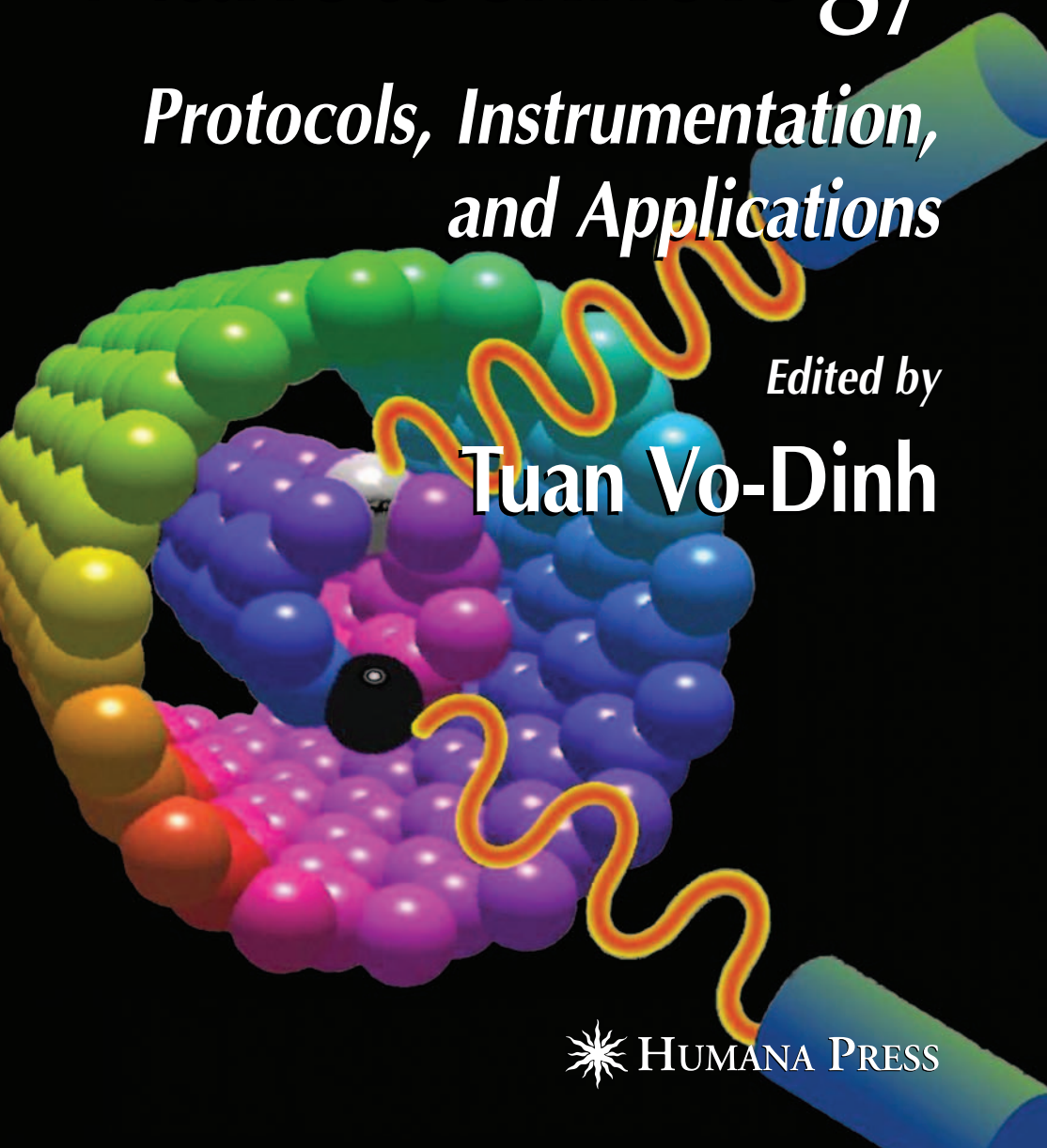


# Protein Nanotechnology

*Protocols, Instrumentation,  
and Applications*

*Edited by*

**Tuan Vo-Dinh**



## Protein Nanotechnology

*The New Frontier in Biosciences*

Tuan Vo-Dinh

### Summary

The combination of nanotechnology and molecular biology has led to a new generation of nanoscale-based devices and methods for probing the cell machinery and elucidating intimate life processes occurring at the molecular level that were heretofore invisible to human inquiry. This chapter provides a brief overview of the field of nanotechnology and its applications to the study, design, and use of protein systems in biology and medicine.

**Key Words:** Nanotechnology; protein; nanosensor; nanoprobe; DNA; RNA; molecular motor.

### 1. Introduction: An Historical Perspective on Nanotechnology

Nanotechnology involves research and development on materials and species at length scales between 1 and 100 nm. The term *nano* is derived from the Greek word meaning “dwarf.” In dimensional scaling, *nano* refers to  $10^{-9}$ , i.e., one billionth of a unit. Thus, a nanometer is  $10^{-9}$  m (0.000000001 m), or about the size of a molecule such as benzene. *Nanotechnology* therefore, refers to the techniques and methods for studying, designing, and fabricating things at the nanometer scale. The initial concept of investigating materials and biological systems at the nanoscale dates to more than 40 yr ago, when Richard Feynman presented a lecture in 1959 at the annual meeting of the American Physical Society at the California Institute of Technology. This lecture, entitled “There’s Plenty of Room at the Bottom” (*1*), is generally considered to be the first look into the world of materials, species, and structures at nanoscale levels.

Nanostructures are similar in size to many biological species such as proteins. These species comprise a wide variety of basic structures such as

From: *Methods in Molecular Biology*, vol. 300:  
*Protein Nanotechnology, Protocols, Instrumentation, and Applications*  
Edited by: T. Vo-Dinh © Humana Press Inc., Totowa, NJ

polymers, carbohydrates (sugars), and lipids; thus, they have a great variety of chemical, physical, and functional properties. This structural variety and the versatility of these biological nanomaterials and systems have important implications for the design, development, and manufacturing of new and artificial assemblies (such as lipid vesicles, dendritic polymers, DNA aggregates, and nano rods or tubes) that are critical to industrial, biotechnological, and medical applications.

To understand complex biological nanosystems at the cellular level, we urgently need to develop a next-generation nanotechnology tool kit. This is technology on the scale of molecules, and it has the potential of developing devices smaller and more efficient than anything currently available. It is believed that the new advances in genetic engineering, genomics, proteomics, medicine, and biotechnology will depend on our mastering nanotechnology in the coming decades. If we can assemble biological systems and devices at the atomic and molecular levels, we will achieve a versatility in design, a precision in construction, and a control in operation heretofore hardly dreamed of. Such a dream was foreseen by Eric K. Drexler in his book *Engines of Creation* (2), in which he envisioned that major processes in molecular technology could be based on protein engineering.

## 2. The Importance of Protein Nanotechnology

The living cell, with its myriad of biological components, may be considered the ultimate nanoscale device. **Figure 1** shows a schematic diagram of the cell with its various components. Some typical sizes of proteins and biological species are given in **Table 1**. Chemistry also deals with atoms and molecules, which are of nanometer sizes. However, nanotechnology differs from chemistry in a very fundamental aspect. Whereas chemistry deals with atoms and molecules at the bulk level (we do not see the molecules in chemical solutions), nanotechnology seeks to actually “manipulate” individual atoms and molecules in very specific ways.

Proteins are major cellular components that play an essential role in maintaining the functioning of the cell. Proteins have a number of functions. They can function as enzymes, which are the driving force for biochemical reactions. Also, they can serve as antibodies that recognize invading elements and allow the immune system to neutralize and eliminate unwanted invaders. Proteins have functions within physiological as well as pathophysiological processes in a cell or organism. Because diseases, therapy, and drugs can alter protein profiles, a determination of protein profiles can provide useful information for understanding disease and designing therapy. Therefore, understanding the structure, metabolism, and function of proteins at the molecular (i.e., nanoscale) level is absolutely critical to our understanding of biological

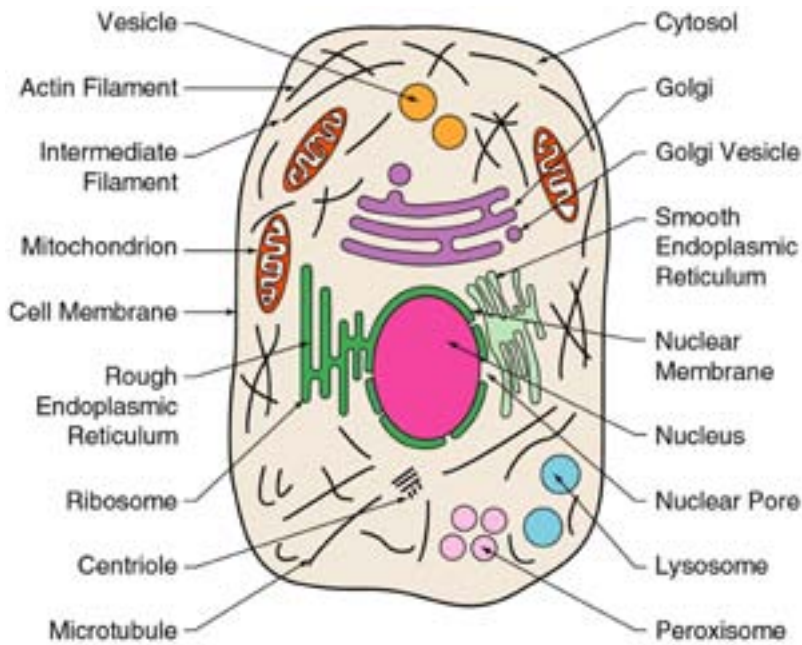


Fig. 1. Schematic diagram of a cell and its components.

**Table 1**  
**Typical Sizes of Proteins and Biological Species**

Biological species	Example	Typical size	Typical mol wt (Daltons)
Small proteins	Chymotrypsin	4-nm sphere	$10^4\text{--}10^5$
Large proteins	Aspartate transcarbamoylase	7-nm sphere	$10^5\text{--}10^7$
Small assemblies	Ribosome	20-nm sphere	$10^5\text{--}10^7$
Large assemblies	Viruses	100-nm sphere	$10^7\text{--}10^{12}$
Nucleic acids	tRNA	10-nm rod	$10^4\text{--}10^5$

processes. This knowledge will contribute to improving our ability to manipulate biological species in molecular manufacturing, enhancing energy production using biofuel-based microbial systems, or detecting the health status of a living organism in order to effectively diagnose and ultimately prevent disease.

Proteins and genes are closely related. Briefly, DNA, the genetic code encrypted in chromosomes, is translated into a corresponding sequence of RNA, which is then read by the ribosome to fabricate a sequence of amino acids. These amino acid chains fold up into a three-dimensional (3D) shape



and become a specific protein, which is designed to perform a particular role in some part of the cell or the body. For example, some proteins are created in an inactive form, then enzymatically cleaved at the site of activity to become a new, active form. We have recently begun to understand the importance of a special type of proteins called chaperonins. These proteins are designed to assist in the folding of other proteins within the cell into their final shape and function. A gene can also undergo different splicings, and posttranslational modifications can result in several active forms of proteins. Thus, knowledge of the sequence information in genes is not sufficient to describe life. It is also critical to determine the function of the corresponding proteins, which are the actual players in the process of life.

### 3. Protein Structure: The Basic Building Blocks

Proteins are long chains of molecules consisting of polymers assembled from a large number of amino acids like beads on a necklace. The sequence of the amino acids in the polymer backbone is the *primary structure* of any given protein. There are 20 normal amino acids. Typical polypeptide chains contain about 100 to 600 amino acid molecules and have a molecular weight of about 15,000 to 70,000. Since amino acids have hydrophilic, hydrophobic, and amphilic groups, in an aqueous environment they tend to fold to form a locally ordered, 3D structure, called the *secondary structure*, that is characterized by a low-energy configuration with the hydrophilic groups outside and the hydrophobic groups inside. In general, simple proteins have a natural  $\alpha$ -helix configuration. Another natural secondary configuration is a  $\beta$ -sheet. These two secondary configurations ( $\alpha$ -helix and  $\beta$ -sheet) are the building blocks that assemble to form the final *tertiary structure*, which is held together by extensive-secondary interactions, such as van der Waals bonding. The tertiary structure is the complete 3D structure of one indivisible protein unit (i.e., one single covalent species). Sometimes, several proteins are bound together to form supramolecular aggregates that make up a *quarternary structure*. The quarternary structure, which is the highest level of structure, is formed by the noncovalent association of independent tertiary structure units.

Knowing the 3D structure of proteins is essential in understanding their function. The sequence (primary structure) provides little information about the function of proteins. To carry out their function, proteins must take on a particular shape, often referred to as an active form, through the folding process. **Figure 2** shows an example of the 3D structure of bovine serum albumin (BSA). Folded proteins, such as egg albumin, can be unfolded by heating. Following heating, the albumin, which has undergone an irreversible folding conformation change, turns white. In this form albumin is said to be denatured. Denatured albumin cannot be reversed into its natural state. However, some

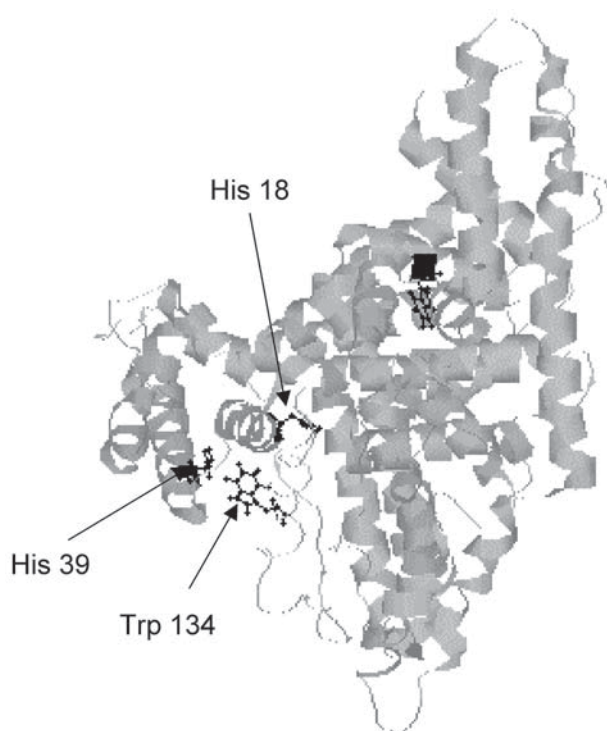


Fig. 2. Three-dimensional structure of BSA.

proteins can be denatured and renatured repeatedly; that is, they can be unfolded and refolded back to their natural configuration. Diseases such as Alzheimer's disease, cystic fibrosis, mad cow disease, an inherited form of emphysema, and even many cancers are believed to result from protein misfolding.

Extensive experimental and theoretical research efforts have been devoted to determine the structure of proteins. By using a combination of computational methods, mass spectroscopy, and nuclear magnetic resonance (NMR) techniques, researchers have identified an optimal set of small molecules for use in synthesizing novel bidentate antidotes or detection agents for clostridial neurotoxins, such as tetanus and botulinus. The crystal structure of the tetanus toxin C fragment (TetC, Protein Data Bank access code 1A8D) is shown with doxorubicin and a peptide computationally docked into sites 1 and 2, respectively, in **Fig. 3**. The structures of sialic acid and lavendustin A are shown about an NMR stack plot showing that lavendustin A binds to TetC (3).

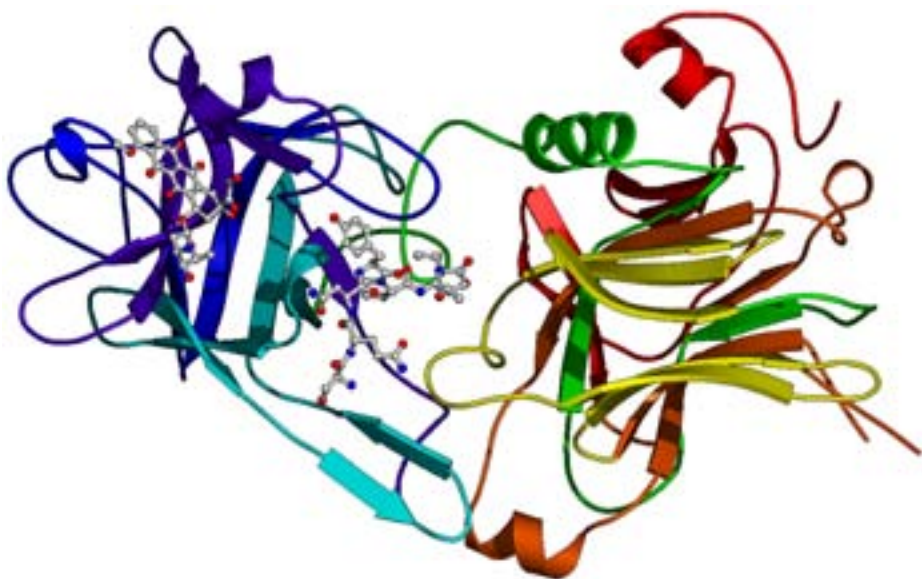


Fig. 3. Crystal structure of TetC. (Adapted from **ref. 3.**)

The goal of understanding the structure and function of proteins as integrated processes in cells, often referred to as “system biology,” presents a formidable challenge, much more difficult than that associated with determination of the human genome. Therefore, proteomics, which involves determination of the structure and function of proteins in cells, could be a research area that presents more challenges than genomics. Proteomics research directions can be categorized as structural and functional. Structural proteomics, or protein expression, measures the number and types of proteins present in normal and diseased cells. This approach is useful in defining the structure of proteins in a cell. However, the role of a protein in a disease is not defined simply by knowledge of its structure. An important function of proteins is in the transmission of signals through intricate protein pathways. Proteins interact with each other and with other organic molecules to form pathways. Functional proteomics involves the identification of protein interactions and signaling pathways within cells and their relationship to disease processes. Elucidating the role that proteins play in signaling pathways allows a better understanding of their function in cellular behavior and permits diagnosis of disease and, ultimately, identification of potential drug targets for preventive treatment. As described in the various chapters of this book, protein nanotechnology holds the promise of providing the critical tools needed to obtain real-time information about the signaling processes in cells.

#### 4. Protein Machines: Nature's Engines of Life

Life is made possible by the action of a series of biological molecular nanomachines in the cell machinery. By evolutionary modification over trillions of generations, living organisms have perfected an armory of molecular machines, structures, and processes. The simplest cells used nanoscale manipulators for building molecule-sized objects. They are now used to build proteins and other molecules atom by atom according to defined instructions encrypted in the DNA. The cellular machinery uses rotating bearings that are found in many forms; for example, some protein systems found in the simplest bacteria are used as clamps that encircle DNA and slide along its length. Human cells contain a rotary motor that is used to generate energy. A wide variety of molecule-selective pumps are used by cells to absorb ions, amino acids, sugars, vitamins, and all of the other nutrients needed for living. Cells also use molecular sensors that can detect the concentration of surrounding molecules and compute the proper functional outcome.

Consider a well-known molecular machine, the ribosome. Ribosomes are biological species that play the role of nanomachines in living cells. Ribosomes build proteins essential to the functioning of the cell. Although the size of a typical ribosome is only  $8000 \text{ nm}^3$ , this nanomachine is capable of manufacturing almost any protein by stringing together amino acids in a precise linear sequence following instructions from a messenger RNA copied from the host DNA. To perform its molecular manufacturing task, the ribosome grasps a specific transfer RNA (tRNA), which, in turn, is chemically bonded by a specific enzyme to a specific amino acid. It has the means to grasp the growing polypeptide and to cause the specific amino acid to react with, and be added to, the end of the polypeptide. In other words, DNA can be considered the biological software of the cellular machinery, ribosomes are large-scale molecular constructors, and enzymes are functional molecular-sized assemblers. These proteins are truly nature's engines of life processes.

Cells use other protein-based nanomachines to separate chromosomes during cell division, to move material, to crawl on surfaces, and to propel themselves in water. For example, during cell division in animal cells, the disassembly of the microtubule (a 25-nm-diameter hollow cylinder) moves replicated DNA to the two emerging daughter cells. The movement of another well-known molecular motor, myosin, along double helical filaments of a protein called actin (approx 10 nm across) produces the contraction of muscle cells during each heartbeat.

Classic and quantum molecular simulation methods have provided an invaluable tool in the development of nanomaterials and in feasibility studies of nanotechnology designs (**Fig. 4**). For example, fundamental classic and quantum simulation studies of model nanobearings and nanomotors composed

Figure not available in electronic version of this product because the copyright owner has either withheld permission or permission could not be obtained.

Fig. 4. Example of nanostructures designed using classic and quantum molecular simulation methods. (Used by permission from Sumpter and Noid, personal communication.)

of concentric carbon nanotubes have shown strong effects of internal mode coupling on key aspects of the performance of the motors and bearings. Over the last several years, Noid and Sumpter have investigated the performance of nanobearings, nanomotors, and fluid flow through nanotubes using fully dynamic (molecular dynamics) simulation (4,5). Various types of molecular bearings and other mechanical devices have recently been proposed in the growing nanotechnology literature. One desired capability to be derived in the later stages of nanotechnology development, and an interesting scientific problem in its own right, is the introduction of controlled motion at the nanometer size scale. In a development closely related to molecular bearings, Noid, Tuzun, and Sumpter have simulated several model graphite nanometer-scale laser-driven motors (**Fig. 5**). The motors consist of two concentric graphite cylinders

Figure not available in electronic version of this product because the copyright owner has either withheld permission or permission could not be obtained.

Fig. 5. Model graphite laser-driven nanomotors designed using simulation methods. The laser-driven motors consist of two concentric graphite cylinders (shaft and sleeve) with one positive and one negative electric charge attached to opposite ends of one of the end rings of the shaft. (Used by permission from Noid et al. [5].)

(shaft and sleeve) with one positive and one negative electric charge attached to opposite ends of one of the end rings of the shaft. Rotational motion of the shaft is induced by applying one or sometimes two oscillating laser fields. The shaft cycles between periods of rotational pendulum-like behavior and unidirectional rotation (motor-like behavior). Motor performance was mapped as a function of size, field strength and frequency, and relative location of the attached positive and negative charges. Drawing on observations of multilaser-enhanced energy absorption in small molecular systems, Noid and Sumpter also mapped motor performance as a function of one- vs two-laser excitation.

## 5. The Nano Toolkit

Recently, nanotechnology has been revolutionizing many important areas in molecular biology, especially in the detection and manipulation of proteins and biological species at the molecular and cellular level. The combination of molecular biology and nanotechnology opens the possibility of detecting and manipulating atoms and molecules using nanodevices, with the potential for a wide variety of medical uses at the cellular level.



Today, the amount of research in biomedical science and engineering at the molecular level is growing exponentially because of the availability of new investigative nanotools based on protein nanotechnology. These new analytical tools are capable of probing the nanometer world and will make it possible to characterize the chemical and mechanical properties of cells, discover novel phenomena and processes, and provide science with a wide range of tools, including materials, devices, and systems with unique characteristics. The marriage of electronics, biomaterials, and molecular biology and nanotechnology is expected to revolutionize many areas of biology and medicine in the 21st century.

The combination of nanotechnology and molecular biology has already led to a new generation of devices for probing the cell machinery and elucidating molecular-level life processes heretofore invisible to human inquiry. Tracking biochemical processes within intracellular environments can now be performed *in vivo* with the use of fluorescent molecular nanoprobe and nanosensors (6). With powerful microscopic tools using near-field optics, scientists are now able to explore the biochemical processes and nanoscale structures of living cells at unprecedented resolutions. It is now possible to develop nanocarriers for targeted delivery of drugs that have their shells conjugated with antibodies for targeting antigens and fluorescent chromophores for *in vivo* tracking.

The development of metallic nanoprobe that can produce a surface-enhancement effect for ultrasensitive biochemical analysis is another area of active nanoscale research. *Plasmonics* refers to the research area dealing with enhanced electromagnetic properties of metallic nanostructures. The term is derived from *plasmons*, which are the quanta associated with longitudinal waves propagating in matter through the collective motion of large numbers of electrons. Incident light irradiating these surfaces excites conduction electrons in the metal and induces excitation of surface plasmons, which, in turn, leads to enormous electromagnetic enhancement for ultrasensitive detection of spectral signatures through surface-enhanced Raman scattering (SERS) (7) and surface-enhanced fluorescence. **Figure 6** shows a scanning electron micrograph of SERS-active nanospheres (300-nm diameter coated with a 100-nm layer of silver). Nanoparticle-based SERS technology has enabled sensitive detection of a variety of compounds of medical interest. SERS nanoprobe technology has also been incorporated into the design of several fiberoptic probes for diagnostics (8). The development of a SERS gene probe technology based on solid surface-based technology has also been reported. One study demonstrated the selective detection of human immunodeficiency virus DNA and a cancer gene (9).

Optical nanosensors, which have dimensions on the nanometer size scale, have been developed to probe individual chemical species in specific locations

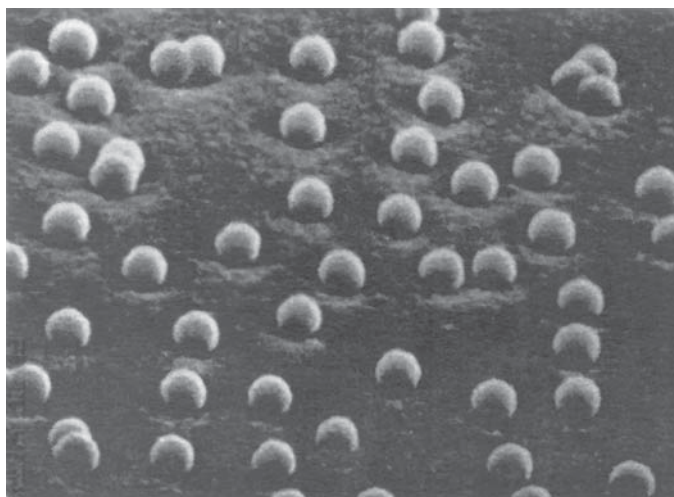


Fig. 6. Nanoprobes consisting of nanospheres coated with nanoshells of silver.

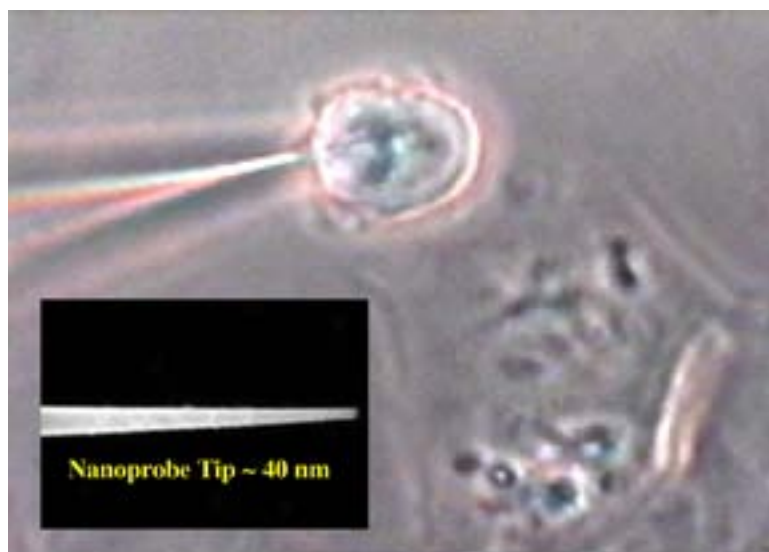


Fig. 7. Fiberoptic nanosensor for single-cell analysis. (Adapted from **ref. 10.**)

throughout a living cell (*10*). **Figure 7** is a photograph of a fiberoptic nanoprobe with an enzyme substrate designed to detect caspase 9, a protein expressed during apoptosis in a single cell (*11*). An important advantage of the optical sensing modality is its capability to measure biological parameters in a

noninvasive or minimally invasive manner owing to the extremely small size of the nanoprobe. Following measurements using the nanobiosensor, cells have been shown to survive and undergo mitosis (12). Biomedical nanosensors, both in vivo and ex vivo, will play an important role in the future of medicine. The capability to detect important biological molecules at ultratrace concentrations in vivo is central to many advanced diagnostic techniques. Early detection of diseases will be made possible by tracking down trace amounts of biomarkers in tissue.

The development of nanotechnology-based devices and techniques has allowed measurements of fundamental parameters of proteins and biological species at the molecular level. With “optical tweezer” techniques, small particles may be trapped by radiation pressure in the focal volume of a high-intensity, focused beam of light. This technique, also called “optical trapping,” may be used to move small cells or subcellular organelles around at will by the use of a guided, focused beam (13). Ingenious optical-trapping systems have also been used to measure the force exerted by individual motor proteins (14). A bead coated with an immobilized, caged bioactive probe was inserted into tissue or even a cell and moved to a strategic location by an optical-trapping system. The cage could then be photolyzed by multiphoton uncaging in order to release and activate the bioactive probe. Optical tweezers can also be used to determine the precise mechanical properties of single molecules of collagen, an important tissue component and a critical factor in diagnosing cancer and the aging process (15). The optical tweezer method uses the momentum of focused laser beams to hold and stretch single collagen molecules bound to polystyrene beads. The collagen molecules are stretched through the beads using the optical laser tweezer system, and the deformation of the bound collagen molecules is measured as the relative displacement of the microbeads, which are examined by optical microscopy.

The study of biological applications of nanotechnology will be important to the future of biological research and medical science. Medical applications of nanomaterials will revolutionize health care in much the same way that materials science changed medicine 30 yr ago with the introduction of synthetic heart valves, nylon arteries, and artificial joints. The protein nanotechnologies discussed previously are just some examples of a new generation of nanotools that have the potential to detect, identify, and manipulate single proteins in vivo and drastically change our fundamental understanding of the life process itself. They could ultimately lead to the development of new modalities of early diagnostics and medical treatment and prevention beyond the cellular level to that of individual proteins, the building blocks of the life process.

## References

1. Feynman, R. (1960) There's plenty of room at the bottom: an invitation to enter a new field of physics. *Eng. Sci.* February Issue.
2. Drexler, E. K. (1986) *Engines of Creation*, Anchor Books, New York.
3. Cosman, M., Lightstone, F. C., Krishnan, V. V., Zeller, L., Prieto, M. C., Roe, D. C., and Balhorn, R. (2002) Screening mixtures of small molecules for binding to multiple sites on the surface of tetanus toxin C fragment by bioaffinity NMR. *Chem. Res. Toxicol.* **15**, 1218–1228.
4. Tuzun, R. E., Noid, D. W., and Sumpter, B. G. (1995) The dynamics of molecular bearings. *Nanotechnology* **6**, 64–74.
5. Noid, D. W., Tuzun, R. E., and Sumpter, B. G. (1997) On the importance of quantum mechanics for nanotechnology. *Nanotechnology* **8**, 119–125.
6. Vo-Dinh, T. (ed.) (2003) *Biomedical Photonics Handbook*, CRC Press, Boca Raton, FL.
7. Vo-Dinh, T. (1998) Surface-enhanced Raman spectroscopy using metallic nanostructures. *Trends Anal. Chem.* **17**, 557–582.
8. Isola, N., Stokes, D. L., and Vo-Dinh, T. (1998) Surface-enhanced Raman gene probes for HIV detection. *Anal. Chem.* **70**, 1352–1356.
9. Vo-Dinh, T., Stokes, D. L., Griffin, G. D., Volkan, M., Kim, U. J., and Simon, M. I. (1999) Surface-enhanced Raman scattering (SERS) method and instrumentation for genomics and biomedical analysis. *J. Raman Spectrosc.* **30**, 785–793.
10. Vo-Dinh, T., Alarie, J. P., Cullum, B., and Griffin, G. D. (2000) Antibody-based nanoprobe for measurements in a single cell. *Nat. Biotechnol.* **18**, 764–767.
11. Vo-Dinh, T. (2003) Nanosensors: probing the sanctuary of individual living cells. *J. Cell. Biochem.* **39(Suppl.)**, 154–161.
12. Vo-Dinh, T., Cullum, B. M., and Stokes, D. L. (2001) Nanosensors and biochips: frontiers in biomolecular diagnostics. *Sens. Actuators B Chem.* **74(1–3)**, 2–11.
13. Askin, A., Dziedzic, J. M., and Yamane, T. (1987) Optical trapping and manipulation of single cells using infrared laser beam. *Nature* **330**, 769–771.
14. Kojima, H., Muto, E., Higuchi, H., and Yanagido, T. (1997) Mechanics of single kinesin molecules measured by optical trapping nanometry. *Biophys. J.* **73(4)**, 2012–2022.
15. Luo, Z. P., Bolander, M. E., and An, K. N. (1997) A method for determination of stiffness of collagen molecules. *Biochem. Biophys. Res. Commun.* **232(1)**, 251–254.



## Kinetics and Mechanisms of Protein Crystallization at the Molecular Level

Peter G. Vekilov

### Summary

This chapter focuses on the processes by which a protein molecule in a supersaturated solution joins a protein crystal. The pair of proteins ferritin/apoferritin is used as an example. The most commonly used technique in such investigations has been atomic force microscopy. I discuss the modifications and tests of the atomic force microscope necessary to obtain real-time, *in situ* molecular resolution imaging. Then, I review tests that establish a quantitative correspondence between the continuous models of crystal growth and the discrete nature of the processes at the molecular level. I address the issue of whether the incorporation of a molecule from a solution into a growth site on the crystal surface is limited by the slow rate of decay of an Eyring-type transition state. The conclusion is that, on the contrary, a scenario, envisioned by Smoluchowski and Debye, is followed in which the kinetics is only limited by the rate diffusion over the free-energy barrier of interaction between two molecules, or an incoming molecule and a surface. Review of the data for many other protein and nonprotein systems suggests that this conclusion is valid not only for the crystallization of ferritin/apoferritin, but also for many other protein and small-molecule crystallization systems. Finally, I review results establishing that the pathway that a molecule from a solution takes on its way to an incorporation site on the crystal surface is indirect: it includes adsorption on the surface and two-dimensional diffusion toward the incorporation site. These results will likely contribute to the understanding at the molecular level not only of the processes of crystallization of proteins and small molecules, but also of the deposition of layers of proteins and other soft materials on substrates, and of other processes of self-assembly in solution.

**Key Words:** Crystallization; solution thermodynamics; atomic force microscopy; diffusion-limited kinetics; transition states; activation energy; growth mechanisms; surface diffusion; direct incorporation.

From: *Methods in Molecular Biology*, vol. 300:  
*Protein Nanotechnology, Protocols, Instrumentation, and Applications*  
Edited by: T. Vo-Dinh © Humana Press Inc., Totowa, NJ



## 1. Introduction

Crystallization of proteins, as any other phase transition, occurs through a combination of processes at molecular, mesoscopic, and macroscopic length scales. During phase transitions in solution, molecular-level phenomena include the interactions between the molecules that alter the free energy landscape to cause the formation of the new phase and determine the driving force for the phase transformation; attachment of molecules to the new phase during growth; formation of sites suitable for molecular attachment; and generation of defects. On the mesoscopic length scale, one could consider the nucleation of droplets, clusters, or crystallites of the new phase; generation of new layers of a crystal controlled by capillarity; and interactions between growth steps as they propagate along the crystal's surfaces. Macroscopic length scales govern the fluxes of energy and mass through the interface (i.e., the transport of building blocks to the growing phase and the dissipation of heat away from it), as well as the balance and distribution of stress and strain in a solid and the transition from elastic to plastic deformations.

In this chapter, I focus on the molecular-level processes during the growth of crystals of the pair of proteins ferritin and apoferritin. Ferritin is the main nonheme iron storage protein in cytosol (1–3). The protein shell consists of 24 subunits, arranged in pairs along the 12 facets of a rhombododecahedron (4,5). Ferritins have been extensively studied as an example of biological mineralization occurring in vivo (6,7). The iron-containing core of ferritin can be replaced with other organic, inorganic, and bioorganic compounds for potential applications in the areas of nanoassembly, drug delivery, biomineralization, and so on (8,9). Apoferritin is the protein shell from which the ferrite core has been removed by dissolution into an acidic solution. The structures of the proteins from various species are known down to 1.90 Å resolution (5).

In the presence of  $\text{Cd}^{2+}$ , ferritin and apoferritin crystallize in the cubic F432 group (3,5). Contrary to typical protein crystallization cases, in which the electrolyte serves to screen the repulsion between the similarly charged protein molecules, in the case of apoferritin,  $\text{Cd}^{2+}$  is involved in specific bonds between the molecules (5). This specificity makes the case of apoferritin crystallization a relevant first-approximation model of other self-assembling systems, such as viri, protein complexes, and nanoparticles.

The crystals, such as the one in **Fig. 1**, are typically faceted by octahedral (111) faces pierced by the threefold axis belonging to the symmetry group. The highly symmetric shape of the ferritin and apoferritin molecules makes the approximation of isotropic molecular shape realistic. In addition, the symmetry of the environment of a molecule in a crystal makes quantitative insight easier to obtain and comprehend. Because of these two factors, ferritin and apoferritin crystallization is a particularly appealing system for in-depth investigations of the thermodynamics and kinetics of phase transitions.

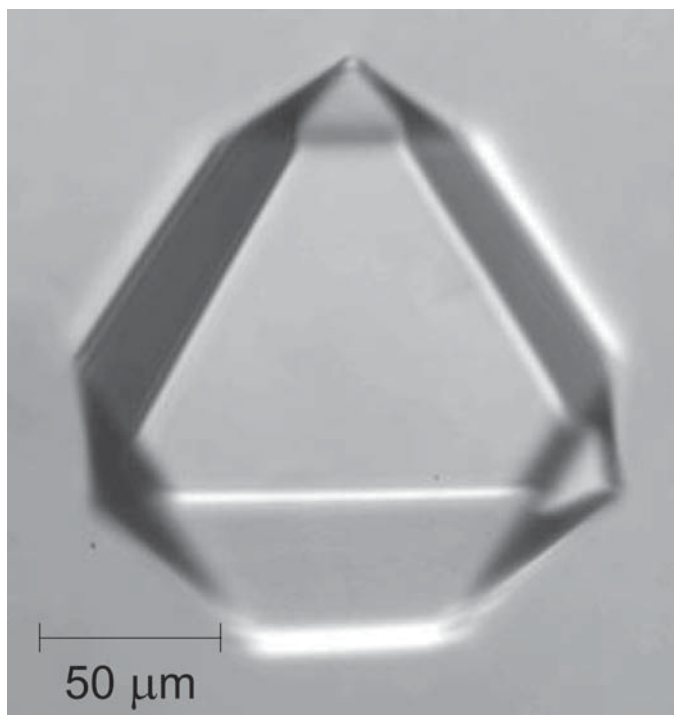


Fig. 1. Typical octahedral crystal of apoferritin, resting on cell bottom with a (111) face facing upward. Ferritin crystals appear identical except for the ruby red color.

In this chapter, I first define the methods used to characterize the growth kinetics on the molecular length scale. Then, I discuss tests of the correspondence between discrete approaches to the kinetics of attachment, in which the growth rate and other spatial and temporal characteristics of the growth process are represented as a statistical averages of events involving individual atoms or molecules, and continuous approaches, in which fluxes of matter toward the growth interface are evaluated. Finally, I show that the kinetics of incorporation of the molecules into growth sites on the surface of a crystal are not determined by decay of a high-energy transition state but are only limited by the diffusion of the incoming molecule over a barrier owing to the hydration shells around incoming molecules.

## 2. Methods

### 2.1. Atomic Force Microscopy

In our laboratory, we used Nanoscope IIIa or Nanoscope IV Multimode atomic force microscopes from Digital Instruments, equipped with a 120- $\mu\text{m}$  (“J”)

scanner and a Tapping Mode fluid cell. The preparation of crystals and solutions and the cell loading are very similar to those used in numerous other investigations and are discussed in detail in **ref. 10**.

Temperature in the laboratory was stabilized to approx  $22 \pm 0.5^\circ\text{C}$ . To control the temperature in the crystallization solution, we mounted the sample onto a Peltier-cooled disk firmly attached to the scanner. This allowed imaging in the range of 28 to  $45^\circ\text{C}$ ; to access 25 and  $20^\circ\text{C}$ , the room temperature was set at 18 to  $20^\circ\text{C}$ . Temperature in the fluid cell was monitored with a thermocouple imbedded into the metal disk under the solution droplet and was found to be steady within  $0.1^\circ\text{C}$ .

All images were collected *in situ* during growth of the crystals using the less intrusive tapping-imaging mode (**11,12**). This allows visualization of adsorbed protein and impurity species (tip impact in the contact-imaging mode often prevents such imaging).

We used standard SiN tips and tapping drive frequency was adjusted in the range of 25 to 31 kHz to the resonance value for the specific tip used. Other scanning parameters were adjusted such that continuous imaging affected neither the surface structure nor the process dynamics. For verification, we varied the scan sizes and the time elapsed between image collections and saw that neither the spatial nor the temporal characteristics of the processes changed.

## 2.2. Atomic Force Microscopy Data

We employed three types of atomic force microscopy (AFM) data collection. The first type consisted of images of 200 nm to 1 mm, such as the one in **Fig. 2**, on which the protein molecules, 13 nm in size were clearly detectable. Calibration of the microscope was verified by determining the spacing of molecules along a densely, packed direction in the lattice and the thickness of the top crystalline layer. As **Fig. 2** reveals, the respective numbers for one of the systems, used for the studies summarized here, the protein apoferritin, are 13.1 and 10.5 Å. These are in good agreement with the evaluations from the X-ray structure of the crystal. Using the crystal lattice parameter of  $a = 18.4$  nm for the crystallographic group F432 (**4,5**), the intermolecular spacing is  $(1/2)(2a^2)^{1/2} = 13.0$  nm, and the layer thickness is  $(1/3)(3a^2)^{1/2} = 10.6$  nm.

To evaluate the maximum resolution of molecular-scale imaging attainable with ferritin/apoferritin *in situ*, during crystallization, we scanned a  $200 \times 200$  nm square on the surface of a ferritin crystal (*see Fig. 3A*). The two-dimensional Fourier transform of the image in **Fig. 3B** has the expected hexagonal symmetry, with the distance between the peaks in the first hexagon and the center of the plot corresponding to resolution equal to the molecular size of 13 nm. The maximum resolution, determined from the location of the most distant

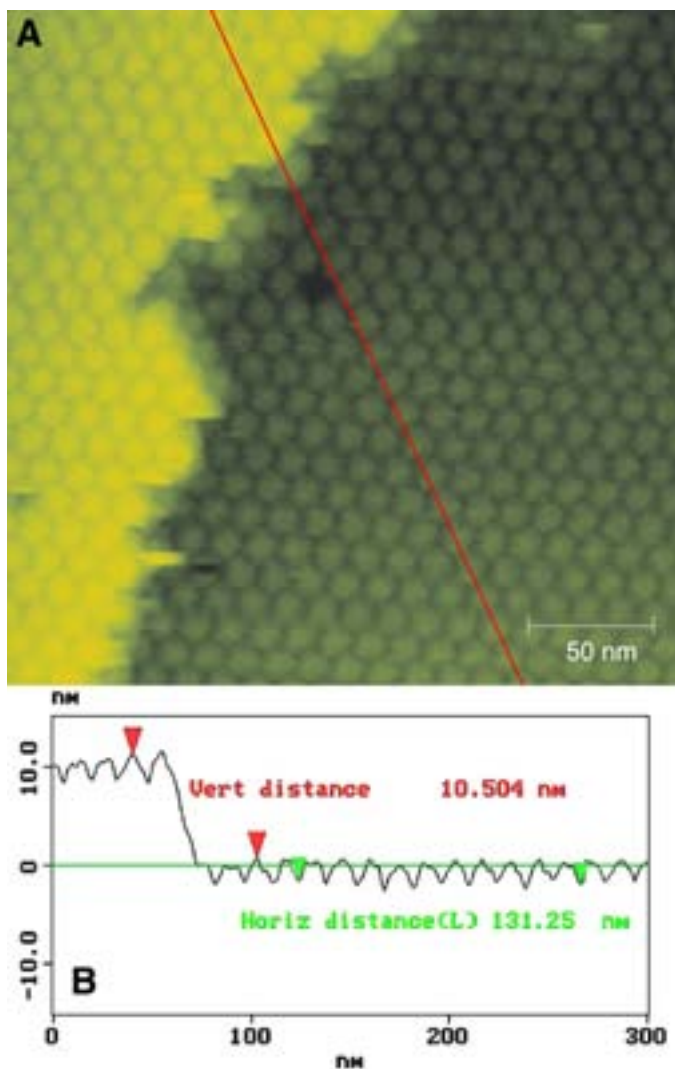


Fig. 2. Accuracy of AFM imaging. (A) View of a (111) apoferritin crystal face; (B) height profile along line in (A) allowing determination of layer thickness and molecular spacing. (From **ref. 10.**)

peak, is 1.6 nm. This resolution allows us to distinguish some of the submolecular-level details of the molecules on the crystal surface in **Fig. 3C**. Comparison with the structure of the molecules coming from an X-ray determination in **Fig. 3D (5)** shows that the triangular formation in **Fig. 3C** likely corresponds to bundles of  $\alpha$ -helices.

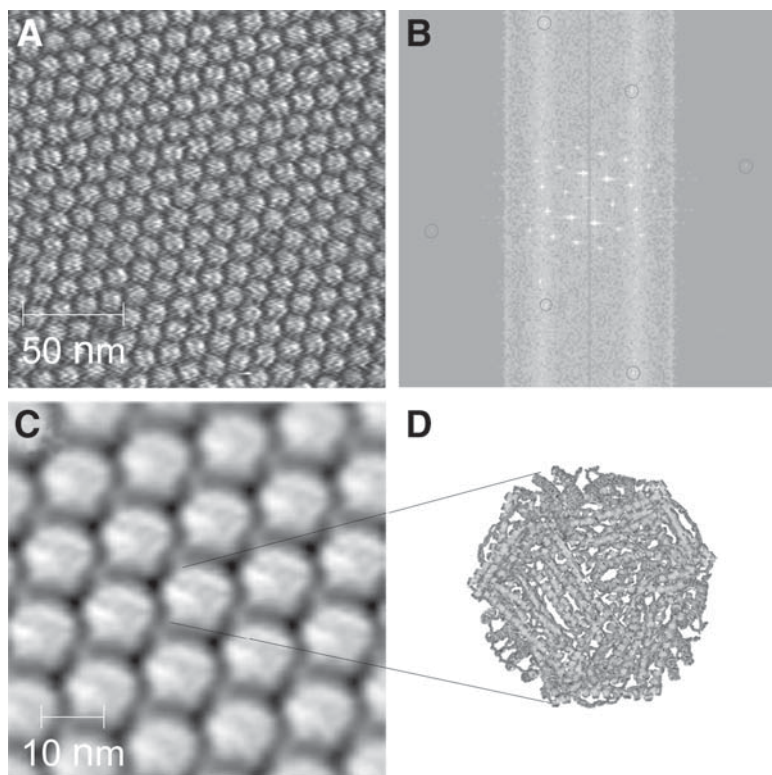


Fig. 3. Resolution of AFM imaging. **(A)** Real-space high-resolution image of a (111) apoferritin crystal face. (From **ref. 10**.) **(B)** Fourier transform of A: circles highlight high-resolution peaks; eighth-order peaks at the top and bottom of the image correspond to a resolution of approx 1.6 nm. (From **ref. 10**.) **(C)** Real-space image in which each molecule is replaced by average of all molecules in frame; processed with SEMPER Software package (N. Braun, S. Weinkauff, personal communication). **(D)** Ribbon presentation of X-ray structure of apoferritin molecule viewed along (111) direction. Images of molecules in C appear to have similar triangular features.

The second type of AFM data consisted of images on the mesoscopic length scales from several tens of nanometers to several micrometers, as in many previous AFM studies of crystallization from solution (**13–24**). These images, similar to the one in **Fig. 4**, with a view-field width between 2 and 40  $\mu\text{m}$ , allow characterization of growth steps and step patterns.

For the third type of AFM data, we employed scans with a disabled y-axis (**25,26**), as in previous scanning tunneling microscopy (STM) work on metals and semiconductors in ultrahigh vacuum (**27–30**). The AFM tip is drawn over a single line of the crystal surface. In the collected pseudoimages, the vertical

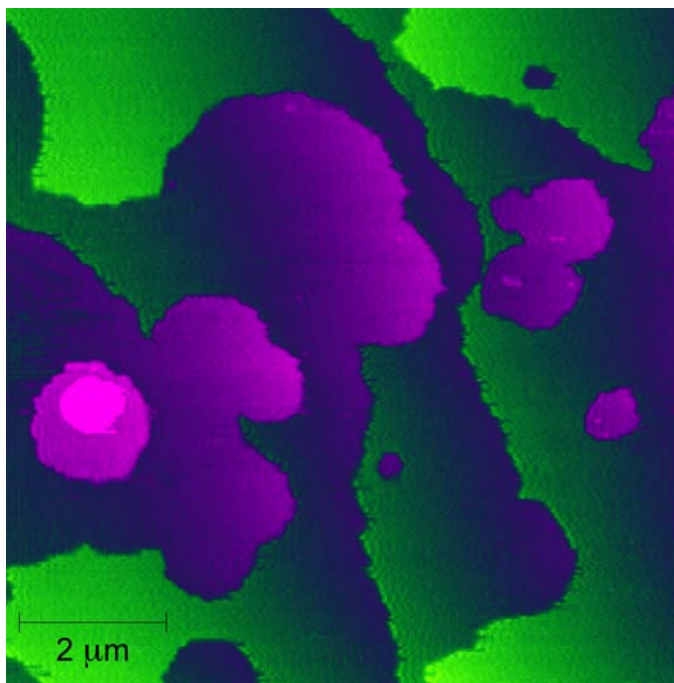


Fig. 4. AFM images of surface of growing apoferritin crystals taken near center of respective facet. Facet size is approx 90  $\mu\text{m}$ , ensuring near-uniform supersaturation over the facet. New crystal layers are generated at random locations by surface nucleation and spread to merge with other islands and cover the whole facet.

axis represents time. The technique allows monitoring of processes with characteristic times of fractions of a second.

If the scan widths were 600 nm and less, the displacement of a single site on the step could be monitored with molecular resolution; that is, we could trace the attachment and detachment of single molecules to and from steps (*10,25,31*). Data collection lasted typically 2 to 3 min. Immediately after such scans, area scans included the line along which the tip was drawn. In about 80% of cases, these tests revealed that the tip impacted over the same location had delayed the growth. These data were discarded, and only data sets that did not show tip impact are discussed herein.

### **2.3. Determination of Step Velocities**

During growth of crystals by the generation and spreading of layers, the rate of growth of the newly formed layers, often called step velocity, is the main kinetic variable, and its link to the driving force determines the main kinetic



parameter, the step kinetic coefficient. In the studies discussed here, we employed three methods of step velocity determination.

As a first method, we used sequences of molecular resolution *in situ* AFM images of the advancing steps, as in **Fig. 2**. The step velocities were determined as the ratio  $Na/\Delta t$ , in which  $N$  is the number of molecular sizes  $a$  that the step advances for the time between two sequential images  $\Delta t$ . For each concentration of ferritin or apoferritin, approx 20 determinations of  $v$  were done and averaged (32). This method is applicable to step velocities  $<5 \text{ nm s}^{-1}$ , at which a step would advance by several molecular sizes for the time required for image collection, approx 1 min (10,25).

For step velocity data at higher driving forces, we disabled the slow scanning axis of the AFM (25). This allowed us to monitor for times of 60 to 90 min with a frequency of 2 to 4  $\text{s}^{-1}$  the propagation of 15 to 30 steps within 10- $\mu\text{m}$  segments of a growing crystal surface (26).

To ensure the veracity of the kinetics data, we crosschecked the results of the AFM determinations with interferometry. This method is applicable to step velocities as fast as 100 nm/s. We extracted averaged values of the step velocities from time traces of this variable recorded with a frequency of 1  $\text{s}^{-1}$  at chosen points on the growing crystal surface using laser interferometry. Each point represents the average of approx 1000 measurements (33,34); the data scatter intervals were evaluated as 90% confidence interval for this average (32). Complete details about this method are provided in refs. 34–36.

### 3. Characterization of Test System

#### 3.1. Molecular Mass, Size, and Intermolecular Interactions

The molecular mass of apoferritin has been determined by many techniques to be  $M_w = 450,000 \text{ g/mol}$  (2,3), with the mass of a molecule  $m = 7.47 \times 10^{-19} \text{ g}$ . However, the average  $M_w$  of ferritin varies between 550,000 and 950,000 g/mol, depending on the size of the ferrite core (2,3). To determine the  $M_w$  of ferritin in the samples used here, we performed static light scattering (37) in 0.05  $M$   $\text{NaOOCCH}_3$  solutions. The molecular masses  $M_w$  and the second osmotic virial coefficients  $A_2$  in dimensional form were determined from the Debye plots,  $(KC/R_0) = [(1/M_w) + 2A_2C]$ , in **Fig. 5**, in which  $R_0$  is the Raleigh ratio of the scattered to the incident light intensity;  $K$  is a system constant,  $K = (1/N_A) (2\pi n_0/\lambda^2)^2 (dn/dC)^2$ ;  $n_0 = 1.3320$  is the refractive index of the solvent at the wavelength of the laser beam  $\lambda = 0.6328 \text{ mm}$  (38,39); and  $dn/dC$  is the  $n$ -increment with the protein concentration  $C$ , determined for each protein at  $\lambda = 0.628 \text{ mm}$  by a differential refractometer—for ferritin  $dn/dC = 0.290 \text{ cm}^3/\text{g}$ , and for apoferritin,  $dn/dC = 0.159 \text{ cm}^3/\text{g}$ .

The Debye plots in **Fig. 5** show that for ferritin,  $M_w = 780,000 \text{ g/mol}$ ,  $m = 1.30 \times 10^{-18} \text{ g}$ , and, as expected, for apoferritin,  $M_w = 450,000 \text{ g/mol}$ .

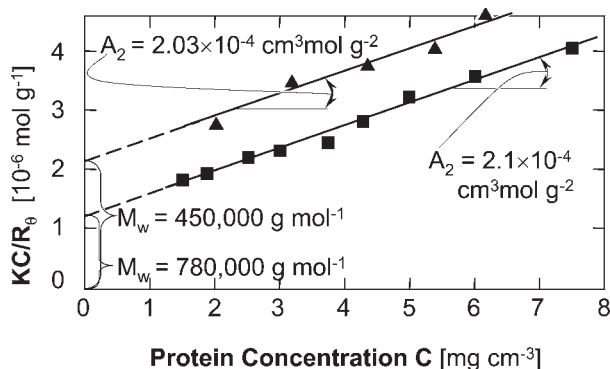


Fig. 5. Static light-scattering characterization of ferritin (■) and apoferritin (▲) molecules in 0.05 *M* NaOOCCH<sub>3</sub> solutions. The Debye plots are  $(KC/R_\theta) = [(1/M_w) + 2A_2C]$  ( $R_\theta$  is the Raleigh ratio of the scattered to the incident light intensity,  $K$  is a system constant, and  $C$  is protein concentration in mg/mL). The molecular masses,  $M_w$ , and the second osmotic virial coefficients in the dimensional form,  $A_2$ , of the two proteins are shown in the plot. The repulsion between the protein molecules (37,82) ensures nonaggregating sample of well-separated monomers. (From ref. 40.)

**Figure 5** also shows that values of the second osmotic virial coefficients,  $A_2$ , for the two proteins are similar. This is not surprising since  $A_2$  characterizes the pair interactions between the solute molecules, determined by the identical surfaces of the molecules.

As expected, the size distributions of the scatterers in solutions of the two proteins resulting from a dynamic light-scattering determination (37) are narrow, and the two proteins have identical diameters of 13 nm (40). This is equal to their identical crystallographic diameters (2–4). Since these sizes are calculated from the set of experimentally determined diffusivities using the Einstein-Stokes law of Brownian motion, the equality to the crystallographic data indicates that the diffusion of both molecules obeys this law (41).

### 3.2. Solubility and Driving Force for Crystallization

The crystallization driving force is written as

$$\{\exp[-(\mu_c - \mu_s)/k_B T] - 1\} \cong (C/C_e - 1) = (n/n_e - 1) \quad (1)$$

in which

$$\mu_s = \mu_0 + k_B T \ln(\gamma C) \text{ and } \mu_c = \mu_0 + k_B T \ln(\gamma_e C_e) \quad (2)$$

In these expressions, subscripts *c* and *s* denote crystal and solute, respectively; *C* and *n* are, respectively, the protein mass and molecular concentrations,  $n = C/m$ ; for determinations of the molecular masses *m* of ferritin and apoferritin,

see **Subheading 3.1.**; and the subscript  $e$  indicates their values at equilibrium with the crystal.

To determine the solubility of ferritin and apoferritin at 27°C, we monitored trains of growth steps and gradually decreased the apoferritin concentration in the solution. We found that at a certain  $C$ , the propagation of the steps stopped, and when the concentration was lowered below this value, the step movement was backward, and the crystal was dissolving. The concentration of equilibrium between crystal and solution  $C_e = 35 \pm 5$  mg/mL for ferritin, and  $C_e = 23 \pm 4$  mg/mL for apoferritin.

Characterization using static light scattering of the solution nonideality in crystallizing solution containing  $\text{Cd}^{2+}$  in addition to the  $\text{NaOOCCH}_3$  (**10**) revealed that the activity coefficients  $\gamma$  were 0.996 in a 100  $\mu\text{g/mL}$  solution of ferritin, and 0.998 in an apoferritin solution of the same concentration, and correspondingly closer to unity at a lower concentration of the proteins.

### 3.3. Statistical Thermodynamics Arguments of Independence of Solubility on Molecular Mass

The values for  $n_e$ , determined as discussed in **Subheading 3.2.** and in **refs. 10,25** for ferritin and apoferritin are, respectively,  $(2.7 \pm 0.5) \times 10^{13} \text{ cm}^{-3}$  and  $(3.0 \pm 0.5) \times 10^{13} \text{ cm}^{-3}$ . They are equal within the error limits, suggesting that the solubilities of these proteins do not depend on their molecular mass. Next, I provide statistical-mechanical arguments that indicate that this may be the case for protein molecules with near-spherical symmetry.

To rationalize the apparently equal solubility of ferritin and apoferritin, we consider the equilibrium between the solution and a crystal. This is equivalent to equilibrium between the states of a molecule in a kink on the crystal surface and in the solution (**42–44**). At constant temperature and pressure, the activity of a molecule in the crystal does not depend on the concentration of the solute and is equal to the activity of the standard crystal state (**45,46**). Then, the equilibrium constant  $K_{\text{cryst}}$  can be written as

$$K_{\text{cryst}} = (\gamma_e C_e)^{-1} \cong C_e^{-1} \quad (3)$$

in which  $g_e$  is the protein activity coefficient at a protein concentration equal to the solubility, and  $C_e$  is the solubility. The activity coefficient depends on the protein concentration and on the intermolecular interactions. Hence, we expect equal  $\gamma$ s in solutions of ferritin and apoferritin of equal concentration. As shown in **Subheading 3.2.**, determinations of  $\gamma$  for apoferritin solutions of concentrations up to 20-fold higher than the solubility have yielded  $\gamma \cong 1$  (**10**). We expect the same to be true for ferritin, and this is the basis of the second equality in **Eq. 13** above for these two proteins.

From the point of view of statistical thermodynamics, the equilibrium constant for crystallization  $K_{cryst}$  can be written as (47)

$$K_{cryst} = q_0 \exp(\mu_0/k_B T) \quad (4)$$

in which  $q_0$  is the partition function of a molecule in a kink (which is only a function of temperature and pressure), and  $\mu_0$  is the standard chemical potential of a molecule in the solution.

To evaluate  $q_0$  and  $\mu_0$ , we assume that the internal molecular vibrations in the solution are the same as in the crystal and are decoupled from the other degrees of freedom. This allows us to neglect the internal vibrational partition function for both states. Furthermore, we limit ourselves to only translational contributions to the solute partition function, neglecting the rotational contributions, and those stemming from the intermolecular interactions. This limits the validity of the considerations below to molecules similar to the ferritin-apoferritin pair: with symmetry close to spherical, and that only exhibit very weak intermolecular interactions and activity coefficients close to 1.

We do not take into account the contribution of the release or binding of the solvent molecules to the free-energy changes in the phase transition. Although arguments presented in **Subheading 5.2.** indicate that these contributions may be significant (10), we expect the contributions of the solvent effects to be identical for ferritin and apoferritin. This justifies neglecting them while aiming at comparisons between the two proteins. We also neglect the rotational vibrations in the crystal.

With these assumptions, we can use the expressions for the partition functions from **ref. 47**, and write

$$q_0 = q_x q_y q_z \cong (q_{vib})^3 \quad (5)$$

in which  $q_i$  ( $i = x, y, z$ ) are the partition functions for translational vibrations along the respective coordinate. In turn, with  $h$  the Planck constant,  $n$  the vibration frequency, and  $U$  the mean-force potential of a molecule in a kink,

$$q_{vib} = \frac{\exp\left(-\frac{h\nu}{k_B T}\right)}{1 - \exp\left(-\frac{h\nu}{k_B T}\right)} \approx \frac{k_B T}{h\nu}, \quad \nu = \frac{1}{2\pi} \sqrt{\frac{f}{m}}, \quad \text{where } f = \left(\frac{\partial^2 U}{\partial i^2}\right)_{\min} \quad (6)$$

Combining, we obtain for  $q_{vib}$  and  $q_0$

$$q_{vib} = \frac{2\pi k_B T}{h} \sqrt{\frac{m}{f}}, \quad q_0 = \left(\frac{2\pi k_B T}{h}\right)^3 \left(\frac{m}{f}\right)^{3/2} \quad (7)$$

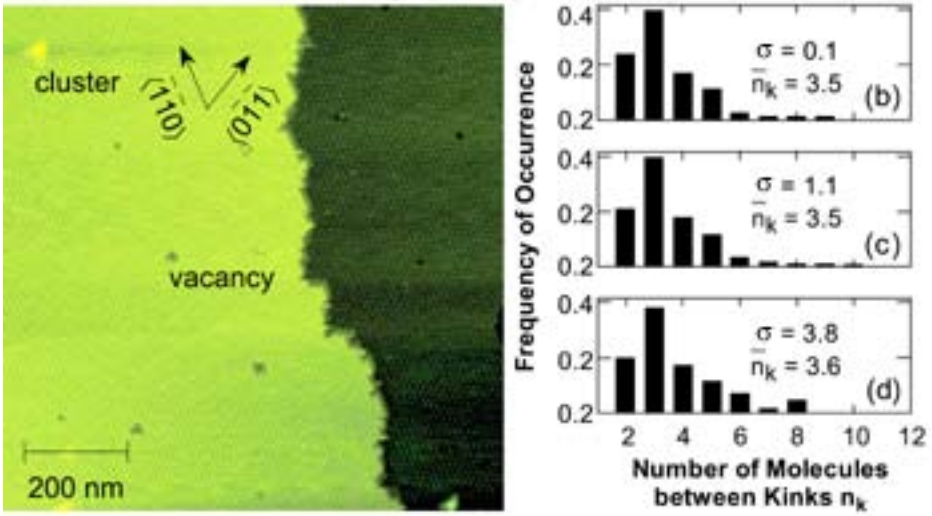


Fig. 6. (A) Molecular structure of growth step on apoferritin crystal at protein concentration of 70 mg/mL, corresponding to supersaturation  $\sigma = \Delta\mu/k_B T = 1.1$ ,  $(C/C_e - 1) = 2.04$ . Dark area: lower layer; light area: advancing upper layer. Adsorbed impurity clusters and surface vacancies are indicated. (B–D) The distribution of the number of molecules between kinks on steps located  $>0.5 \mu\text{m}$  apart, obtained from images similar to **Fig. 1**, at the three supersaturations  $s$  indicated in the plots is shown. The mean values of the distributions for each case are also shown. The protein concentrations corresponding to these  $\sigma$ 's are (B) 25  $\mu\text{g/mL}$ , (C) 70  $\mu\text{g/mL}$ , and (D) 1  $\mu\text{g/mL}$ . (From **ref. 10**.)

For  $m_0$ , we have (47)

$$\frac{\mu_0}{k_B T} = -\ln \left[ \left( \frac{2\pi m k_B T}{h^2} \right)^{3/2} k_B T \right] \quad \text{and} \quad \exp \left( \frac{\mu_0}{k_B T} \right) = \frac{1}{k_B T} \left( \frac{h^2}{2\pi m k_B T} \right)^{3/2} \quad (8)$$

We see that  $q_0$  contains  $m^{3/2}$ , while  $\exp(\mu_0/k_B T)$  is proportional to  $m^{-3/2}$ ; that is, their product  $K_{\text{cryst}}$ , and  $C_e$  do not depend on the mass of the molecule.

## 4. Growth Sites

### 4.1. Kinks and Kink Density

Under all conditions used in the experiments reported here, the crystals of ferritin and apoferritin as seen in the optical microscope attached to the atomic force microscope had the typical octahedral shapes with sharp edges. Accordingly, the AFM images in **Fig. 4, 6–9** and all figures below indicate growth by layer generation and spreading to cover the whole facet.

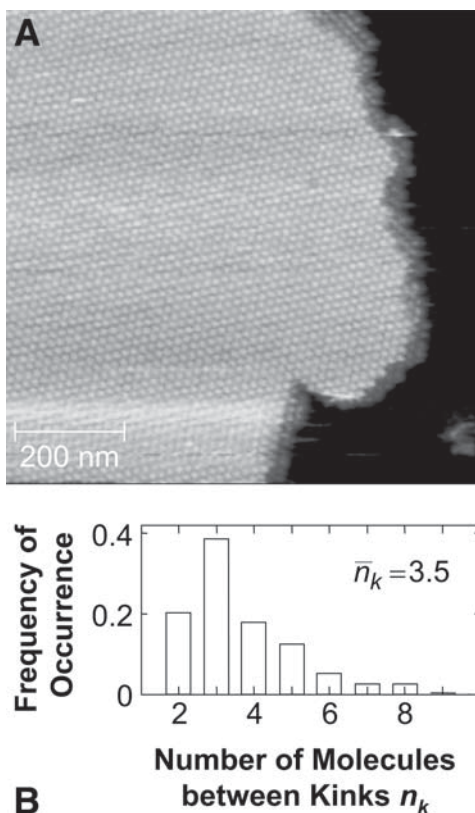


Fig. 7. (A) Molecular structure of growth step on ferritin crystal at protein concentration of 70 mg/mL, corresponding to supersaturation  $\sigma = \Delta\mu/k_B T = 0.7$ ,  $(C/C_e - 1) = 1$ . Dark area: lower layer; light gray: advancing upper layer. (B) Distribution of molecules between kinks on steps located approx 0.5 mm apart, obtained from images similar to (A) at same  $(C/C_e - 1) = 1$ . (From **ref. 31**.)

The molecular structures of a (111) apoferritin face and of a growth step are shown in **Fig. 6**. The kinks at a step are the sites where incoming molecules attach. A molecule attached at a kink has half of the neighbors that a molecule in the crystal bulk has; in the f.c.c. lattice of ferritin and apoferritin, the half-number equals six, with three molecules belonging to the underlying layer, and three molecules from the step (**42,43,48**). Thus, the kink density is a fundamental variable that determines the ability of the crystal to incorporate solute molecules and grow (**49,50**).

From **Fig. 6** and approx 15 other similar images, we determine the kink density along a step by counting the molecules between two kinks,  $n_k$ , also called kink length (**51**) and plot their distribution in **Fig. 6B–D** for apoferritin, and in **Fig. 7B** for



ferritin. Note that kink density is affected by the presence of surface point defects, such as vacancies or vacancy clusters, seen in **Fig. 6A**, as well as impurity cluster adsorbed on the surface (37). These features act as stoppers: straight step segments as long as eight molecules form and the step propagation is locally delayed (25). Hence, for the statistics in **Figs. 6** and **7**, we did not consider step segments around such stoppers. We obtain  $\bar{n}_k = 3.5$  for both proteins. Comparing **Fig. 6A–C**, we see that the  $n_k$  distributions are nearly the same near equilibrium, as well as at very high supersaturations.

#### 4.2. Energy of Kinks and Molecular Interaction Energy

The lack of dependence of the kink density on the thermodynamic supersaturation suggests that the kinks are not created by nucleation of molecular rows along a step; such nucleation would result in a steep dependence of kink density on supersaturation (52,53). Hence, the kink density  $1/n_k$  appears to be an equilibrium property of this surface even during growth in a supersaturated environment. In this case, the number of molecules between the kinks  $n_k$  is solely determined by the balance of molecular interactions and thermal fluctuations in the top crystal layer (28,29,54,55) and should be a function of the energy  $w$  needed to create a kink. Derivations have shown (49) that the average  $\bar{n}_k$

$$\bar{n}_k = \frac{1}{2} \exp(w/k_B T) + 1 \quad (9)$$

From the value of  $\bar{n}_k$  in **Figs. 6** and **7**,  $w = 1.6 k_B T$ . Quite surprisingly, this value of  $w$  is only slightly lower than the energy of kinks on Si crystals (30); one would expect the strong covalent bonds in the Si crystal lattice to lead to significantly higher kink energies. For the orthorhombic form of lysozyme, it was found that  $w = 7.4 k_B T$  (52). This significantly higher value leads to an extremely low kink density with  $n_k$  as high as 400 to 800, and step propagation limited by the rate of kink generation (52).

If we assume only first-neighbor interactions, we can evaluate the intermolecular bond energy,  $\phi$ . When a molecule is moved from within the step on a (111) face of an f.c.c. crystal to a location at the step, four kinks are created. For this, seven bonds (four in the top layer and three with molecules from the underlying layer) are broken, and five are formed. Then,  $w = \phi/2$  and  $\phi = 3.2 k_B T \cong 7.8 \text{ kJ/mol} = 0.09 \text{ eV}$ .

The intermolecular bonds in ferritin and apoferritin crystals involve two chains of bonds Asp — Cd<sup>2+</sup> — Glu between each pair of adjacent molecules (4,5). The preceding value of  $\phi$  seems significantly lower than the typical coordination bond energies. This low value may stem from the need to balance Cd<sup>2+</sup> coordination with the amino acid residues and with the water species

(H<sub>2</sub>O and OH<sup>-</sup>), or from free-energy loss owing to spatially and energetically unfavorable contacts by the other amino acid residues involved in the intermolecular contacts.

## 5. Thermodynamics of Crystallization and Crystal Morphology

### 5.1. Aspects of Macroscopic Thermodynamics

In the search for temperature dependence of the solubility, crystals were grown in the flat cell, allowing good optical microscopic observation. At various stages in the development of the individual crystals, corresponding to crystal sizes between 20 and 400  $\mu$ m, the temperature was varied between 0 and 40°C. A significantly faster growth rate that would correspond to a higher supersaturation at a lower solubility was not noticed at either the low or the high limits of this temperature range. Furthermore, no rounding of the crystal edges was detected that would indicate crystal dissolution owing to higher solubility. These observations are interpreted as an indication of none or very weak temperature dependence of the solubility (56).

Temperature-independent solubility means that the equilibrium constant of crystallization is also independent of temperature. Hence (57),

$$\left(\frac{\partial \ln K}{\partial T}\right)_p = -\left(\frac{\partial \Delta G^\circ / RT}{\partial T}\right) = \frac{\Delta H^\circ}{RT^2} = 0 \quad (10)$$

in which  $R$  is the gas constant, or

$$\left(\frac{\partial \Delta G^\circ}{\partial T}\right) = \frac{\Delta G^\circ}{T} \quad (11)$$

Equation 11 has a simple solution:

$$\Delta G^\circ = \text{const} \times T \quad (12)$$

Using  $\Delta G^\circ = \Delta H^\circ - T\Delta S^\circ$ , we obtain that  $\Delta H^\circ = 0$  and  $\Delta S^\circ = \text{const}$ .

The lack of temperature dependencies of the solubility leads to the following conclusions: (1) the enthalpy of crystallization is zero (or extremely small), and (2) the entropy of crystallization is temperature independent (or a weak function of temperature).

### 5.2. Molecular Processes Underlying Enthalpy, Entropy, and Free Energy for Crystallization

The intermolecular bond energy  $\phi$  contains both enthalpy and entropy components. The enthalpy ones are owing to the ion-mediated, hydrogen, and other bonds between the molecules, and the entropy components stem from the net

release or binding of water and other small molecules on crystallization (45). With this in mind, we can write an expression for the free energy for crystallization as follows:

$$\Delta G^\circ = \Delta H^\circ - T\Delta S^\circ_{\text{solvent}} - T\Delta S^\circ_{\text{protein}} \quad (13)$$

Here,  $\Delta H^\circ - T\Delta S^\circ_{\text{solvent}}$  are contributions associated with  $\phi$ , and  $\Delta S^\circ_{\text{protein}}$  is the loss of entropy of the protein molecules. A crude estimate of  $\Delta S^\circ_{\text{protein}}$  and of the relative weights of the two entropy contributions can be obtained by comparing the standard free-energy change for apoferritin crystallization  $\Delta G^\circ$  determined from the solubility to the value corresponding to the intermolecular bond free energy  $\phi$ .

By converting the solubility of the apoferritin (23 mg/mL) to molality,  $C_e = 5.2 \times 10^{-8}$  mol/kg. At equilibrium between crystal and solution, for apoferritin

$$\Delta G = G^\circ(\text{crystal}) - [G^\circ(\text{solution}) + N_A k_B T \ln(C_e)] = 0 \quad (14)$$

in which  $N_A$  is the Avogadro number, and the product  $N_A k_B = R$  is the universal gas constant. Hence,

$$\Delta G^\circ = G^\circ(\text{crystal}) - G^\circ(\text{solution}) = N_A k_B T \ln C_e \quad (15)$$

in which  $\Delta G^\circ = -42$  kJ/mol.

To get  $\Delta H^\circ - T\Delta S^\circ_{\text{solvent}}$  from  $\phi = 3 k_B T \cong 7.3$  kJ/mol, we have to multiply  $\phi$  by  $Z_1/2 = 6$ , the half-number of neighbors in the crystal lattice (two molecules partake in a bond, in an f.c.c. lattice  $Z_1 = 12$ ) and, accounting for the sign, we get  $-44$  kJ/mol. The closeness of  $\Delta H^\circ - T\Delta S^\circ_{\text{solvent}}$  to  $\Delta G^\circ$  indicates the insignificance of  $\Delta S^\circ_{\text{protein}}$  for the free energy of crystallization.

As shown above, the enthalpy of crystallization and the related energy of pair interactions in the solution are close to zero. In combination with the insignificance of  $\Delta S^\circ_{\text{protein}}$ , this allows us to conclude that crystallization is mostly driven by the maximization of the entropy of the solvent. Such disordering may stem from the release on crystallization of the water and other solvent components bound to the protein molecules in the solution. A similarity can be traced to the processes that underlie hydrophobic attraction, which governs many processes in nature (58), including some stages of protein folding (59).

The standard free energy of formation of a single intermolecular bond in apoferritin crystals is  $-7.8$  kJ/mol (see **Subheading 4.2.**) and is fully attributable to the entropy gain caused by the release of water,  $\Delta S^\circ_{\text{solvent}} = 26.6$  J/(mol·K) per intermolecular bond (10).

This conclusion allows us to estimate crudely the number of water molecules  $n_w$  released at the contact between two hemoglobin molecules. Following an analogy first put forth by Tanford (60), we compare the entropy effect of Hb crystallization to the entropy change for melting of ice = at 273 K,  $\Delta S^\circ_{\text{ice}} =$

22 J/(mol·K) (**45,61,62**). Similarly, estimates of the entropy loss owing to the tying up of hydration water in crystals have yielded 25 to 29 J/(mol·K) (**62**). Using these numbers, the values of  $\Delta S^{\circ}_{\text{solvent}}$  reflect the release of one or two water molecules per intermolecular bond.

This low number of water molecules can be tentatively linked to the structure of the intermolecular bonds in the face-centered cubic apoferritin crystals. The X-ray structure reveals that each of the 12 such bonds consists of a pair of  $\text{Cd}^{2+}$  ions (**4**). Around each  $\text{Cd}^{2+}$  ion of the pair, two of the six coordination spots are occupied by an aspartic acid residue from the one apoferritin molecule partaking in the bond and a glutamic acid residue from the other (**5**). The fact that the entropy change corresponds to the release of one or two, rather than four, water molecules suggests that the  $\text{Cd}^{2+}$  ions may be prebound to either the incoming apoferritin molecule or the apoferritin molecules already in the crystal.

Thus, as suggested by the crystal structures of ferritin and apoferritin (**3–5**), the main component of the crystallization driving force stems from the strong  $\text{Cd}^{2+}$ -mediated bond between each pair of molecules. The unexpected part of our conclusion is that this driving force is not of enthalpy origin (the likely large negative enthalpy of such a bond must have been compensated for by unfavorable enthalpy effects of other patches of the molecules), but comes from the entropy of the water released during the formation of this bond.

## 6. Molecular-Level Kinetics of Growth

While the kink density is a thermodynamic growth variable that characterizes the affinity of the crystal to the solute molecules, the kinetics of incorporation are reflected by the flux of molecules into a growth site. To monitor these fast incorporation events, we disabled the slow scanning axis of the atomic force microscope. The advance of a step site is shown in **Figs. 8** and **9**. Area scans immediately following the trace in **Figs. 8** and **9** revealed that step motion is not inhibited or accelerated at the location of scanning; that is, the chosen scanning parameters ensured that step propagation was not affected by scanning over the same line for approx 3 min.

Despite the relatively high solution supersaturation  $\sigma = 1.1$ , the time trace in **Fig. 8** reveals not only 25 arrivals to, but also 22 departures of molecules from the monitored site. All arrivals and departures of molecules to and from the monitored site involve single molecules. Thus, in contrast to claims of pre-formed multiple-molecule growth units for the protein lysozyme (**63–65**), apoferritin and ferritin crystal grow by the attachment of single molecules.

This type of data collection does not allow observations of the neighboring sites at the step. Hence, we cannot distinguish between attachment and detachment from molecules in the kinks or at the steps. Still, we notice that the resi-

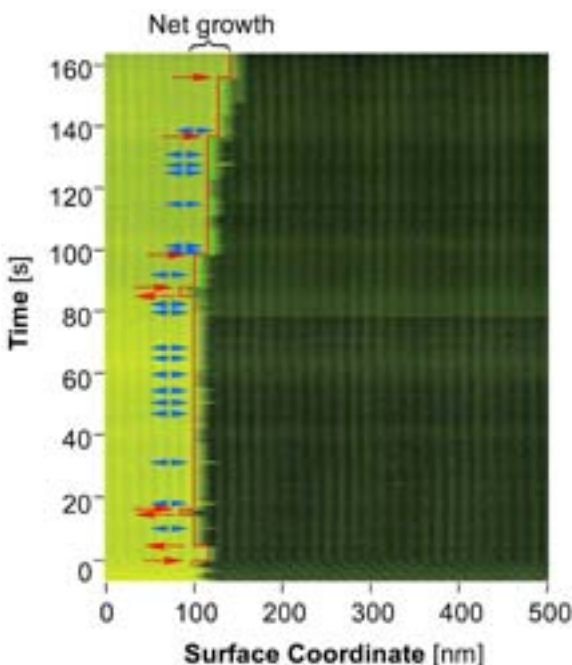


Fig. 8. Incorporation of molecules into steps at apoferritin concentration of 70 mg/mL,  $\sigma = 1.1$ , and  $(C/C_e - 1) = 2.04$ . The pseudoimage recorded using a scanning frequency of 3 Hz with the  $y$  scan axis disabled at time = 0 shows displacement of one step site. The contour traces the step position. Red arrows indicate attachment and detachment events with a residence time  $> 1$  s, and blue double-sided arrows with a residence time  $< 1$  s; for details, see the text. The appearance of 1/2 molecule attachments at times  $> 80$  s, highlighted in green, is owing to events at a neighboring site that entered the image owing to scanner drift. (From **ref. 10**.)

dence times  $t$  between these events fall into either  $t \leq 1$  s or  $t > 5$  s. **Figure 8** shows six events of the second type and 19 events of the first. Their ratio is roughly equal to the kink density along the step, suggesting that the longtime events may be attachments and detachments to and from a kink, and the short ones may be sightings of molecules at the step edge.

Furthermore, molecules may enter the line of observation owing to molecular diffusion along the step, or to exchange with the terrace between the steps or the adjacent solution. Whereas the latter results in step propagation and growth, the former is a process that only involves rearrangement of molecules already belonging to the crystals and that may not be associated with growth. To distinguish between the two, as done previously for steps on metal and semiconductor surfaces (28,54,66–68), we calculated the time correlation func-

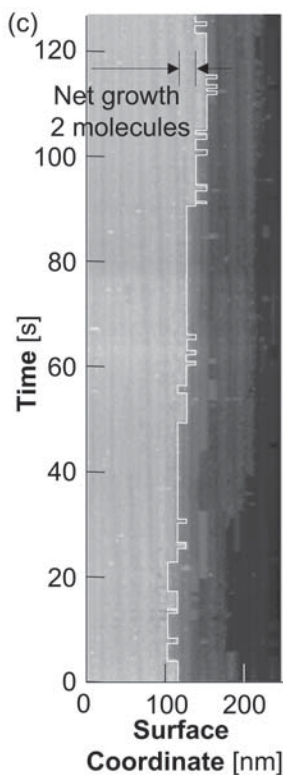


Fig. 9. Incorporation of molecules into steps on ferritin crystal at protein concentration of 70 mg/mL, corresponding to supersaturation  $\sigma = \Delta\mu/k_B T = 0.7$ ,  $(C/C_e - 1) = 1$ . A pseudomicroimage recorded with the scan axis parallel to the step disabled at time = 0 shows the displacement of one molecular site at the step. In this imaging mode, the molecules in the upper and lower layers appear as vertical columns. The red contour traces the step position. Left shifts of this contour indicate detachment of a molecule from the monitored site, and right shifts indicate molecular attachment into the monitored site. (From **ref. 31**.)

tion of the step position  $x$  (in molecular size units) as  $([x(t + \Delta t) - x(t)]^2)_{\Delta t}$ , with averaging over the respective  $\Delta t$ . In **Fig. 10**, it is plotted as a function of  $\Delta t$ . Theoretical analyses of the exchange of the steps with the medium at equilibrium (28,54,68–70) predict that if diffusion along the step edge dominates the advance of the step site, the cross-correlation should follow  $\Delta t^{1/4}$  dependence (28,54,68–70). We found no theory dealing with supersaturated conditions. However, motion of a site on the step edge is similar to Brownian motion (68,69). For Brownian diffusion, the coefficient relating  $([x(t + \Delta t) - x(t)]^2)_{\Delta t}$  and  $\Delta t^{1/2}$  may vary, but the exponent 1/2 of  $\Delta t$  does not depend on the presence

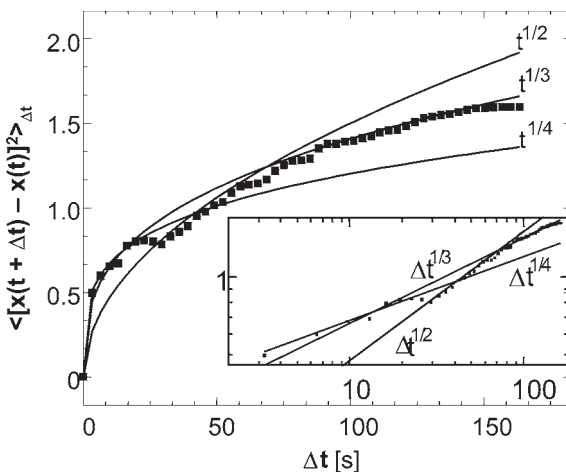


Fig. 10. Time correlation curve, characterizing mean square displacement of a location at a step for a time interval  $\Delta t$  as a function of this  $\Delta t$ , corresponding to trace of step location in **Fig. 8**; inset: logarithmic plot. Solid squares indicate data; lines fits with exponential dependencies on time as indicated in the plots. (From **ref. 25**.)

or absence of concentration/chemical potential gradients (57). Hence, we use only the exponents of  $\Delta t$  stemming from the data in **Fig. 10** for further discussion.

The data in **Fig. 10** do not fit a single exponential. The deviation from 1/4 at times longer than 20 s allows us to conclude that the trace in **Fig. 8** likely reflects exchange of molecules between the step and interstep terraces or the adjacent solution. This conclusion allows us to extract from **Figs. 8** and **9** net frequencies of attachment of molecules to kinks. For apoferritin at  $(C/C_e - 1) = 2$ , from the net attachment of three molecules for 162 s and the probability of viewing a kink of  $1/n_k = 1/3.5$ , we get  $(j_+ - j_-) = 0.065 \text{ s}^{-1}$ , or one molecule per approx 15 s. For ferritin at  $(C/C_e - 1) = 1$ , **Fig. 9** shows net growth of two molecules for 128 s, leading to an average net flux  $(j_+ - j_-) = 0.054 \text{ s}^{-1}$  into the growth sites distributed with mean density = 0.28. Thus, even at the relatively high supersaturation in **Figs. 8** and **9**, incorporation of molecules into the crystal is extremely slow and occurs over macroscopic time scales

The step velocities  $v$  for the two proteins, determined using the three methods discussed in **Subheading 2.3**, are shown in **Fig. 11**. The data fit well the proportionality

$$v = \beta \Omega C_e (C/C_e - 1) = \beta \Omega n_e (n/n_e - 1) \quad (16)$$

with  $\Omega = 1/4 a^3 = 1.56 \times 10^{-18} \text{ cm}^3$ —the crystal volume per ferritin or apoferritin molecule, and step kinetic coefficient  $\beta$  (50,71) is  $(6.0 \pm 0.4) \times 10^{-4} \text{ cm/s}$  for ferritin and  $(6.0 \pm 0.3) \times 10^{-4} \text{ cm/s}$  for apoferritin.



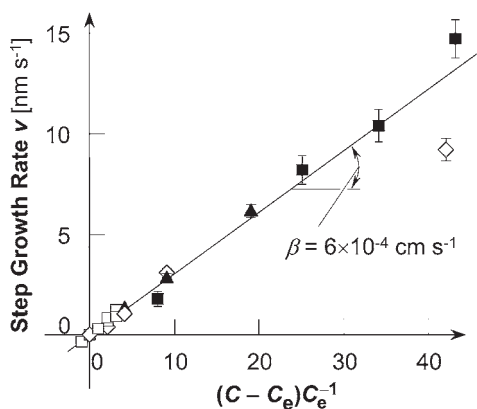


Fig. 11. Determination of kinetic coefficients for step growth for ferritin and apoferritin. Dependencies of the step growth rates  $v$  on the crystallization driving force  $(C/C_e - 1)$ . ( $\square$ ,  $\diamond$ )  $v$ -Values for, respectively, ferritin and apoferritin, from sequences of molecular resolution *in situ* AFM images of the advancing steps. The reason for the lower value of the point for apoferritin at  $(C/C_e - 1) = 42$  is not well understood. This point was not used in the determination of the kinetic coefficient  $\beta$ . ( $\blacktriangle$ ) Data for apoferritin extracted from disabled y-axis scans. ( $\blacksquare$ ) Data for ferritin from time traces of the step growth rate using laser interferometry. The straight line corresponds to the step kinetic coefficient  $\beta = 6 \times 10^{-4}$  cm/s. (From **ref. 40**.)

Since there are no sources or sinks of molecules at the step other than the attachment sites, the step growth rate  $v$  should equal  $\bar{a}\bar{n}_k^{-1}(j_+ - j_-)$  (**50,72**). At  $(C/C_e - 1) = 1$ , at which all data on ferritin in **Fig. 9** were collected, the value of the step growth rate for ferritin from **Fig. 11** is  $v = 0.20$  nm/s, equal to the product  $\bar{a}\bar{n}_k^{-1}(j_+ - j_-)$ . For apoferritin, the average step velocity at  $(C/C_e - 1) = 2$ ,  $\sigma = 1.1$  is  $v = 0.26$  nm/s. The product  $\bar{a}\bar{n}_k^{-1}(j_+ - j_-)$  determined at the same conditions is 0.24 nm/s.

The closeness of the values of the product  $\bar{a}\bar{n}_k^{-1}(j_+ - j_-)$  and measured  $v$ s indicates that the step propagation in ferritin crystallization occurs only owing to incorporation of molecules into the kinks along the steps (**10,25**).

## 7. What Limits the Rate of Incorporation of a Molecule in a Kink?

### 7.1. Diffusion-Limited or Transition-State Kinetics

Next, I discuss the factors that determine the rate of the last stage, the chemical stage, in the growth mechanism—the incorporation into a kink of a molecule standing in front of this kink. In this way, I eliminate from consideration the rate of supply of the molecules from the solution bulk to the kink, constituting the transport stage of the growth mechanism.

The kinetics of chemical reactions in solutions are either limited only by the rate of diffusion of the species (73) or additionally slowed down by a high-energy transition state (74). The former kinetics pathway does not exclude the presence of potential free-energy barriers. It has been shown that if molecules have to overcome a repulsive maximum to reach the bonding minimum, the rate of binding can be evaluated as diffusion over the barrier. The resulting kinetic law contains an exponential dependence on the height of the barrier (74).

For the kinetics of the phase transitions in solutions, it is generally accepted that colloid particles follow the diffusion-limited model, while the growth rates of new phases of small molecules are thought to be governed by a transition state (71,72,75–77). For the intermediate case of protein solid phases, the growth kinetics largely resemble those of small molecules, and it was assumed that transition-state laws apply (78). Although rate laws reminiscent of diffusion-limited mechanisms have been postulated for small-molecule phase transitions (49,79,80), they were viewed as equivalent to respective transition-state expressions (79,80), and no critical tests to discriminate between the two mechanisms were suggested or performed.

In the transition-state kinetics, the rate coefficients are (1) mass dependent (50,81); (2) independent on the diffusivity (74); and (3) faster for high-symmetry molecules, because of the transition-state entropy (72). I discuss next evidence indicating that (no. 1) is violated for the ferritin/apoferritin pair of proteins, and that nos. 2 and 3 are violated for many other systems, suggesting that the rate of many phase transitions is in fact diffusion limited.

The data in **Fig. 11** show that at equal driving forces, the step growth rates are equal for the two proteins. Since in the preceding subsections we have shown that the mechanism of attachments of molecules to kinks are identical for the two proteins, we conclude that this observation is in apparent contradiction with transition-state-type kinetic laws, in which the vibrational components of the transition-state partition function lead to proportionality of  $\beta$  to  $m^{-1/2}$ , characteristic of no. 1 of the transition-state kinetics just discussed. We conclude that the kinetics of incorporation into the kinks are only limited by diffusion (40).

## **7.2. Evaluation of Flux of Molecules Into a Kink in the Case of Diffusion-Limited Kinetics**

We derive an expression for the kinetic coefficient of growth of crystals from solution as diffusion over an energy barrier  $U$ , followed by unimpeded incorporation (73,74). The barrier  $U$  may be of electrostatic origin (74); however, for the ferritin/apoferritin pair, it probably accounts for the need to expel the water molecules attached to the incoming molecules and to the growth site (82). Repulsive potentials owing to water structuring at hydrophobic and hydrophilic surface patches can have significant strength and range (83,84).

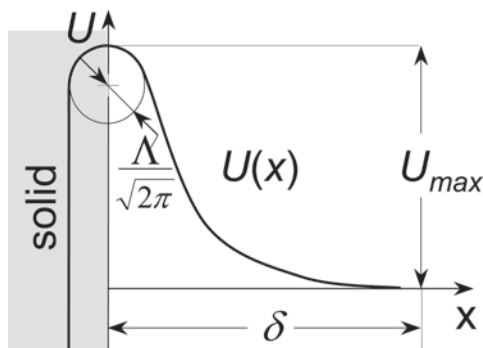


Fig. 12. Schematic illustration of the potential energy relief in front of growth interface. For details, see the text. (From **ref. 40.**)

In **Fig. 12**, the resulting potential relief is schematically depicted. The potential reaches its maximum value  $U_{\max}$  at the crossing of the increasing branch, owing to the repulsion between the incoming solute molecules and the crystal surface at medium separations, and the receding branch, which corresponds to the short-range attraction required if the molecules should enter the growth site. We position the beginning of the coordinate axis  $x = 0$  at the location of this maximum. We assign a finite curvature of  $U(x)$  about this maximum and link it with the expulsion of the last few solvent molecules as an incoming solute molecule joins the crystal. The finite curvature assumption follows previous solutions to similar problems (**85,86**). The distance  $d$ , used as the upper integration limit, is bound from below by the range of interaction of the solute molecules with the surface, which can be a few solute molecular sizes, and from above by the distances between the solute molecules in the solution bulk,  $n^{-1/3} \approx 0.2$  nm. Thus,  $d$  can be chosen significantly longer than the molecular sizes and kink lengths, and using a one-dimensional model is justified. Since the rate of diffusion over a sharp barrier only depends on the curvature around the maximum (**85,86**), the choice of  $d$  does not affect the result

To calculate the flux  $J$  of molecules with concentration  $n$  that, driven by a concentration gradient, overcome a barrier to reach the surface, we orient the coordinate  $x$  perpendicular to a growing surface and denote the potential relief close to this surface as  $U(x)$ . From the generalized Fick law,  $J = (nD/k_B T) d\mu/dx$ , with  $\mu(T, x) = \mu_0(T) + k_B T \ln[\gamma n(x)] + U(x)$  and  $\gamma \approx 1$  (**10**),  $J$  is linked to  $U(x)$ ,  $n(x)$  and the gradient of  $n$  as (**73,86**)

$$J = D \left\{ \frac{dn(x)}{dx} + n(x) \frac{d[U(x)/k_B T]}{dx} \right\}, x > 0 \quad (17)$$

with  $D$  being the Stokes diffusion coefficient of the molecules. In search of a steady  $J = \text{const}$ , we integrate **Eq. 17** with two sets of boundary conditions: (1) that at a certain distance from the surface  $\delta$ ,  $x \geq \delta$ ,  $U = 0$ , and  $n = n_\delta$ ; and (2) that in the crystal, i.e., at  $x \leq 0$ ,  $n = 0$ .

Dividing by  $D$  and multiplying both sides by  $\exp[U(x)/k_B T]$ , we get

$$\frac{J}{D} \exp[U(x)/k_B T] = \frac{d}{dx} \left\{ n(x) \exp[U(x)/k_B T] \right\} \quad (18)$$

Integrating from  $x = 0$  to  $x = \delta$ , using the boundary conditions at  $x = 0$  and  $x \geq \delta$ , we get

$$J = \frac{n_\delta D}{\int_0^\delta \exp[U(x)/k_B T] dx} \quad (19)$$

an analog to equation 9.51 in **ref. 74** and the Fuchs expression for coagulation of particles interacting through  $U(x)$ .

If  $U(x)$  has a sharp maximum at  $x = 0$ , we can represent it with a symmetric function around the point of the maximum. As shown below, in many cases  $|d^2 U/dx^2| < a$ , and this justifies the assumption of a sharp maximum. We use only the first two members of the Taylor series:  $U(x) = U_{\text{max}} - 1/2 |d^2 U/dx^2| x^2$ . The minus sign stems from  $d^2 U/dx^2 < 0$  at the maximum. Then, the integral

$$\int_0^\delta \exp[U(x)/k_B T] dx \cong \exp\left(\frac{U_{\text{max}}}{k_B T}\right) \left[ \frac{2}{\pi} \left| \frac{\partial^2 (U/k_B T)}{\partial x^2} \right|_{x=0} \right]^{-1/2} \quad (20)$$

The approximate equality above is based on  $\delta \gg [1/2 |d^2 U/dx^2|]^{-1/2}$ , the half-width of the Gaussian function in **Eq. 20**. Finally,

$$J = D \sqrt{\frac{2}{\pi k_B T}} \left\{ \left| \frac{\partial^2 U}{\partial x^2} \right|_{\text{max}} \right\}^{1/2} \exp\left(-\frac{U_{\text{max}}}{k_B T}\right) n_\delta \quad (21)$$

Note that only half of the flux  $J$  from **Eq. 21** contributes to growth: on top of the barrier, the force driving the molecules into the crystal is zero, and a molecule has equal chances of getting incorporated, or going back to the solution (87). With this, and introducing the parameter  $L$  as the radius of curvature of  $U(x)/k_B T$  at its maximum

$$\Lambda = \left( \frac{1}{2\pi} \left| \frac{\partial^2 (U/k_B T)}{\partial x^2} \right|_{\text{max}} \right)^{-1/2} \quad (22)$$

the expression for  $J$  becomes

$$J = \frac{D}{\Lambda} \exp\left(-\frac{U_{\max}}{k_B T}\right) n_\delta \quad (23)$$

**Equation 23** is essentially identical to the nucleation rate expression derived by Zeldovich (86) as a diffusion flux over a potential barrier in the space of cluster sizes.

If  $U_{\max}$  is owing to the hydration of the incoming molecule and the site where it attaches, the radius of curvature of  $U(x)$  around  $U_{\max}$  should be the size of a few water molecules, 2 to 4 Å, and the length  $\Lambda$  should be approx 5–10 Å. Note that in this evaluation, we apply discrete considerations to a continuous model. Still, we expect the estimate of  $\Lambda$  to be roughly correct.

If all molecules that overcome the barrier are incorporated into a kink, the incoming flux into a kink is  $j_+ = JDS_{\text{kink}} \approx Ja^2$ , in which  $a^2$  is an effective surface area of a kink. If there are no solute transport constraints (kinetic growth regime),  $n_d$  is equal to that in the solution bulk  $n$ . Furthermore, in equilibrium, when  $n$  equals the solubility,  $n_e$ ,  $j_+ = j_-$ . Since  $j_-$  does not depend on  $n$  in the solution, the step velocity  $v$  is

$$v = \frac{a}{n_k} (j_+ - j_-) = \frac{a^3}{n_k} \frac{D}{\Lambda} \exp\left(-\frac{U_{\max}}{k_B T}\right) (n - n_e) \quad (24)$$

Because Brownian diffusion does not depend on the molecular mass, the above model yields a mass-independent kinetic coefficient (for details, see the supplementary information). The resulting step growth rate  $v$  is

$$v = \frac{a}{n_k} (j_+ - j_-) = \frac{a^3}{n_k} \frac{D}{\Lambda} \exp\left(-\frac{U_{\max}}{k_B T}\right) (n - n_e) \quad (25)$$

in which  $L$  contains the radius of curvature of  $U(x)$  around its maximum and, hence, is likely the size of a few water molecules, approx 5–10 Å.

With  $a^3 = W$ , we can rewrite **Eq. 25** in the typical form of **Eq. 16** that is readily comparable to experimental data (40). This defines  $\beta$  as

$$\beta = \frac{1}{n_k} \frac{D}{\Lambda} \exp\left(-\frac{U_{\max}}{k_B T}\right) \quad (26)$$

The parameters in this expression,  $\bar{n}_k$ ,  $D$ ,  $\Lambda$ , and  $U_{\max}$ , have a clear physical meaning and can be independently measured (40).

### 7.3. How Broad Is the Class of Molecules That Follow Diffusion-Limited Kinetics Law?

The ratio  $D/\Lambda\bar{n}_k$  has been used (88) as a kinetic coefficient for crystallization from the melt, with  $L$  defined as the “free path” of the building blocks, atoms, or molecules in the melt. In further work, this law was shown to poorly predict the behavior of metals during solidification (89). Note that in contrast to the above expression for melt growth, **Eq. 26** treats growth from solutions with Einstein-Stokes diffusion of the solute molecules.

In a classic paper (49), the ratio of the diffusivity to the mean distance between kinks,  $D/a\bar{n}_k$ , was used as a kinetic coefficient. This definition misses the energy barrier for growth, demonstrated by numerous later experiments (81). In a further development (79), the kinetic coefficients for motion of steps were postulated as  $\beta = (D/\Lambda)\exp(-U/k_B T)$ , with  $\Lambda$  introduced as a “jump length in the solution.” Comparing this formula with our **Eq. 26**, we see that **Eq. 26** explicitly accounts for the mean kink density  $\bar{n}_k^{-1}$  and provides a clear definition of  $\Lambda$ .

Evidence for diffusion-limited kinetics in other solution crystallization systems can be found in experiments on growth of protein crystals in gels, in which the protein diffusivity is significantly lower than in a “free” solution. It was found with two proteins that the maximum value of the growth rate, recorded at the early stages of growth before solution depletion and transport control set in, is 1.5 to 3 times lower than the equivalent value in free solutions (90). This suggests that the kinetic coefficient of growth is correlated to the diffusivity. In another work with the protein lysozyme, it was found that in gelled media, the protein concentration at the growth interface is essentially equal to the one in free solutions, while the concentration gradient at the interface, proportional to the growth rate, is lower by approx 1.5 times (91). This is only possible if the kinetic coefficient in gels is lower, supporting the correlation between  $\beta$  and  $D$  and contradicting characteristic no. 2 of the transition-state kinetic laws, discussed in **Subheading 7.1**.

**Table 1** shows that the known kinetic coefficients for crystallization of about a dozen proteins, protein complexes, and viri are in the range of  $0.8$  to  $400 \times 10^{-4}$  cm/s (17,22,25,92,93). The molecular symmetry groups have orders ranging from 1 to 3, to 24 for the ferritins, and 60 for the satellite tobacco mosaic virus. No correlation exists between higher molecular symmetry and higher kinetic coefficients. This suggests that the rate-limiting step is not the decay of a transition state that should be facilitated for high-symmetry molecules with higher transition-state entropies, characteristic no. 3 discussed in **Subheading 7.1**.

Evidence in favor of the applicability of the diffusion-limited kinetics also applies for phase transitions involving small-molecule substances and comes from detailed data on the adsorption kinetics on the surface of a growing

**Table 1**  
**Kinetic Coefficients ( $\beta$ ), Diffusivities ( $D$ ),**  
**Effective Molecular Diameter ( $a$ ), Point Symmetry Group of Molecule ( $G$ ),**  
**and Order of Symmetry Group ( $Z$ ) for Various Systems**

System	$\beta$ , $10^{-4}$ (cm/s)	$D$ , $10^{-6}$ (cm <sup>2</sup> /s)	$a$ (nm)	$G$	$Z$	Reference
Insulin			6.5	$\bar{3}m$	6	<b>103</b>
No acetone	90	0.79				
approx 5% acetone	420					
Apo ferritin	6	0.32	13	432	24	<b>25</b>
Ferritin	6	0.32	13	432	24	<b>40</b>
Canavalin, R3 form	5.8–26	0.4	3.5–8	3	3	<b>22</b>
Lumasine synthase	3.6	0.16	18	m5	60	O. Gliko, unpublished
Catalase	0.32	NA <sup>a</sup>	11.5	222	4	<b>104</b>
Lysozyme (101)		0.73	3	1	1	
Typical	2–3					<b>105</b>
No step bunching	22–45					<b>93</b>
Lysozyme (110)	2–3					<b>106</b>
STMV	4–8	0.2	16	m5	60	<b>17</b>
Thaumatococcus	2	0.6	4.0	1	1	<b>107</b>
Various inorganic systems (ADP, KDP, alums, etc.)	~100–1000	~1–5	0.5	1, 2, $\bar{2}$ , m, etc.	1, 2	<b>108</b>

<sup>a</sup>NA, not available; ADP, ammonium-dihydrogen phosphate; KDP, potassium-dihydrogen phosphate.

ammonium-dihydrogen phosphate (ADP) crystal (**94,95**). The data for the temperature range of 29–67°C were fitted to an equivalent of **Eq. 26** with  $\bar{n}_k^{-1} = 1$  to account for the suspected density of the adsorption sites (**94,95**); for the surface diffusion mechanism selected by this system, adsorption is the process to be limited by either diffusion or a transition-state decay rate. The fit yielded  $\Lambda = 13 \text{ \AA}$  and  $U = 27 \text{ kJ/mol}$ . The closeness of  $L$  to the range just suggested for the diffusion-limited case suggests that this mechanism is the rate-determining one for the investigated phase transition.

Further evidence in favor of the applicability of this mechanism to small molecules comes from the unusually narrow grouping of the kinetic barriers for growth of approx 10 diverse substances at  $28 \pm 7 \text{ kJ/mol}$  (**81**). The chemical nature of these substances ranges from inorganic salts, to organic molecular compounds, to proteins and viri. Hence, the narrow range of the activation barriers is unexpected for transition-state kinetics, in which the activated com-



plexes should reflect the chemical variety of the crystallizing compounds. On the other hand, assuming diffusion-limited kinetics, we note that the diffusivities in aqueous solutions have effective activation energies of approx 8–17 kJ/mol (38,96). If, as suggested by Eq. 26, we subtract these values from the barriers of  $28 \pm 7$  kJ/mol (81), characterizing the overall kinetics, only approx 10–20 kJ/mol remain for the barriers owing to the interactions between the solute and the crystal surface. The range of  $28 \pm 7$  kJ/mol is sufficiently broad to accommodate the chemical specificity of the solutes.

Thus, our experimental data in the context of other recent findings show that the kinetics of attachment of molecules to a growing phase during crystallization or other phase transitions in solution are, in many cases, diffusion limited. This applies to proteins, as well as to small-molecule systems. It is important to once again state that this result concerns the kinetics of incorporation of the solute molecules into existing attachments sites. In cases in which such sites are few, or transport from the solution bulk is slow, the kinetics of creation of attachment sites or of transport may control the overall kinetics. What we argue is that after an attachment site exists, and the solute molecules are standing in front of it, the rate of incorporation is solely limited by diffusion, and not restricted by the decay of an intermediate state (40).

## 8. Molecular Pathway From Solution to Crystal

During crystal growth from solution, the solute molecules have two possible pathways between the solution and the kinks: they can be directly incorporated (49,71), or they can first adsorb on the terraces between the steps, diffuse along them, and then reach the steps (48,49).

If a crystal grows by the direct incorporation mechanism, the competition for supply between adjacent steps is mild (71). By contrast, competition for supply confined to the adsorption phase is acute (79); it retards step propagation and acts as a strong, effective attraction between the steps. This dramatically affects the stability of the step train; the appearance and evolution of step bunches (51); and, ultimately, the crystal's quality and utility (97).

The two mechanisms can be directly discerned by monitoring the adsorbed solute molecules on the crystal surface, similar to experiments with metal atoms at lowered temperatures (98). However, during solution growth at room temperature, the diffusivity of the adsorbed species is approx  $10^{-8}$  cm<sup>2</sup>/s (22,94); that is, a molecule passes 100 nm in approx 0.01 s. With *in situ* AFM, this distance is covered by the scanning tip typically approx 0.1 s; that is, imaging is too slow to detect and monitor the adsorbed molecules. Electron microscopy of flash-frozen samples has, in several cases, revealed the presence of adsorbed solute molecules on the crystal's surface (99); however, their participation in growth cannot be confidently judged by this technique. Because direct tests

appear impossible, indirect evidence for the growth mechanism of several systems has been sought.

For several solution-grown crystals, the growth mechanism has been deduced by comparing the velocities of isolated steps with those of closely spaced steps. Similar values of the two velocities for silver (100) and calcite (15,16) were taken as evidence for the direct incorporation mechanism. Conversely, slower growth of dense step segments was interpreted in favor of the surface diffusion mechanism for KDP/ADP (21,94), lysozyme (101), and canavalin (22). A known problem for such mesoscale data is that the data sets interpreted in favor of direct incorporation could also reflect a surface diffusion range shorter than the shortest step separation probed (15,16). Thus, critical evidence about the growth mode should be sought by studying the growth processes at the molecular level (10,25).

As shown in **Subheading 7.3.**, in the case of direct incorporation from the solution (*see also refs. 72 and 78*),

$$j_+ - j_- = v_+ C_e \Omega \exp \left( - \frac{U_{\max}}{k_B T} \right) \left[ \frac{C}{C_e} - 1 \right], \quad v_+ = \frac{D}{\Lambda a}, \quad \text{and} \quad \frac{j_+}{j_-} = \frac{C}{C_e} \quad (27)$$

Here,  $U_{\max}$  is the energy barrier for incorporation into the kinks (50,71); in the case of ferritin, it likely accounts for the need to expel the water molecules structured around hydrophilic patches on the surfaces of the incoming molecules and the molecules forming the kink (82).  $\Omega = 1.56 \times 10^{-18} \text{ cm}^3$  is the crystal volume per ferritin molecule;  $D = 3.2 \times 10^{-7} \text{ cm}^2/\text{s}$  is the ferritin diffusivity (37); and  $\Lambda$  is the radius of curvature of the surface-molecule interaction potential around its maximum at  $U_{\max}$  (73,74) and, hence, should be of the order of a few water molecule sizes, approx 5–10 Å (95). The step velocity  $v$  for this growth mode is

$$v = \frac{a}{n_k} (j_+ - j_-) = \frac{\Omega C_e}{n_k} \frac{D}{\Lambda} \exp \left( - \frac{U_{\max}}{k_B T} \right) \left[ \frac{C}{C_e} - 1 \right] \quad (28)$$

Analogous considerations for the case of growth via surface diffusion yield for the net flux into the step from the surface are

$$j_{s+} - j_{s-} = v_{s+} n_e a^2 \exp \left( - \frac{U_{s0}}{k_B T} \right) \left[ \frac{n_s}{n_e} - 1 \right], \quad v_{s+} = \frac{D_s}{\Lambda_s a}, \quad \text{and} \quad \frac{j_{s+}}{j_{s-}} = \frac{n_s}{n_e} \quad (29)$$

in which  $n_s$  and  $n_e$  are the surface concentration of adsorbed ferritin and its equilibrium value, respectively;  $U_{s0}$  is the energy barrier for incorporation into the kink from the surface; and  $D_s$  and  $\Lambda_s$  are, respectively, the surface diffusivity

and curvature of the surface  $U_s$ . For the step velocity, one gets through  $v = a/\bar{n}_k(j_{s+} - j_{s-})$  an expression analogous to **Eq. 25**.

To evaluate the ratios of the fluxes in and out of step, we use that **Fig. 9** reveals that for ferritin at  $C/C_e = 2$ ,  $j_+/j_- \leq 1.105$ . For apoferritin, similar experiments in **Fig. 8** show that at  $C/C_e = 3$ ,  $j_+/j_- \leq 25/22 = 1.14$ . For both proteins, these ratios represent gross violations of the last equality of **Eq. 27**. These violations cannot be attributed to depletion of the solution layer adjacent to the crystal. This factor becomes significant at approx 100 times higher growth rates (**102**) and suggests that the direct incorporation mechanism may not apply. In the case of Langmuir adsorption,  $n_s = n_s C(B + C)^{-1}$  ( $B$  – Langmuir constant) and  $n_s/n_e < C/C_e$ . Hence, the lower ratios of the in- to out-flux are compatible with a mechanism of incorporation from the state of adsorption on the surface.

For further tests of the growth mode, we examine the step velocity law in **Eq. 28**. The only unknown parameter here is the energy barrier  $U_0$ . Determinations of  $v$  at four temperatures and two ferritin concentrations in **Fig. 13** yield  $E_{\text{total}} = 41 \pm 3$  kJ/mol. In **Eq. 28**,  $C_e$  (**56**) and  $\Omega$  do not depend on temperature, and  $\Lambda$  is about the size of a few water molecules and in a first approximation does not depend on  $T$  (**95**). For a molecule following the Stokes law,  $D = D_0 \exp(-E_{\text{visc}}/k_B T)$ , where  $E_{\text{visc}}$  is the temperature factor in an Arrhenius-type expression for the dependence of the solvent viscosity on temperature. For NaCl solutions in Na acetate buffer,  $E_{\text{visc}} = 7.4$  kJ/mol (**38**). As shown in **Eq. 28**,  $\bar{n}_k$  has a weak near-exponential dependence on  $T$  through the kink energy  $w = 3.8$  kJ/mol. This leaves  $U_0 \approx 30$  kJ/mol. This value is close to the 28 kJ/mol found as the average over systems ranging from inorganic salts, through organics, to proteins and viri (**81**).

Substituting into **Eq. 28**, we get at  $C/C_e = 2$ ,  $v = 0.0014$  nm/s, and at  $C/C_e = 3$ ,  $v = 0.0028$  nm/s. These values are more than two orders of magnitude lower than actually observed. The measured values of 0.20 and 0.31 nm/s would require  $U_{\text{max}} \approx 18$  kJ/mol, beyond the range of the determination in **Fig. 13**. This discrepancy supports the assertion that the direct incorporation mechanism is inapplicable to the growth of ferritin. We conclude that a mechanism involving adsorption on the terraces better corresponds to the available data for ferritin. As noted, in the ferritin/apoferritin system, the steps only exhibit attraction at very short separations. We conclude that the characteristic surface diffusion length (**49**) must be shorter than a few lattice parameters to account for this. Note that an investigation limited to data on the mesoscale step kinetics would have concluded that the growth mechanism is direct incorporation.

A relevant question is: why do the energetics of the system select the surface diffusion mechanism over the direct incorporation? This question can only be addressed with the molecular-level data available for the system. We note that when the surface diffusion mechanism operates, the energy barrier determined

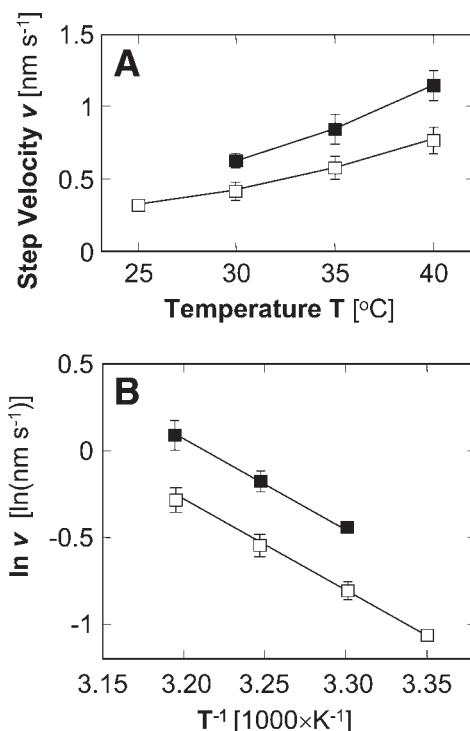


Fig. 13. Dependencies of step velocity  $v$  for growth of ferritin on temperature (A), and in Arrhenius coordinates (B). (■) at  $C/C_e = 4$ ; (□) at  $C/C_e = 3$ . For each point, positions of advancing steps were compared in sequences of molecular resolution *in situ* AFM images; approx 20 such determinations of  $v$  were averaged. The error bars represent the 90% confidence interval of the average. (From ref. 31.)

from the data in **Fig. 13** is a function of the barriers of the elementary steps of this mechanism and should be denoted as  $U_{\text{sum}}$ . As shown in refs. 79 and 95,  $U_{\text{sum}} = U_{\text{ads}} - U_{\text{desorb}} + U_{\text{SD}} + U_{\text{step}}$ , which are the barriers, respectively, for adsorption, desorption, surface diffusion, and incorporation into the step (see **Fig. 14**). Since the energy effect of one intermolecular bond of ferritin should be equal to that of apoferritin,  $\phi \approx 3k_B T = 7.4$  kJ/mol (25), we can safely assume that for adsorption – desorption on a (111) f.c.c. surface,  $U_{\text{ads}} - U_{\text{desorb}} = DH_{\text{ads}} = -3\phi = -22$  kJ/mol. When interactions between the adsorbed molecules are ignored, the lowest possible value of  $U_{\text{SD}}$  occurs when only one bond is broken on passage between two adsorption sites; hence,  $U_{\text{SD}} \geq \phi$ . This yields  $U_{\text{step}} \leq 44$  kJ/mol, similar to the ADP value (95). Since an equal number of bonds, three, are created during adsorption and incorporation into the step, we can roughly assume  $U_{\text{ads}} \approx U_{\text{step}}$ . Thus, the highest barrier encountered by a

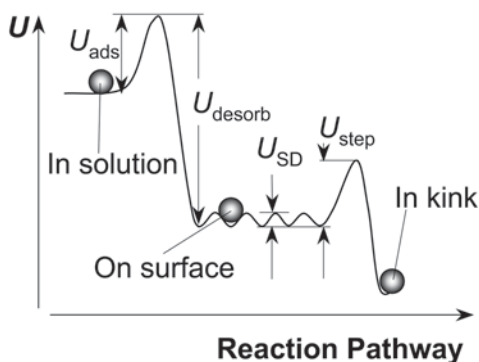


Fig. 14. Energy landscape of surface diffusion mechanism. For notations, see the text. (Modified from **ref. 109.**)

molecule en route to the kink is  $\leq 44$  kJ/mol. For direct incorporation into kinks, for which all of the six bonds are created simultaneously,  $U_{\text{kink}} \sim U_{\text{ads}} + U_{\text{step}} \approx 88$  kJ/mol. A crude estimate yields that this would make growth via this pathway slower by a factor of  $\sim \exp[(88,000 - 44,000)/RT] \sim 10^8$ .

## Acknowledgments

These studies would not have been possible without the dedicated work of my collaborators who took part in the original investigations reviewed here: S. T. Yau, K. Chen, and D. Petsev. I thank O. Galkin for critical comments on the manuscript. Generous financial support throughout the years has been provided by the Office of Biological and Physical Research, NASA.

## References

1. Theil, E. C. (1987) Ferritin: structure, gene regulation, and cellular function in animals, plants and microorganisms. *Annu. Rev. Biochem.* **56**, 289–315.
2. Massover, W. H. (1993) Ultrastructure of ferritin and apoferritin: a review. *Micron* **24**, 389–437.
3. Harrison, P. M. and Arosio, P. (1996) The ferritins: molecular properties, iron storage function and cellular regulation. *Biochim. Biophys. Acta* **1275**, 161–203.
4. Lawson, D. M., Artymiuk, P. J., Yewdall, S. J., et al. (1991) Solving the structure of human H ferritin by genetically engineering intermolecular crystal contacts. *Nature* **349**, 541–544.
5. Hempstead, P. D., Yewdall, S. J., Fernie, A. R., Lawson, D. M., Artymiuk, P. J., Rice, D. W., Ford, G. C., and Harrison, P. M. (1997) Comparison of the three dimensional structures of recombinant human H and horse L ferritins at high resolution. *J. Mol. Biol.* **268**, 424–448.
6. Taft, K. L., Papaefthymiou, G. C., and Lippard, S. J. (1993) A mixed-valent polyiron oxo complex that models the biomineralization of the ferritin core. *Science* **259**, 1302–1305.

7. Pereira, A. S., Tavares, P., Lloyd, S. G., Danger, D., Edmondson, D. E., Theil, E. C., and Huynh, B. H. (1997) Rapid and parallel formation of Fe<sup>3+</sup> multimers, including a trimer, during H-type subunit ferritin mineralization. *Biochemistry* **36**, 7917–7927.
8. Gider, S., Awschalom, D. D., Douglas, T., Mann, S., and Chaparala, M. (1995) Classical and quantum magnetic phenomena in natural and artificial ferritin proteins [see comments]. *Science* **268**, 77–80.
9. Yang, D. and Nagayama, K. (1995) Permeation of small molecules into the cavity of ferritin as revealed by proton nuclear magnetic resonance relaxation. *Biochem. J.* **307**, 253–256.
10. Yau, S. T., Petsev, D. N., Thomas, B. R., and Vekilov, P. G. (2000) Molecular-level thermodynamic and kinetic parameters for the self-assembly of apoferritin molecules into crystals. *J. Mol. Biol.* **303**, 667–678.
11. Hansma, P. K., Cleveland, J. P., Radmacher, M., et al. (1994) Tapping mode atomic force microscopy in liquids. *Appl. Phys. Lett.* **64**, 1738–1740.
12. Noy, A., Sanders, C. H., Vezenov, D. V., Wong, S. S., and Lieber, C. M. (1998) Chemically sensitive imaging in tapping mode by chemical force microscopy: relationship between phase lag and adhesion. *Langmuir* **14**, 1508–1511.
13. Durbin, S. D. and Carlson, W. E. (1992) Lysozyme crystal growth studied by atomic force microscopy. *J. Crystal Growth* **122**, 71–79.
14. Durbin, S. D., Carson, W. E., and Saros, M. T. (1993) In situ studies of protein crystal growth by atomic force microscopy. *J. Phys. D: Appl. Phys.* **26**, B128–B132.
15. Hillier, P. E., Manne, S., Hansma, P. K., and Gratz, A. J. (1993) Atomic force microscope: a new tool for imaging crystal growth processes. *Faraday Discuss.* **95**, 191–197.
16. Gratz, A. J., Hillner, P. E., and Hansma, P. K. (1993) Step dynamics and spiral growth on calcite. *Geochim. Cosmochim. Acta* **57**, 491–495.
17. Malkin, A. J., Land, T. A., Kuznetsov, Y. G., McPherson, A., and DeYoreo, J. J. (1995) Investigation of virus crystal growth mechanism by in situ atomic force microscopy. *Phys. Rev. Lett.* **75**, 2778–2781.
18. McPherson, A., Malkin, A. J., and Kuznetsov, Y. G. (1995) The science of macromolecular crystallization. *Structure* **3**, 759–768.
19. Malkin, A. J., Kuznetsov, Y. G., Land, T. A., DeYoreo, J. J., and McPherson, A. (1996) Mechanisms of growth of protein and virus crystals. *Nat. Struct. Biol.* **2**, 956–959.
20. Ng, J. D., Kuznetsov, Y. G., Malkin, A. J., Keith, G., Giege, R., and McPherson, A. (1997) Visualization of RNA crystal growth by atomic force microscopy. *Nucleic Acids Res.* **25**, 2582–2588.
21. De Yoreo, J. J., Land, T. A., and Dair, B. (1994) Growth morphology of vicinal hillocks on the {101} face of KH<sub>2</sub>PO<sub>4</sub>: from step flow to layer-by-layer growth. *Phys. Rev. Lett.* **73**, 838–841.
22. Land, T. A., DeYoreo, J. J., and Lee, J. D. (1997) An in-situ AFM investigation of canavalin crystallization kinetics. *Surf. Sci.* **384**, 136–155.

23. Yip, C. M. and Ward, M. D. (1996) Atomic force microscopy of insulin single crystals: direct visualization of molecules and crystal growth. *Biophys. J.* **71**, 1071–1078.
24. Yip, C. M., DePhelippis, M. R., Frank, B. H., Brader, M. L., and Ward, M. D. (1998) Structural and morphological characterization of ultralente insulin crystals by atomic force microscopy: evidence of hydrophobically driven assembly. *Biophys. J.* **75**, 1172–1179.
25. Yau, S. T., Thomas, B. R., and Vekilov, P. G. (2000) Molecular mechanisms of crystallization and defect formation. *Phys. Rev. Lett.* **85**, 353–356.
26. Lin, H., Yau, S. T., and Vekilov, P. G. (2003) Dissipating step bunches during crystallization under transport control. *Phys. Rev. E* **67**, 0031606.
27. Giesen-Seibert, M., Jentjens, R., Poensgen, M., and Ibach, H. (1993) Time dependence of step fluctuations on vicinal copper (111) surfaces investigated by tunneling microscopy. *Phys. Rev. Lett.* **71**, 3521–3524.
28. Poensgen, M., Wolf, J., Frohn, J., Giesen, M., and Ibach, H. (1992) Step dynamics on Ag(111) and Cu(100) surfaces. *Surf. Science* **274**, 430–440.
29. Kitamura, N., Lagally, M. G., and Webb, M. B. (1993) Real-time observations of vacancy diffusion on Si(001)-(2×2) by scanning tunneling microscopy. *Phys. Rev. Lett.* **71**, 2081–2085.
30. Swartzentruber, B. S., Mo, Y. W., Kariotis, R., Lagally, M. G., and Webb, M. B. (1990) Direct determination of site and kink energies of vicinal Si(001). *Phys. Rev. Lett.* **65**, 1913–1916.
31. Chen, K. and Vekilov, P. G. (2002) Evidence for the surface diffusion mechanism of solution crystallization from molecular-level observations with ferritin. *Phys. Rev. E* **66**, 021606.
32. Choi, S. C. (1978) *Introductory Applied Statistics in Science*, Prentice Hall, Englewood Cliffs, NJ.
33. Vekilov, P. G., Alexander, J. I. D., and Rosenberger, F. (1996) Nonlinear response of layer growth dynamics in the mixed kinetics-bulk transport regime. *Phys. Rev. E* **54**, 6650–6660.
34. Gliko, O., Booth, N. A., Rosenbach, E., and Vekilov, P. G. (2002) Phase-shifting interferometry for the study of the step dynamics during crystallization of proteins. *Crystal Growth Design* **2**, 381–385.
35. Gliko, O., Booth, N. A., and Vekilov, P. G. (2002) Step bunching in a diffusion-controlled system: phase-shifting interferometry investigation of ferritin. *Acta Crystallogr. Sect. D* **58**, 1622–1627.
36. Gliko, O. and Vekilov, P. G. (2002) Spatio-temporal step patterns during crystal growth in a transport controlled system. *J. Phys. Chem.* **106**, 11,800–11,804.
37. Petsev, D. N., Thomas, B. R., Yau, S. T., and Vekilov, P. G. (2000) Interactions and aggregation of apoferritin molecules in solution: effects of added electrolytes. *Biophys. J.* **78**, 2060–2069.
38. Fredericks, W. J., Hammonds, M. C., Howard, S. B., and Rosenberger, F. (1994) Density, thermal expansivity, viscosity and refractive index of lysozyme solutions at crystal growth concentrations. *J. Crystal Growth* **141**, 183–192.



39. Muschol, M. and Rosenberger, F. (1995) Interaction in undersaturated and supersaturated lysozyme solutions: static and dynamic light scattering results. *J. Chem. Phys.* **103**, 10,424–10,432.
40. Petsev, D. N., Chen, K., Gliko, O., and Vekilov, P. G. (2003) Diffusion-limited kinetics of the solution-solid phase transition of molecular substances. *Proc. Natl. Acad. Sci. USA* **100**, 792–796.
41. Sun, S. F. (1994) *Physical Chemistry of Macromolecules*, John Wiley & Sons, New York.
42. Stranski, I. N. (1928) Zur Theorie des Kristallwachstums. *Z. Phys. Chem.* **136**, 259–278.
43. Stranski, I. N. and Kaischew, R. (1934) Über den Mechanismus des Gleichgewichtes kleiner Kriställchen. I. *Z. Phys. Chem.* **B26**, 100–113.
44. Kaischew, R. and Stranski, I. N. (1937) Über die Thomson-Gibbs'sche Gleichung bei Kristallen. *Z. Phys. Chem.* **B35**, 427–432.
45. Eisenberg, D. and Crothers, D. (1979) *Physical Chemistry with Applications to Life Sciences*, Benjamin/Cummins, Menlo Park, NJ.
46. Berry, P. S., Rice, S. A., and Ross, J. (2000) *Physical Chemistry*, Oxford University Press, New York.
47. Hill, T. L. (1986) *Introduction to Statistical Thermodynamics*, New York.
48. Volmer, M. (1939) *Kinetik der Phasenbildung*, Steinkopff, Dresden, Germany.
49. Burton, W. K., Cabrera, N., and Frank, F. C. (1951) The growth of crystals and equilibrium structure of their surfaces. *Philos. Trans. R. Soc. Lond. Ser. A* **243**, 299–360.
50. Chernov, A. A. (1984) *Modern Crystallography III, Crystal Growth*, Springer, Berlin.
51. Williams, E. D. and Bartelt, N. C. (1991) Thermodynamics of surface morphology. *Science* **251**, 393–400.
52. Chernov, A. A., Rashkovich, L. N., Yamlinski, I. V., and Gvozdev, N. V. (1999) Kink kinetics, exchange fluxes, 1D “nucleation” and adsorption on the (010) face of orthorhombic lysozyme crystals. *J. Phys.:Condens. Matter* **11**, 9969–9984.
53. Teng, H. H., Dove, P. M., Orme, C. A., and De Yoreo, J. J. (1998) Thermodynamics of calcite growth: baseline for understanding biomineral formation. *Science* **282**, 724–727.
54. Kuipers, L., Hoogeman, M., and Frenken, J. (1993) Step dynamics on Au(110) studied with a high-temperature, high-speed scanning tunneling microscope. *Phys. Rev. Lett.* **71**, 3517–3520.
55. Swartzentruber, B. S. (1998) Fundamentals of surface step and island formation mechanisms. *J. Crystal Growth* **188**, 1–10.
56. Petsev, D. N., Thomas, B. R., Yau, S.-T., Tsekova, D., Naney, C., Wilson, W. W., and Vekilov, P. G. (2001) Temperature-independent solubility and interactions between apoferritin monomers and dimers in solution. *J. Crystal Growth* **232**, 21–29.
57. Atkins, P. (1998) *Physical Chemistry*, Freeman, New York.

58. Israelachvili, J. N. (1995) *Intermolecular and Surface Forces*, Academic, New York.
59. Eaton, W. A., Munoz, V., Thompson, P. A., Chan, C. K., and Hofrichter, J. (1997) Submillisecond kinetics of protein folding. *Curr. Opin. Struct. Biol.* **7**, 10–14.
60. Tanford, C. (1980) *The Hydrophobic Effect: Formation of Micelles and Biological Membranes*, John Wiley & Sons, New York.
61. Eisenberg, D. and Kauzmann, W. (1969) *The Structure and Properties of Water*, Oxford, New York, University Press.
62. Dunitz, J. D. (1994) The entropic cost of bound water in crystals and biomolecules. *Nature* **264**, 670.
63. Li, M., Nadarajah, A., and Pusey, M. L. (1999) Growth of (101) faces of tetragonal lysozyme crystals: determination of the growth mechanism. *Acta Cryst. Sect. D* **55**, 1012–1022.
64. Li, M., Nadarajah, A., and Pusey, M. L. (1999) Determining the molecular-growth mechanisms of protein crystal faces by atomic force microscopy. *Acta Cryst. Sect. D* **55**, 1036–1045.
65. Nadarajah, A. and Pusey, M. L. (1997) Growth mechanism of the (110) face of tetragonal lysozyme crystals. *Acta Cryst. Sect. D* **53**, 524–534.
66. Alfonso, C., Bermond, J. M., Heyraud, J. C., and Metois, J. J. (1992) The meandering of steps and the terrace width distribution on clean Si(111). *Surf. Sci.* **262**, 371–381.
67. Bartelt, N. C., Einstein, T. L., and Williams, E. D. (1990) The influence of step-step interactions on step wandering. *Surf. Sci. Lett.* **240**, L591–L598.
68. Ihle, T., Misbah, C., and Pierre-Louis, O. (1998) Equilibrium step dynamics of vicinal surfaces revisited. *Phys. Rev. B* **58**, 2289–2309.
69. Pimpinelli, A., Villain, J., Wolf, D. E., Metois, J. J., Heyraud, J. C., Elkinari, I., and Uimin, G. (1993) Equilibrium step dynamics on vicinal surfaces. *Surf. Sci.* **295**, 143–153.
70. Kuipers, L., Hoogeman, M. S., and Frenken, J. W. M. (1995) Step and kink dynamics on Au(110) and Pb(111) studied with a high-speed STM. *Phys. Rev. B* **52**, 11,387–11,397.
71. Chernov, A. A. (1961) The spiral growth of crystals. *Sov. Phys. Uspekhi* **4**, 116–148.
72. Chernov, A. A. and Komatsu, H. (1995) Topics in crystal growth kinetics, in *Science and Technology of Crystal Growth* (van der Eerden, J. P. and Bruinsma, O. S. L., eds.), Kluwer Academic, Dordrecht, The Netherlands, pp. 67–80.
73. Smoluchowski, M. (1916) Drei Vorträge über Diffusion, Brownsche Bewegung und Koagulation von Kolloidteilchen. *Physik Z.* **17**, 557–585.
74. Eyring, H., Lin, S. H., and Lin, S. M. (1980) *Basic Chemical Kinetics*, John Wiley & Sons, New York.
75. Neilsen, A. E. (1967) Nucleation in aqueous solutions, in *Crystal Growth* (Peiser, S., ed.), Pergamon, Oxford, UK, pp. 419–426.

76. Kahlweit, M. (1969) Nucleation in liquid solutions, in *Physical Chemistry* vol. VII (Eyring, H., ed.), Academic, New York, pp. 675–698.
77. Walton, A. G. (1969) Nucleation in liquids and solutions, in *Nucleation* (Zettlemoyer, A. C., ed.), Marcel Dekker, New York, pp. 225–307.
78. Chernov, A. A. and Komatsu, H. (1995) Principles of crystal growth in protein crystallization, in *Science and Technology of Crystal Growth* (van der Eerden, J. P. and Bruinsma, O. S. L., eds.), Kluwer Academic, Dordrecht, The Netherlands, pp. 329–353.
79. Gilmer, G. H., Ghez, R., and Cabrera, N. (1971) An analysis of combined volume and surface diffusion processes in crystal growth. *J. Crystal Growth* **8**, 79–93.
80. van der Eerden, J. P. (1994) Crystal growth mechanisms, in *Handbook of Crystal Growth* vol. 1a (Hurle, D., ed.), North Holland, Amsterdam, pp. 307–476.
81. De Yoreo, J. J. (2001) Eight years of AFM: what has it taught us about solution crystal growth, in *Thirteenth International Conference on Crystal Growth* (Hibiya, T., Mullin, J. B., and Uwaha, M., eds.), Elsevier, Kyoto, Japan.
82. Petsev, D. N. and Vekilov, P. G. (2000) Evidence for non-DLVO hydration interactions in solutions of the protein apoferritin. *Phys. Rev. Lett.* **84**, 1339–1342.
83. Israelachvili, J. and Pashley, R. (1982) The hydrophobic interaction is long range decaying exponentially with distance. *Nature* **300**, 341,342.
84. Israelachvili, J. and Wennerstrom, H. (1996) Role of hydration and water structure in biological and colloidal interactions. *Nature* **379**, 219–225.
85. von Smoluchowski, M. (1918) Versuch einer matematischen theorie der koagulationskine. *Z. Phys. Chem.* **92**, 129–135.
86. Zeldovich, J. B. (1942) On the theory of formation of new phases: cavitation. *J. Theor. Exp. Phys. (USSR)* **12**, 525–538.
87. Zwanzig, R. (2001) *Nonequilibrium Statistical Mechanics*, Oxford University Press, Oxford, UK.
88. Frenkel, J. (1932) *Phys. J. USSR* **1**, 498–510.
89. Broughton, J. Q., Gilmer, G. H., and Jackson, K. A. (1982) Crystallization rates of a Lennard-Jones liquid. *Phys. Rev. Lett.* **49**, 1496–1500.
90. Garcia-Ruiz, J. M. and Moreno, A. (1997) Growth kinetics of protein single crystals in the gel acupuncture technique. *J. Crystal Growth* **178**, 393–401.
91. Hou, W. B., Kudryavtsev, A. B., Bray, T. L., DeLucas, L. J., and Wilson, W. W. (2001) Real time evolution of concentration distribution around tetragonal lysozyme crystal: case study in gel and free solution. *J. Crystal Growth* **232**, 265–272.
92. Malkin, A. J., Kuznetsov, Y. G., Glanz, W., and McPherson, A. (1996) Atomic force microscopy studies of surface morphology and growth kinetics of thaumatin crystallization. *J. Phys. Chem.* **100**, 11,736–11,743.
93. Vekilov, P. G., Thomas, B. R., and Rosenberger, F. (1998) Effects of convective solute and impurity transport on protein crystal growth. *J. Phys. Chem.* **102**, 5208–5216.
94. Vekilov, P. G., Kuznetsov, Y. G., and Chernov, A. A. (1992) Interstep interaction in solution growth; (101) ADP face. *J. Crystal Growth* **121**, 643–655.
95. Vekilov, P. G., Kuznetsov, Y. G., and Chernov, A. A. (1992) The effect of temperature on step motion: (101) ADP face. *J. Crystal Growth* **121**, 44–52.

96. Borchers, H., ed. (1955) Landoldt-Bornstein numerical data and functional relationships, in *Materials Values and Mechanical Behaviour of Nonmetals*, vol. IV, pt. II, Springer, Berlin.
97. Bauser, E. (1994) Atomic mechanisms in semiconductor liquid phase epitaxy, in *Handbook of Crystal Growth*, vol. 3b (Hurle, D. T. J., ed.), North Holland, Amsterdam, pp. 879–911.
98. Ehrlich, G. and Hudda, F. G. (1966) Asymmetric capture at steps. *J. Chem. Phys.* **44**, 1039–1052.
99. Braun, N., Tack, J., Fischer, M., Bacher, A., Bachmann, L., and Weinkauf, S. (2000) Electron microscopic observations on protein crystallization: adsorption layers, aggregates and crystal defects. *J. Crystal Growth* **212**, 270–282.
100. Bostanov, V., Staikov, G., and Roe, D. K. (1975) Rate of propagation of growth layers on cubic crystal faces in electrocrystallization of silver. *J. Electrochem. Soc.* **122**, 1301–1305.
101. Vekilov, P. G., Monaco, L. A., and Rosenberger, F. (1995) Facet morphology response to non-uniformities in nutrient and impurity supply. I. Experiments and interpretation. *J. Crystal Growth* **156**, 267–278.
102. Lin, H., Petsev, D. N., Yau, S. T., Thomas, B. R., and Vekilov, P. G. (2001) Lower incorporation of impurities in ferritin crystals by suppression of convection: modeling results. *Crystal Growth Design* **1**, 73–79.
103. Reviakine, I., Georgiou, D. K., and Vekilov, P. G. (2003) Capillarity effects on the crystallization kinetics: insulin. *J. Am. Chem. Soc.* **125**, 11,684–11,693.
104. Malkin, A., Kuznetsov, Y., and McPherson, A. (1997) An in situ AFM investigation of catalase crystallization. *Surf Sci.* **393**, 95–107.
105. Vekilov, P. G., Ataka, M., and Katsura, T. (1993) Laser Michelson interferometry investigation of protein crystal growth. *J. Crystal Growth* **130**, 317–320.
106. Vekilov, P. G. and Rosenberger, F. (1996) Dependence of lysozyme growth kinetics on step sources and impurities. *J. Crystal Growth* **158**, 540–551.
107. Kuznetsov, Y. G., Konnert, J., Malkin, A. J., and McPherson, A. (1999) The advancement and structure of growth steps on thaumatin crystals visualized by atomic force microscopy at molecular resolution. *Surf. Sci.* **440**, 69–80.
108. Vekilov, P. G. and Chernov, A. A. (2002) The physics of protein crystallization, in *Solid State Physics* vol. 57 (Ehrenreich, H. and Spaepen, F., eds.), Academic, New York, pp. 1–147.
109. Bennema, P. (1967) Analysis of crystal growth models for slightly supersaturated solutions. *J. Crystal Growth* **1**, 278–286.

## Nanostructured Systems for Biological Materials

Esther H. Lan, Bruce Dunn, and Jeffrey I. Zink

### Summary

The sol-gel process is a chemical technique for immobilizing biomolecules in an inorganic, transparent matrix. The dopant biomolecules reside in an interconnected mesoporous network and become part of the nanostructured architecture of the entire material. In this chapter, we review the sol-gel immobilization approach and discuss how it leads to the stabilization of a number of proteins against aggressive chemical and thermal environments. We also review the sensor applications of this material that result from having analyte molecules diffuse through the matrix and reach the immobilized biomolecule.

**Key Words:** Sol-gel; aerogel; xerogel; sol-gel encapsulation; butyrylcholinesterase; creatine kinase; cortisol.

### 1. Introduction

There are a variety of methods for immobilizing biomolecules including entrapment, microencapsulation, covalent attachment, and adsorption. In this chapter, we review our work involving an immobilization process that has features common to both entrapment and microencapsulation. In this method, biomolecules are encapsulated in the pores of an inorganic material that is prepared using sol-gel chemistry, one of a variety of “soft chemistry” approaches in which solid-state materials are synthesized at room temperature under mild conditions. The resulting matrix constitutes a nanostructured material. It possesses two phases: there is a network of solid colloidal particles arranged with interpenetrating mesoporosity that is filled with the solvent phase. The dopant biomolecules reside in the mesoporous network, in a solvent-rich environment, and become part of the nanostructured architecture of the entire material.

The nanostructure of the material has a profound effect on properties. When the molecular sizes of the dopant molecules are less than the average pore

From: *Methods in Molecular Biology*, vol. 300:  
*Protein Nanotechnology, Protocols, Instrumentation, and Applications*  
Edited by: T. Vo-Dinh © Humana Press Inc., Totowa, NJ

diameter, these molecules (usually of low molecular weight) are mobile within the solvent-filled pores. The high molecular weight biomolecules, however, are confined within the cages formed by the developing sol-gel nanostructure. The biomolecules have local mobility, but no translational mobility. A diverse range of proteins has been immobilized in sol-gel-derived materials including globular and membrane-bound proteins, enzymes, and other biosystems. In almost all cases, the chemistry of the dopant biomolecule in the nanostructured environment is analogous to that in solution, with the subtle difference being that now the system involves a porous inorganic matrix. The properties of both the solid phase and the solution phase are evident in the sol-gel-encapsulated materials, and frequently it is the interactions of the dopant biomolecules with the sol-gel matrix that determine the reaction pathways for a particular biological system.

In this chapter, we first review the basic aspects of sol-gel chemistry and their application to the encapsulation of biomolecules. Then we review the details of protein stabilization, one of the most significant properties provided by sol-gel encapsulation. After reviewing the different types of stabilization, we detail the remarkable encapsulation properties of creatine kinase. Finally, we present recent research in our laboratory in which we have combined organic and biological molecules in sol-gel matrices to achieve greater functionality. The latter work is directed at sensor applications.

### **1.1. The Sol-Gel Process**

The sol-gel process is a low-temperature synthesis technique for producing amorphous inorganic solids, i.e., glasses. A sol is generally defined as a colloidal solution with particles of <100 nm suspended in a liquid, whereas a gel is a semisolid colloid. One of the distinct advantages of the sol-gel process is that glasses can be prepared at room temperature with excellent homogeneity and high purity. The glasses fabricated using this process are highly porous, so that selected dopants can be incorporated into the porous glass matrix. Moreover, it is possible to make these sol-gel materials optically transparent, so that they can be used as sensors. There has long been considerable interest in making transparent glasses that contain various organic and inorganic dopants, and the ability to make glasses at low temperatures is extremely useful because many dopants undergo irreversible changes at high temperatures.

In the sol-gel process, a colloidal sol forms from the hydrolysis and polycondensation of metalorganic precursors. The precursors are typically metal alkoxides,  $M(OR)_n$ , in which OR is  $OCH_3$  (methoxy),  $OC_2H_5$  (ethoxy), and so on. The most commonly used alkoxides for making silica-based materials are tetramethoxysilane (TMOS) ( $OR = OCH_3$ ) and tetraethoxysilane ( $OR = OC_2H_5$ ), because hydrolysis and condensation can be well controlled. An over-

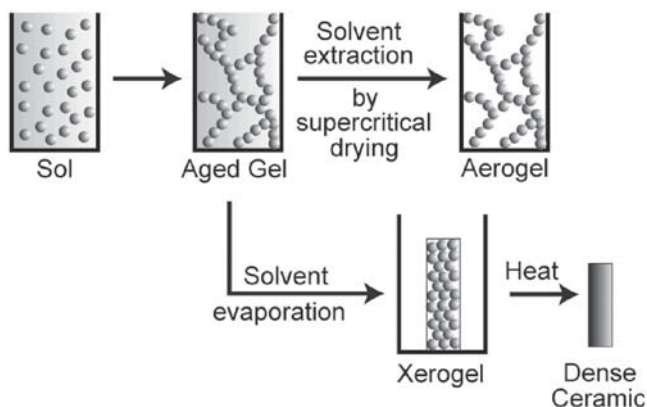


Fig. 1. Overview of sol-gel processing in fabrication of wet (aged) gels, aerogels, and xerogels. (Adapted from **ref. 4.**)

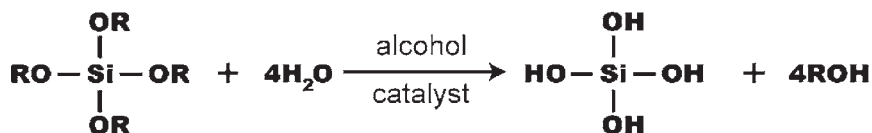
view of the sol-gel process can be divided into the following steps: sol formation, gelation, drying, and densification, as illustrated in **Fig. 1**. As can be seen, the method of drying (solvent evaporation or extraction) can greatly affect the final matrix structure, pore size, and pore volume. The resulting material can be in the form of a monolith, thin film, or fiber, depending on the fabrication method.

In the hydrolysis reaction, the precursor (metal alkoxide) is mixed with water in the presence of a catalyst. An alcohol can be added as a cosolvent since alkoxides and water are immiscible, but both are soluble in ethanol and methanol. The hydrolysis step leads to formation of silanol groups ( $\text{Si-OH}$ ), which are intermediates, and alcohol as a byproduct. Hydrolysis is followed by condensation, as silanol groups condense to form siloxane groups ( $\text{Si-O-Si}$ ), releasing alcohol or water as a byproduct. Note that the hydrolysis and condensation reactions occur concurrently. Both of these reactions are depicted in **Fig. 2**.

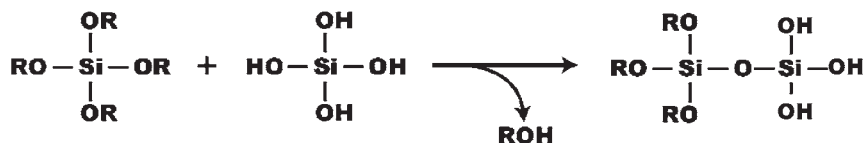
A variety of factors affect the hydrolysis and condensation reactions and final microstructure of the gel. These factors include the solution pH, temperature, nature of alkoxide, amount of alcohol, ratio of alkoxide to water to alcohol, and type of catalyst used. The relative rates of hydrolysis and condensation determine the final structure of the gel (**1**), and there have been extensive studies on the effect of these factors on the polymerization reactions and final microstructure (**1–5**). The final structure of the glass can be controlled to a large degree by controlling the hydrolysis and condensation reactions. A fast hydrolysis and slow condensation favor formation of more highly condensed silicate polymers, whereas slow hydrolysis and fast condensation result in less



### Hydrolysis of metal alkoxides:



### Condensation:



where R can be H or any alkyl group, CH<sub>3</sub>, CH<sub>2</sub>CH<sub>3</sub>, etc.

Fig. 2. Hydrolysis and condensation reactions in sol-gel processing.

condensed polymers (2). The ratio of water to metal alkoxide, in which  $r_w = [\text{water}]/[\text{metal alkoxide}]$ , can also be used to tailor the gel network. For  $r_w < 4$ , the structure is primarily that of linear polymers, whereas if  $r_w > 4$ , the structure is primarily crosslinked, three-dimensional (3D) networks (5). Another critical factor controlling gel structure is pH. Silicate sols prepared under acidic conditions (acid catalyzed) form primarily linear polymers, and on drying, a dense gel forms with relatively small pores (**Fig. 3A**). On the other hand, silicate sols prepared under basic conditions (base catalyzed) form primarily branched clusters, and on drying, the gel network is more open, with a larger pore network (**Fig. 3B**) (3).

As hydrolysis and condensation polymerization reactions continue, the sol becomes a gel. The gelation point is defined as the time at which the silica matrix forms a continuous solid (6) or the point at which the material can support a stress elastically (1). After the sol-to-gel transition, there is a sharp increase in viscosity and the polymer structure becomes rigid. The sol-to-gel transition is irreversible, with essentially no change in volume. The material after gelation is composed of two distinct phases: amorphous silica particles (5–10 nm in diameter) and an interstitial liquid phase (6). This material is described as a “wet” gel, as long as the interstitial liquid phase (i.e., pore liquid) is maintained. As the gel ages, polycondensation continues, increasing the connectivity of the network, and its structure and properties continue to change.

It is possible to prepare sol-gel materials in a wide range of geometries, from bulk monolith materials (dimensions >1 mm) to thin films (thickness of

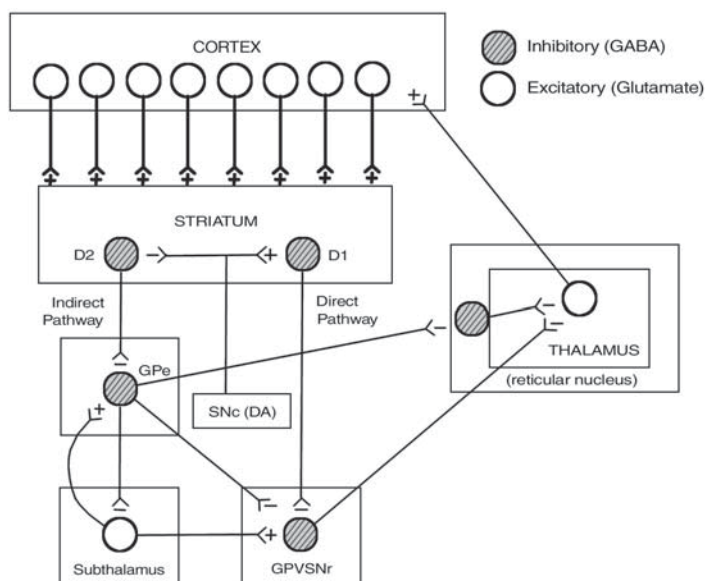


Fig. 3. (A) Acid catalysis in sol-gel processing of silica leads to primarily linear polymers, and upon drying, a dense gel forms with relatively small pores. (B) Base catalysis in sol-gel processing of silica leads to primarily branched clusters, and on drying, the gel network is more open, with a larger pore network. (Adapted from **ref. 3.**)

tens to hundreds of nanometers). In the fabrication of these materials, if the pore liquid is allowed to evaporate, the gel begins to dry. The drying process is accompanied by considerable weight loss and volume shrinkage. Typically, gel drying is accomplished under ambient conditions. As the interstitial liquid evaporates from the pores, there are large capillary forces, causing pore collapse and material shrinkage. The dried gel is described as a “xerogel” (see **Fig. 1**). For silica sol-gel materials, xerogels are typically  $\leq 50\%$  of their original volume. Alternatively, solvent extraction can be performed using supercritical drying. This supercritically dried gel is called an “aerogel” (see **Fig. 1**). Under these conditions, pore liquid can be removed without pore collapse and subsequent shrinkage, resulting in a lightweight material with relatively large pore sizes and high pore volume.

## 2. Encapsulation of Biomolecules in Sol-Gel Matrices

The encapsulation of proteins and other biomolecules in sol-gel-derived glasses is an intriguing research area because it involves placing delicate biological molecules with well-defined structures in the pores of a matrix that is, by comparison, hard and disordered. The encapsulation of biomolecules in sol-

gel-derived glasses has been ongoing for more than a decade, with the first research in this area published in 1990 (7). The first studies of biodoped sol-gel materials reported alkaline phosphatase encapsulated in base-catalyzed silica, and the resulting sol-gel material was opaque with low enzymatic activity. In subsequent work, a sol-gel synthesis route that was able to produce optically transparent monoliths was developed (8). The proteins copper-zinc superoxide dismutase, cytochrome-*c* (cyt-*c*), and myoglobin were immobilized in the pores of transparent silica glasses, and the biological function and activity of these proteins were monitored spectroscopically. Since that time, a variety of biomolecules, including antibodies, enzymes, other proteins, and even bacteria, have been successfully immobilized in sol-gel matrices, many of which were optically transparent. Research results have been described and summarized in a number of published reviews (9–12).

One of the most important aspects of using the sol-gel method to encapsulate biomolecules is that the method can be tailored so as not to denature the proteins. That is, the sol-gel-encapsulated biomolecules retain their characteristic reactivities and spectroscopic properties. Some important factors that need to be considered include pH, pore size, and the presence of alcohol. A synthesis protocol that has been successfully used to fabricate optically transparent and biologically active silica gels is illustrated in **Fig. 4**. The protocol consists of (1) mixing alkoxide precursor(s) with water in the presence of dilute acid (catalyst); (2) sonicating the mixture to fully hydrolyze the alkoxide, usually in the absence of alcohol; (3) adding a pH-buffered solution containing the biomolecule of interest; and (4) casting the solution into the desired geometry and shape (monolith or thin film). In this protocol, alcohol concentration is minimized, and the pH of the biomolecule-doped sol is raised to a level that ensures the viability of the biomolecule.

Using the synthesis protocol described in **Fig. 4**, gelation occurs typically between 2 and 30 min. The gelation time depends on a variety of factors, including ionic strength of the buffer, concentration of biomolecules, addition of alcohol (or lack thereof), and temperature. To lengthen the gelation time, one can reduce the buffer ionic strength, reduce the biomolecular concentration, add alcohol, and/or lower the temperature. Another means to lengthening the gelation time is to include an additive such as polyethylene glycol (PEG) or polyvinyl alcohol. We have successfully extended the gelation time for sols synthesized with the TMOS precursor and biological buffers by tens of minutes or even hours by altering the synthesis conditions. After gelation, polycondensation continues, and the gel network grows in mechanical stability and strength. Retaining sol-gel materials in the wet gel state can be easily accomplished by storing the materials in sealed containers so that pore liquid is not

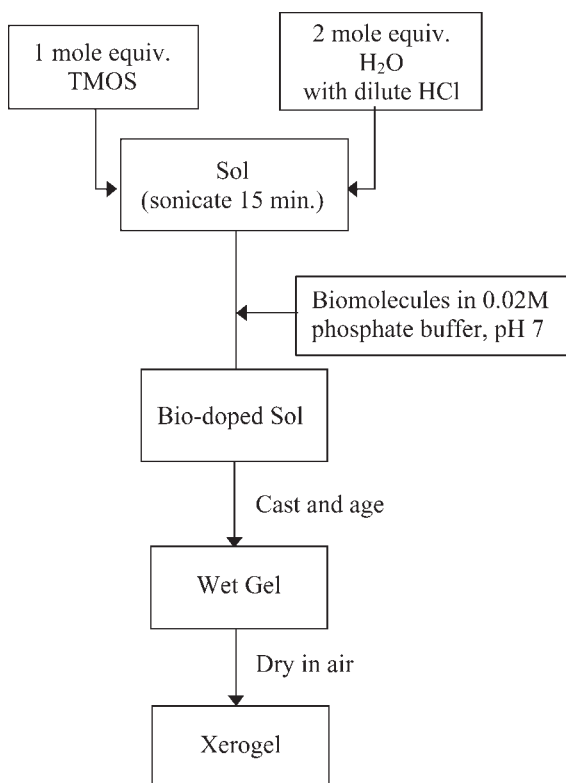


Fig. 4. Synthesis protocol for immobilization of biomolecules in transparent sol-gel silica glasses. TMOS = tetramethylorthosilicate or tetramethoxysilane.

allowed to evaporate. If a xerogel is desired, evaporation should be performed slowly so as to prevent cracking in the matrix.

### 3. Stabilization of Biomolecules by Sol-Gel Encapsulation

One of the most important benefits of sol-gel immobilization that has emerged is the ability to stabilize biomolecules through encapsulation (13–17). There is indirect evidence that a biomolecule designs a self-specific pore as the silicate network forms around it during sol-gel hydrolysis and condensation reactions (15). There is a silicate “cage” that defines the pore according to the size and shape requirements of the biomolecule. Consequently, the biomolecule prevents its surrounding pore from collapsing while the matrix protects the biomolecule from unfolding and aggregation. In addition, the matrix prevents contact with proteases or microorganisms. In the following sections, we review the enhanced stability in terms of thermal, storage, and chemical stability for biomolecules as a result of sol-gel immobilization.

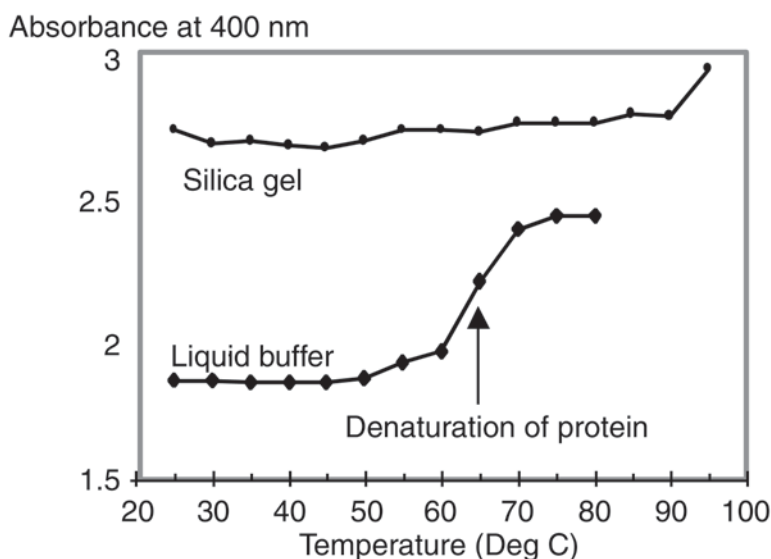


Fig. 5. Thermal denaturation profile of cyt-*c* in liquid buffer and in a wet silica gel shows a substantial improvement in thermal stability as a result of sol-gel encapsulation. The transition temperature,  $T_m$ , is approx 65°C in liquid buffer but at least 90°C in the wet gel. (Reproduced from **Ref. 15** with permission.)

### 3.1. Thermal Stability

A marked improvement in thermal stability as a result of sol-gel encapsulation has been observed for three flavoprotein oxidases: glucose oxidase, lactate oxidase (LOX), and glycolate oxidase (GLyOX) (**13**). When encapsulated in xerogels, where smaller pore sizes were likely to enhance electrostatic interactions between the silicate and the protein, glucose oxidase was reported to be stabilized by immobilization. The extent of the stabilization was impressive; the half-life at 63°C was increased 200-fold on sol-gel encapsulation compared to enzyme in water. Interestingly, LOX and GLyOX were initially destabilized by sol-gel encapsulation. The three oxidases have different *pI* values: 3.8 for glucose oxidase, 4.6 for LOX, and 9.6 for GLyOX. It was apparent that electrostatic interactions between the enzyme and charged silicate matrix caused the destabilization since both LOX and GLyOX experienced a dramatic improvement in stability *if* the enzymes were electrostatically complexed with a base *prior* to sol-gel immobilization. Once electrostatically complexed, LOX experienced a 150-fold increase and GLyOX a 100-fold increase in enzyme half-life at 63°C compared to enzyme in water (**13**). These findings show the benefit of increased stability as a result of encapsulation, yet they also under-

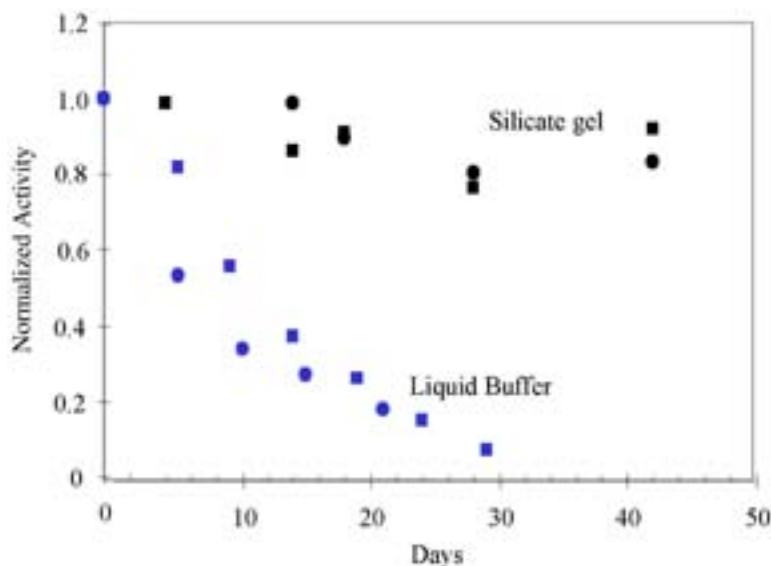


Fig. 6. Normalized enzyme activity of butyrylcholinesterase as a function of storage time at 4°C shows that activity was substantially better retained in the sol-gel-immobilized enzyme than in the free enzyme (enzyme in buffer solution).

score the importance of electrostatic interactions between biomolecules with the highly charged surfaces of the sol-gel-derived matrix.

Increased thermal stability has also been observed in the heme protein cyt-*c* (15). Thermally induced unfolding of proteins in solution, in general, exhibits a sharp transition over a small temperature range, and the transition point at which half of the molecules are denatured is termed  $T_m$ . For cyt-*c*, the unfolding can be monitored using optical absorption of the heme Soret band. As shown in Fig. 5,  $T_m$  for cyt-*c* in liquid buffer was approx 65°C, whereas  $T_m$  for cyt-*c* in the sol-gel matrix was at least 90°C. It is possible that the sol-gel-encapsulated cyt-*c* was stable beyond 90°C because boiling of the buffer led to gel cracking at approx 95°C.

### 3.2. Storage Stability

Whereas thermal stability studies were conducted at elevated temperatures, the storage stability of proteins and enzymes was evaluated at or below room temperature. In experiments with cholinesterase, sol-gel-immobilized enzyme retained enzymatic activity during storage significantly better than enzyme in buffer solution. Figure 6 shows the activity of butyrylcholinesterase as a function of storage time at 4°C. As seen, the sol-gel-encapsulated enzyme lost almost no activity after 40 d of storage, whereas the enzyme in solution experienced a steady decline in activity during the same period.

### 3.3. Chemical Stability

Improved chemical stability is also possible. Studies have shown that antibodies immobilized via the sol-gel route better retained their ability to bind antigen after exposure to acid compared with antibodies immobilized via traditional surface attachment. After exposure to 0.01 *N* HCl (pH approx 2.0) for 24 h, sol-gel-encapsulated antitrinitrotoluene (anti-TNT) antibodies experienced essentially no loss in their ability to bind TNT, whereas antibodies immobilized via traditional surface attachment experienced >30% loss (16).

Results of the chemical stability of cyt-*c* in alcohol indicated that this heme protein partially denatured (unfolded) in buffered solutions with <60 vol% methanol (MeOH), with the degree of denaturation increasing as the amount of methanol increased. Furthermore, at concentrations >60 vol% MeOH, aggregation occurred, depending on the buffer. When encapsulated in silicate gels, however, protein denaturation (unfolding) owing to MeOH was fully reversible; the protein reverted to its native form when samples were soaked in pure buffer. Moreover, protein aggregation did *not* occur for the sol-gel-immobilized protein even when the gels were soaked in pure methanol for several weeks (18). The results confirm that isolating biomolecules in the pores of the matrix prevented aggregation and at least partially constrained the mobility of the protein.

### 3.4. Other Considerations

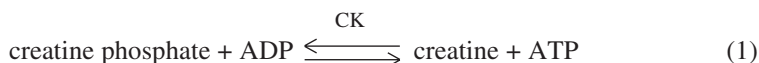
The collective results have shown that, at least for some proteins and enzymes, sol-gel encapsulation has led to a marked improvement in stability. The exact mechanism is not yet understood, although isolation of biomolecules in the pores of the matrix prevents protein aggregation, a known denaturation pathway (19). Moreover, the matrix may protect the protein from unfolding. It has also been demonstrated that additives present in sol-gel matrices may help stabilize encapsulated biomolecules. For example, PEG added to sol-gel matrices enhanced the activity in lipase (20) and the half-life of trypsin, and acid phosphatase (21). There are, however, important considerations if the sol-gel route is selected. The first is the electrostatic interactions between the biomolecule, especially its “active site,” and the silicate matrix, because both are likely to be highly charged. Another consideration is that the observed rates of reactions are likely to be lower owing to diffusion limitations. Finally, depending on the size of the immobilized biomolecule, the effect of protein crowding may result in destabilization of the protein conformation (22).

## 4. Case Study of Stabilization Owing to Sol-Gel Encapsulation: Enzyme Creatine Kinase

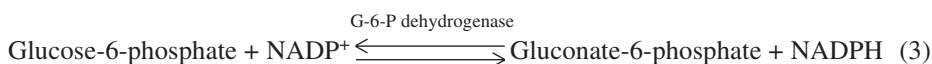
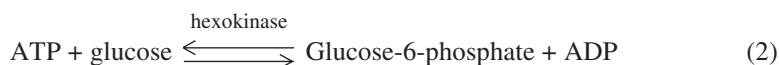
We present here a case study of the stabilization of an enzyme as a direct result of sol-gel encapsulation. The enzyme creatine kinase (CK) is a key



enzyme in cellular energetics. It exists as a dimer held together by hydrogen bonds, with a total mol wt of 82 kDa. The enzyme catalyzes the following reaction:



To monitor the enzyme activity (rate of reaction), it is extremely difficult to measure the generation of adenosine triphosphate (ATP) directly. As an alternative, the generation of ATP can be measured by coupled enzyme reactions using the enzymes hexokinase and glucose-6-phosphate dehydrogenase (G-6-P dehydrogenase), as described in the following reactions:



When these three reactions are coupled, the rate of formation of NADPH is proportional to the rate of formation of ATP in a linear fashion. The concentration of NADPH can be measured by its absorbance at 340 nm. In the experimental testing of the enzymatic activity of CK, the CK enzyme was the only component immobilized in the sol-gel silica matrix. The solid CK-doped gel was then immersed in a liquid buffer containing the required substrates creatine phosphate, glucose, adenosine 5'-diphosphate (ADP), and  $\text{NADP}^+$ ; the required enzymes hexokinase and glucose-6-phosphate dehydrogenase; and a thiol activator, *N*-acetylcysteine. The results showed that the CK enzyme was stabilized owing to encapsulation in sol-gel silica and that there were unusual temperature effects on its activity (17). These features are discussed in the following sections.

#### 4.1. Long-Term Storage at Room Temperature

Silica gel monoliths with immobilized CK were prepared and stored in near-neutral pH buffer solution at room temperature for as long as 6 mo. As a comparison, CK in liquid buffer was also stored under the same conditions. **Figure 7** shows the relative activity of the enzyme in the sol-gel matrix compared with in liquid buffer. The activity in both the sol-gel monoliths and in solution was normalized to the initial rate. As seen in **Fig. 7**, the encapsulated enzyme retained 90% of its activity after about 5 mo. Thereafter, the activity began to decline and decreased to 50% of its maximum value after 6 mo. By contrast, the activity of CK in liquid buffer dropped to approx 50% of its original activity after only 10 d of storage at room temperature.

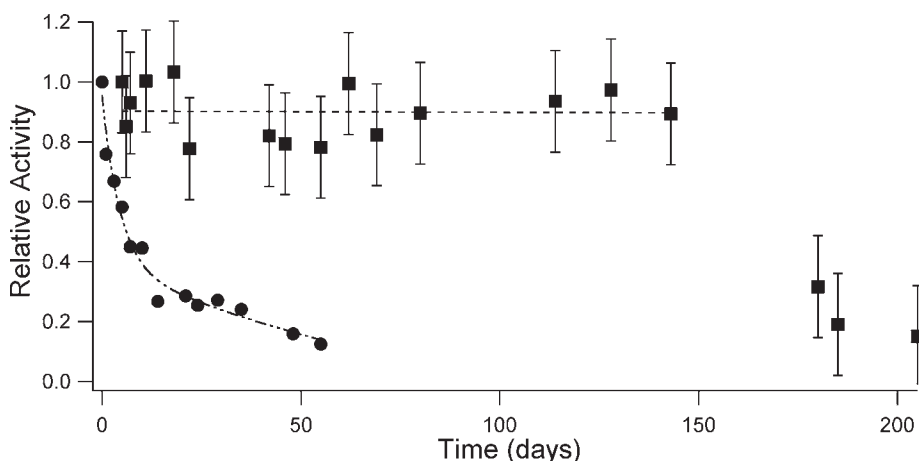


Fig. 7. Relative activity as a function of time for CK when stored at room temperature in pH 7.0 HEPES buffer solution (●) and in sol-gel silica (■) shows that the enzyme had enhanced storage stability as a result of sol-gel encapsulation. The maximum activities per milligram of enzyme for the solution and sol-gel were  $0.2$  and  $7 \times 10^{-5}$ , respectively. (Reproduced from **Ref. 17** with permission.)

#### 4.2. Effect of Elevated Temperature and Increase in Activity Following Heating

CK in sol-gel monoliths and buffer solutions were stored at 37, 47, and 60°C for varying lengths of time to evaluate enzyme stability. At the elevated temperatures, for both monoliths and solution, there was a faster loss in CK activity as the temperature was increased. There was, however, significantly higher activity for the sol-gel-encapsulated CK compared with CK in solution at all temperatures. For example, at 60°C, no activity was observed in the CK solution after 1 h, whereas the sol-gel-immobilized enzyme still retained 50% activity after 5 h of heating. Similarly, at 47°C, activity in the solution dropped to essentially zero after about 1 d, whereas the sol-gel-immobilized enzyme retained 50% of its activity after 5 d of heating. Furthermore, the activity remained at approx 50% of its maximum value after 12 d. **Figure 8** shows a comparison of CK activity in both sol-gel monolith and buffered solution after heating at 47°C.

One unusual and unexpected observation from our results was that CK sol-gel monoliths that were heated exhibited a sharp initial *increase* in activity, which was then followed by a gradual decrease. This phenomenon was observed at all elevated temperatures (i.e., 37, 47, and 60°C). The increase in

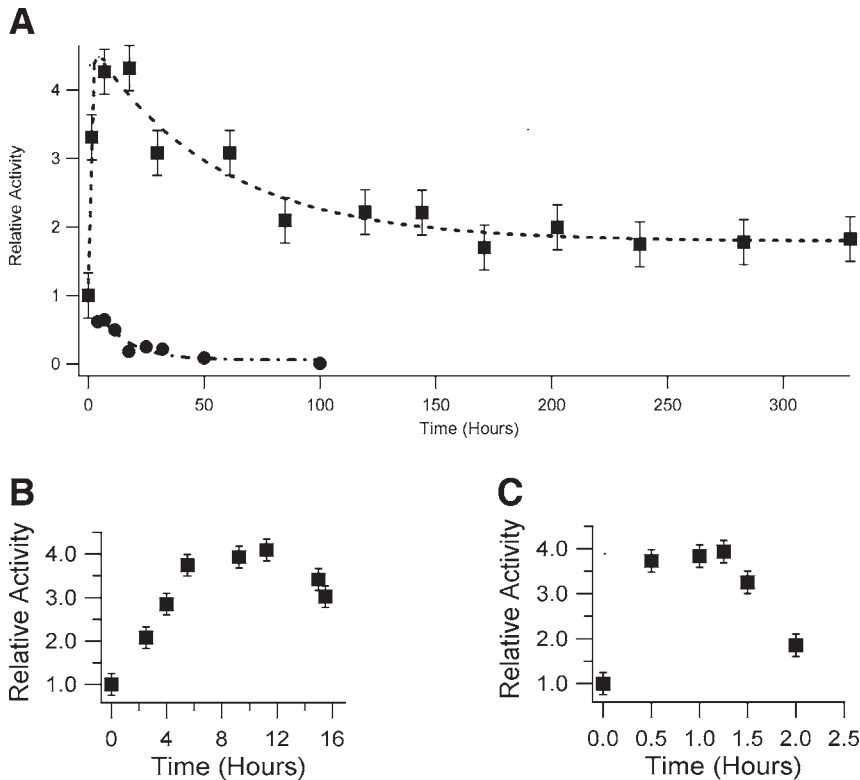


Fig. 8. (A) Relative activity as a function of time for CK heated at 47°C in solution (●) and in sol-gel silica (■) shows that the activity in solution decreases immediately, but the activity in sol-gel silica increases before it decreases. (B) Activity vs time as a function of heat treatment at 47°C in a CK-doped wet silica gel. (C) Activity vs time as a function of heat treatment at 60°C in a CK-doped wet silica gel. (Reproduced from Ref. 17 with permission.)

activity as a result of heat treatment is shown in **Fig. 8**. The apparent activation energy for the activity enhancement was  $2.6 \pm 0.6$  kJ/mol. The activity increased generally about fourfold as a result of heat treatment. Note that heating the enzyme in liquid buffer did not cause an increase in the activity but, rather, caused an immediate decrease.

The average pore sizes of the sol-gel monoliths were determined using nitrogen adsorption and desorption isotherms. The pore size, pore volume, and surface area as a function of temperature are listed in **Table 1**. There was a relatively narrow pore size distribution in which 80% of the pore volume was within  $\pm 10\%$  of the average pore size. The nitrogen adsorption and desorption

**Table 1**  
**Pore Size as Function of Heating for Sol-Gel Monoliths**

Heating condition	Average pore size (nm)	Pore volume (m <sup>2</sup> /g)	Surface area (m <sup>2</sup> /g)
Room temperature	8.3	2.0	900
37°C for 3 h	8.8	1.9	780
47°C for 3 h	9.3	2.2	800
60°C for 3 h	10.9	2.2	730

data indicate that there were heat-induced changes in the silica matrix. The pore size increased as a function of temperature, which offers a materials-based explanation for the increase in enzyme activity in the heat-treated samples. With a larger pore size, the enzyme was able to rearrange to a more desirable conformation. In the synthesis of the sol-gel monoliths, gelation occurred on the order of minutes. Although the material experienced a liquid-to-solid transition at gelation, polycondensation continued to occur. As the matrix forms around the enzyme, the enzyme molecules may not be trapped in their native state. By enlarging the pores, the process of enzyme rearrangement becomes more favorable. Maintaining an elevated temperature for an extended period of time, however, induces enzyme denaturation, resulting in a decrease in activity. There are, therefore, two opposing effects, which may explain why the initial activity increased with short-term heating whereas the activity decreased with long-term heating.

To monitor the structural changes and maintenance of the structural integrity of CK, circular dichroism (CD) spectra were taken. CD utilizes circularly polarized light to probe the secondary structure ( $\alpha$  helices and  $\beta$  sheets) of proteins. CD spectra are sensitive to conformational changes and are a common spectroscopic method for studying protein structure (23). The CD spectra of CK in buffer solution and sol-gel monoliths (with and without heat treatment) were obtained, as shown in **Fig. 9 (17)**. The CD spectrum of the enzyme in liquid buffer, which represents the properties of unconfined enzyme in its native state, exhibited a minimum at 220 nm. The CD spectrum of sol-gel-encapsulated enzyme (no heat treatment) showed a minimum at 225 nm, indicating that a large fraction of the enzyme was in a different, nonnative conformational state. On heating the monoliths for 3 h at 37, 47, or 60°C, however, the CD minimum of 220 nm was restored. We can infer from these results that, with heating, the encapsulated enzyme was able to revert to a more native conformation (i.e., the secondary structure of the enzyme became more like that of the enzyme in solution). Enabling the enzyme structure to match more

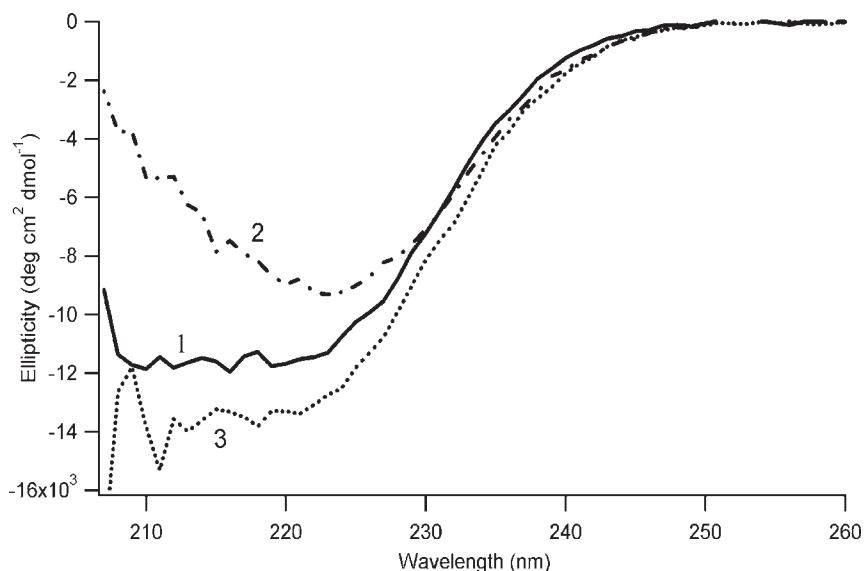


Fig. 9. CD spectra of CK in (1) a freshly made solution, (2) an unheated sol-gel silica monolith, and (3) a monolith heated for 3 h at 47°C. The spectra suggest that the enzyme is confined in a nonnative conformation on initial encapsulation, but after heating the monolith for 3 h, the enzyme conformation becomes more like that of free enzyme (enzyme in solution). (Reproduced from **Ref. 17** with permission.)

closely its native state may explain why there was an initial increase in its activity.

In a second set of experiments, we monitored the thermal transitions of CK by monitoring changes in the ellipticity at 220 nm (characteristic wavelength) as a function of temperature. Ellipticity is an indication of the  $\alpha$ -helical content, and protein unfolding is indicated by an increase in ellipticity. As seen in **Fig. 10 (17)**, on heating the monolith and solution to 90°C, the encapsulated enzyme did not fully denature like the enzyme in solution. The midpoint temperature of the unfolding transition, termed  $T_m$ , was 75°C for the CK in solution, whereas  $T_m$  could not be determined for the monoliths because the enzyme did not unfold completely. In other words, the sol-gel-immobilized CK did not unfold to the same extent as CK in solution. When the temperature was cooled to 20°C, there was virtually no change in ellipticity, indicating that in both cases protein unfolding was not reversible. Nevertheless, these results clearly show that when immobilized in the pores of the sol-gel matrix, the enzyme was able to better withstand thermal denaturation.

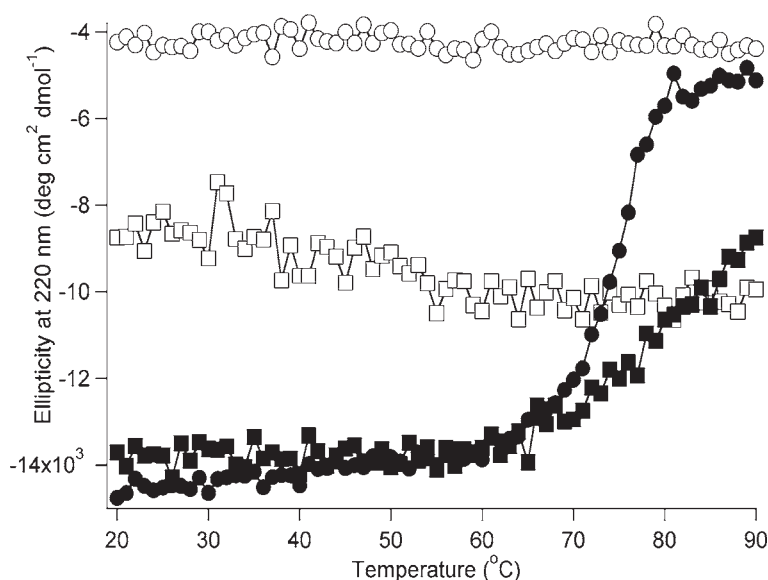


Fig. 10. Thermal unfolding transition of CK in monoliths and in solution monitored by ellipticity at 220 nm: (●) solution during heating; (○) solution during cooling; (■) sol-gel monolith during heating; (□) sol-gel monolith during cooling. The sol-gel-encapsulated enzyme unfolded to a lesser extent compared with free enzyme (enzyme in solution), but in both cases the denaturation was irreversible. The sample was heated at 2°C/min from 20 to 90°C and then cooled from 90 to 20°C. (Reproduced from Ref. 17 with permission.)

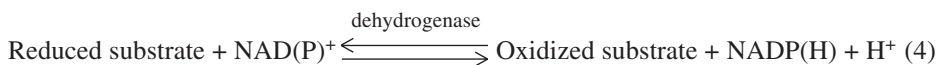
### 4.3. Matrix–Enzyme Surface Interactions

The body of work with CK suggests that the enzyme may act as a pore template during the sol-gel process; that is, the matrix forms around the enzyme during gelation. As to the mechanism of stabilizing CK using sol-gel immobilization, it is plausible to assume that there are favorable interactions between the enzyme and the silica matrix. The outer surface of CK contains more positively charged patches than negative patches, as shown by electron density calculations (24). When sol-gel silica is immersed in buffer of near-neutral pH, the silica walls are negatively charged, because the *pI* of silica is approx 2 (4). Therefore, electrostatic attraction between the silica matrix surface and the enzyme surface is expected. Although the outer surface of CK interacts significantly with the matrix, the active site of the enzyme does not. The active site of CK is embedded in the interior of the enzyme and experiences essentially no interaction with the silica. It is important that the active site not be altered or blocked in order to retain maximum enzyme activity. The combination of exte-

rior structural stabilization caused by enzyme–pore wall electrostatic interactions and the absence of significant perturbations of the active site in a cleft that is spatially separated from the surface results in a stabilized and active biomaterial (17).

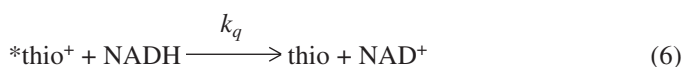
## 5. Photochemical Coenzyme Regeneration in Sol-Gel Matrices

For many enzymes, a cofactor (also referred to as a coenzyme) is required, and this is true of dehydrogenase enzymes, which require NAD or NADP as a cofactor (Eq. 4):



In optical sensing, enzyme activity in dehydrogenase enzymes can be measured conveniently because the reduced form of the coenzyme, NADH or NADPH, fluoresces. Sensors based on this reaction, however, cannot operate continuously without a renewable supply of the coenzyme. We have shown in recent work that a photooxidizer can be incorporated into the sol-gel matrix, along with the enzyme and cofactor, to regenerate by oxidation the reduced cofactor (25). The organic dye thionine was selected as the photooxidizing agent, because it is stable in the silica matrix, retains its excited-state properties, and is compatible and unreactive with the other components.

Thionine,  $\text{thio}^+$ , absorbs light in the visible range with  $\lambda_{\text{max}} = 596 \text{ nm}$  (Eq. 5). In solution, excited thionine,  $^*\text{thio}^+$ , oxidizes NADH (Eq. 6). As NADH is oxidized, the fluorescence emission of the excited thionine is quenched. Therefore, by exciting thionine ( $\text{thio}^+$ ) using visible light (596 nm), it is possible to regenerate  $\text{NAD}^+$ .



The enzyme isocitrate dehydrogenase (ICDH) was used as a model dehydrogenase in this research because the Gibbs free energy of the ICDH reaction strongly favors the oxidation of isocitrate, thereby reducing experimental complications from back reactions (26). ICDH catalyzes the oxidation of isocitrate to  $\alpha$ -ketoglutarate using  $\text{NADP}^+$  as the electron acceptor (Eq. 7):



The scheme for photochemical oxidation of NADPH by thionine coupled to the enzymatic reaction of ICDH is shown in Fig. 11.



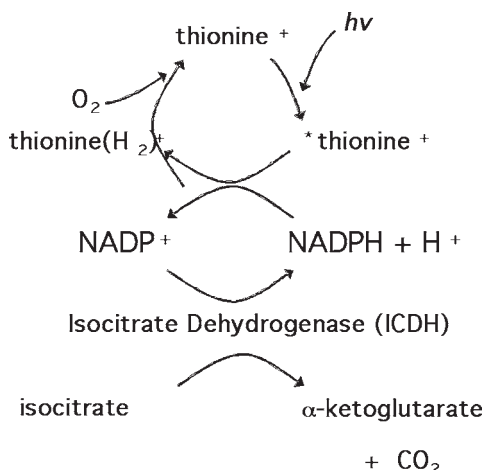


Fig. 11. Enzyme cofactor regeneration for continuous isocitrate oxidation. The photochemical oxidation of NADPH by thionine is coupled to enzymatic oxidation of isocitrate by ICDH. When thionine is excited, it reacts with NADPH to reform  $\text{NADP}^+$ . The regenerated  $\text{NADP}^+$  becomes available for another isocitrate oxidation. (Reproduced from **Ref. 25** with permission.)

We first established that NADPH undergoes a reaction similar to NADH with thionine (**Eq. 6**) in that the fluorescence of thionine is quenched as it oxidizes NADPH. The fluorescence emission spectra of thionine in buffer solution and encapsulated in wet silica gels showed essentially no difference, indicating that the optical properties of the thionine photooxidizer itself were not altered as a result of encapsulation. When NADPH-doped silica gels and NADPH buffer solutions were exposed to excited thionine, fluorescence quenching was observed in both the gels and solution. **Figure 12** shows the NADPH concentration, expressed as a percentage of the initial NADPH concentration, over time in the presence of excited thionine ( $\text{*thio}^+$ ). The oxidation of NADPH can be described by a decay constant,  $k_{\text{oxidize}}$ , and the rate of oxidation of NADPH was about one order of magnitude slower in the sol-gel matrix.  $k_{\text{oxidize}}$  was  $8.8(\pm 1.0) \times 10^{-4} \text{ s}^{-1}$  in sol-gel silica, compared with  $9.8(\pm 2.9) \times 10^{-3} \text{ s}^{-1}$  for buffer solution. The slower observed rate in the sol-gel material may be explained by mass transport limitations. NADPH was immobilized in the gel, whereas thionine was added at time 0 and needed time to diffuse through the pores of the network.

The photochemical oxidation of NADPH can be coupled to the enzymatic oxidation of isocitrate by ICDH (**Fig. 11**). ICDH and thionine were coencapsulated in wet silica gels and incubated with  $\text{NADP}^+$ , and isocitrate was then

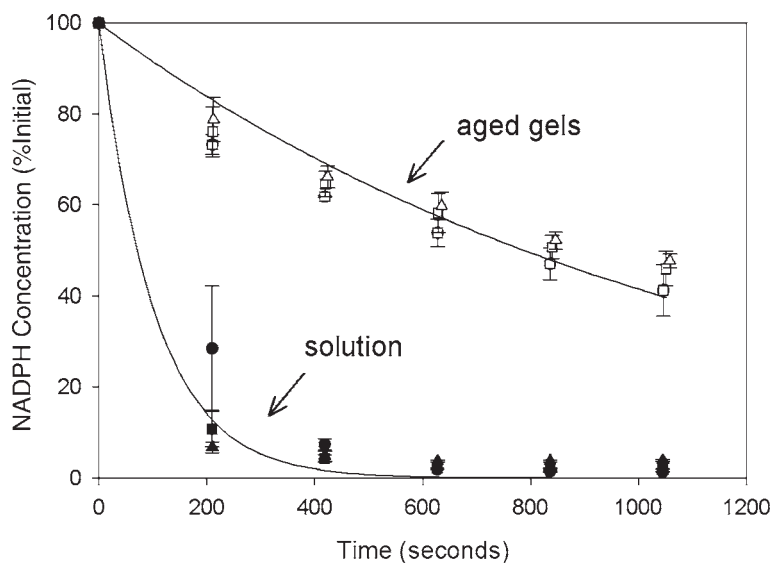


Fig. 12. Disappearance of NADPH during exposure to excited thionine in buffer solution and in wet silica gels. The NADPH concentration is expressed as a percentage of the initial NADPH concentration at time 0. Open symbols show the decrease in NADPH in wet gels, and closed symbols show the decrease in NADPH in solution. Three starting NADPH concentrations were used for each sample type: (○) wet gel, 120  $\mu\text{M}$  NADPH; (□) wet gel, 80  $\mu\text{M}$  NADPH; (△) wet gel, 40  $\mu\text{M}$ ; (●) buffer solution, 120  $\mu\text{M}$  NADPH; (■) buffer solution, 80  $\mu\text{M}$  NADPH; (▲) buffer solution, 40  $\mu\text{M}$  NADPH. The data for the six conditions were fit individually to a single exponential decay,  $y = 100e^{-bt}$ . The decay parameter,  $b$ , for the wet gels and the solution samples was  $8.8(\pm 1.0) \times 10^{-4} \text{ s}^{-1}$  and  $9.8(\pm 2.9) \times 10^{-3} \text{ s}^{-1}$ , respectively. (Reproduced from **Ref. 25** with permission.)

injected into the sample at different times. As shown in **Fig. 13**, at each injection of enzyme substrate, the ICDH reaction was observed by the production of NADPH, as indicated by an increase in its fluorescence. When thionine was excited, NADPH was oxidized, resulting in a decrease in its fluorescence. Moreover, the enzymatic reduction of  $\text{NADP}^+$  to NADPH by ICDH followed by the photochemical oxidation of NADPH to  $\text{NADP}^+$  by thionine can be cycled. We generated a calibration curve to correlate the NADPH produced as a function of isocitrate concentration and the curve was essentially linear (**Fig. 14**). The data presented in **Figs. 13** and **14** show that a photo-oxidizer can indeed regenerate the NADPH coenzyme, and that photochemical regeneration is possible in a bioactive solid-state silica glass (**25**). The collective results suggest that it is possible to utilize dehydrogenase enzymes as optical biosensors

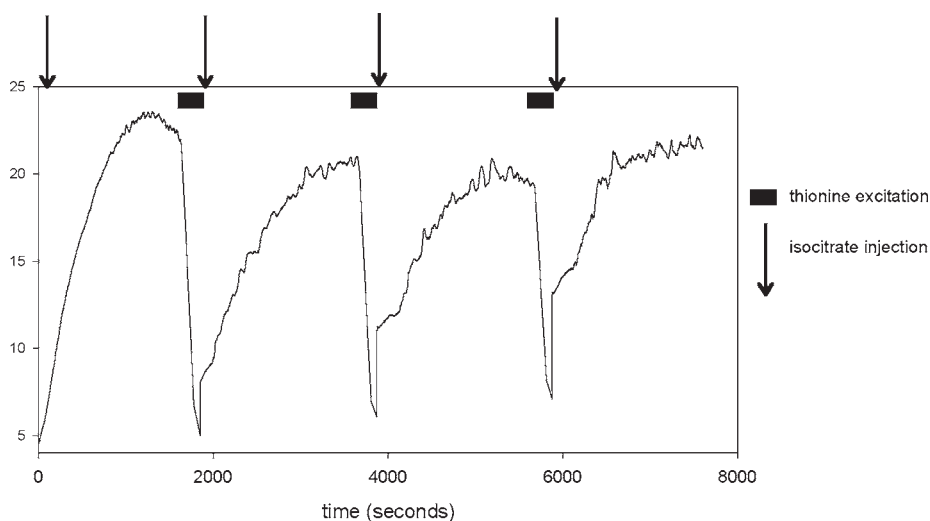


Fig. 13. Repeated ICDH reactions in a sol-gel silica monolith. ICDH, thionine, and  $\text{NADP}^+$  were encapsulated in a silica gel, and isocitrate was injected onto the gel at the times indicated by the arrows. To monitor the enzyme oxidation of isocitrate, the fluorescence at 460 nm was measured, which indicates generation of NADPH. Subsequently, thionine was excited (at the times indicated by the solid bars) to induce the oxidation of NADPH back to  $\text{NADP}^+$ . This process could be repeated for at least four cycles. (Reproduced from **Ref. 25** with permission.)

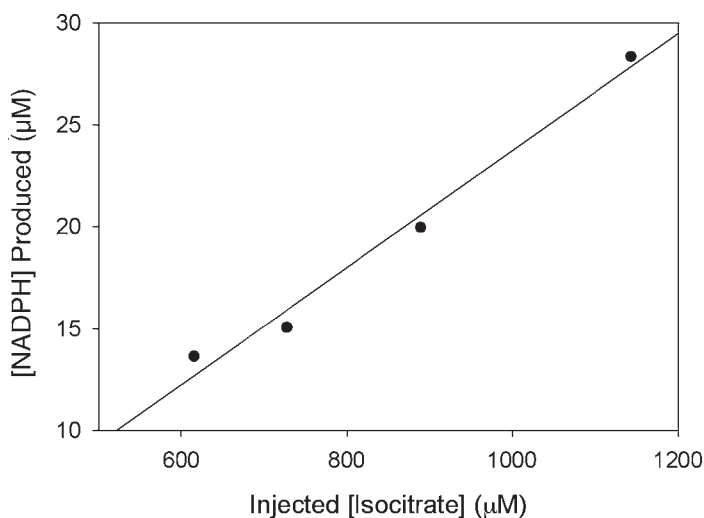


Fig. 14. Calibration curve generated from repeated measurements using the same ICDH-doped gel. The maximum NADPH concentration produced during each cycle is plotted as a function of isocitrate concentration, and a linear curve was observed. (Reproduced from **Ref. 25** with permission.)

without compromising the continuity of sensor function owing to depletion of coenzyme.

## 6. Biosensing Elements Using Biologically Active Sol-Gel Thin Films

The potential use of sol-gel-based materials as sensing elements has made these materials the subject of intensive study (27,28). Although it is possible to use monoliths, for biosensing applications, the use of thin films is preferred. The primary reason is that thin films have a reduced diffusion length for the target analyte, and, therefore, there is a greatly reduced response time, because diffusion distance varies with  $t^{1/2}$ . The sol-gel matrix has an interconnected network of pores and presents a tortuous path for diffusion of analytes. For thin films, there is an important interplay among porosity and pore size, diffusion coefficient, and response time (29).

Sol-gel thin films are usually deposited on substrates using either dip coating or spin coating. In dip coating, the thickness can be generally controlled by the withdrawal speed, and it is possible to fabricate coatings with excellent optical transparency. Moreover, it is possible to dip coat onto substrates with a variety of geometries, from planar substrates to optical fibers. If spin coating is used, the thickness can be tailored using the spin rate, and, again, films can have excellent optical transparency.

The fabrication of high-quality sol-gel thin films with functional and active biomolecules is by no means trivial. Generally, biomolecules prefer a near-neutral pH and low-alcohol environment. Under these conditions, the condensation reaction in sol-gel synthesis is accelerated, leading to rapid gelation. A major factor in thin film synthesis is that a reasonable gelation time is required, especially for dip coating. One of the most effective means not only to lengthen the gelation time, but also to lower the viscosity of the sol, is the addition of alcohol. Large and delicate proteins can be particularly sensitive to the presence of alcohol, but apparently some proteins, such as antibodies, still retain their biological function. The fabrication of reproducible thin films with uniform thickness is also necessary if these materials are to be used on a large scale. One advantage of sol-gel coatings is that by matching the coating material with the substrate (e.g., silica coatings on silica substrates), strong adhesion between coating and substrate can be attained.

We have successfully prepared biologically active thin films with immobilized antibodies. The encapsulation of antibodies in sol-gel matrices has been studied extensively (16,30–40) although only limited work has been performed with thin films. The synthesis protocol for thin films is similar to that for monoliths, except for the addition of methanol to the silica sol and buffered protein mixture. The thin films were deposited on glass substrates by dip coat-

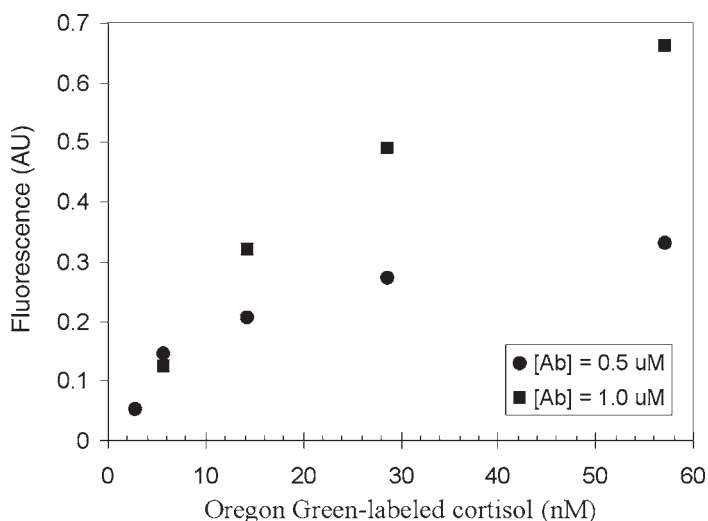


Fig. 15. Fluorescence signal as a function of Oregon Green–cortisol concentration for sol-gel silica thin films containing 0.5 or 1.0  $\mu\text{M}$  anticortisol antibody. The sol-gel-encapsulated antibodies retained their ability to bind antigen, and by increasing the antibody concentration, higher signals can be obtained. (Reproduced from **Ref. 41** with permission.)

ing. We encapsulated anticortisol antibodies in sol-gel silica thin films and used these materials as sensing elements in an immunoassay for cortisol (**41**). The antibody-doped thin films were of excellent quality and optical transparency, with a thickness of approx 1  $\mu\text{m}$  for films in the “wet” state, and a thickness of approx 0.5  $\mu\text{m}$  for films in the “dried” state. Although a significant amount of methanol was used (approx 30 vol%) in the dip-coating solution, the immobilized antibodies retained the ability to bind their target antigen (cortisol in this case). In our experiments, antibody-antigen binding was detected optically using fluorescent Oregon Green–labeled cortisol. Oregon Green is a derivative of fluorescein and experiences excitation and emission in the visible region (495 and 527 nm, respectively). As seen in **Fig. 15**, with a constant antibody concentration in the thin films, the fluorescence signal increased with increasing concentration of labeled antigen. Moreover, by raising the antibody concentration in the thin films, one can obtain higher optical signals.

Note that all experiments were conducted with “wet” films, in which pore sizes remain relatively large. When films were allowed to dry fully, no antibody-antigen binding could be observed. We conducted competitive immunoassays for cortisol using the anticortisol-doped silica thin films. In these immunoassays, in which labeled and unlabeled antigen compete for a fixed number of antibody molecules, the measured signal varies logarithmically with

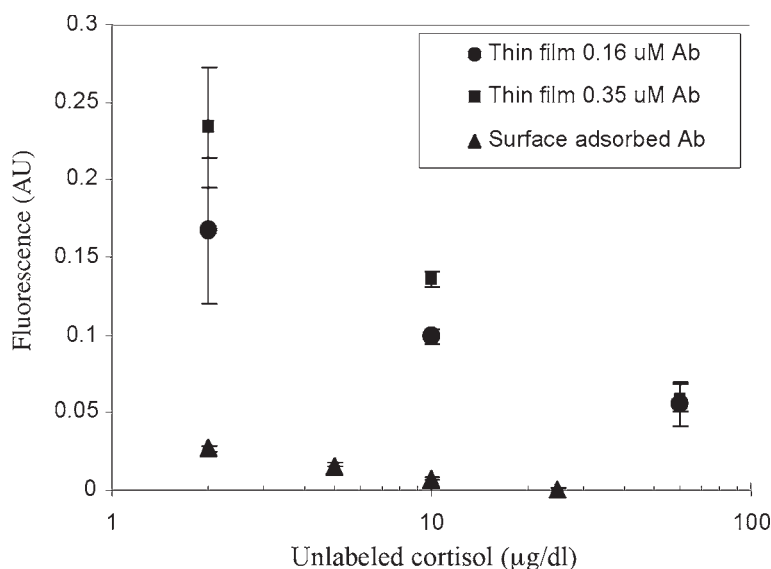


Fig. 16. Calibration curves from competitive immunoassays conducted with sol-gel silica thin films containing anticortisol and with surface-adsorbed anticortisol. With sol-gel encapsulation, we were able to obtain substantially higher signals because of the ability to immobilize a substantially higher number of biomolecules per unit area compared to traditional monolayer surface adsorption. (Reproduced from **Ref. 41** with permission.)

unlabeled antigen concentration, and the slope is negative (**42,43**). The competitive immunoassays with anticortisol sol-gel thin films exhibited the expected behavior; a calibration curve with a negative slope was obtained (**Fig. 16**). Moreover, with a higher antibody concentration in the thin film, higher signals were achieved.

When immobilizing biomolecules, one distinct advantage of sol-gel encapsulation is the ability to create 3D architectures. With traditional immobilization methods, such as surface adsorption or covalent attachment, monolayer coverage of the biomolecule is usually obtained. With sol-gel encapsulation, however, one can achieve a substantially higher number of biomolecules per unit area because of the 3D nature of the bioactive material. The total number of biomolecules immobilized depends on the thickness of the material. This feature was demonstrated by comparing competitive immunoassay results for anticortisol encapsulated in sol-gel thin films (approx 1  $\mu\text{m}$  thickness) and surface adsorbed on polystyrene. As seen in **Fig. 16**, the fluorescence signals from the sol-gel films were as much as 10 times higher than those measured using surface-adsorbed antibody.

Finally, there is a distinct advantage with thin films in terms of reduced response times. The immunoassay with anticortisol thin films (approx 1  $\mu\text{m}$  thickness) required an incubation of only 20 min, and experiments showed that a plateau in the signal was reached after approx 10 min (data not shown). When analogous immunoassays were performed with anticortisol-doped silica monoliths of 1-mm thickness, the required incubation time for the assay was at least 3 h. For biological assays, therefore, thin films are far more effective than monoliths because limitations owing to analyte diffusion through the porous matrix can be minimized.

## 7. Conclusion

Immobilization of biomolecules in sol-gel-derived matrices leads to a wide variety of bioactive materials. The flexible processing inherent in sol-gel synthesis and the ability to use chemical modifications are attributes that make sol-gel methods an attractive platform for biosensors. The prospect of using sol-gel immobilization to better retain the activity of enzymes and enhance the chemical and thermal stability of proteins makes these bioactive materials especially promising. Some important considerations for the widespread use of these materials in biosensing include the size limitations on target analytes, continuous biosensing, and incorporation into devices. With current synthesis procedures, relatively large biomolecules (e.g., proteins) are immobilized in the pores of the matrix, but small analytes diffuse through the porous network. For future applications, a nanostructured material that permits the diffusion of some large biomolecules and yet allows other large biomolecules to remain encapsulated in the pores would be highly desirable. The feasibility of using sol-gel-based biosensors for continuous sensing has not been adequately explored, because most research has been directed at demonstrating proof of concept. Future work directed at continuous monitoring, along with incorporating sol-gel-sensing elements into actual devices, will enable these materials to make a wide impact on biosensing technology.

## Acknowledgments

We greatly appreciate the contributions of Dr. Dorothy Nguyen, Dr. Jenna Rickus, Jing C. Zhou, James R. Lim, Maria H. Chuang, and Pauline Chang to the work described in this review. We also gratefully acknowledge support for this research from NSF (DMR 0103952 and DMR 0099862) and NASA (NAG9-1252). This work was also partially supported by the Center for Cell Mimetic Space Exploration, a NASA University Research, Engineering and Technology Institute, through award no. NCC 2-1364.



## References

1. Hench, L. L. and West, J. K. (1990) The sol-gel process. *Chem. Rev.* **90**, 33–72.
2. Brinker, C. J., Keefer, K. D., Schaeffer, D. W., and Ashley, C. S. (1982) Sol-gel transition in simple silicates. *J. Non-Cryst. Solids* **48**, 47–64.
3. Brinker, C. J. and Scherer, G. W. (1985) Sol-gel glass: gelation and gel structure. *J. Non-Cryst. Solids* **70**, 301–322.
4. Brinker, C. J. and Scherer, G. W. (1990) *The Physics and Chemistry of Sol-Gel Processing*, Academic, San Diego.
5. Sakka, S. (1982) Gel method for making glass, in *Treatise on Materials Science and Technology*, vol. 22, (Herman, H. and Tomozawa, M., eds.), Academic, New York, pp. 129–167.
6. Rickus, J. L., Dunn, B., and Zink, J. I. (2002) Optically based sol-gel biosensor materials, in *Optical Biosensors: Present and Future* (Ligler, F. S. and Rowe-Taitt, C. A., eds.), Elsevier Science, Amsterdam, The Netherlands, pp. 427–456.
7. Braun, S., Rappoport, S., Zusman, R., Avnir, D., and Ottolenghi, M. (1990) Biochemically active sol-gel glasses—the trapping of enzymes. *Mater. Lett.* **10**, 1–5.
8. Ellerby, L. M., Nishida, C. R., Nishida, F., Yamanaka, S. A., Dunn, B., Selverstone Valentine, J., and Zink, J. I. (1992) Encapsulation of proteins in transparent porous silicate-glasses prepared by the sol-gel method. *Science* **255**, 1113–1115.
9. Avnir, D., Braun, S., Lev, O., and Ottolenghi, M. (1994) Enzymes and other proteins entrapped in sol-gel materials [review]. *Chem. Mater.* **6**, 1605–1614.
10. Livage, J., Coradin, T., and Roux, C. (2001) Encapsulation of biomolecules in silica gels [review]. *J. Phys. Condensed Matter* **13**, R673–R691.
11. Gill, I. (2001) Bio-doped nanocomposite polymers: sol-gel bioencapsulates [review]. *Chem. Mater.* **13**, 3404–3421.
12. Zink, J. I., Valentine, J. S., and Dunn, B. (1994) Biomolecular materials based on sol-gel encapsulated proteins. *N. J. Chem.* **18**, 1109–1115.
13. Chen, Q., Kenausis, G. L., and Heller, A. (1998) Stability of oxidases immobilized in silica gels. *J. Am. Chem. Soc.* **120**, 4582–4585.
14. Heller, J. and Heller, A. (1998) Loss of activity or gain in stability of oxidases upon their immobilization in hydrated silica: significance of the electrostatic interactions of surface arginine residues at the entrances of the reaction channels. *J. Am. Chem. Soc.* **120**, 4586–4590.
15. Lan, E. H., Dave, B. C., Fukuto, J. M., Dunn, B., Zink, J. I., and Valentine, J. S. (1999) Synthesis of sol-gel encapsulated heme proteins with chemical sensing properties. *J. Mater. Chem.* **9**, 45–53.
16. Lan, E. H., Dunn, B., and Zink, J. I. (2000) Sol-gel encapsulated anti-trinitrotoluene antibodies in immunoassays for TNT. *Chem. Mater.* **12**, 1874–1878.
17. Nguyen, D. T., Smit, M., Dunn, B., and Zink, J. I. (2002) Stabilization of creatine kinase encapsulated in silicate sol-gel materials and unusual temperature effects on its activity. *Chem. Mater.* **14**, 4300–4306.
18. Miller, J. M., Dunn, B., Valentine, J. S., and Zink, J. I. (1996) Synthesis conditions for encapsulating cytochrome C and catalase in SiO<sub>2</sub> sol-gel materials. *J. Non-Cryst. Solids* **202**, 279–289.

19. Eggers, D. K. and Valentine, J. S. (2001) Molecular confinement influences protein structure and enhances thermal protein stability. *Protein Sci.* **10**, 250–261.
20. Kawakami, K. and Yoshida, S. (1995) Sol-gel entrapment of lipase using a mixture of tetramethoxysilane and methyltrimethoxysilane as the alkoxide precursor—esterification activity in organic media. *Biotechnol. Techniques* **9**, 701–704.
21. Shtelzer, S., Rappoport, S., Avnir, D., Ottolenghi, M., and Braun, S. (1992) Properties of trypsin and of acid-phosphatase immobilized in sol-gel glass matrices. *Biotechnol. Appl. Biochem.* **15**, 227–235.
22. Eggers, D. K. and Valentine, J. S. (2001) Crowding and hydration effects on protein conformation: a study with sol-gel encapsulated proteins. *J. Mol. Biol.* **314**, 911–922.
23. Schmid, F. X. (1990) *Protein Structure: A Practical Approach*, IRL Press, Oxford, UK.
24. Nayal, M., Hitz, B. C., and Honig, B. (1999) GRASS: a server for the graphical representation and analysis of structures. *Protein Sci.* **8**, 676–679.
25. Rickus, J. L., Chang, P. L., Tobin, A. J., Zink, J. I., and Dunn, B. (2004) Photochemical coenzyme regeneration in an enzymatically active optical material. *J. Phys. Chem. B.* **108**, 9325–9332.
26. Lehninger, A. L., Nelson, D. L., and Cox, M. M. (1993) *Principles of Biochemistry*, Worth Publishers, New York.
27. Maccraith, B. D., McDonagh, C., McEvoy, A. K., Butler, T., Okeeffe, G., and Murphy, V. (1997) Optical chemical sensors based on sol-gel materials—recent advances and critical issues. *J. Sol-Gel Sci. Technol.* **8**, 1053–1061.
28. Maccraith, B. D., McDonagh, C. M., Okeeffe, G., McEvoy, A. K., Butler, T., and Sheridan, F. R. (1995) Sol-gel coatings for optical chemical sensors and biosensors. *Sens. Actuators B Chem.* **29**, 51–57.
29. McDonagh, C., Bowe, P., Mongey, K., and MacCraith, B. D. (2002) Characterisation of porosity and sensor response times of sol-gel-derived thin films for oxygen sensor applications. *J. Non-Cryst. Solids* **306**, 138–148.
30. Altstein, M., Aharonson, N., Segev, G., Ben-Aziz, O., Avnir, D., Turniansky, A., and Bronshtein, A. (2000) Sol-gel-based enzymatic assays and immunoassays for residue analysis. *Italian J. Food Sci.* **12**, 191–206.
31. Bronshtein, A., Aharonson, N., Avnir, D., Turniansky, A., and Altstein, M. (1997) Sol-gel matrixes doped with atrazine antibodies—atrazine binding properties. *Chem. Mater.* **9**, 2632–2639.
32. Doody, M. A., Baker, G. A., Pandey, S., and Bright, F. V. (2000) Affinity and mobility of polyclonal anti-dansyl antibodies sequestered within sol-gel-derived biogels. *Chem. Mater.* **12**, 1142–1147.
33. Grant, S. A. and Glass, R. S. (1999) Sol-gel-based biosensor for use in stroke treatment. *IEEE Trans. Biomed. Eng.* **46**, 1207–1211.
34. Jiang, D. C., Tang, J., Liu, B. H., Yang, P. Y., and Kong, J. L. (2003) Ultrathin alumina sol-gel-derived films: allowing direct detection of the liver fibrosis markers by capacitance measurement. *Anal. Chem.* **75**, 4578–4584.
35. Jordan, J. D., Dunbar, R. A., and Bright, F. V. (1996) Aerosol-generated sol-gel-derived thin films as biosensing platforms. *Anal. Chim. Acta* **332**, 83–91.

36. Roux, C., Livage, J., Farhati, K., and Monjour, L. (1997) Antibody-antigen reactions in porous sol-gel matrices. *J. Sol-Gel Sci. Technol.* **8**, 663–666.
37. Shabat, D., Grynszpan, F., Saphier, S., Turniansky, A., Avnir, D., and Keinan, E. (1997) An efficient sol-gel reactor for antibody-catalyzed transformations. *Chem. Mater.* **9**, 2258–2260.
38. Turniansky, A., Avnir, D., Bronshtein, A., Aharonson, N., and Altstein, M. (1996) Sol-Gel entrapment of monoclonal anti-atrazine antibodies. *J. Sol-Gel Sci. Technol.* **7**, 135–143.
39. Vazquez-Lira, J. C., Camacho-Frias, E., Pena-Alvarez, A., and Vera-Avila, L. E. (2003) Preparation and characterization of a sol-gel immunosorbent doped with 2,4-D antibodies. *Chem. Mater.* **15**, 154–161.
40. Wang, R., Narang, U., Prasad, P. N., and Bright, F. V. (1993) Affinity of antifuorescein antibodies encapsulated within a transparent sol-gel glass. *Anal. Chem.* **65**, 2671–2675.
41. Zhou, J. C., Chuang, M. H., Lan, E. H., Dunn, B., Smith, S. M., and Gillman, P. L. (2004) Immunoassays for cortisol using antibody-doped sol-gel silica. *J. Mater. Chem.* **14**, 2311–2316.
42. Ashkar, F. S. (1983) *Radiobioassay*, CRC Press, Boca Raton, FL.
43. Pesce, A. J. and Kaplan, L. A. (1987) *Methods in Clinical Chemistry*, C. V. Mosby, St. Louis, MO.



## Nanomaterials of Drug Delivery Systems for Tissue Regeneration

Yasuhiko Tabata

### Summary

A new therapeutic trial aimed at assisting tissue regeneration at a body defect in size too large for self-repair has recently begun. The objective is to substitute the biological functions of damaged and injured organs by taking advantage of cells. For successful tissue regeneration, it is absolutely indispensable not only to have cells of high proliferation and differentiation potential, but also to create an environment suitable for inducing regeneration. Such creation can be artificially achieved only by providing various biomaterials to promote cell proliferation and differentiation, such as cell scaffold and growth factors. Growth factors are often required to promote tissue regeneration because they can induce angiogenesis, which promotes a sufficient supply of oxygen and nutrients to effectively maintain the biological functions of cells transplanted for organ substitution. However, because of their poor in vivo stability, the biological effects of growth factors cannot always be expected unless these drug delivery systems (DDSs) are contrived. In this chapter, several research approaches to tissue regeneration are reviewed to emphasize the significance of biomaterials and DDS technologies in regenerative medicine.

**Key Words:** Tissue engineering; tissue regeneration; regenerative medicine; biomaterials; drug delivery systems; growth factor release.

## 1. Introduction

### 1.1. Technologies Necessary for Tissue Regeneration

When a body tissue or organ is severely injured, largely lost, or malfunctioning, it is clinically treated using either reconstructive surgery or organ transplantation. Although there is no doubt that these procedures have saved and improved the lives of countless patients, these therapies at present are facing several clinical challenges. One promising alternative to such complications is to allow patients to induce regeneration of their body tissues and organs by

From: *Methods in Molecular Biology*, vol. 300:  
*Protein Nanotechnology, Protocols, Instrumentation, and Applications*  
Edited by: T. Vo-Dinh © Humana Press Inc., Totowa, NJ

making use of their self-healing potential. A new biomedical field focused at bringing about this new therapeutic approach is tissue engineering. Tissue engineering is one of the biomedical technologies aimed at assisting clinical applications of basic research, which results in “regenerative” medicine and “regenerative” medical therapy for patients, including regeneration of natural tissues as well as creation of biological substitutes for defective or lost tissues and organs, starting at the cellular level (*I*).

To successfully achieve tissue regeneration, it is undoubtedly necessary not only to increase the number of cells constituting the tissue, but also to reconstruct a structure to support the proliferation and differentiation of the cells’ so-called extracellular matrix (ECM). In addition, growth factors are often required to promote tissue regeneration, depending on the type of tissue. In summary, the components necessary for tissue engineering include cells, the scaffolds for cell proliferation and differentiation, and growth factors.

Recently, it has been well recognized that the ECM not only physically supports cells, but also plays an important role in both cell proliferation and differentiation (or morphogenesis), which results in tissue regeneration and organogenesis. It is unlikely that a large defect of tissue will be naturally regenerated and repaired by merely supplying cells to the defect. Nonetheless, there are a few cases in which successful tissue regeneration is achieved by simply adding healthy cells to the appropriate site. For example, one practical approach is to provide an environment suitable for induction of tissue regeneration at the defect site by first building a scaffold as an artificial ECM that temporarily promotes cell attachment and the subsequent cell proliferation and differentiation. It is highly expected that self-derived cells residing around the scaffold or the cells preseeded in the scaffold will proliferate and differentiate on the foundation of the provided scaffold if the artificial ECM is compatible with the cells. Once the regeneration process of a new tissue is initiated, the cells constituting tissue eventually produce the natural and appropriate ECM. However, any remaining cell scaffolds physically hinders tissue regeneration during the process. Thus, for successful tissue regeneration, a period of scaffold degradation at the defect should be optimized and controlled. For cases in which the tissue to be repaired has a high activity toward regeneration, a new tissue will be formed in the biodegradable scaffold matrix by active, immatured cells infiltrated by the surrounding healthy tissue. However, additional means are required if the regeneration potential of tissue is very low, because of, e.g., the poor infiltration of cells and low concentration of growth factors responsible for new tissue generation. The simplest method to offset these conditions is to supply growth factors to the site of regeneration for cell differentiation and proliferation.

However, the direct injection of growth factors in solution form into sites to be regenerated is often not effective, because injected growth factors are rapidly diffused out and excreted from the site. One promising way to enhance growth factor efficiency *in vivo* is to use drug delivery systems (DDSs). For example, the controlled release of growth factor at the site of action over an extended time period is readily possible by incorporating the factors into appropriate carriers. It is likely that a growth factor is protected against proteolysis, as long as it is held within the carrier, hence enabling prolonged retention of the activity *in vivo*. After the release of the growth factor, the carrier should be degraded in the body because it is no longer needed. Thus, for tissue regeneration or organ substitution, it is of prime importance to create an environment suitable for induction of tissue regeneration by making use of the biodegradable scaffold and DDS technologies. Even if the basic biology of and medicine for cells are greatly advanced, “regenerative” medical therapy for patients will never be realized by the research results alone unless this regeneration environment is provided appropriately.

## 1.2. Overview of Tissue Engineering

Tissue engineering is classified into two categories in terms of the site where tissue engineering is performed: *in vitro* and *in vivo* (**Fig. 1**). *In vitro* tissue engineering involves tissue reconstruction and organ substitution, otherwise known as bioartificial organs. **Table 1** provides tissues and organs undergoing tissue engineering. The targeted tissues and organs have been extensively investigated based on combinations of cells, scaffolds, and growth factors (**1**).

If tissues can be reconstructed *in vitro* in factories or laboratories on a large scale, the tissue constructs can be supplied to patients when they are needed. This approach would be very attractive for commercialization once the feasibility is established. However, it is quite difficult to completely reconstruct the event *in vitro* using the cell culture technologies currently available. Another approach to *in vitro* tissue engineering is the substitution of organ functions by the use of allogenic or xenogenic cells. Such engineered organs have been called bioartificial organs because they are composed of heterogeneous cells and man-made membranes or porous constructs for immunoisolation to protect the cells from host attack and maintain cell function. This approach has been performed for the liver, pancreas, and kidney (**2,3**).

Distinct from *in vitro* tissue engineering, *in vivo* tissue engineering has the advantage of using the native environment for induction of tissue regeneration. Most of the materials necessary for tissue regeneration are automatically supplied by the host living body. Therefore, almost all the approaches to tissue engineering have been currently performed *in vivo* with or without biodegradable scaffolds. This approach is more realistic and clinically acceptable if it



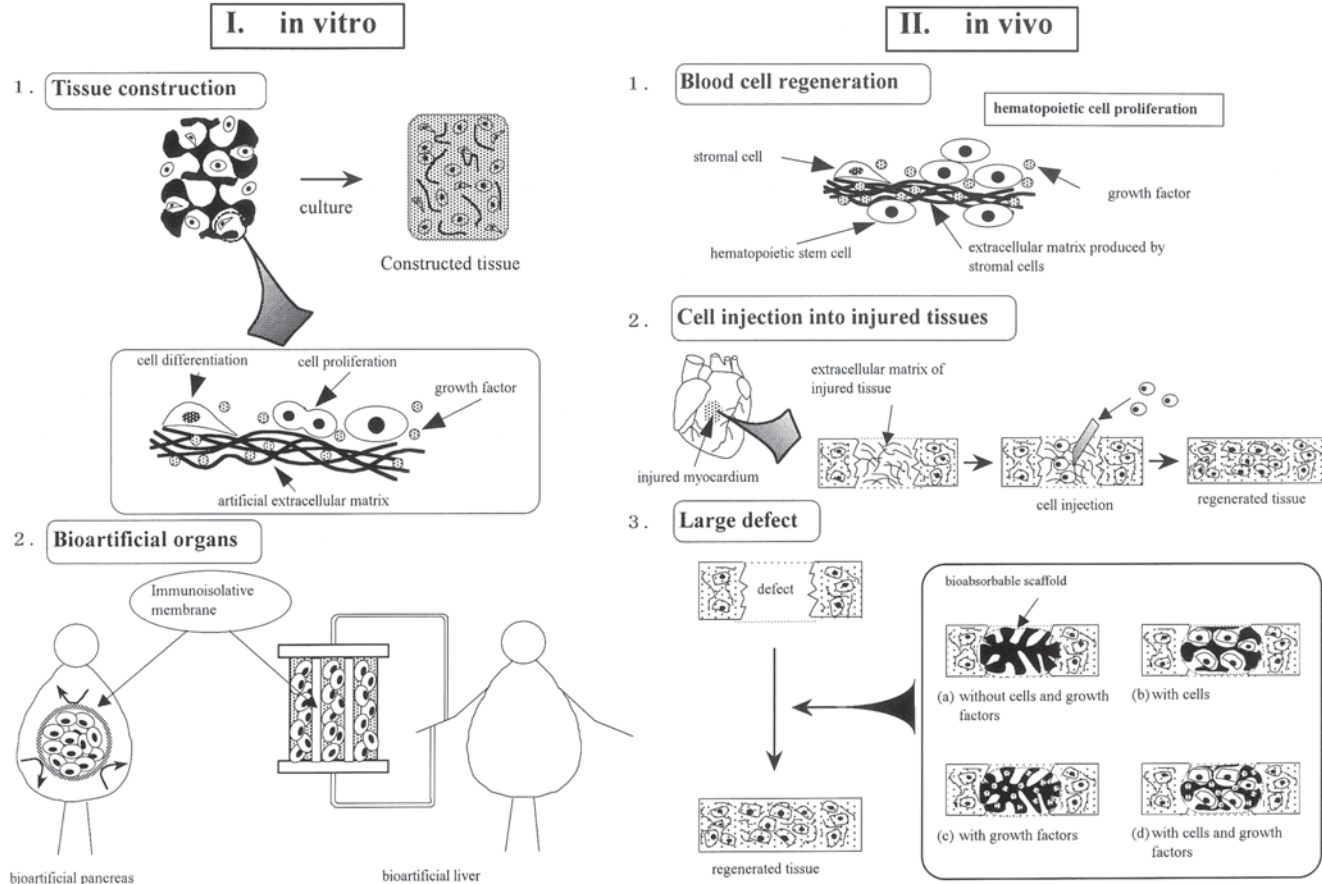


Fig. 1. Basic principle of tissue engineering.

**Table 1**  
**Tissues and Organs Being Regenerated or Reconstructed by Tissue Engineering**

Fabricated site	Cell	Tissue regeneration			Organ substitution
		Scaffold	Scaffold + growth factor	Barrier membrane	Barrier membrane
In vitro	Necessary	Skin (epidermis + dermis), articular cartilage, bone, artery, myocardium	—	—	Liver, pancreas, kidney
In vivo	Not necessary	Dermis, dura mater, esophagus, trachea	Bone (skull, jaw, long), hair, arteriole, smooth muscle, bladder, periodontal tissue	Peripheral nerve, periodontal tissue, alveolar bone	—
In vivo	Necessary	Skin, cornea, retina, artery, cartilage (fibrous and hyaline), bone (skull, jaw, long), myocardium, trachea, esophagus, small intestine, stomach, smooth muscle, bladder, ureter, central nerve	Mamma, fat, hair, myocardium, liver, kidney	Peripheral nerve	Liver, pancreas, chromaffin cells (angiogenesis)

works well. If the healthy ECM is still available in the body, no artificial scaffold is needed. In addition to bone marrow transplantation, eye-related stem cells are being used for regeneration of defective cornea and retina (4), and the transplantation of myocardial cells has been experimentally tried for the treatment of myocardial infarction (5). For the regeneration of a large defect, it is absolutely necessary to use a biodegradable scaffold. The scaffold is implanted with or without cell seeding. For example, sponge form collagen is the most popular material (6), because a collagen scaffold is compatible with cells and is degraded in the body, hence preventing a physical hindrance to new tissue construction. In vivo tissue engineering using a collagen sponge or a biodegradable polymer sheet with no cell seeding has succeeded in inducing regeneration of the skin dermis (7), trachea (8), esophagus (9), and dura mater (10).

There are many body tissues that cannot be regenerated unless the scaffold used is seeded with the cells specifically needed for tissue regeneration. Regeneration of epidermis and cartilage necessitates seeding of the scaffold with keratinocytes and chondrocytes, respectively. Cells isolated from blood vessels and small intestines have been combined with biodegradable scaffolds to achieve in vivo regeneration of the respective organs (11,12). Bone marrow cells have also been widely used to this end; bone marrow cells contain mesenchymal stem cells (MSCs) that can differentiate into the osteocytic lineage (13,14). It is possible to seed more than one type of cell for regeneration of tissue composed of several subtissues. For example, phalanges and small fingers could be reconstructed by using three different scaffolds combined with periosteum, chondrocytes, and tenocytes for reconstruction of bone, cartilage, and tendon (ligament), respectively (15).

Sometimes successful tissue regeneration cannot be achieved by merely combining cells and their scaffolds. In such cases, one practical, possible way to promote tissue generation is to use suitable growth factors as well. The type of growth factor depends not only on the target tissue under investigation but also the site where the tissue is expected to generate. Besides the single use of growth factor, sometimes a combination of multiple growth factors with the scaffold preseeded with cells is required to accelerate tissue regeneration.

When a body defect is incurred, the defect space is soon filled with fibrous tissue produced by fibroblasts, which are ubiquitously present in the body and can rapidly proliferate. Once this ingrowth of fibrous connective tissue takes place, further repair or regeneration of other tissues is effectively terminated. To prevent tissue ingrowth, additional biomaterials, known as barrier membranes, are needed. The objective is to make space for tissue regeneration and prevent the undesirable tissue ingrowth, thereby permitting repair of the defect by natural tissue. Some successful examples include guided channels for lost peripheral nerve fibers (16) and guided regeneration of lost periodontal tissues

and alveolar bone (17). Barrier membranes should be prepared from biodegradable materials, because they are no longer needed after completion of tissue regeneration. This chapter presents an overview of several research trials on tissue regeneration based on the use of DDS growth factors with or without cells and/or the scaffolds.

## 2. Materials

An aqueous solution of human recombinant basic fibroblast growth factor (bFGF) with a *pI* of 9.6 (10 mg/mL) was kindly supplied by Kaken (Tokyo, Japan). A gelatin sample with a *pI* of 5.0 (Nitta Gelatin, Osaka, Japan) was extracted from bovine bone (type I collagen) by an alkaline process. Na<sup>125</sup>I aqueous solution in 0.1 *N* NaOH (NEZ033, 740 MBq/mL) and *N*-succinimidyl-3-(4-hydroxy-3,5-di<sup>125</sup>I iodophenyl) propionate (<sup>125</sup>I-Bolton-Hunter reagent, NEX-120H, 147 MBq/mL in anhydrous benzene) were purchased from NEN, DuPont (Wilmington, DE). Glutaraldehyde, glycine, and other chemicals were purchased from Wako (Osaka, Japan) and used without further purification.

## 3. Methods

### 3.1. Preparation of Gelatin Hydrogel Incorporating Growth Factor

Gelatin hydrogel was prepared by glutaraldehyde crosslinking of a gelatin aqueous solution. Briefly, after mixing 40  $\mu$ L of aqueous glutaraldehyde solution (25 wt%) with 40 mL of aqueous gelatin solution (5 wt%) preheated at 40°C, the mixed aqueous solution was cast into a polypropylene tray (18  $\times$  18 cm<sup>2</sup>); the mixture was left for 12 h at 4°C to allow chemical crosslinking of the gelatin. The resulting hydrogel sheet was then punched out to obtain gelatin hydrogel disks (6 mm in diameter, 3 mm thick), and the disks were placed in 50 mL of 100 mM glycine aqueous solution, followed by agitation at 37°C for 1 h to block residual aldehyde groups of unreacted glutaraldehyde. The crosslinked hydrogel disks were twice washed with double-distilled water (ddH<sub>2</sub>O), freeze-dried, and sterilized with ethylene oxide gas. The water content of gelatin hydrogel (the weight ratio of water present in the hydrogel to the wet hydrogel) was 96.0 wt%, as calculated from the hydrogel weight before and after swelling in phosphate-buffered saline solution (pH 7.4) for 24 h at 37°C.

The original bFGF solution was diluted with ddH<sub>2</sub>O to adjust the solution concentration. The aqueous bFGF solution (20  $\mu$ L) was dropped onto a freeze-dried gelatin hydrogel disk for impregnation of bFGF into the disk. The bFGF solution was completely sorbed into the hydrogel disk at 25°C for 2 h, because the solution volume was less than that theoretically required for the equilibrated swelling of hydrogels. Similarly, empty gelatin hydrogels without bFGF were prepared by adding ddH<sub>2</sub>O as the solution.

### 3.2. Characterization of Gelatin Hydrogel Incorporating Growth Factor

In vivo degradation of gelatin hydrogels was evaluated in terms of the loss of radioactivity of implanted  $^{125}\text{I}$ -labeled gelatin hydrogels. Gelatin hydrogels were radioiodinated using  $^{125}\text{I}$ -Bolton-Hunter reagent. Briefly, 100  $\mu\text{L}$  of  $^{125}\text{I}$ -Bolton-Hunter reagent solution in anhydrous benzene was bubbled with dry nitrogen gas until benzene evaporation was completed. Then, 1 mL of 0.1 M sodium borate-buffered solution (pH 8.5) was added to the dried reagent to prepare an aqueous solution of  $^{125}\text{I}$ -Bolton-Hunter reagent. The aqueous solution was impregnated into freeze-dried disks of gelatin hydrogels at a volume of 20  $\mu\text{L}$ /disk. The resulting swollen hydrogels were kept at 4°C for 3 h to introduce  $^{125}\text{I}$  residues into the amino groups of gelatin. The radioiodinated gelatin hydrogels were placed in ddH<sub>2</sub>O, which was exchanged periodically at 4°C for 4 d to exclude noncoupled, free  $^{125}\text{I}$ -labeled reagent from  $^{125}\text{I}$ -labeled gelatin hydrogels. When measured periodically, the radioactivity of the ddH<sub>2</sub>O returned to a background level after 3 d of rinsing. The resulting swollen hydrogels were freeze-dried. In vivo degradation of gelatin hydrogels was evaluated in terms of the loss of radioactivity of implanted  $^{125}\text{I}$ -labeled gelatin hydrogels. Various types of  $^{125}\text{I}$ -labeled gelatin hydrogels were implanted into the back subcutis of ddY mice (three mice per group, 6 to 7 wk old). At 1, 3, 5, 7, 10, 14, and 21 d after hydrogel implantation, the radioactivities of explanted hydrogels were measured on a gamma counter. Next, the mouse back skin around the hydrogel site was cut into a 3  $\times$  5 cm strip, and the corresponding fascia site was thoroughly wiped off with filter paper and measured to evaluate the remaining radioactivity of tissue around the implanted hydrogel. The ratio of total radioactivity measured to the radioactivity of the initially implanted hydrogel was expressed as the percentage of remaining activity for hydrogel degradation.

An aqueous solution of  $^{125}\text{I}$ -labeled bFGF was sorbed into freeze-dried gelatin hydrogel disks to prepare gelatin hydrogel incorporating  $^{125}\text{I}$ -labeled bFGF.  $^{125}\text{I}$ -labeled bFGF was prepared according to the chloramines T method reported previously (18). Various types of gelatin hydrogels incorporating  $^{125}\text{I}$ -labeled bFGF were implanted into the backs of mice. An aqueous solution of  $^{125}\text{I}$ -labeled bFGF was subcutaneously injected into the backs of mice. At different time intervals, areas of mouse skin containing the implanted hydrogels or directly injected  $^{125}\text{I}$ -labeled bFGF were thoroughly wiped off with filter paper in a way similar to that just described. The radioactivities of the residual gelatin hydrogels and the skin strip plus filter paper were measured on a gamma counter, and their radioactivity ratios to the bFGF initially used were expressed as the percentage of remaining activity for in vivo bFGF release.

Recently, much research has been devoted to tissue regeneration through combinations of growth factors with various carrier materials (Table 2).

**Table 2**  
**Experimental Trials for Tissue Regeneration by Combination of Growth Factor With Carrier<sup>a</sup>**

Growth factor	Carrier	Animal	Tissue regenerated
BMP	PLA	Dog	Long bone
	Collagen sponge	Rat	Long bone
		Dog, monkey	Periodontal ligament and cementum
rhBMP-2	$\beta$ -TCP	Rabbit	Long bone
	Porous HA	Rabbit	Skull bone
	Porous PLA	Dog	Spinal bone
		Rat	Skull bone
	PLA microsphere	Rabbit	Skull bone
	Collagen sponge	Dog	Periodontium
	Gelatin	Rabbit	Skull bone
rhBMP-7	PLA-coating gelatin sponge	Dog, monkey	Long bone, jaw bone, skull bone
	Porous HA	Monkey	Skull bone
	PLA-PEG copolymer	Rat	Long bone
	Collagen	Dog	Spinal bone
		Dog	Long bone
EGF	Agarose	Hamster	Angiogenesis
aFGF	PVA	Rat	Dermis
	PVA	Mouse	Angiogenesis
bFGF	Alginate	Mouse	Angiogenesis
	Alginate	Mouse	Angiogenesis
	Agarose/heparin	Mouse, pig	Angiogenesis
	Amylopectin	Mouse	Angiogenesis
	Gelatin	Mouse	Angiogenesis, dermis, adipogenesis
NGF		Rabbit, monkey	Skull bone
		Dog	Nerve
	Fibrin gel	Mouse	Angiogenesis
	Collagen minipellet	Rabbit	Long bone
	Collagen	Mouse	Cartilage
	Poly(ethylene-co-vinyl acetate)	Rat	Nerve
	Collagen minipellet	Rabbit	Nerve
TGF- $\beta$ 1	PLGA	Rat	Nerve
	PEG	Rat	Dermis
	Gelatin	Rabbit	Skull bone
	Plaster of Paris, PLGA	Rat	Skull bone
	TCP	Dog	Long bone
	Porous HA	Dog	Long bone
	Collagen	Baboon	Skull bone
PDGF-BB		Mouse	Dermis
	Porous HA	Rabbit	Long bone
	Collagen	Rat	Dermis
	Chitosan	Rat	Periodontal bone
VEGF	Collagen	Mouse	Angiogenesis
	Alginate	Mouse	Angiogenesis
HGF	Gelatin	Mouse	Angiogenesis
IGF-1	PLGA-PEG	Rat	Adipogenesis
IGF-1/bFGF	PLGA-PEG	Rat	Adipogenesis
PDGF/IGF-1	Titanium implant	Dog	Jaw bone

<sup>a</sup>aFGF, acid fibroblast growth factor; bFGF, basic fibroblast growth factor; BMP, bone morphogenetic protein; EGF, epidermal growth factor; HA, hydroxyapatite; HGF, hepatocyte growth factor; IGF-1, insulin-like growth factor-1; NGF, nerve growth factor; PDGF-BB, platelet-derived growth factor-BB; PEG, poly(ethylene glycol); PLA, polylactide; PLGA, glycolide-lactide copolymer; PVA, poly(vinyl alcohol); rhBMP, recombinant human bone morphogenetic protein; TCP, tricalcium phosphate; TGF, transforming growth factor; VEGF, vascular endothelial growth factor.

All results claim the necessity of combining the growth factors with carriers to induce in vivo tissue regeneration. In addition to proteinaceous growth factor, the gene encoding growth factor has recently been applied to promote tissue regeneration (19). If the corresponding gene is transfected into the cells existing in the site of regeneration, it is highly possible that the cells can secrete the growth factor for a certain time period, resulting in promoted tissue regeneration. The angiogenetic therapy of ischemic diseases (20) and bone tissue regeneration (21) have been attempted by using the corresponding growth factor genes.

#### 4. Notes

1. *Characteristics of gelatin hydrogel for controlled release of growth factor.*

One of the largest problems in protein release technology is the loss of biological activity of proteins released from protein-carrier formulations. It has been demonstrated that this loss of activity results mainly from denaturation and deactivation of proteins during preparation of carrier formulations. Therefore, a method to prepare protein release carriers with inert biomaterials should be exploited to minimize protein denaturation. From this viewpoint, a polymer hydrogel may be a preferable candidate for use as a protein release carrier because of its biocompatibility and its high inertness toward protein drugs.

We have created a release system for growth factors that mimics the native mode of growth factor delivery in the living body. **Figure 2** shows a conceptual illustration for the controlled release of growth factor from a biodegradable polymer hydrogel based on physicochemical interaction forces between the growth factor and polymer molecules. For example, a hydrogel is prepared from a biodegradable polymer with negative charges. The growth factor with a positively charged site is electrostatically attracted to the polymer chain and thereby is physically immobilized in the hydrogel carrier. If an environmental change, such as increased ionic strength, occurs, the immobilized growth factor is released from the factor-carrier formulation. Even if such an environmental change does not take place, degradation of the carrier itself also leads to growth factor release. Because the latter is more likely to happen in vivo than the former, it is preferred that the release carrier be prepared from biodegradable polymers. This complexation protects the growth factor from denaturation and enzymatic degradation in vivo.

As the material for growth factor release, we have selected gelatin because it has the desired physicochemical properties and has been extensively used for industrial, pharmaceutical, and medical purposes. The biosafety of gelatin has been proven through its long clinical uses. Another unique advantage is the electrical nature of gelatin, which can be changed by the processing method. For example, an alkaline process of collagen results in hydrolysis of amide groups of the asparagine and glutamine residues, having a high density of carboxyl groups, which makes the gelatin negatively charged. The *pI* of gelatin is about 5.0.



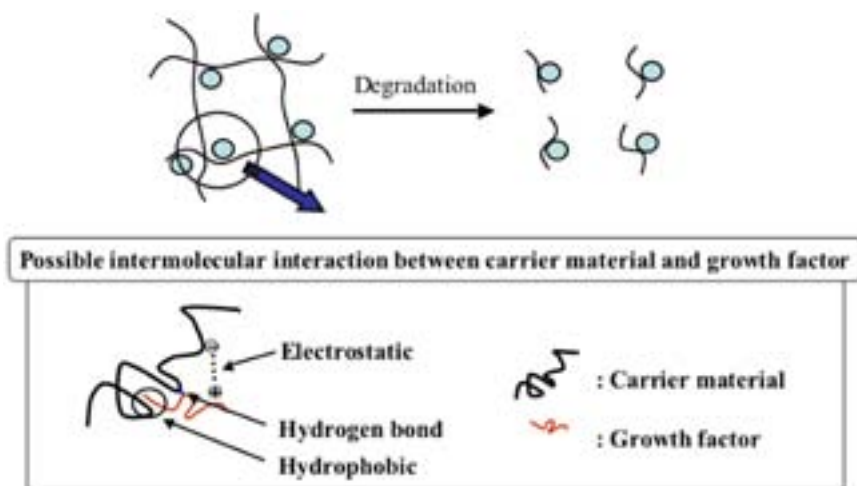


Fig. 2. Conceptual illustration of growth factor release from a biodegradable hydrogel based on physical interaction forces.

By contrast, the nature of a gelatin is much different for an acidic process. A positively charged gelatin of “basic” type is prepared and the  $pI$  is about 9.0. If a growth factor to be released has the positively charged site in the molecule that interacts with acidic polysaccharides present in the ECM, the negatively charged gelatin of “acidic” type is preferable as the carrier material. Considering the electrostatic interaction, the “basic” gelatin is preferable for release of molecules with the negative charged site. It was found that, as expected, bFGF, transforming growth factor- $\beta 1$  (TGF- $\beta 1$ ), or platelet-derived growth factor was sorbed into the acidic gelatin hydrogel mainly owing to the electrostatic interaction (22).

Animal experiments revealed that the hydrogels prepared from the acidic gelatin were degraded in the body (23). The degradation period of hydrogels depends on their water content, which is a measure of crosslinking extent: the higher the water content of the hydrogels, the faster their *in vivo* degradation. The water content of hydrogels increased with increasing concentrations of chemical crosslinking agents and gelatin concentration used in the preparation of the hydrogels. The time profile of *in vivo* bFGF retention was in accordance with that of hydrogel degradation, irrespective of the hydrogel biodegradability. It seems reasonable to suppose that bFGF was released from the gelatin hydrogel along with degraded gelatin fragments in the body as a result of hydrogel degradation. These findings strongly indicate that growth factor release is governed mainly by hydrogel degradation, as described in Fig. 2. As a result, in this release system, the release period is not influenced by the hydrogel’s shape at all, but controllable only by changing the degradation rate of hydrogel (24). Note that gelatin hydrogels can be formed into different shapes of disks, tubes, sheets, granules, and microspheres (24,25).



2. *Tissue regeneration by gelatin hydrogel incorporating bFGF.* As described in the previous section, the gelatin hydrogel was found to be a superior carrier for the controlled release of growth factor. Hereafter, concrete experimental results on angiogenesis, bone regeneration, and adipogenesis are described as achieved by this release system alone or in combination with stem cells.
3. *Angiogenesis.* bFGF has been reported to have a variety of biological functions (26) and to be effective in enhancing wound healing through induction of angiogenesis and regeneration of bone, cartilage, and nerve tissue. Among its biological actions, the gelatin hydrogel was effective in enhancing the *in vivo* angiogenic effect of bFGF. When gelatin hydrogels incorporating bFGF were subcutaneously implanted into a mouse's back, the angiogenic effect was observed around the implanted site, in marked contrast to the sites implanted with bFGF-free, empty gelatin hydrogels or injected with an aqueous solution of bFGF (22). No angiogenesis was induced by the injection of bFGF solution even when the dose was increased to 1 mg/site. This result must be owing to a rapid elimination of bFGF from the injection site (27). By contrast, the gelatin hydrogel incorporating bFGF induced significant angiogenesis even when the dose was as low as 30  $\mu$ g/site. The maintenance period of the hydrogel-induced angiogenic effect could be changed by prolonging the hydrogel's water content as the water content became lower (27). It is likely that the hydrogels with lower water contents were more slowly degraded and consequently released bFGF of biological activity *in vivo* less rapidly than those with higher water contents, leading to a prolonged angiogenic effect. A similar enhanced and prolonged angiogenic effect was also observed when using gelatin hydrogels incorporating bFGF of the microsphere type (24).

The technology to induce artificially *in vivo* angiogenesis is indispensable for tissue engineering. Two objectives of angiogenesis induction include the therapy of ischemic disease and advanced angiogenesis for cell transplantation. As an example of the former, the therapy of ischemic myocardium by gelatin hydrogels incorporating bFGF is introduced here. Myocardial infarction was induced by ligating the left anterior descending (LAD) coronary artery of dog heart. Gelatin microspheres incorporating bFGF were intramuscularly injected into both sides of the LAD 10 mm distal from the ligated site. As a control, an aqueous solution of bFGF at the same dose level was injected. Injection of the gelatin microspheres containing bFGF induced regeneration of collateral coronary arteries at the site of ligated LAD and increased the blood flow in the left circumflex coronary artery (LCX) (**Fig. 3**). More interesting, the injection of microspheres was also effective in recovering the motion of myocardium in the ischemic region. Neither of these therapeutic effects were observed for the injection of bFGF solution at the same dose level (1).

There is no doubt that a sufficient supply of nutrients and oxygen to the cells transplanted in the body is indispensable for cell survival and the maintenance of biological functions. Without sufficient supply, cells preseeded in a scaffold for tissue regeneration would hardly survive following implantation of the scaffold

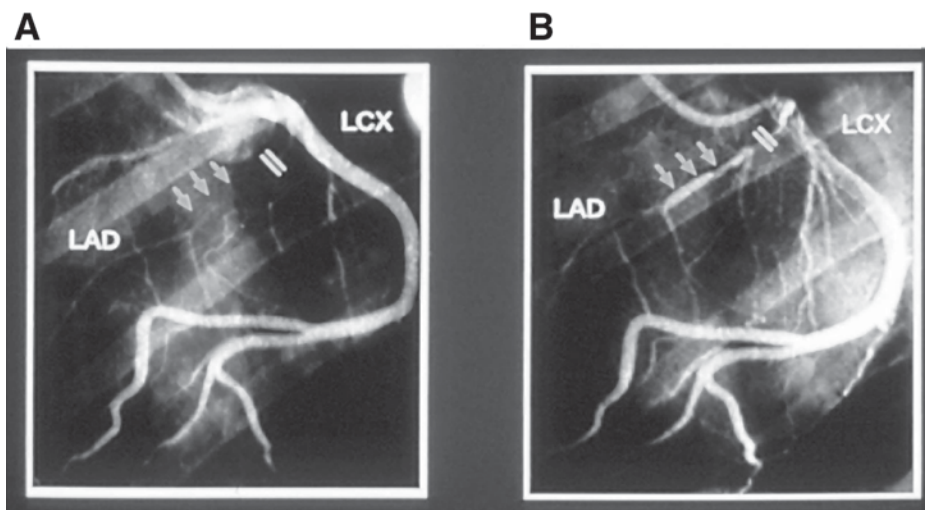


Fig. 3. Left coronary angiograms of ischemic dog heart 1 wk after intramyocardial injection of (A) bFGF solution and (B) gelatin microspheres incorporating bFGF. bFGF was bilaterally injected at the distal side of the LAD ligated portion (indicated by Mark II) at a dose of 100  $\mu$ g/heart. The hydrogel water content was 95.0 wt%.

into the body. Such a situation is caused by allo- or xenogeneic cells transplanted into the body for organ substitution. For successful cell transplantation, the nutrient and oxygen supply is the dominant challenge relative to immunoisolation. For both of the supplies, it is promising to induce angiogenesis throughout the transplanted site of cells by using angiogenic growth factors. In a recent study, pancreatic islets were encapsulated by a hydrogel bag effective for immunoisolation and implanted into the sc tissue of streptozotocin-induced diabetic mice. Advanced angiogenesis at the site of cell transplantation induced by gelatin microspheres containing bFGF enabled the encapsulated islets to improve the survival rate, resulting in a prolonged maintenance period of normal glucose level in the blood (**Fig. 4**) (28). This finding demonstrates that *in vivo* angiogenesis induced by the gelatin microspheres containing bFGF could be achieved in the subcutis of even diabetic mice, which have an inferior injury-repairing capability relative to healthy mice. It is of prime importance to induce tissue regeneration even in the bodies of patients who have diseases or are elderly. Little tissue engineering research has been performed on aged animals. This area of study will undoubtedly become important when considering clinical applications for tissue engineering. This angiogenic effect for the prolonged cell survival was observed for transplantation of hepatocytes (29) and cardiomyocytes (30).

4. *Bone regeneration.* Gelatin hydrogels incorporating bFGF were found to have a promising potential for bone repair (31,32). For example, when implanted into a monkey skull defect, the gelatin hydrogel incorporating bFGF promoted bone

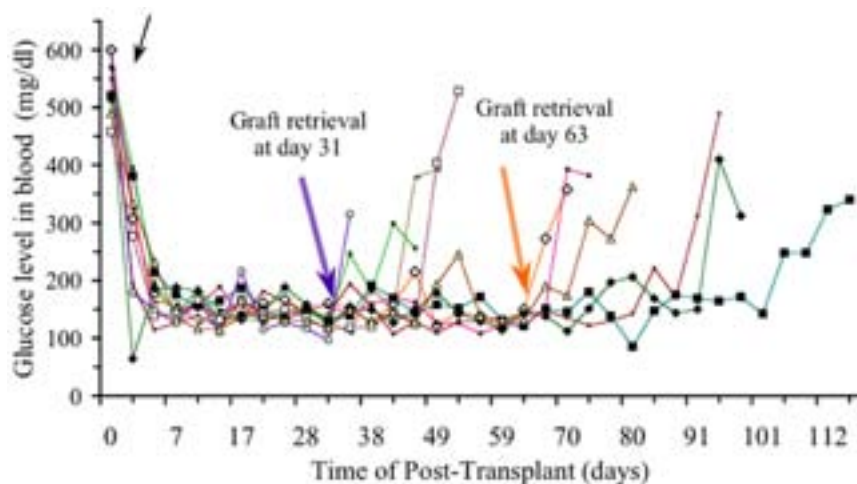


Fig. 4. Time course of glucose level in blood of diabetic mice after sc xenograft of rat pancreas islets encapsulated by an agarose/PSSa hydrogel membrane into vascularized site induced by advance injection of gelatin microspheres containing bFGF (small arrow, transplantation). Two of 10 recipients became hyperglycemic again when the grafts were respectively retrieved at d 31 ( $\circ$ ,  $*$ , and  $\square$ ) and d 63 ( $\diamond$ ,  $\times$ ,  $\triangle$ ,  $+$ ,  $\blacklozenge$ , and  $\blacksquare$ ) (large arrows). This strongly indicates that the encapsulated islets functioned normally in the subcutis of diabetic mice. The average normoglycemic period was  $68.4 \pm 25.6$  d.

regeneration at the defect and closed the defect by 21 wk after implantation. By contrast, both the use of bFGF-free gelatin hydrogels and the use of a similar dose of bFGF in the solution resulted in a total lack of bone regeneration, and a remarkable ingrowth of soft connective tissues at the bone defect. Measurement of bone mineral density (BMD) at the skull defect revealed that gelatin hydrogels containing bFGF enhanced the BMD to a significantly higher extent than did free bFGF, irrespective of the hydrogel water content. The BMD resulting from the bFGF-free gelatin hydrogel implant was similar to that of the untreated group, indicating that the presence of hydrogel did not impair bone healing at the defect. In a histological study, hydrogel implantation increased the number of osteoblasts residing near the edge of the bone defect and retained it at a significantly high level over the time range studied.

It is known that both TGF- $\beta$ 1 and bone morphogenetic protein (BMP) also promote bone regeneration (33–36). We have succeeded in repairing bone and skull defects of rabbits and monkeys by the controlled release of TGF- $\beta$ 1 from gelatin hydrogels, in marked contrast to the use of free TGF- $\beta$ 1 even at higher doses (34). However, the degree of repair depended on the water content of hydrogels, which could be reduced or increased. It is possible that too rapid degradation of the hydrogel causes a short period of bFGF release, resulting in no

induction of bone regeneration. Conversely, a long-term residue of hydrogels owing to slow degradation would physically hinder bone regeneration. As a result, it is likely that the hydrogel with an optimal biodegradability induced complete bone regeneration at the skull defect (34). As with previously described studies, hydrogels function as carriers of growth factors as well as barriers to prevent the ingrowth fibrous tissues into bone defects. Balance of the time course between the two hydrogel functions would result in better bone repairing. We have recently succeeded in the controlled release of BMP-2 by hydrogels of a gelatin type. This controlled-release system enabled BMP-2 to induce formation of bone tissue ectopically or orthotopically at doses lower than used for the application of free BMP-2 in solution.

There are some cases in which a combination of the controlled release of growth factor and stem cells is effective in achieving bone repair. In one trial, we utilized cells with osteogenic potentials and combined them with the growth factor release system. MSCs were isolated from the bone marrow of a rabbit fibula. We demonstrated that application of a combination of MSCs and gelatin microspheres containing TGF- $\beta$  allowed completely repaired defects in rabbit skulls by newly formed bone tissue, in marked contrast to that of either material used alone (37). In this case, however, the TGF- $\beta$  release system when used alone was not effective because the dose was too low.

5. *Adipogenesis.* When gelatin microspheres incorporating bFGF were mixed with a basement membrane extract (Matrigel) and subcutaneously implanted into a mouse's back, *de novo* formation of adipose tissue was observed at the implanted site (38). Recently, we also succeeded in inducing *de novo* adipogenesis by combining preadipocytes isolated from fat tissues, gelatin microspheres incorporating bFGF, and a collagen sponge (Fig. 5). When the preadipocytes and the microspheres were placed into the collagen sponge and implanted into the back subcutis of a mouse, *de novo* formation of adipose tissue was observed at the implanted sponge site. Combination of all three materials was needed to induce this adipogenesis (39). These results experimentally justify the strategy of *in vivo* tissue engineering asserting that tissue regeneration can be achieved by creating a suitable environment in the body site to be regenerated.
6. *Conclusion.* For regeneration of body tissues, a variety of growth factors act on cells by forming a complex network while the action timing, action site, and concentration of growth factors are delicately regulated in the body. It is likely that the mechanisms of tissue regeneration in living systems will be clarified with rapidly advancing progress in cell biology, molecular biology, and embryology. Even so, it will be impossible to imitate living systems by solely making use of the scientific knowledge and technologies currently available. However, clarification of living mechanisms will help researchers to understand which growth factor is key to induce the regeneration of a target tissue. If such a key growth factor is supplied to the necessary site at a suitable time period and concentration, I believe that the living body will be stimulated toward the process of natural tissue regeneration. Once the right direction toward tissue regeneration is

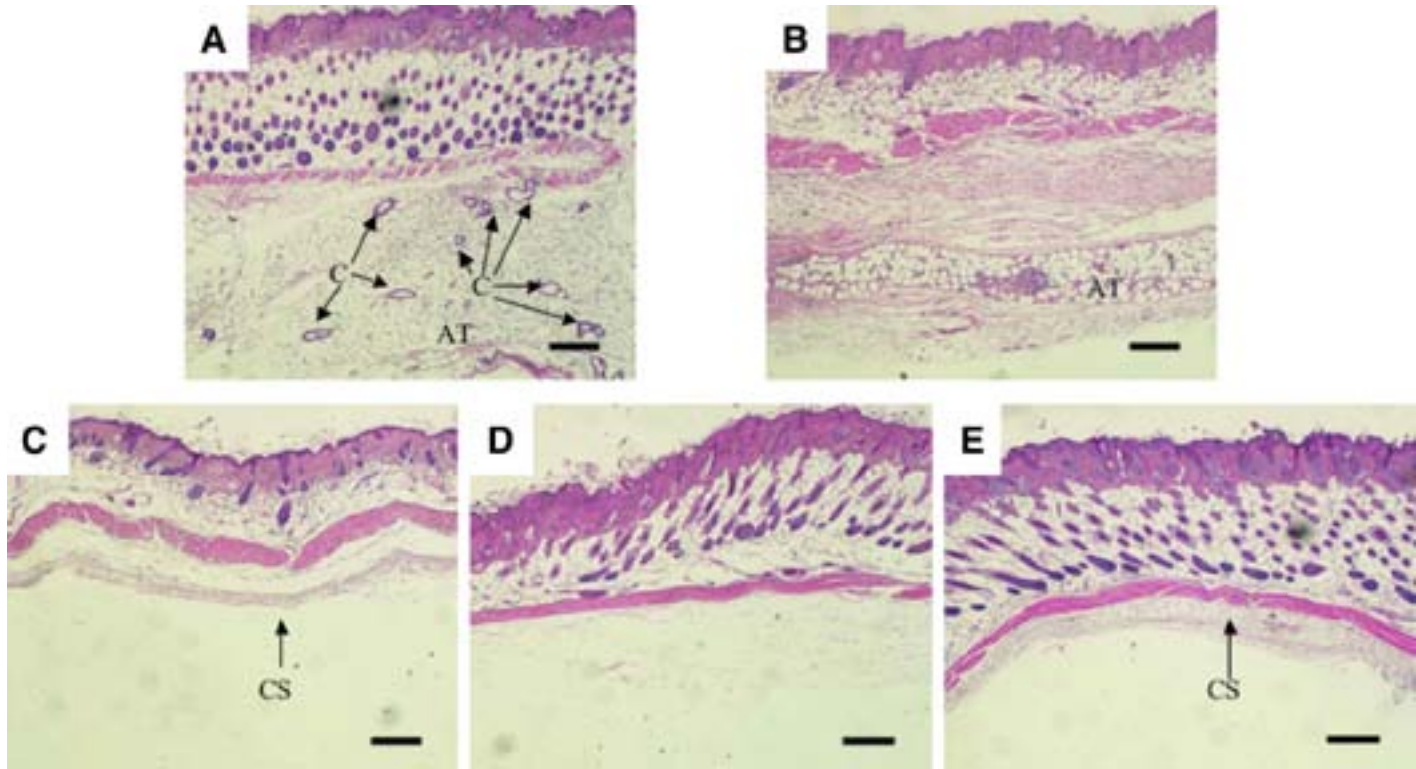


Fig. 5. *De novo* formation of adipose tissue in mouse subcutis 6 wk after implantation of a collagen sponge containing a mixture of preadipocytes and gelatin microspheres incorporating bFGF: (A) collagen sponge containing mixture of preadipocytes and gelatin microspheres incorporating bFGF; (B) collagen sponge containing mixture of preadipocytes and free bFGF; (C) collagen sponge containing preadipocytes; (D) mixture of preadipocytes and gelatin microspheres incorporating bFGF; (E) collagen sponge containing gelatin microspheres incorporating bFGF. (Magnification:  $\times 100$ ; Sudan III staining). The gelatin microspheres incorporating bFGF were completely degraded to disappear from the injected site. The bFGF dose was  $10 \mu\text{g}/\text{site}$  and the hydrogel water content was 95.0 wt%. Bar =  $300 \mu\text{m}$ . CS, collagen sponge; AT, adipose tissue newly formed; C, capillary newly formed.



taken, the intact system of the body will start to act and function, resulting in automatic achievement of tissue regeneration. There is no doubt that as long as growth factors are used, their controlled release will be an essential technology in the future. Recently, bFGF has been on the Japanese market as a therapeutic agent for skin ulcer and decubitus. I expect that this will be a cue to encourage clinical application of tissue regeneration based on growth factor DDS technology.

If tissue engineering matures to be the third choice of therapeutic medicine relative to reconstructive surgery and organ transplantation, it will give patients many therapeutic choices and privileges. To this end, substantial collaborative efforts among researchers in materials, pharmaceutical, biological, and medical sciences, and clinical medicine are needed to reach academic and technical maturity in tissue engineering. Because tissue engineering is still in its infancy, it will take much more time before its full potential is realized. Without the cell scaffold and DDS technologies to induce tissue regeneration, any developmental results of medicine, biology, and molecular biology regarding stem cells will never be realized in medical therapy for patients, which is the final goal of "regenerative" medicine. Tissue engineering is one of the indispensable tools to make regenerative medicine clinically available. Little DDS research aiming at tissue regeneration as well as organ substitution has been conducted. I am confident that the majority of the readers of this chapter will get a better understanding of the magnified significance of biomaterials as well as DDSs in the future progress of tissue engineering. It is hoped that this article will increase readers' interest in this research field.

## References

1. Tabata, Y. (2001) Significance of biomaterials and drug delivery systems in tissue engineering. *Connect. Tissue* **33**, 315–324.
2. Prokop, A., Hunkeler, D., and Cherrington, A. D. (1997) Bioartificial organs, sciences, medicine, and technologies. *Ann. NY Acad. Sci. USA* **831**, 249–298.
3. Humes, H. D., Buffington, D. A., MacKay, S. M., Funke, A. J., and Weitzel, W. F. (1999) Replacement of renal function in uremic animals with a tissue-engineered kidney. *Nat. Biotechnol.* **17**, 451–455.
4. Tsubota, K., Satake, Y., Kaido, M., Shinozaki, M., Shimmura, S., Bissen-Miyajima, H., and Shimazaki, J. (1999) Treatment of severe ocular-surface disorders with corneal epithelial stem-cell transplantation. *N. Engl. J. Med.* **340**, 1697–1703.
5. Li, R. K., Jia, Z.-Q., Weisel, R. D., Mickle, D. A., Zhang, J., Mohabeer, M. K., Rao, V., and Ivanov, J. Cardiomyocyte transplantation improves heart function. (1996) *Ann. Thorac. Surg.* **62**, 654–660.
6. Shimizu, Y. (1998) Tissue engineering for soft tissue, in *The Tissue Engineering for Therapeutic Use 2* (Ikada, Y. and Enomoto, S., eds.), Elsevier Science B.V. Publisher, Amsterdam, The Netherlands, pp. 119–122.
7. Yannas, I. V. and Burke, J. F. (1980) Design of an artificial skin. 1. Basic design principle. *J. Biomed. Mater. Res.* **14**, 65–81.

8. Okumura, N., Nakamura, T., Shimizu, Y., Tomihata, K., Ikada, Y., and Shimizu, Y. (1994) Experimental study on a new tracheal prosthesis made from collagen-conjugated mesh. *J. Thorac. Cardiovasc. Surg.* **108**, 337–341.
9. Takimoto, Y., Nakamura, T., Yamamoto, Y., Kiyotani, T., Teramachi, M., and Shimizu, Y. (1998) The experimental replacement of a central esophageal segment with an artificial prosthesis with the use of collagen matrix and a silicone stent. *J. Thorac. Cardiovasc. Surg.* **116**, 98–106.
10. Yamada, K., Miyamoto, S., Nagata, I., Kikuchi, H., Ikada, Y., Iwata, H., and Yamamoto, K. (1997) Development of a dural substitute from synthetic bio-absorbable polymers. *J. Neurosurg.* **86**, 1012–1017.
11. Shinoka, T., Shum-Tim, D., Ma, P. X., Tanel, R. E., Isogai, N., Langer, R., Vacanti, J. P., and Mayer, J. E. Jr. (1998) Creation of viable pulmonary artery autografts through tissue engineering. *J. Thorac. Cardiovasc. Surg.* **115**, 536–546.
12. Kaihara, S., Kim, S. S., Kim, B. S., Mooney, D., Tanaka, K., and Vacanti, J. P. (2000) Long-term follow-up of tissue-engineered intestine after anastomosis to native small bowel. *Transplantation* **69**, 1927–1932.
13. Ohgushi, H. and Caplan, A. I. (1999) Stem cell technology and bioceramics: from cell to gene engineering. *J. Biomed. Mater. Res. (Appl. Biomater.)* **48**, 913–927.
14. Pittenger, M. F., Mackay, A. M., Beck, S. C., Jaiswal, R. K., Douglas, R., Mosca, J. D., Moorman, M. A., Simonetti, D. W., Craig, S., and Marshak, D. R. (1999) Multilineage potential of adult human mesenchymal stem cells. *Science* **284**, 143–147.
15. Isogai, N., Landis, W., Kim, T. H., Gerstenfeld, L. C., Upton, J., and Vacanti, J. P. (1999) Formation of phalanges and small joints by tissue-engineering. *J. Bone Joint Surg.* **81**, 306–316.
16. Valentini, R. F. (1995) Nerve guidance channels, in *The Biomedical Engineering Handbook* (Brozine, J. D., ed.), CRC Press, Boca Raton, FL, pp. 1985–1996.
17. Ishikawa, I. and Arakawa, S. (1998) Awareness of periodontal disease—the role of industry. *Intern. Dent. J.* **48**, 261–267.
18. Parker, C. W. (1990) Radiolabelling of proteins. *Methods Enzymol.* **182**, 721–737.
19. Bonadio, J., Goldstein, S. A., and Lecy, R. J. (1998) Gene therapy for tissue repairing and regeneration. *Adv. Drug Deliv. Rev.* **33**, 53–69.
20. Lee, J. S. and Feldman, A. M. (1998) Gene therapy for therapeutic myocardial andiogenesis: a promising synthesis of two emerging technologies. *Nat. Med.* **4**, 739–742.
21. Bonadio, J., Smiley, E., Patil, P., and Goldstein, S. (1999) Localized, directed plasmid gene delivery in vivo: prolonged therapy results in reproducible tissue engineering. *Nat. Med.* **5**, 753–759.
22. Tabata, Y. and Ikada, Y. (1998) Protein release from gelatin matrices. *Adv. Drug Deliv. Rev.* **31**, 287–301.
23. Tabata, Y., Nagano, A., and Ikada, Y. (1999) Biodegradation of hydrogel carrier incorporating fibroblast growth factor. *Tissue Eng.* **5**, 127–138.
24. Tabata, Y., Hijikata, S., Munirzzaman, M. D., and Ikada, Y. (1999) Neo-vascularization through biodegradable gelatin microspheres incorporating basic fibroblast growth factor. *J. Biomater. Sci. Polym. Ed.* **10**, 79–94.

25. Tabata, Y., Morimoto, K., Katsumata, H., Yabuta, T., Iwanaga, K., Kakemi, M., and Ikada, Y. (1999) Surfactant-free preparation of biodegradable hydrogel microspheres for protein release. *J. Bioactive Compatible Polym.* **14**, 371–384.
26. Rifkin, D. B. and Moscatelli, D. (1989) Structural characterization and biological functions of basic fibroblast growth factor. *J. Cell Biol.* **109**, 1–6.
27. Tabata, Y. and Ikada, Y. (1999) Vascularization effect of basic fibroblast growth factor released from gelatin hydrogels with different biodegradabilities. *Biomaterials* **20**, 2169–2175.
28. Wang, W., Gu, Y., Tabata, Y., Miyamoto, M., Hori, H., Nagata, N., Touma, M., Balamurugan, A. N., Kawakami, Y., Nozawa, M., and Inoue, K. (2002) Reversal of diabetes in mice by xenotransplantation of a bioartificial pancreas in a prevascularized subcutaneous site. *Transplantation* **73**, 122–129.
29. Ogawa, K., Asonuma, K., Inamoto, Y., Tabata, Y., and Tanaka, K. (2001) The efficacy of prevascularization by basic FGF for hepatocyte transplantation using polymer devices in rats. *Cell Transplant.* **83**, 281–302.
30. Sakakibara, Y., Nishimura, K., Tambara, K., Yamamoto, M., Lu, F., Tabata, Y., and Komeda, M. (2002) Prevascularization with gelatin microspheres containing basic fibroblast growth factor enhances the benefits of cardiomyocyte transplantation. *J. Thorac. Cardiovasc. Surg.* **124**, 50–56.
31. Tabata, Y., Yamada, K., Miyamoto, S., Nagata, I., Kikuchi, H., Aoyama, I., Tamura, M., and Ikada, Y. (1998) Bone regeneration by basic fibroblast growth factor complexed with biodegradable hydrogel. *Biomaterials* **19**, 807–815.
32. Tabata, Y., Yamada, K., Hong, L., Miyamoto, S., Hashimoto, N., and Ikada, Y. (1999) Skull bone regeneration in primates in response to basic fibroblast growth factor. *J. Neurosurg.* **91**, 851–856.
33. Hong, L., Tabata, Y., Yamamoto, M., Miyamoto, S., Yamada, K., Hashimoto, N., and Ikada, Y. (1998) Comparison of bone regeneration in a rabbit skull defect by recombinant human BMP-2 incorporated in biodegradable hydrogel and in solution. *J. Biomater. Sci. Polym. Ed.* **9**, 1001–1014.
34. Hong, L., Tabata, Y., Miyamoto, S., Yamamoto, M., Yamada, K., Hashimoto, N., and Ikada, Y. (2000) Bone regeneration at rabbit skull defects treated with transforming growth factor- $\beta$ 1 incorporated into hydrogels with different levels of biodegradability. *J. Neurosurgery* **92**, 315–325.
35. Yamamoto, M., Tabata, Y., Hong, L., Miyamoto, S., Hashimoto, N., and Ikada, Y. (2000) Bone regeneration by transforming growth factor  $\beta$ 1 released from a biodegradable hydrogel. *J. Control. Release* **64**, 133–142.
36. Hong, L., Tabata, Y., Miyamoto, S., Yamada, K., Aoyama, I., Tamura, M., Hashimoto, N., and Ikada, Y. (2000) Promoted bone healing at rabbit skull gap between autologous bone fragment and the surrounding intact bone with biodegradable microspheres containing transforming growth factor  $\beta$ 1. *Tissue Eng.* **6**, 331–340.
37. Tabata, Y., Hong, L., Miyamoto, S., Miyao, M., Hashimoto, N., and Ikada, Y. (2000) Bone formation at a rabbit skull defect by autologous bone marrow combined with gelatin microspheres containing TGF- $\beta$ 1. *J. Biomater. Sci. Polym. Ed.* **11**, 891–901.



38. Tabata, Y., Miyao, M., Inamoto, T., Ishii, T., Hirano, Y., Yamaoki, Y., and Ikada, Y. (2000) De novo formation of adipose tissue by controlled release of basic fibroblast growth factor. *Tissue Eng.* **6**, 279–289.
39. Kimura, Y., Ozeki, M., Inamoto, T., and Tabata, Y. (2003) Adipose tissue engineering based on human preadipocytes combined with gelatin microspheres containing basic fibroblast growth factor. *Biomaterials* **24**, 2513–2521.

## Nanotechnology With S-Layer Proteins

Bernhard Schuster, Erica Györvary, Dietmar Pum, and Uwe B. Sleytr

### Summary

The cross-fertilization of biology, chemistry, material sciences, and solid-state physics is opening up a great variety of new opportunities for innovation in nanosciences. One of the key challenges is the technological utilization of self-assembly systems wherein molecules spontaneously associate under equilibrium conditions into reproducible supramolecular aggregates. The attractiveness of such processes lies in their capability to build uniform, ultrasmall functional units and the possibility of exploiting such structures at meso- and macroscopic scale for life and nonlife science applications. The use of crystalline bacterial cell-surface proteins (S-layer proteins) provided innovative approaches for the assembly of supramolecular structures and devices with dimensions of a few to tens of nanometers. S-layers have proven to be particularly suited as building blocks in a molecular construction kit involving all major classes of biological molecules. The immobilization of biomolecules in an ordered fashion on solid substrates and their controlled confinement in definite areas of nanometer dimensions are key requirements for many applications including the development of bioanalytical sensors, biochips, molecular electronics, biocompatible surfaces, and signal processing among functional membranes, cells, and integrated circuits.

**Key Words:** Surface layers; S-layers; two-dimensional protein crystals; biomimetics; self-assembly; nanotechnology; nanobiotechnology; nanoparticle; construction kit; supported lipid membranes.

### 1. Introduction

Many prokaryotic organisms have regular arrays of (glyco)proteins on their outermost surface (for a compilation, *see ref. 1*). These monomolecular crystalline surface layers, termed S-layers (2), are found in members of nearly every taxonomic group of walled bacteria and cyanobacteria and represent an almost universal feature of archaeal cell envelopes (*see Fig. 1*). S-layers are generally composed of a single protein or glycoprotein species with a molecular mass of

From: *Methods in Molecular Biology*, vol. 300:  
*Protein Nanotechnology, Protocols, Instrumentation, and Applications*  
Edited by: T. Vo-Dinh © Humana Press Inc., Totowa, NJ

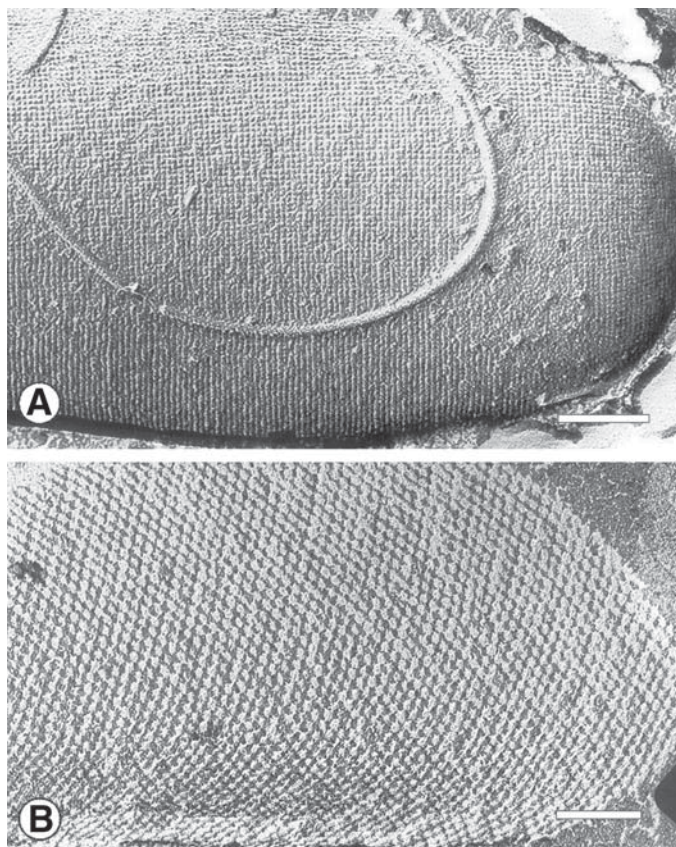


Fig. 1. Electron micrographs of freeze-etching preparations of whole cells of (A) *B. sphaericus*, showing a square S-layer lattice; (B) *Thermoplasma thermohydrosulfuricus*, revealing a hexagonally ordered array. Bars: (A) 200 nm; (B) 100 nm. (Reprinted from **ref. 45** with permission from the publisher; © 2001, Elsevier Science.)

40,000 to 230,000 Daltons and exhibit either oblique (p1, p2), square (p4), or hexagonal (p3, p6) lattice symmetry with unit cell dimensions in the range of 3 to 30 nm (see **Fig. 2**). One morphological unit consists of one, two, three, four, or six identical subunits, respectively. The monomolecular arrays are generally 5 to 10 nm thick and show pores of identical size (diameter of 1.5–8 nm) and morphology. In most S-layers, the outer face is less corrugated than the inner face. Moreover, S-layers are highly anisotropic structures regarding the net charge and hydrophobicity of the inner and outer surface (3,4). Owing to the crystalline character of S-layers, functional groups (e.g., carboxyl, amino, hydroxyl groups) are repeated with the periodicity of the protein lattice.

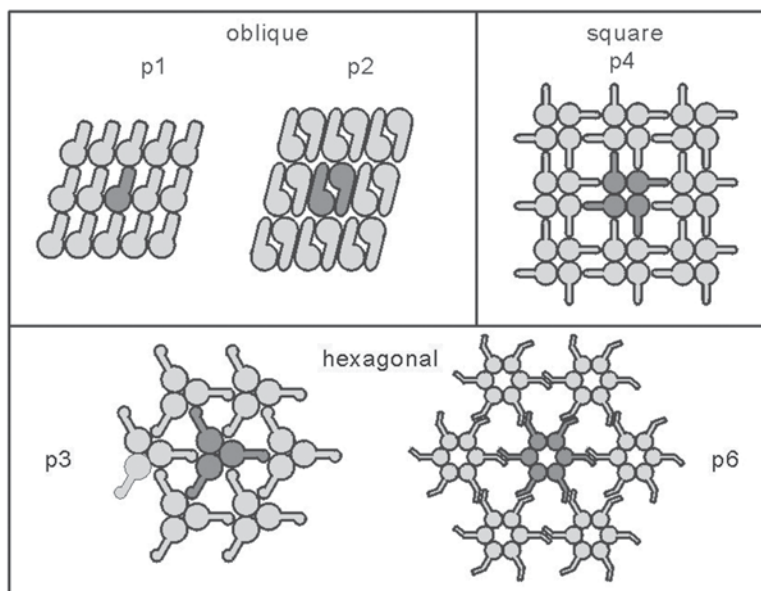


Fig. 2. Schematic representation of types of S-layer lattice grouped according to possible 2D space group symmetries. Morphological units were chosen arbitrarily and are shown in dark gray. (Reprinted from **ref. 8** with permission from the publisher; © 2003, Wiley-VCH.)

Because S-layers possess a high degree of structural regularity and the constituent subunits are the most abundant of all bacterial cellular proteins, these crystalline arrays are excellent models for studying the dynamic aspects of assembly of a supramolecular structure *in vivo* and *in vitro*. Moreover, the use of S-layers provided innovative approaches for the assembly of supramolecular structures and devices. S-layers have proven to be particularly suited as building blocks and patterning elements in a biomolecular construction kit involving all major classes of biological and chemically synthesized molecules or nanoparticles. In this context, one of the most important properties of isolated S-layer (glyco)protein subunits is their capability to reassemble into monomolecular arrays in suspension, at the air interface, on a solid surface, on floating lipid monolayers (*see Fig. 3*), and on liposomes or particles (for a review, *see refs. 5–8*).

An important line of development in S-layer-based technologies is presently directed toward the genetic manipulation of S-layer proteins. These strategies open new possibilities for the specific tuning of their structure and function. S-layer proteins incorporating specific functional domains of other proteins while maintaining the self-assembly capability will lead to new ultrafiltration

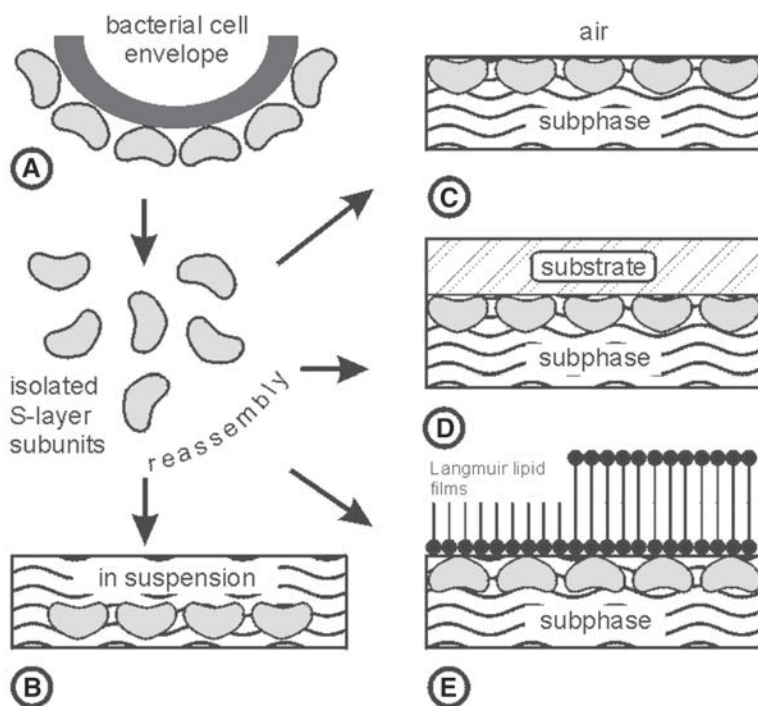


Fig. 3. (A) Schematic illustration of recrystallization of isolated S-layer subunits into crystalline arrays. The self-assembly process can occur (B) in suspension, (C) at the air-liquid interface, (D) on solid supports, and (E) on Langmuir lipid films. (Reprinted from ref. 5 with permission from the publisher; © 1999, Wiley-VCH.)

membranes, affinity structures, enzyme membranes, metal-precipitating matrices, microcarriers, biosensors, diagnostics, biocompatible surfaces, and vaccines (6,7).

Although up to now most S-layer technologies developed concerned life sciences, an important emerging field of future applications relates to nonlife sciences. Native or genetically modified S-layers recrystallized on solid supports can be used as patterning elements for accurate spatial positions of nanometer-scale metal particles or as matrices for chemical deposition of metals as required for molecular electronics and nonlinear optics.

## 2. Materials

### 2.1. Bacterial Strain, Growth in Continuous Culture, and Isolation

#### 2.1.1. Bacterial Strains

1. *Geobacillus stearothermophilus* PV72, kindly provided by F. Hollaus (Österreichisches Zuckerforschungsinstitut, Tulln, Austria).

2. *Bacillus sphaericus* CCM 2177 (Czech Collection of Microorganisms, Brno, Czech Republic).

### 2.1.2. Growth in Continuous Culture

1. SVIII medium: 10 g/L of peptone, 5 g/L of yeast extract, 5 g/L of lab lemco, 1.2 g/L of  $K_2HPO_4 \cdot 3H_2O$ , 0.1 g/L of  $MgSO_4 \cdot 7H_2O$ , 0.6 g/L of sucrose.
2. Bioreactor type Biostat E (Braun, Melsungen, Germany).
3. Mass flow controller (Brooks, Veenendaal, The Netherlands).
4. 1 N NaOH and 2 N  $H_2SO_4$  (Merck, Darmstadt, Germany).
5. pH and redox probes of gel paste type and an amperometric probe (Ingold, Urdorf, Switzerland).
6. Spectrophotometer (model 25; Beckman, Fullerton, CA).
7. Sodium dodecyl sulfate-polyacrylamide gel electrophoresis (SDS-PAGE) apparatus (Bio-Rad, Hercules, CA).
8. Densitometer (Elscript 400AT/SM; Hirschmann, Neuried, Germany).
9. Centrifuge (Sepatech 17RS; Heraeus, Hanau, Germany).
10. Buffer A: 50 mM Tris-HCl (Fluka, Buchs, Switzerland) buffer, adjusted to pH 7.2.

### 2.1.3. Preparation of Cell-Wall Fragments

1. Ultrasonicator treatment (Ultrasonics Sonicator W-385; Farmingdale, NY).
2. Centrifuge (JA-HS; Beckmann).
3. 0.75% Triton X-100 (Serva, Heidelberg, Germany) dissolved in buffer A.

### 2.1.4. Isolation of S-Layer Proteins

1. 5 M Guanidine hydrochloride (Fluka) in buffer A.
2. Ultracentrifuge (Beckmann L5-65).
3. 10 mM  $CaCl_2$  in distilled water (Fluka).
4. Dialysis tube with a cutoff of 12 to 16 kDa and a pore size of 25 Å (Biomol, Hamburg, Germany).
5. Spectrophotometer (Hitachi U 2000; Tokyo, Japan).

## 2.2. S-Layer Proteins on Solid Supports

### 2.2.1. Solid Supports

1. Silicon nitride and silicon wafers (100 orientation, p-type, boron-doped, resistivity of 25 to 45  $\Omega$ cm, native oxide layer; MEMC, Novara, Italy, or Wacker Chemitronic, Burghausen, Germany).
2. Metallic wafers: gold-coated supports (Pharmacia, Peapack, NJ), titanium, aluminum, palladium.
3. Polymers: polyester, polypropylene, poly(ethylene terephthalate), poly(methacrylic acid methylester), polycarbonate (Wettlinger Kunststoffe, Wien, Austria).



4. Glass slides (Assistant Micro Slides, No. 2400; Elka, Sondheim, Germany), cellulose, mica, highly oriented pyrolytic graphite.

### 2.2.2. Cleaning and Modification of Solid Supports

1. Solvents (acetone, propan-2-ol, ethanol, ammonia [29%], hydrogen peroxide [30%], HCl [37%], and dried toluene; Merck), Milli-Q water (Millipore, Bedford, MA), and N<sub>2</sub> gas (Linde, Wien, Austria).
2. Silanes: octadecyltrichlorosilane, (3-methacryloyloxypropyl)-trimethoxysilane, trimethoxysilane, decyldimethylsilane, hexamethyldisilane, 2-aminopropyl-trimethoxysilane, 3-mercaptopropyltrimethoxysilane (ABCR, Karlsruhe, Germany).
3. Plasma cleaner (Gala, Bad Schwalbach, Germany) and O<sub>2</sub> gas (Linde).
4. Kruss contact angle measurement system G1 (Hamburg, Germany).

### 2.2.3. Crystallization of S-Layer Proteins on Solid Supports

1. Buffer B: 1 mM citrate buffer (Fluka) adjusted to pH 4.0 with NaOH and HCl (Merck).
2. Buffer C: 10 mM CaCl<sub>2</sub> in 0.5 mM Tris-HCl (Fluka) buffer adjusted to pH 9.0 with NaOH and HCl (Merck).
3. pH Meter (Mettler Toledo MP 220; Schwerzenbach, Switzerland).
4. *G. stearothermophilus* PV72 (0.1 mg/mL) (see **Subheading 2.1.1.**) in buffer B.
5. *B. sphaericus* CCM 2177 (0.1 mg/mL) (see **Subheading 2.1.1.**) in buffer C.
6. Rotator (Reax2; Heidolph, Schwabach, Germany).

### 2.2.4. Atomic Force Microscopy

1. Digital Instruments Nanoscope IIIa (Santa Barbara, CA) or other nanoscope with an E-scanner (nominal scan size: 12  $\mu\text{m}$ ) or a J-scanner (nominal scan size: 130  $\mu\text{m}$ ).
2. Standard 200- $\mu\text{m}$ -long oxide-sharpened silicon nitride cantilevers (NanoProbes; Digital Instruments) with a nominal spring constant of 0.06  $\text{Nm}^{-1}$ .

## 2.3. Patterning of Crystalline S-Layer Proteins

### 2.3.1. S-Layer Protein-Covered Solid Supports

1. S-layer protein SbpA of *B. sphaericus* CCM2177 (see **Subheading 2.1.1.**).
2. Buffer C (see **Subheading 2.2.3.**).
3. Cleaning and characterization materials (see **Subheading 2.2.2.**).

### 2.3.2. Lithographic Masks

1. Chromium coating 100 nm thick on quartz glass consisting of lines and squares (feature sizes ranging from 200 to 1000 nm) with different line-and-space ratios.

### 2.3.3. Excimer Laser

1. ArF excimer laser (model EMG 102E; Lambda Physik, Göttingen, Germany).

#### 2.3.4. Poly(dimethylsiloxane) Molds

1. Silicon mold master: 4-in. silicon wafers, photoresist (Clariant AZ 9260; Microchemicals, Ulm, Germany), photolithography.
2. Poly(dimethylsiloxane) (PDMS) (Sylgard 184; Dow Corning, Midland, MI).
3. Oven (Memmert, U 25; Schwabach, Germany), exsiccator.

#### 2.3.5. Microscopy

1. Materials for atomic force microscopy (AFM) (*see Subheading 2.2.4.*).
2. Materials for epifluorescence microscopy:
  - a. Buffer D: 0.1 M NaHCO<sub>3</sub>-Na<sub>2</sub>CO<sub>3</sub> buffer adjusted to pH 9.2 with NaOH and HCl (Merck).
  - b. Fluorescence marker (fluorescein isothiocyanate [FITC]), and dimethyl sulfoxide (DMSO) (both from Sigma-Aldrich, Wien, Austria).
  - c. Fluorescence microscope (Nikon, Tokyo, Japan).

### 2.4. Formation of Nanoparticle Arrays

#### 2.4.1. Preparation of Supports

1. Standard formvar- and carbon-coated electron microscope grids (Groepl, Tulln, Austria).
2. SiO<sub>2</sub>, to coat grids by evaporation (EPA 100; Leybold-Heraeus, Köln, Germany).
3. O<sub>2</sub> plasma, to treat SiO<sub>2</sub>-coated grids in a plasma cleaner (*see Subheading 2.2.2.*).

#### 2.4.2. Electrostatic Binding of Nanoparticles to S-Layers

1. S-layer protein SbpA of *B. sphaericus* CCM 2177 (0.1 mg/mL) in buffer C (*see Subheading 2.2.3.*) and O<sub>2</sub>-treated SiO<sub>2</sub>-coated grids.
2. Nanoparticles: citrate-stabilized gold nanoparticles (mean diameter of 5 nm; Sigma-Aldrich) and amino-modified cadmium selenide (CdSe) nanoparticles (mean diameter of 4 nm; University of Hamburg, Germany).

#### 2.4.3. Transmission Electron Microscopy

1. Uranyl acetate (2.5% in Milli-Q water; Merck) for negative staining.
2. Transmission electron microscope (TEM CM12; Philips, Eindhoven, The Netherlands).

### 2.5. S-Layer-Supported Lipid Membranes

#### 2.5.1. Painted and Folded Membranes

1. 1,2-Diphytanoyl-*sn*-glycero-3-phosphocholine (DPhyPC) (Avanti, Alabaster, AL).
2. Hexadecane, *n*-decane, *n*-hexane, and pentane (Fluka).
3. Chloroform and ethanol (Merck).
4. Electrolyte: 0.01 to 1 M KCl or NaCl in Milli-Q water and, if desired, 10 mM CaCl<sub>2</sub> (all chemicals obtained from Merck).



5. Painted membranes: homemade Teflon chamber with a drilled orifice, 0.9 mm in diameter, dividing the two compartments with a volume of about 12 mL each (for more details, see refs. 9–11).
6. Copper wire (approx 1 mm in diameter) covered with a Teflon (polytetrafluoroethylene) tube and bent in an L shape to form a brush.
7. Folded membranes: homemade Teflon chamber with a Teflon film (25  $\mu\text{m}$  thick; Goodfellow, Cambridge, England) which divided the two compartments with a volume of about 3.5 mL, each. Into the Teflon film a hole, approx 140  $\mu\text{m}$  in diameter, was punched by a perforating tool (syringe needle that has been sharpened inside and outside; for further details see refs. 9, 10, 12).
8. Two 1-mL single-use syringes (B. Braun, Melsungen, Germany), or others, two plastic tubes.

### 2.5.2. Technical Equipment

1. Patch-clamp amplifier (EPC9; HEKA, Lamprecht, Germany), or others, with corresponding software (Pulse+PulseFit 8.11; HEKA).
2. Two silver/silver chloride (Ag/AgCl) electrodes (see Note 1).
3. Vibration isolation unit (Newport, Darmstadt, Germany) with a Faraday cage on top.

## 3. Methods

### 3.1. Bacterial Strain, Growth in Continuous Culture, and Isolation

#### 3.1.1. Growth in Continuous Culture

*G. stearothermophilus* PV72 (3,13,14) was grown on 50 mL of SVIII medium (15) in a 300-mL shaking flask at 57°C to mid-logarithmic growth. Two hundred milliliters of this suspension was used as the inoculum for 5 L of SVIII medium sterilized in a bioreactor. Before inoculation, 20 mL of a sterile glucose solution (6 g of glucose in total) was added. Cultivation was performed at 57°C and a stirring speed of 300 rpm. In continuous culture, the dilution rate was kept at 0.1 h<sup>-1</sup>. The rate of aeration was 0.5 L of air/min. The pH of the culture was kept at 7.2  $\pm$  0.2 by the addition of either 1 N NaOH or 2 N H<sub>2</sub>SO<sub>4</sub>. Aeration rate was controlled by a mass flow controller. Redox potential was measured by a platinum contact redox probe. The partial oxygen pressure was monitored with an amperometric probe. The cell density was measured at 600 nm in a spectrophotometer. In principle, *B. sphaericus* CCM 2177 (16) was cultivated under the same conditions, but because this organism is a mesophilic one, the temperature was lowered to 32°C (see Note 2).

For controlling the homogeneity of the culture, 10-mL samples were taken from the bioreactor at different times. Aliquots were plated on SVIII agar, and the grown biomass (at 57°C for 18 h) was used for SDS-PAGE (13). The gel system contained a 4% stacking gel and a 10% separation gel. Single-cell colonies grown on SVIII agar plates were subjected to SDS-PAGE for final identi-

fication. The relative amounts from both types of S-layer proteins were estimated from SDS gels by densitometric evaluation.

For biomass harvesting, the culture suspension from the overflow of continuous culture was collected in heat-sterilized bottles at 2 to 4°C. Cells were separated from spent medium by continuous centrifugation at 16,000g and 4°C, washed with buffer A, and stored at -20°C.

### 3.1.2. Preparation of Cell-Wall Fragments

The frozen biomass (100 g) was suspended in 350 mL of buffer A. The suspension was separated into three parts and the cells were broken by ultrasonic treatment for 2 min at maximal output. To avoid autocatalytic processes, all preparation steps must be done on ice at 4°C. Subsequently, the intact and broken cells were separated by centrifuging at 28,000g for 10 min. The upper, lighter pellet was detached and collected. The lower, darker pellet was again suspended in buffer A, ultrasonically treated, and sedimented. This procedure was repeated four times. To remove contaminating plasma membrane fragments, the crude cell-wall preparations (collected pellets) were extracted with 250 mL of 0.75% Triton X-100 (dissolved buffer A) and stirred for 10 min at room temperature ( $22 \pm 2^\circ\text{C}$ ). Subsequently, the cell-wall fragments were sedimented at 40,000g for 10 min. The extraction step was repeated three times. Finally, the pellet was frozen in aliquots at -20°C.

### 3.1.3. Isolation of S-Layer Proteins

Cell-wall fragments (2 mg) were suspended in 30 mL of guanidine hydrochloride solution in buffer A and stirred at room temperature for 30 min. Subsequently, the suspension was sedimented at 30,000 rpm and 4°C for 45 min in an ultracentrifuge. The supernatant was dialyzed either against a  $\text{CaCl}_2$  solution (*G. stearothermophilus* PV72) or against distilled water (*B. sphaericus* CCM 2177) three times for at least 2 h each, at 4°C (see **Note 3**). Finally, the S-layer self-assembly products (see **Note 4**) were sedimented for 15 min at 40,000g and 4°C. The supernatant containing single subunits and oligomeric precursors were stored at 4°C and used within 5 d. For determination of the protein concentration, the measured adsorption at 280 nm was multiplied by 1.75 and 1.64 for the S-layer protein SbsB of *G. stearothermophilus* PV72 and SbpA of *B. sphaericus* CCM 2177, respectively. The protein solutions were adjusted to a concentration of 1 mg of protein/mL and used for all recrystallization experiments described later (**Fig. 3**).

## 3.2. S-Layer Proteins on Solid Supports

### 3.2.1. Preparation of Solid Supports

Silicon wafers were immersed in hot acetone followed by rinsing in propan-2-ol and finally washed with ethanol and Milli-Q water. The advancing contact

angle of water on the clean silicon surface was  $65^\circ$ . To increase the hydrophilicity of the substrates, the silicon wafers were treated in an  $O_2$  plasma (20-s leaning time, 0.01-bar plasma pressure, 70% power density, high-purity-grade  $O_2$ ). The plasma-treated silicon substrates with an advancing contact angle of water of  $5^\circ$  were used immediately for the recrystallization studies. Other solid supports (e.g., metals, polymers, glass) were only rinsed with ethanol and Milli-Q water before use.

Silanization procedures (solution or vapor phase) using different silanes were applied to obtain silicon or glass substrates with more-hydrophobic surfaces (17,18). The substrates were cleaned in a solution containing 1:1:5 parts of ammonia (29%), hydrogen peroxide (30%), and Milli-Q water at  $80^\circ\text{C}$  for 10 min. Subsequently, the silicon or glass substrates were treated with 1:1:6 parts of concentrated hydrogen chloride (37%), hydrogen peroxide (30%), and deionized water at  $80^\circ\text{C}$  for 15 min. Finally, the substrates were rinsed thoroughly with Milli-Q water and dried in a stream of nitrogen gas. This procedure is known as RCA cleaning.

For silanization out of a solution, the substrates were further rinsed with acetone and dried with toluene. Subsequently, the supports were put into anhydrous toluene containing 1% silane. Silanization (e.g., with decyldimethylsilane), was carried out for 30 min to 2 h with mild shaking at room temperature. Finally, the silanized supports were rinsed with toluene, methanol, and Milli-Q water.

Silanization from vapor phase was performed with silanes of shorter chain lengths (e.g., hexamethyldisilane). Supports were baked with some drops of silane in an airtight glass vessel at  $60^\circ\text{C}$  for 2 h and finally rinsed with methanol.

### 3.2.2. S-Layer Protein Recrystallization on Solid Supports

For recrystallization of the S-layer protein SbsB of *G. stearothermophilus* PV72 and SbpA of *B. sphaericus* CCM 2177, buffer B and buffer C were used, respectively. The protein concentration in all experiments was 0.1 mg/mL. Recrystallization on solid supports was carried out either in rotating Eppendorf tubes that had been previously filled with the protein solution or in glass wells. In the latter case, the substrates were placed onto the air-liquid interface. After a recrystallization time of 4 h at room temperature, the supports were removed by tweezers, washed, and stored in Milli-Q water ( $4^\circ\text{C}$ ).

### 3.2.3. Atomic Force Microscopy

Scanning was carried out in contact mode in a liquid cell filled with a 100 mM NaCl solution (Fig. 4). The applied force was kept to a minimum during scanning to prevent modification of the sample surface by the tip. Scan speed was approx 6 Hz. Images were flattened line by line during recording using the microscope's software.

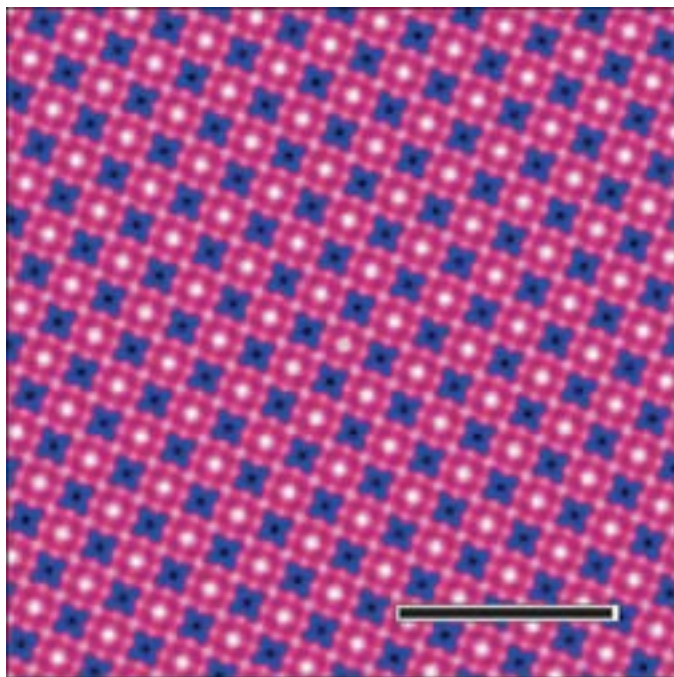


Fig. 4. Scanning force microscopic image of S-layer protein SbpA from *B. sphaericus* CCM 2177 recrystallized on a silicon wafer. The image was recorded in contact mode in a liquid cell (bar = 50 nm). (Reprinted from **ref. 8** with permission from the publisher; © 2003, Wiley-VCH.)

AFM studies showed crystalline domains with average diameters of 10 to 20  $\mu\text{m}$  for SbsB and 0.1 to 10  $\mu\text{m}$  for SbpA, when crystallized on a variety of solid supports (*see Table 1*). In particular, SbsB generated crystalline monolayers only on hydrophobic solid supports, whereas SbpA formed extended crystalline domains on hydrophilic surfaces, but only small patches on hydrophobic ones.

### 3.3. Patterning of Crystalline S-Layer Proteins

#### 3.3.1. Excimer Laser Patterning

Silicon wafers were cleaned with several solvents and  $\text{O}_2$  plasma treated (*see Subheading 3.2.*). Recrystallization of isolated S-layer protein on the silicon wafer was carried out as previously described (*see Subheading 3.2.*).

Prior to irradiation, the recrystallized S-layer was carefully dried in a stream of high-purity nitrogen gas in order to remove excess water not required for maintaining the structural integrity of the protein lattice (*see Note 5*). Then, the

**Table 1**  
**Supports and Their Modifications**  
**Used in Formation of Crystalline S-Layer Protein Layers<sup>a</sup>**

Support	Surface and modifications	SbsB	SbpA
Silicon wafers (100 orientation, p-type)	Si (native oxide layer) RCA cleaned	–	–
	Si (native oxide layer)	+	+ <sup>b</sup>
	Si (native oxide layer) O <sub>2</sub> plasma treated	–	+
	Si <sub>3</sub> N <sub>4</sub>	+	+
	Octadecyltrichlorosilane	+	+
	(3-Methacryloyloxypropyl)-trimethoxysilane	+	+
	Trimethoxysilane	+	+
	Decyldimethylsilane	+	+
	Hexamethyldisilane	+	+
	2-Aminopropyltrimethoxysilane	+	+
	3-Mercaptopropyltrimethoxysilane	+	+
Metallic supports	Gold	+	+
	Titanium	+	+
	Aluminum	n	+
	Palladium	+	+
Polymers	Polyester	+	n
	Polypropylene	+	+
	Poly(ethylene terephthalate)	n	+
	Poly(methacrylic acid methylester)	n	+
	Polycarbonate	+	n
Others	Glass	+	+
	Cellulose	+	+
	Mica	–	+
	Highly oriented pyrolytic graphite	–	+

<sup>a</sup>+, crystallization; –, no crystallization; n, not tested.

<sup>b</sup>Very large crystalline domains.

lithographic mask was brought into direct contact with the S-layer-coated silicon wafer (**Fig. 5**). The whole assembly was irradiated by the ArF excimer laser (*see Note 6*) in a series of one to five pulses with an intensity of about 100 mJ/cm<sup>2</sup> per pulse (pulse duration: 8 ns; 1 pulse/s). Finally, the mask was removed and the S-layer-coated silicon wafer was immediately immersed in buffer.

S-layers that have been patterned by ArF excimer laser radiation may also be used as high-resolution etching masks in nano/microlithography. This application requires enhancement of the patterned protein layer by electro-less

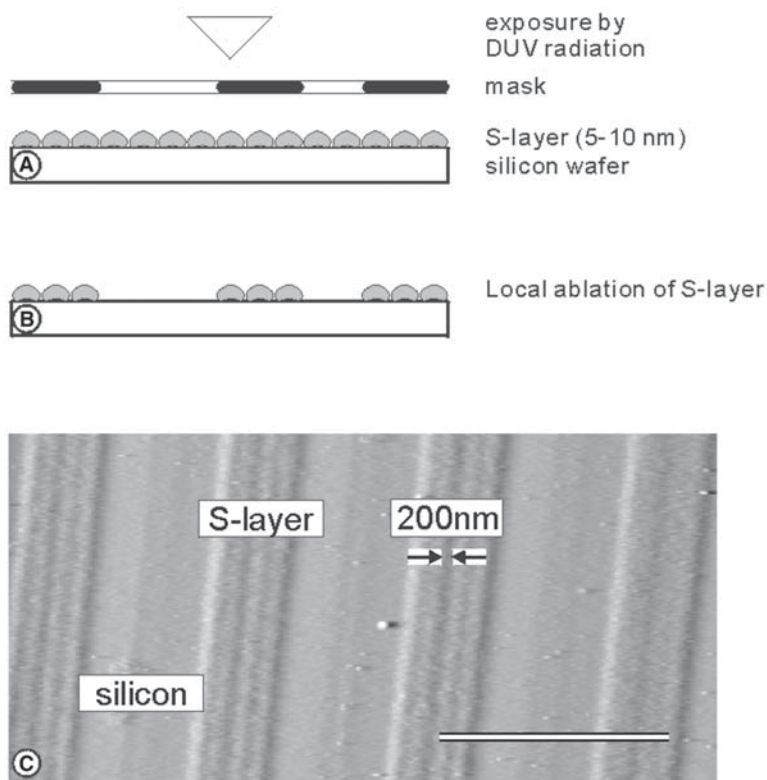


Fig. 5. Schematic drawing of patterning of S-layers by exposure to deep ultraviolet (DUV) radiation. (A) A pattern is transferred onto the S-layer by exposure to ArF excimer laser radiation through a microlithographic mask. (B) The S-layer is specifically removed from the silicon surface in the exposed areas. (C) A scanning force microscopic image of a patterned S-layer on a silicon wafer is shown. Bar = 3  $\mu\text{m}$ . (Modified after **ref. 5** with permission from the publisher; © 1999, Wiley-VCH.)

metallization prior to subsequent reactive ion etching. Since S-layers are only 5 to 10 nm thick, and thus much smaller than conventional resists (500–1000 nm mean thickness), proximity effects are strongly reduced, yielding a considerable improvement in edge resolution. For the development of bioanalytical sensors, patterned S-layers may also be used as electrode structures for binding biologically active molecules at specified target areas.

### 3.3.2. Soft Lithography Patterning

A well-known soft lithography technique, micromolding in capillaries (MIMIC) (**19,20**), can be used for patterning and self-assembly of 2D S-layer protein arrays on silicon supports. For mold formation, 6- $\mu\text{m}$ -high mesa-struc-



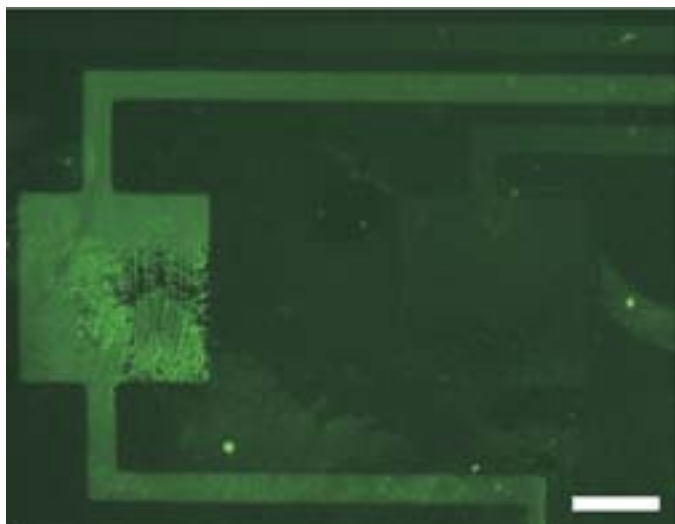


Fig. 6. Fluorescence image of FITC-labeled S-layer protein SbpA patterned at a plasma-treated native silicon oxide support using a PDMS mold. Bar = 50  $\mu\text{m}$ .

ture mold masters were fabricated in photoresist on 4-in. silicon wafers using photolithography. PDMS was used to generate the molds from the masters (21,22). Ten parts of PDMS and one part of elastomer were mixed and degassed in an exsiccator. The PDMS solution was put on the master, which was placed in a Petri dish, and again the solution was degassed until no bubbles were observed. The PDMS mold was baked at 50°C for at least 4 h and subsequently removed from the master and cut to a proper size. Microchannels were formed when the recessed grooves in the PDMS mold were brought into conformal contact with the planar support, typically a native oxide-terminated silicon wafer.

The microchannels were subsequently filled from one end with protein solution (0.1 mg/mL of SbpA in buffer C) by capillary action. The silicon supports (solvent cleaned) were O<sub>2</sub> plasma treated before application of the mold in order to increase the wettability of the surface and to improve channel filling (*see Note 7*). After self-assembly and crystallization of the S-layer protein (30 min to 24 h), the PDMS mold was removed under Milli-Q water, leaving the patterned S-layer arrays on the support. The patterning was detected either by AFM (*see Subheading 3.2.*) or by epifluorescence microscopy.

For microscopic detection of fluorescence, the protein structures were labeled with FITC (*see Note 8*). The solid-supported S-layer patterns were incubated with the FITC suspension (1 mg of FITC in 100  $\mu\text{L}$  of DMSO, diluted with 2 mL of buffer D) for 1 h at room temperature in the dark. After labeling,

the samples were washed with buffer D and, finally, the patterning was investigated by epifluorescence microscopy (**Fig. 6**).

The MIMIC technique can be utilized for lateral patterning of simple and moderately complex crystalline S-layer arrays ranging in critical dimension from submicrons to hundreds of microns. Furthermore, the native chemical functionality of the S-layer protein is completely retained, as demonstrated by attachment of human IgG antibody and subsequent binding of anti-human IgG antigen on the patterned S-layer substrates (**23**). This versatile MIMIC patterning technique can also be combined with immobilization techniques (*see Subheading 3.4.*), such as for controlled binding of nanoparticles with well-defined locations and orientations.

### **3.4. Formation of Nanoparticle Arrays**

#### *3.4.1. Preparation of Supports*

To obtain comparable surface properties with those of silicon wafers, standard formvar- and carbon-coated electron microscope grids were coated with a 1- to 10-nm-thick layer of SiO<sub>2</sub> by evaporation and subsequent O<sub>2</sub> plasma treatment as described before (*see Subheading 3.2.*).

#### *3.4.2. S-Layer Recrystallization*

A solution of SbpA of *B. sphaericus* CCM 2177 (0.1 mg of SbpA/mL of buffer C) was used to fill glass wells. Subsequently, the SiO<sub>2</sub>-coated grids were placed horizontally at the liquid-air interface and removed after 4 h. In most cases, there was not only a crystalline SbpA layer on the grid but also adsorbed self-assembly products. The S-layer protein-coated grids were washed and stored in Milli-Q water at 4°C.

#### *3.4.3. Nanoparticles*

Citrate-stabilized gold nanoparticles with a mean diameter of 5 nm were negatively charged. The amino-modified, positively charged CdSe nanoparticles were prepared according to the literature (**24,25**) (*see Note 9*). For noncovalent, electrostatic binding of nanoparticles to S-layer lattices, SbpA-coated grids (with or without attached S-layer self-assembly products; *see Note 4*) were incubated in the nanoparticle solution for 1 h at room temperature and washed with Milli-Q water.

#### *3.4.4. Transmission Electron Microscopy*

Transmission electron microscopy (TEM) analysis was performed on negatively stained but most frequently on untreated preparations. The structural (lattice constants, symmetries) and chemical diversity (surface-active functional groups) of S-layer proteins allows the formation of nanocrystal



superlattices with a spatially controlled packing. Owing to electrostatic interactions, anionic citrate-stabilized gold nanoparticles (5 nm in diameter) formed a superlattice at those sites where the inner face of the S-layer lattice was exposed. By contrast, cationic semiconductor nanoparticles (such as amino functionalized CdSe particles) formed arrays on the outer face of the solid-supported S-layer lattices (26).

### 3.5. S-Layer-Supported Lipid Membranes

#### 3.5.1. Formation of Painted Lipid Membranes

Lipid membranes (**Fig. 7A**) were made from a 1% (w/w) solution of DPhyPC in *n*-decane (27,28). The stock solution was stored at  $-20^{\circ}\text{C}$ . The orifice was prepaigned with DPhyPC dissolved in chloroform (10 mg/mL) and dried with nitrogen for at least 20 min. Subsequently, the compartments were filled with the electrolyte (12 mL each). The *cis* cell was grounded, and the *trans* cell was connected by another Ag/AgCl electrode to the patch-clamp amplifier. A drop of lipid mixture was put on the Teflon brush and stroked up the orifice. Membrane formation should be seen immediately (see **Note 10**). Thinning of the membranes was followed by measuring the capacitance of the lipid membrane. After a constant capacitance was reached (takes approx 20–40 min), experiments to study the intrinsic parameters of the lipid membrane were performed.

#### 3.5.2. Formation of Folded Lipid Membranes

DPhyPC was dissolved in *n*-hexane/ethanol (9:1). The stock solution was stored at  $-20^{\circ}\text{C}$  at a concentration of 5 mg of lipid/mL. At least 30 min before the formation of the membrane, the aperture was preconditioned with a small drop of hexadecane/pentane (1:10) (**Fig. 7B**). Both compartments were filled to just below the aperture with electrolyte (29). A volume of 2  $\mu\text{L}$  of the lipid stock solution was spread on the aqueous surface of each compartment, and the solvent was allowed to evaporate for at least 20 min. Raising the level of the electrolyte within the compartments to above the aperture by means of the syringes led to formation of a lipid membrane, which was checked by measuring its conductance and capacitance (see **Note 11**).

The current response from given voltage functions was measured to provide the capacitance and conductance of the lipid membranes (30,31). A triangular voltage function (+40 to  $-40$  mV, 20 ms) may be used to determine the capacitance of the lipid membrane. The specific capacitance is about 0.4 to 0.5 and 0.6 to 0.8  $\mu\text{F}/\text{cm}^2$  for the painted and folded membranes, respectively (9,11,32,33) (see **Note 12**). Membrane conductance is usually  $<10^{-8}$  S/ $\text{cm}^2$ . The settings of the two built-in Bessel filters of the amplifier for the current monitor signal were 10 and 1.5 kHz, respectively. All experiments should be performed at room temperature (see **Note 13**). After each experiment, the Teflon aperture

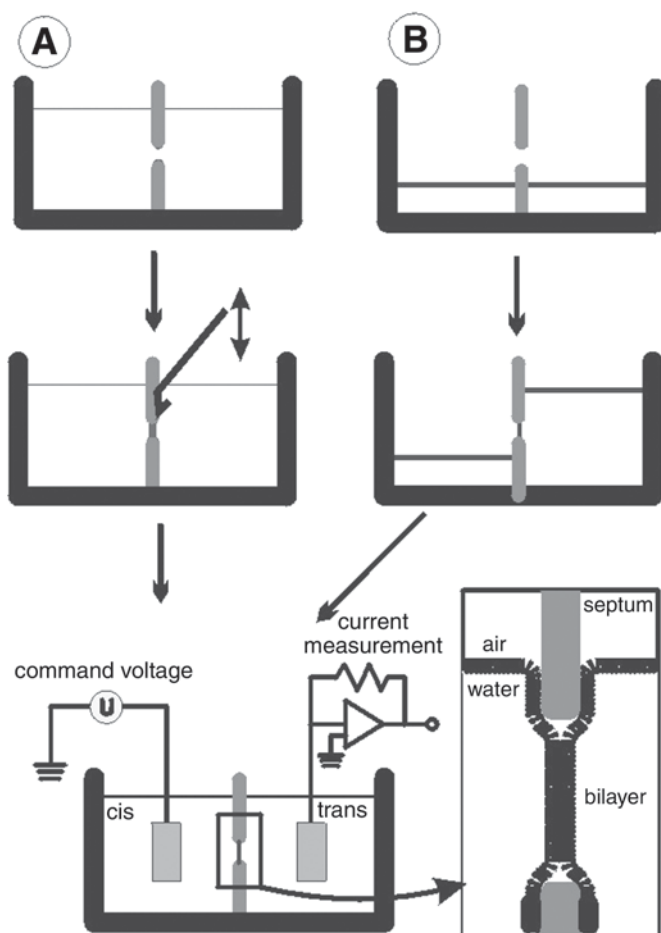


Fig. 7. Schematic illustration of formation of (A) painted and (B) folded lipid membrane. On the lower left is an illustration of the setup (not drawn to scale), and the inset shows a drawing of the bilayer lipid membrane.

was cleaned extensively with chloroform, methanol, and ethanol and finally rinsed with Milli-Q water.

### 3.5.3. Recrystallization of S-Layer Proteins *SbpA* and *SbsB*

After forming the painted or folded lipid membrane, the S-layer solution was carefully injected into the *trans* compartment to a final protein concentration of 0.1 mg/mL. The same volume of buffer was added to the *cis* compartment. According to our experience, the recrystallization process of S-layer subunits on lipid membranes was generally completed within 3 h (34). If the

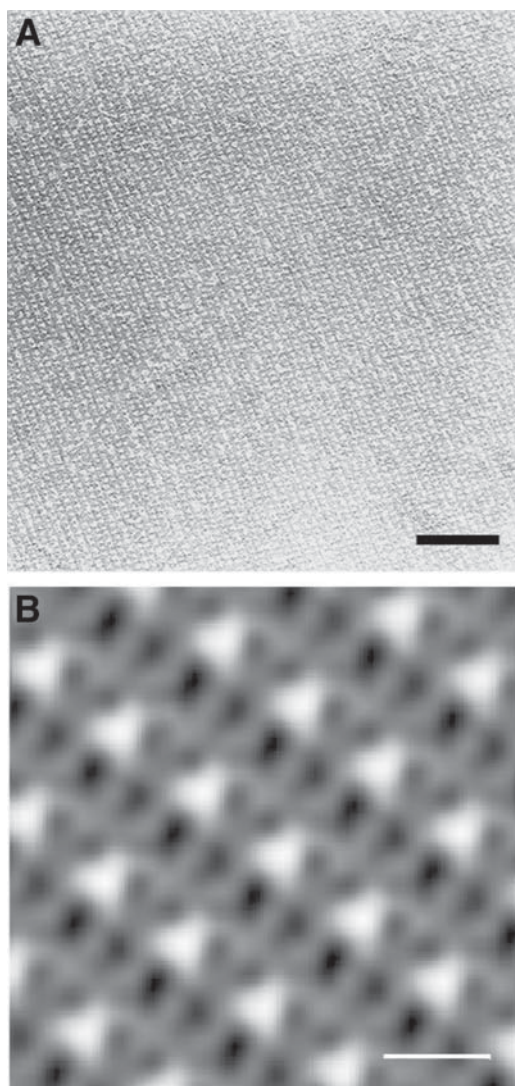


Fig. 8. **(A)** Electron micrograph of negatively stained preparation of S-layer protein SbsB isolated from *G. stearotheophilus* PV72 recrystallized on a monolayer made of DPhPC/hexadecylamine (molar ratio of 10:4). Bar = 100 nm. **(B)** Computer image reconstitution of transmission electron microscopic images of oblique S-layer lattice of SbsB. Bar = 10 nm. (Reprinted from **ref. 35** with permission; © 2002, Elsevier Science.)

lipid membrane should be supported by the S-layer protein SbpA from *B. sphaericus* CCM 2177, 10 mM  $\text{CaCl}_2$  has to be added to the electrolyte to make recrystallization possible. On the other hand, no  $\text{CaCl}_2$  is needed for the recrystallization of the S-layer SbsB protein of *G. stearotheophilus* PV72 (**Fig. 8**). The closely attached S-layer lattice did not affect the specific capacitance, whereas the resistance of the membranes increased slightly (**32,35–38**). Recrystallization of the S-layer protein can be investigated by TEM (*see Subheading 2.4.3.*) on deposited negatively stained preparations or by AFM investigations (*see Subheading 2.2.4.*) of the lipid-coated polymer septum.

The advantages of S-layer-supported lipid membranes are the enhanced long-term stability (**37,38**); the stability against voltage ramps even up to 500 mV and more (**39**); the increased bending stiffness (**40**); and, hence, the higher robustness against hydrostatic pressure gradients (**34,35**). Thus, it might be possible to distinguish at mechanosensitive ion channels (**41–43**), reconstituted in S-layer-supported lipid membranes, between the curvature-induced mechanical activation and the flow-induced activation (**35**). In addition, the tightly attached S-layer lattice allows complete reconstitution of membrane-active peptides (**37,44**) but also of complex membrane proteins such as  $\alpha$ -hemolysin (**36,38,39**).

#### 4. Notes

1. For chlorination, immerse silver wire as anode in a 0.1 N HCl solution and pass a current of 10 mA for 5 min through the wire.
2. *B. sphaericus* CCM 2177 tends to make the medium alkaline and, thus, one has to be prepared to add  $\text{H}_2\text{SO}_4$  early enough to maintain a pH of 7.2.
3. The S-layer-containing solutions should be dialyzed against large volumes, usually 3 L of distilled water, with or without  $\text{CaCl}_2$  taken at each dialysis step. Be sure to cool the distilled water to 4°C before performing dialysis.
4. Single isolated S-layer subunits from many prokaryotic organisms have shown the ability to assemble into regular lattices identical to those observed on intact cells on removal of the disrupting agents used for their isolation (e.g., on dialysis). The S-layer self-assembly processes lead to the formation of flat sheets, open-ended cylinders, or spheres. Ionic strength, temperature, protein concentration, and polymer associated with S-layers can determine both the rate and extent of assembly (for a review, *see refs. 5–8*).
5. Excess water has to be carefully removed before patterning in order to prevent interference fringes caused by the water film.
6. S-layer protein is completely removed by ArF ( $\lambda = 193$  nm) irradiation at a dose of 100 to 200 mJ/cm<sup>2</sup>.
7. Rapid filling of the micron-scale channels may be followed with an optical microscope, and capillaries may be filled even when the solution enters from both ends of the mold.

8. FITC binds to the free amino groups of the S-layer protein.
9. The amino-modified CdSe nanoparticles were prepared by an organometallic synthesis using a mixture of highly boiling primary aminoalkanes and tri-octylphosphine as the coordinating solvent. The CdSe nanocrystals from about 1 mL of freshly prepared sol were precipitated by adding a small amount of methanol. After removal of the supernatant, the particles were transferred in 5 mL of aqueous solution of 20 mM *N,N*-dimethyl-mercaptoethylammonium chloride and 1 mM 2-(butylamino)-ethanethiol in the case of an additional functionalization with a secondary amine. Five minutes of ultrasonic treatment led to an optically clear solution.
10. Push the Teflon brush very tightly against the septum when the lipid is stroked up the orifice. If the membrane ruptures, try it again with the Teflon brush without dropping new lipid on it.
11. If no membrane formation can be achieved, remove the lipid of the air-water interface using a suction pump, and try it again with a smaller amount of lipid. In addition, be very careful that all solutions and the electrolytes are free of any dust or other contaminants.
12. The dielectric constant for lipid membranes is taken as  $\epsilon = 2.1$ , corresponding to the average dielectric constant of a long-chain hydrocarbon.
13. If the humidity is too high or the weather is sultry, membrane formation is very rare and the membranes are usually not very stable.

## Acknowledgments

This work was supported by the Ludwig Boltzmann Society; by grants from the Austrian Science Foundation (projects P-14419-MOB and P-16295-B07); and by the Volkswagen Foundation, Germany (project I/77 710).

## References

1. Sleytr, U. B., Messner, P., Pum, P., and Sára, M. (eds.) (1996) *Crystalline Bacterial Cell Surface Proteins*, Academic, Austin, TX.
2. Sleytr, U. B. (1978) Regular arrays of macromolecules on bacterial cell walls: structure, chemistry, assembly and function. *Int. Rev. Cytol.* **53**, 1–64.
3. Pum, D., Sára, M., and Sleytr, U. B. (1989) Structure, surface charge, and self-assembly of the S-layer lattice from *Bacillus coagulans* E38-66. *J. Bacteriol.* **171**, 5296–5303.
4. Sára, M., Pum, D., and Sleytr, U. B. (1992) Permeability and charge-dependent adsorption of the S-layer lattice from *Bacillus coagulans* E38-66. *J. Bacteriol.* **174**, 3487–3493.
5. Sleytr, U. B., Messner, P., Pum, D., and Sára, M. (1999) Crystalline bacterial cell surface layers (S layers): from supramolecular cell structure to biomimetics and nanotechnology. *Angew. Chem. Int. Ed.* **38**, 1034–1054.
6. Sleytr, U. B., Sára, M., and Pum, D. (2000) Crystalline bacterial cell surface layers (S-layers): a versatile self-assembly system, in *Supramolecular Polymerization* (Ciferri, A., ed.), Marcel Dekker, New York, pp. 177–213.

7. Sleytr, U. B., Sára, M., Pum, D., and Schuster, B. (2001) Molecular nanotechnology and nanobiotechnology with two-dimensional protein crystals (S-layers), in *Nano-Surface Chemistry* (Rosoff, M., ed.), Marcel Dekker, New York, pp. 333–389.
8. Sleytr, U. B., Sára, M., Pum, D., Schuster, B., Messner, P., and Schäffer, C. (2003) Self assembly protein systems: microbial S-layers, in *Biopolymers*, vol. 7 (Steinbüchel, A. and Fahnestock, S., eds.), Wiley-VCH, Weinheim, Germany, pp. 285–338.
9. Hanke, W. and Schlue, W. R. (1993) Planar lipid bilayers: methods and applications, in *Biological Techniques Series* (Sattelle, D. B., ed.), Academic, London, UK, pp. 24–43.
10. Alvarez, O. (1986) How to set up a bilayer system, in *Ion Channel Reconstitution* (Miller, C., ed.), Plenum, New York, pp. 115–130.
11. Benz, R., Fröhlich, O., Läger, P., and Montal, M. (1975) Electrical capacity of black lipid films and of lipid bilayers made from monolayers. *Biochim. Biophys. Acta* **394**, 323–334.
12. Montal, M. (1974) Formation of bimolecular membranes from lipid monolayers. *Methods Enzymol. B* **32**, 545–554.
13. Messner, P., Hollaus, F., and Sleytr, U. B. (1984) Paracrystalline cell wall surface layers of different *Bacillus stearotherophilus* strains. *Int. J. Syst. Bacteriol.* **34**, 202–210.
14. Sleytr, U. B., Sára, M., Küpcü, Z., and Messner, P. (1986) Structural and chemical characterization of S-layers of selected strains of *Bacillus stearotherophilus* and *Desulfotomaculum nigrificans*. *Arch. Microbiol.* **146**, 19–24.
15. Bartelmus, W. and Perschak, F. (1957) Schnellmethode zur Keimzahlbestimmung in der Zuckerindustrie. *Z. Zuckerind.* **7**, 276–281.
16. Pum, D. and Sleytr, U. B. (1995) Anisotropic crystal growth of the S-layer of *Bacillus sphaericus* CCM 2177 at the air/water interface. *Colloids Surf. A* **102**, 99–104.
17. Pum, D., Stangl, G., Sponer, C., Fallmann, W., and Sleytr, U. B. (1997) Deep ultraviolet patterning of monolayers of crystalline S-layer protein on silicon surfaces. *Colloids Surf. B* **8**, 157–162.
18. Pum, D., Stangl, G., Sponer, C., Riedling, K., Hudek, P., Fallmann, W., and Sleytr, U. B. (1997) Patterning of monolayers of crystalline S-layer proteins on a silicon surface by deep ultraviolet radiation. *Microelectron. Eng.* **35**, 297–300.
19. Xia, Y. and Whitesides, G. M. (1998) Soft lithography. *Angew. Chem. Int. Ed.* **37**, 550–575.
20. Michel, B., Bernard, A., Bietsch, A., et al. (2001) Printing meets lithography: soft approaches to high resolution patterning. *IBM J. Res. Dev.* **45**, 697–719.
21. Kumar, A., Biebuyck, H. A., and Whitesides, G. M. (1994) Patterning self-assembled monolayers: applications in materials science. *Langmuir* **10**, 1498–1511.
22. Kim, E., Xia, Y., and Whitesides, G. M. (1995) Making polymeric microstructures: capillary micromolding. *Nature* **376**, 581–584.
23. Györfvay, E. S., O’Riordan, A., Quinn, A. J., Redmond, G., Pum, D., and Sleytr, U. B. (2003) Biomimetic nanostructure fabrication: nonlithographic lateral



- patterning and self-assembly of functional bacterial S-layers at silicon supports. *Nano Lett.* **3**, 315–319.
24. Talapin, D. V., Rogach, A. L., Kornowski, A., Haase, M., and Weller, H. (2001) Highly luminescent monodisperse CdSe and CdSe/ZnS nanocrystals synthesized in a hexadecylamine-trioctylphosphine oxide-trioctylphosphine mixture. *Nano Lett.* **1**, 207–211.
  25. Talapin, D. V., Rogach, A. L., Mekis, I., Haubold, S., Kornowski, A., Haase, M., and Weller, H. (2002) Synthesis and surface modification of amino-stabilized CdSe, CdTe and InP nanocrystals. *Colloids Surf. A* **202**, 145–154.
  26. Györvary, E., Schroedter, A., Talapin, D. V., Weller, H., Pum, D., and Sleytr, U. B. (2004) Formation of nanoparticle arrays on S-layer protein lattices. *J. Nanosci. Nanotechnol.* **4**, 115–120.
  27. Mueller, P., Rudin, D. O., Tein, H. T., and Wescott, W. C. (1962) Reconstitution of cell membrane structure *in vitro* and its transformation into excitable systems. *Nature* **194**, 979–981.
  28. Fettiplace, R., Gordon, L. G. M., Hladky, S. B., Requena, J., Zingsheim, H. P., and Haydon, D. A. (1975) Techniques in formation and examination of black lipid bilayer membranes, in *Methods of Membrane Biology*, vol. 4 (Korn, E. D., ed.), Plenum, New York, pp. 1–75.
  29. Montal, M. and Mueller, P. (1972) Formation of bimolecular membranes from lipid monolayers and a study of their electrical properties. *Proc. Natl. Acad. Sci. USA* **69**, 3561–3566.
  30. Darszon, A. (1983) Strategies in the reassembly of membrane proteins into lipid bilayer systems and their functional assay. *J. Bioenerg. Biomembr.* **15**, 321–334.
  31. Schindler, H. (1989) Planar lipid-protein membranes: strategies of formation and of detection dependencies of ion transport functions on membrane conditions. *Methods Enzymol.* **171**, 225–253.
  32. Schuster, B. and Sleytr, U. B. (2000) S-layer supported lipid membranes. *Rev. Mol. Biotechnol.* **74**, 233–254.
  33. Tien, H. T. and Ottova, A. L. (2001) The lipid bilayer concept and its experimental realization: from soap bubbles, kitchen sink, to bilayer lipid membranes. *J. Membr. Sci.* **189**, 83–117.
  34. Schuster, B., Sleytr, U. B., Diederich, A., Bähr, G., and Winterhalter, M. (1999) Probing the stability of S-layer-supported planar lipid membranes. *Eur. Biophys. J.* **28**, 583–590.
  35. Schuster, B. and Sleytr, U. B. (2002) The effect of hydrostatic pressure on S-layer supported lipid membranes. *Biochim. Biophys. Acta* **1563**, 29–34.
  36. Schuster, B. and Sleytr, U. B. (2002) Single channel recordings of  $\alpha$ -hemolysin reconstituted in S-layer-supported lipid bilayers. *Bioelectrochemistry* **55**, 5–7.
  37. Schuster, B., Pum, D., and Sleytr, U. B. (1998) Voltage clamp studies on S-layer-supported tetraether lipid membranes. *Biochim. Biophys. Acta* **1369**, 51–60.
  38. Schuster, B., Pum, D., Braha, O., Bayley, H., and Sleytr, U. B. (1998) Self-assembled  $\alpha$ -hemolysin pores in an S-layer-supported lipid bilayer. *Biochim. Biophys. Acta* **1370**, 280–288.



39. Schuster, B., Pum, D., Sára, M., Braha, O., Bayley, H., and Sleytr, U. B. (2001) S-layer ultrafiltration membranes: a new support for stabilizing functionalized lipid membranes. *Langmuir* **17**, 400–503.
40. Hirn, R., Schuster, B., Sleytr, U. B., and Bayerl, T. M. (1999) The effect of S-layer protein adsorption and crystallization on the collective motion of a lipid bilayer studied by dynamic light scattering. *Biophys. J.* **77**, 2066–2074.
41. Chang, G., Spencer, R. H., Lee, A. T., Barclay, M. T., and Rees, D. C. (1998) Structure of the MscL homolog from *Mycobacterium tuberculosis*: a gated mechanosensitive ion channel. *Science* **282**, 2220–2226.
42. Jones, S. E., Naik, R. R., and Stone, M. O. (2000) Use of small fluorescent molecules to monitor channel activity. *Biochem. Biophys. Res. Commun.* **279**, 208–212.
43. Booth, I. R. and Louis, P. (1999) Managing hypoosmotic stress: aquaporins and mechanosensitive channels in *Escherichia coli*. *Curr. Opin. Microbiol.* **2**, 166–169.
44. Schuster, B., Weigert, S., Pum, D., Sára, M., and Sleytr, U. B. (2003) New method for generating tetraether lipid membranes on porous supports. *Langmuir* **19**, 2392–2397.
45. Sleytr, U. B., Sára, M., Pum, D., and Schuster, B. (2001) Characterization and use of 2D protein crystals (S-layers). *Prog. Surf. Sci.* **68**, 231–278.



## Folding of $\beta$ -Structured Fibrous Proteins and Self-Assembling Peptides

Anna Mitraki and Mark J. van Raaij

### Summary

Natural fibrous proteins include families found in natural materials such as wool and silk; in tissue components such as collagen and elastin; or in virus and bacteriophage adhesins. They have long fascinated scientists and engineers because of their mechanical and elastic properties, and considerable efforts have been made in order to produce artificial materials inspired from these natural proteins. The understanding of their structure, folding, and assembly properties is necessary in order to achieve these objectives. However, because of their complexity, structural information is quite often extremely difficult to obtain for these proteins. In this chapter, we focus on a particular family of fibrous proteins: trimeric,  $\beta$ -stranded viral adhesins. We describe folding strategies that led to the identification of stable domains that could be crystallized, and the novel structural motifs that are emerging. We also discuss self-assembling peptides derived from these motifs. Finally, we review the possibilities of designing novel macroscopic materials as well as nanoscale fibrous objects with controlled dimensions and properties based on these novel structural motifs.

**Key Words:** Fibrous proteins;  $\beta$ -structure; protein folding; triple  $\beta$ -helix; triple  $\beta$ -spiral; self-assembling peptides; amyloid fibers.

### 1. Introduction

Natural fibrous proteins can be made up from collagen triple helices,  $\alpha$ -helical coiled structures, or  $\beta$ -structured motifs (**1–3**). Collagen triple helices and coiled coils have been much more extensively studied from a biochemical, structural, and biophysical point of view, and they are not discussed in this chapter. Until recently, much less structural and folding information has been available for  $\beta$ -structured fibrous proteins. Their intrinsic structural complexity and notorious tendency to aggregate makes  $\beta$ -structured proteins more difficult to fold and handle.

From: *Methods in Molecular Biology*, vol. 300:  
*Protein Nanotechnology, Protocols, Instrumentation, and Applications*  
Edited by: T. Vo-Dinh © Humana Press Inc., Totowa, NJ

One class of  $\beta$ -structured fibrous proteins is used by viruses as their attachment organelles (4–6). They are often homotrimers composed of an N-terminal domain attached to the viral capsid, a central shaft, and a C-terminal receptor-binding or chemosensor domain (7,8). The long, thin fiber shaft appears to act as a mechanical device capable of reaching the virus. These fibrous proteins have evolved to survive in harsh extracellular environments; they are, therefore, extremely stable proteins, resistant to sodium dodecyl sulfate (SDS), urea, temperature, and proteases (9). The primary sequence of the shaft parts often comprises sequence repeats, suggesting that these parts fold into regular, repetitive structures.

Owing to their elongated and asymmetric nature, these proteins have intrinsic crystallization difficulties. Because they are resistant to proteases, proteolytic domains cannot be isolated. However, studying their folding pathways can reveal folding intermediates comprising stable domains; these stable domains can be crystallized and can lead to structural information (10–12). The use of such a strategy revealed that the structure of such stable domains has novel  $\beta$ -structured motifs for some of these viral adhesins (13–16). We believe that this kind of strategy can be applicable to other fibrous proteins of yet unknown structure. In this chapter, we underline such strategies, and discuss the structure, folding, and assembly of two case studies: the fibers of human adenoviruses and the short tail fiber of bacteriophage T4. The structure, folding, and assembly of phage P22 fibers that remain a paradigm in this area have been extensively reviewed before (17,18) and are not discussed herein. We finally discuss how the knowledge of structural building blocks and folding pathways can lead to rational design of novel nanofibers with controlled dimensions and properties.

## 2. Methods

### 2.1. *Unfolding Studies and Identification of Stable Domains*

For many  $\beta$ -structured fibrous proteins, complete unfolding requires denaturing treatments that can be considered extreme relative to the average globular protein, such as temperatures higher than 70°C. To look for eventual long-lived and stable unfolding intermediates, one needs to explore milder denaturing conditions. These include lower temperatures, and moderate concentrations (0.1–0.5%) of detergents such as SDS, or denaturing agents such as urea or guanidine hydrochloride. One attractive property of the viral adhesins that we studied so far is that the native trimers are not dissociated by SDS at ambient temperatures; dissociation into monomers is achieved only after heating. The native proteins bind very little SDS and migrate slowly in distinct positions in SDS-polyacrylamide-containing gels (10,11). This resistance to

SDS is particularly useful because it allows separation of native trimers from partially folded and misfolded chains directly by SDS-polyacrylamide gel electrophoresis (PAGE). Partially unfolded, but not dissociated, chains can quite often be directly visualized in SDS-PAGE gels (**10,11**).

Another advantage of big fibrous proteins is that their native forms are visible in electron microscopy, and stable, partially folded intermediates can be visualized directly as well (**11**). To identify the borders between the unfolded part and the stable domain, limited proteolysis can be used, utilizing proteases that can act under these mildly denaturing conditions. Proteases such as endoproteinase Glu-C, endoproteinase Lys-C, chymotrypsin, trypsin, and elastase can act in 0.1% SDS (endoproteinase Glu-C can act in up to 0.5% SDS). Endoproteinase Glu-C, endoproteinase Lys-C, and trypsin can tolerate denaturing conditions up to 5 M urea. Two proteases with contrasting specificities can be used, in order to assess the borders with certainty. The identity of the stable fragments can subsequently be confirmed by N-terminal sequencing and/or mass spectroscopy. Another option is to partially unfold the fiber of interest at an intermediate temperature; cool down the sample without allowing refolding; and then proceed with proteolysis at the optimum, lower temperature of the protease. If metal ions, cofactors, and so on are known to be essential for the protein, they might contribute to the stability of the domains. Therefore, it is useful to compare the proteolysis results in the presence and absence of cofactors (*see Subheading 2.5.*). **Figure 1** illustrates the various steps of the aforementioned strategy for a generic fibrous protein.

## **2.2. Recombinant Production of Fibrous Proteins**

During the production of a fibrous protein by recombinant methods, the risk of obtaining insoluble aggregates (inclusion bodies) has to be considered. To avoid inclusion body formation, standard described strategies can be applied (**19**). However, fibrous proteins might present some additional difficulties. Cellular chaperones can participate in the folding and assembly of viral fibers; for example, Hsp70 and Hsp90 are necessary for the formation of the reovirus fibers (**20,21**). Sometimes specific chaperones are used to ensure correct folding and assembly of fibrous proteins. The T4 short fibers that we describe in **Subheading 2.5.** use such a specific, phage-encoded chaperone, called gp57. In the absence of this protein, the T4 short fibers form insoluble aggregates when expressed in *Escherichia coli*; expression in their correctly folded, trimeric state requires coexpression with gp57 (**22**). gp57 is also necessary for the folding and assembly of long tail fibers, but its mechanism of action is currently unknown. Thus, when a chaperone requirement exists, the fibrous protein of interest has to be overexpressed in the presence of this cellular or virally encoded chaperone.

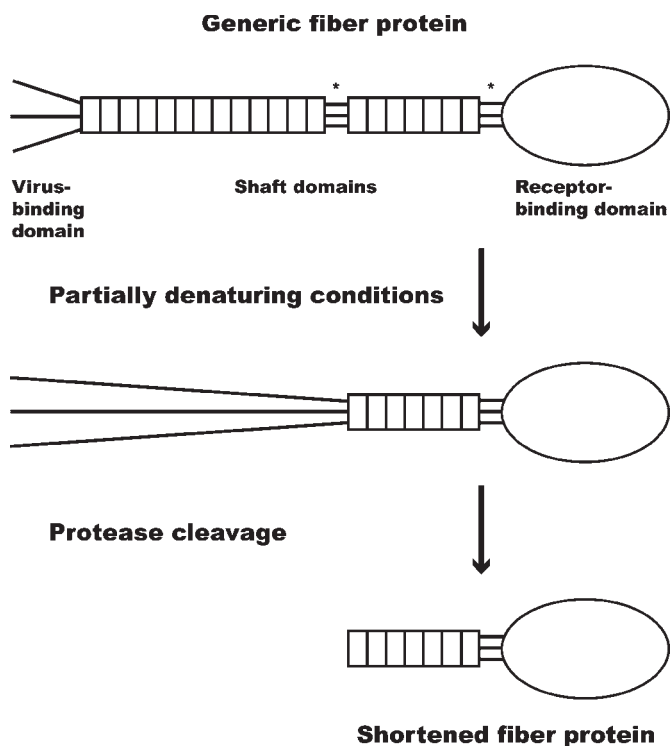


Fig. 1. Generalized strategy for producing shortened fiber protein fragments suitable for crystallization. Shown at the top is a generic fiber protein with an N-terminal virus-binding domain, central shaft domains, and a C-terminal receptor-binding domain. Asterisks indicate hinge regions. In partially denaturing conditions (which may consist of raising the temperature or adding intermediate concentrations of detergents or denaturants), the protein partially unfolds. Protease is then added, which cleaves off the unfolded domains. Note that although N-terminal unfolding is shown here, unfolding may also take place elsewhere.

### 2.3. Crystallization

Fiber proteins can in principle be crystallized using the same strategies as globular proteins, trying different precipitants, pHs, additives, and temperatures. The virus-binding regions in fiber proteins may, however, in the absence of the rest of the virus or bacteriophage, be unfolded and lead to a specific aggregation, hindering crystallization. Furthermore, because they often have specific regions where the fiber is bent or kinked, this can lead to lower success rates in crystallization and, in the case of successful structural determination, regions that are disordered in the crystallographic electron density. The identification of a stable domain, eliminating some or all of the binding regions,

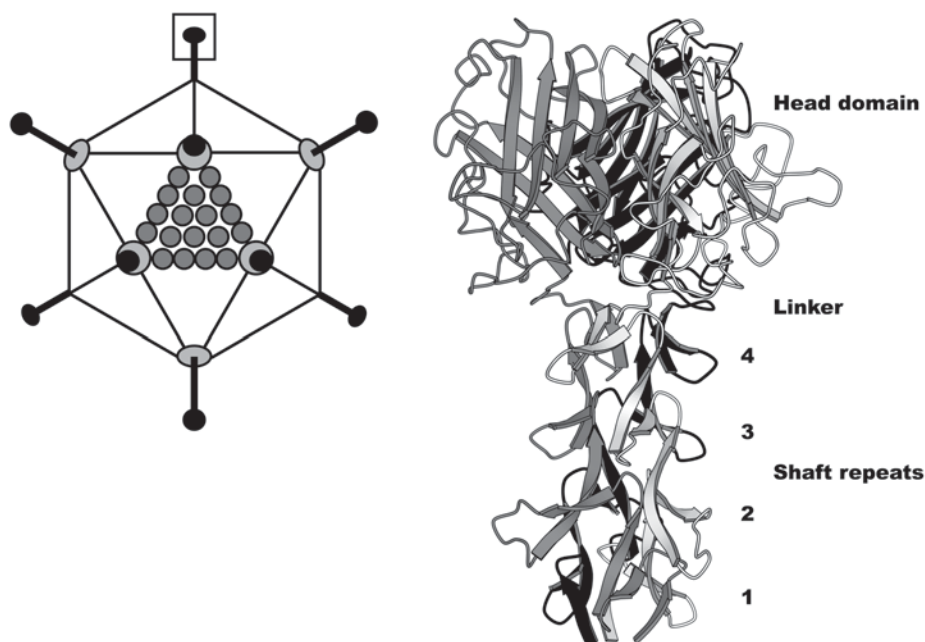


Fig. 2. Schematic drawing of adenovirus (**left**) and structure of adenovirus type 2 fiber stable fragment (**right**). The head domain, linker region, and shaft repeats are labeled. In the full-length fiber proteins up to 22 repeats are present. The part of the fiber of which the structure is shown is boxed. The shown adenovirus particle is about 80 nm wide (not counting the fibers, which can measure up to 35 nm each), and the part of the structure shown is about 10 nm long. The figures were produced using Molscript (56) and atomic coordinates publicly available from the PDB protein structure database (<http://www.rcsb.org>). One of the chains is shown in black and the other two in gray. The PDB code for the adenovirus type 2 stable fragment is 1QIU.

greatly aids in obtaining diffracting crystals. As with globular proteins, important for the success of crystallization is purity, conformational homogeneity, and the ability to obtain the protein in reasonable amounts (upward from about 0.5 mg) and at relatively high concentrations (5–50 mg/mL).

#### 2.4. Case Study #1: Adenovirus Fiber

Adenoviruses cause respiratory, gastroenteric, and ocular infections in humans (23). The fibers (parallel homotrimers, with each monomer containing 582 amino acids) protrude from the 12 vertices of the icosahedral capsid, and they are responsible for cell attachment (**Fig. 2**). The C-terminal, globular head domain attaches to the cell receptor (7). The central shaft contains a repeating sequence motif with an invariant glycine or proline and a conserved pattern of



hydrophobic residues (24). The shaft can be as long as 30 nm in some serotypes, featuring 22 such repeats. The fiber is imbedded to the viral capsid with a short, N-terminal part (about 45 residues).

Unfolding experiments of the entire adenovirus type 2 fiber (11) led to the identification of a long-lived unfolding intermediate. In the presence of SDS at moderate temperatures (4–22°C), partial unfolding of the fiber starts from the N-terminus, and a stable intermediate accumulates that has the C-terminal head and part of the shaft structured as seen by electron microscopy. This unfolding intermediate is directly visible in SDS-containing polyacrylamide gels, running slower than the native trimer (11). After digestion of the unfolded parts by limited proteolysis and N-terminal sequencing, the stable domain has been identified to span residues 319 to 582. This domain was subsequently cloned and expressed in *E. coli*; it has been obtained in its trimeric, properly folded form, and its successful crystallization led to the solving of its crystal structure (14).

The crystal structure uncovered the fold of four shaft repeats, which form a triple  $\beta$ -spiral (Fig. 2). The basic structural motif is a strand-loop-strand motif; these motifs are connected by a type 2  $\beta$  turn that contains a conserved glycine (in the solved part of the shaft) or a proline (in the rest of the shaft). The three chains wrap around each other to give a highly intertwined structure (one-third of the surface area of the monomer is buried in the trimer). To superimpose one repeat onto the next repeat at its C-terminus, a translation along the shaft of about 1.3 nm and a clockwise rotation of about 50° are necessary. Stabilizing features of the structure are a central longitudinal hydrophobic core, to which three hydrophobic amino acid side chains from every shaft repeat contribute; hydrophobic patches at greater radius formed by two additional conserved hydrophobic side chains; and conserved intra- and interchain hydrogen bonds. The loop in the strand-loop-strand motif has a variable sequence and is solvent exposed; these solvent-exposed loops are a unique structural feature among the so-far known fibrous folds.

The crystal structures of fiber head domains of types 5 (25), 2 (26), 12 (27), and 3 (28) are known and virtually identical apart from differences in the loop regions. Each fiber head monomer contains an antiparallel  $\beta$  sandwich, formed by two four-stranded  $\beta$  sheets packing together at an angle of about 30°. In the globular trimer, the  $\beta$  sandwiches make up a three-bladed propeller (Fig. 2). The trimeric head contains three receptor-binding sites on the sides of the trimer at monomer-monomer interfaces (27). The three receptor-binding sites per trimer lead to tighter binding owing to avidity enhancement of affinity (29). A linker region (residues 393–398) between the head and shaft domains may lead to flexibility between the two domains; indeed, in the crystal structure of the stable fragment (14), the central threefold axes of the two domains

were displaced by about 2°. Whether this flexibility has a role in receptor-binding is currently not known.

Interestingly, a C-terminal fragment of mammalian reovirus fiber ( $\sigma$  1 protein) has been obtained by tryptic digestion of a deletion mutant, and its structure has been solved (30). Its structure showed a  $\beta$ -structured globular head domain similar to adenovirus fiber head and three triple  $\beta$ -spiral shaft repeats.

### 2.5. Case Study #2: Bacteriophage T4 Short Tail Fiber

Bacteriophage T4 acts like a self-powered nanoscopic syringe. It is also one of the largest and most complex viruses known and contains more than 40 different structural proteins (31). It is very efficient, since one particle is generally sufficient to productively infect its *E. coli* host and several hundred daughter phages can be produced in 30 min at 37°C. During infection, first the long tail fibers bind to the bacterial lipopolysaccharide or OmpC (outer membrane protein C). Once at least three long tail fibers have bound, the phage base-plate changes conformation from the hexagon form to the star form (32). This leads the short tail fibers to extend and bind to the bacterial lipopolysaccharide core region (Fig. 3). The next step is contraction of the outer tail tube, driving the inner tail tube through the bacterial membrane (Fig. 3). The inner tail tube is capped by a needle (33) with lysozyme activity, helping the puncturing of the bacterial cell wall. The phage DNA passes through the tail tube into the bacterium and directs the production of daughter phage.

The long tail fibers are a complex of four different proteins (34). The proximal half of the fiber (or “thigh”) is formed by a gp34 trimer (1289 amino acids per subunit), the hinge (or “knee”) contains a monomer of gp35 (372 amino acids), and the distal half of the fiber (or “shin”) is made up of trimers of gp36 and gp37. gp37 (1026 residues per monomer) is responsible for receptor binding and makes up the bulk of the distal fiber half, which gp36 (221 amino acids per monomer) connects the gp37 trimer to the hinge. The crystal structures of the long tail fiber proteins have not yet been reported.

Short tail fibers are composed of a single protein, gp12, of 527 residues, which forms parallel homotrimers. Coexpression of gp12 with the T4 chaperone protein gp57 (22) in *E. coli* and subsequent purification led to the availability of material of suitable quantity, purity, and solubility. However, despite extensive trials, crystals could not be obtained from this material. Like the adenovirus fiber, its N-terminus is flexible and/or unstable, and 37 to 41 amino acids can be digested away already at 37°C. This common pattern may be owing to the fact that the N-termini of both proteins are attached to the viral capsid or the base plate in their native context and, therefore, may become destabilized in the isolated, purified form. On further increase in the temperature at 56°C followed by protease digestion, the first 83 amino acids are

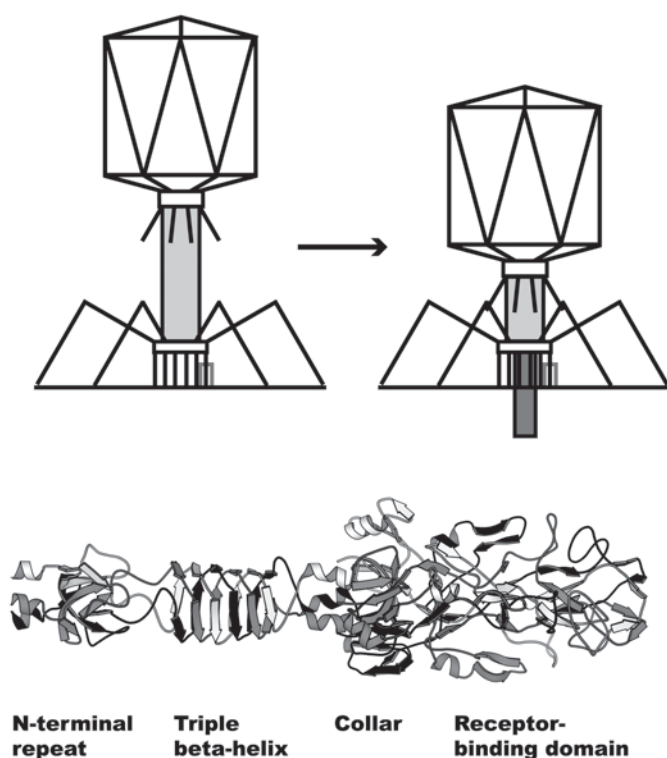


Fig. 3. Schematic drawing of uncontracted bacteriophage T4 (**top left**) and contracted T4 (**top right**). Only four of the six fibrillin and long tail fibers are shown for clarity. Uncontracted T4 particles are about 300 nm high. At the bottom is a composite structure of the known domains of the bacteriophage T4 short tail fiber (combined from PDB codes 1H6W and 1OCY). One of the chains is shown in black and the other two in gray. The receptor-binding domain, collar domain, triple  $\beta$ -helix, and resolved N-terminal repeat are labeled. Five more N-terminal repeats are present in the full-length protein. In the schematics, the part of the short tail fiber of which the structure is known is boxed in gray. Full-length short tail fibers are about 35 nm long, and the part of the structure shown is about 15 nm.

removed and a second cleavage site is uncovered after Arg-395. This heat- and protease-stable fragment crystallized successfully (12). Another fragment, prepared in the same way except in the presence of divalent zinc cations, led to a fragment in which only the N-terminal 83 amino acids are removed. The resulting crystal structures (15,16) allowed the identification of several new folds, although parts of the crystallized protein were not visible in the crystallographic electron density because of static disorder. This is true for amino acids 85 to

245 in the first fragment, and for residues 85 to 329 in the second. Nevertheless, the combined crystal structures allowed us to describe the structure of amino acids 246 to 527 (**Fig. 3**).

The N-terminal domain contains six 17-residue sequence repeats comprising conserved hydrophobic residues such as alanines and threonines, and conserved glutamic acid residues. Of these repeats, one has been resolved in the crystal structure (residues 255–271); it basically comprises two  $\beta$  strands connected by a solvent-exposed type 1  $\beta$  turn. Eight of these sequence repeats are also present in gp34 and one in gp37. Because the residues between the repeats are not conserved and the spacing between the repeats is variable, it appears that the T4 fiber shaft structures are not as regular as the structure of the adenovirus fiber shaft.

The region comprising amino acids 290 to 327 forms a right-handed triple-stranded  $\beta$ -helix, in which each monomer contributes six, six-residue  $\beta$  strands in two  $360^\circ$  turns (**Fig. 3**). Two amino acids of each  $\beta$  strand contribute hydrophobic side chains to a central hydrophobic core, and the framework of the triple  $\beta$ -helix is held together by interchain hydrogen bonds between the  $\beta$  strands. In the  $\beta$ -helix domain, each monomer has 57% of its surface buried in the complex. Interestingly, the needle at the bottom of the tail tube, which is a trimer of gp5, also contains a triple  $\beta$ -helix, but with longer  $\beta$  strands of eight residues and comprising seven  $360^\circ$  turns (**33**).

The arrow-shaped C-terminal head domain has a globular collar domain (**15**) and a strongly intertwined zinc-containing receptor-binding domain (**16**). The collar domain has weak structural homology to a part of bacteriophage T4 gp11, suggesting a possible distant evolutionary relationship. The receptor-binding domain has yet another, unique fold. It contains few regular secondary structure elements, although the normal requirements for a stable protein fold are fulfilled: it has a hydrophobic core and hydrogen-bonding requirements are met. In the center of the trimeric receptor-binding domain, we found a single zinc ion, octahedrally coordinated by the NE2 atoms of two histidine residues from each monomer. In the absence of zinc ions, this domain unfolds at  $56^\circ\text{C}$ , whereas in the presence of zinc it does not.

### 3. Self-Assembling Peptides

It has recently been shown that a number of peptides derived from natural protein sequences can self-assemble into  $\beta$ -structured supramolecular assemblies (**35,36**). These supramolecular assemblies can adopt the form of fibrils, tubes, sheets, or monolayers (**37**) and can serve as biomaterials with a variety of potential applications. They can be used as, e.g., vehicles for encapsulation and delivery of therapeutics or as biological scaffolds for cell attachment or biomineralization templates (**38,39**). Repetitive sequences derived from natu-

ral fibrous proteins that are  $\beta$  structured and extremely stable such as the viral adhesins are, of course, very attractive candidates for the design of peptides that could self-assemble into nanofibers. Information on the crystal structure of the native protein is a very important factor because it allows rational design; however, as we will see, this information will need to be coupled with folding and assembly information.

Synthetic peptides corresponding to shaft sequences of the adenovirus fiber shaft repeats 3 and 4 (**Fig. 2**) do not adopt the triple  $\beta$ -spiral conformation in the absence of the head. Instead, they self-assemble into long, unbranched fibrils that can reach the order of microns. These fibrils, called amyloid-type fibrils, adopt a cross- $\beta$  structure, i.e., a structure where the  $\beta$  strands lie perpendicular to the fibril axis (**40,41**). The adenovirus head domain is essential for trimerization, because deletions or mutations in this part were found to hinder the trimerization process in vivo (**42,43**). This domain may act as a registration signal necessary for the correct alignment and assembly of the three chains, as do the procollagen regions in collagen folding (**44**) or the C-terminal domain of phage T4 fibritin (**45**). This short (27 amino acids) domain in a  $\beta$ -propeller conformation serves as a template for the correct trimerization of the triple coiled-coil N-terminal domain of the fibritin. (Fibritin fibers can be seen protruding from the “collar” part of the phage T4 particle in **Fig. 3**.) Registration signals are often used to ensure correct folding and assembly of fibrous proteins, and this has to be taken into account while engineering fibrous constructs based on repetitive fibrous sequences. If engineering of a construct that adopts the native structure is desired, then a registration signal has to be included in the design. Otherwise, out-of-register polymerization of the repetitive sequences will give fibers that could adopt a different structure and have different properties. It is important, though, to keep in mind that these properties could be interesting in their own right and could be used toward different applications.

The advantages and disadvantages of peptide synthesis vs bacterial expression also have to be considered. Short peptides (up to about 40 amino acids) are easy to design and synthesize; however, obtaining synthetic peptide material at higher scales is usually more expensive than protein material produced by recombinant methods. Another advantage of chemical synthesis is that it also allows the combination of peptide and nonpeptide moieties, such as alkyl chains, in order to create hybrid structures. Such hybrid structures comprising hydrophilic peptides linked to alkyl chains designed for biomineralization have been recently described. They can organize into cylindrical micelles, and phosphorylated serine residues on their surface organize the deposition of calcium ions, leading to hydroxyapatite nanofibers (**46**).

#### 4. Applications

The first steps toward applications of  $\beta$ -structured, viral fibrous proteins in materials science and nanotechnology have been made. These proteins could be useful for the design of nanoscale fibrous objects with specified dimensions and properties, and the fabrication of novel biocompatible and biodegradable materials. Engineering fibrous constructs for experimental gene therapy is another rapidly developing field concerning adenovirus fibers.

Novel gene therapy vectors are being designed to specifically target certain tissues, and for this purpose fibers with modified tropism are needed. This rapidly advancing field recently provided a wealth of information about and considerable insight into engineering possibilities of the adenovirus fiber (reviewed in **ref. 47**). It has been shown that the protein can be modified in several ways and still be folded correctly. The length of the shaft can be increased by nine repeats (**48**), and other receptor binding domains can be inserted in loops or at the C-terminus (**47**). Hybrid adenovirus fibers where the knob domain or the knob plus some or many shaft repeats have been replaced by foreign trimerization domains have been incorporated into experimental adenovirus-based gene therapy vehicles (**47**).

Artificial (macroscopic) fibers with sequences based on adenovirus shaft repeats were produced by recombinant gene technology long before a crystal structure became available. O'Brien et al. (**49**) have designed polymers with fiber shaft repeats as building blocks that were bacterially expressed as inclusion bodies. After refolding, purification, and spinning, they reported properties "comparable to commercial textile fibers" for the fibers obtained (**49**). Although no detailed structure and assembly studies have been conducted on this material, powder diffraction patterns together with Raman studies suggest that these fibers might adopt a cross- $\beta$ , amyloid-like conformation (**49,50**). Construction of nanoarrays based on bacteriophage T4 long fiber proteins gp34 and gp37 is being pioneered by Edward Goldberg's group (**51**). Their strategy is, first, to engineer self-assembling protein rod units; second to insert functional moieties at precise positions in these protein rods without perturbing folding and assembly; and, finally, to assemble two-dimensional or three-dimensional nanoarrays from these functionalized rods. gp34 and gp37 trimers are both approx 70 nm long. gp12 and adenovirus fiber could perhaps also be used for this purpose; they are both about 35 nm long.

A question is, can  $\beta$ -structured fibers be made longer? In the case of adenovirus, adding nine repeats (to a total length of 45 nm) is possible in vivo (**48**). The addition of more repeats may be difficult, because N-termini have to be held apart until the C-terminal trimerization domain is synthesized and can fold, and putting the trimerization domain at the N-terminus may lead to protein synthesis problems in *E. coli*.

## 5. Conclusion

We have reviewed in this chapter strategies that recently led to the X-ray structures of several building blocks of viral and bacteriophage fiber proteins. Using these building blocks, artificial nanoscale fibrous constructs can be obtained by rational design based on the crystal structures, provided that folding considerations are taken into account.

The structures of many viral and bacteriophage fibrous proteins remain unresolved. In the near future, further structural information on these natural fibrous proteins and their interaction partners (chaperones and receptors) should become available. This additional structural information and the eventual emergence of new motifs will provide a sounder basis for engineering materials based on stable trimeric viral fibers.

Combining the various motifs and building blocks from these fibers in order to make artificial fusion proteins is the next challenge toward the design of fibrous nanoconstructs. The first steps in this direction have been made: the trimerization motif of the T4 fibrin (27 amino acids) can be fused to fibrous parts of a variety of proteins, ranging from T4 short tail fibers to collagen helices giving stable, trimeric proteins (52,53). Stetefeld et al. (54) have determined the structure of such an artificial collagen triple helix fused to the fibrin trimerization motif. Their structure shows how the staggered collagen triple helix (without a central threefold axis) is accommodated by the threefold symmetric foldon by a 60° bend. A fusion protein carrying the trimerization domain plus most of the coiled-coil of the fibrin was also successfully fused to the two most N-terminal repeats of the adenovirus fiber shaft. A linker sequence (SQNV) present in both fusion partners was used in this construct in order to avoid potential structural conflicts between motifs (55). These examples prove that combination of fibrous motifs varying from coiled-coils to the triple  $\beta$ -spiral is feasible, provided that the appropriate linkers are used.

The strategies that we have described underline some general trends in the folding and assembly of  $\beta$ -structured fibrous proteins. We believe that these strategies can be helpful if followed for other fibrous proteins of yet-unknown structure. However, an important thing to keep in mind is that every protein can be different; only a rigorous and detailed understanding of its own folding and assembly pathway can lead to structural information, and further rational design based on this information.

## Acknowledgments

We acknowledge support from the Centre National de la Recherche Scientifique and from the Direction d'Objectifs Matériaux of the Commissariat à l'Energie Atomique. Mark van Raaij is a Ramón y Cajal investigator sponsored by the Spanish Ministry of Science and Technology.



## References

1. Beck, K. and Brodsky, B. (1998) Supercoiled protein motifs: the collagen triple-helix and the alpha-helical coiled coil. *J. Struct. Biol.* **122**, 17–29.
2. Jenkins, J. and Pickersgill, R. (2001) The architecture of parallel  $\beta$ -helices and related folds. *Prog. Biophys. Mol. Biol.* **77**, 111–175.
3. Mitraki, A., Miller, S., and van Raaij, M. J. (2002) Review: conformation and folding of novel beta-structural elements in viral fiber proteins: the triple beta-spiral and triple beta-helix. *J. Struct. Biol.* **137**, 236–247.
4. Iwashita, S. and Kanegasaki, S. (1976) Enzymic and molecular properties of base-plate parts of bacteriophage P22. *Eur. J. Biochem.* **65**, 87–94.
5. Philipson, L., Lonberg-Holm, K., and Pettersson, U. (1986) Virus-receptor interaction in an adenovirus system. *J. Virol.* **2**, 1064–1075.
6. Riede, I. (1987) Receptor specificity of the short tail fibres (gp12) of T-even type *Escherichia coli* phages. *Mol. Gen. Genet.* **206**, 110–115.
7. Ruigrok, R. W. H., Barge, A., Albiges-Rizo, C., and Dayan, S. (1990) Structure of adenovirus fiber. II. Morphology of single fibers. *J. Mol. Biol.* **215**, 589–596.
8. Makhov, A. M., Trus, B. L., Conway, J. F., Simon, M. N., Zurabishvili, T. G., Mesyanzhinov, V. V., and Steven, A. C. (1993) The short tail-fiber of bacteriophage T4: molecular structure and a mechanism for its conformational transition. *Virology* **194**, 117–127.
9. King, J. and Laemmli, U. K. (1971) Polypeptides of the tail fibres of bacteriophage T4. *J. Mol. Biol.* **62**, 465–477.
10. Chen, B. and King, J. (1991) Thermal unfolding pathway for the thermostable P22 tailspike endorhamnosidase. *Biochemistry* **30**, 6260–6269.
11. Mitraki, A., Barge, A., Chroboczek, J., Andrieu, J. P., Gagnon, J., and Ruigrok, R. W. H. (1999) Unfolding studies of human adenovirus type 2 fiber trimers: evidence for a stable domain. *Eur. J. Biochem.* **264**, 599–606.
12. van Raaij, M. J., Schoehn, G., Jaquinod, M., Ashman, K., Burda, M. R., and Miller, S. (2001) Identification and crystallisation of a heat- and protease-stable fragment of the bacteriophage T4 short tail fibre. *Biol. Chem.* **382**, 1049–1055.
13. Steinbacher, S., Seckler, R., Miller, S., Steipe, B., Huber, R., and Reinemer, P. (1994) Crystal structure of P22 tailspike protein: interdigitated subunits in a thermostable trimer. *Science* **265**, 383–386.
14. van Raaij, M. J., Mitraki, A., Lavigne, G., and Cusack, S. (1999) A triple beta-spiral in the adenovirus fiber shaft reveals a new structural motif for a fibrous protein. *Nature* **401**, 935–938.
15. van Raaij, M. J., Schoehn, G., Burda, M. R., and Miller, S. (2001) Crystal structure of a heat- and protease-stable part of the bacteriophage T4 short tail fibre. *J. Mol. Biol.* **314**, 1137–1147.
16. Thomassen, E., Gielen, G., Schütz, M., Schoehn, G., Abrahams, J. P., Miller, S., and van Raaij, M. J. (2003) The structure of the receptor-binding domain of the bacteriophage T4 short tail fibre reveals a knitted trimeric metal-binding fold. *J. Mol. Biol.* **331**, 361–373.

17. Seckler, R. (1998) Folding and function of repetitive structure in the homotrimeric phage P22 tailspike protein. *J. Struct. Biol.* **122**, 216–222.
18. Betts, S. and King, J. (1999) There's a right way and a wrong way: in vivo and in vitro folding, misfolding and subunit assembly of the P22 tailspike. *Struct. Fold. Des.* **7**, R131–R139.
19. Mitraki, A. and King, J. (1989) Protein folding intermediates and inclusion body formation. *Bio/Technology* **7**, 690–697.
20. Lee, P. W. K., and Gilmore, R. (1998) Reovirus cell attachment protein sigma1: structure-function relationships and biogenesis. *Curr. Top. Microbiol. Immunol.* **233**, 137–153.
21. Gilmore, R., Coffey, M. C., and Lee, P. W. K. (1998) Active participation of Hsp90 in the biogenesis of the trimeric reovirus cell attachment protein sigma1. *J. Biol. Chem.* **273**, 15,227–15,233.
22. Burda, M. R. and Miller, S. (1999) Folding of coliphage T4 short tail fiber in vitro: analysing the role of a bacteriophage-encoded chaperone. *Eur. J. Biochem.* **265**, 771–778.
23. Horwitz, M. S. (1996) Adenoviruses, in *Fields Virology*. (Fields, B. N., Knipe, D. M., and Howley, P. M., eds.), Lippincott-Raven, Philadelphia, pp. 2149–2171.
24. Green, N. M., Wrigley, N. G., Russel, W. C., Martin, S. R., and McLachlan, A. D. (1983) Evidence for a repeating cross-beta sheet structure in the adenovirus fiber. *EMBO J.* **2**, 1357–1365.
25. Xia, D., Henry, L. J., Gerard, R. D., and Deisenhofer J. (1994) Crystal structure of the receptor-binding domain of adenovirus type 5 fiber protein at 1.5 Å resolution. *Structure* **2**, 1259–1270.
26. van Raaij, M. J., Louis, N., Chroboczek, C., and Cusack, S. (1999) Structure of the human adenovirus serotype 2 fiber head domain at 1.5 Å resolution. *Virology* **262**, 333–343.
27. Bewley, M. C., Springer, K., Zhang, Y. B., Freimuth, P., and Flanagan, J. M. (1999) Structural analysis of the mechanism of adenovirus binding to its human cellular receptor, CAR. *Science* **286**, 1579–1583.
28. Durmort, C., Stehlin, C., Schoehn, G., Mitraki, A., Drouet, E., Cusack, S., and Burmeister, W. P. (2001) Structure of the fiber head of Ad3, a non-CAR-binding serotype of adenovirus. *Virology* **285**, 302–312.
29. Lortat-Jacob, H., Chouin, E., Cusack, S., and van Raaij, M. J. (2001) Kinetic analysis of adenovirus fiber binding to its receptor reveals an avidity mechanism for trimeric receptor-ligand interactions. *J. Biol. Chem.* **276**, 9009–9015.
30. Chappell, J. D., Protá, A. E., Dermody, T. S., and Stehle, T. (2002) Crystal structure of reovirus attachment protein sigma1 reveals evolutionary relationship to adenovirus fiber. *EMBO J.* **21**, 1–11.
31. Karam, J. D. (1994) *Molecular Biology of Bacteriophage T4*, ASM Press, Washington, DC.
32. Crowther, R. A., Lenk, E. V., Kikuchi, Y., and King, J. (1977) Molecular reorganization in the hexagon to star transition of the baseplate of bacteriophage T4. *J. Mol. Biol.* **116**, 489–523.

33. Kanamaru, S., Leiman, P. G., Kostyuchenko, V. A., Chipman, P. R., Mesyanzhinov, V. V., Arisaka, F., and Rossmann, M. G. (2002) Structure of the cell-puncturing device of bacteriophage T4. *Nature* **415**, 553–557.
34. Cerritelli, M. E., Wall, J. S., Simon, M. N., Conway, J. F., and Steven A. C. (1996) Stoichiometry and domainal organization of the long tail-fiber of bacteriophage T4: a hinged viral adhesin. *J. Mol. Biol.* **260**, 767–780.
35. Zhang, S., Holmes, T., Lockshin, C., and Rich, A. (1993) Spontaneous assembly of a self-complementary oligopeptide to form a stable macroscopic membrane. *Proc. Natl. Acad. Sci. USA* **90**, 3334–3338.
36. Aggeli, A., Bell, M., Boden, N., Keen, J. N., Knowles, P. F., McLeish, T. C., Pitkeathly, M., and Radford, S. E. (1997) Responsive gels formed by the spontaneous self-assembly of peptides into polymeric beta-sheet tapes. *Nature* **386**, 259–262.
37. Aggeli, A., Nyrkova, I. A., Bell, M., Harding, R., Carrick, L., McLeish, T. C., Semenov, A. N., and Boden, N. (2001) Hierarchical self-assembly of chiral rod-like molecules as a model for peptide beta-sheet tapes, ribbons, fibrils, and fibers. *Proc. Natl. Acad. Sci. USA* **98**, 11,857–11,862.
38. Zhang, S. and Altman, M. (1999) Peptide self-assembly in functional polymer science and engineering. *React. Funct. Polym.* **41**, 91–102.
39. Zhang, S., Marini, D. M., Hwang, W., and Santoso, S. (2002) Design of nanostructured biological materials through self-assembly of peptides and proteins. *Curr. Opin. Chem. Biol.* **6**, 865–871.
40. Luckey, M., Hernandez, J., Arlaud, G., Forsyth, V. T., Ruigrok, R. W., and Mitraki, A. (2000) A peptide from the adenovirus fiber shaft forms amyloid-type fibrils. *FEBS Lett.* **468**, 23–27.
41. Mitraki, A., van Raaij, M. J., Ruigrok, R., Cusack, S., Hernandez, J.-F., and Luckey, M. (2001) Structure, folding and assembly of adenovirus fibers, in *Self-Assembling Peptide Systems in Biology, Medicine and Engineering* (Aggeli, A., Boden, N., and Zhang, S., eds.), Kluwer Academic, Dordrecht, The Netherlands, pp. 221–233.
42. Novelli, A. and Boulanger, P. A. (1991) Deletion analysis of functional domains in baculovirus-expressed adenovirus type 2 fiber. *Virology* **185**, 365–376.
43. Hong, J. S. and Engler, J. A. (1996) Domains required for assembly of adenovirus type 2 fiber trimers. *J. Virol.* **70**, 7071–7078.
44. McLaughlin, S. H. and Bulleid, N. J. (1998) Molecular recognition in procollagen chain assembly. *Matrix Biol.* **16**, 369–377.
45. Tao, Y., Strelkov, S. V., Mesyanzhinov, V. V., and Rossmann, M. G. (1997) Structure of bacteriophage T4 fibrillin: a segmented coiled coil and the role of the C-terminal domain. *Structure* **5**, 789–798.
46. Hartgerink, J. D., Beniash, E., and Stupp, S. I. (2001) Self-assembly and mineralization of peptide-amphiphile nanofibers. *Proc. Natl. Acad. Sci. USA* **294**, 1684–1688.
47. Barnett, B. G., Crews, C. J., and Douglas, J. T. (2002) Targeted adenoviral vectors. *Biochim. Biophys. Acta* **1575**, 1–14.

48. Seki, T., Dmitriev, I., Kashentseva, E., Takayama, K., Rots, M., Suzuki, K., and Curiel, D. T. (2002) Artificial extension of the adenovirus fiber shaft inhibits infectivity in coxsackievirus and adenovirus receptor-positive cell lines. *J. Virol.* **76**, 1100–1108.
49. O'Brien, J. P., Hoess, R. H., Gardner, K. H., Lock, R. L., Wasserman, Z. R., Weber, P. C., and Salemme, F. R. (1994) Design, synthesis, and fabrication of a novel self-assembling fibrillar protein, in *Silk Polymers, Materials Science and Biotechnology*, ACS Symposium Series 544 (Kaplan, D., Adams, W. W., Farmer, B., and Viney, C., eds.), American Chemical Society, Washington, DC, pp. 104–117.
50. Gillespie, D. B., Thiel, B. L., Trabbic, K. A., Viney, C., and Yager, P. (1994) Structural investigation of (AdII)<sub>26</sub> fiber, a novel bioengineered material based on a viral spike protein. *Macromolecules* **27**, 6177–6182.
51. Hyman, P., Valluzzi, R., and Goldberg, E. (2002) Design of protein struts for self-assembling nanoconstructs. *Proc. Natl. Acad. Sci. USA* **99**, 8488–8493.
52. Miroshnikov, K. A., Marusich, E. I., Cerritelli, M. E., Cheng, N., Hyde, C. C., Steven, A. C., and Mesyanzhinov, V. V. (1998) Engineering trimeric fibrous proteins based on bacteriophage T4 adhesins. *Protein Eng.* **11**, 329–332.
53. Frank S., Kammerer, R. A., Mechling D., Schulthess, T., Landwehr, R., Bann, J., Guo, Y., Lustig, A., Bächinger, H. P., and Engel, J. (2001) Stabilization of short collagen-like triple helices by protein engineering. *J. Mol. Biol.* **308**, 1081–1089.
54. Stetefeld, J., Frank, S., Jenny, M., Schulthess, T., Kammerer, R. A., Boudko, S., Landwehr, R., Okuyama, K., and Engel, J. (2003) Collagen stabilization at atomic level: crystal structure of designed (GlyProPro)(10)foldon. *Structure* **11**, 339–346.
55. Krasnykh, V., Belousova, N., Korokhov, N., Mikheeva, G., and Curiel, D. T. (2001) Genetic targeting of an adenovirus vector via replacement of the fiber protein with the phage T4 fibritin. *J. Virol.* **75**, 4176–4183.
56. Kraulis, P. J. (1991) MOLSCRIPT: a program to produce both detailed and schematic plots of protein structures. *J. Appl. Cryst.* **24**, 946–950.

## Application of NMR Methods to Identify Detection Reagents for Use in Development of Robust Nanosensors

Monique Cosman, Viswanathan V. Krishnan, and Rod Balhorn

### Summary

Nuclear magnetic resonance (NMR) spectroscopy is a powerful technique for studying bimolecular interactions at the atomic scale. Our NMR laboratory is involved in the identification of small molecules, or ligands, that bind to target protein receptors such as tetanus neurotoxin (TeNT) and botulinum neurotoxin, anthrax proteins, and HLA-DR10 receptors on non-Hodgkin lymphoma cancer cells. Once low-affinity binders are identified, they can be linked together to produce multidentate synthetic high-affinity ligands (SHALs) that have very high specificity for their target protein receptors. An important nanotechnology application for SHALs is their use in the development of robust chemical sensors or biochips for the detection of pathogen proteins in environmental samples or body fluids. Here we describe a recently developed NMR competition assay based on transferred nuclear Overhauser effect spectroscopy that enables the identification of sets of ligands that bind to the same site, or a different site, on the surface of TeNT fragment C (TetC) than a known “marker” ligand, doxorubicin. Using this assay, one can identify the optimal pairs of ligands to be linked together for creating detection reagents, as well as estimate the relative binding constants for ligands competing for the same site.

**Key Words:** Nuclear magnetic resonance; structure-based drug design; transferred nuclear Overhauser effect spectroscopy; tetanus toxin; biosensors.

### 1. Introduction

Nuclear magnetic resonance (NMR) spectroscopy has evolved into an important technique in support of structure-based drug design because of its long tradition in the study of molecular interactions (1,2). Several NMR experiments have been used in generic binding assays to identify weak, but specific, binding between small molecules and a target protein. The advantage of these NMR screening methods is that they can be applied as soon as a target

From: *Methods in Molecular Biology*, vol. 300:  
*Protein Nanotechnology, Protocols, Instrumentation, and Applications*  
Edited by: T. Vo-Dinh © Humana Press Inc., Totowa, NJ

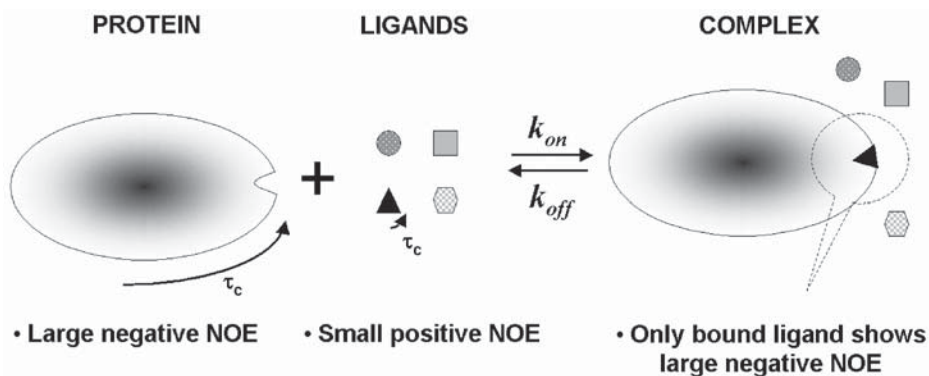


Fig. 1. Principle of the trNOESY experiment. The trNOE is only operative when the ligand is bound, because the ligand experiences a long correlation time ( $\tau_c$ ) only in the bound state. The NOE is transferred and measured on the resonances of the ligand in the free state.

protein is available without the need for extensive assay development. NMR screening methods have been reviewed extensively by others (3–5) and are not described in detail here, with the exception of the transferred nuclear Overhauser effect spectroscopy (trNOESY) experiment.

trNOESY experiments (6–8) are routinely used to detect ligand binding to a target protein under conditions of fast exchange (ligands that bind with micromolar to millimolar dissociation constants). The advantages of the trNOESY method are that it does not require large amounts of pure, labeled protein; it is not limited by the size of the protein; and it can provide information about the structure of the bound form of the ligand. In the experiment, the intensity of each intraligand nuclear Overhauser effect (NOE) crosspeak is governed by the population-weighted cross-relaxation rate (9) (Fig. 1). Thus, the binding event is relatively straightforward to detect and does not require time-consuming chemical shift assignments. A strong negative NOE crosspeak is observed for binders, as opposed to weakly positive or zero NOE crosspeaks for the same compounds in the absence of the target receptor, as shown for MP-biocytin in Fig. 2. Thus, the sign flip of the NOE crosspeak between the free vs bound states acts as a simple binary filter to distinguish binders from nonbinders (10,11) (see Note 1).

An important parameter in selecting a reagent for use in a sensor is its relative binding affinity. Very recently, several laboratories, including our own, have begun to address the issue of whether NMR screening methods can simultaneously and rapidly provide this information (12–14). For the preparation of multivalent ligands that consist of two or more ligands that are weak

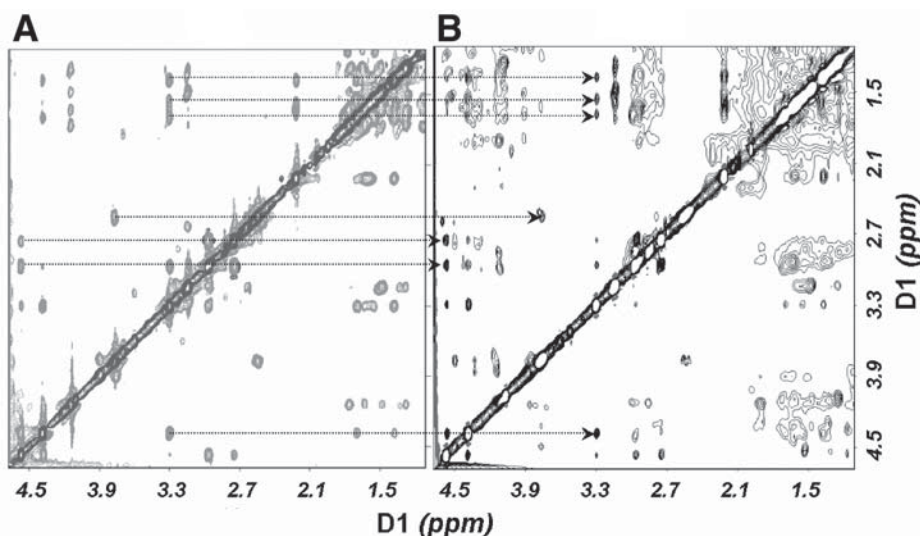


Fig. 2. trNOESY experiment: (A) A 900-ms NOESY spectrum of MP-biocytin (approx 1 mM) exhibits weak positive crosspeaks (in gray). (B) The addition of TetC (approx 0.05 mM) results in the MP-biocytin crosspeaks in the 300-ms trNOESY to flip their sign to negative (in black) and increase in intensity, indicating that MP-biocytin binds to TetC. Several of the crosspeaks in both spectra are designated by the dashed arrows and the 900-ms spectrum in (A) is plotted at a two times lower level than the 300-ms trNOESY spectrum in (B) for presentation purposes. The spectra were acquired at 30°C.

binders, it is also useful to determine whether each ligand is binding with specificity to the same site or to a different site from another ligand. Although the individual ligands that comprise a linked bidendate compound may only bind weakly to the protein, as expected because of their small size, the free energy of binding of the linked compound is, in principle, the sum of the free energies of each fragment plus a term owing to linking (15). Thus, linked compounds with less than micromolar dissociation constants can be obtained by linking two fragments that each dissociate in the greater than micromolar range (16). Here, we present the methods in detail for carrying out a trNOESY competition binding assay for tetanus toxin fragment C (TetC).

Tetanus toxin and the botulinum toxins (BoNTs) are structurally and functionally related members of the family of *Clostridial* neurotoxins. Recent interest in these neurotoxins arises from the increased frequency of the use of BoNTs in medicine, occasional dairy cattle and wildfowl deaths that have resulted from toxin ingestion, and the potential threat that this protein might be used by terrorist groups or other nations as a biological weapon (17,18).



Both toxins selectively concentrate at the synapse of axons in vertebrate motor neurons and are the most potent toxins known to humans (19). The entry of these toxins into neuronal cells requires the initial binding of the toxin to gangliosides on the cell surface. Thus, effective inhibitors that block neuronal cell binding can be developed for use as antidotes or serve as molecular recognition materials for affinity-based chemical sensors that detect and identify these highly toxic proteins.

## 2. Materials

1. High-field NMR instrument ( $\geq 500$  MHz) (*see Note 2*).
2. Available Chemical Directory (ACD) or similar library of compounds to screen.
3. Recombinant TetC (Roche, Indianapolis, IN).
4. 100% Deuterium oxide ( $D_2O$ ) (Isotech, Miamisburg, OH).
5. 100% Deuterated dimethyl sulfoxide (DMSO) (Isotech).
6. Doxorubicin hydrochloride (Sigma-Aldrich, St. Louis, MO). **Caution:** the anti-tumor drug doxorubicin is an inhibitor of reverse transcriptase and RNA polymerase, is an immunosuppressive agent, and intercalates into DNA (20–22).
7. 3'-Sialyllactose (Sigma-Aldrich).
8. Sarcosine-Arg-Gly-Asp-Ser-Pro (Sar-RGDSP) (Sigma-Aldrich).
9. 3-(*N*-maleimidopropionyl)biocytin (MP-biocytin) (Sigma-Aldrich).
10. Lavendustin A (Sigma-Aldrich). **Caution:** lavendustin A is a protein tyrosine kinase inhibitor (23).
11. Naphthofluorescein-di- $\beta$ -D-galactopyranoside (NF-GalPyr) (Sigma-Aldrich).
12. Ser-Gln-Asn-Tyr-Pro-Ile-Val (SQNYPIV) (Calbiochem-Novabiochem, La Jolla, CA).
13. Sialic acid (Calbiochem-Novabiochem).

## 3. Methods

### 3.1. Theory of the *trNOESY* Experiment

At spectrometer frequencies of 500 to 600 MHz ( $H_v$ ), small molecules (molecular weight  $< 1500$ ) in the free state yield small, positive NOEs, whereas large protein molecules (molecular weight  $> 10,000$ ) yield large, negative NOEs. In the fast-exchange regime (binding constant between  $10^{-3}$  and  $10^{-7}$  M), the ligand acquires the NOE characteristics of the large molecule during the reversible binding and shows large negative NOEs (Fig. 1). These characteristics are transferred from the bound state of the ligand to its free state, and, therefore, the ligand signals are still sharp owing to the rapid total rotational correlation time,  $\tau_c$ , of the free ligand. The ligand-binding event is thus identified by both the change in sign and the intensity buildup rate of its intramolecular NOEs.

The theory behind the mechanism of trNOE has been well developed over the years (24–29). The dynamics of the NOE is governed by the three species equilibrium processes given by



in which  $[P]$ ,  $[L]$ , and  $[PL]$  are the molar concentrations of the protein, the ligand, and the complex, respectively; and  $k_{\text{on}}$  and  $k_{\text{off}}$  are the association and dissociation constants, respectively. In the trNOE experiment, the exchange of the ligand between the free and bound states alters the relaxation dynamics of the ligand more significantly than of the protein. Under equilibrium conditions, the binding constant,  $K_D$ , is the ratio of  $k_{\text{off}}$  to  $k_{\text{on}}$ . The exchange rate that is relevant to the NMR experiments,  $k_{\text{ex}}$ , depends on the relative populations of the protein and ligand as well as the binding constant and is defined as

$$k_{\text{ex}} = k_{\text{on}}[P] + k_{\text{off}} = k_{\text{off}}/(1 - L_b) \quad (2)$$

in which  $L_b$  is the bound ligand fraction. For a single ligand-binding site,  $L_b$  is given by

$$L_b = \{(P_T + L_T + K_D) - \sqrt{(P_T + L_T + K_D)^2 - 4P_T L_T}\}/2L_T \quad (3)$$

in which  $P_T$  and  $L_T$  are the total protein and ligand concentrations, respectively; and  $K_D$  is the binding constant. In the performance of trNOE experiments, it is useful to have the protein-binding site at least half-saturated ( $L_T \approx K_D$ ). This is accomplished by using a large molar excess of the ligand of approx 5 to 50 times that of the protein. Exchange of the magnetization between the protein-bound form and the free form of the ligand produces an averaged NOE.

The exchange-averaged NOE depends on the rate of exchange and the magnitude of the NOE between the free ( $\text{NOE}_f$ ) and bound ( $\text{NOE}_b$ ) forms. The exchange rate,  $k_{\text{ex}}$ , is considered fast, intermediate, or slow if  $k_{\text{ex}} \gg [\text{NOE}_f - \text{NOE}_b]$ ,  $k_{\text{ex}} \approx [\text{NOE}_f - \text{NOE}_b]$ , and  $k_{\text{ex}} \ll [\text{NOE}_f - \text{NOE}_b]$ , respectively. In the fast-exchange regime ( $k_{\text{ex}} \gg [\text{NOE}_f - \text{NOE}_b]$ ), the trNOE experiments are extremely useful because the observed NOE is then a population weighted average.

The dynamic interplay between the ligand intramolecular NOEs and the ligand/protein intermolecular exchange NOEs can be described by combining Solomon's equations and chemical exchange equations (30–32). Using this approach, Clore and Gronenborn (25,26) described the observed effect of trNOE by using matrix notation. The combined matrix includes the pairwise interactions in a multiple-spin system undergoing exchange, which accounts for the spin diffusion effects as well (29,33,34). The evolution of the intensity in a two-dimensional (2D) trNOE experiment (trNOESY) is given by (30,32)

$$\frac{d}{d\tau_m} \mathbf{V}(\tau_m) = -\Gamma \mathbf{V}(\tau_m) \quad (4)$$

in which  $\tau_m$  is the mixing time, and the elements of the matrix  $\mathbf{V}(\tau_m)$  are the measured peak volumes of the crosspeaks in the trNOESY spectrum, which are described in terms of the exchange-relaxation matrix  $\Gamma$ . The exchange rates ( $k_{ex}$ ) as well as the self- ( $\rho_{ij}$ ) and cross-relaxation ( $\sigma_{ij}$ ) rates of the various proton pairs are included in  $\Gamma$ . When the exchange is fast relative to the relaxation rates, the effective rate constants are molar fraction weighted averages of the rate constants of the free and bound forms. Thus, if  $i$  and  $j$  are the ligand spins, the effective cross-relaxation rate  $\sigma_{ij}^{avg}$  is

$$\sigma_{ij}^{avg} = L_b \sigma_{ij}^b + (1 - L_b) \sigma_{ij}^f \quad (5)$$

In this fast-exchange regime, as pointed out by Landy and Rao (35), the relaxation + exchange matrix,  $\Gamma$ , can be symmetrized, and, thus, the rate equation for the  $m$ -spin ligand and  $n$ -spin protein simplifies to an  $(n + m)$  differential equation (36). The relative concentrations of the ligand and protein, following Zabell and Post (37) and Eq. 2, can be written as

$$\frac{d}{d\tau_m} \begin{bmatrix} (V_l^b + V_l^f) & \sqrt{\mu_p^b} \\ (V_p^b + V_p^f) & \sqrt{\mu_l^b} \end{bmatrix} = - \begin{pmatrix} \mu_l^b \Gamma_l^b + \mu_l^f \Gamma_l^f & \sqrt{(\mu_l^b \mu_p^b) \Gamma_{lp}^b} \\ \sqrt{(\mu_l^b \mu_p^b) \Gamma_{lp}^b} & \mu_p^b \Gamma_p^b + \mu_p^f \Gamma_p^f \end{pmatrix} \times \begin{bmatrix} (V_l^b + V_l^f) & \sqrt{\mu_p^b} \\ (V_p^b + V_p^f) & \sqrt{\mu_l^b} \end{bmatrix} \quad (6)$$

in which  $\Gamma_l^b$  and  $\Gamma_l^f$  represent the symmetrical  $n \times n$  relaxation matrices of the ligand in the bound and free forms, respectively; and  $\Gamma_p^b$  and  $\Gamma_p^f$  have analogous definitions for the protein. The relative concentrations are defined by “ $\mu$ ” as follows:

$$\begin{aligned} \mu_l^b &= [PL]/([PL] + [L]) \\ \mu_l^f &= [L]/([PL] + [L]) \\ \mu_p^b &= [PL]/([PL] + [P]) \\ \mu_p^f &= [P]/([PL] + [P]) \end{aligned} \quad (7)$$

These equations are generally used in cases in which quantification of ligand crosspeaks in the trNOESY spectra is needed to determine the structure of the bound form of the ligand. This information is especially useful when combined with computational approaches in order to optimize models of protein/ligand complexes, which, in turn, are used to develop new ligands with higher affinity and specificity for the target site on the protein.

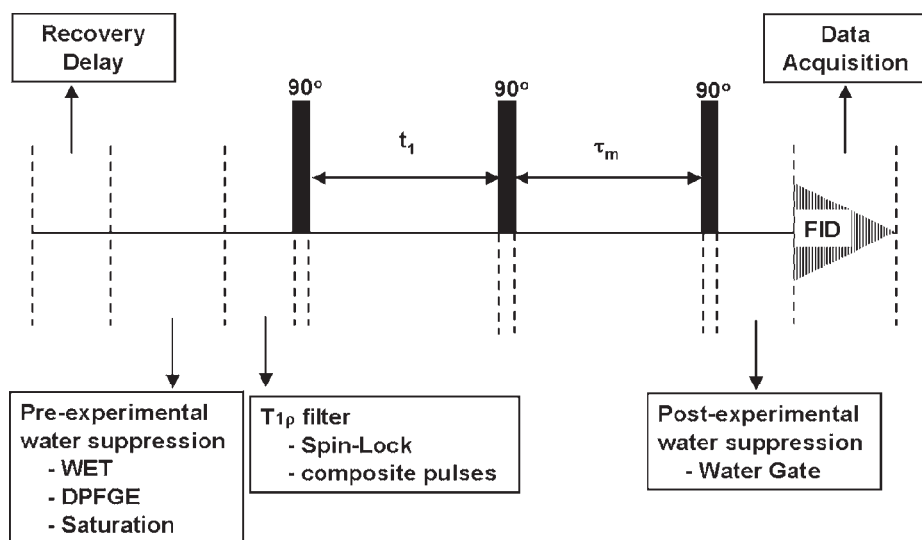


Fig. 3. trNOESY pulse sequence. Bars represent 90° radiofrequency pulses and FID stands for free induction decay. The pulses and the receiver are phase cycled to select the NOE and perform phase-sensitive detection along  $t_1$ . WET, water suppression enhanced through  $T_1$  effects; DPFGE, double pulsed field gradient echo.

## 3.2. NMR Experimental Setup

### 3.2.1. NMR Pulse Sequences

NMR pulse sequences, which are composed of a series of radiofrequency pulses interspersed with delays, are the actual NMR experiments. The pulse sequence for the trNOESY experiment differs slightly from the conventional three-pulse NOESY experiment (38), as shown in Fig. 3.

#### 3.2.1.1. FILTERING OUT PROTEIN SIGNALS (SEE NOTE 3)

One common modification is the insertion of a relaxation filter to suppress extraneous protein signals, which may interfere with the detection of the ligand signal. This can be achieved by the  $T_{1\rho}$  (or  $R_2$ ) filter. This filter can be introduced either prior to or after the first 90° pulse. If introduced prior to the first pulse, the filter needs to be flanked by additional 90° pulses or windowless multiple pulse sequences such as DIPSI (39) need to be used, so that the magnetization is along the Z-axis after the filter is employed. If the filter is introduced after the first 90° pulse, as in the original experiment proposed by Scherf and Anglister (40), care must be taken to acquire the first  $t_1$  point to avoid the need for large phase corrections in the indirect dimension.

### 3.2.1.2. SUPPRESSION OF WATER SIGNAL (SEE NOTE 4)

Another common modification to the pulse sequence is the control or suppression of the water magnetization. A variety of preexperimental water suppression schemes are available, such as excitation sculpting–based suppression (41) or WET (42,43). Postexperimental elimination of water signal using methods such as watergate or its modifications (44,45) are also a viable alternative to preelimination. When considering water suppression schemes in a trNOESY experiment, it is critical to consider how the water suppression will affect detection of the ligand signals. For example, if the ligand contains exchangeable protons, then it is desirable to avoid presaturation because it tends to saturate these resonances as well. It is also important to note that all the postexperimental water suppression schemes (e.g., watergate) have a nonuniform excitation profile near the water frequency. Under such conditions, it is advisable to adjust the sample temperature to move the water signal so that any nearby ligand resonances do not get suppressed as well.

### 3.2.2. Selection of Mixing Times

For screening purposes, it is first useful to identify where the ligand protons resonate when protein is not present. This requires that a NOESY spectrum of the ligand be obtained. A direct comparison of the spectrum with ligand alone and the spectrum of the ligand or mixtures of ligands in the presence of the TetC protein provides a simple and rapid way of identifying those crosspeaks that belong to that particular ligand without having to assign the chemical shifts. Assignment of chemical shifts can often be a very time-consuming process and would only be needed if the structure of the bound form of the ligand is to be determined.

In the absence of protein, NOESY experiments are carried out at longer (600–900 ms) mixing times, whereas mixtures of ligands in the presence of TetC are carried out at shorter (200–300 ms) mixing times. Long mixing times are necessary for detection of NOEs for small molecules (<1- to 2-kDa molecular weight) because the product of  $\omega_0$  ( $2\pi \times$  spectrometer frequency) and  $\tau_c$  (rotational correlation time) is  $<1$  ( $\omega_0\tau_c < 1$ ). By contrast, shorter mixing times are required for large molecules or ligands binding to large molecules because  $\omega_0\tau_c \gg 1$  (46).

### 3.2.3. Experiment Time

Typically, 300 increments are collected in  $t_1$ , each with 48 or 64 scans, and 1024 complex data points are collected in  $t_2$ . Our NMR data were processed using the program VNMR (version 6.1C; Varian, Palo Alto, CA) and analyzed using the program FELIX (version 97; Accelrys, San Diego, CA).

The time required for performing a trNOESY or NOESY experiment is dependent on the concentration of the ligands and the mixing time. For example, at concentrations of approx 0.3 mM, 20 h is required for both the ligand alone (900-ms mixing time, 48 scans) and the ligand in the presence of TetC (300-ms mixing time, 64 scans). At ligand concentrations of 1 mM, the time required can be reduced by half. Collecting data on mixtures of ligands instead of single ligands further decreases the total time required for the trNOESY experiment.

#### 3.2.4. Effects of Temperature

In our studies, we arbitrarily chose to carry out the trNOESY experiments at either 20 or 30°C, empirically discovering that the data improved slightly at the higher temperature for most ligands. Changing the temperature can alter the rate of exchange between ligand and TetC and thereby increase the possibility of detection of trNOEs in some cases in which binding was not observed. Lower temperatures slow the exchange rate, whereas higher temperatures increase the exchange rate. Thus, one way to address the important limitation of the trNOESY competition assay—that binding can only be detected for those compounds that have millimolar to micromolar dissociation constants—is to change the temperature and, consequently, the rate of exchange (*see Note 5*).

### 3.3. Preparation of Sample

#### 3.3.1. Identification of Optimal Set of Ligands to Screen for Binding to TetC

There are several strategies, including random screening of a suitable chemical database, that can be employed to identify sets of potential binders. In this study, two crystal structures of TetC are available (PDB access codes 1AF9 and 1A8D [47,48], <http://www.rcsb.org/pdb/>), so we employed a structure-based approach.

##### 3.3.1.1. COMPUTATIONAL METHODS TO IDENTIFY SUITABLE LIGANDS

The first step involved using the crystal structure of the protein is to identify binding sites and to carry out a virtual screen of the ACD. Two surface binding sites, Site-1 and Site-2, are identified by calculating the solvent-accessible surface and using the SPHGEN routine from DOCK 4.01 (49), which packs clusters of spheres into structural pockets. A sphere-atom matching scheme in the DOCK 4.01 program (50–52) is then used to computationally screen the ACD, which currently contains more than 300,000 commercially available compounds, and to predict which molecules will likely bind to Site-1 and Site-2. A variety of structurally diverse ligands are chosen to represent the spectrum of possible candidates, and the best candidates are ranked by energy and contact scores. The top 100 compounds are then visually examined qualitatively to assess the interactions that they form with the site.

### 3.3.1.2. FURTHER REDUCTION AND OPTIMIZATION OF SET OF LIGANDS

The next step is to scale down further the top 100 compounds obtained from the virtual screen to approx 10 to 20 compounds for each site, using a selection criterion based on cost and availability. The final cut is made by checking the remaining compounds for binding activity by electrospray ionization mass spectroscopy (ESI-MS) (**53,54**; **Table 1**). Although this step is not required, it does help to significantly speed up the process in narrowing down the number of likely candidates. The sequential funneling of 300,000 ligands to about a dozen for each site resulted in optimizing the short list of compounds (**Fig. 4**) to use in our NMR screening studies for binding activity in an aqueous environment. There are several reasons why checking for binding activity in solution is important. In particular, it is a prerequisite for identifying detection reagents that will be used in an aqueous environment. In addition, the synthesis of novel bidendate ligands requires that the individual compounds be compatible with one another and with TetC under similar solvent conditions.

### 3.3.2. Preparation of Stock Solutions and Sample Solutions

1. Store dry recombinant TetC at  $-15$  to  $-25^{\circ}\text{C}$  (*see Note 6*).
2. Dissolve 1 to 3 mg of dry (lyophilized) TetC protein samples in 500  $\mu\text{L}$ /experiment of 100%  $\text{D}_2\text{O}$  to obtain a final concentration between 38 and 72  $\mu\text{M}$  (*see Note 7*).
3. Centrifuge at highest speed for 5 min to remove any insoluble material before adding ligands.
4. Prepare concentrated stock solutions of ligands in either 100  $\mu\text{L}$  of  $\text{D}_2\text{O}$  or deuterated DMSO. The goal is to keep the total concentration of DMSO at or below 5% (v/v). The addition of this small amount of DMSO would not be expected to affect the stability of the protein, as previously demonstrated by other NMR studies (**16**), but it should be checked experimentally for each protein by determining whether the binding activity is still detectable for a known binder when the protein is in a 5% DMSO solution. Three ligands, MP-biocytyl, lavendustin A, and NF-galactopyranoside, were dissolved in deuterated DMSO; the remaining ligands (**Fig. 4**) were all soluble in  $\text{D}_2\text{O}$ .
5. Calculate the volume of ligand stock solution required to prepare an approx 0.3 to 1 mM concentration in the final 500- to 600- $\mu\text{L}$  sample volume. Test different molar ratios of TetC:doxorubicin ranging from 1:5 to 1:50 in order to determine the best ratios for use in the experiments (*see Note 8*).
6. Prepare protein–ligand complexes by one of the following two methods:
  - a. Dissolve 3 mg of TetC in 1.0 mL of  $\text{D}_2\text{O}$  (57.9  $\mu\text{M}$ ) and centrifuge for 5 min in an Eppendorf microcentrifuge at highest speed to remove insoluble material prior to adding the ligands.
  - b. Prepare mixtures of ligands in approx 500–800  $\mu\text{L}$  of  $\text{D}_2\text{O}$  (0.2–1 mM) prior to the addition of 1 to 3 mg of dry TetC (38–72  $\mu\text{M}$ ) to a final ratio of TetC:ligand of approx 1:20.



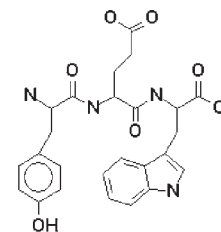
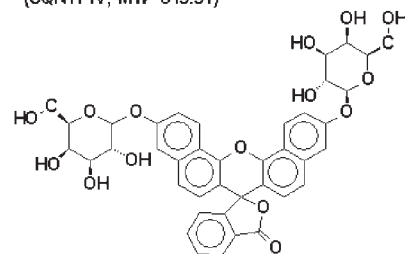
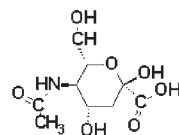
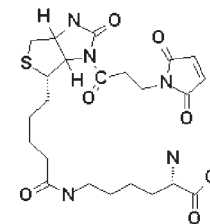
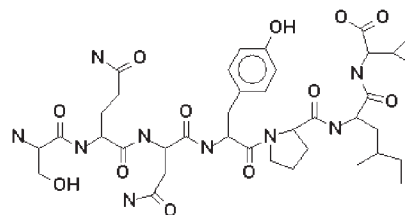
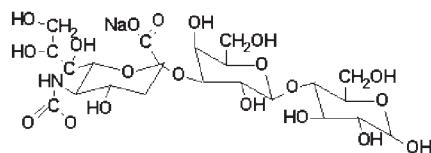
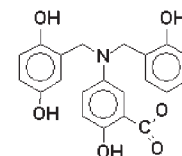
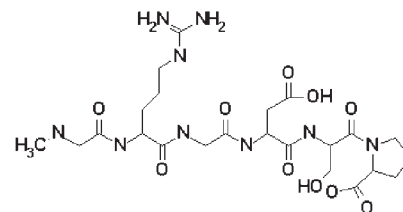
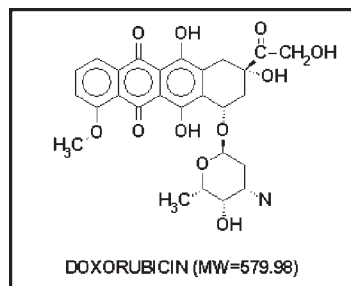


Fig. 4. Structures and molecular weights of ligands used in this study. The marker ligand, doxorubicin, is boxed.

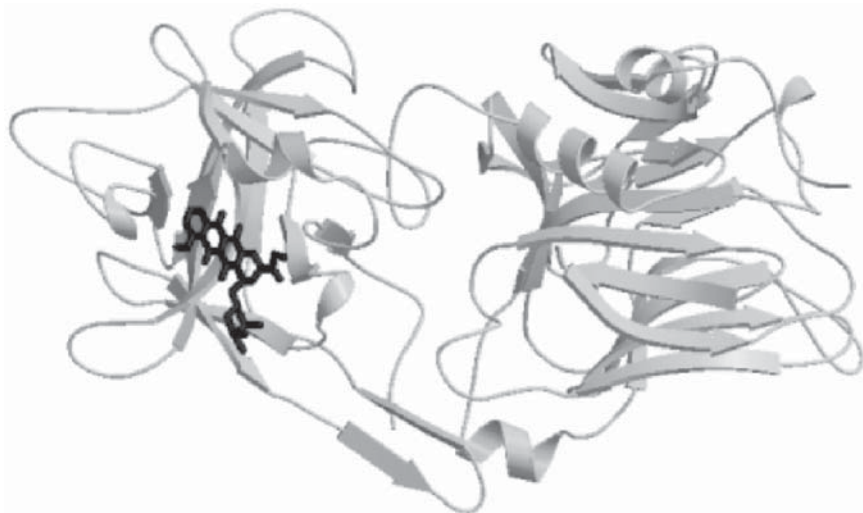


Fig. 5. Crystal structure of TetC with doxorubicin, the marker ligand, computationally docked into Site-1. This figure was made using Molscript (60) and Raster3D (61) programs.

### 3.4. Screening/Competition trNOESY Assay

The trNOESY competition assay requires a “marker” ligand, for which the binding site on the protein and preferably the binding constant are known. The crystal structures of BoNT/B ligand complexes show that doxorubicin (55) and 3'-sialyllactose (56) bind to Site-1 (Fig. 5). Site-1 is a common surface feature found in the structures of both TetC and BoNT, and preliminary results obtained from the crystal structure of TetC in complex with doxorubicin indicate that doxorubicin also binds to Site-1 on TetC (S. Swaminathan, personal communication, March 2002). Furthermore, the dissociation constant for the doxorubicin/TetC complex is known and is approx 10  $\mu\text{M}$  (57). Doxorubicin is thus an ideal marker ligand to use in this study.

Competition experiments are used to identify those compounds that bind to Site-1 or a different site by determining whether binding of doxorubicin to TetC is disrupted by a competing ligand binding to the same site. This is evidenced by an absence of trNOEs for doxorubicin and the presence of trNOEs for the other ligand. However, it must be stressed that these assays cannot identify the exact site of ligand binding, only whether the sites are different or the same (see Note 9 for additional caveats).

#### 3.4.1. Method 1: Sequential Addition of Ligands

Sequential addition of each of the computationally predicted Site-2 ligands is used as a negative control to show whether any of these ligands will also

**Table 1**  
**Ligands Tested Positive by ESI-MS**  
**for Noncovalent Complex Formation With TetC**

Predicted Site-1	Predicted Site-2
Doxorubicin <sup>a,b</sup>	Tyr-Glu-Trp
3'-Sialyllactose <sup>2</sup>	Lavendustin A
D-(+)-Cellotetraose <sup>a</sup>	Sar-RGDSP
Neohesperidin diHCl <sup>a</sup>	NF-GalPyr
Gly-Arg-Gly-Asp-Ser <sup>a</sup>	MP-biocytin
Hemorphin-5 <sup>a</sup>	SGNYPIV
Etoposide phosphate	

<sup>a</sup>Reported in ref. 57.

<sup>b</sup>Binds Site-1 in BoNT/B (55).

**Table 2**  
**Concentrations of Ligands and TetC and Observation of Binding Activity**

	Ligand	[Lig] ( $\mu$ M)	[TetC] ( $\mu$ M)	[TetC]:[Lig]	Binding
<b>Fig. 6</b>					
A	Doxorubicin	1081.4	54.3	1:20	Yes
B	Sar-RGDSP	1116.3	50.6	1:22	No
C	SGNYPIV	1050.6	47.4	1:22	Yes
D	Lavendustin A	993.3	45.0	1:22	Yes
E	NF-GalPyr	926.6	43.3	1:21	Maybe <sup>a</sup>
<b>Fig. 8</b>					
A	Sialic acid	386.7	22.3	1:17	No
BC	Doxorubicin	365.6	21.5	1:17	Yes, no <sup>b</sup>
C	3'-Sialyllactose	351.9	20.7	1:17	Yes

<sup>a</sup>Precipitation was observed, resulting in a decrease in the intensities of all crosspeaks.

<sup>b</sup>Doxorubicin binding was observed in Fig. 8B but not in Fig. 8C.

bind to Site-1 by displacement of doxorubicin. The results also show whether two or more ligands can bind simultaneously to TetC, thus identifying suitable pairs of ligands to link together in developing the synthetic high-affinity ligands (SHALs) as detection reagents for the *Clostridium* neurotoxins.

1. Prepare a TetC:doxorubicin complex with the concentrations approx [50  $\mu$ M]/[1000  $\mu$ M] or a ratio of 1:20. Collect trNOESY data.
2. Add approx 1 mM each of the predicted Site-2 ligands sequentially (Table 2), collecting trNOESY data after each addition.

3. Analyze trNOESY data after each addition of ligand to determine whether crosspeaks belonging to doxorubicin or added ligand become weaker, positive, or disappear, indicating that doxorubicin has been displaced. The appearance of strong negative crosspeaks indicates that the ligand is able to bind simultaneously with doxorubicin and is thus a good candidate for linking to another ligand (**Fig. 6**).

#### *3.4.2. Method 2: Evaluation of Ligands Binding Sequentially in Reverse Order to TetC*

It is important to carry out the positive control, or the reverse experiment of method 1. Each ligand shown in **Fig. 4** is first added to TetC in a 20-fold excess to determine whether binding could be observed without the interference possible owing to the presence of another ligand. Doxorubicin is next added to the mixture to determine whether it can displace the bound ligand being tested, and to confirm that the protein is active if no binding had occurred with ligand-1. If displacement occurs, then ligand-1 is identified as a Site-1 binder that exhibits a weaker binding affinity than the marker ligand, doxorubicin. Next, another ligand, ligand-3, is added to determine whether the ligand-1 or doxorubicin is displaced. If ligand-1 is displaced but not doxorubicin, then ligand-1 and -3 must compete for the same site, with ligand-3 having the higher binding affinity. A comprehensive analysis of the optimized short list of compounds using this strategy yielded the results shown in **Fig. 7**. Here is a step-by-step example of the method:

1. Add a 20-fold excess of sialic acid to TetC (**Table 2**) and acquire a 300-ms trNOESY spectrum (**Fig. 8A**). Sialic acid does not appear to bind.
2. Add a 20-fold excess of doxorubicin to the sialic acid/TetC solution. Acquire a 300-ms trNOESY spectrum (**Fig. 8B**) to confirm that the protein has not lost its activity or that the batch of protein used was bad.
3. Add a 20-fold excess of 3'-sialyllactose (another Site-1 binder) to the sialic acid/TetC/doxorubicin solution. Acquire a 300-ms trNOESY spectrum. In this case, 3'-sialyllactose will displace doxorubicin, confirming that both ligands bind to Site-1, with 3'-sialyllactose having a higher binding affinity constant than doxorubicin.

#### *3.4.3. Method 3: Addition of TetC to Different Combinations of Ligands*

This method screens multiple ligands simultaneously for binding to TetC in a more high-throughput manner. Up to 10 ligands at a time can be rapidly screened, but since the set of ligands had been prescreened by computational and mass spectroscopy methods, we limited our combinations to three at a time, as shown in **Fig. 8**. The time lost by running a larger number of trNOESY experiments is easily regained by having to analyze much less complicated, and unambiguous, data sets. The experimental results also provided key

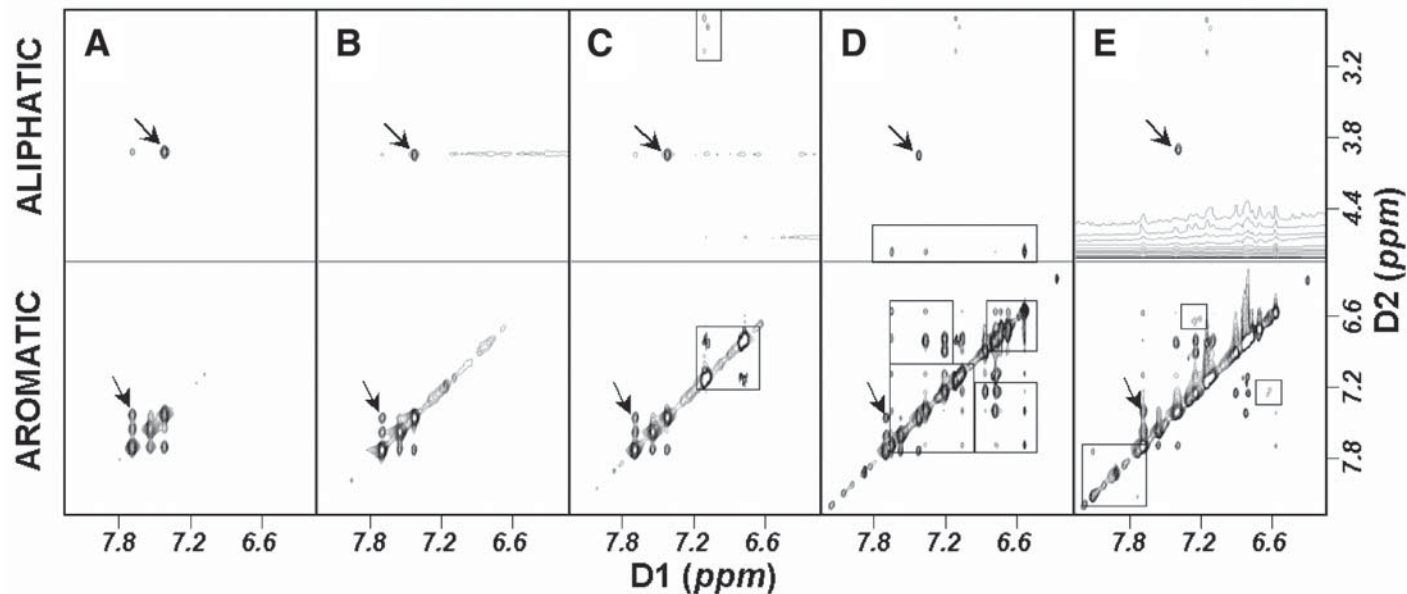


Fig. 6. Effect of doxorubicin binding in Site-1 on predicted Site-2 ligands binding to TetC: expanded regions of the 2D trNOESY spectra of TetC/ligand complexes at 200-ms mixing time and 20°C showing binding of (A) doxorubicin (Site-1 marker ligand). The arrows indicate one aliphatic and one aromatic crosspeak that belongs to doxorubicin, which remains bound throughout the sequential additions of (B) Sar-RGDSP, (C) SQNYPIV, (D) lavendustin A, and (E) NF-GalPyr. The appearance of new, negative crosspeaks in the panels is indicated by a box, and these crosspeaks indicate that Sar-RGRSP does not bind when doxorubicin is present, but that both SQNYPIV and lavendustin A do bind. The addition of NF-GalPyr (E) appears to partially displace lavendustin A, but not doxorubicin and SQNYPIV.

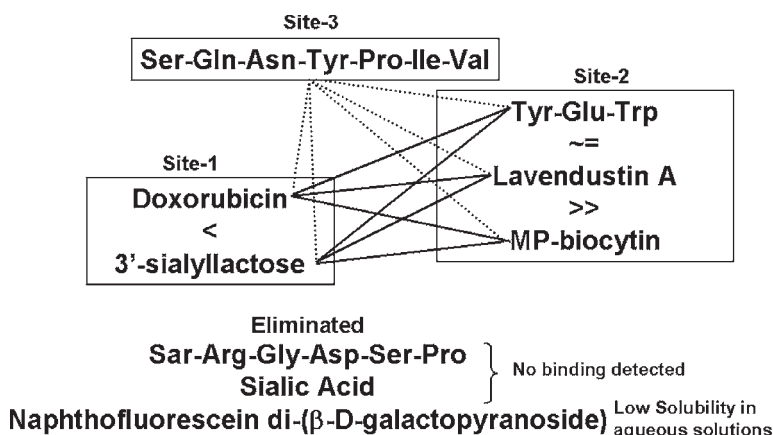


Fig. 7. Grouping of optimized set of ligands tested by trNOESY competition assay into three different binding sites on TetC. The lines indicate how a ligand from each site can be linked in unique ways to develop SHALs as detection reagents in nanosensors. Three ligands were eliminated because either binding was not detected or the ligand was insoluble in aqueous solutions.

information about the compatibility of the ligands under the same solvent conditions.

#### 4. Notes

1. Negative NOE crosspeaks for small molecules in the absence of TetC were sometimes observed when the molecule contains protons attached to large ring systems, such as the protons attached to the four-ring system of doxorubicin. These protons exhibit less internal motion than those located in more flexible long carbon chains. However, although the sign of the trNOE crosspeaks corresponding to these aromatic resonances remained the same regardless of whether TetC was present or not, their intensities were always much stronger for the bound ligand. Thus, both the sign and intensity of the crosspeaks must be taken into consideration when distinguishing ligands that bind from those that do not.
2. Our experiments were carried out on a Varian Inova 600-MHz spectrometer. Although the experiments can be carried out on a lower-field instrument, higher concentrations of both protein and ligands will be required because the sensitivity of the experiment decreases with decreasing magnetic field strength.
3. This step is only necessary if the protein concentration is high and/or the molecular weight of the protein is low. Either case would result in the detection of protein signals that may interfere with observation of the ligand signals. In our case, the TetC concentration is kept low (approx 50  $\mu M$ ). Although TetC signals could be detected at higher concentrations (approx 72  $\mu M$ ), they did not interfere with the detection of the ligand signals. In addition, the molecular weight of TetC is

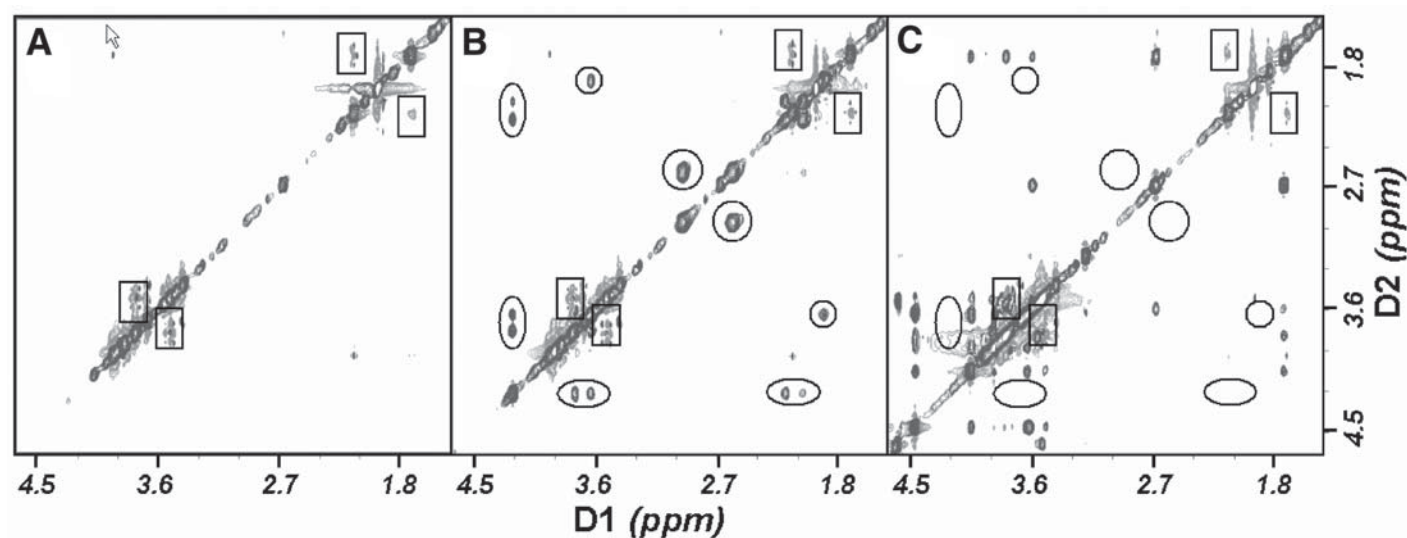


Fig. 8. A 300-ms trNOESY spectra at 2°C of (A) sialic acid does not appear to bind to TetC, as evidenced by weak and positive trNOEs (boxed gray crosspeaks). (B) The addition of doxorubicin to a mixture of TetC and sialic acid results in doxorubicin binding, as evidenced by the strong negative trNOEs (circled black crosspeaks). (C) The addition of 3'-sialyllactose to a mixture of sialic acid, doxorubicin, and TetC shows that 3'-sialyllactose displaces doxorubicin from binding in Site-1. The circled positions of doxorubicin crosspeaks from (B) and the boxed gray sialic acid crosspeaks are shown in (C) for comparison.



sufficiently large (51 kDa) and it is known to dimerize, so that the protein signals are broadened out into the baseline.

4. If the ligands and proteins can be dissolved in deuterated solvents and buffers, then a simple presaturation pulse of the water signal can suffice to eliminate any residual water signal. However, if the samples need to be prepared in solvents or buffers that contain a high ratio of  $\text{H}_2\text{O}/\text{D}_2\text{O}$ , then it is necessary to implement one of these water suppression schemes.
5. Sialic acid did not bind TetC at 2, 10, 20, 30, or 37°C, as evidenced by the presence of weak positive crosspeaks in the spectra at all of these temperatures. However, a crystal structure of a TetC/sialic acid complex by Emsley et al. (58) shows that sialic acid binds to a site that is adjacent to Site-1. One possible explanation for the discrepancies between the NMR and X-ray results is that sialic acid binds TetC with  $<10^3$  M or  $>10^6$  M affinity in the temperature range that we tested. Another reason, however, may be owing to differences in binding between the crystal state and the solution state.
6. Whereas TetC can be purchased as a dry, lyophilized powder, other proteins may not be available dried or they cannot be dried without compromising their activity or risking their precipitation. In these cases, either the protein is dialyzed against deuterated buffer or the experiment is carried out in 90%  $\text{H}_2\text{O}/10\%$   $\text{D}_2\text{O}$ .
7. The minimum volume needed for the NMR experiment in a standard 5-mm tube is approx 500  $\mu\text{L}$ . However, other NMR tubes and probes could be used instead to reduce the amount of sample needed in cases in which the protein is rare or has limited solubility. For example, 5-mm Shigemi tubes (200–300  $\mu\text{L}$ ) or a microprobe (2  $\mu\text{L}$ ) can be used to reduce the volumes. However, note that these are more expensive options and not always available in every NMR laboratory.
8. Ligand:protein ratios between 5 and 50 can be used, depending on the amount of protein available. The optimal molar ratio of TetC:doxorubicin was found to be between 1:15 and 1:25. These ratios provided good sensitivity for detection of trNOEs for a large range of structurally unrelated ligands
9. Several limitations of trNOESY competition assays need to be considered: the possibility that two or more ligands can bind the same site simultaneously cannot be completely ruled out based only on their lack of competition. Recently, Ma et al. (59) have proposed that a protein can preexist in ensembles of substrates, as a result of its conformational flexibility, and present a range of different binding site shapes to the incoming ligands, such that one site may recognize and bind multiple, diverse ligands. An assumption has been made that the ligands are binding specifically to only one site, which may not always be the case. For example, *N*-acetylgalactosamine binds to two different sites in the crystal structure of the TetC complex (58). Similarly, if a predicted Site-2 ligand is binding with specificity to more than one site, a stronger competitor can displace it from one site, but not necessarily from the other sites. In such a case, both ligands would bind simultaneously to TetC. Nonspecific association of a ligand with TetC is also possible, especially at very high concentrations of ligand.

## Acknowledgments

We wish to thank Felice Lightstone for carrying out the computation studies, and Maria Prieto and Loreen Zeller for carrying out the mass spectroscopy experiments. We thank the Department of Energy's Chemical and Biological Security Program and the Lawrence Livermore National Laboratory Exploratory LDRD 01-ERD-046 for generous support of this project. This work was performed under the auspices of the US Department of Energy by Lawrence Livermore National Laboratory under contract W-7405-Eng-48.

## References

1. Pellecchia, M., Sem, D. S., and Wuthrich, K. (2002) NMR in drug discovery. *Nat. Rev. Drug Discov.* **1**, 211–219.
2. Pellecchia, M., Meininger, D., Dong, Q., Chang, E., Jack, R., and Sem, D. S. (2002) NMR-based structural characterization of large protein-ligand interactions. *J. Biomol. NMR* **22**, 165–173.
3. Peng, J. W., Lepre, C. A., Fejzo, J., Abdul-Manan, N., and Moore, J. M. (2001) Nuclear magnetic resonance-based approaches for lead generation in drug discovery. *Methods Enzymol.* **338**, 202–230.
4. Diercks, T., Coles, M., and Kessler, H. (2001) Applications of NMR in drug discovery. *Curr. Opin. Chem. Biol.* **5**, 285–291.
5. van Dongen, M., Weigelt, J., Uppenberg, J., Schultz, J., and Wikstrom, M. (2002) Structure-based screening and design in drug discovery. *Drug Discov. Today* **7**, 471–478.
6. Clore, G. M., Gronenborn, A. M., Mitchinson, C., and Green, N. M. (1982) <sup>1</sup>H-NMR studies on nucleotide binding to the sarcoplasmic reticulum Ca<sup>2+</sup>-ATPase: determination of the conformations of bound nucleotides by the measurement of proton-proton transferred nuclear Overhauser enhancements. *Eur. J. Biochem.* **128**, 113–117.
7. Gronenborn, A. M. and Clore, G. M. (1982) Conformation of NAD<sup>+</sup> bound to yeast and horse liver alcohol dehydrogenase in solution: the use of the proton-proton transferred nuclear Overhauser enhancement. *J. Mol. Biol.* **157**, 155–160.
8. Roberts, G. C. K. (1999) NMR spectroscopy in structure-based drug design. *Curr. Opin. Biotechnol.* **10**, 42–47.
9. Blommers, M. J. J., Stark, W., Jones, C. E., Head, D., Owen, C. E., and Jahnke, W. (1999) Transferred cross-correlated relaxation complements transferred NOE: structure of an IL-4R-derived peptide bound to STAT-6. *J. Am. Chem. Soc.* **121**, 1949–1953.
10. Peng, J. W., Lepre, C. A., Fejzo, J., Abdul-Manan, N., and Moore, J. M. (2001) Nuclear magnetic resonance-based approaches for lead generation in drug discovery, in *Methods in Enzymology: Nuclear Magnetic Resonance of Biological Macromolecules, Part A* (James, T. L., Dotsch, V., and Schmitz, U., eds.), Academic, San Diego, pp. 202–229.

11. Henrichsen, D., Ernst, B., Magnani, J. L., Wang, W. T., Meyer, B., and Peters, T. (1999) Bioaffinity NMR spectroscopy: identification of an E-selectin antagonist in a substance mixture by transfer NOE. *Angew. Chem. Int. Ed.* **38**, 98–102.
12. Cosman, M., Lightstone, F. C., Krishnan, V. V., Zeller, L., Prieto, M. C., Roe, D. C., and Balhorn, R. (2002) Identification of novel small molecules that bind to two different sites on the surface of tetanus toxin C fragment. *Chem. Res. Toxicol.* **15**, 1218–1228.
13. Dalvit, C., Flocco, M., Knapp, S., Mostardini, M., Perego, R., Stockman, B. J., Veronesi, M., and Varasi, M. (2002) High-throughput NMR-based screening with competition binding experiments. *J. Am. Chem. Soc.* **124**, 7702–7709.
14. Jahnke, W., Floersheim, P., Ostermeier, C., Zhang, X. L., Hemmig, R., Hurth, K., and Uzunov, D. P. (2002) NMR reporter screening for the detection of high-affinity ligands. *Angew. Chem. Int. Ed.* **41**, 3420–3423.
15. Jencks, W. P. (1980) What everyone wanted to know about tight binding and enzyme catalysis, but never thought of asking. *Mol. Biol. Biochem. Biophys.* **32**, 3–25.
16. Hajduk, P. J., Meadows, R. P., and Fesik, S. W. (1997) Discovering high-affinity ligands for proteins. *Science* **278**, 497, 499.
17. Henderson, D. A. (2000) Bioterrorism. *Int. J. Clin. Pract. Suppl.* **115**, 32–36.
18. Arnon, S. S., Schechter, R., and Ingleby, T. V., et al. (2001) Botulinum toxin as a biological weapon: medical and public health management. *JAMA* **285**, 1059–1070.
19. Montecucco, C. and Schiavo, G. (1995) Structure and function of tetanus and botulinum neurotoxins. *Q. Rev. Biophys.* **28**, 423–472.
20. Kraus-Berthier, L., Jan, M., Guilbaud, N., Naze, M., Pierre, A., and Atassi, G. (2000) Histology and sensitivity to anticancer drugs of two human non-small cell lung carcinomas implanted in the pleural cavity of nude mice. *Clin. Cancer Res.* **6**, 297–304.
21. Friesen, C., Fulda, S., and Debatin, K. M. (1999) Cytotoxic drugs and the CD95 pathway. *Leukemia* **13**, 1854–1858.
22. Sparano, J. A. (1999) Doxorubicin/taxane combinations: cardiac toxicity and pharmacokinetics. *Semin. Oncol.* **26**, 14–19.
23. Onoda, T., Iinuma, H., Sasaki, Y., Hamada, M., Isshiki, K., Naganawa, H., Takeuchi, T., Tatsuta, K., and Umezawa, K. (1989) Isolation of a novel tyrosine kinase inhibitor, lavendustin A, from *Streptomyces griseolavendus*. *J. Nat. Prod.* **52**, 1252–1257.
24. Bothner-By, A. A. and Gassend, R. (1972) Binding of small molecules to proteins. *Annu. NY Acad. Sci.* **222**, 668–676.
25. Clore, G. M. and Gronenborn, A. M. (1982) Theory and applications of the transferred nuclear Overhauser effect to the study of the conformations of small ligands. *J. Magn. Reson.* **48**, 402–417.
26. Clore, G. M. and Gronenborn, A. M. (1983) Theory of the time dependent transferred nuclear Overhauser effect: application to the structural analysis of ligand-protein complexes in solution. *J. Magn. Reson.* **53**, 423–442.

27. Campbell, A. P. and Sykes, B. D. (1993) The 2-dimensional transferred nuclear Overhauser effect—theory and practice [review]. *Annu. Rev. Biophys. Biomol. Struct.* **22**, 99–122.
28. Ni, F. and Scheraga, H. A. (1994) Use of the transferred nuclear Overhauser effect to determine the conformations of ligands bound to proteins. *Accounts Chem. Res.* **27**, 257–264.
29. Ni, F. (1994) Recent developments in transferred NOE methods. *Prog. Nucl. Magn. Reson. Spectrosc.* **26**, 517–606.
30. Solomon, I. (1955) Relaxation process in a two-spin system. *Phys. Rev. A* **99**, 559–565.
31. McConnell, J. (1987) *The Theory of Nuclear Magnetic Relaxation in Liquids*, Cambridge University Press, New York.
32. Kaplan, J. I. and Frankel, G. (1980) *NMR of Chemically Exchanging Systems*, Academic, New York.
33. Krishnan, V. V., Murali, N., and Kumar, A. (1988) A diffusion equation approach to spin diffusion in biomolecules. *J. Magn. Reson.* **84**, 255–267.
34. Krishnan, V. V., Hegde, U., and Kumar, A. (1991) Spin diffusion in biomolecules: effect of higher order terms in transient NOE experiments. *J. Magn. Reson.* **94**, 605–611.
35. Landy, S. B. and Rao, B. D. N. (1989) Dynamical NOE in multiple-spin systems undergoing chemical exchange. *J. Magn. Reson.* **81**, 371–377.
36. Zheng, J. and Post, C. B. (1993) Protein indirect relaxation effects in exchange-transferred Noesy by a rate-matrix analysis. *J. Magn. Reson. Ser. B* **101**, 262–270.
37. Zabell, A. P. R. and Post, C. B. (2002) Intermolecular relaxation has little effect on intra-peptide exchange-transferred NOE intensities. *J. Biomol. NMR* **22**, 303–315.
38. Kumar, A., Ernst, R. R., and Wüthrich, K. (1980) A two-dimensional nuclear Overhauser enhancement (2D NOE) experiment for the elucidation of complete proton-proton cross-relaxation networks in biological macromolecules. *Biochem. Biophys. Res. Commun.* **95**, 1–6.
39. Shaka, A. J., Lee, C. J., and Pines, A. (1998) Iterative schemes for bilinear operators: application to spin decoupling. *J. Magn. Reson.* **77**, 274–293.
40. Scherf, T. and Anglister, J. (1993) A T1ρ filtered two-dimensional transferred NOE spectrum for studying antibody interactions with peptide antigens. *Biophys. J.* **64**, 754–761.
41. Hwang, T. L. and Shaka, A. J. (1995) Water suppression that works—excitation sculpting using arbitrary waveforms and pulsed field gradients. *J. Magn. Reson. Ser. A* **112**, 275–279.
42. Smallcombe, S. H., Patt, S. L., and Keifer, P. A. (1995) Wet solvent suppression and its applications to Lc Nmr and high-resolution Nmr spectroscopy. *J. Magn. Reson. Ser. A* **117**, 295–303.
43. Ogg, R. J., Kingsley, R. B., and Taylor, J. S. (1994) Wet, a T1- and B1-insensitive water-suppression method for in vivo localized H-1 Nmr spectroscopy. *J. Magn. Reson. Ser. B*, **104**, 1–10.

44. Sklenar, V., Piotto, M., Leppik, R., and Saudek, V. (1993) Gradient-tailored water suppression for  $^1\text{H}/^{15}\text{N}$  HSQC experiments optimized to retain full sensitivity. *J. Magn. Reson. A* **102**, 241–245.
45. Liu, M. L., Mao, X. A., Ye, C. H., Huang, H., Nicholson, J. K., and Lindon, J. C. (1998) Improved watergate pulse sequences for solvent suppression in Nmr spectroscopy. *J. Magn. Reson.* **132**, 125–129.
46. Noggle, J. H. and Schirmer, R. E. (1971) *The Nuclear Overhauser Effect: Chemical Applications*, Academic, New York.
47. Knapp, M., Segelke, B., and Rupp, B. R. (1998) The 1.61 Å structure of the tetanus toxin ganglioside binding region solved by MAD and MIR phase combination. *Am. Crystallogr. Assoc.* **25**, 90.
48. Umland, T. C., Wingert, L. M., Swaminathan, S., Furey, W. F., Schmidt, J. J., and Sax, M. (1997) Structure of the receptor binding fragment HC of tetanus neurotoxin. *Nat. Struct. Biol.* **4**, 788–792.
49. Ewing, T. J., Makino, S., Skillman, A. G., and Kuntz, I. D. (2001) DOCK 4.0: search strategies for automated molecular docking of flexible molecule databases. *J. Comput. Aided Mol. Des.* **15**, 411–428.
50. DesJarlais, R. L., Sheridan, R. P., Seibel, G. L., Dixon, J. S., Kuntz, I. D., and Venkataraghavan, R. (1988) Using shape complementarity as an initial screen in designing ligands for a receptor binding site of known three-dimensional structure. *J. Med. Chem.* **31**, 722–729.
51. Kuntz, I. D., Blaney, J. M., Oatley, S. J., Langridge, R., and Ferrin, T. E. (1982) A geometric approach to macromolecule-ligand interactions. *J. Mol. Biol.* **161**, 269–288.
52. Meng, E. C., Shoichet, B. K., and Kuntz, I. D. (1992) Automated docking with grid-based energy evaluation. *J. Computat. Chem.* **13**, 505–524.
53. Pramanik, B. N., Bartner, P. L., Mirza, U. A., Liu, Y. H., and Ganguly, A. K. (1998) Electrospray ionization mass spectrometry for the study of non-covalent complexes: an emerging technology. *J. Mass Spectrom.* **33**, 911–920.
54. Gao, J., Cheng, X., and Chen, R., et al. (1996) Screening derivatized peptide libraries for tight binding inhibitors to carbonic anhydrase II by electrospray ionization-mass spectrometry. *J. Med. Chem.* **39**, 1949–1955.
55. Eswaramoorthy, S., Kumaran, D., and Swaminathan, S. (2001) Crystallographic evidence for doxorubicin binding to the receptor-binding site in Clostridium botulinum neurotoxin B. *Acta Crystallogr. D Biol. Crystallogr.* **57**, 1743–1746.
56. Swaminathan, S. and Eswaramoorthy, S. (2000) Structural analysis of the catalytic and binding domains of Clostridium botulinum neurotoxin type B. *Nat. Struct. Biol.* **7**, 693–699.
57. Lightstone, F. C., Prieto, M. C., Singh, A. K., Piqueras, M. C., Whittall, R. M., Knapp, M. S., Balhorn, R., and Roe, D. C. (2000) Identification of novel small molecule ligands that bind to tetanus toxin. *Chem. Res. Toxicol.* **13**, 356–362.
58. Emsley, P., Fotinou, C., Black, I., Fairweather, N. F., Charles, I. G., Watts, C., Hewitt, E., and Isaacs, N. W. (2000) The structures of the H(C) fragment of tetanus toxin with carbohydrate subunit complexes provide insight into ganglioside binding. *J. Biol. Chem.* **275**, 8889–8894.

59. Ma, B., Shatsky, M., Wolfson, H. J., and Nussinov, R. (2002) Multiple diverse ligands binding at a single protein site: a matter of pre-existing populations. *Protein Sci.* **11**, 184–197.
60. Kraulis, P. J., Domaille, P. J., Campbellburk, S. L., Vanaken, T., and Laue, E. D. (1994) Solution structure and dynamics of *ras* P21-center-dot-GDP determined by heteronuclear 3-dimensional and 4-dimensional NMR spectroscopy. *Biochemistry* **33**, 3515–3531.
61. Merritt, E. A. and Bacon, D. J. (1997) Raster3D photorealistic molecular graphics. *Methods Enzymol.* **277**, 505–524.





## Studying 3D Subdomains of Proteins at the Nanometer Scale Using Fluorescence Spectroscopy

Pierre M. Viallet and Tuan Vo-Dinh

### Summary

Databases devoted to the crystal structure of proteins have dramatically increased in size during the last two decades. Moreover, X-ray and NMR technology studies have shown that proteins belonging to the same family generally share the same global 3D architecture. These results suggest that the need for experimental determination of protein structure will be reduced to those that are suspected to have sufficiently novel structures. Furthermore, NMR and other techniques have demonstrated that a protein in solution experiences constant random thermal motions that occur over large time scales, ranging from picoseconds to seconds and perhaps hours. Such changes may have important functional consequences, but identifying which changes are functionally relevant remains a difficult task even if this problem has been addressed both with experimental and computational methods. For that specific purpose, there is a need for methods allowing a fast and accurate monitoring of conformation changes (that occur at specific subdomains of proteins. Fluorescence resonance energy transfer (FRET) is a suitable tool for monitoring conformational changes at the nanoscale level. This chapter describes the various FRET methods that are used for monitoring the 3D sub-domain conformation of proteins in solution, in single living cells and at the single molecular level.

**Key Words:** Fluorescence spectroscopy; fluorescence resonance energy transfer; fluorescence lifetime imaging measurements; lifetime measurements; energy transfer; near-field scanning optical microscope; protein subdomain.

### 1. Introduction

Databases devoted to protein structures have dramatically increased in size during the last decade. Besides X-ray studies that have depicted the three-dimensional (3D) crystal structure of larger and larger molecules with amazing accuracy, nuclear magnetic resonance (NMR) and other techniques are used to monitor protein conformational changes in solution. A protein in solution is now considered as experiencing, within a stable equilibrium structure, constant random thermal motions that occur over time scales ranging from pico-

From: *Methods in Molecular Biology*, vol. 300:  
*Protein Nanotechnology, Protocols, Instrumentation, and Applications*  
Edited by: T. Vo-Dinh © Humana Press Inc., Totowa, NJ

seconds to seconds, and even hours. NMR methods are very attractive, for they can provide comprehensive information on movements occurring at different sites throughout the macromolecule. For instance,  $^{15}\text{N}$ -NMR relaxation studies indicate that the movements of the backbone of a stable protein are generally restricted to the picosecond to nanosecond time scale (**1**). By contrast, side-chain dynamics, as revealed by  $^{13}\text{C}$  or deuterium NMR relaxation methods, have indicated that protein hydrophobic cores are heterogeneously dynamic (**2–4**). Besides studies mainly devoted to folding and unfolding processes in proteins, recent articles deal with conformational changes related to protein functions (*see refs. 5–7 and references therein*). Both random thermal motions and the average conformation may be strongly modified when a protein experiences ligand or substrate binding, docking to another macromolecule, or phosphorylation. Such changes may have important functional consequences. Nevertheless, identifying which changes are functionally relevant is a difficult task. An even more fascinating challenge is to monitor structural rearrangement that might occur when a substrate is added to an enzyme (**7–10**).

Monitoring conformational changes may require the use of several techniques of investigation (**11**). Sometimes in association with NMR studies, differential scanning calorimetry, far-ultraviolet (UV) circular dichroism (CD), labeling with fluorescent markers, and site-directed spin labeling have been extensively used (**11–14**). The last two methods provide information on conformational changes only around specific amino acids, but this could be an advantage when monitoring 3D changes associated with enzyme activity. Furthermore, it is known that proteins belonging to the same family generally share the same global 3D architecture. It is thought that progress in protein structure modeling will reduce the need for experimental determination of the whole 3D structure of proteins, because structural description of all proteins in a family is possible when the structure of a single member is known (**15**). As a consequence, the interest in methods allowing easy monitoring of conformational change occurring at specific locations of the proteins must be reconsidered, especially when they can be used *in vivo*. One may argue that both fluorescence and spin labeling require slight modifications of the studied protein, but then this is also often the case for NMR studies.

Among the different techniques using fluorescence, fluorescence resonance energy transfer (FRET) is the best adapted for conformational change monitoring, although other methods have also been used. Of course, because of the high sensitivity of the fluorescence quantum yield to the microenvironment of the fluorescent molecule, other techniques are also available. Changes in fluorescence intensity or fluorescence lifetime have been used for monitoring changes in the polarity, hydrophobicity, and acidity of the environment of tryptophan(s) or fluorescent tags linked to proteins. For instance, the pH sensitivity of the fluorescence intensity of dansyl has been used for monitoring a

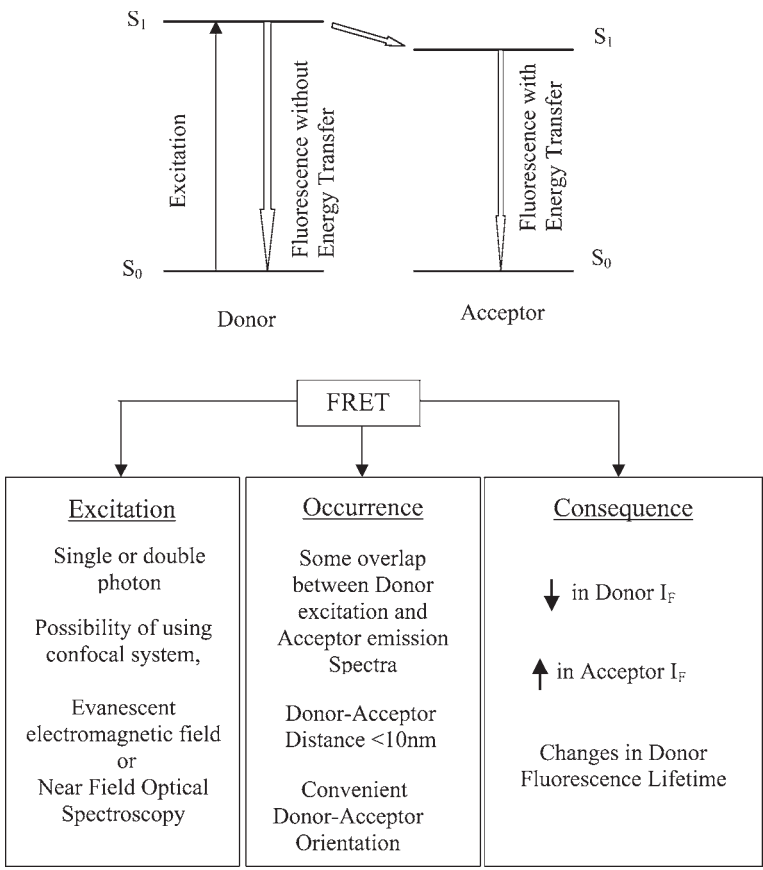


Fig. 1. Principle of FRET.  $I_F$ , fluorescence intensity.

proton transfer between a dansyl molecule bound to a protein and one of its endogenous amino acids (lysine) (11). However, FRET has the unique property of occurring only when the distance between the two involved molecules is <10 nm. Only FRET allows quantification of subtle conformational changes below the light diffraction limits. Furthermore, such a molecular ruler at the nanoscale can be easily used in living cells.

2. Methods

The basic fundamentals of FRET have been known for many years (16–18). FRET consists of a quantum mechanical process resulting in radiationless energy transfer from the first excited state of a fluorescent molecule, called the donor (D), to the first excited state of another fluorescent molecule, called the acceptor (A). As a consequence, under conditions that are given subsequently, excitation of the donor may induce the fluorescence of the acceptor (Fig. 1).

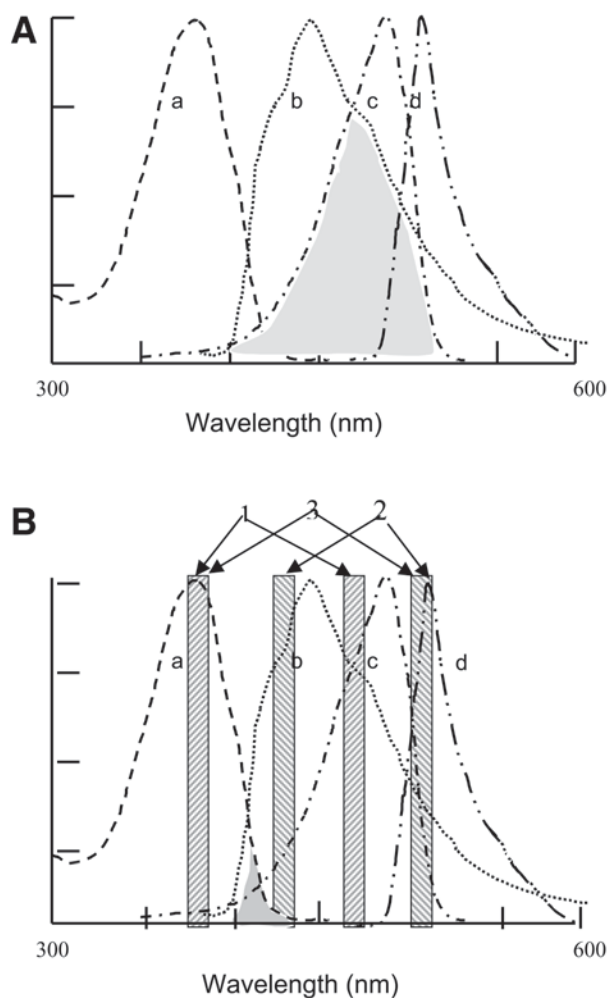


Fig. 2. FRET. (A) Example of overlap spectral region (in gray) required for FRET: a, donor absorption spectrum; b, acceptor absorption spectrum; c, donor emission spectrum; d, acceptor emission spectrum. (B) Minimal filter set required for FRET monitoring: 1, recording of donor fluorescence intensity; 2, recording of acceptor fluorescence intensity without FRET; 3, recording of FRET intensity.

For FRET to occur, the two fluorophores must be conveniently selected: the donor emission spectrum must significantly overlap the absorption spectrum of the acceptor, and the reabsorption of the fluorescence emitted by the donor must be minimal to avoid tedious data corrections (**Figs. 1,2**). Furthermore, FRET intensity is sensitive to the relative orientation of the transition dipoles

of the fluorophores. Then, because FRET has to compete with other deactivation processes of the donor excited state, the donor should have a high fluorescence quantum yield. Finally, the distance between D and A must be  $<10$  nm, for FRET efficiency decreases with the sixth power of the distance between them. It is just this last property that makes FRET an invaluable tool for probing protein conformation and protein conformational changes. Moreover, both D and A must be insensitive to photobleaching when FRET is used for probing protein conformational changes, for that goal requires successive periods of irradiation.

Application of FRET techniques to biomedical research started quite recently (19,20). As a matter of fact, interpretation of FRET data on biological events is a difficult task for the following reasons. Observation is generally carried out on a population of biological molecules that are known to experience different 3D conformations even when sharing the same free-energy level. Thus, even if the time necessary for data collection is “ideally short,” data will reflect the distribution of individual molecules in the same energy level, i.e., the relative weight of their different potential 3D conformations. Furthermore, technical limitations do not allow the collection of significant amounts of data within periods of time short enough compared to intracellular movements. Such a situation is common to every optical method of collecting information, making it difficult to assign an experimental value to a precise conformation. For these reasons, FRET is often used as an “all or nothing” method, separating the studied molecules into two subpopulations, that in which FRET occurs ( $D-A < 10$  nm) and that in which FRET does not ( $D-A > 10$  nm).

As indicated before, FRET can be used for experiments in solution with a conventional spectrofluorometer or under the microscope for studying biomolecules in living cells. In the latter case, owing to the concentration of light at the objective, the risk of photobleaching is highly increased. Thus, besides the use of direct single-photon irradiation, other methods have been developed. Multiphoton microscopy takes advantage of the existence of the “optical window,” the wavelength domain between 700 and 1100 nm where the biological material is practically transparent to radiation (21,22). The simultaneous absorption of two photons at 800 nm may allow reaching the first excited state, since it is usually done with a single 400-nm photon. This occurs when two coherent photons “reach” the fluorescent target at the same time and requires the use of a high-energy, high-frequency ( $<100$  fs) pulsed laser. The efficiency of two-photon excitation follows a power-squared relation and can be achieved only inside a tiny volume of the sample at a time. The whole cell is then not damaged by irradiation, and the risk of photobleaching is restricted to the tiny volume where the two photons collide. Nevertheless, some risk of photobleaching may remain for some fluorescent probes (23).

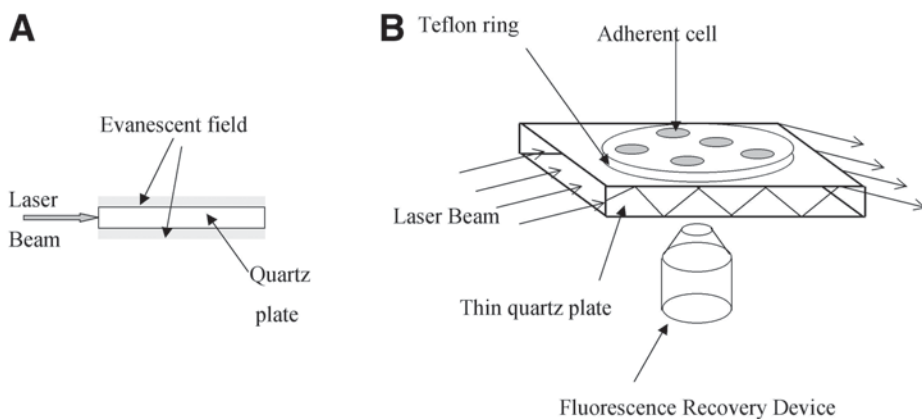


Fig. 3. Total internal reflection fluorescence microscopy. **(A)** Irradiation through the quartz plate used to support cells generates an evanescent field in thin volumes located on both sides of the plate. **(B)** Illustration of a device allowing grabbing of data from many cells at a time.

Because the source of potential photobleaching is the concentration of the excitation light through the objective, it has been suggested that cells be irradiated in another way. When cells are grown on a thin quartz plate, this plate can be used as a laser light guide inducing an evanescent electromagnetic field in the 0- to 100-nm range above the plate surface, a distance long enough to excite preferentially molecules inside the living cells (24). Moreover, this elegant technique allows the simultaneous collection of data on many individual cells (**Fig. 3**).

As indicated in **Fig. 1**, FRET affects the fluorescence intensity of both D and A and changes the lifetime of D. Methods that allow monitoring either fluorescence intensities or lifetime measurements can be used in quantification. When protein conformational changes are studied in solution, fluorescence spectroscopy can be used with conventional equipment (**Fig. 4**). The fluorescence spectrum resulting from a partial energy transfer will be a combination of the respective fluorescence spectra of the donor and the acceptor. The relative weight of these spectra will depend on the respective quantum yields of D and A for the wavelength used for excitation. The relative contribution of these spectra can be easily obtained even in the presence of other fluorophores or relatively noisy signals, using previously published methods of spectra resolution (25). By contrast, experiments performed on living cells require the use of excitation and emission filter sets (**Fig. 5**) (26). The use of three sets of filters is generally necessary, which is time-consuming (27). A simplification can be obtained by using fluorophores with minimal overlap of their respective excitation spectra and selecting excitation wavelengths out of this overlap

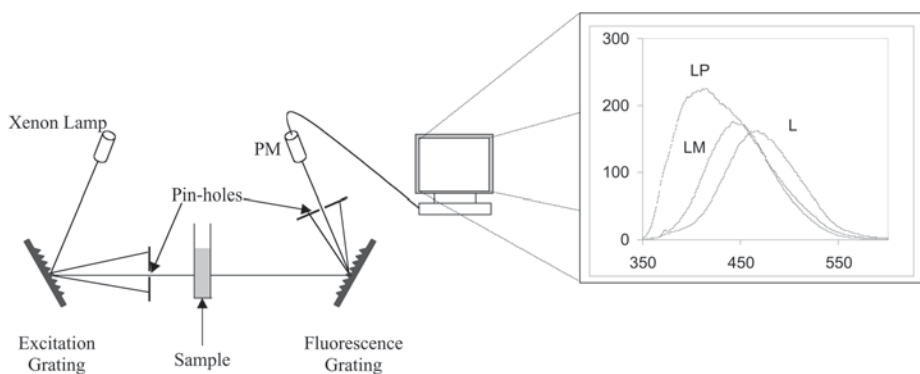


Fig. 4. Schematic drawing of a conventional spectrofluorometer (PM) photomultiplier. Respective fluorescence spectra of protein-bound (LP), cation-bound (LM), and free (L) Mag-into 1 are shown.

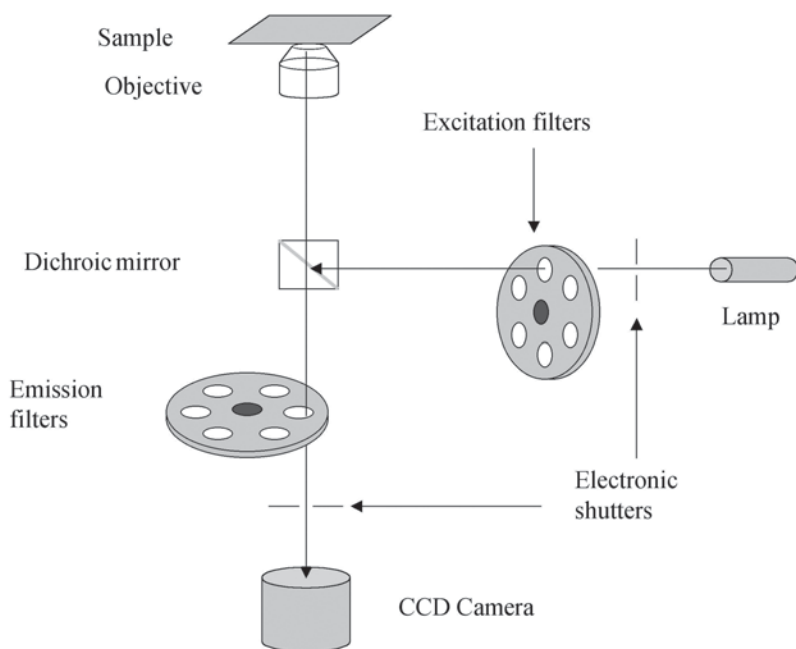


Fig. 5. Schematic drawing (not to scale) of a FRET multiwavelength fluorescence imaging microscope. The electronic shutters are necessary to minimize the cell irradiation resulting from illumination and data recording at different wavelengths. CCD, charge-coupled device.



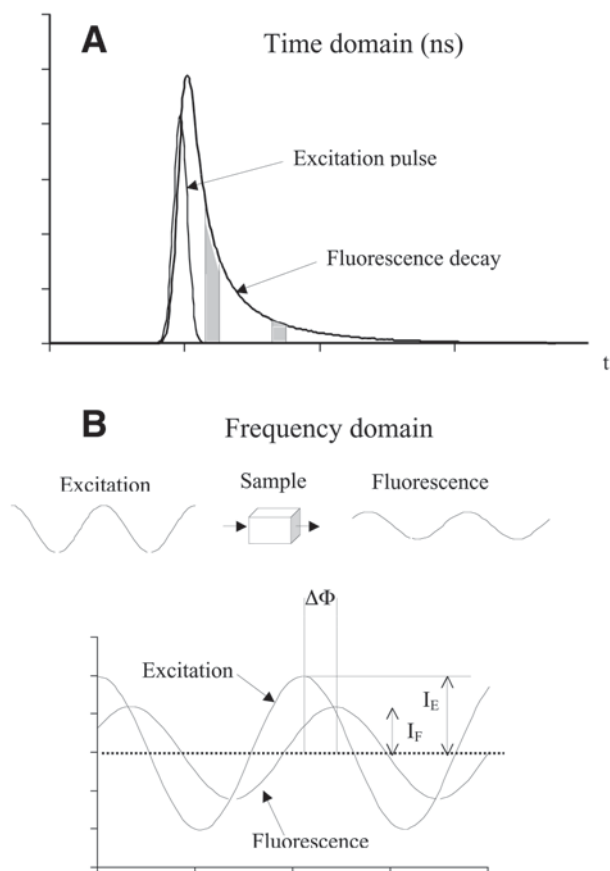


Fig. 6. Fluorescence lifetime imaging. **(A)** In the time domain method, a fast-gated camera is used to repeatedly record during very short periods of time (in gray) data from the multiexponential decay of the fluorescence (bold curve) excited by a very short excitation pulse (light curve). **(B)** In the frequency domain approach, measurable parameters are the phase shift  $\Delta\Phi$  and the relative reduction of amplitude of the fluorescence signal ( $I_F$ ) compared with that of the excitation pulse ( $I_E$ ).

range. As shown in **Fig. 2B**, the first set of filters will allow the monitoring of whole changes of the donor and acceptor fluorescence, respectively, and the second set will measure changes in the acceptor fluorescence resulting only from changes in the chemical microenvironment (without FRET). A combination of these data will allow monitoring of changes in FRET specifically.

Time life measurements can also be used to quantify FRET either in protein solution or in living cells. The fluorescence lifetime is independent of the concentration of the fluorophore, which is an important advantage because the

probe concentration is expected to vary inside a living cell. On the contrary, the lifetime strongly depends on molecular interactions between the probe and its chemical environment. Energy transfer itself is expected to influence the lifetime of the donor, for it competes with other deactivation processes of the donor excited state. Thus, a 3D conformational change inducing a change in energy transfer will affect in a complex way the donor lifetime. Nevertheless, fluorescence lifetime imaging has recently been extensively used for FRET monitoring (28–30). Two fundamentally different approaches have been used. In the time domain approach, the fluorescence lifetime ( $\tau_f$ ) is measured by excitation of the sample with a short pulse of light, much shorter than the fluorescence lifetime (**Fig. 6**). Such a method requires a camera capable of fast gating, allowing the collection of the fluorescence signal during precise short periods of time (31–33). The use of the time domain approach is thus limited by the difficulty of gating a camera fast enough to collect information during the lifetime of a fluorescence decay (**Fig. 6A**).

In the frequency domain approach, the sample is excited with sinusoidally modulated light. The optical angular frequency of the light is reciprocal to the fluorescence lifetime to be measured. As a result, the emitted fluorescence is sinusoidally modulated at the same frequency but with a reduction in the modulation depth,  $M$ , and shifted in phase,  $\Delta\Phi$  (**Fig. 6B**). This technique requires a detector capable of high-frequency modulation. Parameters related to the respective intensities of the excitation pulse and the fluorescence signal, and to the phase shift  $\Delta\phi$ , are used to calculate two other parameters, the phase lifetime,  $\tau_\phi$ , and the modulation lifetime,  $\tau_M$ . These last lifetimes are equal only when the sample contains only one fluorescent species, which is never the case inside a cell, owing to molecular interactions. When more than one fluorescent species is present, the phase and modulation lifetimes differ. In such a situation, the true lifetime composition can be obtained by measuring the phase and modulation lifetimes over a range of frequencies and fitting the results to a set of dispersion relationships. Fluorescence lifetime imaging measurements (FLIMs) may become more usual in the near future owing to several advantages associated with spectral discrimination. Simultaneous readout of data and the requirement of only one dichroic and long-pass emission filter result in the use of a lower light dose and reduce the risk of photochemical damage to the cells. Recent articles have reported on progress in numerical analysis of data and on the feasibility of multiwavelength frequency domain FLIM (34–38).

### 3. Results

Among amino acids, only tryptophan experiences a significant fluorescence, and this fluorescence requires excitation wavelengths that cannot go through most microscope objectives. Thus, proteins must be previously tagged with

fluorescent chemicals to make it possible to study their conformational changes through fluorescence techniques. Depending on the protein and the actual goal, different tagging processes have been used. Examples are discussed next in some detail.

### **3.1. Noncovalent Binding**

It is well known that some chemicals have a preferential location inside specific pockets of the 3D protein structures. When fluorescent, they can be used for reporting conformational changes in and around these specific subdomains, for most of the fluorescence properties are sensitive to changes in the microchemical environment. That is specifically the case when the preferential location results from a noncovalent binding to a specific amino acid. Then, changes in protein conformation may influence fluorescent properties through either changes in the microchemical environment, a change in binding conditions, or even both at the same time. Sometimes, the binding of the exogenous fluorophore may induce some energy transfer from a neighboring tryptophan, which makes it possible to probe the interaction through FRET techniques.

Some years ago, it was demonstrated that Mag-indo 1, a fluorescent chemical initially used for probing intracellular calcium concentration, was able to interact with some proteins through a noncovalent binding with some histidine residue(s). Such a binding induces a specific shift in the fluorescence spectrum of Mag-indo 1, making it possible to quantify this binding using specific data treatments (**Fig. 4**) (25,26,39). The interaction of Mag-indo 1 with turkey egg white lysozyme (Tlys) in the absence of calcium has been studied using the synchronous fluorescence technique (40,41). This technique, in which both excitation and emission wavelengths are scanned simultaneously with a constant  $\delta\lambda$ , compresses the spectral information to a relatively narrow domain of wavelengths. This generally reduces the spectral overlap from various fluorescent components. In this study, it allows the simultaneous recording of synchronous fluorescence spectra both of free Mag-indo 1 and protein-bound Mag-indo 1 and of the protein itself. Moreover, a potential energy transfer from one of the protein tryptophans cannot affect the fluorescence intensity of the synchronous fluorescence spectrum of the protein-bound Mag-indo 1. As a consequence, the value of the dissociation constant characteristic of the interaction can be easily obtained. On the contrary, changes in the intensity of the protein fluorescence spectrum may reflect both a change in the chemical microenvironment of a tryptophan close to the interaction site and some energy transfer from this tryptophan to the protein-bound Mag-indo 1. The energy transfer resulting from the interaction can be monitored through changes in the intensity of the Mag-indo 1 excitation spectrum when excited in the range of

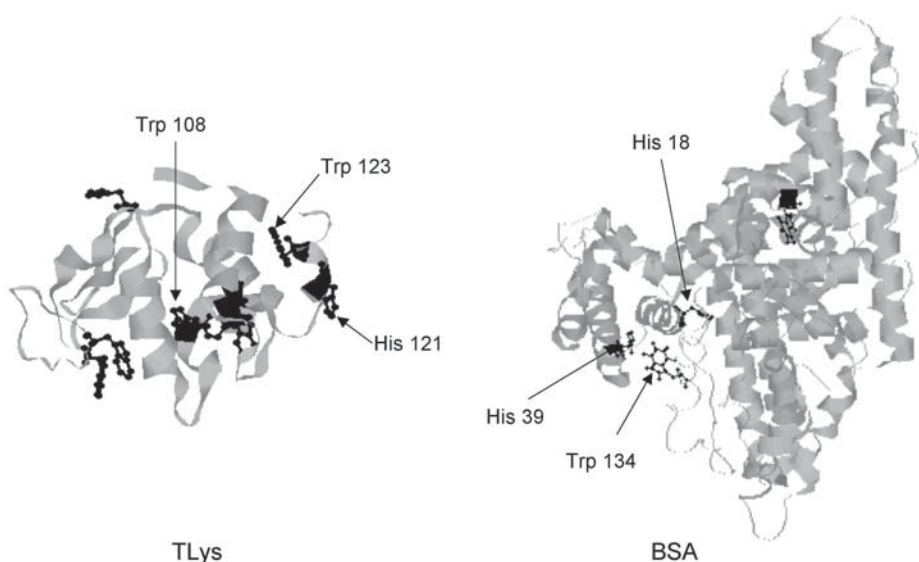


Fig. 7. Respective 3D conformations of TLys (**left**) and BSA (**right**). Chemical structures of tryptophan and histidine residues appears as balls and sticks.

wavelengths of tryptophan absorption (42). Furthermore, the amino acid sequence of TLys has only two histidine residues, and only one of them, His 121, is located in the vicinity of one tryptophan in the stable 3D conformation. Thus, the existence of some energy transfer allows easy determination of the protein subdomain accessible through this interaction (**Fig. 7**).

Fluorescence techniques were also used to monitor conformational changes resulting from the binding of fluorescent substrates (4-methylumbelliferyl chitobiosides or chitotriosides) to turkey or hen egg white lysozyme. In both cases, a quenching of the protein fluorescence was observed when the substrates were engulfed in the enzyme cleft, but no energy transfer was evidenced. This finding suggests that the quenching results only from a change in the chemical environment of one tryptophan, probably Trp 108, associated with the presence of the substrate inside the cleft (unpublished results).

Interactions of bovine serum albumin (BSA) and human serum albumin (HSA) with Mag-indo 1 have also been studied (42). These homologous proteins present two hydrophobic pockets but differ in their number of tryptophan residues: BSA has two tryptophans, one in each hydrophobic pocket, but HSA has only one, lacking the Trp 134 present in BSA. It was demonstrated that both proteins interact with Mag-indo 1 but that interaction induces a quenching of the protein fluorescence only for BSA. This quenching was associated with an energy transfer from BSA to Mag-indo 1 that parallels the protein-probe

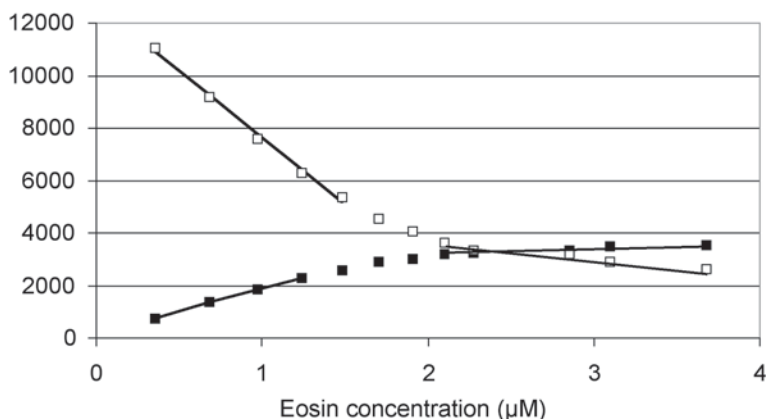


Fig. 8. Influence of increasing eosin concentrations on fluorescence intensity of BSA tryptophans (□) and on fluorescence intensity of BSA-bound eosin (■). Fluorescence intensities on the y-axis are in arbitrary units. BSA concentration was 1.8  $\mu$ M.

binding. These results suggest that interaction takes place in the vicinity of Trp 134 and can be used for monitoring unfolding and refolding processes of this BSA subdomain in the presence of guanidine hydrochloride (43).

Recently, interactions of eosin with, respectively, BSA and HSA have been reconsidered from the conformational change point of view (J. M. Salmon and L. Bilia, personal communication 2001). The interaction of eosin with these proteins induces both an increase in intensity and a red shift in the eosin fluorescence spectrum that allows quantifying the interaction. The stoichiometry of the interaction is 1/1 for HSA and 1/2 for BSA. Moreover, this interaction induces a quenching of the fluorescence of both tryptophans of BSA (Fig. 8). Comparison with results obtained with HSA confirmed that the eosin interaction occurs with amino acid(s) located in the two hydrophobic pockets of BSA.

### 3.2. Tagging Protein With Variants of Green Fluorescent Protein

Green fluorescent protein (GFP) is a spontaneously fluorescent polypeptide of 27 kDa (238 amino acid residues) from the jellyfish *Aequorea victoria* that absorbs UV-blue light and emits in the green region of the spectrum (44). Its structure and potential uses for studying living cells have recently been reviewed in detail (45–50). The GFP chromophore results from a cyclization of three adjacent amino acids (S65, Y66, and G67) and the subsequent 1,2-dehydrogenation of the tyrosine (45–50). Although the chromophore by itself is able to absorb light, its fluorescent properties are associated with the presence of an 11-stranded  $\beta$ -barrel. GFP has been expressed in both bacteria and eukaryotic cells and has been produced by in vitro translation of the GFP mRNA. More-

over, GFP retains its fluorescence when fused to heterologous proteins on the N- and C-terminals, and this binding generally does not affect the functionality of the tagged protein (45,46,49). This leads the way for the use of GFP as an intracellular reporter even if the fluorescence intensity of the native GFP is not bright enough for most intracellular applications. Variants have been engineered that have different excitation and/or emission spectra that better match available light sources (46,48–50). The use of brighter mutants was also found necessary in the case of low expression levels in specific cellular microenvironments (46–50). Some of them, such as the cyan (ECFP) and yellow (EYFP) fluorescent protein, have been specifically engineered to match the FRET criteria.

Although the use of GFP and GFP-variants chimera have given amazing information on protein synthesis, translocation, and intracellular localization, their structure limits their use for monitoring conformational changes in proteins. Because of their own size, GFP variants may modify the kinetics of conformational changes when used for tagging small proteins. Furthermore, these variants are fused to the N- and/or C-terminals of the tagged protein, which is generally not the best location to be sensitive to conformational changes resulting from binding to other proteins or enzyme substrates. Thanks to recent progress in structural genomics, it has become easier to determine which kind of protein biological activities may change the distance between the N- and C-terminal tags above or below 10 nm (15).

Actually, GFP chimeras have demonstrated their potential for functional studies of proteins. This research field has been well covered by recent reviews (see refs. 28, 46, 47, 51, 52, and references therein). Intramolecular FRET was used to monitor protein activity especially for detecting UV-induced apoptosis and testing novel apoptosis inducers or inhibitors (53–57). All these studies were carried out with caspase fluorescent substrates that are labeled to show FRET when the substrate is intact. Caspase activity disrupts the substrate, inducing the disappearance of FRET. Unfortunately, this elegant method for monitoring enzyme activity is unable to give any information about potential associated conformational changes in the protein.

Phosphorylation is an efficient posttranscriptional way of modifying proteins to modulate protein functions. Different methods have been tested for monitoring phosphorylation through FRET methods. In special cases, phosphorylation induces significant conformational changes that can be evidenced by FRET methods if the peptide can be tagged at both ends by GFP mutants. In this scheme, chimeric reporters have been constructed based on a double-tagged appropriate substrate peptide sequence for a given protein kinase (58,59). In this approach, a flexible linker sequence and a phosphorylation recognition domain that binds the phosphorylated substrate domain were included

between two GFP variants. Thus, phosphorylation induces a huge conformational change that will change the distance and/or relative orientation between the GFP mutants. These changes will change the FRET conditions between the GFP mutants. In principle, this approach can be extended to any kind of kinases and the specific reporters can be expressed in both bacteria and mammalian cells (60,61). Nevertheless, although allowing efficient monitoring of the kinases' activity, this method does not give any information on the conformational changes experienced by kinases during the phosphorylation or dephosphorylation processes.

Intermolecular FRET techniques have also been used for monitoring an interaction between a nuclear receptor and its specific activator that is required for transcription of transiently transfected and chromosomally integrated reporter genes (62). High-resolution FRET microscopy was used for the study of the potential role of "lipid rafts" in the interaction between cholera toxin  $\beta$ -subunits and GPI-anchored proteins in the plasma membrane of HeLa cells (63). The interaction of epidermal growth factor receptor and Grb2 in living cells has also been monitored using FRET imaging (64). In addition, in a study by Janetopoulos et al. (65), receptor-mediated activation of heterotrimeric G-proteins was visualized in living cells by monitoring FRET between  $\alpha$ - and  $\beta$ -subunits fused to cyan and yellow fluorescent proteins (65). Their study deserves special mention because the protocol used allowed the determination of both the kinetics and the sites of G-protein activation in cells and tissues. For that purpose, the subunits  $G\alpha_2$  and  $G\beta$  of *Dictyostelium discoideum* were respectively tagged with cyan and yellow fluorescent proteins. FRET intensity was used to monitor changes in the G-protein concentration, reporting both protein activity and associated conformational changes.

### 3.3. Other Types of Covalent Binding

In 1995 it was demonstrated that lysine<sub>75</sub> is the most reactive lysine residue in calmodulin and is therefore labeled extensively and selectively when calmodulin is treated with amine-reactive fluorophores (66–69). This labeling process was used to build up a fluorescent protein usable for visualizing the binding of  $Ca^{2+}$  to calmodulin, monitoring  $Ca^{2+}$  activation-dependent and -independent localization of calmodulin, and investigating the role of calmodulin in the control of mitotic transition (66,67,70). Moreover, this binding was found to be insensitive to enzyme digestion of the protein with chymotrypsin and trypsin, allowing a quite easy identification of the binding site through conventional methods of peptide characterization. Another potentially interesting method of chemically tagging protein with fluorescent markers is to use available cysteine residues that are generally limited in number in the protein sequence compared to the frequency of other amino acids.



The potential use of these chemical bindings will be enhanced if they are performed in the frame of a close scientific cooperation among scientists involved in the determination of the 3D structure of proteins and enzyme-substrate complexes. Scientists interested in the chemical tagging of proteins with small fluorescent molecules will take advantage of the recently published 3D structures for identification of the best candidate(s) among the amino acid sequence (71). When the fluorescent analog(s) has been synthesized, scientists may benefit from the powerful crystallographic, X-ray, and NMR techniques to check if the tag has induced some unwanted change in the 3D conformation.

Another exciting approach has been developed recently that consists of a chemical synthesis of a specific domain of a protein. This method, which takes full advantage of the 3D conformation protein databanks and progress in Proteomic, has been used for studying the unfolding of the peripheral subunit-binding domain of the dihydrolipoamide succinyltransferase (the E2 subunit) from the 2-oxoglutarate dehydrogenase multienzyme complex of *Escherichia coli* (11). The synthetic protein was tagged with a naphthyl-alanine at the NH<sub>2</sub> terminus and with a dansylated lysine at the COOH terminus to investigate the end-to-end distance variation during unfolding through FRET techniques. Differential scanning calorimetry and far-UV CD were also used in this study.

Compared with tagging through genomic protocols, chemical tagging may present some lack of specificity. Amino acids usable for chemical binding are generally not unique in the amino acid sequence of a protein. Thus, contrary to what happened with calmodulin, it can be expected that chemical tagging will result in different tagged proteins, and potentially multitagged proteins. Although this may require further purification to separate the tagged proteins, that may prove to be useful for probing conformational changes in different subdomains. In any case, chemical tagging seems an alternative to GFP tagging, allowing the use of far smaller fluorescent markers. It may provide researchers with fluorescent analogs that will match all the requirements for studying protein conformational changes in solution. These modified proteins should also be efficient for studying the efficacy of electroporation or any other process of assisted endocytosis (72–77).

#### 4. What Next?

Whatever valuable information FRET methods yield on protein activity and conformational changes, this information is obtained from data that are generally collected from a molecular population. Because it is generally admitted that many 3D conformations may correspond to the same level of free energy, such data may as well reflect the heterogeneity of the molecular population or characterize a homogeneous intermediate conformation. For that reason, a quest for methods allowing the visualization of the conformational change of a

single molecule appears necessary, especially for monitoring intermediate conformations occurring during protein activity. Although the earlier optical methods were devoted to monitoring diffusion of macromolecules, recent developments are now focused on what is called “dynamic structural biology.” In such a research field, methods allowing detection of changes of distance and/or orientation between two precise sites located on a macromolecule, or two different macromolecules, are required. Two optical methods, FRET and fluorescence polarization anisotropy (FPA), have been recently adapted for single-molecule detection (78). Whereas FRET efficiency depends on both the relative distance and the orientation of donor and acceptor, FPA efficiency depends only on changes in the orientation of one fluorophore. Thus, optimal experiments will consist of using both techniques at a time, a situation that is rarely met. On one hand, FPA requires only one fluorescent tag per macromolecule, which limits investigation of chemical synthesis. On the other hand, FPA consists of comparing the intensity of fluorescence polarized in the same direction as that of the excitation light ( $I_{par}$ ) with that of the fluorescence polarized in a perpendicular direction ( $I_{perp}$ ). Such a comparison may be difficult to quantify when the signal intensities are low and in the presence of a large background signal. However, when a fluorophore is either rigidly attached or tethered to a macromolecule, changes in FPA can be interpreted in terms of angular movements of that macromolecule, but bulk averaging may mask important information on dynamic changes in orientation.

Recording the fluorescence issued from a single molecule is not an easy task owing to the low-intensity signal. First of all, it is necessary to be sure that the recorded signal really comes from a unique molecule, which is generally achieved by using ultralow fluorophore concentrations and confocal microscopy. As an example, concentrations of fluorescent molecules are usually in the range of 10 to 30 pmol. Under these conditions, in a diffraction-limited excitation volume of about 0.5 fL, the probability of single-molecule occupancy is about 0.01, compared with the probability of simultaneous double-molecule occupancy of  $5 \times 10^{-5}$ . Thus, the signal intensity is generally far lower than that of the background, especially when measurements are performed with living cells, and must be extracted from this background. This can be achieved with single-photon-counting avalanche photodiodes, allowing detection of single-molecule photon bursts with integration times compatible with the rate of most biological events (<1 ms).

Techniques of single-pair FRET (spFRET) and single-molecule fluorescence polarization anisotropy (smFPA) have been developed for observing the conformational fluctuations and catalytic activities of enzymes at single-molecule resolution. They were first used for studying conformational changes and interactions of Staphylococcal nuclease (SNase) (79). In this study,

intramolecular spFRET was measured between donor and acceptor fluorophores attached to single SNase protein immobilized on glass cover slips by means of hexahistidine tags. smFPA was performed with single-tagged SNase, and intermolecular spFRET was measured between donor-labeled SNase and acceptor-labeled DNA substrate. The use of spFRET has been extended to the study of conformational changes experienced by single molecules of chymotrypsin inhibitor 2 when denatured in solution (80). Although single molecules have been detected in single living cells using fluorescent chimera such as transferrin-tetramethylrhodamine, it seems that the spFRET technique has not yet been used in living cells (81). One reason for this situation may be that, in living cells, autofluorescence results in too large of a background signal. Nevertheless, in another recent study, lateral motion of lipid microdomains in native muscle cell membrane was imaged, which could be considered as a pilot application of single-molecule microscopy to a living cell (82). The behavior of membrane-bound proteins tagged with GFP variants has also been recently studied at the single-molecule level (83–85).

To our knowledge, the first biological application of smFPA was reported on the axial rotation of actin filaments sliding over myosin motor molecules fixed on a glass surface (86). The conformational states of the myosin motor from the same biological system were studied 1 yr later (87). Orientation dependence of single-fluorophore intensity was used for monitoring conformational changes in F1-ATPase in real time. The fluorophore used, Cy3, was attached to the central subunit of this molecule and revealed that the subunit rotates in discrete 120° steps, each step being driven by the hydrolysis of one adenosine triphosphate molecule (88). Although these experiments were performed with enzymes fixed on a glass surface, they lead the way to studies of rotations of molecular motors.

Obviously, the use of both spFRET and smFPA at the intracellular level requires an increase in signal/background ratio. This cannot result from an increase in the integration time, which must remain in the millisecond range to be consistent with the speed of intracellular events. Likewise, the acquisition rate has its own technical limitations. Thus, the most efficient way to increase the signal/background ratio is to decrease the background intensity, which can be achieved by decreasing the irradiated intracellular volume. Three optical techniques are now available for that purpose.

Owing to the marvelous background rejection in total internal reflection fluorescence microscopy, this technique seems perfectly suitable for detecting signals of low intensity. It has been recently used for monitoring intracellular events such as chemotactic signaling, nucleocytoplasmic transport of proteins, and actin filament turnover (*see* **ref. 89** and references therein).

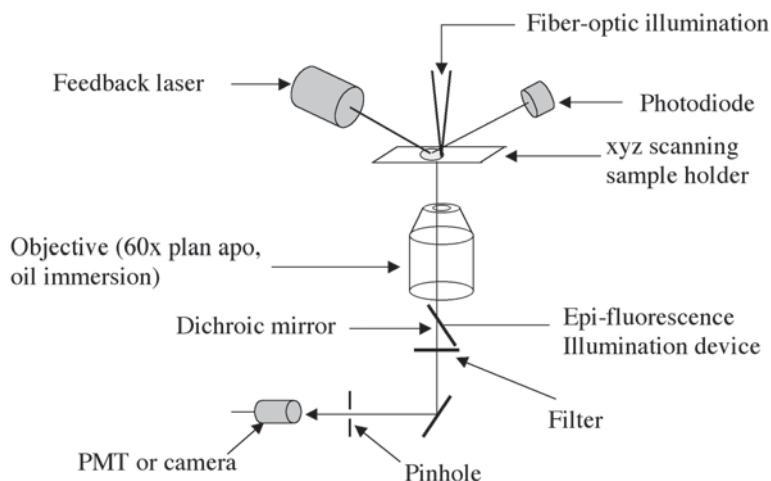


Fig. 9. Schematic diagram of a near-field scanning optical microscope. PMT, photo-multiplier tube.

Near-field scanning optical microscopy (NSOM) allows the creation of a subwavelength light source in close proximity to the surface of a sample to generate optical images with a lateral optical resolution below the diffraction limit. The optical probe is a tapered optical fiber chemically etched into a conical tip and metallized with an opaque metal coating leaving a clear aperture of about 20 to 100 nm at its apex. Excitation light issued from the optical fiber creates a nanometer-size excitation light source. When the tip is maintained a few nanometers above the cell surface, only fluorescent molecules located in the near field under the tip are excited (*90*). Thus, besides the classic mechanism used for scanning the cell, a feedback mechanism is necessary for maintaining the tip at a fixed distance from the cell surface during the scanning process (**Fig. 9**). This technique is of particular interest for studies of plasma membrane proteins or for proteins located close to or linked with the plasma membrane (*91–93*).

As mentioned earlier, multiphoton microscopy requires that two coherent photons “reach” the fluorescent target at the same time, so this technique only delivers efficient irradiation inside a tiny volume of the cell. Furthermore, this technique is not limited to exploration of the vicinity of the plasma membrane. Improvements in both equipment and data treatment have resulted in a spatial resolution in the 10-nm range (*93,94*). An elegant association of NSOM with the two-photon technology that has been described could well be the best way to reduce the background signal (*85*) and makes spFRET and smFPA usable in intact living cells.

Besides potentially invaluable information in the biomedical domain, optical studies of individual molecules already provide information about the dynamics of photophysical processes of these fluorophores (95,96). The existence of unexpected long-lasting “dark states” populated through irradiation has been evidenced and correlated to the protonated state of the fluorophore. This is a striking example of potential perturbations of biomolecules induced by the used exploration technique. Optical studies of single fluorescent molecules might also be used to address the question of potential differences in quantum yield for molecules that populate the different conformations associated with the same value of the free-energy scale during the protein-folding pathway (97).

There is no doubt that fluorescence microscopy at the single-molecule level will bring new insights into the dynamics of cellular molecular biology. However, that will require a perfect knowledge of the biophysical and photophysical properties of the used fluorescent reporters. It is anticipated that studies performed on specific 3D subdomains will be necessary to achieve these goals.

## References

1. Palmer, A. G. (1997) III. Probing molecular motion by NMR. *Curr. Opin. Struct. Biol.* **7**, 732–737.
2. Nicholson, L. K., Kay, L. E., Baldissari, D. M., Arango, J., Young, P. E., Bax, A., and Torchia, D. A. (1992) Dynamics of methyl groups in proteins as studied by proton-detected  $^{13}\text{C}$ -NMR spectroscopy: application to the leucine residues of staphylococcal nuclease. *Biochemistry* **31**, 5253–5263.
3. Wand, A. J., Urbauer, J. L., McEvoy, R. P., and Bieber, R. J. (1996) Internal dynamics of human ubiquitin revealed by  $^{13}\text{C}$ -relaxation studies of randomly fractionally labeled protein. *Biochemistry* **35**, 6116–6125.
4. Le Master, D. M. (1999) NMR relaxation order parameter analysis of the dynamics of protein side chains. *J. Am. Chem. Soc.* **121**, 1726–1742.
5. Wang, C. W., Pawley, N. H., and Nicholson, L. K. (2001) The role of backbone motions in ligand binding to the c-Src SH3 domain. *J. Mol. Biol.* **313**, 873–887.
6. Lee, A. L. and Wand, A. J. (2001) Microscopic origins of entropy, heat capacity and the glass transition in proteins. *Nature* **411**, 501–504.
7. Wand, A. J. (2001) Dynamic activation of protein function: a view emerging from NMR spectroscopy. *Nat. Struct. Biol.* **8**, 926–931.
8. Kay, L. E. (1998) Protein dynamics from NMR. *Nat. Struct. Biol.* **5**, 513–517.
9. Hoogstraten, C. J., Wank, J. R., and Pardi, A. (2000) Active site dynamics in the lead-dependent ribozyme. *Biochemistry* **39**, 9951–9958.
10. Eisenmesser, E. Z., Bosco, D. A., Akke, M., and Kern, D. (2002) Enzyme dynamics during catalysis. *Science* **295**, 1520–1523.
11. Garcia-Mira, M. M., Sadqi, M., Fischer, N., Sanchez-Ruiz, J. M., and Munoz, V. (2002) Experimental identification of downhill protein folding. *Science* **298**, 2191–2194.

12. Dunham, T. D. and Farrens, D. L. (1999) Conformational changes in rhodopsin. *J. Biol. Chem.* **274**, 1683–1690.
13. Mayor, U., Johnson, C. M., Dagget, V., and Fersht, A. R. (2000) Protein folding and unfolding in microseconds to nanoseconds by experiment and simulation. *Proc. Natl. Acad. Sci. USA* **97**, 13,518–13,522.
14. Hubbel, W. L., Cafiso, D. S., and Altenbach, C. (2000) Identifying conformational changes with site-directed spin labeling. *Nat. Struct. Biol.* **7**, 735–739.
15. Sanchez, R., Pieper, U., Melo, F., Eswar, N., Marti-Renom, M. A., Madhusudhan, M. S., Mirkovic, N., and Sali, A. (2000) Protein structure modeling for structural genomics. *Nat. Struct. Biol.* **7**, 986–990.
16. Förster, T., (1965) Delocalized excitation and excitation transfer, in *Modern Quantum Chemistry*, vol. 3 (Sinanoglu, O., ed.), Academic, New York, pp. 93–137.
17. Stryer, L. (1978) Fluorescence energy transfer as a spectroscopic ruler. *Annu. Rev. Biochem.* **47**, 819–846.
18. Lakowicz, J. R. (ed.). (1999) *Principles of Fluorescence Spectroscopy*, 2nd ed., Plenum, New York.
19. Jurgens, L., Arndt-Jovin, D., Pecht, I., and Jovin, T. M. (1996) Proximity relationships between the type I receptor for Fc epsilon (Fc epsilon RI) and the mast cell function associated antigen (MAFA) studied by donor photobleaching fluorescence resonance energy transfer microscopy. *Eur. J. Immunol.* **26**, 84–91.
20. Clegg, R. M. (1996) Fluorescence resonance energy transfer, in *Fluorescence Imaging Spectroscopy and Microscopy*, vol. 137, Chemical Analysis Series (Wang, X. F. and Herman, B. eds.), Wiley, New York, pp. 179–251.
21. König, K. (1999) Multiphoton microscopy in life science. *J. Microsc.* **200**, 83–104.
22. Diaspro, A. and Robello, M. (2000) Two-photon excitation of fluorescence for three-dimensional optical imaging of biological structures. *J. Photochem. Photobiol.* **55**, 1–8.
23. Patterson, G. H. and Piston, D. W. (2000) Photobleaching in two-photon excitation microscopy. *Biophys. J.* **78**, 2159–2162.
24. Teruel, M. N. and Meyer, T. (2002) Parallel single-cell monitoring of receptor-triggered membrane translocation of a calcium-sensing protein module. *Science* **295**, 1910–1912.
25. Salmon, J.-M., Vigo, J., and Viallet, P. (1988) Resolution of complex fluorescence spectra recorded on single unpigmented living cells using a computerized method. *Cytometry* **9**, 25–32.
26. Vigo, J., Yassine, M., Viallet, P., and Salmon, J.-M. (1995) Multiwavelength fluorescence imaging: the prerequisite for the intracellular applications. *J. Trace Microprobe Techniques* **13**, 199–207.
27. Gordon, G. W., Berry, G., Liang, X. H., Levine, B., and Herman, B. (1998) Quantitative Fluorescence resonance energy transfer measurements using fluorescence microscopy. *Biophys. J.* **74**, 2702–2713.
28. Bastiaens, P. I. H. and Squire, A. (1999) Fluorescence lifetime imaging microscopy: spatial resolution of biochemical processes in the cell. *Trends Cell Biol.* **9**, 48–52.

29. Emptage, N. J. (2001) Fluorescence imaging in living systems. *Curr. Opin. Pharmacol.* **1**, 521–525.
30. Wouters, F. S., Verveer, P. J., and Bastiaens P. I. H. (2001) Imaging biochemistry inside cells. *Trends Cell Biol.* **11**, 203–211.
31. Dong, C. Y., So, P. T., French, T., and Gratton, E. (1995) Fluorescence lifetime imaging by asynchronous pump-probe microscopy. *Biophys. J.* **69**, 2234–2242.
32. Schneckenburger, H., Gschwend, M. H., Sailer, R., Mock, H. P., and Strauss, W. S. (1998) Time-gated fluorescence microscopy in cellular and molecular biology. *Cell Mol. Biol.* **44**, 795–805.
33. Schneckenburger, H., Gschwend, M. H., Sailer, R., Strauss, W. S., Lyttek, M., Stock, K., and Zipfl, P. (2000) Time-resolved in situ measurement of mitochondrial malfunction by energy transfer spectroscopy. *J. Biomed. Opt.* **5**, 362–366.
34. Despa, S., Vecer, J., Steels, P., and Ameloot, M. (2000) Fluorescence lifetime microscopy of the Na<sup>+</sup> indicator sodium green in HeLa cells. *Anal. Biochem.* **281**, 159–175.
35. Jakobs, S., Subramaniam, V., Schönle, A., Jovin, T. M., and Hell, S. W. (2000) EGFP and DsRed expressing cultures of *Escherichia coli* imaged by confocal, two-photon and fluorescence lifetime microscopy. *FEBS Lett.* **479**, 131–135.
36. Squire, A., Verveer, P. J., and Bastiaens, P. I. H. (2000) Multiple frequency fluorescence lifetime imaging microscopy. *J. Microsc.* **197**, 136–149.
37. Tadrous, P. J. (2000) Methods for imaging the structure and function of living tissues and cells: fluorescence lifetime imaging. *J. Pathol.* **191**, 229–234.
38. Hanley, Q. S., Subramaniam, V., Arndt-Jovin, D. J., and Jovin, T. M. (2001) Fluorescence lifetime imaging: multi-point calibration, minimum resolvable differences, and artifact suppression. *Cytometry* **43**, 248–260.
39. Bancel, F., Salmon, J.-M., Vigo, J., and Viallet, P. M. (1992) Microspectrofluorometry as a tool for investigations of non calcium interactions of indo-1. *Cell Calcium* **13**, 59–68.
40. Vo-Dinh, T. (1978) Multicomponents analysis by synchronous luminescence spectroscopy. *Anal. Chem.* **50**, 396–401.
41. Stevenson, C. L., Johnson, R. W., and Vo-Dinh, T. (1994) Synchronous luminescence: a new detection technique for multiple fluorescent probes used for DNA sequencing. *Biotechniques* **16**, 1104–1110.
42. Viallet, P. M., Vo-Dinh, T., Bunde, T., Ribou, A.-C., Vigo, J., and Salmon, J.-M. (1999) Fluorescent molecular reporter for the 3-D conformation of protein subdomains: the Mag-indo 1 system. *J. Fluoresc.* **9**, 153–161.
43. Viallet, P. M., Vo-Dinh, T., Ribou, A.-C., Vigo, J., and Salmon, J.-M. (2000) Native fluorescence and Mag-indo-1-protein interaction as tools for probing unfolding and refolding sequences of the bovine serum albumin subdomain in the presence of guanidine hydrochloride. *J. Protein Chem.* **19**, 431–439.
44. Prasher, D. C., Eckenrode, V. K., Ward, W. W., Predergast, F. G., and Cormier, M. J. (1992) Primary structure of the *Aequorea victoria* green-fluorescent protein. *Gene* **111**, 229–233.



45. Ludin, B. and Matus, A. (1998) GFP illuminates the cytoskeleton. *Trends Cell Biol.* **8**, 72–77.
46. Bajno, L. and Grinstein, S. (1999) Fluorescent proteins: powerful tools in phagocyte biology. *J. Immun. Methods* **232**, 67–75.
47. Chamberlain, C. and Hahn, K. M. (2000) Watching proteins in the wild: fluorescence methods to study dynamics in living cells. *Traffic* **1**, 755–762.
48. Latif, R. and Graves, P. (2000) Fluorescent probes: Looking backward and looking forward. *Thyroid* **10**, 407–412.
49. Sacchetti, A., Ciccocioppo, R., and Alberti, S. (2000) The molecular determinants of the efficiency of green fluorescent protein mutants. *Histol. Histopathol.* **15**, 101–107.
50. Whitaker, M. (2000) Fluorescent tags of protein function in living cells. *BioEssays* **22**, 180–187.
51. Miyawaki, A. and Tsien, R. Y. (2000) Monitoring protein conformations and interactions by fluorescence resonance energy transfer between mutants of green fluorescent protein. *Methods Enzymol.* **327**, 472–500.
52. Truong, K. and Ikura, M. (2001) The use of FRET imaging microscopy to detect protein-protein interactions and protein conformation changes in vivo. *Curr. Opin. Struct. Biol.* **11**, 573–578.
53. Xu, X., Gerald, A. L., Huang, B. C., Anderson, D. C., Payan, D. G., and Luo, Y. (1998) Detection of programmed cell death using fluorescence energy transfer. *Nucleic Acid Res.* **26**, 2034, 2035.
54. Mahajan, N. P., Harrison-Shostak, D. C., Michaux, J., and Henman, B. (1999) Novel mutant green fluorescent protein protease substrates reveal the activation of specific caspases during apoptosis. *Chem. Biol.* **6**, 401–409.
55. Jones, J., Heim, R., Hare, E., Stack, J., and Pollok, B. A. (2000) Development and application of a GFP-FRET intracellular caspase assay for drug screening. *J. Biomol. Screen.* **5**, 307–318.
56. Luo, K. Q., Yu, V. C., Pu, Y., and Chang, D. C. (2001) Application of the fluorescence resonance energy transfer method for studying the dynamics of caspase-3 activation during UV-induced apoptosis in living HeLa cells. *Biochem. Biophys. Res. Commun.* **283**, 1054–1060.
57. Tawa, P., Tam, J., Cassady, R., Nicholson, D. W., and Xanthoudakis, S. (2001) Quantitative analysis of fluorescent caspase substrate cleavage in intact cells and identification of novel inhibitors of apoptosis. *Cell Death Differ.* **8**, 30–37.
58. Ng, T., Squire, A., Hansara, G., et al. (1999) Imaging protein kinase C $\alpha$  activation in cells. *Science* **283**, 2085–2089.
59. Nagay, Y., Miyazaki, M., Aoki, R., Zama, T., Inouye, S., Hirose, K., Iino, M., and Hagiwara, M. (2000) A fluorescent indicator for visualizing cAMP-induced phosphorylation in vivo. *Nat. Biotechnol.* **18**, 313–318.
60. Zhang, J., Ma, Y., Taylor, S. S., and Tsien, R. Y. (2001) Genetically encoded reporters of protein kinase A activity reveal impact of substrate tethering. *Proc. Natl. Acad. Sci. USA* **98**, 14,997–15,002.

61. Ting, A. Y., Kain, K. H., Klemke, R. L., and Tsien, R. Y. (2001) Genetically encoded fluorescent reporters of protein tyrosine kinase activities in living cells. *Proc. Natl. Acad. Sci. USA* **98**, 15,002–15,008.
62. Llopis, J., Westin, S., Ricote, M., et al. (2000) Ligand-dependent interactions of coactivators steroid receptor coactivator-1 and peroxisome proliferator-activated receptor binding protein with nuclear hormone receptors can be imaged in living cells and are required for transcription. *Proc. Natl. Acad. Sci. USA* **97**, 4363–4368.
63. Kenworthy, A. K., Petranova, N., and Edidin, M. (2000) High-resolution FRET microscopy of cholera toxin B-subunit and GPI-anchored proteins in cell plasma membranes. *Mol. Biol. Cell* **11**, 1645–1655.
64. Sorkin, A., McLure, M., Huang, F., and Carter, R. (2000) Interaction of EGF receptor and Grb2 in living cells visualized by fluorescence resonance energy transfer (FRET) microscopy. *Curr. Biol.* **10**, 1395–1398.
65. Janetopoulos, C., Jin, T., and Devreotes, P. (2001) Receptor-mediated activation of heteromeric G-proteins in living cells. *Science* **291**, 2408–2411.
66. Wilding, M., Török, K., and Whitaker, M. (1995) Activation-dependent and activation-independent localization of calmodulin to the mitotic apparatus during the first cell cycle of the *Lytechinus pictus* embryo. *Zygote* **3**, 219–224.
67. Wilding, M., Wright, E. M., Patel, R., Ellis-Davies, G., and Whitaker, M. (1996) Local perinuclear calcium signals associated with mitosis-entry in early sea urchin embryos. *J. Cell Biol.* **135**, 191–199.
68. Torok, K., Wilding, E. M., Groigno, L., Patel, R., and Whitaker, M. (1998) Imaging the spatial dynamics of calmodulin activation during mitosis. *Curr. Biol.* **8**, 692–699.
69. Whitaker, M. (2000) Fluorescent tags of protein function in living cells. *BioEssays* **22**, 180–187.
70. Zimprich, F., Török, K., and Bolsover, S. R. (1995) Nuclear calmodulin responds rapidly to calcium influx at the plasmalemma. *Cell Calcium* **17**, 233–238.
71. Falke, J. J. (2002) A moving story. *Science* **295**, 1480, 1481.
72. Baron, S., Poast, J., Rizzo, D., McFarland, E., and Kieff, E. (2000) Electroporation of antibodies, DNA, and other molecules into cells: a highly efficient method. *J. Immunol. Methods* **242**, 115–126.
73. Zelphati, O., Wang, Y., Kitada, S., Reed, J. C., Felgner, P. L., and Corbeil, J. (2001) Intracellular delivery of proteins with a new lipid-mediated delivery system. *J. Biol. Chem.* **276**, 35,103–35,110.
74. Boyle, D. L., Carman, P., and Takemoto, L. (2002) Translocation of macromolecules into whole rat lenses in culture. *Mol. Vis.* **8**, 226–234.
75. Fortugno, P., Wall, N. R., Giodini, A., O'Connor, D. S., Plescia, J., Padgett, K. M., Tognin, S., Marchisio, P. C., and Altieri, D. C. (2002) Survivin exists in immunologically distinct subcellular pools and is involved in spindle microtubule function. *J. Cell Sci.* **115**, 575–585.
76. Anantharam, V., Kitazawa, M., Wagner, J., Kaul, S., and Kanthasamy, A. G. (2002) Caspase-3-dependent proteolytic cleavage of protein kinase C is essential

- for oxydative stress-mediated dopaminergic cell death after exposure to methylcyclopentadienyl manganese tricarbonyl. *J. Neurosci.* **22**, 1738–1751.
77. Fernando, P., Kelly, J. F., Balazsi, K., Slack, R. S., and Megeney, L. A. (2002) Caspase 3 activity is required for skeletal muscle differentiation. *Proc. Natl. Acad. Sci. USA* **99**, 11,025–11,030.
78. Weiss, S. (2000) Measuring conformational dynamics of biomolecules by single molecule fluorescence spectroscopy. *Nat. Struct. Biol.* **7**, 724–729.
79. Ha, T., Ting, A. Y., Liang, J., Caldwell, W. B., Deniz, A. A., Chemla, D. S., Schultz, P. G., and Weiss, S. (1999) Single-molecule fluorescence spectroscopy of enzyme conformational dynamics and cleavage mechanism. *Proc. Natl. Acad. Sci. USA* **96**, 893–898.
80. Deniz, A. A., Laurence, T. A., Beligere, G. S., Dahan, M., Martin, A. B., Chemla, D. S., Dawson, P. E., Schultz, P. G., and Weiss, S. (2000) Single-molecule protein detection protein folding: diffusion fluorescence energy transfer studies of the denaturation of chymotrypsin inhibitor 2. *Proc. Natl. Acad. Sci. USA* **97**, 5179–5184.
81. Byassee, T. A., Chan, W. C. W., and Nie, S. (2000) Probing single molecules in single living cells. *Anal. Chem.* **72**, 5606–5611.
82. Schütz, G. H., Kada, G., Pastuhenko, V. P., and Schindler, H. (2000) Properties of lipid microdomains in a muscle cell membrane visualized by single molecule microscopy. *EMBO J.* **19**, 892–901.
83. Harms, G. S., Cognet, L., Lommerse, P. H. M., Blad, G. A., and Schmidt, T. (2001) Autofluorescent proteins in single-molecule research: applications to live cell imaging microscopy. *Biophys J.* **80**, 2396–2408.
84. Harms, G. S., Cognet, L., Lommerse, P. H. M., et al. (2001) Single-molecule imaging of L-type  $\text{Ca}^{2+}$  channels in live cells. *Biophys. J.* **80**, 2639–2646.
85. Iino, R., Koyama, I., and Kusumi, A. (2001) Single-molecule imaging of green fluorescent proteins in living cells: E-cadherin forms oligomers on the free cell surface. *Biophys. J.* **80**, 2667–2677.
86. Sase, I., Miyata, H., Ishiwata, S., and Kinoshita, K. Jr. (1997) Axial rotation of sliding actin filaments revealed by single fluorescence imaging. *Proc. Natl. Acad. Sci. USA* **94**, 5646–5650.
87. Warshaw, D. M., Hayes, E., Gaffney, D., Lauzon, A. M., Wu, J., Kennedy, G., Tribus, K., Lowey, S., and Berger, C. (1998) Myosin conformational states determined by single fluorophore polarization. *Proc. Natl. Acad. Sci. USA* **95**, 8034–8039.
88. Adachi, K., Yasuda, R., Noji, H., Itoh, H., Yoshida, M., and Kinoshita, K. Jr. (2000) Stepping rotation of F1-ATPase visualized through angle-resolved single-fluorophore imaging. *Proc. Natl. Acad. Sci. USA* **97**, 7243–7247.
89. Sako, Y. and Uyemura, T. (2002) Total internal reflection fluorescence microscopy for single-molecule imaging in living cells. *Cell Struct. Funct.* **27**, 357–365.
90. Marchese-Ragona, S. P. and Haydon, P. G. (1997) Near-field scanning optical microscopy and near-field confocal optical spectroscopy: emerging techniques in biology, in *Imaging Brain Structure and Function* (Lester, E. D., Felder, C. C.,

- and Lewis, E. N., eds.), Annals of the New York Academy of Sciences, New York, pp. 196–207.
91. Enderle, T., Ha, T., Ogletree, D. F., Chemla, D. S., Magowan, C., and Weiss, S. (1997) Membrane specific mapping and colocalization of malarial and host skeletal proteins in the plasmodium falciparum infected erythrocyte dual-color near field scanning optical microscopy. *Proc. Natl. Acad. Sci. USA* **94**, 520–525.
  92. Kirsch, A. K., Subramaniam, V., Jenei, A., and Jovin, T. M. (1999) Fluorescence resonance energy transfer detected by scanning near-field microscopy. *J. Microsc.* **194**, 448–454.
  93. Korchev, Y. E., Raval, M., Lab, M. J., Gorelik, J., Edwards, C. R., and Rayment-Klenerman, D. (2000) Hybrid scanning ion conductance and scanning near-field optical microscopy for the study of living cells. *Biophys. J.* **78**, 2675–2679.
  94. Doyle, R. T., Szulcowski, M. J., and Haydon, P. G. (2001) Extraction of near-field fluorescence from composite signals to provide high resolution images of glial cells. *Biophys. J.* **80**, 2477–2482.
  95. Dickson, R. M., Cubitt, A. E., Tsien, R. Y., and Moerner, W. E. (1997) On/off blinking and switching behaviour of single molecules of green fluorescence protein. *Nature* **388**, 355–358.
  96. Petermann, E. J. G., Brasselet, S., and Moerner, W. E. (1999) The fluorescence dynamics of single molecules of green fluorescence protein. *J. Phys. Chem. A* **103**, 10,553–10,560.
  97. Dill, K. E. (1999) Polymer principles and protein folding. *Protein Sci.* **8**, 1166–1180.



## Carbon Nanotubes and Nanowires for Biological Sensing

Jun Li, Hou Tee Ng, and Hua Chen

### Summary

This chapter reviews the recent development in biological sensing using nanotechnologies based on carbon nanotubes and various nanowires. These 1D materials have shown unique properties that are efficient in interacting with biomolecules of similar dimensions, i.e., on a nanometer scale. Various aspects including synthesis, materials properties, device fabrication, biofunctionalization, and biological sensing applications of such materials are reviewed. The potential of such integrated nanobiosensors in providing ultrahigh sensitivity, fast response, and high-degree multiplex detection, yet with minimum sample requirements is demonstrated. This chapter is intended to provide comprehensive updated information for people from a variety of backgrounds but with common interests in the fast-moving interdisciplinary field of nanobiotechnology.

**Key Words:** Carbon nanotube; single-walled carbon nanotube; multiwalled carbon nanotube; nanowires; chemical vapor deposition; lithography; self-assembly; scanning probe microscopy; field-effect-transistor; nanoelectronics.

### 1. Introduction

Efficient biological sensing requires directly interrogating individual biomolecules with a physical dimension of about 1 to 100 nm. Development in this field strongly demands techniques and probing tools extending to similar length scales. This has been one of the major driving forces for nanotechnology in recent years. As the size of the materials is reduced to the nanometer regime, they show many new electronic, optical, and mechanical properties, which are more directly associated with the environment and target samples. Although the majority of raw nanomaterials are nanoparticles, high-aspect ratio one-dimensional (1D) materials such as carbon nanotubes (CNTs) and various nanowires (NWs) are more attractive as building blocks in the fabrication of

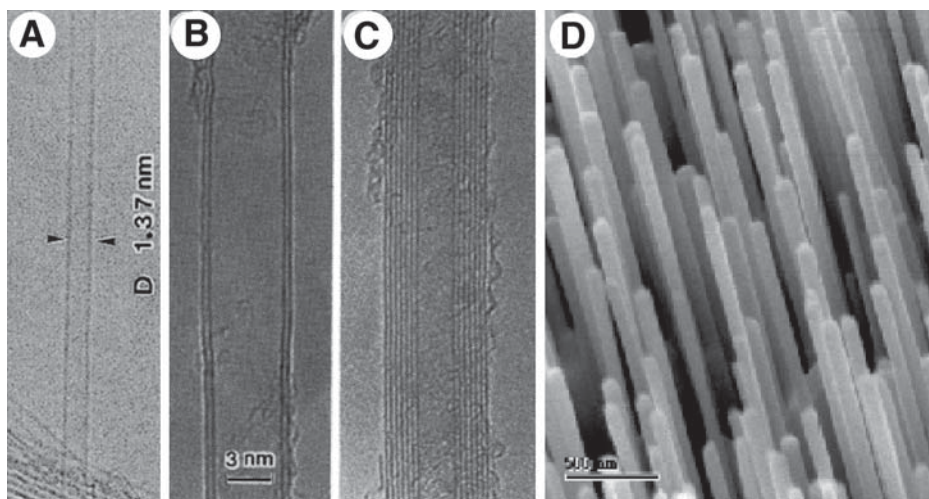


Fig. 1. Transmission electron microscopy (TEM) images of (A) a SWCNT and (B,C) two types of MWCNTs, and (D) scanning electron microscopy (SEM) image of an array of ZnO NWs. (Panel [A] is reprinted from **ref. 10** with permission and panels [B] and [C] are reprinted from **ref. 9** with permission. Copyright 1991 and 1993, respectively, Nature Publishing Group, <http://www.nature.com>.)

devices. The potential of CNTs and NWs as sensing elements and tools for biological applications as well as for detecting gases and small chemicals has been recently recognized. Promising results in improving sensitivity, lowering detection limit, reducing sample amount, and increasing the degree of multiplex and miniaturization have been reported based on CNTs (1,2) and NWs (3,4). Even though these studies are still in early research stages, they have shown great potential for future biotechnologies. This chapter summarizes, from a technology development point of view, the recent progress in the development of biological sensors using CNTs and NWs, it is our hope to attract interest in exploring the potential applications of such technologies in biomedical research.

CNTs belong to a family of materials consisting of seamless graphitic cylinders with extremely high aspect ratios (5–8). The typical diameter varies from about 1 nm to hundreds of nanometers, and the length spans from tens of nanometers to hundreds of microns or even centimeters. Scientists in NEC Corporation originally discovered the cylindrical structure of CNTs in 1991 (9). A CNT may consist of one graphitic layer, referred to as single-walled CNTs (SWCNTs) (10), as shown in **Fig. 1A**, or multi graphitic layers, referred to as multiwalled CNTs (MWCNTs) (9), as shown in **Fig. 1B,C**. SWCNTs normally give a smaller diameter (down to 7 Å) and show electronics properties strongly



dependent on the helicity, namely the  $(m,n)$  lattice vector in the graphitic sheet along which it is rolled into a tube (11). It is known that SWCNTs are semiconducting if their chirality  $(m,n)$  satisfies  $m - n \neq 3 \times \text{integer}$  (5–8). MWCNTs consist of a random mixture of all possible helicities in each shell (12).

Owing to the intriguing nanometer-scale structures and unique properties, CNTs have quickly attracted intensive attention in the past few years in many fields such as nanoelectronic devices (12–20), composite materials (21), field-emission devices (22,23), atomic force microscope probes (24–27), and hydrogen/lithium ion storage (28,29). Many studies reported potential for ultrahigh sensitivity sensors as well (1,20,30–32). The extremely high surface-to-volume ratio of CNTs is ideal for efficient adsorption. The (1D) quantum wire nature makes their electronic properties extremely sensitive to gas or chemical adsorption. Both of these factors are essential for high-sensitivity sensors. In the past few years, CNT sensors have been demonstrated in many applications involving gas molecules, liquid-phase chemicals, and biomolecules, showing improved performance compared with conventional sensors utilizing micro- or macromaterials and thin films (2). Depending on applications, sensing devices can be fabricated using single free-standing CNTs (25,26), semiconducting SWCNT field-effect-transistors (FETs) (1,20,33,34), well-defined nanoelectrode arrays (35), or porous films (32,36,37).

NWs, on the other hand, typically refer to highly crystalline, wirelike 1D materials consisting of metals (38), semiconductors (3,39), or inorganic compounds (4,40). They can be synthesized with a high aspect ratio similar to that of CNTs, i.e., about a few to hundreds of nanometers in diameter and more than microns in length. **Figure 1D** shows a well-aligned array of ZnO NWs with an average diameter of approx 100 nm and length more than microns. Besides showing similar properties, such as high aspect ratio and large surface-to-volume ratio, CNTs, NWs have well-defined crystalline structure. The broad choice of various crystalline materials and doping methods makes the electronic and optical properties of NWs tunable with a high degree of freedom and precision. With the development of new synthesis methods, NWs have attracted more and more attention for sensor applications.

Another category of NWs is based on templating methods. These materials are the assembly of intrinsically heterogeneous biological and solid-state nanomaterial components instead of homogeneous structures. The nano-/bio-assembly NWs consist of two approaches: (1) CNTs or crystalline NWs serving as templates on which biomolecules aggregate into nanoscale wirelike structures (41), and (2) DNA or protein macromolecular backbones or assembly serving as templates on which nanoparticles are deposited to form nanoscale wirelike structures (42). Both of these approaches have been demonstrated in heterogeneously integrated nano-biosystems for biological sens-

ing, which combine the biorecognition-driven self-assembly functionalities with desired solid-state electronics properties.

## 2. Growth of Materials and Device Fabrication

### 2.1. Growth of CNTs

Finding the solutions to grow CNTs with desired quantities and qualities is an active, ongoing research topic. A host of experimental approaches have been explored, improved, and modified to successfully synthesize CNTs, both single- and multiwalled, for sensor applications. The typical techniques used include electrical arc discharge, laser ablation, and chemical vapor deposition. In most growth processes, a catalyst that is either a metal or a mixed alloy is used.

Iijima and Ichihashi (10) and Bethune et al. (43) first demonstrated the growth of SWCNTs, though in small quantities, by using the electrical arc-discharge techniques. The SWCNTs were typically accompanied by a substantial amount of amorphous carbon, carbon nanoparticles, and other carbon-based materials. By using the laser ablation method, Thess et al. (44) further improved the purity and synthesized SWCNTs on the grams quantity. The as-synthesized SWCNTs present mostly in the form of ropes with individual nanotubes aggregating into hexagonal crystals owing to the van der Waals interaction. Subsequent studies by other groups have improved on either the designs or experimental formulations to obtain better quality and larger quantity products. For example, Kajiura et al. (45) used a newly designed chamber that was equipped with a filtering zone to produce a high content of SWCNT ropes under controlled gas flow conditions. Journet et al. (46) optimized the growth of SWCNTs by incorporating yttrium and nickel into a carbon anode. Both of these techniques have also been successfully used to synthesize MWCNTs.

Recently, chemical vapor deposition (CVD) has gained popularity in synthesizing both SWCNTs and MWCNTs with good yields and particularly for direct growth device fabrication. A typical growth process involves passing a hydrocarbon gas over a heated catalyst at high temperature for a period of time. Kong et al. (47) demonstrated using the techniques to synthesize SWCNTs with high quality by passing methane over alumina-supported catalyst in a temperature range of 850 to 1000°C. By optimizing the catalyst preparation and growth conditions, the quality and yields of the nanotubes could be further improved as demonstrated by many studies (48–51). More recently, Bronikowski et al. (52) demonstrated large-scale production (10 g/d) of high-purity SWCNTs using a gas-phase CVD process, termed HiPco process. SWCNT material of up to 97 mol% purity could be produced at a rate of 450 mg/h.

Plasma enhanced CVD (PECVD), with the advantage of compatibility with semiconductor processes, has attracted extensive attention in the growth of CNTs for device fabrication (53–55). A single or an array of CNTs can be grown at sites precisely defined by lithographic techniques down to tens of nanometers (55). The alignment can also be precisely controlled by an electrical field. The only drawback is that the CNTs grown by PECVD are more defective, with the graphitic layer not perfectly parallel to the tube axis. Many bamboo-like close shells are formed along the tube instead of forming perfect hollow channels running from one end all the way to the other end. However, such defective structures were found not critical for many sensor applications (35). With continual effort in the development of growth techniques and methodology, it is expected that CNTs with the desired properties, qualities, and quantities will be obtained in the near future.

## 2.2. Growth of Crystalline NWs

Crystalline 1D NWs can be formed with metals, semiconductors, or inorganic compounds. They have shown potential in a wide range of applications including nanoelectronics, nanosensors, and nanobiotechnology. Different synthetic strategies have been developed for obtaining desired 1D NWs, which can be divided into two categories using wet chemical methods and vapor-phase methods, respectively.

In the growth of 1D nanowires dictated by the anisotropic crystallographic nature of the material, Stejny et al. (56) demonstrated that inorganic NWs of poly(sulfur nitride) having a diameter of approx 20 nm and a length of hundreds of micrometers could be synthesized by taking advantage of their highly anisotropic structural bonding. Using a similar strategy, Golden et al. (57) and Venkataraman and Lieber (58) showed the synthesis of  $(\text{Mo}_3\text{Se}_3^-)_n$  and molybdenum selenide molecular wires, respectively. Making use of the hexagonally packed helical chains of Se atoms along their *c*-axis, Gates et al. (59) demonstrated that a generic, solution-phase approach could be used for the large-scale synthesis of uniform NWs of t-Se.

Another strategy involves using a template to assist in the synthesis of 1D NWs. The template serves as a scaffold within (or around) which a desired material could be *in situ* generated with its morphology complementary to that of the template. For example, Limmer et al. (60) showed the growth of uniform arrays of NWs of  $\text{Pb}(\text{Zr}, \text{Ti})\text{O}_3$  in porous alumina membranes. Although the synthesized NWs are typically polycrystalline, single crystalline NWs could be obtained with careful selection of the growth conditions. Barbic et al. (61) and Molaes et al. (62) demonstrated growth of single crystalline silver and copper NWs, respectively, using electrodeless and pulse electrodeposition methods. Using a different templating platform, Müller et al. (63) showed that

it is possible to fabricate large arrays of Ge NWs by templating against the V-grooves etched into the surfaces of Si(100) substrates. Sugawara et al. (64) further demonstrated that three-dimensional (3D) arrays of iron NWs could be obtained by templating against relief features existing on the surfaces of NaCl crystals. Other templating schemes involving forming self-assembled molecular structures against existing nanostructures have also been successfully used to obtain a variety of NWs (65).

Vapor-phase synthesis, on the other hand, is probably the most extensively explored method for the fabrication of 1D NWs. By maintaining a low supersaturation level and vapor pressure, 1D nanostructures could, in principle, be synthesized from their bulk materials. A main advantage of the vapor-phase method lies in its simplicity and accessibility. In a typical growth process, the vapor species are first formed by evaporation, followed by chemical reduction, transportation, and condensation of gas species onto suitable substrates. In the direct vapor-phase method, Zhang et al. (66) showed successful growth of  $\text{Si}_3\text{N}_4$ , SiC,  $\text{Ga}_2\text{O}_3$ , and ZnO NWs by heating the powders of these materials at elevated temperatures. Using an indirect vapor-phase method, Yang and Lieber (67) showed the growth of MgO NWs using a carbothermal reduction process. Recently, Shi et al. (68) observed the growth of Si NWs by using a mixture of Si and  $\text{SiO}_2$  in the feedstocks. Laser ablation was used to assist in the vaporization of these bulk materials.

Among the various vapor-based methods, a growth process involving a vapor-liquid-solid (VLS) mechanism is poised to be the most successful approach for generating NWs with single crystalline structures. Numerous groups have synthesized a variety of NWs from their respective inorganic materials (69–73). A critical component of the VLS mechanistic growth approach involves dissolution of the gaseous reactants into a liquid catalytic nanoparticle, which acts as a soft template for the nucleation and growth of 1D NWs.

A major challenge in the synthesis of 1D NWs is how to tailor their diameter, length, and properties uniformly in a single growth process. This is particularly important in many practical applications that require high homogeneity in their structural, physical, and electronic properties.

### 2.3. Nanobiosensing Devices

**Figure 2** summarizes four types of the most commonly used biological sensing devices based on CNTs and NWs, which covers most studies reported in the literature by now. Depending on the sensing applications, different device architectures and fabrication routes are required to achieve successfully their desired functions. Common to all, CNTs or NWs are critical components of the sensing devices, which are integrated either directly or indirectly during the fabrication routes. A variety of methods, ranging from advanced micro- or

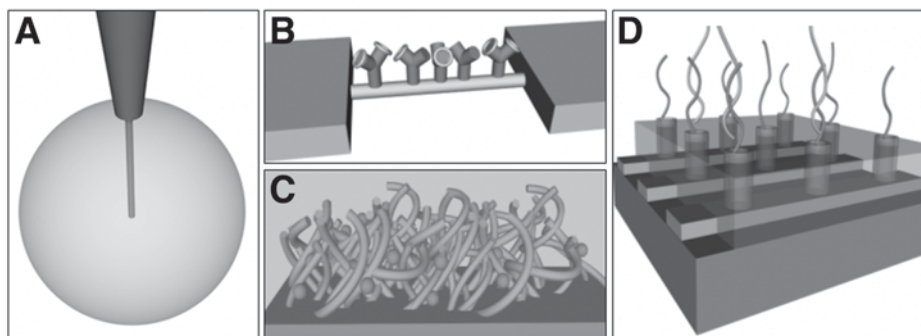


Fig. 2. Schematic of four types of CNT/NW devices for biological sensing: (A) single CNT or NW extended from a microtip to probe a single cell or single molecules; (B) FET device using a single semiconducting CNT or NW; (C) porous CNT/NW film as electrochemical biosensor; (D) nanoelectrode array-based electrochemical biosensor.

nanolithographic techniques to handmade processes, have been demonstrated by various researchers to build functional devices. Generally, CNTs/NWs could be the sensing elements whose properties are changed on occurrence of the biological events' or the transducers that transfer the changed signal to the measuring units. The sensing device could use a single CNT/NW or an ensemble of such materials.

The most straightforward biological sensing employs a single CNT or NW to probe the biochemical environment in a single living cell or interrogate a single biomolecule (as shown in **Fig. 2A**). The CNT/NW probe can be attached to the pulled tip of an optical fiber for optical detection (74) or an electrode for electrical or electrochemical measurements (75). Normally, for such applications, the sidewalls of the nanoprobe have to be shielded or insulated to reduce the background so that the small signal from the very end of the probe can be detected. The CNT/NW probes provide the best spatial resolution as well as ultrahigh sensitivity and short response time. The small size, high aspect ratio, and mechanical robustness of CNTs were also employed as the physical probe for high-resolution scanning probe microscopy (SPM). This technique is powerful for illustrating the structure of single molecules such as DNA and proteins with the resolution down to a few nanometers.

A semiconducting CNT or NW can be used to construct a FET, as shown in **Fig. 2B**, using nanolithographic techniques. Such a device consists of a semiconducting CNT or NW connected to two contact electrodes (source and drain) on an oxide-covered Si substrate that could serve as the gate electrode (1,13). Conventional FETs fabricated with semiconductors such as Si have been

configured as sensors by modifying the gate oxide (without the gate electrode) with molecular receptors or ion-selective membranes for the analytes of interest (76). The binding or adsorption of charged species could produce an electric field that depletes or accumulates carriers within the semiconducting material similar to the gate potential. As a result, the conductance between the source and drain electrodes is dramatically changed. Chemical sensors based on such a mechanism referred to as chemical field-effect-transistors (76) have been used for many applications since the 1980's.

As we mentioned in the Introduction, SWCNTs have well-defined structures. The helicity of the SWCNT determines whether it is metallic or semiconducting. It has been demonstrated that a semiconducting SWCNT (S-SWCNT) FET exhibits p-type transistor characteristics with the conductance tunable over several orders of magnitude by changing the gate voltage applied on the Si substrate (1). Such a phenomenon was attributed to the adsorption of  $O_2$  as the electron acceptor in an ambient environment. Since every carbon atom is exposed at the surface, SWCNTs are highly efficient for gas adsorption. In addition, a theoretical work predicts about 0.1 electron transfers per  $O_2$  molecule (77). Owing to the small size, this gives a big carrier density in the "bulk" SWCNT that would dramatically change the electronic behavior of the FET. The quantum wire nature of the SWCNT makes the conductance of the tube even more sensitive because any partial point charge could completely deplete the local carrier along the 1D wire. Therefore, the sensitivity of single-molecule adsorption/desorption could, in principle, be achieved with such miniaturized S-SWCNT FETs. Semiconducting NWs (S-NWs) such as Si (3) and  $In_2O_3$  (4) have also been recently demonstrated in FET sensing devices. The applications of such devices in biological sensing are discussed in **Subheading 3.2**.

The large surface-to-volume ratio and good electrical conductance along the tube axis make CNTs attractive for enzyme-based electrochemical sensors. CNTs can be cast as a thin film on conventional electrodes (78–80) or used as a 3D porous film (32,36,37) (as shown in **Fig. 2C**). Such crude CNT ensembles serve both as large immobilization matrices and as mediators to improve the electron-transfer between the enzyme-active site and the electrochemical transducer. Improved electrochemical behavior of NADH (80), neurotransmitters (32), and enzymes (79) has been reported.

The last type of CNT/NW device is also an electrochemical sensor based on an array of vertically aligned CNTs embedded in  $SiO_2$  matrices, as schematically shown in **Fig. 2D**. The electrochemical signal is characteristic of the reduction/oxidation (redox) reaction of the analytes instead of nonspecific charges sensed by FETs, resulting in very good specificity comparable to fluorescence-based optical techniques that are commonly used in today's biology research. In addition, a high degree of miniaturization and multiplex detection



can be realized for molecular diagnosis using individually addressed micro-electrode array integrated with microelectronics and microfluidics systems (81–84), which is more attractive than optical techniques, particularly for quick and simple diagnostics. However, the sensitivity of electrochemical techniques using traditional macro- and microelectrodes is orders of magnitude lower than those of optical techniques, which limits their use in many applications. Nanoscale sensing elements have been actively pursued to seek solutions for improving the sensitivity of electrochemical techniques.

The performance of electrodes with respect to speed and spatial resolution is known to scale inversely with the electrode radius (85–87). It is of interest for biosensing to reduce the radius of electrodes to 10–100 nm, approaching the size of biomolecules. Li et al. (35) demonstrated that nanoelectrodes, particularly a MWCNT-based nanoelectrode array, with an average diameter of 30 to 100 nm, can be integrated into an electrochemical system for ultrasensitive chemical and DNA detection. The nanoelectrode array is fabricated with a bottom-up scheme resulting in a precisely positioned and well-aligned MWCNT array embedded in a planarized SiO<sub>2</sub> matrix (55,88). The vertically aligned MWCNTs were first grown using direct current (DC)-biased hot-filament plasma CVD on a metal film-covered silicon substrate. They were then subjected to tetraethyloxysilicate CVD for gap filling of SiO<sub>2</sub>. SiO<sub>2</sub> dielectrics was found to fill conformally in the gap between individual MWCNTs and hence reinforced the MWCNT array. Excess SiO<sub>2</sub> was subsequently removed, allowing exposure of the MWCNT tips via a mechanical polishing step. The open ends of MWCNTs exposed at the dielectric surface act as nanoelectrodes. **Figure 3** shows SEM images of a CNT array grown on multiplex microelectrodes with different densities defined by lithographic techniques. The surface of an encapsulated and planarized array shows only the very end of CNTs exposed as well-defined nanoelectrodes. Such a nanoelectrode array showed characteristic electrochemical behavior for redox species both in bulk solution and immobilized at the CNT ends. Dramatic improvements in sensitivity and time constant were observed (35).

CNTs have demonstrated many advantages in nanoelectrode applications. The wide electropotential window, flexible surface chemistry, and biocompatibility make the MWCNT array an attractive electrode similar to other widely used carbon electrodes. The open end of an MWNT is expected to show a fast electron transfer rate (ETR) similar to that of the graphite edge-plane electrode, whereas the sidewall is inert like the graphite basal plane (89). Fast ETR is demonstrated along the tube axis (75,90). Such an MWCNT electrode could interrogate target species, down to the single-molecule level, at one end and sustain electron transport along the tube axis to the measuring circuit with minimum interference from the environment. Whereas a single



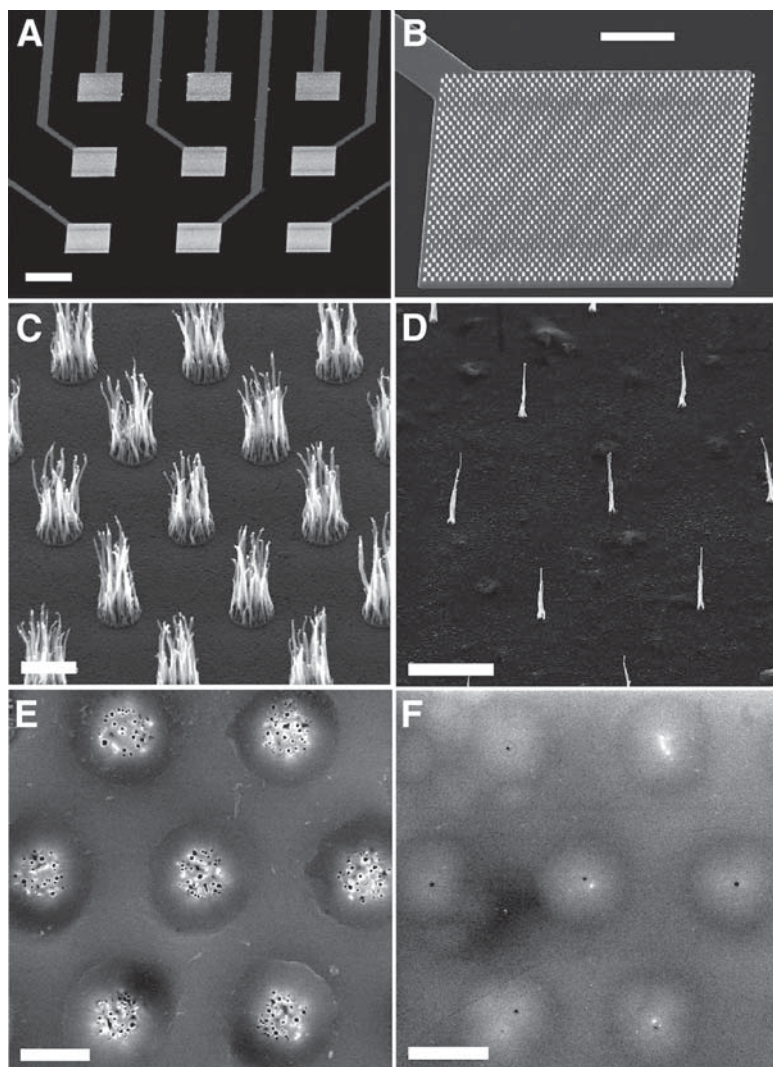


Fig. 3. SEM images of (A)  $3 \times 3$  electrode array; (B) array of MWCNT bundles on one of the microelectrode pads; (C,D) array of MWCNTs at UV-lithography- and e-beam-patterned Ni spots, respectively; (E,F) surface of polished MWCNT array electrodes grown on 2- $\mu\text{m}$  and 100-nm spots, respectively. Panels (A–D) are  $45^\circ$  perspective views and panels (E) and (F) are top views. Bars = 200, 50, 2, 5, 2, and 2  $\mu\text{m}$ , respectively.

nanoelectrode can provide the desired temporal and spatial advantages, the nanoelectrode array serves the needs for analytical applications requiring reliable statistics and multiplex detection.

## 2.4. Functionalization of CNTs/NWs for Biological Sensing

A common feature for biological sensing is the requirement of immobilization of biomolecules with specific functionalities to the sensing device. These biomolecules serve as probes either to specifically bind particular species in the testing sample or to specifically catalyze the reaction of the analyte. Such an event produces a change in chemical or physical properties that can be converted into a measurable signal by the transducer. The specific recognition of the target molecules is the essential feature for biological sensing. The common probe and target (analyte) recognition mechanisms include (1) antibody–antigen interactions, (2) nucleic acid hybridizations, (3) enzymatic reactions, and (4) cellular interactions. Depending on the device and its sensing mechanism, different functionalization methods have to be adapted. We can separate the functionalization methods into three categories to cover all the biological sensing methods that are summarized in the next section. These are (1) covalent binding to the open ends of CNTs, (2) noncovalent binding to the sidewall of CNTs, and (3) covalent binding to NWs.

CNTs, from a structural point of view, are quite similar to a roll of graphitic sheets. The sidewalls have very inert chemical properties similar to graphite basal planes. The open ends of CNTs, on the other hand, are similar to graphite edge planes, which are much more reactive owing to the dangling  $sp^2$  bonds. For measuring the chemical force of single molecules or single-cell surfaces with CNT SPM tips and using CNT nanoelectrodes for biosensing (35), the open end of the CNTs needs to be functionalized. Lieber et al. (25,91) demonstrated that the open end of an SWCNT is rich with the  $-COOH$  group and thus can be used for selective covalent bonding of primary amine molecules through amide bonds facilitated by the coupling reagents *N*-hydroxysuccinimide, sometimes aided with dicyclohexylcarbodiimide. Williams et al. (92) used similar methods to functionalize the open end of an SWCNT with a peptide nucleic acid (PNA) with the sequence  $NH_2$ -Glu-GTGCTCATGGTG- $CONH_2$ , in which Glu is a glutamate amino acid residue and the central block represents nucleic acid bases. A National Aeronautics and Space Administration (NASA) group demonstrated that primary amine-terminated DNA oligoprobes can be covalently functionalized to the open ends of an array of vertically aligned MWCNTs imbedded in  $SiO_2$  matrix by a similar carbodiimide chemistry using the water-soluble coupling reagents 1-ethyl-3(3-dimethyl aminopropyl) carbodiimide hydrochloride and *N*-hydroxysulfo-succinimide (93).

For FET sensors, functionalization to the sidewall of CNTs is required (33,34,94,95). Because semiconducting SWNTs are used as the conducting channels whose electronic properties are monitored up on the binding of charged target molecules at the surface, the graphitic  $sp^2$  sidewall structure has

to be preserved to maintain its inherent properties. Such a sidewall structure is strongly hydrophobic and chemically inert, which raises problems in biocompatibility and biofunctionalization for specific recognition. It has been reported that proteins such as streptavidin and HupR can adsorb strongly onto the MWCNT surface presumably via hydrophobic interactions between the aromatic CNT surface and hydrophobic domains of the proteins (41). A designed amphiphilic  $\alpha$ -helical peptide has been found to spontaneously assemble onto the SWCNT surface in aqueous solution with the hydrophobic face of the helix noncovalently interacting with the CNT surface and the hydrophilic amino acid side chains extending outward from the exterior surface (96). Chen et al. (94) reported a noncovalent sidewall functionalization scheme whereby a variety of proteins were immobilized on SWCNTs functionalized by  $\pi$ -stacking of the conjugate pyrenyl group of 1-pyrenebutanoic acid succinimidyl ester. The succinimidyl ester group reacts with amine groups on lysine residues of proteins to form covalent amide linkages (94). However, all such noncovalent interaction-based immobilization methods lack specificity; in particular, the direct nonspecific binding of proteins to the CNTs needs to be suppressed for biological sensing. Extensive washing using conventional protocols was not sufficient to remove such nonspecifically bound proteins. For this purpose, a surfactant (Triton-X 100) was coadsorbed on the CNT surface with polyethylene glycol (PEG) (95). Such a coating was found to be effective in resisting nonspecific adsorption of streptavidin. Amine-terminated PEG can be used so that the biotin moiety can be added to the PEG chains through covalent linking with an amine-reactive biotin reagent, biotinamidocaproic acid 3-sulfo-N-hydroxysuccinimide ester (95). The functionalized CNTs have demonstrated specific recognition to streptavidin. A similar method using mixed polyethylene imine (PEI) and PEG coating was reported for functionalizing biotin to the sidewall of SWCNTs in FET devices (34). These methods can be extended to the recognition of other biomolecules based on specific interactions of antibody-antigen and complementary DNA strands.

Besides the application in FET sensing devices, the biofunctionalized CNTs also show much better solubility so that further chemistry or biochemistry can be applied. In addition, biorecognition can be employed to regulate the assembly of supramolecular structures, which may lead to new sensing devices. Since the integrity of the CNT structure is not as critical in such applications as in FETs, covalent sidewall functionalizations are also actively pursued by the direct attachment of functional groups to the graphitic surface such as fluorination and hydrogenation or the use of carboxylic acids at the defect sites to form amide or ester linkages (97). Such sidewall functionalizations may particularly be applicable to MWCNT sensors in which CNTs only serve as the probe materials to transduce signals from the measured molecules and their own elec-

tronic properties are insensitive to the environment. For example, a MWCNT electrode functionalized with antibody or enzyme can be used as a single electrochemical probe to study biochemistry in a single cell (75). Sidewall functionalization of the MWCNT array can also greatly increase the enzyme (glucose oxidase) loading in the electrochemical glucose sensor (37). Some other studies on enzyme-based sensors using CNT-cast glassy carbon electrodes have demonstrated that even spontaneous adsorption or polymer wrapping can improve enzyme loading and electron transfer (78–80). From the biological side, peptides with selective affinity for CNTs were recently reported (98), which could lead to new methods for bio-nanointegration.

For metal NWs, such as Au, Ag, and Cu, strongly chemisorbed thiol molecules are commonly used as linkers for immobilizing biomolecules (99). Si or Ge NWs present a thin (approx 1 to 2 nm thick) native oxide film at the surface. Such NWs and other oxide NWs present abundant hydroxyl groups at the surface. Various silane molecules can be used as linkers to functionalize biomolecules (100,101). Polymer wrapping can also be applied to functionalize various NWs. Nonspecific adsorption could be used as well. Cui et al. (3) simply dipped Si NWs in biotinamidocaproyl-labeled bovine serum albumin followed by rinsing with phosphate buffer and demonstrated that specific binding with streptavidin target can be detected with a FET device down to at least a picomolar concentration range.

### 3. Applications and Mechanisms for Biological Sensing

#### 3.1. Single-Cell/Single-Molecule Probes

The most direct application of CNTs/NWs for biological sensing is to use them as single probes, which gives great spatial resolution. With the small size, such probes can be inserted into a single cell for *in situ* measurements with minimum disturbance as well as ultrahigh sensitivity. Vo-Dinh et al. (74) demonstrated antibody-based nanobiosensors for the detection of benzo[*a*] pyrene tetrol (BPT), a biomarker for human exposure to the known carcinogen benzo[*a*] pyrene, by simply pulling an optical fiber to nanometer sizes at the tip. The distal end was covalently coated with anti-BPT antibodies through silane linkers. The nanobiosensors were inserted into individual cells, incubated for 5 min to allow antigen-antibody binding, and then removed for detection. The small size of the tips of these optical fiber nanosensors gives them several advantages over normal probes, including decreased response time and increased sensitivity. Such a nanobiosensor, based on fluorescence spectroscopy, shows a sensitivity down to approx  $1.0 \times 10^{-10}$  M for BPT (74,102) and an absolute limit of detection for BPT of approx 300 zeptomol ( $10^{-21}$  mol) (103).

With the recent development in CNTs and NWs, such wirelike nanomaterials can be adapted for similar techniques. In particular, ZnO NWs have been found

with nanolasing properties along the axial direction (40,104), which could be explored for optical-biomolecular detection. CNTs or metal NWs, on the other hand, can be used as nanoelectrodes (75) to measure the electrochemical reaction in a single cell or the reactivity of a single molecule. The electrical signal has the potential to reach single molecular sensitivity, by using a nanoelectrode (87).

Single CNTs attached to a scanning probe microscope tip have also attracted intensive interest owing to their small diameter, high aspect ratio, large Young's modulus, and mechanical robustness (24). They can be used as physical probes to obtain the highest resolution in studying the structure of macromolecules or cell surfaces. Li et al. (26) demonstrated the method for implementing and characterizing CNTs attached to a scanning probe microscope (SPM) tip for *in situ* imaging of DNA molecules on a mica surface within a buffer solution. They used a magnetically driven oscillating probe atomic force microscope with a silicon nitride cantilever (spring constant of  $k = 0.1$ ) driven at a frequency of approximately kHz. A bundle of MWCNTs was attached to the pyramidal tip with an acrylic adhesive. The diameter of the bundles ranged from tens to hundreds of nanometers. Typically, a single MWCNT extended out and was used as a probe for SPM imaging.  $\lambda$  DNA molecules were spontaneously bound to the surface from 2  $\mu\text{g/mL}$  solutions with the presence of approx 1 mM  $\text{MgCl}_2$  for enhancing the DNA/mica interaction. **Figure 4** shows a SPM image of DNA molecules in a  $2.3 \times 2.3 \mu\text{m}^2$  area. Single DNA molecules were clearly resolved. The resolution of DNA images is very uniform and consistent with the diameter of the CNT tip (approx 5 nm). SWCNT tips could provide even higher resolution (25,91). The double-helix structure of DNA may be resolved in the future by SPM techniques using SWCNT tips. The tip can also be functionalized to provide additional information about chemical force (25,91).

Woolley et al. (105) reported the direct haplotyping of kilobase-size DNA using SWCNT SPM probes. The haplotype of a subject—the specific alleles associated with each chromosome homolog—is a critical element in single-nucleotide polymorphism (SNP) mapping that leads to a greater comprehension of the genetic contribution to risk of common diseases such as cancer and heart disease. However, current methods for determining haplotypes have significant limitations that have prevented their use in large-scale genetic screening. For example, molecular techniques for determining haplotypes, such as allele-specific or single-molecule polymerase chain reaction (PCR) amplification, are hampered by the need to optimize stringent reaction conditions and the potential for significant error rates. Using SPM with high-resolution SWCNT probes, multiple polymorphic sites can be directly visualized by hybridizing specifically labeled oligonucleotides with the template DNA frag-



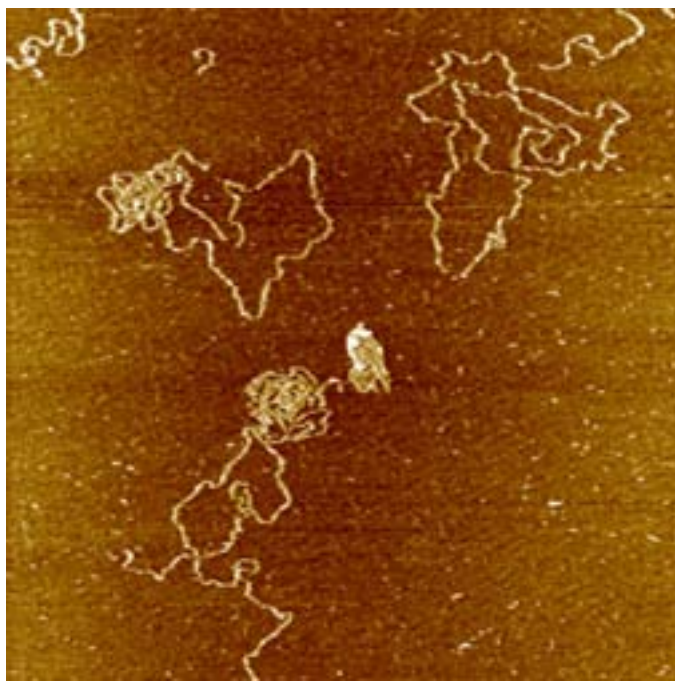


Fig. 4. SPM image of DNA molecules on  $2.3 \times 2.3 \mu\text{m}^2$  mica surface submerged under 1 mM  $\text{MgCl}_2$  buffer solution obtained with a single MWCNT tip.

ments of approx 100 to 10,000 bases. The positions of streptavidin and IRD800 labels at two sequences in M13mp18 were demonstrated. The SWCNT tips, with tip radii  $<3$  nm and resolution of approx 10 base, made it possible for high-resolution multiplex detection to differentiate between labels such as streptavidin and the fluorophore IRD800 based on their size. This concept has been further applied to the determination of haplotypes on the UGT1A7 gene (*105*), which is under study for its role in cancer epidemiology. Direct haplotyping using SWCNT SPM probes represents a significant advance over conventional approaches and could facilitate the use of SNPs for association and linkage studies of inherited diseases and genetic risk (*106*).

The electronic properties of biomolecules such as DNAs have been extensively studied in the past few years owing to their potential for single molecular sensing. However, DNA molecules were found to be not very conductive even in the duplex form. There are also difficulties in assembling them into reliable devices. Williams et al. (*92*) reported on a study to couple SWCNTs covalently with PNA (an uncharged DNA analog). Hybridization of DNA fragments to the PNA sequence was measured with an atomic force microscope

under ambient conditions and indicated that the functionalization is specific to the open ends of SWCNTs with rare attachment to the sidewall. PNA was chosen owing to its chemical and biological stability. The uncharged PNA backbone gives rise to PNA-DNA duplexes that are more thermally stable than their DNA-DNA counterparts because there is no electrostatic repulsion. This method unites the unique properties of SWCNTs with the specific molecular recognition features of DNA, which may provide new means to incorporate SWCNTs into larger electronic devices by recognition-based assembly as well as biological sensing.

### 3.2. FET Biosensors

FETs fabricated with S-SWCNTs (**1**) and S-NWs (**4**) have shown ultrahigh sensitivity for detecting gas molecules such as  $\text{NH}_3$ ,  $\text{O}_2$ , and  $\text{NO}_2$ . The high sensitivity and potential for fabricating high-density sensor array makes the nanoscale FETs very attractive. The same principle can be extended to biosensing, particularly since biomolecules such as DNA and proteins are heavily charged under most conditions. S-SWCNT FETs are more sensitive to the binding of such charged species than chemisorbed gas molecules. However, the wet chemical environment that involves various ions and other biomolecules is much more complicated than the operation for gas sensing. So far no direct measurement of the binding of biomolecules on S-SWCNT FETs in the liquid environment has been successfully demonstrated. Only a recent study by Star et al. (**34**) has demonstrated the effectiveness of the device structure for specific biotin-streptavidin binding by measurements in the *dried* condition after incubation and washing. A PEI/PEG polymer coating layer has been employed to avoid nonspecific binding. Biotin molecules were attached to the polymer layer for specific molecular recognition. Biotin-streptavidin binding has been detected by changes in the characteristics of a device. Nonspecific binding was observed in devices without the polymer coating, whereas no binding was found for polymer-coated but not biotinylated devices. Streptavidin, in which the biotin-binding sites were blocked by reaction with excess biotin, produced essentially no change in the characteristics of the biotinylated polymer-coated devices.

Besides the difficulty in obtaining direct measurements in liquids, S-SWCNT FET sensors face the problem that the property of the SWCNTs, whether it is semiconducting or metallic, is not controllable with current synthetic methods. A mixture of CNTs with properties varying in a wide range is produced, which makes systematic studies difficult. NWs of semiconductors such as Si and  $\text{In}_2\text{O}_3$  do not have this limitation because they are always semiconducting, and the dopant type and concentration can be controlled. As a result, the sensitivity can be tuned in the absence of an external gate.



Figure not available in electronic version of this product because the copyright owner has either withheld permission or permission could not be obtained.

Fig. 5. **(A)** Schematic of a biotin-modified SiNW in FET device (**left**) and after bound with streptavidin (**right**). **(B)** Plot of conductance vs time for a biotin-modified SiNW, in which region 1 corresponds to buffer solution, region 2 corresponds to addition of 250 nM streptavidin, and region 3 corresponds to pure buffer solution. **(C)** Conductance vs time for an unmodified SiNW; regions 1 and 2 are the same as in **(B)**. **(D)** Conductance vs time for a biotin-modified SiNW, in which region 1 corresponds to buffer solution and region 2 to addition of a 250 nM streptavidin solution preincubated with 4 eq of d-biotin. **(E)** Conductance vs time for a biotin-modified SiNW, in which region 1 corresponds to buffer solution, region 2 corresponds to addition of 25 pM streptavidin, and region 3 corresponds to pure buffer solution. Arrows mark the points when solutions were changed. (Reprinted from **ref. 3** with permission. Copyright 2001 American Association for the Advancement of Science.)

The functionalization of biorecognition probes to the oxide surface with silane linkers is also much more mature. Cui et al. (**3**) successfully demonstrated that boron-doped (p-type) SiNW FETs can be used to create highly sensitive, real-time electrically based sensors for biological and chemical species in buffer solutions. The SiNWs with the native oxide surface modified with

3-aminopropyltriethoxysilane exhibited pH-dependent conductance that was linear over a large dynamic range and could be understood in terms of the change in surface charge during protonation and deprotonation. Biotin-modified SiNWs were used to detect streptavidin down to at least a picomolar concentration range. As shown in **Fig. 5B**, the conductance of biotin-modified SiNWs increased almost instantly to a constant value (from region 1 to region 2) on the addition of 250 nM streptavidin in 1 mM phosphate buffer (pH 9.0) with 10 mM NaCl. This conductance value was maintained after switching to a flow of pure buffer solution (region 3), indicating that a negatively charged species was irreversibly bound to the p-type SiNW surface, consistent with the small dissociation constant ( $K_d \sim 10^{-15} M$ ) for biotin-streptavidin. By contrast, the conductance did not show any change on the addition of (1) the streptavidin solution with an unmodified SiNW (**Fig. 5C**) and (2) a streptavidin solution in which the biotin-binding sites were blocked by reaction with 4 eq of d-biotin with a biotin-modified SiNW (**Fig. 5D**), indicating no nonspecific binding of streptavidin in either case. A similar conductance change resulting from biotin-streptavidin binding was observed when the streptavidin concentration was lowered to 25 pM (**Fig. 5E**) with a possible detection limit of about 10 pM. In addition, biotin-functionalized SiNWs showed a decrease in conductance on the reversible specific binding of positively charged antibody (monoclonal antibiotin). Concentration-dependent detection was demonstrated in real time down to a concentration of a few nanomolar. Finally, detection of the reversible binding of the metabolic indicator  $\text{Ca}^{2+}$  was demonstrated using a calmodulin-modified SiNW. The small size, great reliability, and capability of these semiconductor NW FETs for sensitive, label-free, and real-time detection of a wide range of chemical and biological species have great potential for molecular diagnostics.

### 3.3. Nanoelectrode Array-Based Electrochemical Biosensors

The embedded CNT array minimizes background from the sidewalls while the well-defined graphitic chemistry at the exposed open ends allows the selective functionalization of  $-\text{COOH}$  groups with primary amine-terminated oligonucleotide probes through amide bonds. The wide electropotential window of carbon makes it possible to measure directly the oxidation signal of guanine bases immobilized at the electrode surface. The probe [Cy3]5'-CTIIAT TTCICAIITCCT-3'[AmC7-Q] and the target [Cy5]5'-AGGACCTGCGAA ATCCAGGGGGGGGGGG-3' are used, which are related to the wild-type (Arg1443stop) *BRCA1* gene (**107**). A 10-bp polyG is attached to the target sequence as the signal moiety and the guanine bases in the probe are replaced with inosine to ensure that guanine signal is only from target DNA. Hybridization is carried out at 40°C for about 1 h in approx 100 nM target solution in

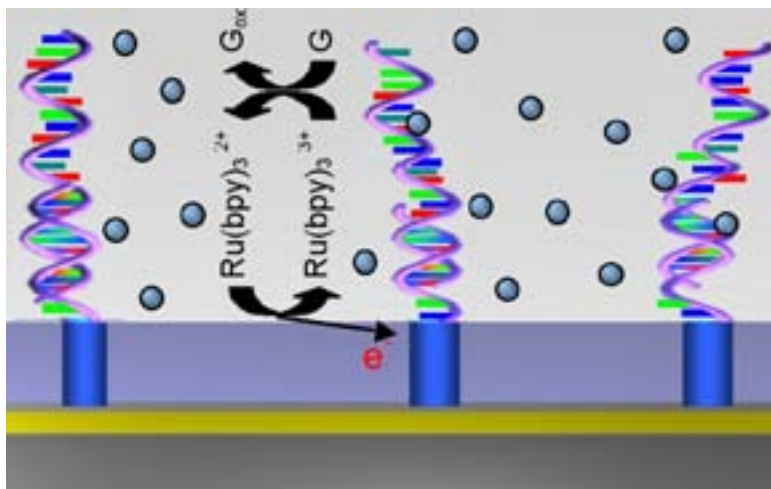


Fig. 6. Schematic of MWCNT nanoelectrode array combined with  $\text{Ru}(\text{bpy})_3^{2+}$ -mediated guanine oxidation for ultrasensitive DNA detection.

X3 saline sodium citrate (SSC) buffer solution. Rigorous washing using X3 SSC, X2 SSC with 0.1% sodium dodecyl sulfate, and X1 SSC, respectively, at  $40^\circ\text{C}$  for 15 min after each probe functionalization and target hybridization process are applied to get rid of the nonspecifically bound DNA molecules, which is critical for obtaining reliable electrochemical data.

Such a solid-state nanoelectrode array has great advantages in stability and processing reliability over other electrochemical DNA sensors based on mixed self-assembled monolayers of small organic molecules. The density of a nanoelectrode can be controlled precisely using lithographic techniques, which, in turn, define the number of probe molecules. The detection limit can be optimized by lowering the nanoelectrode density. However, the electrochemical signal is defined by the number of electrons that can be transferred between the electrode and analytes, which is observable only if it is over the level of the background. In particular, guanine oxidation occurs at rather high potential (approx 1.05 V vs saturated calomel electrode [SCE]) at which a high background is produced by carbon oxidation and water electrolysis. This problem can be solved by introducing  $\text{Ru}(\text{bpy})_3^{2+}$  mediators to amplify the signal based on an electrocatalytic mechanism (108). Combining the CNT nanoelectrode array with the  $\text{Ru}(\text{bpy})_3^{2+}$ -mediated guanine oxidation method (as schematically shown in Fig. 6), Li et al. (35) demonstrated that the hybridization of less than a few attomoles of oligonucleotide targets can be easily detected with a  $20 \times 20 \mu\text{m}^2$  electrode, with orders-of-magnitude improvement in sensitivity compared to previous electrochemically based DNA detections.

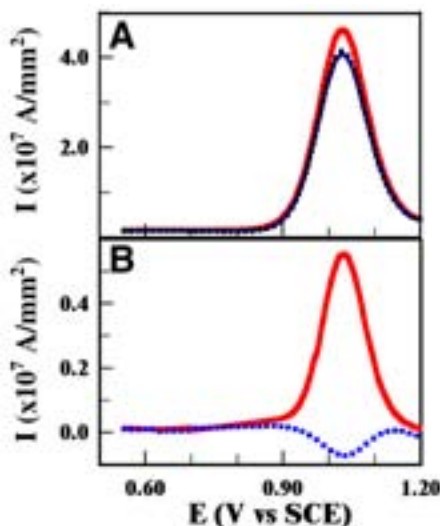


Fig. 7. (A) Three consecutive ACV measurements of low-density MWCNT array electrode functionalized with oligonucleotide probes with sequence [Cy3]5'-CTIAT TTCICAIITCCT-3'[AmC7-Q] and hybridized with oligonucleotide targets with sequence [Cy5]5'-AGGACCTGCGAAATCCAGGGGGGGGGG-3'. The thick, thin, and dotted lines correspond to the first, second, and third scan, respectively. Measurements were carried out in 5 mM Ru(bpy)<sub>3</sub><sup>2+</sup> in 0.20 M NaOAc supporting electrolyte (at pH 4.8) with an AC sinusoidal wave of 10 Hz and 25-mV amplitude on top of a staircase DC ramp. (B) Difference between first and second scans (solid line), and between second and third scans (dotted line), respectively. The positive peak corresponds to the increase in Ru(bpy)<sub>3</sub><sup>2+</sup> oxidation signal owing to the guanine bases on the surface. The negative peak serves as a control representing the behavior of a bare electrode.

**Figure 7A** shows three consecutive alternating current voltammetry (ACV) scans in 5 mM Ru(bpy)<sub>3</sub><sup>2+</sup> in 0.20 M NaOAc buffer solutions after hybridizing the polyG-tagged BRCA1 targets on an MWCNT array electrode (with average tube-tube spacing of approx 1.5 μm). The AC current is measured by applying a sinusoidal wave of 10-Hz frequency and 25-mV amplitude on a staircase potential ramp. Well-defined peaks are observed around 1.04 V, with the first scan clearly higher than the almost superimposed subsequent scans. The background is almost a flat line at zero. As shown in **Fig. 7B**, subtracting the second scan from the first gives a well-defined positive peak (continuous line), whereas subtracting the third scan from the second gives a small negative peak (dashed line) serving as an unambiguous negative control. The high quality of the data indicates that there is still plenty of room to lower the detection limit of target DNAs. In practical diagnosis, the target DNA consists of hun-

dreds of guanine bases as active signal moieties giving a much higher signal. Thus, the detection limit could be reduced well below 1 attomol. Successful electrochemical detection of PCR products using this platform was recently demonstrated. Other advantages of electrochemical detection, such as the ability to apply extra stringency control using an electrical field, could possibly be realized with this system.

The nanoelectrode array platform can also be extended to other electrode materials such as Au and Pt NWs. Different functionalization schemes and signal moieties have to be employed for different applications to take advantage of the spatial and temporal resolution of nanoelectrodes. This platform is also applicable for enzyme-based biosensors or for electrochemically based pathogen detection by immobilizing proteins such as enzymes and antibodies at the electrodes.

### **3.4. CNT Porous Film Electrodes**

Besides being used as building elements in well-defined devices, both SWCNTs and MWCNTs can be cast as a thin film on conventional electrodes (78–80) or used as a 3D porous film (32,36,37). CNTs serve both as large immobilization matrices and as mediators to improve electron transfer between the enzyme-active site and the electrochemical transducer. CNT-modified glassy carbon electrodes exhibit a substantial (490 mV) decrease in the overpotential for  $\beta$ -nicotinamide adenine dinucleotide oxidation. Various enzymes such as glucose oxidase and flavin adenine dinucleotide can spontaneously adsorb onto the CNT surface and maintain their substrate-specific enzyme activity over a prolonged period of time (78). Biosensors based on enzymes that catalyze important biological redox reactions (such as glucose oxidation) can be developed.

### **3.5. CNT/NW Templated Bioassembly**

It is of great interest to modify the external surface of CNTs or NWs with biological macromolecules, such as oligonucleotides (109), proteins (41,94), and peptides (96). Such bio-nanoassembly could promote the development of new biosensors and bioelectronic nanomaterials, which could take advantage of the specific biomolecular recognition properties associated with the bound macromolecules. For such purposes, the specific recognition function has to be densely packed on the outer surface of CNTs/NWs and the biomolecules such as proteins have to remain functional. A good criterion for the conservation of the functional properties of the protein is its ability to form ordered arrays.

Balavoine et al. (41) reported on a study of streptavidin assembly on CNTs to form helical crystallization. Streptavidin is very useful in many biochemical assays, such as labeling and affinity chromatography, owing to its high affinity

for (+) biotin ( $K_a \sim 10^{15}$ ). The assembly was carried out in solutions by spontaneous adsorption. MWCNTs were prepared by the arc-discharge method and stored as a suspension in methanol (approx 2 mg/mL). One hundred microliters of MWCNT suspension was dried under an ethane gas flow and resuspended in 20 mL of a 40% aqueous solution of methanol. This suspension was sonicated to disperse the MWCNTs prior to the addition of 20  $\mu$ L of streptavidin solution (approx 10  $\mu$ g/mL) in a buffer containing 10 mM Tris (pH 8.0) and 50 mM NaCl, and then it was allowed to stand at room temperature for 45 min. Such a sample was deposited on a carbon film-covered grid and was negatively stained with a 2% uranyl acetate solution for TEM imaging. In appropriate conditions, the MWCNT surface was found almost completely covered with streptavidin, presumably owing to the interaction with its hydrophobic domains. Even though most assemblies are disordered, some regular-spaced helical structures were observed at proper conditions. Another water-soluble protein, HupR, was also studied and showed ordered arrays on a wider range of MWCNT diameters than streptavidin.

A 29-residue amphiphilic  $\alpha$ -helical peptide was also specifically designed to coat and solubilize CNTs as well as control the assembly of the peptide-coated CNTs into macromolecular structures through peptide-peptide interactions (96). **Figure 8** shows a cross-sectional view of the molecular structure and a perspective view of the helical backbones of the model illustrating the assembly of such molecules on an SWCNT surface. Six such  $\alpha$ -helices are sufficient to surround the circumference of an individual SWCNT, while maintaining typical interhelical interactions. The hydrophobic face of the helix with apolar amino acid side chains (Val and Phe) presumably interacts non-covalently with the aromatic surface of CNTs, and the hydrophilic face extends outward to promote self-assembly through charged peptide-peptide interactions. Electron microscopy and polarized Raman studies reveal that the peptide-coated CNTs assemble into fibers with CNTs aligned along the fiber axis. The size and morphology of the fibers can be controlled by manipulating solution conditions that affect peptide-peptide interactions.

While the aforementioned studies are based on nonspecific adsorptions, Wang et al. (98) have used phage display to identify peptides with selective affinity for CNTs. Binding specificity has been confirmed by demonstrating direct attachment of nanotubes to phage and free peptides immobilized on microspheres. Consensus binding sequences show a motif rich in histidine and tryptophan at specific locations. Analysis of peptide conformations shows that the binding sequence is flexible and folds into a structure matching the geometry of CNTs. The hydrophobic structure of the peptide chains suggests that they act as symmetric detergents. An IgG monoclonal antibody against the fullerene C<sub>60</sub> (110) was also studied to show binding to CNTs with some selectivity (111).



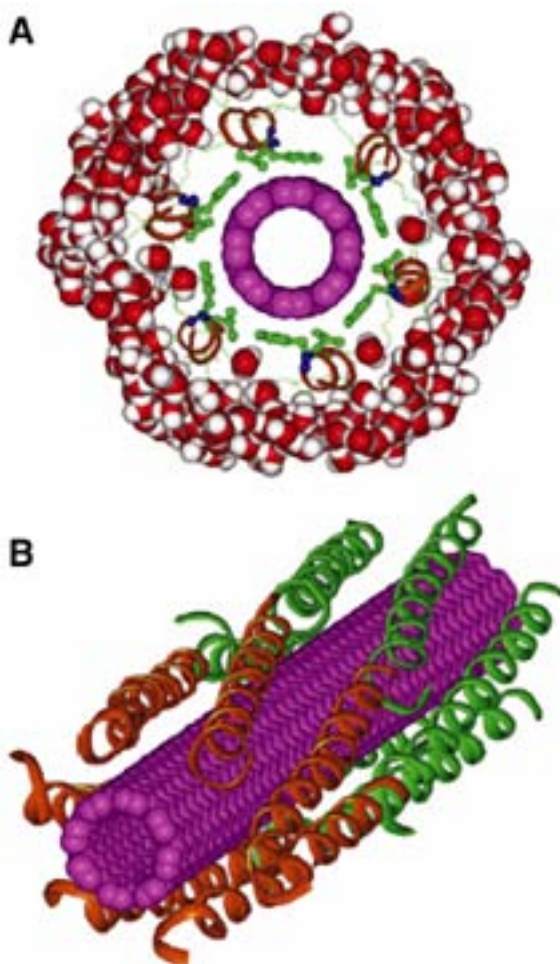


Fig. 8. Model of amphilphilic peptide helices assembled on an SWCNT surface. (A) Cross-section view showing six peptide helices wrapped around an SWCNT. A helical ribbon denotes the backbone of each peptide. The hydrophobic Val and Phe side chains are packed against the SWCNT surface. A 5-Å-thick water shell was used in the energy refinement. (B) View of a peptide-wrapped SWCNT with 12 peptide helices. The peptide formed two layers with head-to-tail alignment. (Reprinted from **ref. 96** with permission. Copyright 2003 American Chemical Society.)

### 3.6. Biomolecular Templated NW Assembly

The steady trend in the electronics industry toward components having ever-smaller dimensions has stimulated the development of alternative “bottom-up” fabrication technologies to compete with conventional micro- and nano-



lithography, which are expected to become extremely expensive as the feature sizes of future electronic circuits approach the limits of optical lithography (112). Bottom-up approaches, which rely on self-assembly (or self-organization) that often utilizes biological molecules, could provide viable solutions. Low fabrication costs and feature sizes below the current limit of optical lithography are two of the major advantages of bottom-up approaches. Biomolecules can also be employed as templates to deposit various solid materials to form nonhomogeneous NWs, which could possibly be used in electronics-based biosensors.

The chemical deposition of metals such as silver (42), gold (113), platinum (114,115), palladium (116,117), copper (118), and functionalized gold particles (119,120) on DNA has been investigated as a potential approach for creating conductive NWs. The molecular recognition properties of biomolecules are used for the defined buildup of a nanostructured circuit, and the electrical functionality is installed by the directed construction of a metallic wire on the biotemplate. Saxl (112) and Keren et al. (113) demonstrated that not only can conducting gold and silver NWs be constructed from DNA templates but also that specific regions of DNA molecules can be protected from metal deposition by associating proteins along sections of the DNA. The ability to control metallization spatially provides an important step toward the bottom-up assembly of functional nanocircuits. However, a nonconducting gap was sometimes observed at small bias voltages. Richter et al. (117) reported that palladium NWs chemically deposited on a DNA template showed highly conductive ohmic transport behavior. **Figure 9** shows low-voltage (1 kV) SEM images of a single palladium metallized DNA strand with a length of approx 16  $\mu\text{m}$  corresponding to the length of a linear  $\lambda$ -DNA molecule of 48,502 bp. The DNA molecule was positioned between macroscopic Au electrodes and metallized afterward with a two-step chemical deposition method, involving (1) activation of the template by treatment with Pd(II) complexes, which in part bind on the DNA strands, and (2) subsequent reduction of the complexes to form metallic clusters. Two-terminal I-V curves of such NWs showed a linear curve with a bias voltage down to 1  $\mu\text{V}$  (117). The specific conductivity for NWs with a diameter >50 nm was found only one order of magnitude below that of bulk palladium.

Recently, specific sequences of peptides were used to mineralize specific metals and semiconductors to produce highly crystalline nanocrystals that form nonhomogeneous NW assemblies. A good example is a new biological approach developed by Djalali et al. (121) to fabricate Au NWs using sequenced histidine-rich peptides as templates. Histidine-containing peptides are known to have high affinities to metal ions that damage central nervous systems by altering protein conformations into abnormal forms via histidine-

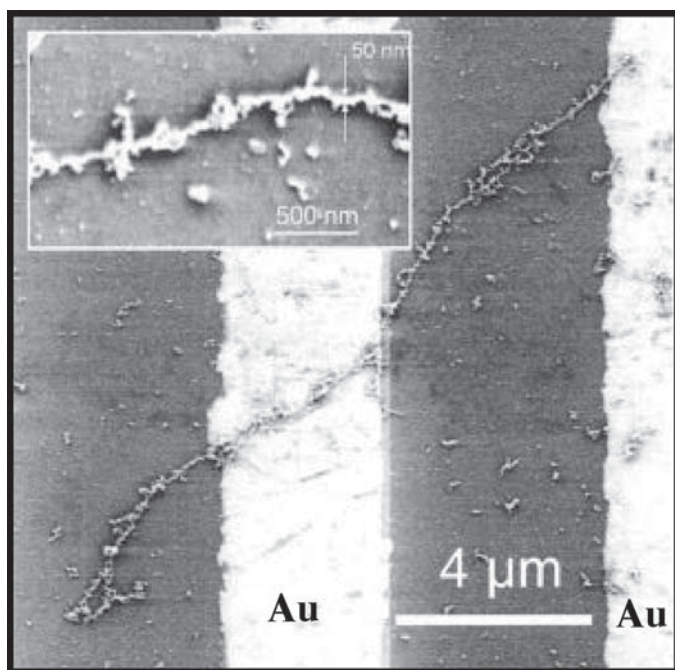


Fig. 9. SEM image of a single palladium metallized DNA strand with length of approx 16  $\mu\text{m}$  corresponding to length of a  $\lambda$ -DNA molecule. Two gold electrodes are deposited on the strands to measure the electrical property across the strand. The inset shows a magnification of the middle part with a diameter of 50 nm. (Reprinted from **ref. 117** with permission. Copyright 2001 American Institute of Physics.)

metal complexation, and this protein deformation may cause Parkinson disease and Alzheimer disease. Fabrication of the histidine-rich peptide involved four steps. First, *bis*(*N*- $\alpha$ -amido-glycylglycine)-1,7-heptane dicarboxylate molecules (10 mM) were self-assembled into NWs in a pH 5.5 citric acid/NaOH solution. Such NWs incorporate binding sites that have high affinity to biological molecules such as DNAs and proteins. Second, a histidine-rich peptide with the sequence A-H-H-A-H-H-A-A-D was immobilized on the heptane dicarboxylate NWs at the binding sites. Third, the histidine-rich peptide NWs were mixed with a  $\text{ClAuPMe}_3$  solution and incubated for 5 d to allow complete immobilization of Au ions. Finally, a reducing agent,  $\text{NaBH}_4$ , was added to produce Au nanocrystals. By using this method, monodispersed Au nanocrystals were uniformly coated on the histidine peptide NWs with high-density coverage, and the crystalline phases of the Au nanocrystals were observed with TEM.

#### 4. Conclusion

We have summarized recent progress in the development of biological sensors based on CNTs and NWs. The potential of these nanodevices for ultrasensitive biological sensing has been demonstrated from a technology development point of view. The reduction in the size of sensing and transducing elements approaching the size of biomolecules (i.e., 1–100 nm) makes it possible for detection down to single molecules. The development in this field may revolutionize current biotechnologies. However, while the sensitivity improves, the reliability may pose a problem, particularly at the level that only a handful of molecules are to be detected out from the sample containing many other molecules. Extensive efforts must be made in both device fabrication and assay development to solve this issue before the great potential and practical applications can be realized.

#### Acknowledgments

We wish to thank Drs. M. Meyyappan, Jie Han, Alan Cassell, Wendy Fan, and Harry Partridge for encouragement and technical discussions during preparation of the manuscript. This work was supported by a NASA contract.

#### References

1. Kong, J., Franklin, N. R., Zhou, C. W., Chapline, M. G., Peng, S., Cho, K., and Dai, H. (2000) Nanotube molecular wires as chemical sensors. *Science* **287**, 622–625.
2. Li, J. and Ng, H. T. (2004) Carbon nanotube sensors, in *Encyclopedia of Nanoscience and Nanotechnology* (Nalwa, H. S., ed.), American Scientific Publishers, Santa Barbara, CA, Vol. 1, 591–601.
3. Cui, Y., Wei, Q., Park, H., and Lieber, C. M. (2001) Nanowire nanosensors for highly sensitive and selective detection of biological and chemical species. *Science* **293**, 1289–1292.
4. Li, C., Zhang D., Liu X., Han, S., Tang, T., Han, J., and Zhou C. (2003) In<sub>2</sub>O<sub>3</sub> nanowires as chemical sensors. *Appl. Phys. Lett.* **82**(10), 1613–1615.
5. Dresselhaus, M. S., Dresselhaus, G., and Eklund, P. C. (ed.). (1996) *Science of Fullerenes and Carbon Nanotubes*, Academic, New York.
6. Ebbesen, T. W. (1997) *Carbon Nanotubes: Preparation and Properties*, CRC Press, Boca Raton, FL.
7. Saito, R., Dresselhaus, M. S., and Dresselhaus, G. (1998) *Physical Properties of Carbon Nanotubes*, World Scientific, New York.
8. Tománek, D. and Enbody, R. (2000) *Science and Application of Nanotubes*, Kluwer Academic, New York.
9. Iijima, S. (1991) Helical microtubules of graphitic carbon. *Nature* **354**, 56–58.
10. Iijima, S. and Ichihashi, T. (1993) Single-shell carbon nanotubes of 1-nm diameter. *Nature* **363**, 603–605.
11. Dai, H. (2002) Carbon nanotubes: synthesis, integration, and properties. *Acc. Chem. Res.* **35**(12), 1035–1044.

12. Collins, P. G., Arnold, M. S., and Avouris, P. (2001) Engineering carbon nanotubes and nanotube circuits using electrical breakdown. *Science* **292**, 706–709.
13. Tans, S. J., Verschueren, A. R. M., and Dekker, C. (1998) Room-temperature transistor based on a single carbon nanotube. *Nature* **393**, 49–52.
14. Fuhrer, M. S., Nygard, J., Shih, L., et al. (2000) Crossed nanotube junctions. *Science* **288**, 494–497.
15. Zhou, C. W., Kong, J., Yenilmez, E., and Dai, H. (2000) Modulated chemical doping of individual carbon nanotubes. *Science* **290**, 1552–1555.
16. Rueckes, T., Kim, K., Joselevich, E., Tseng, G. Y., Cheung, C. L., and Lieber, C. M. (2000) Carbon nanotube-based nonvolatile random access memory for molecular computing. *Science* **289**, 94–97.
17. Derycke, V., Martel, R., Appenzeller, J., and Avouris, P. (2001) Carbon nanotube inter- and intramolecular logic gates. *Nano Lett.* **1**(9), 453–456.
18. Bachtold, A., Hadley, P., Nakanishi, T., and Dekker, C. (2001) Logic circuits with carbon nanotube transistors. *Science* **294**, 1317–1320.
19. Liu, X. L., Lee, C., Zhou, C. W., and Han, J. (2001) Carbon nanotube field-effect inverters. *Appl. Phys. Lett.* **79**(20), 3329–3331.
20. Rosenblatt, S., Yaish, Y., Park, J., Gore, J., Sazonova, V., and McEuen, P. L. (2002) High performance electrolyte gated carbon nanotube transistors. *Nano Lett.* **2**(8), 869–872.
21. Vigolo, B., Penicaud, A., Coulon, C., Sauder, C., Pailler, R., Journet, C., Bernier, P., and Poulin, P. (2000) Macroscopic fibers and ribbons of oriented carbon nanotubes. *Science* **290**, 1331–1334.
22. de Heer, W. A., Chatelain, A., and Ugarte, D. (1995) A carbon nanotube field-emission electron source. *Science* **270**, 1179, 1180.
23. Rinzler, A. G., Hafner, J. H., Nikolaev, P., Lou, L., Kim, S. G., Tomanek, D., Nordlander, P., Colbert, D. T., and Smalley, R. E. (1995) Unraveling nanotubes: field emission from an atomic wire. *Science* **269**, 1550–1553.
24. Dai, H., Hafner, J. H., Rinzler, A. G., Colbert, D. T., and Smalley, R. E. (1996) Nanotubes as nanoprobe in scanning probe microscopy. *Nature* **384**, 147–150.
25. Wong, S., Joselevich, E., Woolley, A., Cheung, C., and Lieber, C. M. (1998) Covalently functionalized nanotubes as nanometer-sized probes in chemistry and biology. *Nature* **394**, 52–55.
26. Li, J., Cassell, A., and Dai, H. (1999) Carbon nanotubes as AFM tips: measuring DNA molecules at the liquid/solid interfaces. *Surf. Interface Anal.* **28**, 8–11.
27. Nguyen, C. V., Chao, K. J., Stevens, R. M. D., Delzeit, L., Cassell, A., Han, J., and Meyyappan, M. (2001) *Nanotechnology* **12**, 363–367.
28. Liu, C. F., Fan, Y. Y., Liu, M., Cong, H. T., Chen, H. M., and Dresselhaus, M. S. (1999) Hydrogen storage in single-walled carbon nanotubes at room temperature. *Science* **286**, 1127–1129.
29. Che, G., Lakshmi, B. B., Fisher, E. R., and Martin, C. R. (1998) Carbon nanotubule membranes for electrochemical energy storage and production. *Nature* **393**, 346–349.

30. Collins, P. G., Bradley, K., Ishigami, M., and Zettl, A. (2000) Extreme oxygen sensitivity of electronic properties of carbon nanotubes. *Science* **287**, 1801–1804.
31. Sumanasekera, G. U., Adu, C. K. W., Fang, S., and Eklund, P. C. (2000) Effects of gas adsorption and collisions on electrical transport in single-walled carbon nanotubes. *Phys. Rev. Lett.* **85**(5), 1096–1099.
32. Ng, H. T., Fang, A., Li, J., and Li, S. F. Y. (2001) Flexible carbon nanotube membrane sensory system: a generic platform. *J. Nanosci. Nanotechnol.* **1**(4), 375–379.
33. Besteman, K., Lee, J.-O., Wiertz, F. G. M., Heering, H. A., and Dekker, C. (2003), Enzyme-coated carbon nanotubes as single-molecule biosensors. *Nano Lett.* **3**(6), 727–730.
34. Star, A., Gabriel, J.-C. P., Bradley K., and Gruner, G. (2003), Electronic detection of specific protein binding using nanotube FET devices. *Nano Lett.*, in press.
35. Li, J., Ng, H. T., Cassell, A., Fan, W., Chen, H., Ye, Q., Koehne, J., Han, J., and Meyyappan, M. (2003), Carbon nanotube nanoelectrode array for ultrasensitive DNA detection. *Nano Lett.* **3**(5), 597–602.
36. Li, J., Cassell, A., Delzeit, L., Han, J., and Meyyappan, M. (2002) Novel three-dimensional electrodes: electrochemical properties of carbon nanotube ensembles. *J. Phys. Chem. B* **106**, 9299–9305.
37. Sotiropoulou, S. and Chaniotakis, N. A. (2003) Carbon nanotube array-based biosensor. *Anal. Bioanal. Chem.* **375**, 103–105.
38. Walter, E. C., Penner R. M., Liu, H., Ng, K. H., Zach, M. P., and Favier, F. (2002) Sensors from electrodeposited metal nanowires. *Surf. Interface Anal.* **34**, 409–412.
39. Morales, A. M. and Lieber, C. M. (1998) A laser ablation method for the synthesis of crystalline semiconductor nanowires. *Science* **279**, 208–211.
40. Huang, M. H., Mao, S. Feick, H., Yan, H., Wu, Y., Kind, H., Weber, E., Russo, R., and Yang, P. (2001) Room-temperature ultraviolet nanowires nanolasers. *Science* **292**, 1897–1899.
41. Balavoine, F., Schultz, P., Richard, C., Mallouh, V., Ebbesen, T. W., and Mioskowski, C. (1999) Helical crystallization of proteins on carbon nanotubes: a first step towards the development of new biosensors. *Angew. Chem. Int. Ed.* **38**(13/14), 1912–1915.
42. Braun, E., Eichen, Y., Sivan, U., and Ben-Yoseph, G. (1998) DNA-templated assembly and electrode attachment of a conducting silver wire. *Nature* **391**, 775–778.
43. Bethune, D. S., Kiang, C. H., de Vries, M. S., Gorman, G., Savoy, R., Vazquez, J., and Beyers, R. (1993) Cobalt-catalyzed growth of carbon nanotubes with single-atomic-layer walls. *Nature* **363**, 605–607.
44. Thess, A., Lee, R., Nikolaev, P., et al. (1996) Crystalline ropes of metallic carbon nanotubes. *Science* **273**, 483–487.
45. Kajiura, H., Tsutsui, S., Huang, H., Miyakoshi, M., Hirano, Y., Yamada, A., and Ata, M. (2001) Production of single-walled carbon nanotube ropes under controlled gas flow conditions. *Chem. Phys. Lett.* **346**, 356–360.

46. Journet, C., Maser, W., Bernier, P., Loiseau, A., Delachapelle, M., Lefrant, S., Deniard, P., Lee, R., and Fischer, J. (1997) Large-scale production of single-walled carbon nanotubes by the electric-arc technique. *Nature* **388**, 756–758.
47. Kong, J., Cassell, A. M., and Dai, H. (1998) Chemical vapor deposition of methane for single-walled carbon nanotubes. *Chem. Phys. Lett.* **292**, 567–574.
48. Su, M., Zheng, B., and Liu, J. (2000) A scalable CVD method for the synthesis of single-walled carbon nanotubes with high catalyst productivity. *Chem. Phys. Lett.* **322**, 321–326.
49. Colomer, J.-F., Stephan, C., Lefrant, S., Tendeloo, G., Willems, I., Kónya, Z., Fonseca, A., Laurent, C., and Nagy, J. (2000) Large-scale synthesis of single-wall carbon nanotubes by catalytic chemical vapor deposition (CCVD) method. *Chem. Phys. Lett.* **317**, 83–89.
50. Flahaut, E., Govindaraj, A., Peigney, A., Laurent, C., and Rao, C. N. R. (1999) Synthesis of single-walled carbon nanotubes using binary (Fe, Co, Ni) alloy nanoparticles prepared in situ by the reduction of oxide solid solutions. *Chem. Phys. Lett.* **300**, 236–242.
51. Hafner, J., Bronikowski, M., Azamian, B., Nikolaev, P., Colbert, D., and Smalley, R. E. (1998) Catalytic growth of single-wall carbon nanotubes from metal particles. *Chem. Phys. Lett.* **296**, 195–202.
52. Bronikowski, M. J., Willis, P. A., Colbert, D. T., Smith, K. A., and Smalley, R. E. (2001) Gas-phase production of carbon single-walled nanotubes from carbon monoxide via the HiPco process: a parametric study. *J. Vac. Sci. Technol. A* **19**, 1800–1805.
53. Ren, Z. F., Huang, Z. P., Xu, J. W., Wang, J. H., Bush, P., Siegal, M. P., and Provencio, P. N. (1998) Synthesis of large arrays of well-aligned carbon nanotubes on glass. *Science* **282**, 1105–1107.
54. Delzeit, L., McAninch, I., Cruden, B. A., Hash, D., Chen, B., Han, J., and Meyyappan, M. (2002) Growth of multiwall carbon nanotubes in an inductively coupled plasma reactor. *J. Appl. Phys.* **91**, 6027–6033.
55. Li, J., Ye, Q., Cassell, A., Ng, H. T., Stevens, R., Han, J., and Meyyappan, M. (2003) Bottom-up approach for carbon nanotube interconnects. *Appl. Phys. Lett.* **82**(15), 2491–2493.
56. Stejny, J. J., Trinder, R. W., and Dlugosz, J. (1981) Preparation and structure of poly(sulphur nitride) whiskers. *J. Mater. Sci.* **16**, 3161–3170.
57. Golden, J. H., DiSalvo, F. J., Frecht, J. M. J., Silcox, J., Thomas, M., and Elman, J. (1996) Subnanometer-diameter wires isolated in a polymer matrix by fast polymerization. *Science* **273**, 782–785.
58. Venkataraman, L. and Lieber, C. M. (1999) Molybdenum selenide molecular wires as one-dimensional conductors. *Phys. Rev. Lett.* **83**, 5334–5337.
59. Gates, B., Mayers, B., Cattle, B., and Xia, Y. (2002) Synthesis and characterization of uniform nanowires of trigonal selenium. *Adv. Funct. Mater.* **12**, 219–227.
60. Limmer, S. J., Seraji, S., Wu, Y., Chou, T. P., Nguyen, C., and Cao, G. (2002) Template-based growth of various oxide nanorods by sol-gel electrophoresis. *Adv. Funct. Mater.* **12**, 59–64.



61. Barbic, M., Mock, J. J., Smith, D. R., and Schultz, S. (2002) Single crystal silver nanowires prepared by the metal amplification method. *J. Appl. Phys.* **91**, 9341–9345.
62. Molaes, M. E. T., Buschmann, V., Dobrev, D., Neumann, R., Scholz, R., Schuchert, I. U., and Vetter, J. (2001) Single-crystalline copper nanowires produced by electrochemical deposition in polymeric ion track membranes. *Adv. Mater.* **13**, 62–65.
63. Müller, T., Heinig, K.-H., and Schmidt, B. (2001) Formation of Ge nanowires in oxidized silicon V-grooves by ion beam synthesis. *Nucl. Instrum. Methods Phys. Res.* **175**, 468–473.
64. Sugawara, A., Coyle, T., Hembree, G. G., and Scheinfein, M. R. (1997) Self-organized Fe nanowire arrays prepared by shadow deposition on NaCl(110) templates. *Appl. Phys. Lett.* **70**, 1043–1045.
65. Xia, Y., Yang, P. Sun, Y., Wu, Y., Mayers, B., Gates, B., Yin, Y., Kim, F., and Yan, H. (2003) One-dimensional nanostructures: synthesis, characterization, and applications. *Adv. Mater.* **15**, 353–389.
66. Zhang, Y., Wang, N., Gao, S., He, R., Maio, S., Liu, J., Zhu, J., and Zhang, X. (2002) A simple method to synthesize nanowires. *Chem. Mater.* **14**, 3564–3568.
67. Yang, P. and Lieber, C. M. (1997) Nanostructured high-temperature superconductors: creation of strong-pinning columnar defects in nanorod/superconductor composites. *J. Mater. Res.* **12**, 2981–2996.
68. Shi, W.-S., Peng, H.-Y., Zheng, Y.-F., Wang, N., Shang, N.-G., Pan, Z.-W., Lee, C.-S., and Lee, S.-T. (2000) Synthesis of large areas of highly oriented, very long silicon nanowires. *Adv. Mater.* **12**, 1343–1345.
69. Duan, X. F. and Lieber, C. M. (2000) General synthesis of compound semiconductor nanowires. *Adv. Mater.* **12**, 298–302.
70. Wu, Y. and Yang, P. (2000) Germanium nanowire growth via simple vapor transport. *Chem. Mater.* **12**, 605–607.
71. Chen, C. C., Yeh, C. C., Chen, C. H., Yu, M. Y., Liu, H. L., Wu, J. J., Chen, K. H., Chen, L. C., Peng, J. Y., and Chen, Y. F. (2001) Catalytic growth and characterization of gallium nitride nanowires. *J. Am. Chem. Soc.* **123**, 2791–2798.
72. Wang, Y. W., Zhang, L. D., Liang, C. H., Wang, G. Z., and Peng, X. S. (2002) Catalytic growth and photoluminescence properties of semiconductor single-crystal ZnS nanowires. *Chem. Phys. Lett.* **357**, 314–318.
73. Huang, M. H., Feick, H., Webber, E., and Yang, P. (2001) Catalytic growth of zinc oxide nanowires through vapor transport. *Adv. Mater.* **13**, 113–116.
74. Vo-Dinh, T., Alarie, J.-P., Cullum, B. M., and Griffin, G. D. (2000) Antibody-based nanoprobe for measurement of a fluorescent analyte in a single cell. *Nat. Biotechnol.* **18**, 764–767.
75. Campbell, J. K., Sun, L., and Crooks, R. M. (1999) Electrochemistry using single carbon nanotubes. *J. Am. Chem. Soc.* **121**, 3779–3780.
76. Bard, A. J. (1994) *Integrated Chemical Systems: A Chemical Approach to Nanotechnology*, John Wiley & Sons, New York, pp. 27–33.



77. Zhao, J., Buldum, A., Han, J., and Lu, J. P. (2002) Gas molecule adsorption in carbon nanotubes and nanotube bundles. *Nanotechnology* **13**, 195–200.
78. Guiseppi-Elie, A., Lei, C., and Baughman, R. H. (2002) Direct electron transfer of glucose oxidase on carbon nanotubes. *Nanotechnology* **13**, 559–564.
79. Azamian, B. R., Davis, J. J., Coleman, K. S., Bagshaw, C. B., and Green, M. L. H. (2002) Bioelectrochemical single-walled carbon nanotubes. *J. Am. Chem. Soc.* **124**, 12,664, 12,665.
80. Musameh, M., Wang, J., Merkoci, A., and Lin, Y. (2002) Low-potential stable NADH detection at carbon-nanotube-modified glassy carbon electrodes. *Electrochem. Commun.* **4**, 743–746.
81. Kuhr, W. G. (2000) Electrochemical DNA analysis comes of age. *Nat. Biotechnol.* **18**, 1042, 1043.
82. Sosnowski, R. G., Tu, E., Butler, W. F., O'Connell, J. P., and Heller, M. J. (1997) Rapid determination of single base mismatch mutations in DNA hybrids by direct electric field control. *Proc. Natl. Acad. Sci. USA* **94**, 1119–1123.
83. Umek R. M., Lin, S. W., Vielmetter, J., et al. (2001) Electronic detection of nucleic acids: a versatile platform for molecular diagnosis. *J. Mol. Diagn.* **3**(2), 74–84.
84. Popovich, N. D. and Thorp H. H. (2002) New strategies for electrochemical nucleic acid detection. *Interface* **11**(4), 30–34.
85. Wightman, R. M. (1981) Microvoltammetric electrodes. *Anal. Chem.* **53**, 1125A–1134A.
86. Penner, R. M., Heben, M. J., Longin, T. L., and Lewis, N. S. (1990) Fabrication and use of nanometer-sized electrodes in electrochemistry. *Science* **250**, 1118–1121.
87. Fan, F.-R. F. and Bard, A. J. (1995) Electrochemical detection of single molecules. *Science* **267**, 871–874.
88. Li, J., Stevens, R., Delzeit, L., Ng, H. T., Cassell, A. M., Han, J., and Meyyappan, M. (2002) Electronic properties of multiwalled carbon nanotubes in an embedded vertical array. *Appl. Phys. Lett.* **81**(5), 910–912.
89. McCreery, R. L. (1991) Carbon electrodes: structural effects on electron transfer kinetics, in *Electroanalytical Chemistry* vol. 17 (Bard, A. J., ed.), Marcel Dekker, New York, pp. 221–374.
90. Nugent, J. M., Santhanam, R. A., and Ajayan, P. M. (2001) Fast electron transfer kinetics on multiwalled carbon nanotube microbundle electrodes. *Nano Lett.* **1**(2), 87–91.
91. Wong, S. S., Woolley, A. T., Joselevich, E., Cheung, C. L., and Lieber, C. M. (1998) Covalent-functionalized single-walled carbon nanotube probe tips for chemical force microscopy. *J. Am. Chem. Soc.* **120**, 8557, 8558.
92. Williams, K. A., Veenhuizen, P. T. M., De la Torre, B. G., Eritja, R., and Dekker, C. (2002) Carbon nanotubes with DNA recognition. *Nature* **429**, 761.
93. Nguyen, C. V., Delzeit, L., Cassell, A. M., Li, J., Han, J., and Meyyappan, M. (2002) Preparation of nucleic acid functionalized carbon nanotube arrays. *Nano Lett.* **2**(10), 1079–1081.

94. Chen, R. J., Zhang, Y., Wang, D., and Dai, H. (2001) Noncovalent sidewall functionalization of single-walled carbon nanotubes for protein immobilization. *J. Am. Chem. Soc.* **123**, 3838, 3839.
95. Shim, M., Kam, N. W. S., Chen, R. J., Li, Y., and Dai, H. (2002) Functionalization of carbon nanotubes for biocompatibility and biomolecular recognition. *Nano Lett.* **2**(4), 285–288.
96. Dieckmann, G. R., Dalton, A. B., Johnson, P. A., et al. (2003) Controlled assembly of carbon nanotubes by designed amphiphilic peptide helices. *J. Am. Chem. Soc.* **125**(7), 1770–1777.
97. Sun, Y.-P., Fu, K., Lin, Y., and Huang, W. (2002) Functionalized carbon nanotubes: properties and applications. *Acc. Chem. Res.* **35**, 1096–1104.
98. Wang, S., Humphreys, E. S., Chung, S. Y., et al. (2003) Peptides with selective affinity for carbon nanotubes. *Nat. Mater.* **2**(3), 196–200.
99. Ulman, A. (1991) *An Introduction to Ultrathin Organic Films: From Langmuir-Blodgett to Self-Assembly*, Academic, New York.
100. Guo, Z., Guilfoyle, R. A., Thiel, A. J., Wang, R., and Smith, L. M. (1994) Direct fluorescence analysis of genetic polymorphisms by hybridization with oligonucleotide arrays on glass supports. *Nucleic Acids Res.* **22**(24), 5456–5465.
101. Beier, M. and Hoheisel, J. D. (1999) Versatile derivatisation of solid support media for covalent bonding on DNA-microchips. *Nucleic Acids Res.* **27**(9), 1970–1977.
102. Vo-Dinh, T. (2002) Nanobiosensors: probing the sanctuary of individual living cells. *J. Cell. Biochem. Suppl.* **39**, 154–161.
103. Vo-Dinh, T., Cullum, B. M., and Stokes, D. L. (2001) Nanosensors and biochips: frontiers in biomolecular diagnostics. *Sens. Actuators B* **74**, 2–11.
104. Johnson, J. C., Yan, H., Schaller, R., Haber, L. H., Saykally, R. J., and Yang, P. (2001) Single nanowires lasers. *J. Phys. Chem. B* **105**(46), 11,387–11,390.
105. Woolley, A. T., Guillemette, C., Cheung, C. L., Housman, D. H., and Lieber, C. M. (2000) Direct haplotyping of kilobase-size DNA using carbon nanotube probes. *Nat. Biotechnol.* **18**, 760–763.
106. Andrew, T. and Mirkin, C. A. (2000) Haplotyping by force. *Nat. Biotechnol.* **18**, 713.
107. Miki, Y., Swensen, J., Shattuck-Eidens, D., Futreal, P. A., Harshman K., Tavtigian, S., Liu, Q., Cochran, C., Bennett, L. M., and Ding, W. (1994) A strong candidate for the breast and ovarian cancer susceptibility gene BRCA1. *Science* **266**, 66–69.
108. Sistare, M. F., Holmberg, R. C., and Thorp, H. H. (1999) Electrochemical studies of polynucleotide binding and oxidation by metal complexes: effects of scan rate, concentration, and sequence. *J. Phys. Chem. B* **103**, 10,718–10,728.
109. Guo, Z., Sadler, P. J., and Tsang, S. C. (2002) Immobilization and visualization of DNA and proteins on carbon nanotubes. *Adv. Mater.* **10**(9), 701–703.
110. Braden, B. C. (2000) X-ray crystal structure of an anti-Buckminsterfullerene antibody Fab fragment: biomolecular recognition of C60. *Proc. Natl. Acad. Sci. USA* **97**, 12,193–12,197.

111. Erlanger, B. F., Chen, B.-X., Zhu, M., and Brus, L. (2001) Binding of an anti-fullerene IgG monoclonal antibody to single wall carbon nanotubes. *Nano Lett.* **1**, 465–467.
112. Saxl, O. (2001) *Opportunities for industry in the application of nanotechnology*. The Institute of Nanotechnology, Stirling, Scotland (<http://www.nano.org.uk/contents.htm>).
113. Keren, K., Krueger, M., Gilad, R., Ben-Yoseph, G., Sivan, U., and Braun, E. (2002) Sequence-specific molecular lithography on single DNA molecules. *Science* **297**, 72–75.
114. Ford, W., Harnack, O., Yasuda, A., and Wessels, J. M. (2001) Platinated DNA as precursors to templated chains of metal nanoparticles. *J. Adv. Mater.* **13**, 1793–1797.
115. Seidel, R., Mertig, M., and Pompe, W. M. (2002) Scanning force microscopy of DNA metallization. *Surf. Interface Anal.* **33**, 151–154.
116. Richter, J., Seidel, R., Kirsh, R., Mertig, M., Pompe, W., Plaschke, J., and Schackert, H. K. (2000) Nanoscale palladium metallization of DNA. *Adv. Mater.* **12**, 507–510.
117. Richter, J., Mertig, M., Pompe, W., Mönch, I., and Schackert, H. K. (2001) Construction of highly conductive nanowires on a DNA template. *Appl. Phys. Lett.* **78**, 536–538.
118. Christopher, A., Monon, F., and Woolley, A. T. (2003) DNA-templated construction of copper nanowires. *Nano Lett.* **3**(3), 359–363.
119. Harnack, O., Ford, W. E., Yasuda, A., and Wessels, J. M. (2002) Tris(hydroxymethyl)phosphine-capped gold particles templated by DNA as nanowire precursors. *Nano Lett.* **2**(9), 919–923.
120. Patolsky, F., Weizmann, Y., Lioubashevski, O., and Willner, I. (2002) Au-nanoparticle nanowires based on DNA and polylysine templates. *Angew. Chem. Int. Ed.* **41**(13), 2323–2327.
121. Djalali, R., Chen, Y., and Matsui, H. (2002) Au nanowire fabrication from sequenced histidine-rich peptide. *J. Am. Chem. Soc.* **124**(46), 13,660–13,661.



## Carbon Nanotube Systems to Communicate With Enzymes

J. Justin Gooding and Joe G. Shapter

### Summary

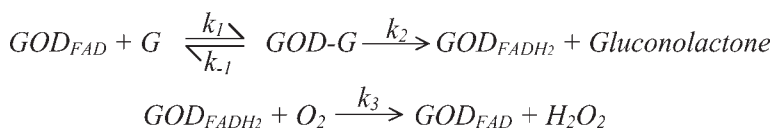
The efficient transfer of electrons between enzymes and electrodes is important for understanding the intrinsic redox properties as well as for developing protein-based biosensors and bioelectronic devices. One strategy to achieve efficient electron transfer to proteins is to build up the electrode inside the protein so that it is close to the redox-active center of the protein. To achieve this requires exceedingly small electrodes. Carbon nanotubes, which are as small as 1 nm in diameter, have the potential to be such electrodes. This chapter outlines recent research toward this goal via the self-assembly of vertically aligned single-walled carbon nanotubes on electrode surfaces followed by the subsequent attachment of proteins to the free ends of the tubes.

**Key Words:** Carbon nanotubes; self-assembly; microperoxidase MP-11; glucose oxidase; electrochemistry; enzyme electrodes; alkanethiols; self-assembled monolayers; atomic force microscopy.

### 1. Introduction

Research into the interaction and electron exchange between redox enzymes and an electrode interface is important for two reasons: first, it is helpful to understand the intrinsic redox properties of proteins (**1,2**); and second, direct electron transfer between enzymes and electrodes is the key to the development of mediatorless, also called third-generation, enzyme biosensors. With a mediatorless biosensor, no cosubstrate is required in the recycling of the enzyme back to its active form. This concept of the mediatorless enzyme biosensor is most applicable to the oxidoreductase enzymes where, as shown in **Scheme 1** for glucose oxidase, the enzyme oxidizes glucose and is reduced in the process. The recycling of the enzyme back to its active oxidized form is achieved using either oxygen in nature or another mediating species such as ferrocene (as used in many glucose meters). The ability of the enzyme

From: *Methods in Molecular Biology*, vol. 300:  
*Protein Nanotechnology, Protocols, Instrumentation, and Applications*  
Edited by: T. Vo-Dinh © Humana Press Inc., Totowa, NJ



Scheme 1. Reaction mechanism for glucose oxidase oxidizing glucose to gluconolactone.

to be oxidized and reduced directly at the electrode would obviate this second reaction, which has implications for reliably sensing *in vivo* and in other environments where cosubstrate concentration may vary.

The redox centers of most redox-active biological molecules are imbedded deep within the glycoprotein (**1**). For example, in the case of glucose oxidase, the closest approach between the exterior of the protein and the redox-active center flavin adenine dinucleotide (FAD) is 13 Å (**3**). As a consequence, electrons cannot be efficiently transferred between the enzyme and the electrode and hence, mediators, or redox relays, are required. There are some exceptions, such as the peroxidase enzymes, laccase and “blue” copper protein, and azurin, in which the redox centers are located close to the surface of the protein and, hence, can be interrogated electrochemically. There have been a variety of approaches to improving the communication between the electrode and the enzyme that usually involve modifying either the electrode or the protein to allow a more intimate association between the protein and the electrode.

Pyrolytic graphite edge-plane electrodes (**4**) and self-assembled monolayer (SAM)-modified gold electrodes (**5**) have most frequently been used to achieve efficient communication to proteins. The edge planes of pyrolytic graphite contain many organic functionalities such as alcohols, phenolics, carboxylic acids, and other carbonyls. These edge planes allow rapid electron transfer while often maintaining the proteins in their functional state. Pyrolytic graphite, however, provides macroscopic surfaces on which many enzyme molecules will bind. Thus, although the communication between enzymes and the electrode is often effective, there is no control over probing individual enzymes or building up bioelectronic systems on the molecular level. However, this may be possible using carbon nanotubes (CNTs) as electrodes with which to communicate with enzymes.

### 1.1. CNT Electrodes for Communicating With Redox Proteins

CNTs are hollow cylinders consisting of graphene sheets wrapped in a cylinder (**6**) with the ends capped or open. In the case of multiwalled CNTs (MWCNTs), the concentric graphite tubules are in the range of 2 to 25 nm in diameter with 0.34 nm between the sheets. With single-walled CNTs (SWCNTs), a single graphene sheet is rolled seamlessly into individual cylinders of typi-

cally 1 to 2 nm with capped ends. All the carbon atoms are  $sp^2$ . SWCNTs can be metallic conductors, semiconductors, or small-band gap semiconductors, depending on their diameter and chirality (7). Closed nanotubes can be opened in oxidizing environments such as nitric acid. Open-ended nanotubes have been shown to have excellent electron transfer properties (2,8–10) compared with closed nanotubes. The open ends of the CNTs typically contain carboxylate and quinone functionalities in common with edge planes of pyrolytic graphite. Hence, the open ends can be likened to edge planes of pyrolytic graphite, and the walls have similar electron transfer properties to the basal planes of pyrolytic graphite.

Electrodes have been made using either MWCNTs or SWCNTs. In most of the nanotube electrodes thus far presented in the literature, the electrode is prepared by forming a paste with a filler compound and packing it into an electrode body or simply by dispersing the tubes in a solvent, drop coating onto the electrode to leave a bed of nanotubes on an electrode surface. Electrodes made in this way have been shown to have electrocatalytic properties for ferricyanide (11) and some biologically relevant molecules (8,12,13). This electrocatalytic performance is well demonstrated in a recent article by Wang et al. (14) in which the oxidation and reduction of hydrogen peroxide, a product of most oxidase enzyme reactions, was observed at potentials far lower than that observed with other carbon surfaces. The low potential then allowed the detection of glucose with only minor interferences from common interferents such as ascorbic acid, acetamidophen, and uric acid. Nanotube-modified electrodes have been further modified with proteins. Proteins have been adsorbed onto the electrodes (15,16) or covalently attached to the tubes (17) to allow communication between the enzyme and the electrode.

Davis et al. (15) provided the first example of achieving electron transfer to proteins using CNT-modified electrodes, in which an electrode of MWCNTs was first opened in nitric acid and then mixed with nujol, bromoform, mineral oil, or water. Cytochrome-*c* and azurin were adsorbed onto and/or within the tubes with retained activity. The nanotubes' electrodes were shown to have an excellent ability to probe the redox sites of these proteins, which was superior to that observed with edge-plane pyrolytic graphite. Similar results have been obtained by others who have probed redox proteins with their active sites close to the protein surface such as cytochrome-*c* (10,18) and horseradish peroxidase (HRP) (19,20). In the case of HRP, the rate constant for electron transfer of  $2.48\text{ s}^{-1}$  is significantly faster than that observed for HRP at an SAM-modified gold electrode of  $0.29\text{ s}^{-1}$  (21). Yamamoto et al. (20) also showed that a CNT electrode modified with HRP could be interfaced with a second enzyme, such as glucose oxidase or lactate oxidase, to give a sensor for glucose or lactate, respectively.



CNT-based electrodes have also been employed in communicating with enzymes that do not normally allow direct communication, namely glucose oxidase (2,22). In an investigation by Guiseppi-Elie et al. (22), a bed electrode of activated SWCNTs was prepared and the enzyme was adsorbed onto this electrode. It was suggested that direct electron transfer to glucose oxidase was possible because adsorption onto the activated nanotubes permitted small assemblies of nanotubes to locate within tunneling distance of the FAD prosthetic group of the enzyme. The rate of electron transfer was found to be  $1.7 \text{ s}^{-1}$ . A very similar rate of  $1.6 \text{ s}^{-1}$  was reported by Zhao et al. (2), in which glucose oxidase-modified nanotube electrodes were fabricated in the same way with the exception that MWCNTs were used. Interestingly, the rate of electron transfer was identical to that quoted for glucose oxidase adsorbed onto anodized graphite electrodes (23) but significantly faster than the  $0.026 \text{ s}^{-1}$  quoted when the glucose oxidase was covalently attached to SAM-modified gold electrodes (24).

The direct electron transfer studies of glucose oxidase illustrate the potential advantages of CNT-modified electrodes. However, all these studies employed randomly entangled nanotubes, which give a poorly defined electrode surface and poorly defined protein immobilization. Such surface studies strongly indicate that the electron transfer is occurring predominantly the ends of the tubes (2,8–10), although it is known from many studies that the proteins are adsorbed along the walls of the tubes as well as the ends (15–17,22,25–27). Sotiropoulou and Chaniotakis (28), however, reported some selectivity of adsorption of glucose oxidase to the ends over the walls of MWCNTs.

Aligned nanotube electrodes will provide a more controlled surface on which to immobilize and communicate with redox proteins. Electrodes of single nanotubes (29) and aligned arrays of nanotubes (11,28,30,31) have been fabricated. Of these initial studies, only Gao et al. (31) and Sotiropoulou and Chaniotakis (28) have modified the aligned nanotube electrodes. Gao et al. (31) electrochemically deposited conducting polymer sheaths around the nanotubes, and Sotiropoulou and Chaniotakis (28) adsorbed glucose oxidase onto the tubes. We also modify aligned nanotube electrodes with redox enzymes with a view to providing efficient direct electron transfer between enzymes and electrodes.

### **1.2. Aligned CNT Electrodes for Achieving Direct Electron Transfer to Enzymes**

The fabrication of aligned CNT electrodes used in our research first relies on the shortening of SWCNTs by modifying the procedure of Liu et al. (32) in which the tubes are oxidized in an acid mixture of concentrated sulfuric and concentrated nitric acid (3:1 ratio) while sonicating. The resultant tubes are reduced to lengths of the order of a few hundred nanometers depending on the cutting times. The ends of the shortened tubes are open and terminated with

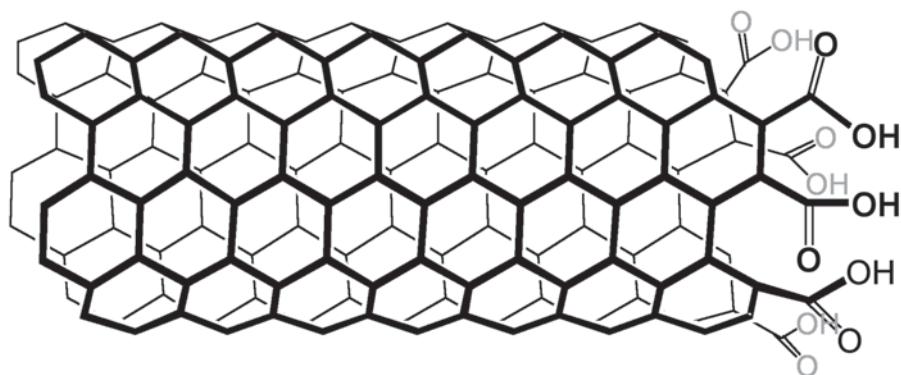
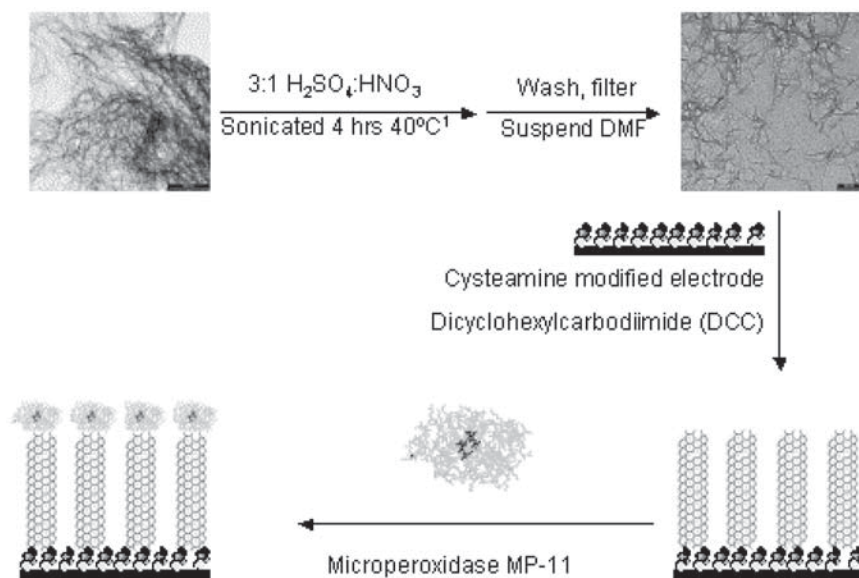


Fig. 1. Representation of shortened SWCNTs with open end showing carboxylic acids formed as consequence of oxidative shortening process.

carboxylic acid moieties (*see Fig. 1*). SWCNTs shortened in this way can be self-assembled aligned normal to a surface in a number of ways including by modifying the ends with the alkanethiol cysteamine ( $\text{HSCH}_2\text{CH}_2\text{NH}_2$ ), which is then attached to a gold surface (**33**). Other methods include simple assembly of the carboxylic acid-terminated tubes onto a silver surface (**34**) or the use of a coordinating ion such as  $\text{Zn}^{2+}$  (**35**) or  $\text{Fe}^{3+}$  (**36**) to anchor the shortened SWCNTs to a surface. We have aligned the shortened SWCNT normal to a gold electrode surface modified with a SAM of cysteamine according to the procedure shown in **Scheme 2**. The nanotubes are covalently linked to the SAM-modified electrode by activating the carboxylic acids with dicyclohexylcarbodiimide (DCC). The aligned CNTs are shown in **Fig. 2**. **Figure 2A** shows what appears to be the SWCNTs standing normally from the gold surface. A cross-section of **Fig. 2A** is shown in **Fig. 2B** in which the height of the tubes attached to the surface appears to be no more than 20 nm. Furthermore, the tubes appear to be in clumps on the surface rather than as individual tubes. If the time the SAM-modified surface is incubated in the tubes is increased, then a greater density of tubes is observed on the surface. Further evidence that these images represent SWCNTs standing from the surface comes from the image in **Fig. 2C**, in which a feature of what appears to be a clump of tubes lying down is visible. The cross section of this image (**Fig. 2D**) shows a large difference in height between this feature and what we believe are the tubes standing normally.

In the activation of the shortened SWCNTs using DCC, both ends of the tubes are activated. Therefore, to the end not attached to the surface, a redox-active species such as an enzyme can be covalently attached (*see Scheme 2*). In our work, we have attached ferrocene and the enzymes microperoxidase



Scheme 2. Steps involved in fabricating aligned shortened SWCNT arrays for direct communication with enzymes such as microperoxidase MP-11 or glucose oxidase.

MP-11 and glucose oxidase. To explore the ability of these aligned SWCNT electrodes to allow direct electron transfer to enzymes, we first investigated the enzyme microperoxidase MP-11 (37) (**Fig. 3**). MP-11 is a small redox protein, 1.9 kDa, obtained by proteolytic digestion of horse heart cytochrome-*c* (38), in which the iron protoporphyrin IX is not shielded by a polypeptide. A number of workers (38–43) have demonstrated that electrons can be efficiently transferred between MP-11 and SAM-modified electrodes.

Attaching MP-11 to the aligned SWCNT-modified gold electrodes and subsequent electrochemical interrogation showed the characteristic peaks for the heme redox-active center of MP-11 with a formal electrode potential of  $-420 \text{ mV}$  vs  $\text{Ag/AgCl}$  (**Fig. 4**). To verify whether the electrochemistry is owing to MP-11 attached to the ends of the SWCNTs, several control experiments were performed. If a SWCNT bed electrode was prepared by drop coating the shortened SWCNT onto a gold electrode and subsequently adsorbing MP-11 onto the nanotubes, the resultant MP-11-modified electrode showed no redox activity. This control suggests that if the MP-11 is adsorbing onto the walls of the nanotubes, as seems likely from previous work on protein adsorption onto nanotubes (15–17,22,25–27), the rate of electron transfer through the walls of the tubes is insufficient to give the discernible redox peaks observed in **Fig. 4**.

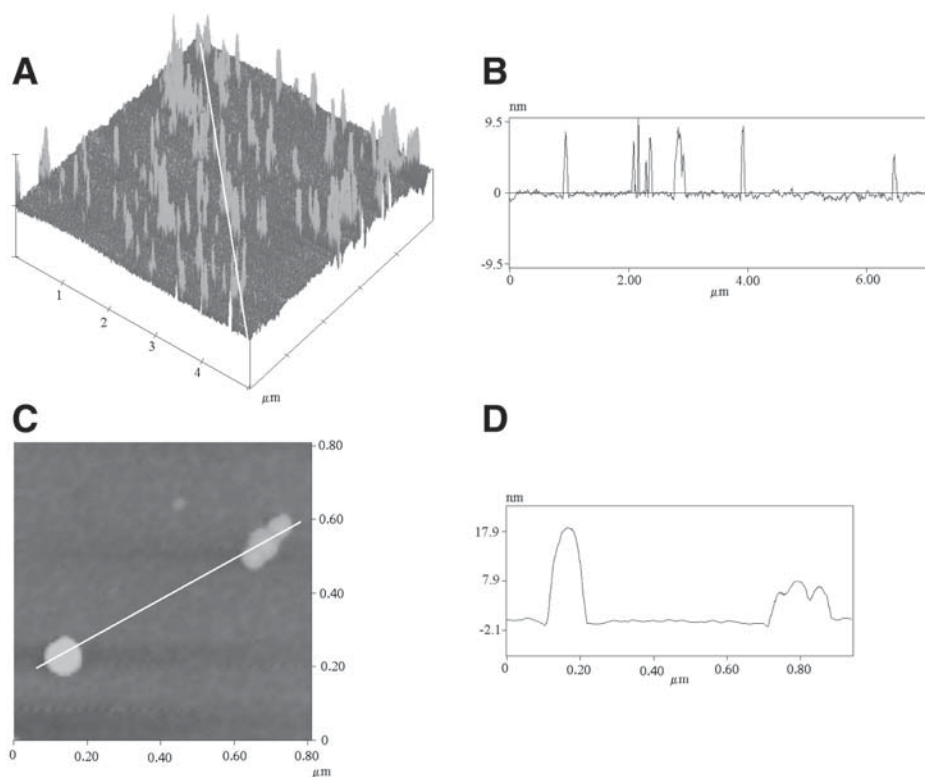


Fig. 2. Atomic force microscopy (AFM) images of shortened SWCNTs aligned onto gold electrode surfaces. **(A)** Tubes cut for 4 h followed by activation with DCC and then incubated with a cysteamine-modified gold electrode for 4 h. The typical heights of the nanotubes are 10 to 20 nm. **(B)** Cross-section of **(A)** diagonally as shown. **(C)** Top view AFM image showing bundle of aligned nanotubes and another bundle of tubes lying flat on surface. **(D)** Differences in heights between standing tubes and those lying down.

To verify that the electrochemistry was not because of the MP-11 adsorbing onto any cysteamine SAM still accessible between the aligned nanotubes, a cysteamine-modified gold electrode was exposed to MP-11 in an analogous manner to the SWCNT-modified electrodes. In this case, very small MP-11 peaks were observed (**Fig. 4A**), but they were significantly smaller than those observed in **Fig. 4B**. Therefore, we can conclude that the electrochemistry observed in **Fig. 4B** is owing to MP-11 attached to the ends of the SWCNTs with the nanotubes allowing effective communication between the electrode and an enzyme located many nanometers away.

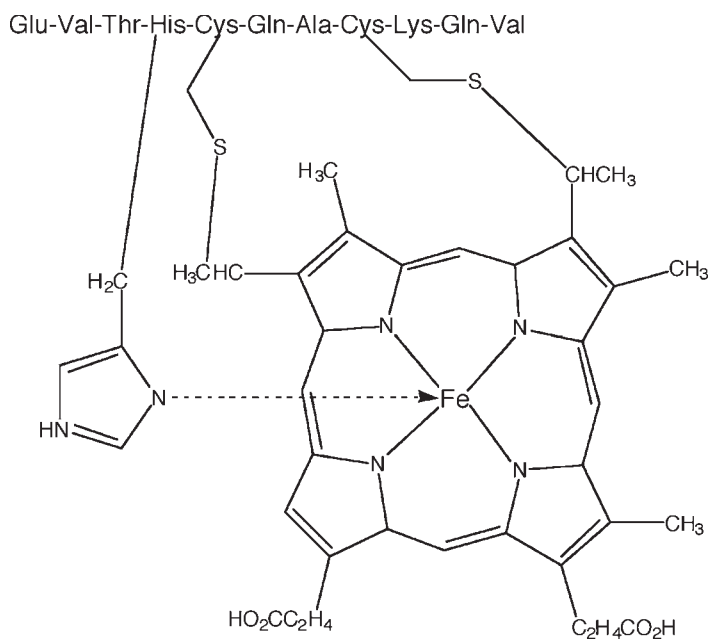


Fig. 3. Microperoxidase MP-11 showing redox-active site and short undeca-peptide backbone.

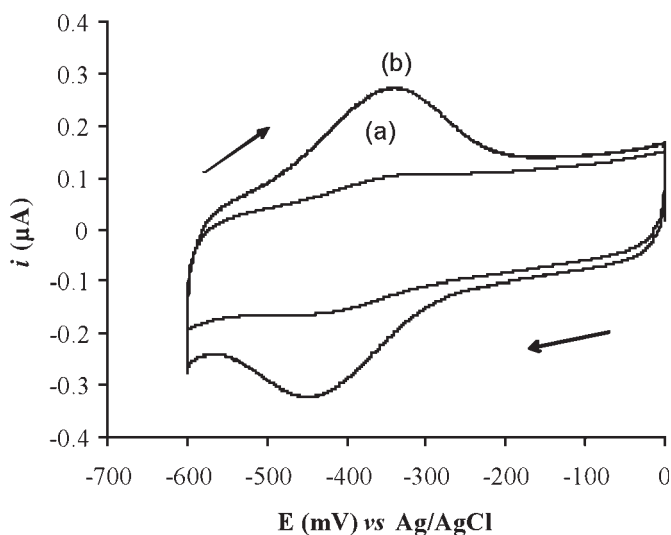


Fig. 4. Cyclic voltammograms of (A) Au/cysteamine after immersion into DMF and MP-11 solution and (B) Au/cysteamine/SWCNTs/MP-11 in 0.05 M phosphate buffer solution (pH 7.0) containing 0.05 KCl under argon gas at scan rate of 100 mV s<sup>-1</sup> vs Ag/AgCl.

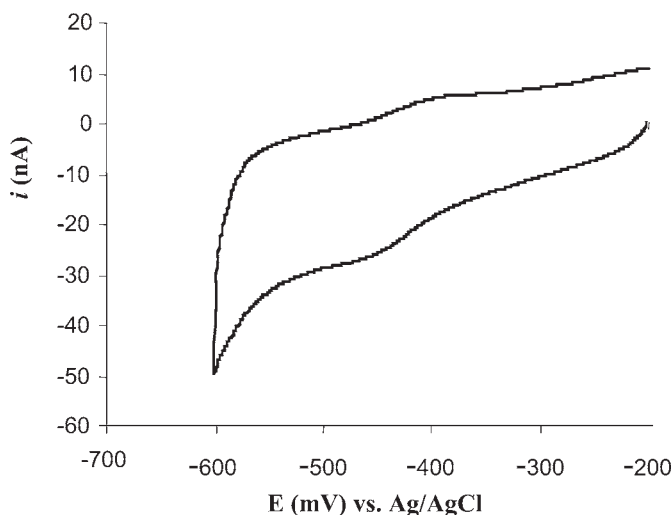


Fig. 5. Cyclic voltammogram of glucose oxidase attached to aligned CNT-modified gold electrode measured in 0.05 *M* phosphate buffer solution (pH 7.0) containing 0.5 *M* KCl under argon gas at scan rate of  $\times 10 \text{ mV s}^{-1}$ .

The variation in cyclic voltammograms with scan rate can be used to calculate the rate of electron transfer between the enzyme and the electrode according to the diffusionless model of Laviron (44). The rate of electron transfer for MP-11 attached to an SWCNT-modified electrode in which the tubes were shortened for 4 h was  $2.8 \pm 0.9 \text{ s}^{-1}$ . This value is only slightly lower than MP-11 attached directly to cysteamine-modified gold electrode ( $6.1 \pm 0.9 \text{ s}^{-1}$ ) and a 3-mercaptopropionic acid-modified gold electrode ( $9.4 \pm 0.6 \text{ s}^{-1}$ ). The very similar rate of electron transfer for the MP-11 attached to the nanotubes compared with the equivalent electrode with the nanotubes removed (the cysteamine-modified electrode) demonstrates the efficiency of the nanotubes as molecular wires.

The virtue of SWCNTs in allowing direct electron transfer to redox proteins is reliant on being able to communicate with enzymes in which the redox-active center is imbedded deep within the glycoprotein. The classic example of such a redox protein, as discussed in **Subheading 1.1.**, is glucose oxidase. **Figure 5** shows the electrochemical response of SWCNT-modified electrodes in which glucose oxidase is attached to the ends of the SWCNTs. The small redox peaks, at a formal potential of about  $-430 \text{ mV}$  vs Ag/AgCl, are attributed to the FAD redox center of glucose oxidase. These preliminary experiments indicate that direct electron transfer to glucose oxidase can be achieved. The remainder of this chapter outlines in detail the experimental protocols used to achieve the results presented in this section.

## 2. Materials

1. Gold working electrode. We used polycrystalline bulk gold electrodes prepared from 1-mm-diameter gold wire (Aldrich, Sydney, Australia) sealed in glass using epoxy (*see Note 1*) as described previously (45). Alternatively, particularly for imaging surfaces, molecularly smooth gold surfaces were prepared by evaporation onto hot mica as described by Mazurkiewicz et al. (46).
2. Ag/AgCl reference electrode (BAS, Lafayette, IN).
3. Platinum flag counterelectrode (homemade) or, alternatively, from BAS.
4. Electrochemical cell for a three-electrode setup (BAS). Alternatively, we use 20-mL sample tubes with the appropriate number of holes cut into the plastic lid.
5. Polishing cloth and 1-, 0.3-, and 0.05- $\mu$  alumina polishing powder (Buehler, Lake Bluff, IL).
6. Ultrasonic cleaner (Unisonics, Sydney, Australia).
7. Potentiostat (BAS 100B).
8. UV-VIS Cary 20 dual beam spectrometer.
9. Scanning Probe Microscopy/Atomic Force Microscopy Digital Instruments Multimode System with a Nanoscope 4 Controller.
10. Phillips CM 200 transmission electron microscope.
11. Carbon nanotubes (Carbon Nanotechnologies, Houston, TX).
12. Solution of concentrated sulfuric acid (98%) and concentrated nitric acid (70%) (3:1 [v/v]).
13. Ethanol (95%).
14. Dimethylformamide (DMF) (Prolabo, Manchester UK).
15. DCC (Aldrich).
16. Teflon membrane, Millipore MF<sup>TM</sup> membrane filters, type 0.45  $\mu$ m HA.
17. Hot-plate stirrer.
18. Cysteamine (2-mercaptoethylamine) (Sigma, Sydney, Australia).
19. Microperoxidase MP-11 (Sigma).
20. Phosphate buffer (0.3 M NaCl, 5 mM phosphate from  $\text{KH}_2\text{PO}_4$  and  $\text{K}_2\text{HPO}_4$ , pH 7.0).
21. 0.01 M HEPES buffer solution, pH 7.5.
22. Eppendorf tubes (500  $\mu$ L).
23. Argon gas.

## 3. Methods

### 3.1. Preparation of Gold Surfaces

1. Polish the gold electrodes to a mirror finish by forming a paste with the alumina powder mixed with Milli-Q water starting with the 1.0- $\mu$  paste, then the 0.3- $\mu$  alumina, and finishing with the 0.05- $\mu$  powder. Polish with each powder for about 5 min by gently drawing figure eights.
2. Place the polished electrodes in a container half filled with Milli-Q water; then place in a sonicator for 10 min.



3. After sonication, fill a clean electrochemical cell with 0.05 M sulfuric acid; place the polished gold electrode, a reference electrode, and a counterelectrode; and connect to the potentiostat.
4. Perform a cyclic voltammogram between  $-300$  and  $1500$  mV with repeated cycling for at least 20 min or until the cyclic voltammogram becomes stable (see **Note 2**).

### 3.2. Cutting of SWCNTs

1. Weigh 2 mg of uncut nanotubes into a sample tube.
2. Add 10 mL of the prepared acid mixture to the nanotubes.
3. Sonicate the sample tubes for the desired time (see **Note 3**).
4. Pour the sonicated solution into a beaker and dilute to 500 mL with Milli-Q water.
5. Collect the nanotubes via vacuum filtration with a Buchner funnel using a  $0.45\text{-}\mu\text{m}$  pore-size Teflon membrane.
6. Discard the acid and filter 1.5 L of Milli-Q water through the nanotubes to reduce their acidity.
7. Test the pH of the filtrate with a universal indicator to ensure a minimum pH of 5.0 before proceeding. Continue washing with Milli-Q water if the pH  $<5.0$ .
8. Immerse the membrane containing the shortened nanotubes in 10 mL of ethanol, sonicate for 15 s (any longer and the membrane will begin to break up), and remove the membrane from the solution with tweezers.
9. Sonicate the ethanol-nanotube solution for 20 min.
10. Pipet 1 mL of the ethanol-nanotube solution into a clean sample tube.
11. Heat the solution to evaporate most of the ethanol, leaving a thin film of ethanol to make the redispersion of the shortened nanotubes easier.
12. Add 10 mL of DMF ( $0.2\text{ mg mL}^{-1}$ ) and shake gently to redisperse the nanotubes. The shortened CNTs are now ready for use.

### 3.3. Characterization of Lengths of Cut SWCNTs

1. Disperse the original and shortened SWCNTs with different cutting times in ethanol.
2. Place a drop or two of this dispersion onto 3-mm-diameter copper grid.
3. Allow the drop or two to evaporate at room temperature overnight.
4. Insert the sample in the transmission electron microscope and take several pictures.
5. Determine the length of each shortened SWCNT prepared at any cutting time simply by manually measuring the length from the transmission electron microscope images. Use at least 100 individual ropes from the images for the distribution determination (see **Notes 3 and 4**).

### 3.4. Assembly of SWCNTs on Electrode Surfaces

#### 3.4.1. Assembly of Aligned Nanotubes

1. Prepare a 1 mM cysteamine solution in 75% aqueous ethanol.
2. Pipet 200  $\mu\text{L}$  of the cysteamine solution into a 500-mL Eppendorf tube.

3. Place a gold electrode (cleaned immediately prior to modification) into the Eppendorf tube so that the gold layer is in the solution.
4. Leave for 5 h for the cysteamine monolayer to self-assemble.
5. Remove the electrode and rinse thoroughly with ethanol.
6. Sonicate the electrode in ethanol for 15 s to remove possible surface contaminants.
7. Pipet 200  $\mu\text{L}$  of the shortened nanotubes dispersed in DMF ( $0.2 \text{ mg mL}^{-1}$ ) into an Eppendorf tube and add 0.5 mg of DCC (to give a concentration of approx 2 mM).
8. Immerse the cysteamine-coated electrode in the nanotube solution for the desired time (typically 4 h) during which the tubes will covalently attach to the cysteamine coated electrode.
9. Remove the shortened SWCNT-modified electrode and wash in DMF, ethanol, and then phosphate buffer (see **Notes 5** and **6**).

#### 3.4.2. Attachment of MP-11

1. Prepare a microperoxidase MP-11 solution at a concentration of  $0.5 \text{ mg mL}^{-1}$  in HEPES buffer at pH 7.5.
2. Place the shortened SWCNT-modified electrode in the MP-11 solution held at  $4^\circ\text{C}$  and incubate overnight.
3. Remove the electrode and rinse in HEPES buffer and then phosphate buffer to remove loosely bound enzyme.

### 3.5. Atomic Force Microscope Imaging of Aligned SWCNTs

1. Freshly prepare the molecularly smooth gold substrates by template stripping as described previously (**46**).
2. Prepare the aligned nanotubes as described in **Subheading 3.4.1**.
3. Use the tapping mode for imaging using commercial Si cantilevers/tips (Olympus) at their fundamental resonance frequencies, which typically varies from 275–320 kHz.
4. Record both height and phase images.
5. Measure the height and length of the SWCNTs using the cross-section analysis using Digital Instruments off-line software (see **Note 7**).

## 4. Notes

1. The cleanliness of the gold surface is all important in determining the quality of the SAM formed on the surface. Hence, even evaporated gold surfaces were cleaned prior to assembly of the modified electrode surface. In the case of polycrystalline gold surfaces, it is important that the epoxy resin used to seal the gold into the glass tube be capable of withstanding the acid conditions used in cleaning. Most epoxy resins will soften in acidic or basic conditions. The epoxy resin that we used was EPON 825 with EPI-CURE 3271 curing agent from Shell Australia, which is resistant to both acidic and basic conditions.
2. The electrochemical cleaning process involves etching away part of the gold surface by oxidizing the surface as the potential is swept anodically (positive). As the potential is swept back negative, the gold oxide that is formed is reduced and a pronounced stripping peak is observed. The additional benefit of the elec-

trochemical cleaning procedure is that the area under this stripping peak can be used to determine the electrochemically accessible area of the gold electrodes. The area of the stripping peak gives the charge passed, and then electrode area can be found using the conversion factor of  $480 \text{ mC cm}^{-2}$  (47).

3. The longer the nanotubes are sonicated, the shorter the length distribution but the thicker the bundles the shorten tubes form. The length and width distribution can be determined using either high-resolution transmission electron microscopy or scanning tunneling microscopy in which the tubes are coated onto molecularly smooth gold surfaces fabricated as described previously (46). Either technique gives the same length distribution, as expected.
4. We have also observed a relationship between the length of the tubes and the mass of the tubes that can be dispersed into various solvents such as DMF. Although we have yet to quantify the length relationship, the amount of tubes that can be dispersed into a given solvent can be monitored via UV-VIS absorption.
5. From this point, they can be used as electrodes or further modified to attach the redox enzymes or other species. The carboxylic acids at both ends of the shortened SWCNTs are activated by the DCC to a carbodiimide that is susceptible to nucleophilic attack from amines. Therefore, to attach species to the other ends of the aligned SWCNTs assembled on the electrode surface simply requires a species with free amines. In our research, we have attached microperoxidase MP-11, glucose oxidase, propylamine, and ferrocene methylamine, synthesized according to the procedure of Kraatz (48). With the enzymes, amino acids with amine side chains provide the nucleophilic amines for covalent attachments to the SWCNTs. In each case, the attachment procedure is the same with the exception of the solvent to which the molecule to be attached is dissolved. The procedure in **Subheading 3.4.2.** is presented for the attachment of microperoxidase MP-11.
6. With the short chain alkanethiols used in this study, a potential problem is that they are easily oxidized in the presence of light. The result of this oxidation is that the gold-thiolate bond is converted into a gold-sulfinate or gold-sulfonate bond (49). Both the gold-sulfinate and gold-sulfonate bonds are much less stable than the gold-thiolate bond. Consequently, when performing an electrochemical control with the SAM-modified electrode alone, via cyclic voltammetry, an oxidation peak, owing to the conversion of the sulfinate to the sulfonate, is sometimes observed at approx +0.3 V vs Ag/AgCl. This peak is suppressed on attachment of the tubes. The presence of such a peak also serves as a good guide to the quality of the SAM prior to tube assembly. If the SAM has been prepared such that there is little or no oxidation of the gold-thiolate bond, then no oxidation process will be observed at such low anodic potentials.
7. An important observation from the preliminary experiments is that, although the transmission electron microscope measurements show that length distributions with a mean of approx 100 nm for 4 h cutting, the heights of the tubes in the atomic force microscope (AFM) images are only 10 to 20 nm from the surface. We believe this anomaly is an artifact of the AFM image. Note that the longer the

cysteamine-modified gold surface is incubated in the nanotubes, the higher the density of tubes on the surface. There is also a concomitant increase in mean length of the aligned tubes. These observations provide good evidence that the AFM images are of aligned nanotubes. Further evidence comes from images as shown in **Fig. 2** in which bundles of tubes standing vertically and lying horizontally can be observed.

## References

1. Heller, A. (1990) Electrical wiring of redox enzymes. *Acc. Chem. Res.* **23**, 128–134.
2. Zhao, Y. D., Zhang, W. D., Chen, H., and Luo, Q. M. (2002) Direct electron transfer of glucose oxidase molecules adsorbed onto carbon nanotube powder microelectrode. *Anal. Sci.* **18**, 939–941.
3. Hecht, H. J., Schomburg, D., Kalisz, H., and Schmid, R. D. (1993) The 3D structure of glucose oxidase from *Aspergillus niger*: implications for the use of GOD as a biosensor enzyme. *Biosens. Bioelectronics* **8**, 197–203.
4. Jeuken, L. J. C. and Armstrong, F. A. (2001) Electrochemical origin of hysteresis in the electron-transfer reactions of adsorbed proteins: contrasting behavior of the “blue” copper protein, azurin, adsorbed on pyrolytic graphite and modified gold electrodes. *J. Phys. Chem. B* **105**, 5271–5282.
5. Gooding, J. J. and Hibbert, D. B. (1999) The application of alkanethiol self-assembled monolayers to enzyme electrodes. *TrAC* **18**, 525–533.
6. Bernholc, J., Brenner, D., Nardelli, M. B., Meunier, V., and Roland, C. (2002) Mechanical and electrical properties of nanotubes. *Ann. Rev. Mater. Res.* **32**, 347–375.
7. Niyogi, S., Hamon, M. A., Hu, H., Zhao, B., Bhowmik, P., Sen, R., Itkis, M. E., and Haddon, R. C. (2002) Chemistry of single-walled carbon nanotubes. *Acc. Chem. Res.* **35**, 1105–1113.
8. Britto, P. J., Santhanam, K. S. V., and Ajayan, P. M. (1996) Carbon nanotube electrode for oxidation of dopamine. *Bioelectrochem. Bioenerg.* **41**, 121–125.
9. Luo, H., Shi, Z., Li, N., Gu, Z., and Zhuang, Q. (2001) Investigation of the electrochemical and electrocatalytic behavior of single-wall carbon nanotube film on a glassy carbon electrode. *Anal. Chem.* **73**, 915–920.
10. Wang, J. X., Li, M. X., Shi, Z. J., Li, N. Q., and Gu, Z. N. (2002) Direct electrochemistry of cytochrome c at a glassy carbon electrode modified with single-wall carbon nanotubes. *Anal. Chem.* **74**, 1993–1997.
11. Nugent, J. M., Santhanam, K. S. V., Rubio, A., and Ajayan, P. M. (2001) Fast electron transfer kinetics on multiwalled carbon nanotube microbundle electrodes. *Nano Lett.* **1**, 87–91.
12. Wang, J. X., Li, M. X., Shi, Z. J., Li, N. Q., and Gu, Z. N. (2002) Electrocatalytic oxidation of norepinephrine at a glassy carbon electrode modified with single wall carbon nanotubes. *Electroanalysis* **14**, 225–230.
13. Wang, J. X., Li, M. X., Shi, Z. J., Li, N. Q., and Gu, Z. N. (2002) Investigation of the electrocatalytic behavior of single-wall carbon nanotube films on an Au electrode. *Microchem. J.* **73**, 325–333.

14. Wang, J. X., Musameh, M., and Lin, Y. (2003) Solubilization of carbon nanotubes by nafion toward the preparation of amperometric biosensors. *J. Am. Chem. Soc.* **125**, 2408, 2409.
15. Davis, J. J., Coles, R. J., and Hill, H. A. O. (1997) Protein electrochemistry at carbon nanotube electrodes. *J. Electroanal. Chem.* **440**, 279–282.
16. Balavoine, F., Schultz, P., Richard, C., Mallouh, V., Ebbesen, T. W., and Mioskowski, C. (1999) Helical crystallization of proteins on carbon nanotubes: A first step towards the development of new biosensors. *Angew. Chem. Int. Ed.* **38**, 1912–1915.
17. Huang, W. J., Taylor, S., Fu, K. F., Lin, Y., Zhang, D. H., Hanks, T. W., Rao, A. M., and Sun, Y. P. (2002) Attaching proteins to carbon nanotubes via diimide-activated amidation. *Nano Lett.* **2**, 311–314.
18. Wang, G., Xu, J. J., and Chen, H. Y. (2002) Interfacing cytochrome c to electrodes with a DNA-carbon nanotube composite film. *Electrochem. Commun.* **4**, 506–509.
19. Zhao, Y. D., Zhang, W. D., Chen, H., Luo, Q. M., and Li, S. F. Y. (2002) Direct electrochemistry of horseradish peroxidase at carbon nanotube powder microelectrode. *Sens. Actuators B* **87**, 168–172.
20. Yamamoto, K., Shi, G., Zhou, T. S., Xu, F., Xu, J. M., Kato, T., Jin, J. Y., and Jin, L. (2003) Study of carbon nanotubes—HRP modified electrode and its application for novel on-line biosensors. *Analyst* **128**, 249–254.
21. Gooding, J. J., Erokhin, P., Losic, D., Yang, W. R., Policarpio, V., Liu, J. Q., Ho, F. M., Situmorang, M., Hibbert, D. B., and Shapter, J. G. (2001) Parameters important in fabricating enzyme electrodes using self-assembled monolayers of alkanethiols. *Anal. Sci.* **17**, 3–9.
22. Guiseppi-Elie, A., Lei, C. H., and Baughman, R. H. (2002) Direct electron transfer of glucose oxidase on carbon nanotubes. *Nanotechnology* **13**, 559–564.
23. Chi, Q. J., Zhang, J. D., Dong, S. J., and Wang, E. K. (1994) Direct electrochemistry and surface characterization of glucose oxidase adsorbed on anodized carbon electrodes. *Electrochim. Acta* **39**, 2431–2438.
24. Jiang, L., McNeil, C. J., and Cooper, J. M. (1995) Direct electron transfer reactions of glucose oxidase immobilised at a self-assembled monolayer. *J. Chem. Soc. Chem. Commun.* 1293–1295.
25. Davis, J. J., Green, M. L. H., Hill, H. A. O., Leung, Y. C., Sadler, P. J., Sloan, J., Xavier, A. V., and Tsang, S. C. (1998) The immobilisation of proteins in carbon nanotubes. *Inorg. Chim. Acta* **272**, 261–266.
26. Azamian, B. R., Davis, J. J., Coleman, K. S., Bagshaw, C. B., and Green, M. L. H. (2002) Bioelectrochemical single-walled carbon nanotubes. *J. Am. Chem. Soc.* **124**, 12,664, 12,665.
27. Shim, M., Kam, N. W. S., Chen, R. J., Li, Y. M., and Dai, H. J. (2002) Functionalization of carbon nanotubes for biocompatibility and biomolecular recognition. *Nano Lett.* **2**, 285–288.
28. Sotiropoulou, S. and Chaniotakis, N. A. (2003) Carbon nanotube array-based biosensor. *Anal. Bioanal. Chem.* **375**, 103–105.

29. Campbell, J. K., Sun, L., and Crooks, R. M. (1999) Electrochemistry using single carbon nanotubes. *J. Am. Chem. Soc.* **121**, 3779, 3780.
30. Diao, P., Liu, Z. F., Wu, B., Nan, X., Zhang, J., and Wei, Z. (2002) Chemically assembled single-wall carbon nanotubes and their electrochemistry. *Chem. Phys. Chem.* **3**, 898–901.
31. Gao, M., Huang, S. M., Dai, L., Wallace, G. G., Gao, R. P., and Wang, Z. L. (2000) Aligned coaxial nanowires of carbon nanotubes sheathed with conducting polymers. *Angew. Chem.-Int. Ed.* **39**, 3664–3667.
32. Liu, J., Rinzler, A. G., Dai, H. J., et al. (1998) Fullerene pipes. *Science* **280**, 1253–1256.
33. Liu, Z., Shen, Z., Zhu, T., Hou, S., Ying, L., Shi, Z., and Gu, Z. (2000) Organizing single-walled carbon nanotubes on gold using a wet chemical self-assembling technique. *Langmuir* **16**, 3569–3573.
34. Wu, B., Zhang, J., Wei, Z., Cai, S. M., and Liu, Z. F. (2001) Chemical alignment of oxidatively shortened single-walled carbon nanotubes on silver surface. *J. Phys. Chem. B* **105**, 5075–5078.
35. Yu, X. F., Mu, T., Huang, H. Z., Liu, Z. F., and Wu, N. Z. (2000) The study of the attachment of a single-walled carbon nanotube to a self-assembled monolayer using X-ray photoelectron spectroscopy. *Surf. Sci.* **461**, 199–207.
36. Chattopadhyay, D., Galeska, I., and Papadimitrakopoulos, F. (2001) Metal-assisted organization of shortened carbon nanotubes in monolayer and multilayer forest assemblies. *J. Am. Chem. Soc.* **123**, 9451–9452.
37. Gooding, J. J., Rahmat, W., Liu, J., Yang, W. R., Losic, D., Orbons, S., Mearns, F. J., Shapter, J. G., and Hibbert, D. B. (2003) Protein electrochemistry using aligned carbon nanotube arrays. *J. Am. Chem. Soc.* **125**, 9006–9007.
38. Lotzbeyer, T., Schuhmann, W., Katz, E., Falter, J., and Schmidt, H.-L. (1994) Direct electron transfer between covalently immobilised enzyme microperoxidase MP-11 and a cystamine-modified gold electrode. *J. Electroanal. Chem.* **377**, 291–294.
39. Lotzbeyer, T., Schuhmann, W., and Schmidt, H.-L. (1996) Electron transfer principles in amperometric biosensors: direct electron transfer between enzymes and electrode surfaces. *Sens. Actuators B* **33**, 50–54.
40. Lotzbeyer, T., Schuhmann, W., and Schmidt, H.-L. (1997) Minizymes: a new strategy for the development of reagentless amperometric biosensors based on direct electron-transfer processes. *Bioelectrochem. Bioenerg.* **42**, 1–6.
41. Narvaez, A., Dominguez, E., Katakis, I., Katz, E., Ranjit, K. T., Ben-Dov, I., and Willner, I. (1997) Microperoxidase-11-mediated reduction of homoproteins: electrocatalyzed reduction of cytochrome c, myoglobin and hemoglobin and electrocatalytic reduction of nitrate in the presence of cytochrome-dependent nitrate reductase. *J. Electroanal. Chem.* **430**, 227–233.
42. Jiang, L., Glidle, A., McNeil, C. J., and Cooper, J. M. (1997) Characterization of electron transfer reactions of microperoxidase assembled at short-chain thiol-monolayers on gold. *Biosens. Bioelectronics* **12**, 1143–1155.
43. Ruzgas, T., Gaigalas, A., and Gorton, L. (1999) Diffusionless electron transfer of microperoxidase-11 on gold electrodes. *J. Electroanal. Chem.* **469**, 123–131.

44. Laviron, E. (1979) General expression of the linear potential sweep voltammogram in the case of diffusionless electrochemical systems. *J. Electroanal. Chem.* **101**, 19–28.
45. Gooding, J. J., Erokhin, P., and Hibbert, D. B. (2000) Parameters important in tuning the response of monolayer enzyme electrodes fabricated using self-assembled monolayers of alkanethiols. *Biosens. Bioelectronics* **15**, 229–239.
46. Mazurkiewicz, J., Mearns, F. J., Losic, D., Rogers, C., Shapter, J. G., and Gooding, J. J. (2002) Cryogenic cleavage used in atomically flat gold surface production. *J. Vac. Sci. Technol. B* **20**, 2265–2270.
47. Hoogvliet, J. C., Dijkema, M., Kamp, B., and van Bennekom, W. P. (2000) Electrochemical pretreatment of polycrystalline gold electrodes to produce a reproducible surface roughness for self assembly: a study in phosphate buffer pH 7.4. *Anal. Chem.* **72**, 2016–2021.
48. Kraatz, H.-B. (1999) Synthesis and electrochemistry of ferrocenemethylamine and its conjugate acid: crystal structure of ferrocenemethylammonium chloride. *J. Organomet. Chem.* **578**, 222–226.
49. Garrell, R. L., Chadwick, J. E., Severance, D. L., McDonald, N. A., and Myles, D. C. (1995) Adsorption of sulfur-containing molecules on gold—the effect of oxidation on monolayer formation and stability characterized by experiments and theory. *J. Am. Chem. Soc.* **117**, 11,563–11,571.





## Molecularly Imprinted Polymers for Biomolecular Recognition

Alexandra Molinelli, Markus Janotta, and Boris Mizaikoff

### Summary

Molecular imprinting of polymers is a concept for the synthetic formation of structurally organized materials providing binding sites with molecular selectivity. Compared to biological receptors, these polymeric recognition systems have the advantage of superior chemical and mechanical stability with potential applications in areas such as biomimetic catalysis and engineering, biomedical analysis, sensor technology, or the food industry. In particular, molecularly imprinted polymers (MIPs) providing selectivity for biorelated molecules are gaining substantial importance. In this context, a self-assembly approach for the synthesis of imprinted polymers against the flavonol quercetin is presented, which is exemplary for the biologically relevant group of flavonoid compounds. The creation of synthetic selective recognition sites for this biomolecule is demonstrated by comparing the separation capabilities of imprinted and nonimprinted polymer particles for several structurally related molecules via high-performance liquid chromatography experiments. The developed quercetin-MIP enables selective extraction of quercetin even from complex mixtures, demonstrating the potential for designing biomimetic recognition materials with improved selectivity for biomolecules with tunable functionality at a nanoscale.

**Key Words:** Molecularly imprinted polymers; synthetic receptors; biomimetic recognition; flavonoids; quercetin; high-performance liquid chromatography.

### 1. Introduction

For the last two decades, the concept of designing synthetic molecular recognition materials that can mimic biological functions has generated substantial interest (1–7) and stimulated research on structurally organized materials. Particularly at a nanoscale level, the technique of molecular imprinting—creating synthetic recognition sites within macromolecular matrices by template inclusion during polymerization—has demonstrated potential for a variety of

From: *Methods in Molecular Biology*, vol. 300:  
*Protein Nanotechnology, Protocols, Instrumentation, and Applications*  
Edited by: T. Vo-Dinh © Humana Press Inc., Totowa, NJ

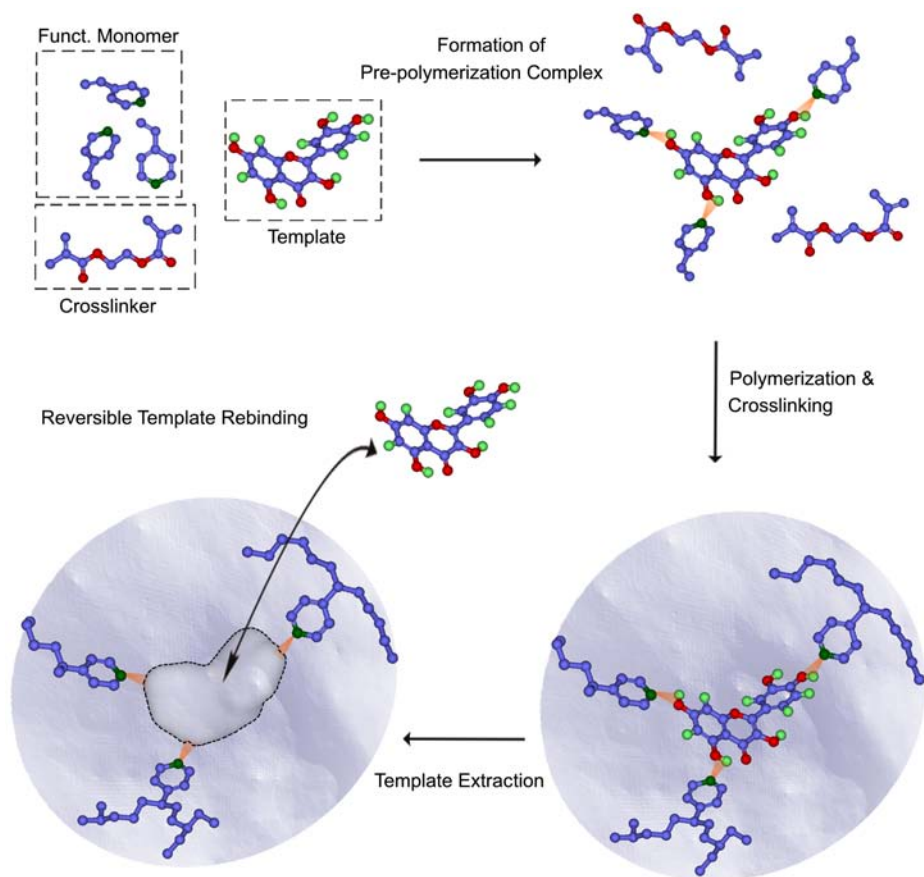


Fig. 1. Schematic concept of molecular imprinting.

applications (8,9). Generally, this methodology is based on utilizing the functionalities of a target molecule (template) to assemble its own recognition cavity by forming interactions with “complementary” functional groups of appropriate functional monomers. These interactions are provided by either cleavable covalent bonds or noncovalent interactions, which are then “frozen” in position by polymerization carried out in the presence of a high concentration of crosslinker (10–13). Subsequent removal of the template creates binding pockets within the polymer matrix that memorize the spatial arrangement of functional groups and the size and shape of the target molecule. Ideally, highly selective recognition of the imprinted analyte is thereby ensured, which favors a reversible rebinding process and selective retention of the templated analyte within the biomimetic recognition matrix (see Fig. 1).

So far, molecular imprinting has mainly been demonstrated for templates with a relatively low molecular weight (**14–16**). In the past few years, successful preparation of molecularly imprinted polymers (MIPs) specifically targeting practically relevant biomolecules such as flavonoids (**17,18**), mycotoxins (**19**), proteins, or carbohydrates (**20–26**) has been discussed in the literature. Nevertheless, the formation of synthetic receptors for macromolecules remains a challenging task, and appropriate procedures for the preparation of MIPs selective for specific biomolecules are of substantial biological and biomedical interest.

In the present study, imprinted polymers against the flavonol quercetin were successfully synthesized and characterized via high-performance liquid chromatography (HPLC) experiments. Because quercetin represents a biomolecule with several functionalities enabling noncovalent interactions with functional monomers, this approach is a suitable example for the formation of synthetic recognition matrices selective for biomolecules.

## 2. Materials

1. Laboratory mortar grinder.
2. Standard testing sieve (25  $\mu\text{m}$ ).
3. HPLC column slurry packer (pressure: 10,000 psi maximum).
4. Blank stainless steel HPLC columns (150 mm or 250  $\times$  4.6 mm id).
5. HPLC system with a UV/Vis diode array detector.
6. Template analyte (quercetin dihydrate).
7. Acetone, purissim (>99%) over molecular sieve (used as porogenic solvent).
8. 4-Vinylpyridine ([4-VP] functional monomer). Reactive monomer; store under refrigeration below  $-10^{\circ}\text{C}$  ( $+14^{\circ}\text{F}$ ). This monomer polymerizes gradually at room temperature. At elevated temperatures, polymerization could occur, generating heat and pressure, which could rupture a closed container.
9. Ethyleneglycol dimethacrylate ([EGDMA] crosslinker).
10. 2,2'-Azobisisobutyronitrile (polymerization initiator).
11. Morin.
12. (+) Catechin.
13. Rutin.
14. 2-Carboethoxy-5,7-dihydroxy-4'-methoxyisoflavone (C-fla).

## 3. Methods

The methods described next outline synthesis of the molecularly imprinted block-polymer; the preparation steps including grinding, sieving, and sedimentation required before application of the polymer; separation experiments applying the prepared polymer particles as HPLC separation matrix; and evaluation of the obtained results.

### 3.1. Synthesis of Polymer

#### 3.1.1. Imprinted Polymer

The pre-polymerization mixture was prepared as follows: 1 mmol of quercetin as the template molecule was dissolved in 15 mL of acetone in a glass vial (30-mL volume). Then 8 mmol of the functional monomer 4-vinylpyridine (*see Note 1*), 40 mmol of the crosslinker ethyleneglycol dimethacrylate (*see Note 2*), and 2% (w/w) 2,2'-azobisisobutyronitrile were added in the denoted order. The solution was next cooled in an ice bath and purged with nitrogen for 5 min. Finally, the polymerization was started (*see Note 3*) by thermal initiation at 60°C in a water bath (*see Note 4*).

#### 3.1.2. Control Polymer

To assess properly the imprinting effect obtained for the target analyte, a non-imprinted control polymer is prepared for control experiments. The same procedure as described in **Subheading 3.1.1.** is applied to synthesize the nonimprinted polymer, but without adding the template.

### 3.2. Processing of Synthesized Polymers

The following steps describe the processing of the block-polymer for application as a separation matrix in liquid chromatography (the same procedure as applied for imprinted and control polymer).

1. Crush a polymer block into small particles using a porcelain mortar and pestle.
2. Grind the polymer particles for 3 min in a mechanical mortar.
3. Wet-sieve the polymer particles with acetone using a 25- $\mu\text{m}$  sieve.
4. After drying, subject the polymer particles, which are detained by the sieve, to additional grinding and wet-sieving by repeating **steps 2 to 4** until most of the polymer particles are sieved.
5. Sediment the collected acetone-polymer particle mixture in approx 250 mL of acetone to eliminate fine particles of grain sizes  $<5\ \mu\text{m}$ . After 1 h, discard the supernatant and add fresh acetone to the precipitated polymer particles. Several sedimentation steps are necessary to eliminate the majority of fine particles (*see Notes 5 and 6*).
6. Wash the polymer particles with methanol and dry at 45°C for 24 h in an oven.

### 3.3. HPLC Separation Experiments

Selective separation matrices based on molecularly imprinted polymers should exhibit selective retention behavior for the template analyte when evaluating the separation capabilities of imprinted and control polymers for the template molecule and structurally related compounds (*see Table 1*). Therefore, the imprinted polymer particles and the control polymer particles were applied as stationary phase during HPLC experiments (27) (*see Note 7*).

1. Sonicate 3 g of polymer particles (either imprinted or control polymer) in approx 50 mL of acetone and pack into stainless-steel HPLC columns ( $250 \times 4.6$  mm id) with acetone at 200 bar using an air-driven fluid pump (slurry packer) (*see Note 8*).
2. Mount the packed HPLC columns (containing either imprinted polymer particles or control polymer particles) into the HPLC system, and perform a template extraction step in order to create the molecule-specific recognition cavities within the polymer matrix.
3. Extract the template molecules from the polymer particles by flushing the columns with methanol:acetic acid (HAc) (7:1 [v/v]) at a flow rate of 1 mL/min until a stable baseline is recorded. To establish comparable conditions, subject the control column to the same procedure. Then equilibrate each column (until a stable baseline is recorded) with acetonitrile (MeCN):H<sub>2</sub>O:HAc (80:10:10 [v/v/v]) as the mobile phase (*see Note 9*), and evaluate with respect to their separation and recognition properties for the template quercetin and several structural analogs (*see Fig. 2*).
4. Using the HPLC column packed with control (nonimprinted) polymer particles as reference, determine the selectivity for the template analyte and crossreactivity of the imprinted polymer.
5. Perform all elutions at ambient temperature at a mobile phase flow rate of 1 mL/min, and monitor spectrophotometrically at 200 to 450 nm using a diode array UV/Vis detector.
6. For each chromatographic run, inject 2  $\mu$ g of the investigated compounds dissolved in 20  $\mu$ L of the mobile phase using 0.2  $\mu$ L of acetone as void marker.

### 3.4. Evaluation

Several characteristic parameters can be interpreted as the main evidence that an imprinting effect has been achieved (*see Fig. 2* and **Table 2**). First, the retention time of quercetin in the column packed with the quercetin imprinted polymer is approx 10 times higher compared to the column packed with the control polymer. The imprinted column shows some cross-selectivity for structurally related compounds, as shown in **Table 2**. Nevertheless, the strongest difference in retention time between the imprinted and the control column occurs for the imprint molecule quercetin (retention index [RI] value of 1). According to **Table 2**, three analytes (Rutin, [+]-Catechin, and C-fla) have low crossreactivity with the generated anti-quercetin recognition cavities, whereas morin, with an RI value of 0.7 (*see Note 10*), shows considerable cross-reactivity owing to the closest structural similarities of the molecular structure to the imprint molecule quercetin. Second, the large difference in capacity factors for quercetin when comparing imprinted and control polymer ( $k'_{\text{MIP}} = 10$ ,  $k'_{\text{CTL}} = 1.4$  in MeCN:H<sub>2</sub>O:HAc [80:10:10]) indicated a strong imprinting effect. Third, the considerably pronounced tailing of the flavonoid peaks in the imprinted column is an indication of a heterogeneous binding site distribution with—more or less—specific and nonspecific sites distributed within the poly-

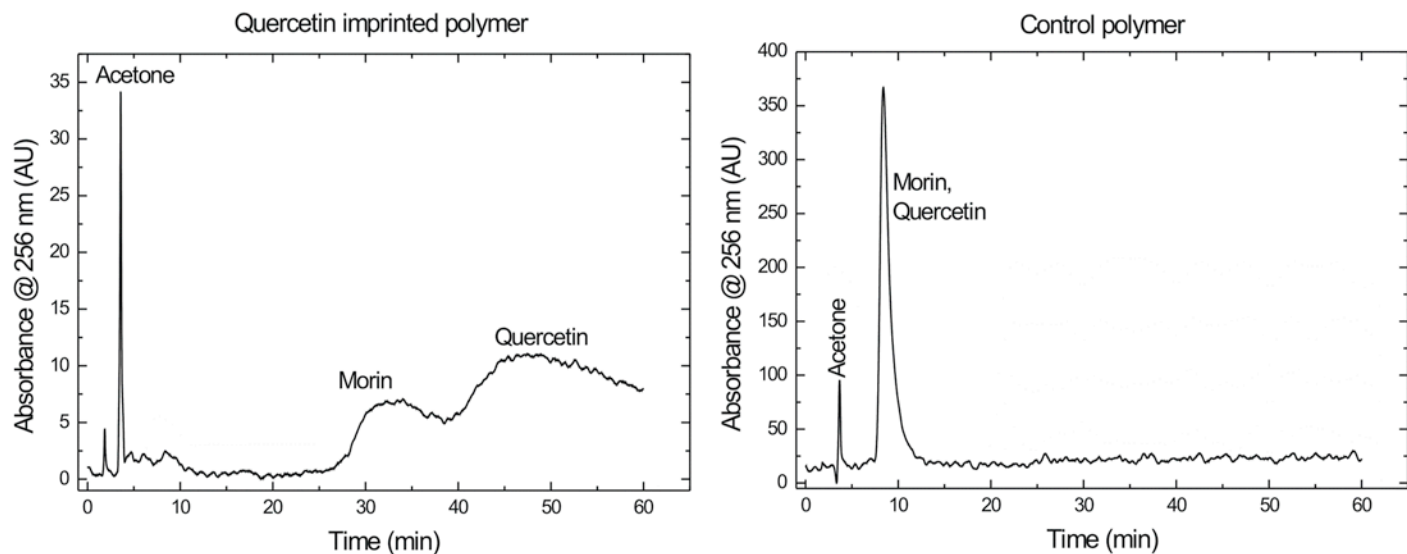


Fig. 2. Chromatograms for (A) imprinted polymer and (B) control polymer with acetone, morin, and quercetin (4-VP/EDMA copolymer) in MeCN:H<sub>2</sub>O:HAc (80:10:10 [v/v/v]) as mobile phase (flow rate: 1 mL/min).



**Table 1**  
**Selected Flavonoid Compounds Used in HPLC Experiments**

Name	<b>Quercetin</b>	<b>Morin</b>	<b>C-Fla</b>
Class	flavonol	flavonol	isoflavone
Formula	C <sub>15</sub> H <sub>10</sub> O <sub>7</sub>	C <sub>15</sub> H <sub>10</sub> O <sub>7</sub>	C <sub>19</sub> H <sub>16</sub> O <sub>7</sub>
CAS#	117-39-5	480-16-0	15485-76-4
Structure			
Name	<b>(+)-Catechin</b>	<b>Rutin</b>	
Class	flavanol	flavonol glycoside	
Formula	C <sub>15</sub> H <sub>14</sub> O <sub>6</sub>	C <sub>27</sub> H <sub>30</sub> O <sub>16</sub>	
CAS#	154-23-4	153-18-4	
Structure			

**Table 2**  
**Results for Capacity Factors, Separation Factors, and RIs for Imprinted and Nonimprinted 4-VP/EDMA Copolymer in MeCN:H<sub>2</sub>O:HAc (80:10:10 [v/v/v]) as Mobile Phase<sup>a</sup>**

	$t_{\text{CTL}}$	$k'_{\text{CTL}}$	$t_{\text{MIP}}$	$k'_{\text{MIP}}$	$\alpha_{\text{CTL}}$	$\alpha_{\text{MIP}}$	RI value
Acetone	3.5	—	3.6	—	—	—	—
Quercetin	<b>8.4</b>	<b>1.4</b>	<b>39.5</b>	<b>10.0</b>	<b>1.0</b>	<b>1.0</b>	<b>1.0</b>
Morin	8.4	1.4	27.8	6.8	1.0	1.5	0.7
(+) Catechin	4.9	0.4	5.9	0.7	3.5	15.2	0.2
Rutin	4.3	0.2	4.9	0.4	6.3	27.9	0.2
C-fla	4.5	0.3	4.7	0.3	5.0	33.5	0.2

<sup>a</sup>Flow rate: 1 mL/min. Bold numbers indicate values for the templated analyte.

mer (**28**). The print molecule interacts differently with these binding sites; it is retained for a longer time in the column owing to these interactions and, consequently, produces a broader peak with pronounced tailing. These results emphasize that HPLC columns packed with imprinted polymer particles are suitable for the separation of structurally closely related analytes based on biomimetic recognition mechanisms within a synthetic receptor matrix.

### 3.5. Application: Molecularly Imprinted Solid-Phase Extraction for Determination of Quercetin From Red Wine

Because HPLC characterization of molecularly imprinted polymers for quercetin has proven the existence of a substantial imprinting effect, the polymer was used as sorbent material for the solid-phase extraction of quercetin from red wine (**18**). The molecularly imprinted polymer enabled facile sample

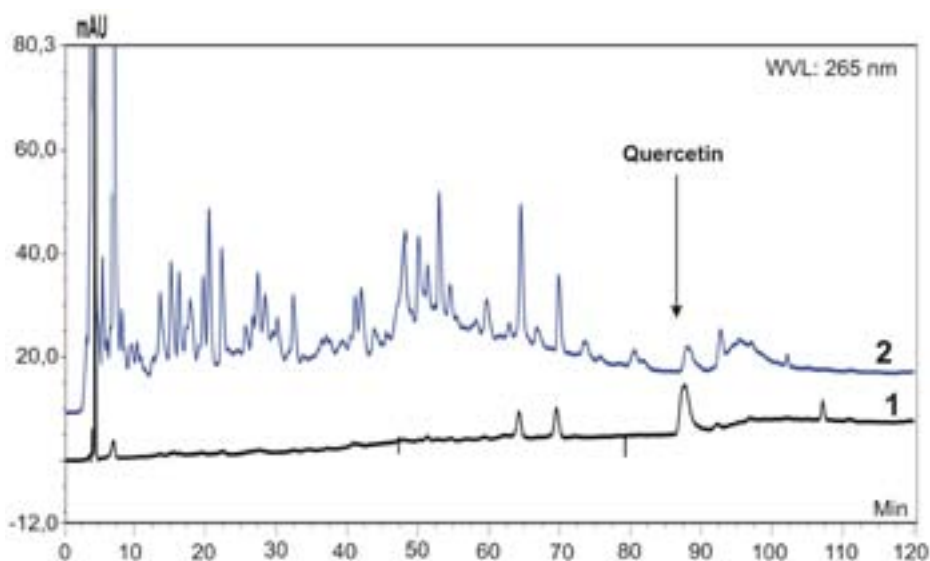


Fig. 3. Chromatogram of a red wine (Merlot) registered at 265 nm (2) before and (1) after MIP solid-phase extraction; (1) after 1.75 mL of elution. (From **ref. 18** with permission.) WVL, wavelength.

cleanup prior to HPLC measurements and selective enrichment of quercetin from the red wine without any further sample cleanup procedures (*see Fig. 3*).

#### 4. Notes

1. Prior to polymerization, 4-vinylpyridine has to be freshly distilled using a microdistillation apparatus in order to remove the inhibitor. The distilled 4-vinylpyridine solution can then be stored in a freezer at temperatures below  $-10^{\circ}\text{C}$  for several months.
2. Depending on the type of template analyte, different functional monomers (including mixtures of functional monomers), crosslinkers, and solvents can be applied (**12,29,30**). One main prerequisite is adequate solubility of sufficient amounts of the selected compounds in the solvent of choice. A typical functional monomer-to-solvent ratio is 3:4 (v/v). The molar ratio selected for the imprinting approach of quercetin is 1:8:40 (template:functional monomer:crosslinker). Depending on the required amount of functional monomer and selected crosslinker, ratios typically vary between 1:4:20 and 1:10:60 (**30–32**). Resulting from losses during the sedimentation procedure (*see Note 5*), a minimum of 0.18 mmol of template in the prepolymerization mixture should be used. A minimum of 2 g of polymer material after the final sedimentation step is necessary for a successful HPLC column packing process. The functional monomer should be selected according to the potential maximum number of interaction sites, because the for-

mation of stable complexes between template molecules and functional monomers in the pre-polymerization mixture and during polymerization will determine the quality of the imprint. The ratio of template to functional monomer and to crosslinker for a defined system is frequently determined by trial and error after characterization of the binding properties of the resulting imprinted polymer. Methods such as nuclear magnetic resonance (NMR) studies of the pre-polymerization mixture facilitate the selection process of suitable ratios between template and functional monomer involved in the formation of complex (33,34).

3. Polymerization must be performed in an airtight glass vial, because oxygen acts as an inhibitor during a radical polymerization.
4. Depending on the properties of the template, thermal polymerization at temperatures  $<60^{\circ}\text{C}$  (radical starter 2,2'-azobis-[2,4-dimethylvaleronitrile]) and ultraviolet polymerization (at room temperature or lower) offer alternatives for starting the radical copolymerization.
5. An ultrasonication processing step is applied prior to each sedimentation to ensure complete mixing between polymer particles and solvent. The accurate removal of fine particles is a crucial step, because the application of fine particles ( $<10\text{-}\mu\text{m}$  diameter) during packing of HPLC stationary-phase materials can result in high back-pressures in the HPLC column. The reduction of the particle size distribution is also necessary for better HPLC column performance, because using particles with a wide size distribution will lead to interfering peak-broadening effects.
6. A clear supernatant solution obtained after 20 to 30 min indicates sufficient removal of most of the fine particles.
7. Radioligand (35,36) and competitive fluorescence (37) binding assays are additional qualified techniques to evaluate the selective recognition performance of imprinted polymers. Analytical techniques such as NMR (33,34), infrared spectroscopy, or mass-sensitive devices (38) can provide supplementary information on the recognition (binding) events. However, in our personal opinion and experience, separation techniques related to affinity chromatographic concepts are particularly suitable for analyzing recognition properties of MIPs and are among the most promising applications of MIP-based recognition matrices for biomolecules.
8. The accurate and careful packing of HPLC columns is of great importance, because enclosure of air bubbles or nonuniform packed columns will result in diminished HPLC performance.
9. The proper choice of mobile phase is crucial and strongly depends on the nature of interactions between the analyte and the stationary phase. It has been shown in the literature that the application of the same solvent previously used for polymerization (39) is beneficial for maximizing the recognition properties in chromatographic applications. Although organic solvents may enhance, e.g., hydrogen bonds and ionic interactions, hydrophobic interactions are mainly amplified when applying aqueous media.
10. Capacity factors are calculated as  $k' = (t - t_0)/t_0$ , in which  $t$  is the retention time for the compound and  $t_0$  corresponds to the retention time for the void marker

(acetone in this experiment). Separation factors are calculated as  $\alpha = k'_{\text{TM}}/k'_{\text{TS}}$ , with TM indicating the template molecule and TS the respective test substance. RI is calculated as  $\text{RI} = \alpha_{\text{CTL}}/\alpha_{\text{MIP}}$ , in which MIP and CTL indicate the MIP and control polymer, respectively. The RI value for the template analyte is 1 per definition and is taken as a reference. Smaller RI values for structurally related molecules indicate less interaction among the analyte, mobile phase, and stationary phase, yielding information on the selectivity and crossreactivity of the MIP.

## Acknowledgments

We gratefully acknowledge funding for this work by the European Union (QLRT-2001-02323) and the Austrian Science Foundation (P14122-CHE).

## References

1. Kempe, M., Fischer, L., and Mosbach, K. (1993) Chiral separation using molecularly imprinted heteroaromatic polymers. *J. Mol. Recogn.* **6**(1), 25–29.
2. Wulff, G., Heide, B., and Helfmeier, G. (1986) Enzyme-analog built polymers. 20. Molecular recognition through the exact placement of functional groups on rigid matrixes via a template approach. *J. Am. Chem. Soc.* **108**(5), 1089–1091.
3. Andersson, L. I. and Mosbach, K. (1990) Enantiomeric resolution on molecularly imprinted polymers prepared with only non-covalent and non-ionic interactions. *J. Chromatogr.* **516**(2), 313–322.
4. Takeuchi, T. and Haginaka, J. (1999) Separation and sensing based on molecular recognition using molecularly imprinted polymers. *J. Chromatogr. B* **728**, 1–20.
5. Owens, P. K., Karlsson, L., Lutz, E. S. M., and Andersson, L. I. (1999) Molecular imprinting for bio- and pharmaceutical analysis. *Trends Anal. Chem.* **18**, 146–154.
6. Haupt, K. and Mosbach, K. (2000) Molecularly imprinted polymers and their use in biomimetic sensors. *Chem. Rev.* **100**, 2495–2504.
7. Andersson, L. I. (2000) Molecular imprinting for drug bioanalysis: a review on the application of imprinted polymers to solid-phase extraction and binding assay. *J. Chromatogr. B* **739**, 163–173.
8. Haupt, K. (2003) Imprinted polymers—tailor-made mimics of antibodies and receptors. *Chem. Commun.* **2**, 171–178.
9. Whitcombe, M. J., Rodriguez, M. E., Villar, P., and Vulfson, E. N. (1995) A new method for the introduction of recognition site functionality into polymers prepared by molecular imprinting: synthesis and characterization of polymeric receptors for cholesterol. *J. Am. Chem. Soc.* **117**, 7105–7111.
10. Mosbach, K. and Ramström, O. (1996) The emerging technique of molecular imprinting and its future impact on biotechnology. *Biotechnology* **14**, 163–170.
11. Wulff, G. (1995) Molecular imprinting in crosslinked materials with the aid of molecular templates—a way towards artificial antibodies. *Angew. Chem. Int. Ed.* **34**, 1812–1832.
12. Sellergren, B. (1999) Polymer- and template-related factors influencing the efficiency in molecularly imprinted solid-phase extractions. *Trends Anal. Chem.* **18**, 164–174.

13. Katz, A. and Davis, M. E. (1999) Investigations into the mechanisms of molecular recognition with imprinted polymers. *Macromolecules* **32**, 4113–4121.
14. Zander, A., Findlay, P., Renner, T., and Sellergren, B. (1998) Analysis of nicotine and its oxidation products in nicotine chewing-gum by a molecularly imprinted solid-phase extraction. *Anal. Chem.* **70**, 3304–3314.
15. Mullet, W. M. and Lai, E. P. C. (2000) Determination of theophylline in serum by molecularly imprinted solid-phase extraction with pulsed elution. *Anal. Chem.* **70**, 3636–3641.
16. Yu, Y., Ye, L., Haupt, K., and Mosbach, K. (2002) Formation of a class of enzyme inhibitors (drugs), including a chiral compound, by using imprinted polymers or biomolecules as molecular-scale reaction vessels. *Angew. Chem. Int. Ed.* **41**, 4460–4462.
17. Weiss, R., Molinelli, A., Jakusch, M., and Mizaikoff, B. (2002) Molecular imprinting and solid phase extraction of flavonoid compounds. *Bioseparation* **10**, 379–387.
18. Molinelli, A., Weiss, R., and Mizaikoff, B. (2002) Advanced solid phase extraction using molecularly imprinted polymers for the determination of quercetin in red wine. *J. Agric. Food Chem.* **50**, 1804–1808.
19. Weiss, R., Freudenschuss, M., Krska, R., and Mizaikoff, B. (2003) Improving the analysis of mycotoxins in beverages—molecularly imprinted polymers for deoxynivalenol and zearalenone. *Food Addit. Contam.* **20(4)**, 386–395.
20. Sellergren, B. (2000) Imprinted polymers with memory for small molecules, proteins, or crystals. *Angew. Chem. Int. Ed.* **39**, 1031–1037.
21. Dabulis, K. and Klibanov, A. M. (1992) Molecular imprinting of proteins and other macromolecules resulting in new adsorbents. *Biotechnol. Bioeng.* **39**, 176–185.
22. Hjertin, S., Liao, J. L., Nakazato, K., Wang, Y., Zamaratskaia, G., and Zhang, H. X. (1997) Gels mimicking antibodies in their selective recognition of proteins. *Chromatographia* **44**, 227–234.
23. Shi, H. Q. and Ratner, B. D. (2000) Template recognition of protein-imprinted polymer surfaces. *J. Biomed. Mater. Res.* **49**, 1–11.
24. Shi, H. Q., Tsai, W.-B., Garrison, M. D., Ferrari, S., and Ratner, B. D. (1999) Template-imprinted nanostructured surfaces for protein recognition. *Nature* **398**, 593–597.
25. Bossi, A., Piletsky, S. A., Piletska, E. V., Righetti, P. G., and Turner, A. P. F. (2001) Surface-grafted molecularly imprinted polymers for protein recognition. *Anal. Chem.* **73**, 5281–5286.
26. Zimmerman, S. C., Wendland, M. S., Rakow, N. A., Zharov, I., and Suslick, K. S. (2002) Synthetic hosts by monomolecular imprinting inside dendrimers. *Nature* **418**, 399–403.
27. Andersson, L. I. (2000) Molecular imprinting: developments and applications in the analytical chemistry field. *J. Chromatogr. B.* **745**, 3–13.
28. Umpleby, R. J. II, Bode, M., and Shimizu, K. D. (2000) Measurement of the continuous distribution of binding sites in molecularly imprinted polymers. *Analyst* **125**, 1261–1265.

29. Whitcombe, M. J., Alexander, C., and Vulfson, E. N. (1997) Smart polymers for the food industry. *Trends Food Sci. Technol.* **8**, 140–145.
30. Yu, C. and Mosbach, K. (1998) Insights into the origins of binding and the recognition properties of molecularly imprinted polymers prepared using an amide as the hydrogen-bonding functional group. *J. Mol. Recogn.* **11**, 69–74.
31. Ramstrom, O., Ye, L., Krook, M., and Mosbach, K. (1998) Screening of a combinatorial steroid library using molecularly imprinted polymers. *Anal. Commun.* **35**, 9–11.
32. Yilmaz, E., Mosbach, K., and Haupt, K. (1999) Influence of functional and cross-linking monomers and the amount of template on the performance of molecularly imprinted polymers in binding assays. *Anal. Commun.* **36**, 167–170.
33. Idziak, I., Benrebouh, A., and Deschamps, F. (2001) Simple NMR experiments as a means to predict the performance of an anti-17 $\alpha$ -ethynylestradiol molecularly imprinted polymer. *Anal. Chim. Acta* **435**, 137–140.
34. Sellergren, B., Lepistoe, M., and Mosbach, K. (1991) Highly enantioselective and substrate-selective polymers obtained by molecular imprinting utilizing non-covalent interactions: NMR and chromatographic studies on the nature of recognition. *J. Am. Chem. Soc.* **110**, 5853–5860.
35. Andersson, L. (1996) Application of molecular imprinting to the development of aqueous buffer and organic solvent based radioligand binding assays for (S)-propranolol. *Anal. Chem.* **68**, 111–117.
36. Jakusch, M., Janotta, M., Mizaikoff, B., Mosbach, K., and Haupt, K. (1999) Molecularly imprinted polymers and infrared evanescent wave spectroscopy: a chemical sensors approach. *Anal. Chem.* **71**, 4786–4791.
37. Suarez-Rodriguez, J. L. and Diaz-Garcia, M. E. (2001) Fluorescent competitive flow-through assay for chloramphenicol using molecularly imprinted polymers. *Biosens. Bioelectron.* **16**, 955–961.
38. Kobayashi, T., Murawaki, Y., Reddy, P. S., Abe, M., and Fujii, N. (2001) Molecular imprinting of caffeine and its recognition assay by quartz-crystal microbalance. *Anal. Chim. Acta* **435**, 141–149.
39. Kempe, M. and Mosbach, K. (1991) Binding studies on substrate- and enantio-selective molecularly imprinted polymers. *Anal. Lett.* **24**, 1137–1145.

## Plasmonics-Based Nanostructures for Surface-Enhanced Raman Scattering Bioanalysis

Tuan Vo-Dinh, Fei Yan, and David L. Stokes

### Summary

Surface-enhanced Raman scattering (SERS) spectroscopy is a plasmonics-based spectroscopic technique that combines modern laser spectroscopy with unique optical properties of metallic nanostructures, resulting in strongly increased Raman signals when molecules are adsorbed on or near nanometer-size structures of special metals such as gold, silver, and transition metals. This chapter provides a synopsis of the development and application of SERS-active metallic nanostructures, especially for the analysis of biologically relevant compounds. Some highlights of this chapter include reports of SERS as an immunoassay readout method, SERS gene nanoprobe, near-field scanning optical microscopy SERS probes, SERS as a tool for single-molecule detection, and SERS nanoprobe for cellular studies.

**Key Words:** Surface-enhanced Raman scattering; genomics; single-molecule detection; near-field scanning optical microscopy; plasmonics; bioanalysis.

### 1. Introduction

Raman spectroscopy is based on vibrational transitions that yield very narrow spectral features that are characteristic of the investigated sample. Thus, it has long been regarded as a valuable tool for the identification of chemical and biological samples as well as the elucidation of molecular structure, surface processes, and interface reactions. Despite such advantages, Raman scattering suffers the disadvantage of extremely poor efficiency. Compared to luminescence-based processes, Raman spectroscopy has an inherently small cross-section (e.g.,  $10^{-30}$  cm<sup>2</sup>/molecule), thus precluding the possibility of analyte detection at low concentration levels without special enhancement processes. Some modes of signal enhancement have included resonance Raman scattering and nonlinear processes such as coherent anti-Stokes Raman scattering.

From: *Methods in Molecular Biology*, vol. 300:  
*Protein Nanotechnology, Protocols, Instrumentation, and Applications*  
Edited by: T. Vo-Dinh © Humana Press Inc., Totowa, NJ



However, the need for high-power, multiple-wavelength excitation sources has limited the widespread use of these techniques.

Nevertheless, there has been a renewed interest in Raman techniques in the past two decades owing to the discovery of the surface-enhanced Raman scattering (SERS) effect, which results from the adsorption of molecules on specially nanotextured metallic surfaces. This large enhancement was first reported in 1974 by Fleischmann et al. (1), who observed the effect for pyridine molecules adsorbed on electrochemically roughened silver electrodes. It was initially believed that the enhancement resulted from the increased surface area produced by the electrochemical roughening, giving rise to increased probed sample density. The teams of Jeanmaire and Van Duyne (2) and Albrecht and Creighton (3) later confirmed the enhancement (up to  $10^8$ ) but attributed the effect to more complex surface enhancement processes, which continue to be the subject of intense theoretical studies. More recent reports have cited SERS enhancements from  $10^{13}$  to  $10^{15}$ , thus demonstrating the potential for single-molecule detection with SERS (4–9).

By the mid-1980s, because of the aggressive development of SERS substrates and application to a wide range of chemicals, the potential of SERS as a routine analytical technique was recognized. The SERS technique has since continued to receive increased interest, as evidenced by the large numbers of articles and review articles (10–21). Furthermore, the scope of SERS has been extended to include other surface-enhanced spectroscopies such as surface-enhanced second-harmonic generation (22) and surface-enhanced hyper-Raman scattering (23).

The SERS effect is based on a combination of several processes, involving electromagnetic enhancement and chemical enhancement (20). Electromagnetic enhancement involves plasmonics, which is related to enhanced electromagnetic properties of metallic nanostructures. The term *plasmonics* is derived from “plasmons,” which are the quanta associated with longitudinal waves propagating in matter through the collective motion of large numbers of electrons. Incident light irradiating these surfaces excites conduction electrons in the metal and induces excitation of surface plasmons leading to enormous electromagnetic enhancement of spectral signatures (such as SERS and surface-enhanced fluorescence) for ultrasensitive detection of biomolecules.

A host of biological compounds (e.g., proteins, amino acids, lipids, fats, fatty acids, DNA, RNA, antibodies, enzymes) has been studied via SERS. Extensive progress in the development of dependable SERS substrates over the past few decades has promoted the application of SERS in the rapidly expanding field of biotechnology, as demonstrated in several excellent reviews (24–28). This chapter provides a synopsis of the development of plasmonics-based nanostructures for SERS analysis of biologically relevant compounds.

Some highlights of this chapter include reports of SERS as an immunoassay readout method, SERS gene nanoprobes, near-field scanning optical microscopy (NSOM) SERS probes, SERS as a tool for single-molecule detection, and SERS nanoprobes for cellular studies.

## 2. Methods

### 2.1. Development of SERS-Active Metal Electrodes

Electrochemically roughened electrodes were the first media with which the SERS effect was observed (1). Observation of this effect resulted in further inaugural studies to confirm it and to establish enhancement factors (2,3,14). Although several metals have been investigated for SERS activity in electrochemical cells (29–33), silver has been the most commonly used. During electrochemical preparation, silver at the electrode surface is first oxidized by the reaction  $\text{Ag} \rightarrow \text{Ag}^+ + \text{e}^-$ ; then, elemental silver is redeposited in the ensuing reduction process,  $\text{Ag}^+ + \text{e}^- \rightarrow \text{Ag}$ . This oxidation-reduction procedure generally produces protrusions on the electrode surface in a size range of 25 to 500 nm. Strong SERS signals appear only after several electrochemical oxidation-reduction cycles, often referred to as “activation cycles.”

Transition metals such as bare Pt, Ru, Rh, Pd, Fe, Co, and Ni electrodes have also been investigated as SERS substrates (34–36). It has been found that transition metals exhibit surface enhancement factors ranging from one to four orders of magnitude, depending on the nature of the metal and the surface morphology. In one study, photoalterations of the copper electrode resulted in a further 10-fold increase in SERS (37).

### 2.2. Development of SERS-Active Metal Nanoparticle Colloids

SERS-active suspensions of elemental metal colloids or nanoparticles of various sizes can be chemically formed in solution. Hence, they can be readily used in suspension for *in situ* solution SERS measurements. Alternatively, they can be immobilized on various solid media for use as surface-based SERS substrates. As with roughened metal electrodes, silver is the most commonly used material. Silver colloids can easily be prepared by reducing a solution of  $\text{AgNO}_3$  with ice-cold  $\text{NaBH}_4$  (38–40), trisodium citrate (41–43), or hydrogen peroxide under basic conditions (44). Other more innovative techniques that reduce the need for wet chemistry have been demonstrated. For example, Ahern and Garrell (45) described a unique *in situ* photoreduction method to produce photocolloids in solutions, and another innovative method involved laser ablation of colloids from silver foils into aqueous solutions (46).

Gold colloids have also been investigated as SERS-active media. Because gold is virtually bioinert, it may prove to be a valuable material for biomedical applications of SERS. Furthermore, gold produces large SERS enhancement

factors when near-infrared (IR) excitation sources are used. Near-IR excitation radiation is particularly useful in biomedical studies because it allows greater penetration depths in tissues while causing less fluorescence background relative to visible radiation. Gold sols have been used for the SERS detection of various dyes (41,47). In particular, Kneipp et al. (7) have observed extremely large enhancement factors (up to  $10^{14}$ ) for dyes adsorbed on gold colloids when using near-IR excitation.

### **2.3. Development of Solid SERS Substrates Based on Metallic Nanostructures**

In addition to immobilized colloids, researchers have developed a variety of solid surface-based SERS substrates that are produced entirely from solid materials, as depicted schematically in **Fig. 1**. In contrast to immobilized colloids, the solid SERS-based probes described subsequently exhibit a high degree of reproducibility. In addition, nanoshells with a dielectric core and a metallic shell (e.g., Au/SiO<sub>2</sub>), or a metallic core and a dielectric shell (e.g., Au core/SiO<sub>2</sub> shell), or a metallic core and a metallic shell (e.g., Au core/Ag shell, Ag core/Ag shell, and Ag core/Au shell), provide a tunable geometry in which the magnitude of the local electromagnetic field at the nanoparticle surface can be precisely controlled (48–51).

#### **2.3.1. Metal Nanoparticle Island Films**

Metallic nanostructured SERS substrates based on metal island films (**Fig. 1A**) are among the most easily prepared surface-based media, granted the availability of a vacuum evaporation system. Such systems are commonly equipped with crystal microbalances for monitoring metal film thickness. Metal island films can be produced by depositing a thin (<10 nm) layer of a metal directly onto a smooth solid base support via sputter deposition (40) or vacuum evaporation. At such a small thickness, the metal layer forms as aggregated, isolated metal islands, the size and shape of which can be influenced largely by the metal thickness, deposition rate, geometry, and temperature, as well as postdeposition annealing. To optimize the production of SERS-active metal island films, various diagnostic techniques have been used, including optical absorption, atomic force microscopy, SERS, or combinations thereof (52,53). More recently, silver island films have been characterized by combining NSOM with Raman spectroscopy, thereby achieving <70-nm resolution (54). A disadvantage of metal island films is that they are easily disturbed by solvents encountered in typical biomedical analyses (55,56). To minimize this disadvantage, buffer metal layers, (3-mercaptopropyl)-trimethoxysilane layers, and organometallic paint layers have been applied to glass supports to stabilize gold island films (57).

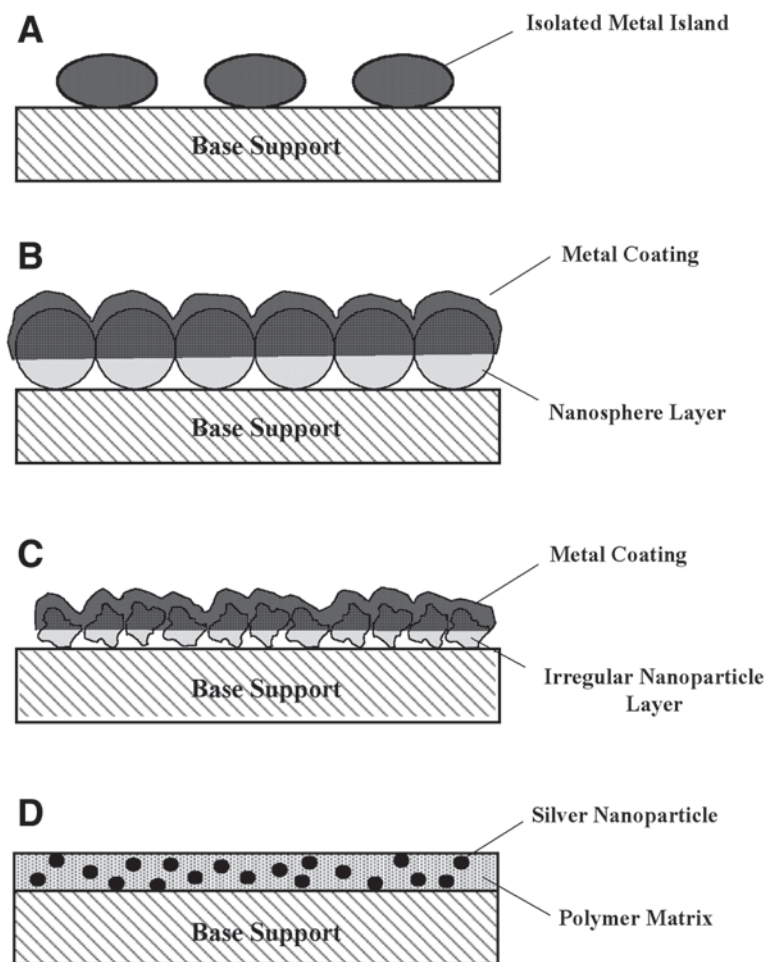


Fig. 1. Various types of SERS-active metallic nanostructures: (A) metal island films; (B) metal-coated nanospheres (seminanoshells); (C) metal-coated random nanostructures; (D) polymer coatings embedded with metal nanoparticles.

### 2.3.2. Metal-Coated Nanosphere Substrates

In our laboratory, we have developed a very dependable solid surface-based SERS substrate technology that can be generally described as metal-coated dielectric nanospheres (**Fig. 1B**) supported by various planar support media. Nanospheres within a specific size range (e.g., 50–500 nm) are spin coated on a solid support in order to produce the roughness required to induce the SERS effect. The resulting nanostructured plate is then coated with a layer of silver (50–150 nm), which provides the conduction electrons required for the surface

plasmon mechanisms. All factors of surface morphology are easily controlled, enabling high batch-to-batch reproducibility. An additional advantage is that the relatively thick layer of silver is less vulnerable to air oxidation than silver islands. Furthermore, the surface is highly resistant to disturbance by sample solvents, making this type of SERS substrate very practical for biomedical applications. Teflon and latex are particularly well suited for SERS substrates because they are commercially available in a wide variety of sizes, which can be selected for optimal enhancement.

Preparation of a nanosphere substrate is relatively easy. A 50- $\mu$ L aliquot of a suspension of nanospheres is deposited evenly over the surface of a dielectric planar support medium, such as filter paper, cellulosic membrane, glass, or quartz (58–62). Using a photoresist to produce uniform monolayer coverage, the substrate is then spun at 800 to 2000 rpm for about 20 s. The spheres adhere to the glass surface, providing uniform coverage. The nanosphere-coated support is then placed in a vacuum evaporator, where silver is deposited on the roughened surface at a rate of 0.15 to 0.2 nm/s.

### 2.3.3. Metal-Coated Nanoparticle Substrates

Nanoparticles with irregular shapes (**Fig. 1C**) can also be used in place of regularly shaped nanospheres in the production of dependable, cost-effective SERS substrates. Dielectric nanoparticle materials investigated in our laboratory have included alumina (63), titanium dioxide (64), and fumed silica (65). The production of irregular nanoparticle-based substrates is achieved with an ease equivalent to that for nanosphere-based substrates described in **Subheading 2.3.2**. Generally, 5 to 10% (w/v) aqueous suspensions of the nanoparticles are spin coated onto solid support media, then coated by 75 to 150 nm of silver via vacuum evaporation. As an alternative to the vacuum evaporation process, other groups have investigated silver coating via chemical processes (66,67). Nevertheless, substrates prepared via vacuum evaporation yield exceptional reproducibility.

Alumina-based substrates produced by vacuum evaporation have proven to be among the most dependable, with a batch-to-batch variability of typically <10% for induced signals of selected model compounds. The surface of an alumina-based substrate consists of randomly distributed surface agglomerates and protrusions in the 10- to 100-nm range. These structures produce large electromagnetic fields on the surface when the incident photon energy is in resonance with the localized surface plasmons. Alumina-based substrates have numerous applications (68–75).

Silver-coated titanium dioxide (64) and fumed silica (65) surfaces also provide efficient SERS-active substrates. Titanium dioxide provides the necessary nanosize surface roughness for the SERS effect; the nominal particle

diameter of  $\text{TiO}_2$  used in our probes is 0.2  $\mu\text{m}$ . When coated with 50 to 100 nm of silver, this type of probe can yield exceptional SERS enhancement with limits of detection of various compounds in the parts-per-billion range. Fumed silica substrates have allowed trace detection of polynuclear aromatic hydrocarbons and pesticides (64,76).

#### 2.3.4. SERS Substrates Based on Metal-Coated Quartz Posts

Silver-coated, regularly spaced submicron posts formed in quartz substrates have proven to be a dependable, yet labor-intensive, SERS substrate. Lithographic techniques have been used to control the surface roughness to a degree suitable for testing the electromagnetic model of SERS (77,78). Although these surfaces produce a Raman enhancement on the order of  $10^7$ , they are difficult to produce with a large surface area. However, an alternative etching procedure for producing quartz posts overcomes this limitation by using an island film as an etching mask on an  $\text{SiO}_2$  substrate (79–83). The preparation of  $\text{SiO}_2$  prolate posts is a multistep operation, as depicted in **Fig. 2**. A 500-nm layer of  $\text{SiO}_2$  is first thermally evaporated onto a fused quartz base support at a rate of 0.1 to 0.2 nm/s. The resulting thermally deposited crystalline quartz is annealed at 950°C to the fused quartz for 45 min. A 5-nm silver layer is then evaporated onto the thermal  $\text{SiO}_2$  layer, and the substrate is flash heated (500°C) for 20 s, causing the thin silver layer to bead up in small globules. These isolated silver globules act as etch masks when the substrate is subsequently etched for 30 to 60 min in a  $\text{CHF}_3$  plasma. This etching produces submicron prolate  $\text{SiO}_2$  posts under the silver globules. Since fused quartz is etched much more slowly than is thermally deposited quartz, the fused quartz base survives the etching process. The posts are then cleaned to remove the silver etch mask and coated with either a continuous 80-nm silver layer (83) or a discontinuous layer with the silver deposition restricted to the tips of the quartz posts (80,81). A disadvantage of quartz post-based substrates is the difficult, time-consuming etching procedure required for post fabrication. Nevertheless, optimized quartz posts can serve as the base for a reusable SERS substrate, provided that the silver coating is replaced between uses.

#### 2.3.5. SERS Substrates Based on Metal Nanoparticle-Embedded Media

Silver nanoparticles embedded in various solid porous media (**Fig. 1D**) have recently been investigated as stable SERS substrates with the potential for selective detection. The *in situ* production of these nanoparticles in solid matrices provides several advantages. For example, a solid matrix not only spatially stabilizes but also physically protects the colloids. In addition, the porosity of such materials as sol-gels, cellulose acetate gels, and polycarbonate films permits interaction of analyte compounds with the embedded metal nanoparticles.

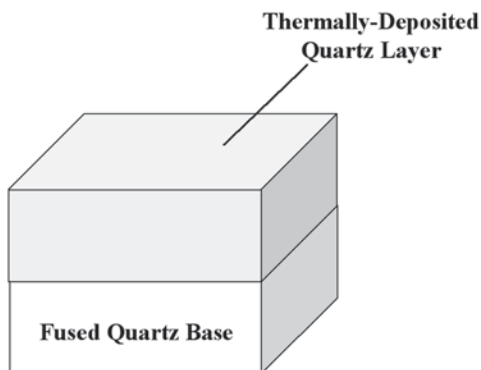
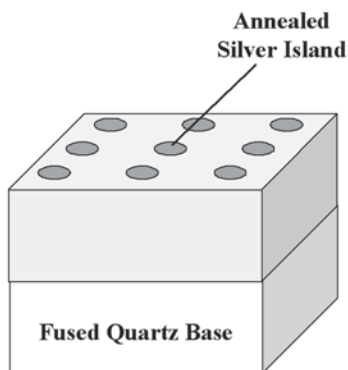
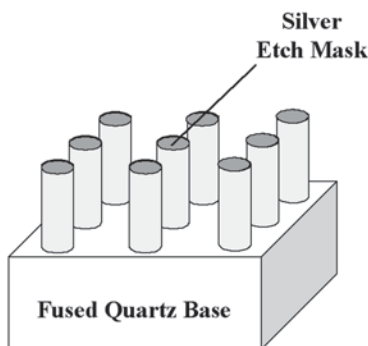
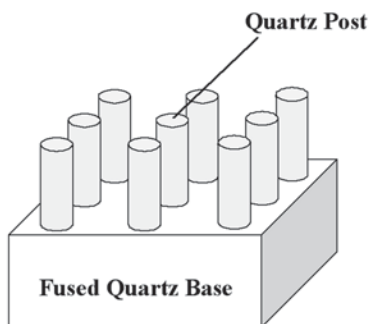
**A** After Thermal Deposition of Quartz on Fused Quartz Base**B** After Deposition and Annealing of Silver Island Film**C** After Plasma Etching**D** After Removal of Silver Etch Mask

Fig. 2. Schematic diagram of production of SERS-active quartz post: (A) after thermal deposition of quartz on fused quartz base; (B) after deposition and annealing of silver island film; (C) after plasma etching; (D) after removal of silver etch mask.

Furthermore, control of pore size and matrix polarity through simple chemical means (particularly when using the sol-gel technique) can impart selectivity. Finally, the chemical processes generally used to prepare such substrates make the SERS technique accessible for general analytical laboratories.

A silver nanoparticle-embedded sol-gel substrate produced through the chemical reduction of silver halide particles distributed in the sol-gel matrix has been reported for the detection of neurotransmitters and dopamine (84,85). *In situ* precipitation of silver chloride nanoparticles via reaction of silver nitrate



with trichloroacetic acid throughout the sol-gel matrix was performed before curing. Immediately prior to use, the silver chloride particles were reduced to elemental silver nanoparticles with  $\text{FeSO}_4 \cdot 7\text{H}_2\text{O}$ . An advantage of this technique is that the sol-gel can be stored for long periods in the nonreduced form, precluding vulnerability to air oxidation.

## 2.4. Overcoatings on SERS Substrates

### 2.4.1. General Organic, Metallic, and Dielectric Overcoatings

Polymer coatings have been applied to a variety of solid surface-based SERS substrates. In one study, a relatively thick layer (approx 10  $\mu\text{m}$ ) of poly(vinylpyrrolidone) (PVP) was applied to alumina-based silver SERS substrates (86). In addition to prolonging shelf life, this procedure demonstrated the preservation of surface features vital to the SERS effect by offering resistance to physical disturbance. Furthermore, chemical selectivity was imparted via selective permeability, particularly for compounds having hydrogen-bonding properties. The procedure involved simply dipping the bare silver SERS probes into a 5% (w/v) methanolic solution of the polymer, followed by room temperature curing on a level surface for approx 30 min. PVP coatings have also been applied to silver island-based SERS probes for selective detection of airborne chemicals (87,88). In these studies (87,88), the coating was observed to preserve the delicate silver island films over a 20-d period.

A combination of polybenzimidazol and mercaptobenzimidazol has been applied to SERS-active, nitric acid-etched copper foils (89). This coating was determined to inhibit corrosion and thus prolong the shelf life of the SERS-active substrate. In addition, treatment of silver SERS substrates with various thiols can provide long-term stability, even for substrates stored in water for 1 mo (90). To promote enhanced adsorption of metal ions ( $\text{Cu}^{+2}$ ,  $\text{Pb}^{+2}$ ,  $\text{Cd}^{+2}$ ), 4-(2-pyridylazo) resorcinol coatings have been applied to SERS-active silver (91). As an example of the enhanced selectivity offered by reactive coatings in the analysis of complex biological matrices, bilirubin and salicylate have been detected at below normal therapeutic levels via direct SERS analysis of whole blood (92). In that study, application of the coating, diazonium, precluded the need for a time-consuming and possibly risky preparation of a less complex serum sample. A reactive coating has also been proposed for the one-step detection of the illicit drugs amphetamine and methamphetamine (93).

Extensive efforts have been devoted to the development of coatings based on inorganic materials. For example, transition metals (Pd, Rh, Pt, Ir, Ru) have been applied to gold substrates as pinhole-free, ultrathin (two to three monolayers) films to enhance adsorption of carbon monoxide and nitric oxide while preserving the SERS-inducing properties of the underlying gold substrates

(94,95). The ultrathin coatings were achieved through a special electrodeposition process. SiO<sub>2</sub>-coated silver island-based substrates have also been reported as viable SERS substrates (96–98). These dielectric-coated substrates have made possible the quantitative detection of dyes adsorbed from solutions. Furthermore, they have been used in fundamental analyte adsorption kinetics studies. SiO<sub>2</sub>-coated substrates could prove especially useful in SERS-based biosensors because of the well-defined hydrophilic and stabilizing properties of the coating. Such substrates could be resistant to oxidation and physical damage, hence both prolonging shelf life and offering the potential for reuse.

#### 2.4.2. Self-Assembled Monolayer Overcoatings

Self-assembled monolayers (SAMs) have proven to be a valuable factor in SERS substrate development and theoretical applications of SERS. For example, they have been used to immobilize SERS-active metal colloids on planar supports in a highly ordered fashion (99–102). In fact, specific colloidal patterns have been prepared by microcontact printing of SAMs on planar surfaces before exposure to SERS-active colloids (101). SAMs have also been used for the production of UV-induced SERS-active photopatterns on silver films coated with *p*-nitrophenol (103). In more fundamental studies, the inherent SERS signals of SAMs have been used to evaluate the surface uniformity of SERS probe surfaces, including electrochemically roughened gold electrodes and immobilized gold colloids (104). The application of SAMs to SERS substrate surfaces also allows selective detection. For example, SAMs of mercaptoalkalinic acids on colloidal silver substrates have been used for the SERS detection of selectively adsorbed cytochrome-c (105) and have formed the basis for anchoring capture DNA probes for SERS-active hybridization platforms (106). Monolayers of cysteamine on silver SERS substrates have also been reported (107,108). Such monolayers could promote the selective adsorption of proteins.

#### 2.4.3. Bioreceptor Monolayer Overcoating

The potential use of SERS in biodiagnostic tests has been demonstrated through the use of immobilized monolayers of bioreceptors, including oligonucleotides and antibodies. The use of surface-enhanced Raman gene (SERG) probes for medical diagnostics (109–113) is covered in greater detail in **Subheading 4**. In the production of SERG probes, SERS-active dye labels can be attached to oligonucleotide primers used in polymerase chain reaction (PCR) amplification of specific target DNA sequences. Following PCR, the resulting labeled amplicons from the targeted DNA region of interest can be denatured, allowing hybridization of specific, single-stranded, labeled DNA to oligonucleotide capture probes, which can be immobilized on solid supports.

Contact with SERS-active media permits subsequent detection of the SERG probe. This method combines the high sensitivity of the SERS technique with the inherent molecular specificity offered by DNA sequence hybridization.

Antibody monolayers have also been the basis of SERS detection with molecular selectivity (*114,115*), thus demonstrating the potential for SERS in immunoassays. In one study, Ni et al. (*115*) demonstrated the simultaneous detection of two antigens in a single sandwich immunoassay using two reporter molecules. Capture antibodies selective for the target antigens were bound to gold colloids. The capture antibody-coated colloids were then exposed to a mixture of target antigens. Finally, reporter antibodies specific to the immobilized target antigens were immobilized on the colloid via interaction with the target antigens. SERS-active markers on the reporter antibodies permitted ultrasensitive detection of the immobilized antigens. Each antigen was assigned a different marker, yet both reporters could be detected in a single measurement because of minimal overlap of the respective Raman spectra. In another study, Dou et al. (*114*) demonstrated the potential for a SERS-based immunoassay with no need for reporter molecules. Instead, they monitored the native SERS signatures of anti-mouse IgG antibodies adsorbed on gold nanoparticles. Because of the structure-specific nature of Raman scattering, they were able to directly confirm conjugation with antigens through the observation of changes in relative intensities of spectral features of the IgG spectrum. Neither reporter probes nor rinsing steps to remove unbound antigens were required in this assay.

### 3. SERS as an Immunoassay Readout Method

Immunoassays have received considerable interest for more than a decade. For example, in 1989, Rohr et al. (*116*) reported on an early example of a SERS-based immunoassay. The same year, Grabbe and Buck (*117*) reported on SERS studies of native human Ig-G. More recently, SERS signatures of native antibodies have been the basis for a simplified immunoassay in which conjugation of the antibody with a target antigen was confirmed through observance of alterations in the SERS spectrum for the native antibody (*114*).

As an alternative, extremely sensitive detection can be achieved with reporter antibody probes tagged with intensely SERS-active compounds or with enzymes that react with substrates to yield SERS-active products. These methods often involve sandwich immunoassay techniques, which increase the number of required steps but offer the advantages of excellent sensitivity and the potential for “label multiplexing.” For example, Ni et al. (*115*) recently reported the simultaneous detection of two types of antigens in a single assay by using two reporter antibodies. The labels of the reporter probes yielded SERS spectral features with minimal overlap, permitting exploitation of a label multiplex advantage. In a sandwich assay format, one set of antibodies

immobilized the target antigens on gold colloids while the reporter antibody probes were subsequently immobilized at allosteric sites of the target antigens.

In other studies, reporter antibodies have been tagged with the enzyme peroxidase (*118,119*). Once the peroxidase-labeled antigen was immobilized on the target, it could be exposed to the substrates, *o*-phenylenediamine and hydrogen peroxide. A sustained reaction of the enzyme with a multitude of substrate molecules yielded an extremely high yield of the SERS-active product, azoaniline. This method has thus far been limited to sandwich immunoassay formats. For example, in a study to detect membrane-bound enzymes in cells, cells were first exposed to primary antibodies specific to the membrane-bound enzymes, then exposed to a peroxidase-tagged reporter antibody specific to the primary antibody (*118*). A format that uses a capture antibody to immobilize a target antigen, and a reporter antibody to bind to a different antigenic site of the immobilized target antigen, has also been reported (*119*).

Recently, successful detection of immunoglobulins using gold nanoshells was achieved in saline, serum, and whole blood (*120*). This system constitutes a simple immunoassay capable of detecting subnanogram-per-milliliter quantities of various analytes in different media within 10 to 30 min. Innovative results have also been reported by Mulvaney et al. (*121*), who prepared "glass-coated, analyte-tagged" nanoparticles for use in multiplexed bioassays. Recently, Doering and Ni (*122*) reported an improved class of core-shell colloidal nanoparticles that are highly efficient for SERS and suitable for multiplexed detection and spectroscopy at the single-particle level. The core-shell structure contains a metallic core for optical enhancement, a reporter molecule for spectroscopic signature, and an encapsulating silica shell for protection and conjugation. With nearly optimized gold cores and silica shells, the core-shell nanoparticles are stable in both aqueous electrolytes and organic solvents, yielding intense single-particle SERS spectra (*122*).

#### 4. SERS Gene Probes

There has been a great deal of interest in the development of optical techniques for genomics analysis such as nonradioactive DNA probes for use in biomedical diagnostics, pathogen detection, gene identification, gene mapping, and DNA sequencing. Hybridization of a nucleic acid probe to DNA biotargets (e.g., gene sequences, bacteria, viral DNA) permits a very high degree of accuracy in identifying DNA sequences complementary to that probe. The possibility of using SERS for low-level detection of DNA bases and oligonucleotides was demonstrated in several studies in the 1980s (*123–126*). More recently, the possibility of using Raman and/or SERS labels for extremely sensitive detection of DNA has been demonstrated. For example, Graham et al. (*113*) have claimed adequate sensitivity for single-molecule DNA detection via sur-

face-enhanced resonance Raman scattering (SERRS). With the use of labeled DNA as gene probes, the SERS technique has been recently applied to the detection of DNA fragments of the human immunodeficiency virus (*112*) as well as B-cell lymphoma 2 gene (*110*).

A critical aspect of sequencing the entire human genome involves defining and identifying large insert clones of DNA corresponding to specific regions of the human genome. An approach that facilitates large-scale genomic sequencing involves developing maps of human chromosomes into maps based on large-insert bacterial clones, such as bacterial artificial chromosomes (BACs) (*127–129*). A time-saving method for detecting multiple BAC clone–labeled probes simultaneously would be especially appealing for the BAC approach to genome sequencing and mapping. The SERS technique can provide this label-multiplex capability. The SERS gene probes described in this section preclude the need for radioactive labels and have great potential to provide sensitivity, selectivity, and label multiplexing for DNA sequencing as well as clinical assays.

A detection system used for recording the SERS spectrum of individual spots is illustrated in **Fig. 3**. An individual spot could correspond to an individual microdot on a hybridization platform. This system can readily be assembled using commercially available or off-the-shelf components. A focused, low-power laser beam is used to excite an individual spot on the hybridization platform. In our studies, a helium-neon laser is used to provide 632.8-nm excitation with approx 5 mW of power. A bandpass filter is used to isolate the 632.8-nm line prior to sample excitation. A signal collection optical module is used to collect the SERS signal at 180° with respect to propagation of the incident laser beam. The collection module includes a Raman holographic filter, which rejects the Rayleigh scattered radiation before it enters the collection fiber. Finally, the collection fiber is coupled to a spectrograph (Instruments S4 Inc., Edison, NJ, HR-320) which is equipped with a Princeton, Trenton, NJ, RE-ICCD-576S detection system. The signal collection module can be coupled directly to the spectrograph, bypassing the optical fiber. However, the optical fiber greatly simplifies measurements and improves reproducibility by minimizing critical optical alignment steps.

Because the SERS gene probe hybridization platform consists of a two-dimensional (2D) array of DNA hybridization spots, a method for recording signals from all spots simultaneously would be highly advantageous, reducing analysis time as well as precluding the need for platform scanning. For analysis of SERS gene probe–based assays, this feat can be accomplished through multispectral imaging (MSI). The concept of MSI is illustrated in **Fig. 4**. With conventional imaging, the optical emission from every pixel of an image is without the capability for tunable wavelength selection (**Fig. 4A**). With con-

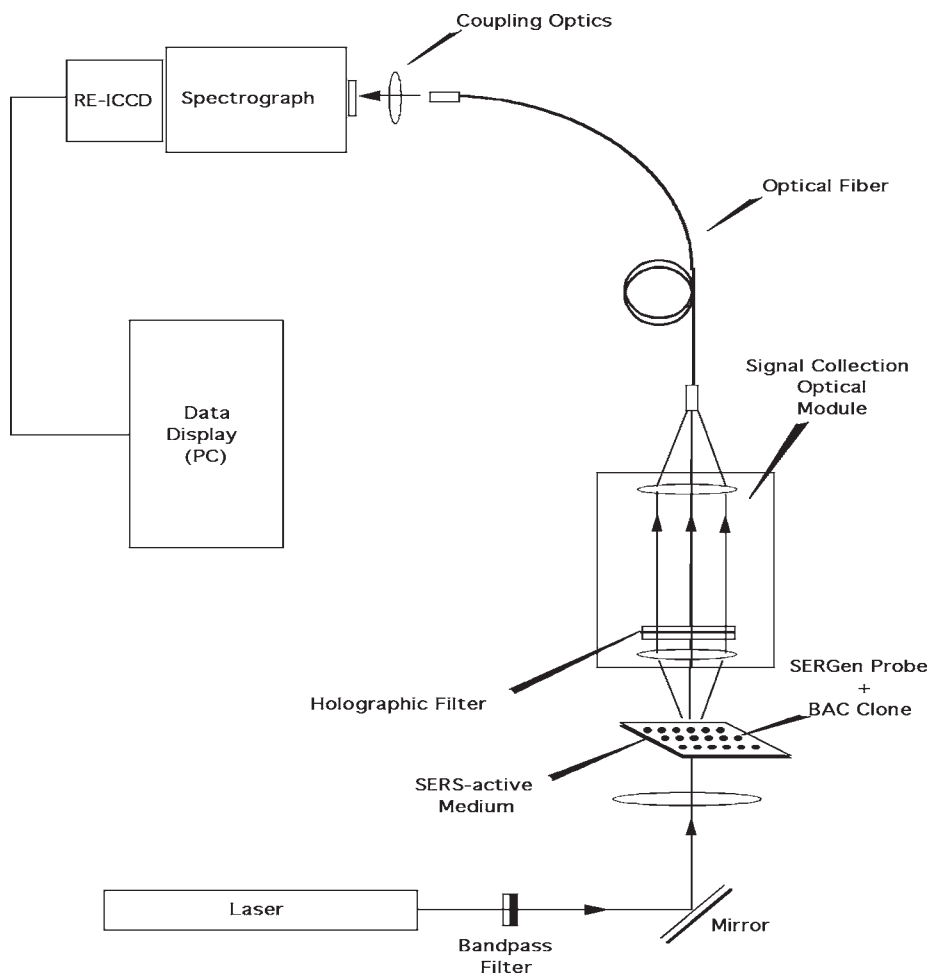


Fig. 3. Instrumental setup for spectral acquisition from individual spots on a bio-assay platform. RE-ICCD, red-enhanced intensified charge-coupled device.

ventional spectroscopy, the signal at every wavelength within a spectral range can be recorded, but for only a single analyte spot. This condition is the basis for the single-point analysis system described above in the previous paragraph. The MSI concept (**Fig. 4C**) combines these two recording modalities, thereby allowing the acquisition of a Raman spectrum for every hybridization spot on the assay platform, provided that the entire platform can be included in the instrument's field of view. Critical to the success of this concept is an imaging spectrometer (**Fig. 5**). In our studies, a rapid-scanning solid-state device, an acousto-optic tunable filter (AOTF), is used for tunable wavelength selection

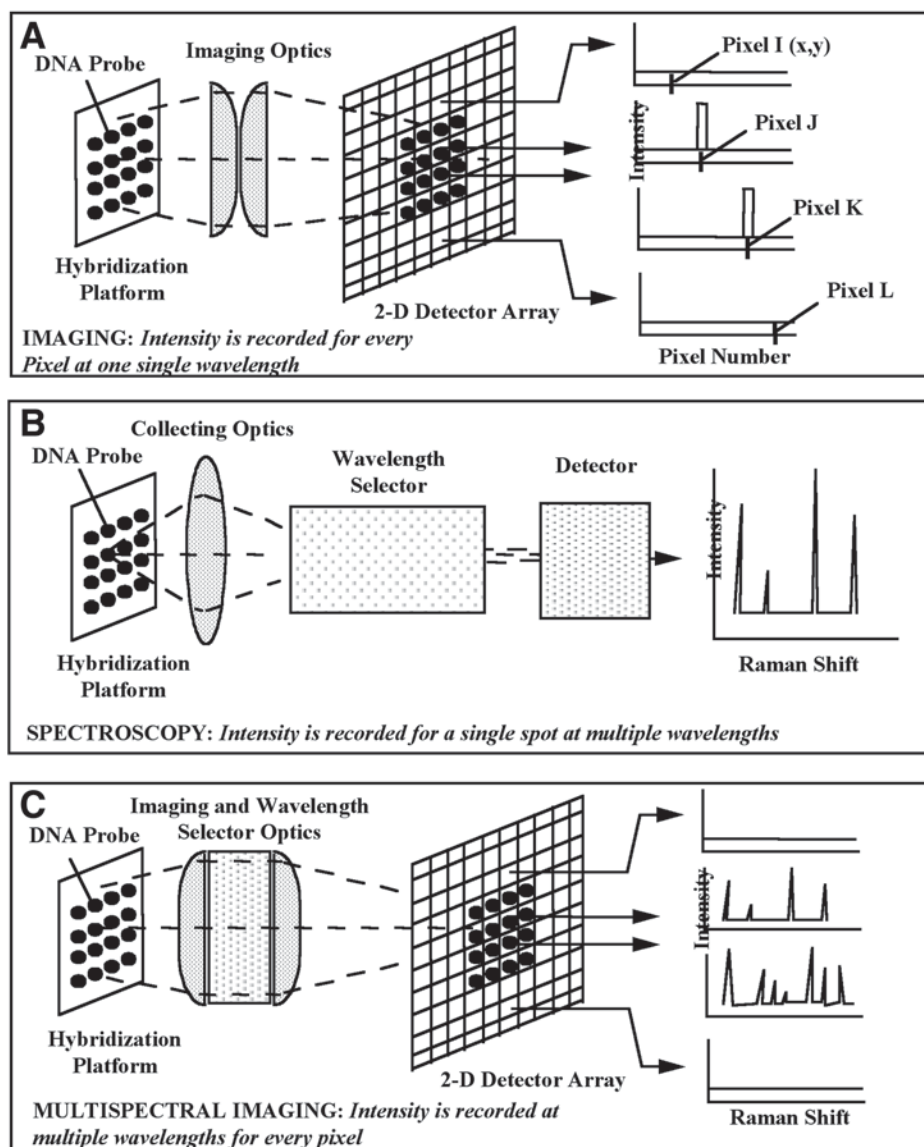


Fig. 4. Various modes of data acquisition from bioassay platforms: (A) imaging; (B) spectroscopy; (C) MSI.

with image-preserving capability. This compact solid-state device has an effective wavelength range of 450 to 700 nm with a spectral resolution of 2 Å and a diffraction efficiency of 70%. Wavelength tuning is achieved simply by supplying the AOTF with a tunable radiofrequency signal.



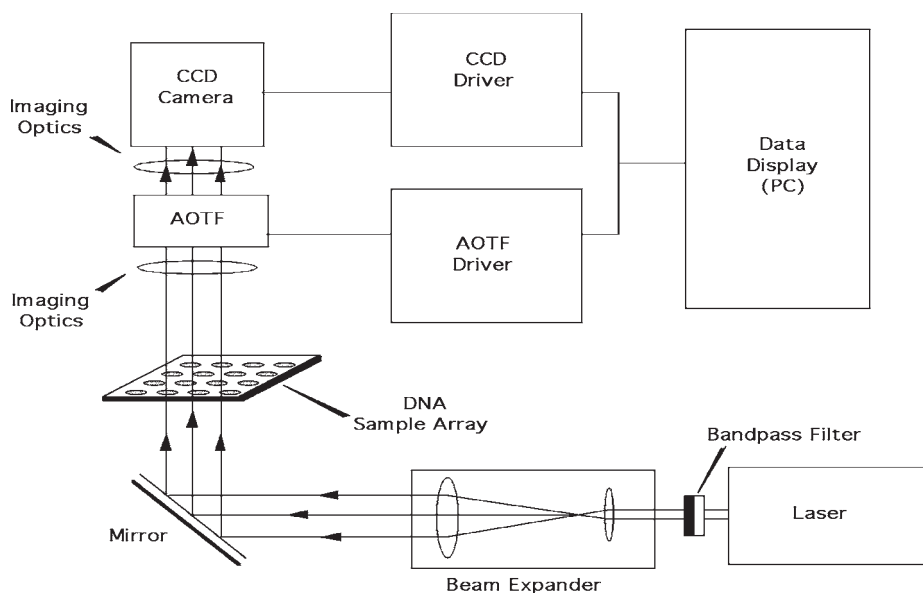


Fig. 5. Schematic diagram of an instrument for MSI of bioassay platforms. CCD, charge-coupled device.

We have recently developed in our laboratory a SERS-active DNA hybridization platform that greatly enhances the utility of the SERS gene probe technology (*106*). In previous work, hybridization of labeled DNA probes was performed on conventional commercially available platforms (e.g., DNA-bind plates), followed by SERS activation of the platform (*24,112*). To make the SERS gene probe technology more practical, we have developed an inherently SERS-active hybridization platform (*106*). No SERS activation of the assay is required following the hybridization step. The new DNA assay platform is an array of oligonucleotide capture probes immobilized directly on a silver island-based substrate prepared on glass. The capture probes were anchored directly to the silver surface via reaction with an SAM of alkyl mercaptans. The coupling approach involved esterification under mild conditions of a carboxylic acid (immobilized mercaptoundecanoic acid) with a labile group; an *N*-hydroxysuccinimide (NHS) derivative; and further reaction with a 5'-amine-labeled DNA capture probe, producing a stable amide (*130*). Our recent study demonstrated the potential of this technology in cancer gene detection (*BRCA1* and *BAX* genes) (*106*).

## 5. NSOM SERS Probes

NSOM is a methodology for obtaining subwavelength resolution (20–200 nm) with the spectroscopic information afforded by conventional optical spectro-

scopic techniques (*131,132*). The high spatial resolution of NSOM permits spectroscopic studies of individual biomolecules in high-density systems such as encountered in *in vivo* experiments (*8,133,134*). In this respect, NSOM combined with a Raman microscope is particularly attractive. So far, this novel scanning probe technique has been restricted to fluorescence and luminescence spectroscopy. With the use of SERS and tapered single-mode fiber probes, near-field Raman spectra have been obtained from single silver nanoparticles with excitation intensities as low as 10 nW (*135*). Recently, the combination of NSOM and SERS to obtain spectral, spatial, and chemical information of molecular adsorbates with subwavelength lateral resolution was reported (*8,9*). Near-field SERS spectra of cresyl fast violet and Rhodamine 6G on silver substrates have been obtained. Spectra from as few as 300 molecules or  $<10^{-2}$  monolayers adsorbed on about 10 silver nanoparticles can be recorded.

## 6. SERS as a Tool for Detection of Single-Molecules

There have been several reports of single-molecule detection using SERS in recent years (*4–7,113,136,137*). A critical factor in these milestone studies has been the development of exceptional SERS substrates. Most of the reports of single-molecule SERS detection have involved the use of metal colloids in suspensions. For example, Kneipp et al. demonstrated single-molecule detection of crystal violet in both silver (*5,6*) and colloid suspensions (*7*). In these studies, an effective cross-section of approx  $10^{-16}$  cm<sup>2</sup>/molecule was observed, corresponding to a  $10^{14}$  enhancement factor. The gold nanoparticles were commercially available but required proper agglomeration through the addition of sodium chloride. These results are promising because these cyanine dyes could be used as bioassay markers.

In some cases, bioassay markers can be resonance enhanced in addition to benefiting from SERS. For example, a DNA marker, 2,5,1',3',7',9'-hexachloro-6-carboxyfluorescein (HEX), has been used to achieve single-molecule detection via SERRS in a silver colloid suspension (*113*). The HEX signature was observed for  $8 \times 10^{-13}$  M DNA, which corresponded to less than 1 molecule per probed volume at any time required for measurement. Single-molecule detection has also been demonstrated on planar surface-based substrates. For example, enhancements to factors of  $10^{14}$ – $10^{15}$  have been observed for Rhodamine-6G molecules adsorbed on silver colloids that had been immobilized on a polylysine-coated glass surface (*4*). Similarly,  $10^{14}$ – $10^{15}$  factor enhancements have been reported for hemoglobin molecules adsorbed on silver nanoparticles immobilized on a polymer-coated silicon wafer (*136*). Researchers in this study reported, however, that single-molecule detection was observed only for hemoglobin molecules situated between and adsorbed to two silver nanoparticles.

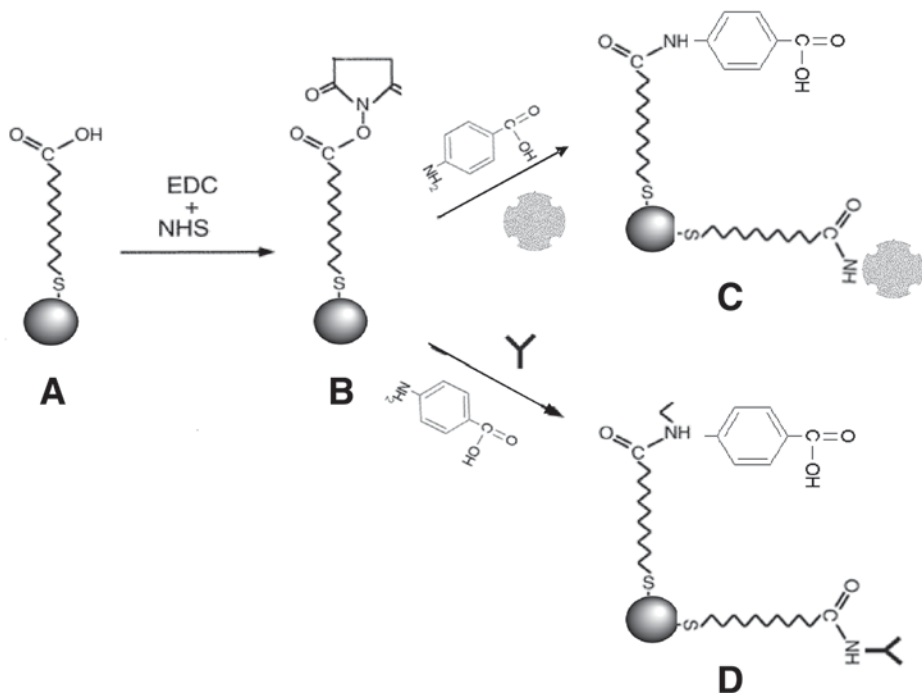


Fig. 6. Chemistry of dual labeling of SERS-active metal nanoparticles. **(A)** Formation of SAM of 11-mercaptoundecanoic acid (MUA) on a metal nanoparticle surface; **(B)** activation of MUA carboxylic acid groups by the carbodiimide, N-(3-dimethylaminopropyl)-N'-ethylcarbodiimide (EDC), and formation of NHS ester by N-hydroxysuccinimide (NHS); **(C,D)** subsequent reaction of activated intermediate with a combination of Raman marker and either streptavidin or amino group-containing biomolecules (e.g., antibodies).

## 7. SERS Nanoprobes for Intracellular Analysis

Direct observation of single molecules and single molecular events inside living cells could dramatically improve our understanding of basic cellular processes (e.g., signal transduction and gene transcription) as well as our knowledge of the intracellular transport and fate of therapeutic agents (e.g., antisense RNA and gene therapy vectors) (*106,138*). Therefore, it is extremely important to develop techniques to measure the reactions of individual molecules in living cells with spatiotemporal resolution (*139*).

In our laboratory, we are developing a strategy for the targeted delivery of SERS active metal colloids into single cells (*140*). **Figure 6** illustrates the surface chemistry involved in the process. The covalent attachment of a Raman-active marker (e.g., *p*-amino benzoic acid [PABA]) and a universal linker (e.g., streptavidin) onto alkanethiol-modified gold surfaces is achieved by

forming amide bonds via an *N*-hydroxysulfosuccinimide ester intermediate. The free carboxylic acid groups of PABA remain available for derivatization with many amino group-containing biomolecules, and the remaining unoccupied binding sites of streptavidin also allow for ready association with a variety of commercially available biotinylated biomolecules (e.g., antibodies, peptides, and nucleotides) via (strept)avidin-biotin interaction. Thus, the dual labeling on the same SERS-active metal nanoparticles provides a generic format for the functionalization of silver/gold nanoparticles. Considering the high sensitivity of SERS and the great flexibility of the surface modification schemes, the methodology is believed to be able to find wide application in numerous biomolecular systems, especially inside single living cells.

The feasibility of measuring SERS of native constituents with a single viable cell using 60-nm gold particles has been demonstrated recently (**139**), in which SERS mapping over a cell monolayer with 1- $\mu\text{m}$  lateral resolution shows different Raman spectra at almost all places, reflecting the highly inhomogeneous chemical organization of the cells. To identify cellular constituents at the single molecule level within single cells, it is clear that many parameters such as excitation wavelength, nanoparticle size, and state of aggregation still need to be optimized.

## 8. Conclusion

The development of dependable SERS-active metallic nanostructures has spurred renewed interest in Raman scattering as a practical analytical tool in bioanalysis. Because of the mainly electromagnetic origin of the SERS enhancement, it may be possible to achieve a strong SERS effect for each molecule. Until such developments were achieved, there was little interest in Raman scattering-based analysis because the cross-section of normal Raman scattering is minuscule ( $10^{-30}$  cm<sup>2</sup>/molecule) relative to the cross-sections available through other molecular spectroscopies, particularly luminescence. In the past, high laser powers were used to compensate for this shortcoming. However, this procedure had limited effectiveness, largely because it induced photodecomposition on probed molecules, particularly at trace-level concentrations. By contrast, SERS-inducing media enable trace-level detection with relatively low laser powers.

Both liquid- and solid-based SERS-inducing media are now being used for the detection of biologically significant compounds; moreover, innovative SERS-based biomedical applications such as gene probes are being developed. The development of such substrates and their use in practical analytical applications has required a triumph over the daunting challenge of producing nanoscale structures in reproducible and cost-effective ways. A significant portion of recent efforts has been devoted to investigating SERS coatings to

improve selectivity, longevity, and ruggedness. It is expected that the current development of SERS-active nanostructures will continue to lead to new exciting opportunities in biological applications such as *in situ* cellular monitoring and sensing.

## Acknowledgments

This work was jointly sponsored by the Federal Bureau of Investigation (Project No. 2051-II18-Y1), and the Office of Biological and Environmental Research, U.S. Department of Energy, under contract DE-AC05-00OR22725 with UT-Battelle, LLC; and by the Laboratory Directed Research and Development Program (Advanced Plasmonics Sensors Project) at Oak Ridge National Laboratory. Fei Yan and David L. Stokes are also supported by an appointment to the Oak Ridge National Laboratory Postdoctoral Research Associates Program, administered jointly by the Oak Ridge National Laboratory and Oak Ridge Institute for Science and Education.

## References

1. Fleischmann, M., Hendra, P. J., and McQuillan, A. J. (1974) Raman-spectra of pyridine adsorbed at a silver electrode. *Chem. Phys. Lett.* **26**, 163–166.
2. Jeanmaire, D. L. and Van Duyne, R. P. (1977) Surface Raman spectro-electrochemistry. 1. Heterocyclic, aromatic, and aliphatic-amines adsorbed on anodized silver electrode. *J. Electroanal. Chem.* **84**, 1–20.
3. Albrecht, M. G. and Creighton, J. A. (1977) Anomalously intense Raman-spectra of pyridine at a silver electrode. *J. Am. Chem. Soc.* **99**, 5215–5217.
4. Nie, S. M. and Emory, S. R. (1997) Probing single molecules and single nanoparticles by surface-enhanced Raman scattering. *Science* **275**, 1102–1106.
5. Kneipp, K., Wang, Y., Kneipp, H., Perelman, L. T., Itzkan, I., Dasari, R., and Feld, M. S. (1997) Single molecule detection using surface-enhanced Raman scattering (SERS). *Phys. Rev. Lett.* **78**, 1667–1670.
6. Kneipp, K., Kneipp, H., Deinum, G., Itzkan, I., Dasari, R. R., and Feld, M. S. (1998) Single-molecule detection of a cyanine dye in silver colloidal solution using near-infrared surface-enhanced Raman scattering. *Appl. Spectrosc.* **52**, 175–178.
7. Kneipp, K., Kneipp, H., Manoharan, R., Hanlon, E. B., Itzkan, I., Dasari, R. R., and Feld, M. S. (1998) Extremely large enhancement factors in surface-enhanced Raman scattering for molecules on colloidal gold clusters. *Appl. Spectrosc.* **52**, 1493–1497.
8. Deckert, V., Zeisel, D., Zenobi, R., and Vo-Dinh, T. (1998) Near-field surface enhanced Raman imaging of dye-labeled DNA with 100-nm resolution. *Anal. Chem.* **70**, 2646–2650.
9. Zeisel, D., Deckert, V., Zenobi, R., and Vo-Dinh, T. (1998) Near-field surface-enhanced Raman spectroscopy of dye molecules adsorbed on silver island films. *Chem. Phys. Lett.* **283**, 381–385.

10. Moskovits, M. (1985) Surface-enhanced spectroscopy. *Rev. Mod. Phys.* **57**, 783–826.
11. Wokaun, A. (1984) Surface-enhanced electromagnetic processes. *Solid State Phys. Adv. Res. Applic.* **38**, 223–294.
12. Schatz, G. C. (1984) Theoretical-studies of surface enhanced Raman-scattering. *Acc. Chem. Res.* **17**, 370–376.
13. Kerker, M. (1984) Electromagnetic model for surface-enhanced Raman-scattering (Sers) on metal colloids. *Acc. Chem. Res.* **17**, 271–277.
14. Chang, R. K. and Furtak, T. E. (1982) *Surface Enhanced Raman Scattering*, Plenum, New York.
15. Garrell, R. L. (1989) Surface-enhanced Raman-spectroscopy. *Anal. Chem.* **61**, 401A–411A.
16. Vo-Dinh, T. (1989) Surface-enhanced Raman spectrometry, in *Chemical Analysis of Polycyclic Aromatic Compounds* (Vo-Dinh, T., ed.), Wiley, New York, pp. 451–482.
17. Pemberton, J. E. (1991) in *Electrochemical interfaces: modern techniques for in-situ characterization* (Abruna, H. D., ed.), VCH Publishers, Inc.: New York, pp. 195–256.
18. Brandt, E. S. and Cotton, T. M. (1993) Surface-enhanced Raman scattering. In *Investigations of Surfaces and Interfaces Part B, Physical Methods of Chemistry Series*, 2nd ed., Rossiter, B. W., (Baetzold, R. C., eds.), Wiley, New York, pp. 663–718.
19. Otto, A., Mrozek, I., Grabhorn, H., and Akemann, W. (1992) Surface-enhanced Raman-scattering. *J. Phys. Condensed Matter* **4**, 1143–1212.
20. Vo-Dinh, T. (1995) Surface-enhanced Raman spectroscopy, in *Photonic Probes of Surfaces* (Halevi, P., ed.), Elsevier, New York, pp. 65–96.
21. Ruperez, A. and Laserna, J. J. (1996) Surface-enhanced Raman spectroscopy, in *Modern Techniques in Raman Spectroscopy* (Laserna, J. J., ed.), Wiley, New York, pp. 227–264.
22. Haller, K. L., Bumm, L. A., Altkorn, R. I., Zeman, E. J., Schatz, G. C., and Vanduyne, R. P. (1989) Spatially resolved surface enhanced 2nd harmonic-generation-theoretical and experimental-evidence for electromagnetic enhancement in the near-infrared on a laser microfabricated Pt surface. *J. Chem. Phys.* **90**, 1237–1252.
23. Golab, J. T., Sprague, J. R., Carron, K. T., Schatz, G. C., and Van Duyne, R. P. (1988) A surface enhanced hyper-Raman scattering study of pyridine adsorbed onto silver—experiment and theory. *J. Chem. Phys.* **88**, 7942–7951.
24. Vo-Dinh, T., Stokes, D. L., Griffin, G. D., Volkan, M., Kim, U. J., and Simon, M. I. (1999) Surface-enhanced Raman scattering (SERS) method and instrumentation for genomics and biomedical analysis. *J. Raman Spectrosc.* **30**, 785–793.
25. Nabiev, I. and Manfait, M. (1993) Industrial applications of the surface-enhanced Raman-spectroscopy. *Rev. Inst. Francais Petrole* **48**, 261–285.
26. Nabiev, I., Chourpa, I., and Manfait, M. (1994) Applications of Raman and surface-enhanced Raman-scattering spectroscopy in medicine. *J. Raman Spectrosc.* **25**, 13–23.

27. Kneipp, K., Kneipp, H., Itzkan, I., Dasari, R. R., and Feld, M. S. (1999) Surface-enhanced Raman scattering: a new tool for biomedical spectroscopy. *Curr. Sci.* **77**, 915–924.
28. Koglin, E. and Sequaris J. M. (1986) Surface enhanced Raman-scattering of biomolecules. *Top. Curr. Chem.* **134**, 1–57.
29. Pemberton, J. E. and Buck, R. P. (1981) Detection of low concentrations of a colored adsorbate at silver by surface-enhanced and resonance-enhanced Raman spectrometry. *Anal. Chem.* **53**, 2263–2267.
30. Pettinger, B., Wenning, U., and Wetzel, H. (1980) Surface-plasmon enhanced Raman-scattering frequency and angular resonance of Raman scattered-light from pyridine on Au, Ag and Cu electrodes. *Surf. Sci.* **101**, 409–416.
31. Loo, B. H. (1983) Surface-enhanced Raman-spectroscopy of platinum. 2. Enhanced light-scattering of chlorine adsorbed on platinum. *J. Phys. Chem.* **87**, 3003–3007.
32. Fleischmann, M., Graves, P. R., and Robinson, J. (1985) The Raman-spectroscopy of the ferricyanide ferrocyanide system at gold, beta-palladium hydride and platinum-electrodes. *J. Electroanal. Chem.* **182**, 87–98.
33. Carrabba, M. M., Edmonds, R. B., and Rauh, R. D. (1987) Feasibility studies for the detection of organic-surface and subsurface water contaminants by surface-enhanced Raman-spectroscopy on silver electrodes. *Anal. Chem.* **59**, 2559–2563.
34. Ren, B., Lin, X. F., Yang, Z. L., Liu, G. K., Aroca, R. F., Mao, B. W., and Tian, Z. Q. (2003) Surface-enhanced Raman scattering in the ultraviolet spectral region: UV-SERS on rhodium and ruthenium electrodes. *J. Am. Chem. Soc.* **125**, 9598, 9599.
35. Yang, Z. L., Wu, D. Y., Yao, J. L., Hu, J. Q., Ren, B., Zhou, H. G., and Tian, Z. Q. (2002) SERS mechanism of nickel electrode. *Chin. Sci. Bull.* **47**, 1983–1986.
36. Tian, Z. Q., Ren, B., and Wu, D. Y. (2002) Surface-enhanced Raman scattering: from noble to transition metals and from rough surfaces to ordered nano-structures. *J. Phys. Chem. B* **106**, 9463–9483.
37. Thierry, D. and Leygraf, C. (1985) The influence of photoalteration on surface-enhanced Raman-scattering from copper electrodes. *Surf. Sci.* **149**, 592–600.
38. Creighton, J. A., Blatchford, C. B., and Albrecht, M. C. (1979) Plasma resonance enhancement of Raman-scattering by pyridine adsorbed on silver or gold sol particles of size comparable to the excitation wavelength. *J. Chem. Soc. Faraday Trans. 2*, 790–798.
39. Sheng, R. S., Zhu, L., and Morris, M. D. (1986) Sedimentation classification of silver colloids for surface-enhanced Raman-scattering. *Anal. Chem.* **58**, 1116–1119.
40. Ni, F., Sheng, R. S., and Cotton, T. M. (1990) Flow-injection analysis and real-time detection of RNA bases by surface-enhanced Raman-spectroscopy. *Anal. Chem.* **62**, 1958–1963.
41. Lee, P. C. and Meisel, D. (1982) Adsorption and surface-enhanced Raman of dyes on silver and gold sols. *J. Phys. Chem.* **86**, 3391–3395.
42. Munro, C. H., Smith, W. E., Garner, M., Clarkson, J., and White, P. C. (1995) Characterization of the surface of a citrate-reduced colloid optimized for use as a substrate for surface-enhanced resonance Raman-scattering. *Langmuir* **11**, 3712–3720.



43. Tarabara, V. V., Nabiev, I. R., and Feofanov, A. V. (1998) Surface-enhanced Raman scattering (SERS) study of mercaptoethanol monolayer assemblies on silver citrate hydrosol: preparation and characterization of modified hydrosol as a SERS-active substrate. *Langmuir* **14**, 1092–1098.
44. Li, Y. S., Cheng, J. C., and Coons, L. B. (1999) A silver solution for surface-enhanced Raman scattering. *Spectrochim. Acta Part A* **55**, 1197–1207.
45. Ahern, A. M. and Garrell, R. L. (1987) In situ photoreduced silver-nitrate as a substrate for surface-enhanced Raman-spectroscopy. *Anal. Chem.* **59**, 2813–2816.
46. Prochazka, M., Mojzes, P., Stepanek, J., Vlckova, B., and Turpin, P. Y. (1997) Probing applications of laser ablated Ag colloids in SERS spectroscopy: improvement of ablation procedure and SERS spectral testing. *Anal. Chem.* **69**, 5103–5108.
47. Hildebrandt, P. and Stockburger, M. (1984) Surface-enhanced resonance Raman-spectroscopy of rhodamine-6G adsorbed on colloidal silver. *J. Phys. Chem.* **88**, 5935–5944.
48. Cao, Y. W., Jin, R., and Mirkin, C. A. (2001) DNA-modified core-shell Ag/Au nanoparticles. *J. Am. Chem. Soc.* **123**, 7961, 7962.
49. Pham, T., Jackson, J. B., Halas, N. J., and Lee, T. R. (2002) Preparation and characterization of gold nanoshells coated with self-assembled monolayers. *Langmuir* **18**, 4915–4920.
50. Graf, C. and van Blaaderen, A. (2002) Metallo-dielectric colloidal core-shell particles for photonic applications. *Langmuir* **18**, 524–534.
51. Jackson, J. B., Westcott, S. L., Hirsch, L. R., West, J. L., and Halas, N. J. (2003) Controlling the surface enhanced Raman effect via the nanoshell geometry. *Appl. Phys. Lett.* **82**, 257–259.
52. Van Duyn, R. P., Hulst, J. C., and Treichel, D. A. (1993) Atomic-force microscopy and surface-enhanced Raman-spectroscopy. 1. Ag island films and Ag film over polymer nanosphere surfaces supported on glass. *J. Chem. Phys.* **99**, 2101–2115.
53. Semin, D. J. and Rowlen, K. L. (1994) Influence of vapor-deposition parameters on SERS active Ag film morphology and optical-properties. *Anal. Chem.* **66**, 4324–4331.
54. Stockle, R. M., Deckert, V., Fokas, C., Zeisel, D., and Zenobi, R. (2000) Sub-wavelength Raman spectroscopy on isolated silver islands. *Vibrational Spectrosc.* **22**, 39–48.
55. Roark, S. E. and Rowlen, K. L. (1994) Thin Ag Films—influence of substrate and postdeposition treatment on morphology and optical-properties. *Anal. Chem.* **66**, 261–270.
56. Roark, S. E., Semin, D. J., Lo, A., Skodje, R. T., and Rowlen, K. L. (1995) Solvent-induced morphology changes in thin silver films. *Anal. Chim. Acta* **307**, 341–353.
57. Mosier-Boss, P. A. and Lieberman, S. H. (1999) Comparison of three methods to improve adherence of thin gold films to glass substrates and their effect on the SERS response. *Appl. Spectrosc.* **53**, 862–873.

58. Vo-Dinh, T., Hiromoto, M. Y. K., Begun, G. M., and Moody, R. L. (1984) Surface-enhanced Raman spectrometry for trace organic-analysis. *Anal. Chem.* **56**, 1667–1670.
59. Goudonnet, J. P., Begun, G. M., and Arakawa, E. T. (1982) Surface-enhanced Raman-scattering on silver-coated Teflon sphere substrates. *Chem. Phys. Lett.* **92**, 197–201.
60. Alak, A. M. and Vo-Dinh, T. (1989) Silver-coated fumed silica as a substrate material for surface-enhanced Raman-scattering. *Anal. Chem.* **61**, 656–660.
61. Moody, R. L., Vo-Dinh, T., and Fletcher, W. H. (1987) Investigation of experimental parameters for surface-enhanced Raman-scattering (SERS) using silver-coated microsphere substrates. *Appl. Spectrosc.* **41**, 966–970.
62. Alak, A. M. and Vo-Dinh, T. (1988) Surface-enhanced Raman spectrometry of chlorinated pesticides. *Anal. Chim. Acta* **206**, 333–337.
63. Bello, J. M., Stokes, D. L., and Vo-Dinh, T. (1989) Silver-coated alumina as a new medium for surface-enhanced Raman-scattering analysis. *Appl. Spectrosc.* **43**, 1325–1330.
64. Bello, J. M., Stokes, D. L., and Vo-Dinh, T. (1989) Titanium-dioxide based substrate for optical monitors in surface-enhanced Raman-scattering analysis. *Anal. Chem.* **61**, 1779–1783.
65. Alak, A. M. and Vo-Dinh, T. (1987) Surface-enhanced Raman-spectrometry of organophosphorus chemical-agents. *Anal. Chem.* **59**, 2149–2153.
66. Li, Y. S., Vo-Dinh, T., Stokes, D. L., and Yu, W. (1992) Surface-enhanced Raman analysis of p-nitroaniline on vacuum evaporation and chemically deposited silver-coated alumina substrates. *Appl. Spectrosc.* **46**, 1354–1357.
67. Li, Y. S. and Wang, Y. (1992) Chemically prepared silver alumina substrate for surface-enhanced Raman-scattering. *Appl. Spectrosc.* **46**, 142–146.
68. Helmenstine, A. M., Li, Y. S., and Vo-Dinh, T. (1993) Surface-enhanced Raman-scattering analysis of etheno adducts of adenine. *Vibrational Spectrosc.* **4**, 359–364.
69. Helmenstine, A., Uziel, M., and Vo-Dinh, T. (1993) Measurement of DNA-adducts using surface-enhanced Raman-spectroscopy. *J. Toxicol. Environ. Health* **40**, 195–202.
70. Vo-Dinh, T. and Stokes, D. L. (1993) Surface-enhanced Raman vapor dosimeter. *Appl. Spectrosc.* **47**, 1728–1732.
71. Alarie, J. P., Stokes, D. L., Sutherland, W. S., Edwards, A. C., and Vo-Dinh, T. (1992) Intensified charge coupled device-based fiberoptic monitor for rapid remote surface-enhanced Raman-scattering sensing. *Appl. Spectrosc.* **46**, 1608–1612.
72. Narayanan, V. A., Begun, G. M., Bello, J. M., Stokes, D. L., and Vo-Dinh, T. (1993) Analysis of the plant-growth regulator Alar (Daminozide) and its hydrolysis products using Raman-spectroscopy. *Analysis* **21**, 107–112.
73. Narayanan, V. A., Begun, G. M., Stump, N. A., Stokes, D. L., and Vo-Dinh, T. (1993) Vibrational-spectra of fluvalinate. *J. Raman Spectrosc.* **24**, 123–128.
74. Narayanan, V. A., Stokes, D. L., and Vo-Dinh, T. (1994) Vibrational spectral-analysis of eosin-y and erythrosin-b—intensity studies for quantitative detection of the dyes. *J. Raman Spectrosc.* **25**, 415–422.

75. Vo-Dinh, T., Houck, K., and Stokes, D. L. (1994) Surface-enhanced Raman gene probes. *Anal. Chem.* **66**, 3379–3383.
76. Vo-Dinh, T., Miller, G. H., Bello, J., Johnson, R., Moody, R. L., Alak, A., and Fletcher, W. R. (1989) Surface-active substrates for Raman and luminescence analysis. *Talanta* **36**, 227–234.
77. Wachter, E. A., Storey, J. M. E., Sharp, S. L., Carron, K. T., and Jiang, Y. (1995) Hybrid substrates for real-time sers-based chemical sensors. *Appl. Spectrosc.* **49**, 193–199.
78. Liao, P. F. (1982) in *Surface Enhanced Raman Scattering* (Chang, R. K. and Furtak, T. E., eds.), Plenum, New York, p. 379–390.
79. Vo-Dinh, T., Hiromoto, M. Y. K., Begun, G. M., and Moody, R. L. (1984) Surface-enhanced Raman spectrometry for trace organic-analysis. *Anal. Chem.* **56**, 1667–1670.
80. Meier, M., Wokaun, A., and Vo-Dinh, T. (1985) Silver particles on stochastic quartz substrates providing tenfold increase in Raman enhancement. *J. Phys. Chem.* **89**, 1843–1846.
81. Vo-Dinh, T., Meier, M., and Wokaun, A. (1986) Surface-enhanced Raman-spectrometry with silver particles on stochastic-post substrates. *Anal. Chim. Acta* **181**, 139–148.
82. Liao, P. F. and Stern, M. B. (1982) Surface-enhanced Raman-scattering on gold and aluminum particle arrays. *Opt. Lett.* **7**, 483–485.
83. Enlow, P. D., Buncick, M., Warmack, R. J., and Vo-Dinh, T. (1986) Detection of nitro polynuclear aromatic-compounds by surface-enhanced raman-spectrometry. *Anal. Chem.* **58**, 1119–1123.
84. Volkan, M., Stokes, D. L., and Vo-Dinh, T. (1999) A new surface-enhanced Raman scattering substrate based on silver nanoparticles in sol-gel. *J. Raman Spectrosc.* **30**, 1057–1065.
85. Volkan, M., Stokes, D. L., and Vo-Dinh, T. (2000) Surface-enhanced Raman of dopamine and neurotransmitters using sol-gel substrates and polymer-coated fiber-optic probes. *Appl. Spectrosc.* **54**, 1842–1848.
86. Pal, A., Stokes, D. L., Alarie, J. P., and Vo-Dinh, T. (1995) Selective surface-enhanced Raman-spectroscopy using a polymer-coated substrate. *Anal. Chem.* **67**, 3154–3159.
87. Vo-Dinh, T. and Stokes, D. L. (1999) Surface-enhanced Raman detection of chemical vapors with the use of personal dosimeters. *Field Anal. Chem. Technol.* **3**, 346–356.
88. Stokes, D. L., Pal, A., Narayanan, V. A., and Vo-Dinh, T. (1999) Evaluation of a chemical vapor dosimeter using polymer-coated SERS substrates. *Anal. Chim. Acta* **399**, 265–274.
89. Carron, K. T., Lewis, M. L., Dong, J. A., Ding, J. F., Xue, G., and Chen, Y. (1993) Surface-enhanced Raman-scattering and cyclic voltammetry studies of synergetic effects in the corrosion inhibition of copper by polybenzimidazole and mercaptobenzimidazole at high temperature. *J. Mater. Sci.* **28**, 4099–4103.

90. Deschaines, T. O. and Carron, K. T. (1997) Stability and surface uniformity of selected thiol-coated SERS surfaces. *Appl. Spectrosc.* **51**, 1355–1359.
91. Crane, L. G., Wang, D. X., Sears, L. M., Heyns, B., and Carron, K. (1995) SERS surfaces modified with a 4-(2-pyridylazo)resorcinol disulfide derivative—detection of copper, lead, and cadmium. *Anal. Chem.* **67**, 360–364.
92. Sulk, R., Chan, C., Guicheteau, J., Gomez, C., Heyns, J. B. B., Corcoran, R., and Carron, K. (1999) Surface-enhanced Raman assays (SERA): measurement of bilirubin and salicylate. *J. Raman Spectrosc.* **30**, 853–859.
93. Sulk, R. A., Corcoran, R. C., and Carron, K. T. (1999) Surface enhanced Raman scattering detection of amphetamine and methamphetamine by modification with 2-mercaptosuccinic acid. *Appl. Spectrosc.* **53**, 954–959.
94. Zou, S. Z. and Weaver, M. J. (1998) Surface-enhanced Raman scattering on uniform transition metal films: toward a versatile adsorbate vibrational strategy for solid-nonvacuum interfaces? *Anal. Chem.* **70**, 2387–2395.
95. Wilke, T., Gao, X. P., Takoudis, C. G., and Weaver, M. J. (1991) Surface-enhanced Raman-spectroscopy as a probe of adsorption at transition metal-high-pressure gas interfaces—NO, CO, and oxygen on platinum-coated gold, rhodium-coated gold, and ruthenium-coated gold. *Langmuir* **7**, 714–721.
96. Tarcha, P. J., DeSaja-Gonzalez, J., Rodriguez-Llorente, S., and Aroca, R. (1999) Surface-enhanced fluorescence on SiO<sub>2</sub>-coated silver island films. *Appl. Spectrosc.* **53**, 43–48.
97. Lacy, W. B., Olson, L. G., and Harris, J. M. (1999) Quantitative SERS measurements on dielectric-overcoated silver-island films by solution deposition control of surface concentrations. *Anal. Chem.* **71**, 2564–2570.
98. Lacy, W. B., Williams, J. M., Wenzler, L. A., Beebe, T. P., and Harris, J. M. (1996) Characterization of SiO<sub>2</sub>-overcoated silver-island films as substrates for surface-enhanced Raman scattering. *Anal. Chem.* **68**, 1003–1011.
99. Fu, X. Y., Mu, T., Wang, J., Zhu, T., and Liu, Z. F. (1998) pH-dependent assembling of gold nanoparticles on p-aminothiophenol modified gold substrate. *Acta Phys.-Chim. Sinica* **14**, 968–974.
100. Zhu, T., Zhang, X., Wang, J., Fu, X. Y., and Liu, Z. F. (1998) Assembling colloidal Au nanoparticles with functionalized self-assembled monolayers. *Thin Solid Films* **329**, 595–598.
101. He, H. X., Zhang, H., Li, Q. G., Zhu, T., Li, S. F. Y., and Liu, Z. F. (2000) Fabrication of designed architectures of Au nanoparticles on solid substrate with printed self-assembled monolayers as templates. *Langmuir* **16**, 3846–3851.
102. Wang, K. and Li, Y. S. (1997) Silver doping of polycarbonate films for surface-enhanced Raman scattering. *Vibrational Spectrosc.* **14**, 183–188.
103. Yang, X. M., Tryk, D. A., Ajito, K., Hashimoto, K., and Fujishima, A. (1996) Surface-enhanced Raman scattering imaging of photopatterned self-assembled monolayers. *Langmuir* **12**, 5525–5527.
104. Zhu, T., Yu, H. Z., Wang, J., Wang, Y. Q., Cai, S. M., and Liu, Z. F. (1997) Two-dimensional surface enhanced Raman mapping of differently prepared gold substrates with an azobenzene self-assembled monolayer. *Chem. Phys. Lett.* **265**, 334–340.

105. Maeda, Y., Yamamoto, H., and Kitano, H. (1995) Self-assembled monolayers as novel biomembrane mimetics. 1. Characterization of cytochrome-c bound to self-assembled monolayers on silver by surface-enhanced resonance Raman-spectroscopy. *J. Phys. Chem.* **99**, 4837–4841.
106. Vo-Dinh, T., Allain, L. R., and Stokes, D. L. (2002) Cancer gene detection using surface-enhanced Raman scattering (SERS). *J. Raman Spectrosc.* **33**, 511–516.
107. Michota, A., Kudelski, A., and Bukowska, J. (2000) Chemisorption of cysteamine on silver studied by surface-enhanced Raman scattering. *Langmuir* **16**, 10,236–10,242.
108. Michota, A., Kudelski, A., and Bukowska, J. (2001) Influence of electrolytes on the structure of cysteamine monolayer on silver studied by surface-enhanced Raman scattering. *J. Raman Spectrosc.* **32**, 345–350.
109. Culha, M., Stokes, D., Allain, L. R., and Vo-Dinh, T. (2003) Surface-enhanced Raman scattering substrate based on a self-assembled monolayer for use in gene diagnostics. *Anal. Chem.* **75**, 6196–6201.
110. Culha, M., Stokes, D., and Vo-Dinh, T. (2003) Surface-enhanced Raman scattering for cancer diagnostics: detection of the BCL2 gene. *Expert Rev. Mol. Diagn.* **3**, 669–675.
111. Vo-Dinh, T., Stokes, D. L., Griffin, G. D., Volkan, M., Kim, U. J., and Simon, M. I. (1999) Surface-enhanced Raman scattering (SERS) method and instrumentation for genomics and biomedical analysis. *J. Raman Spectrosc.* **30**, 785–793.
112. Isola, N. R., Stokes, D. L., and Vo-Dinh, T. (1998) Surface enhanced Raman gene probe for HIV detection. *Anal. Chem.* **70**, 1352–1356.
113. Graham, D., Smith, W. E., Linacre, A. M. T., Munro, C. H., Watson, N. D., and White, P. C. (1997) Selective detection of deoxyribonucleic acid at ultralow concentrations by SERRS. *Anal. Chem.* **69**, 4703–4707.
114. Dou, X., Yamaguchi, Y., Yamamoto, H., Doi, S., and Ozaki, Y. (1998) NIR SERS detection of immune reaction on gold colloid particles without bound/free antigen separation. *J. Raman Spectrosc.* **29**, 739–742.
115. Ni, J., Lipert, R. J., Dawson, G. B., and Porter, M. D. (1999) Immunoassay read-out method using extrinsic Raman labels adsorbed on immunogold colloids. *Anal. Chem.* **71**, 4903–4908.
116. Rohr, T. E., Cotton, T., Fan, N., and Tarcha, P. J. (1989) Immunoassay employing surface-enhanced Raman-spectroscopy. *Anal. Biochem.* **182**, 388–398.
117. Grabbe, E. S. and Buck, R. P. (1989) Surface-enhanced Raman-spectroscopic investigation of human immunoglobulin-G adsorbed on a silver electrode. *J. Am. Chem. Soc.* **111**, 8362–8366.
118. Hawi, S. R., Rochanakij, S., Adar, F., Campbell, W. B., and Nithipatikom, K. (1998) Detection of membrane-bound enzymes in cells using immunoassay and Raman microspectroscopy. *Anal. Biochem.* **259**, 212–217.
119. Dou, X., Takama, T., Yamaguchi, Y., Yamamoto, H., and Ozaki, Y. (1997) Enzyme immunoassay utilizing surface-enhanced Raman scattering of the enzyme reaction product. *Anal. Chem.* **69**, 1492–1495.

120. Hirsch, L. R., Jackson, J. B., Lee, A., Halas, N. J., and West, J. L. (2003) A whole blood immunoassay using gold nanoshells. *Anal. Chem.* **75**, 2377–2381.
121. Mulvaney, S. P., Musick, M. D., Keating, C. D., and Natan, M. J. (2003) Glass-coated, analyte-tagged nanoparticles: A new tagging system based on detection with surface-enhanced Raman scattering. *Langmuir* **19**, 4784–4790.
122. Doering, W. E. and Ni, S. M. (2003) Spectroscopic tags using dye-embedded nanoparticles and surface-enhanced Raman scattering. *Anal. Chem.* **75**, 6171–6176.
123. Sequaris, J. M. L. and Koglin, E. (1987) Direct analysis of high-performance thin-layer chromatography spots of nucleic purine derivatives by surface-enhanced Raman-scattering spectrometry. *Anal. Chem.* **59**, 525–527.
124. Koglin, E. and Sequaris, J. M. (1986) Interaction of proflavine with DNA studied by colloid surface enhanced resonance Raman-spectroscopy. *J. Mol. Struct.* **141**, 405–409.
125. Koglin, E., Sequaris, J. M., and Valenta, P. (1980) Surface Raman-spectra of nucleic-acid components adsorbed at a silver electrode. *J. Mol. Struct.* **60**, 421–425.
126. Koglin, E., Sequaris, J. M., and Valenta, P. (1982) Surface enhanced Raman-spectroscopy of nucleic-acid bases on Ag electrodes. *J. Mol. Struct.* **79**, 185–189.
127. Kim, U. J., Shizuya, H., Deaven, L., Chen, X. N., Korenberg, J. R., and Simon, M. I. (1995) Selection of a sublibrary enriched for a chromosome from total human bacterial artificial chromosome library using DNA from flow-sorted chromosomes as hybridization probes. *Nucleic Acids Res.* **23**, 1838–1839.
128. Kim, U. J., Birren, B. W., Slepak, T., Mancino, V., Boysen, C., Kang, H. L., Simon, M. I., and Shizuya, H. (1996) Construction and characterization of a human bacterial artificial chromosome library. *Genomics* **34**, 213–218.
129. Kim, U. J., Shizuya, H., Kang, H. L., et al. (1996) A bacterial artificial chromosome-based framework contig map of human chromosome 22q. *PNAS* **93**, 6297–6301.
130. Boncheva, M., Scheibler, L., Lincoln, P., Vogel, H., and Akerman, B. (1999) Design of oligonucleotide arrays at interfaces. *Langmuir* **15**, 4317–4320.
131. Pohl, D. W., Denk, W., and Lanz, M. (1984) Optical stethoscopy—image recording with resolution  $\lambda/20$ . *Appl. Phys. Lett.* **44**, 651–653.
132. Betzig, E., Trautman, J. K., Harris, T. D., Weiner, J. S., and Kostelak, R. L. (1991) Breaking the diffraction barrier—optical microscopy on a nanometric scale. *Science* **251**, 1468–1470.
133. Bian, R. X., Dunn, R. C., and Xie, X. S. (1995) Single molecule emission characteristics in near-field microscopy. *Phys. Rev. Lett.* **75**, 4772–4775.
134. Gresillon, S., Aigouy, L., Boccara, A. C., et al. (1999) Experimental observation of localized optical excitations in random metal-dielectric films. *Phys. Rev. Lett.* **82**, 4520–4523.
135. Emory, S. R. and Nie, S. (1997) Surface-enhanced Raman spectroscopy on single silver nanoparticles. *Anal. Chem.* **69**, 2631–2635.

136. Xu, H. X., Bjerneld, E. J., Kall, M., and Borjesson, L. (1999) Spectroscopy of single hemoglobin molecules by surface enhanced Raman scattering. *Phys. Rev. Lett.* **83**, 4357–4360.
137. Bjerneld, E. J., Foldes-Papp, Z., Kall, M., and Rigler, R. (2002) Single-molecule surface-enhanced Raman and fluorescence correlation spectroscopy of horseradish peroxidase. *J. Phys. Chem. B* **106**, 1213–1218.
138. Byassee, T. A., Chan, W. C. W., and Nie, S. (2000) Probing single molecules in single living cells. *Anal. Chem.* **72**, 5606–5611.
139. Kneipp, K., Haka, A. S., Kneipp, H., et al. (2002) Surface-enhanced Raman spectroscopy in single living cells using gold nanoparticles. *Appl. Spectrosc.* **56**, 150–154.
140. Yan, F., Wabuyele, M. B., Griffin, G. D., and Vo-Dinh, T. (2004) Targeted SERS nanoparticles for intracellular sensing. PittCon 2004, Chicago, IL. March 9–12.





## Bacterial Virus $\phi$ 29 DNA-Packaging Motor and Its Potential Applications in Gene Therapy and Nanotechnology

Peixuan Guo

### Summary

A controllable, 30-nm imitating DNA-packaging motor was constructed. The motor is driven by six synthetic adenosine triphosphate (ATP)-binding RNA (packaging RNA [pRNA]) monomers, similar to the driving of a bolt with a hex nut. Conformational change and sequential action of the RNA with fivefold (viral capsid)/sixfold (pRNA hexamer) mismatch could ensure continuous rotation of the motor with ATP as energy. In the presence of ATP and magnesium, a 5- $\mu$ m synthetic DNA was packaged using this motor. On average, one ATP was used to translocate two bases of DNA. The DNA-filled capsids were subsequently converted into up to  $10^9$  PFU/mL of infectious virus. The three-dimensional structures of pRNA monomer, dimer, and hexamer have been probed by photoaffinity crosslinking, chemical modification interference, cryo-atomic force microscopy, and computer modeling. The pRNA's size and shape can be controlled and manipulated at will to form stable dimers and trimers. Cryo-atomic force microscopy revealed that monomers, dimers, and trimers displayed a checkmark outline, elongated shape, and triangular structure, respectively. The motor can be turned off by  $\gamma$ -S-ATP or EDTA and turned on again with the addition of ATP or magnesium, respectively. The formation of ordered structural arrays of the motor complex and its components, the retention of motor function after the 3'-end extension of the pRNA, and the ease of RNA dimer, trimer, and hexamer manipulation with desired shape and size make this RNA-containing motor a promising tool for drug and gene delivery and for use in nanodevices.

**Key Words:** pRNA; bacteriophage  $\phi$ 29; ribozyme; gene therapy; nanomotor; DNA packaging; hexamer; RNA structure and function; nanobiotechnology.

### 1. Introduction

During the life cycle, viral genomic DNA replication and structural protein synthesis are accomplished by two separate cell systems (1–5). After these two subprocesses are complete, the resultant components, protein and nucleic acid,

From: *Methods in Molecular Biology*, vol. 300:  
*Protein Nanotechnology, Protocols, Instrumentation, and Applications*  
Edited by: T. Vo-Dinh © Humana Press Inc., Totowa, NJ

must interact with one another in order to form a complete virion; this process is referred to as viral DNA packaging (6,8–14). Double-stranded DNA (dsDNA) viruses have their lengthy genomic DNA translocated with high velocity into a preformed shell (procapsid), and packaged into near-crystalline density (15,17,18). Because this is an energetically unfavorable motion task, a viral DNA-packaging motor, utilizing adenosine triphosphate (ATP) as energy, is employed (19,20,22–32).  $\phi$ 29, a bacterial dsDNA virus that infects *Bacillus subtilis*, possesses several characteristics common to linear dsDNA viruses, including the use of a pair of noncapsid proteins and ATP to translocate viral DNA into a procapsid, which has been preformed with the aid of scaffolding proteins that are removed before or during DNA packaging, with the presence of at least one component functioning in a manner similar to that of the adenosine triphosphatases (ATPases) (18,33–36); the presence of at least one component functioning in a manner similar to that of the adenosine triphosphatases (ATPases) (30). Examples of viruses with motors similar to  $\phi$ 29 include T4 (37),  $\lambda$  (38,39), T3 and T7 (40–42), phage 21 (43), P22 (44–46), P1 (47), psiM2 (48), Sfi21 (49), herpes simplex virus (HSV) (50–52), cytomegalovirus (CMV) (53), adenovirus (54–56), and poxvirus (57,58). Procapsids of these phages contain a portal vertex (connector or DNA-translocating vertex). Packaging of DNA at this vertex is directional and oriented (5,18,33–36). The pair of noncapsid DNA-packaging proteins can be classified into group 1 proteins, which are smaller and are responsible for DNA binding, and group 2 proteins, which are larger, DNA-dependent ATPases that, as has been proven in some phages, bind specifically to the portal vertex of the procapsid (3,30,41,59–74). As reported earlier (30), the nonstructural DNA-packaging components can be divided into two broad categories based on their role in DNA packaging: (1) procapsid binding, including gpA of  $\lambda$  (14,38), gp2ÄVof  $\phi$ 21 (43), gp19 of T3/T7 (28,76,77), and gp17 of T4 (37); and (2) DNA interaction, including gp18 of T3/T7, gpNu1 of  $\lambda$ , gp1 of  $\phi$ 21, and gp16 of T4 (30). In  $\phi$ 29, the nonstructural components involved in motor function include packaging RNA (pRNA), gp16, and gp3. pRNA and gp16 have been shown to bind procapsid and ATP (79,80), and gp3 binds DNA (81,82). ATP hydrolysis drives DNA translocation. Concatemeric DNA is used as a substrate for packaging except in the case of  $\phi$ 29, which is similar to adenovirus in that a protein is covalently attached to each 5' end of the viral genome (81,82).

Data from HSV (83), equine herpesvirus (84), CMV (85), and avian infectious laryngotracheitis virus (86) indicate that these viruses utilize a packaging pathway similar to that of the dsDNA bacteriophages in most, if not all, packaging stages. For instance, in these viruses, viral DNA is also packaged into a procapsid containing scaffolding protein (85–88). In addition, concatemeric DNA is formed and then cut into monomers during the maturation process (41,83,85,89). The nonstructural DNA-packaging enzyme contains a consen-

**Table 1**  
**Experimental Data for Stoichiometry and Slopes<sup>a</sup>**

Components for $\phi$ 29 virion assembly	Function	Total subunits/ virion	Mathematical quantification of stoichiometry	< of curve (°)	Slopes (tan) empirical	Slopes (tan) theoretical
DNA-gp3	Genome complex	1	1	$45 \pm 4$	1	1
Procapsid	Hold DNA	1	1	$47 \pm 3$	1	1
pRNA trimer	DNA packaging	6	2	$56 \pm 2$	1	1.48
pRNA dimer	DNA packaging	6	3	$64 \pm 5$	2	2.05
pRNA monomer	DNA packaging	6	6	$72 \pm 3$	3	3.14
gp9	Tail-knob protein	10	9	$77 \pm 2$	4	4.33
gp11	Lower collar	12	12	$79 \pm 1$	5	5.67
gp12	Antireceptor	24	12	$80 \pm 2$	6	5.67

<sup>a</sup>Adapted from **ref. 80** with permission.

sus ATP-binding domain (88,90). Furthermore, DNA-filled capsids exhibit a fingerprint-like motif of finely spaced curvilinear striations, similar to some phages, when viewed with cryoelectron microscopy (88). Poxviruses also use concatemeric DNA as a substrate for packaging (91–93). The DNA-packaging enzyme of vaccinia virus has been found to be a potential ATPase (57). Adenovirus also shares similarities to dsDNA bacteriophages, including packing of DNA into preformed procapsids (12,55,94). Given the broad similarities found among different viruses, DNA packaging is an intriguing issue in virology, and it has relevance to many other biochemical processes such as DNA translocation, macromolecular interactions, and bioenergetics.

In vitro assembly of the linear double-stranded (dsDNA) viruses always proceeds in two steps: (1) motor-driven DNA packaging and (2) virion maturation (17,34,95–97). Bacteriophage  $\phi 29$  of *B. subtilis* is a particularly ideal model for studying the function of viral DNA-packaging motor, because virtually every DNA molecule added can be efficiently packaged in vitro, with all components being overproduced and purified (5,9,30,79,98,99,101,102). Procapsids produced from cloned structural genes in  $\phi 29$  are competent for DNA packaging, and the DNA-filled capsids prepared using this system can be converted into infectious virus although the addition of neck and tail proteins (101,102).

Utilizing pRNA's easily manipulable structure, a fully defined in vitro  $\phi 29$  DNA-packaging system has been developed (9). With purified procapsid, gp16, pRNA, and ATP, up to 90% of the added DNA-gp3 can be packaged into the procapsid via the motor constructed with recombinant gene products. After DNA packaging, the in vitro assembly system can convert DNA-filled capsids into infectious  $\phi 29$  virions when purified proteins gp9, gp11, gp12, and gp13 (103,104) are added. Many infectious virions have been assembled in vitro by extract complementation (1–4,74,105–114,116–118), and by the use of synthetic nucleic acid and purified recombinant protein components (103,104). Fully defined in vitro DNA-packaging systems have also been developed and constructed for T3 (8), T4 (37), and  $\lambda$  (119) and  $\phi 29$  (9).

## 2. Components of the $\phi 29$ DNA-Packaging Motor

### 2.1. Procapsid and DNA-Packaging Motor

Procapsids play an active role in the DNA-packaging process of dsDNA viruses. Phage procapsids are largely composed of three structural proteins: (1) the capsid protein, (2) the scaffolding protein, and (3) the connector protein (36,95,120). The three-dimensional (3D) structure of  $\phi 29$ 's empty procapsid precursor has been obtained by reconstruction of cryo-electron microscopy images (121). The icosahedral procapsid of  $\phi 29$  consists of 235 copies of the major capsid protein (gp8), 26 copies of scaffolding protein (gp7), and 12 cop-

ies of the head-tail connector protein (gp10) (260). Studying sequential interactions of these three proteins, (122) found that  $\phi$ 29 procapsid assembly differs considerably from the single-assembly pathway, and that the coexistence of scaffolding protein, major capsid protein, and connector over a threshold concentration is required to form  $\phi$ 29 procapsid. During such a process, scaffolding protein links major capsid protein and connector. The three components interact so quickly that no clear intermediates have been observed.

## 2.2. Capsid Proteins

The capsid proteins are the major structural components for the formation of viral protein shells. Examples include gpE for bacteriophage  $\lambda$  (123,124), gene 23 (major capsid subunit) or gene 24 (pentamer subunit) product for bacteriophage T4 (37), and gp8 for bacteriophage  $\phi$ 29 (122). Besides playing a structural role, it has been found that capsid proteins can play a role in packaging. For example, missense mutations in the capsid proteins of bacteriophage  $\lambda$  can block packaging in proheads that are still morphologically normal (126–128). The procapsid might be involved in an ATP-binding process that has been reported in dsDNA virus  $\phi$ 6 (129).

## 2.3. Scaffolding Proteins

Scaffolding proteins are structural proteins that are required for successful procapsid assembly, but are not part of the mature virion; they are released from procapsids at the initiation of or during DNA packaging. For  $\phi$ 29, the scaffolding protein (gp7) is not required for the competence of procapsids in DNA packaging (4,36). Scaffolding proteins of phage P22 are catalytic and can be utilized in the assembly of a second procapsid once they are released from the first (109). The exact function of scaffolding proteins, however, is not yet clear, and multiple roles are possible. For example, the scaffolding protein may form a core structure around which capsid proteins assemble (130–135). In some cases, they may serve as chaperones to promote the correct folding of capsid proteins. Additionally, they may be involved in mediating a putative capsid protein/connector protein interaction, excluding cellular proteins from the inside of the procapsid, or facilitating the early stages of DNA entrance into the procapsid (97).

## 2.4. Connector

One of the essential components of the motor is the connector complex, a dodecameric structure with a central channel (30–60 Å) through which viral DNA is packaged into the capsid and exits during infection (50,136–141).  $\phi$ 29 connector is a trapezoid-shaped cylinder with a 3.6-nm central channel through which DNA enters the capsid. Although the individual portal

proteins of different viruses share little sequence homology and exhibit large variations in molecular weight, the portal complexes possess a significant amount of morphological similarity (35). In the case of  $\phi 29$ , the structure of one phage portal protein has been determined at atomic resolution (136,137). The connector ring consists of a 12  $\alpha$ -helical subunit, with the central channel being formed by three long helices of each subunit. The ring is 138 Å across at its wide end and 66 Å at the narrow end. The internal channel is 60 Å at the top and 36 Å at the bottom. The wide end of the connector is located in the prohead, and its narrow end partially protrudes out of the capsid. The connector is located at the fivefold vertex of the viral capsid, which leads to a symmetry mismatch between capsid and portal (35,142). It has been proposed that such a mismatch is required for the smooth rotation of the portal protein during DNA packaging (142,143).

## 2.5. Genomic DNA

A virus-encoded protein is covalently linked to each 5' end of the  $\phi 29$  genome (144–146). The terminal protein gp3 functions both as a primer for the initiation of DNA replication (147) and as an essential protein for DNA packaging (5,99). Typically,  $\phi 29$  DNA-gp3 is purified from cells infected by a 4<sup>-</sup> 8<sup>-</sup> suppressor-sensitive mutant (amber mutation) (98). In this mutant, late proteins are not produced when the phage grows in a nonpermissive host, and large quantities of phage DNA-gp3 can be isolated. gp3 has also been purified from cloned gene products (82). Infectious DNA-gp3 can be synthesized in vitro (82,103,145–149).

## 2.6. gp16

The two noncapsid DNA-packaging proteins of various bacteriophages apparently cooperate to link the procapsid to the DNA-packaging substrate, cut monomers of DNA from concatemers, and serve as a DNA-translocation enzyme and/or ATPase. It was found that gp16 of  $\phi 29$  contains both A-type and B-type consensus ATP-binding sequences, and the predicted secondary structure for ATP binding (30). The A-type sequence of gp16 is “basic-hydrophobic region-G-X<sub>2</sub>-G-X-G-K-S-X<sub>7</sub> hydrophobic.” One of the nonstructural DNA-packaging proteins of all dsDNA phages likely functions as an ATPase (30). This prediction has been supported by subsequent studies involving bacteriophages T4 (150),  $\lambda$  (38,152,153), T3 (154), and P22 (155), as well as herpesviruses (88,90) and the vaccinia virus (57).

gp16 is quite hydrophobic, and when overproduced in *E. coli*, it agglutinates into lumps and loses biological activity. A very simple procedure has been developed to purify gp16 to homogeneity in a soluble, active form, in a single purification step (9). The lumps (inclusion bodies) are collected by differential centrifugation, and the protein, denatured and dissolved with guanidine chloride, is passed through a Sephadex column in the presence of 7.5 M urea. gp16



is eluted as a discrete peak with >90% purity. The purified gp16 is then renatured by dialysis against potassium chloride (9). It has been shown that two unique cysteine residues of gp16 are important for biological activity, and, therefore, the reducing agent dithiothreitol is strictly required when guanidine chloride is used for denaturation.

gp16 has been found to bind ATP (19,30,156,157), but the role of gp16 in the  $\phi$ 29 DNA-packaging motor is still a mystery. The hydrophobicity, low solubility, and self-aggregation of  $\phi$ 29 gp16 have long hindered further refinement of the current understanding of its packaging mechanism. Contradictory data regarding ATPase activity, binding location, and the stoichiometry of gp16 have been published (19,30). In the traditional method (30), gp16 was purified in a denatured condition, and active gp16 was obtained by dialysis against 4 mM KCl buffer for 40 min for renaturation, but the renatured gp16 aggregated again within 15 min after renaturation. Recently, it was reported that gp16 was made soluble in the cell by coexpression with groE (157). Indeed, active gp16 was purified through use of this overexpression system. However, although coexpression with groE solved the problem of aggregation within the cell, it could not solve the problem of self-aggregation after purification. PEG and acetone have been used to aid in the purification of gp16 in a homogenous and highly active form (19,259).

## 2.7. pRNA

Even considering its similarities to other dsDNA viruses regarding DNA, several aspects of the specific structure of  $\phi$ 29 are novel and unique, and it is therefore a particularly promising choice for further study. A 120 nt RNA (discovered in 1987 [98]) is vital to proper functioning of the motor. This pRNA binds ATP (80) and enhances the ATPase activity of gp16 (156). A computer model of the pRNA/connector complex has been reported (158). Notably, pRNA binds the connector and participates actively in DNA translocation (79,159), but it leaves the capsid after DNA packaging is completed (160);  $\phi$ 29-encoded pRNA is not present in the mature virion (98). Similar but distinct pRNAs have been revealed through phylogenetic analyses of other phages; there are few conserved bases, but the observed secondary structures are quite similar (161,162). pRNAs from other phages can never replace  $\phi$ 29 pRNA in its DNA packaging (161).

### 2.7.1. Two Domains of pRNA

The two functional domains of pRNA are the procapsid-binding domain, located at its central region (159,163–165), bases 23 to 97, and the DNA translocation domain, located at the 5'/3' paired ends (166). A number of different approaches have been employed to confirm this result, including base deletion

and mutation (**166–169**), ribonuclease probing (**160,161,163**), oligo targeting (**170**), competition assays to inhibit phage assembly (**171–173**), ultraviolet crosslinking to portal protein (**159**), psoralen crosslinking (**160**), and computer modeling (**158**). It has been reported that the C<sup>18</sup>C<sup>19</sup>A<sup>20</sup> bulge of pRNA is solvent exposed when pRNA is bound to procapsid (**174**) and is critical for DNA translocation (**143,162,169**) (**163**). The C<sup>18</sup>C<sup>19</sup>A<sup>20</sup> bulge might be directly involved in interacting with ATP, gp16, DNA-gp3, or capsid components.

### 2.7.2. Formation of Dimers, Trimers, and Hexamers

pRNA dimer is the building block and dimer → tetramer → hexamer is the pathway to hexamer assembly. Six individual  $\phi$ 29 pRNAs form a ring through intermolecular base pairing between the right loop (bases 45–48) and the left loop (bases 82–85) (**143**). Cryo–atomic force microscopy (cryo-AFM) has been used to directly visualize the tertiary structure of pRNA monomers, native and covalently linked dimers, and native trimers. The pRNA monomers fold into a checkmark-shaped structure, the dimers have an elongated shape, and the trimers exhibit a triangular shape. Mg<sup>2+</sup> induces appropriate folding of pRNA for dimerization (**160,174**). pRNA dimers bind to the portal vertex (connector) and serve as the building blocks for hexamer assembly (**164,174**). The DNA-translocating machine is geared by the formation of a hexameric complex; this suggests that the mechanism employed is similar to that of the consecutive firing of six cylinders of a car engine. Base pairing is demonstrated through an experimental procedure in which pRNAs with mutated loop sequences are constructed. Uppercase and lowercase letters have been used in the literature to indicate the right- and left-hand loops of the pRNA, respectively. Complementary sequences are delineated by the same letter in uppercase and lowercase. For example, in pRNA A-a', right loop A (5'GGAC<sub>48</sub>) and left loop a' (3'CCUG<sub>82</sub>) are complementary, whereas in pRNA A-b', the four bases of the right loop A are not complementary to the sequence of the left loop b' (3'UGCG<sub>82</sub>). Mutant pRNAs with complementary loop sequences (such as pRNA I/i') are active in  $\phi$ 29 DNA packaging, whereas mutants with non-complementary loops (such as pRNA A/b') are inactive (**175,176**). It was found that pRNAs A-i' and I-a' were inactive in DNA packaging alone, but when A-i' and I-a' were mixed together, DNA-packaging activity was restored. This result is explained by the transcomplementarity of pRNA loops; the right-hand loop A of pRNA A-i' pairs with the left-hand loop a' of pRNA I-a' (**175,176**).

### 2.7.3. Stoichiometric Determination of pRNA

As a first step in the determination of pRNA's role in DNA packaging, it is important to conclusively determine how many copies of pRNA are used in

each DNA-packaging event. A number of methods have been proven useful in determining the stoichiometry of pRNA and of the other components necessary for motor function (**163,172,175,177,178**). These various approaches have indicated that six pRNAs are present in the  $\phi 29$  DNA-translocation motor. Such methods include binomial distribution (**172,178**); comparing slopes of concentration dependence (**103,172**); and finding the common multiples of 2, 3, and 6 by using sets of two interlocking pRNAs, three interlocking pRNAs, and six interlocking pRNAs (**175**).

### 2.7.3.1. BINOMIAL DISTRIBUTION (**172,178**)

pRNAs mutated at the 5'/3' paired region retain procapsid-binding capacity but lose DNA-packaging function. When mutant pRNA and wild-type (WT) (**Fig. 1**) pRNA are mixed at various ratios for in vitro assembly assays (e.g., 30% mutant and 70% WT), the probability of procapsids possessing a certain amount of mutant and a certain amount of WT pRNA can be determined by expanding the binomial as follows:

$$(p + q)^Z = \binom{Z}{0} p^Z + \binom{Z}{1} p^{Z-1} q + \binom{Z}{2} p^{Z-2} q^2 + \dots + \binom{Z}{Z-1} p q^{Z-1} + \binom{Z}{Z} q^Z = \sum_{M=0}^Z \binom{Z}{M} p^{Z-M} q^M$$

in which  $\binom{Z}{M} = [Z!/M!(Z-M)!]$ ;  $Z$  is the total number of pRNAs per procapsid; and  $p$  and  $q$  are the percentage of mutant and WT pRNA, respectively, used in the reaction mixture. For example, if the total number of pRNA per procapsid required for DNA packaging ( $Z$ ) is 3, then the probability of all combinations of mutant ( $M$ ) and WT ( $N$ ) pRNAs on a given procapsid can be determined by expansion of the binomial:  $(p + q)^3 = p^3 + 3p^2q + 3pq^2 + q^3 = 100\%$ . That is, in the procapsid population, it is possible to determine the probability of a procapsid possessing either three copies of mutant pRNA, two copies of mutant and one copy of WT, one copy of mutant and two copies of WT, or three copies of WT, represented by  $p^3$ ,  $3p^2q$ ,  $3pq^2$ , and  $q^3$ , respectively. Suppose that there are 70% mutant and 30% WT pRNA in a reaction mixture. The percentage of procapsids that possess one copy of mutant and two copies of WT would then be  $3pq^2$ , i.e.,  $3(0.7)(0.3)^2 = 19\%$ . If only one mutant pRNA per procapsid is sufficient to render the procapsid unable to package DNA, then only those procapsids with three bound WT pRNAs (zero mutant pRNA,  $q^3$ ) would package DNA. The yield of virions from the empirical data was plotted and compared to a series of predicted curves to find a best fit. It was found that the experimental inhibition curve most closely resembled, in both slope and magnitude, the predicted curves in which  $Z = 5$  or 6 (**172**).

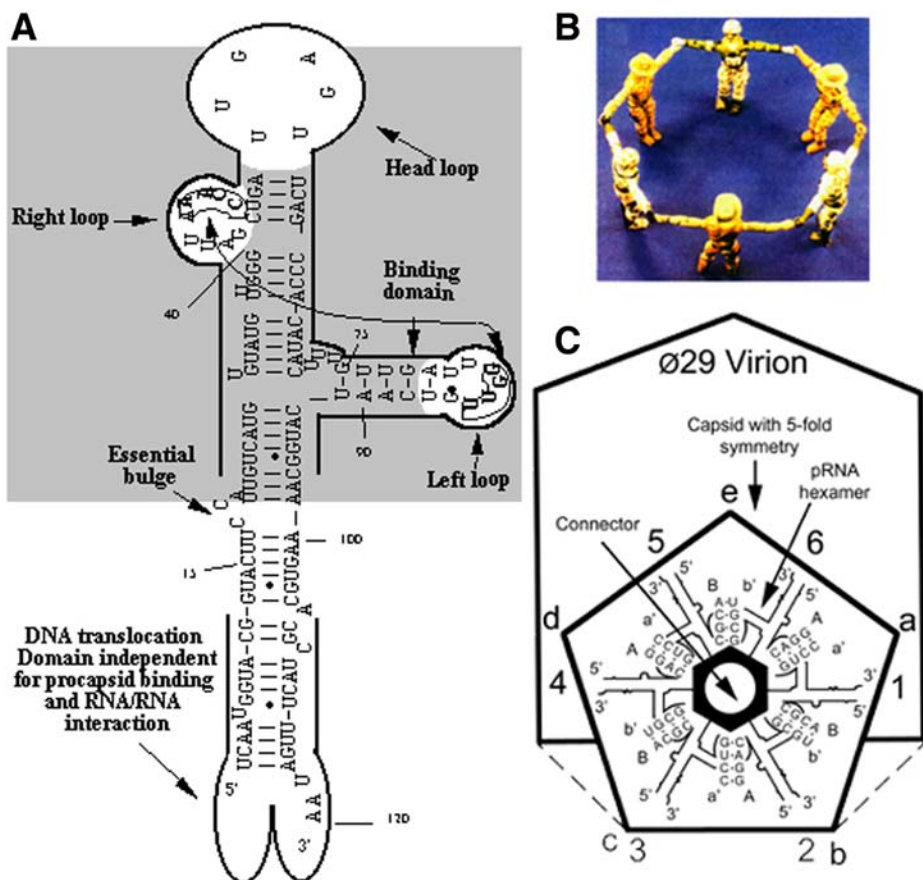


Fig. 1. Structure, domain and location of pRNA on  $\phi 29$  viral particle. **(A)**, Secondary structure of pRNA(A-b'). A and b' are the left and right loops responsible for intermolecular interaction. The intermolecular binding domain (shaded area) and the reactive DNA translocation domain are marked with bold lines. The four bases in the right and left loops, which are responsible for inter-molecule interactions, are placed in boxes. **(B)**, Power Rangers to depict pRNA hexamer by hand-in-hand interaction. **(C)**,  $\phi 29$  particle showing the DNA-packaging motor with pRNA hexamer formed via the interaction of pRNA (A-b') and (B-a'). The surrounding pentagon stands for the fivefold symmetrical capsid vertex, viewed as end-on with the virion as a side view. The central region of pRNA binds to the connector and the 5'/3' paired region extends outward (From **ref. 162** with permission.)

## 2.7.3.2. SLOPES OF CONCENTRATION DEPENDENCE (103,172,179)

The dose response curves of in vitro  $\phi$ 29 assembly vs concentration of various assembly components have been used to approximate the stoichiometry of pRNA.  $\phi$ 29 assembly components with known stoichiometry serve as standard controls. In these curves, the larger the stoichiometry of the component, the more dramatic the influence of the dilution factor on the reaction. A slope of one indicates that one copy of the component is involved in the assembly of one virion, as is the case for genomic DNA in  $\phi$ 29 assembly. A slope larger than one indicates multiple-copy involvement. Using this method, the stoichiometries of DNA-gp3, gp11, gp12, and gp16 have been compared. The result is consistent with other approaches in that the stoichiometry of gp11 and gp12 is greater than the stoichiometry of gp16 and pRNA. It is known that the stoichiometry of gp11 and gp12 in the  $\phi$ 29 assembly is 12, whereas the stoichiometry of pRNA is between 5 and 6. Interestingly, the curves for gp16 and pRNA do not overlap. Whether such a difference is owing to the possible reusability of pRNA or gp16 remains to be elucidated.

## 2.7.3.3. COMMON MULTIPLES OF 3 AND 6

This stoichiometric method begins with mixing two inactive mutant pRNAs intermolecularly with complementary loops, and then assaying the activity of such mixtures in DNA packaging (175,176). The predicted secondary structure of the pRNA reveals two loops, known as the left- and right-hand loops (162). Sequences of these two loops (bases 45–48 of the right-hand loop and bases 85–82 of the left-hand loop) are complementary and were originally proposed to form a pseudoknot (165). However, numerous studies have revealed that these two sequences interact intermolecularly, allowing the formation of pRNA multimers. Several pRNAs with mutated left- and right-hand loop sequences have been constructed.

## 2.7.3.3.1. A Set of Two Interlocking pRNAs (175)

An important finding in pRNA research was that mixing two mutant pRNAs with transcomplementary loops restores full DNA-packaging activity. pRNAs A/b' and B/a' are inactive in packaging when alone, but when they are mixed together, DNA-packaging activity is restored; the right-hand loop A of pRNA A/b' pairs with the left-hand loop a' of pRNA B/a'. Since mixing two inactive pRNAs with interlocking loops—such as when pRNA I-j' and J-i' are mixed in a 1:1 molar ratio—results in the production of infectious virions, the stoichiometry of the pRNA is predicted to be a multiple of two. This, taken together with the results from binomial distribution and serial dilution analyses, strongly indicates that the stoichiometry of pRNA is six.

#### 2.7.3.3.2. A Set of Three Interlocking pRNAs (175)

A similar procedure was used to confirm the formation of trimers through hand-in-hand interaction. Another set of mutants was composed using three pRNAs: A-b', B-c', and C-a'. This set is expected geometrically to form a 3, 6, 9, or 12mer ring that carries each of the three mutants. When tested alone, each individual pRNA exhibited little or no activity. When any two of the three mutants were mixed, again little or no activity was detected. However, when all three pRNAs were mixed in a 1:1:1 ratio, DNA-packaging activity was fully restored. The lack of activity in mixtures of only two mutant pRNAs and the restored activity in mixtures of three mutant pRNAs is to be expected, since the mutations in each RNA are engineered such that only the presence of all three RNAs will produce a closed ring. Since three inactive pRNAs are fully active when mixed together, this suggests that the number of pRNAs in the DNA-packaging complex is a multiple of 3, in addition to being a multiple of 2. Thus, the number of pRNAs required for DNA packaging must be a common multiple of 2 and 3, likely 6 (or 12, but this number has been conclusively excluded by binomial distribution and serial dilution analyses (172), which revealed pRNA's stoichiometry to be between five and six, confirming that the stoichiometry of pRNA is six).

#### 2.7.3.3.3. A Set of Six Interlocking pRNAs (175)

DNA-packaging activity can also be achieved by mixing six mutant pRNAs, each of which is inactive when used alone. Thus, an interlocking hexameric ring is predicted to form by base pairing of the interlocking loops.

#### 2.7.3.3.4. Stoichiometry of Other $\phi$ 29 Components

The highly sensitive in vitro  $\phi$ 29 assembly system has been utilized to determine the stoichiometry of each of the components needed for assembly (103,104,172,173,178). The log/log plot method incorporates only the functional unit (oligo or complex), not the copy number of the subunits. The procapsid, despite containing (26) copies of scaffolding protein gp7, 235 copies of capsid protein gp8, and 12 copies of the portal protein gp10, is a complex that is regarded as one component. DNA-gp3 is also treated as one component since the DNA and terminal protein gp3 are covalently linked. The log/log plot has revealed that the slope of the log/log concentration-dependent curve for procapsid is one; therefore, one copy of procapsid is needed for the assembly of one virion (103,104,172,173,178). The genomic DNA-gp3 acts in the same way. The stoichiometry for pRNA, gp11, and gp12 has been determined to be 6, 12, and 12, respectively, using log/log slope assay (178), binomial distribution (172,178), common multiples of two and three (175,180), migration rates in gel (181), and electron microscopy (EM) (182,183). Although it has been found that six pRNAs form a hexamer as a vital part of the DNA-translocating



motor, the hexamer can be assembled in vitro from individual pRNA molecules or complexes. If the hexamer is assembled from one A-a' or B-b' monomer or six monomers A-b', B-c', C-d', D-e', E-f', F-a' (175), the monomer is regarded as one component and the stoichiometry of the pRNA monomer is six (162). If the hexamer is assembled from purified dimer composed of (I-a')/(A-i'), the dimer is regarded as one component, and the stoichiometry for dimer RNA is three (164,175). If the hexamer is assembled from purified (A-b')/(B-c')/(C-a') trimer, the trimer is regarded as one component and the stoichiometry of trimer-RNA is two (162,175). It was found that gp12 formed a dimer before being packaged into a  $\phi$ 29 assembly intermediate (184,185), and each dimeric gp12 is regarded as one component. Therefore, the stoichiometry of gp12 is 12, instead of 24, disregarding the fact that there are 24 copies of gp12 in each  $\phi$ 29 virion. Purified tail protein gp9, expressed in *Escherichia coli*, has been shown to be active in in vitro  $\phi$ 29 assembly. The absolute copy number of gp9 in one virion has been reported to be nine (181).

## 2.8. ATP: The Source of Motor Energy

Translocation of DNA into the procapsid is energetically quite unfavorable. The DNA arrangement within the capsid is very compact, and the packaged DNA undergoes about a 30- to 100-fold decrease in DNA volume compared with its volume before packaging (15,186). The conclusion that the unfavorable reaction is driven by ATP hydrolysis is derived from studies involving bacteriophages  $\lambda$  (2,152,153,187–189), P22 (155),  $\phi$ 29 (5,9,30), T3/T7 (8,10,28,29,62,63,154,190), T4 (37,150), and P2 (69,70). The first quantification of ATP consumption in DNA packaging was performed in the  $\phi$ 29 system with purified components (30). In the defined in vitro DNA-packaging system, ATP was hydrolyzed to adenosine 5'-diphosphate and  $P_i$ . Approximately one ATP was required to package 2 bp of  $\phi$ 29 DNA. Similarly, with bacteriophage T3, it was found that, on average, one ATP molecule was required to package 1.8 bp of T3 DNA (28). In T3, however, it was found (28) that two separate ATPase activities existed. One of these, called *pac*-ATPase, required viral DNA, and the other, called *non-pac*-ATPase, was stimulated by nonpackagable DNA (i.e., single-stranded or circular) or RNA (nonspecific). However, the *non-pac* ATPase activity continued, after initial activation, in the absence of viral DNA. These individual ATPase activities can be stimulated by mixing with other components. For example, the ATPase activity of prohead was stimulated by the addition of  $\phi$ 29 DNA, and an additional fivefold increase in ATPase activity was found in the complete packaging reaction (30). Recent results indicate that pRNA has an effect on the ATPase activity of gp16, stimulating it fourfold. This ATPase activity continues only when pRNA is present, suggesting the formation of a gp16-pRNA complex. Similarly, procapsids with pRNA



stimulate the ATPase activity of gp16 10-fold, as compared with the lack of stimulation by procapsids alone (156). The results from both the  $\phi$ 29 and T3 systems suggest that the consumption of ATP in the DNA-packaging system is extremely complicated. ATP might be used for the initiation of DNA packaging and translocation. In  $\phi$ 29, all components in the packaging system, including pRNA, procapsid, gp16, and DNA-gp3, are involved in the generation of maximal ATPase activity.

### 3. Mechanisms of Motor Motion to Stuff Viral DNA

#### 3.1. Experimental Attempts to Elucidate Motor Mechanism of $\phi$ 29

##### 3.1.1. Establishment of a Highly Sensitive In Vitro Packaging System

Utilizing pRNA's readily manipulable structure, a defined in vitro  $\phi$ 29 DNA-packaging system has been developed (9). With purified procapsid, gp16, pRNA, and ATP, up to 90% of the added DNA-gp3 can be packaged into the procapsid via the motor constructed with recombinant gene products. After DNA packaging, the in vitro assembly system can convert a DNA-filled capsid into infectious  $\phi$ 29 virions with the addition of purified proteins gp9, gp11, gp12, and gp13 (103,104). With this system, up to  $5 \times 10^9$  infectious virions/mL can be obtained in the presence of all required components, yet not a single infectious virion is detected when even one essential component is absent. This system, with a sensitivity of eight orders of magnitude, has been used to assay the function of the DNA-packaging motor (180,192).

##### 3.1.2. Circularly Permuted pRNA

An important approach in analyzing pRNA function has been the construction of circularly permuted pRNAs (cp-pRNAs), in which any internal base of the pRNA could be reassigned to serve as new 5'- or 3'-termini (169,193). Two tandem pRNA coding sequences separated by a 3- or 17-base loop sequence were cloned into a plasmid. Polymerase chain reaction (PCR) primer pairs such as P6/P5, complementary to various locations within the tandem pRNA coding sequences, were designed to synthesize PCR fragments for the transcription of cp-pRNAs. Results indicated that neither the small nor the large loop interferes with biological activity of the molecule. It has been demonstrated that nonessential bases or ones adjacent to them can be used as new termini for constructing active cp-pRNA; this system greatly facilitates the construction of mutant pRNA via PCR and enables the labeling of any specific internal base by radioisotopes, fluorescence (194), or photoaffinity agents.

##### 3.1.3. Computer Modeling

The goal of modeling pRNA structure is to organize collections of structural data from crosslinking, chemical or ribonuclease probing, chemical modifica-

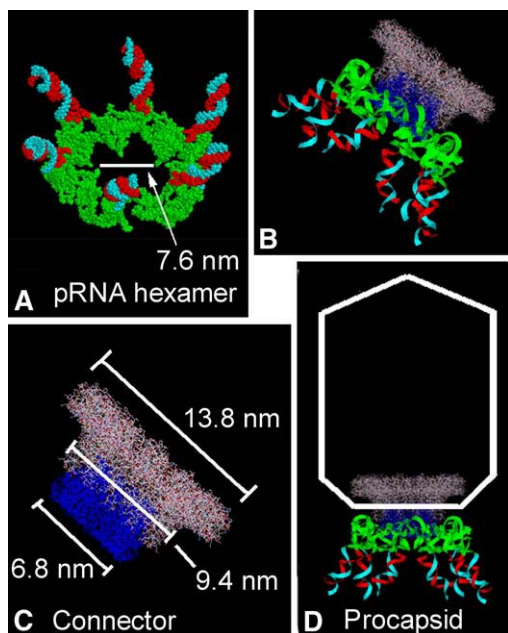


Fig. 2. Computer models of pRNA hexamer and the motor complex of bacterial virus  $\phi$ 29. (A), Hexamer shows the connector binding domain in green, as well as the DNA translocating domain colored red (5'-end) and cyan (3'-end). The DNA translocating domain of the 5'/3'-paired region points up. (B), The crystal structure of the connector (From refs. Valle, Kremer et al., 1999; Valpuesta, Fernandez et al., 1999). The RNA Recognition Motif is blue. (C), Docking of the pRNA hexamer to the RNA binding domain of the connector. (D), Procapsid Bottom view. Adapted from (Shu, Huang et al., 2003) with permission of *J. Biol. Chemistry*.

tion interference, cryo-AFM, and other genetic data into a 3D form. Because a large number of structural constraints are available, computer programs can successfully construct 3D structures (158,195,196) (Fig. 2).

X-ray crystallography studies have revealed that the  $\phi$ 29 connector contains three sections: a narrow end, a central section, and a wider end, with diameters of 6.6, 9.4, and 13.8 nm, respectively (136,137,197). The hexameric pRNA model by Hoepflich and Guo (158) describes a central channel with a diameter of 7.6 nm that perhaps can sheath onto the narrow end of the connector to be anchored by the central section of the connector, which is wider than the central channel of the pRNA hexamer.

The connector-binding domain is located in the middle of the pRNA primary sequence (i.e., bases 23–97), and the DNA-translocation domain is located at the 5'/3' paired ends. It has been predicted that the connector protein (gp10) contains a conserved RNA recognition motif (RRM), located between residues 148 to 214 of each gp10 monomer. This region of gp10 is located at the narrow end of the dodecameric connector that protrudes from the procapsid (**156,198**). The hexamer model by Hoeprich and Guo (**158**) agrees with the aforementioned data, showing that pRNA bases 23 to 97 within the connector-binding domain interact with the predicted RRM motifs of the connector, and the 5'/3' paired region, comprising the DNA-translocation domain, extends away from the connector.

#### *3.1.4. Use of Tweezers to Determine Force of Motor*

Optical tweezers offer an interesting method by which to measure packaging force and speed (**199**). In this procedure, partly packaged motor complex has a microsphere attached to it via unpackaged DNA. This microsphere is caught in an optical trap and tethered to a second bead. When ATP is introduced and packaging initiates, the two beads move closer together. The amount of DNA tension is monitored, and from this, the bead displacement can be calculated; various measurements of packaging dynamics are then possible, including an examination of the presence of packaging “slips” and “pauses,” where irregularities occur in packaging speed. With additional load, the force needed to prevent the DNA from being inserted is about 57 pN, indicating that the  $\phi$ 29 DNA-packaging motor is the strongest biomotor studied to date. Using this method, it has been possible to determine the speed of  $\phi$ 29 DNA packaging, which is initially about 100 bases/s, gradually slowing to a halt as the capsid is filled (**199**). The fivefold/sixfold symmetry mismatch between the procapsid and pRNA has been cited to help explain the mechanism of motor rotation (**142,143,180**), but the precise mechanism by which DNA moves into the capsid during packaging has yet to be elucidated.

#### *3.2. Models for Packaging of DNA by $\phi$ 29*

It is generally understood that pRNA is part of an ATPase and that it possesses at least two conformations: relaxed and contracted. Driven by ATP hydrolysis, which causes an alternation between relaxed and contracted states, the individual parts of the hexameric pRNA complex help rotate the translocation machinery. gp16, a protein that binds ATP, is also involved in ATP hydrolysis.

The requirement of an intermolecular loop/loop interaction between individual pRNA molecules during DNA packaging has led to the belief that pRNA forms a hexamer (**175,176**) and supports a model incorporating the sequential action of pRNA. Individual pRNAs likely need to communicate with each other during DNA packaging to ensure that motion is consecutive. Inter-pRNA

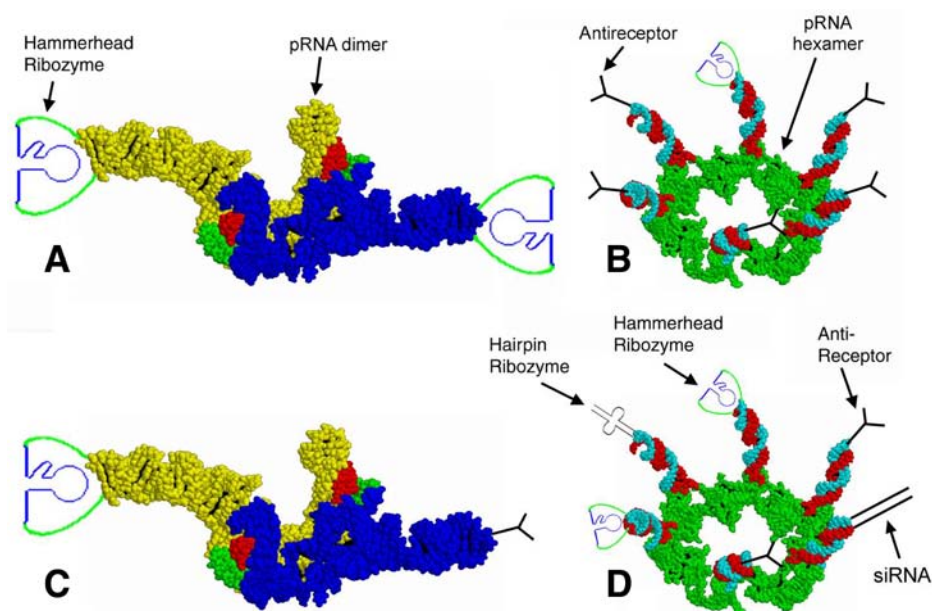


Fig. 3.  $\phi 29$  pRNA as polyvalent vehicles for delivery genes in therapy. pRNA multimers could be used to target a cell receptor and to co-deliver therapeutic siRNA, ribozymes or other biologically active molecules. Adapted from (Shu, Huang et al., 2003) with permission of *J. Biol. Chemistry*.

interactions via loops might serve as a link to pass signals to adjacent pRNAs, regulating sequential conformational changes and/or interactions. Thus, base pairing between the right- and left-hand loops might be necessary to transfer a conformational change from one pRNA to an adjacent one.

Several models for DNA translocation into the  $\phi 29$  procapsid have been proposed (137,143,200–202). It is generally believed that DNA is translocated through the axial hole of the portal vertex, much like a threaded rod moving along a nut. Another model hypothesizes that supercoiled DNA wraps around the portal vertex and that its rotation allows DNA to pass into the procapsid via the outside of the vertex (202). In a model proposed in 1997 (143), sequential action of multiple pRNAs, in conjunction with other components, is vital to DNA packaging. Six copies of pRNA form a hexamer that interacts with the capsid pentamer and moves in discrete  $12^\circ$  steps (Fig. 3). Thirty ATPs are needed for each completed cycle of motor rotation. This model is in good agreement with existing 3D structural data obtained recently by crystallography (137), complementary modification, photoaffinity crosslinking, chemical modification, chemical modification interference, nuclease probing, AFM, and computer-modeling (158) methods.

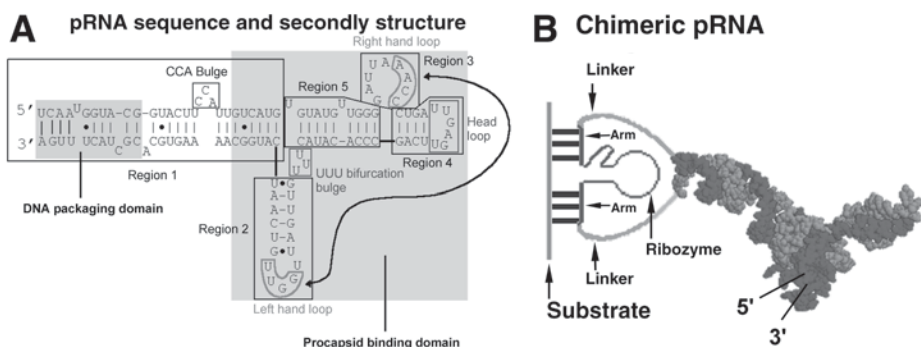


Fig. 4. Sketch showing chimeric pRNA harboring a ribozyme. (A), The sequence and secondary structure of pRNA. The curved line points to the two interacting loops. (B), Structural outline of the pRNA/ribozyme chimera. A ribozyme targeting at the Hepatitis B virus mRNA is connected to both the 5' and 3'-end of pRNA. Adapted from (Hoepflich, Zhou et al., 2003) with permission of Nature Publisher.

In the model proposed in **ref. 137**, DNA located in the central channel interacts with one subunit of the portal. A  $12^\circ$  rotation of the narrow end of the connector leads to lengthwise expansion of the connector via a slight change in the angle of the long helices, and the wide end of the connector follows the narrow end. Such a “following” allows the structure to relax and contract while translating 2 bp of DNA into the capsid (**137**). In addition, the “motor-ratchet” model of DNA packaging has been proposed and reviewed recently (**17**). In this model, the connector rectifies DNA motion via either thermal, biased thermal, or oscillating processes. The motor-ratchet hypothesis has been widely used to interpret data pertaining to biochemistry, genetics, energetics, structure, and dynamics in packaging. The structure of both the connector and pRNA (**158**) exhibits orientational tilting toward one direction.

At least four distinct models can be proposed to describe the specific mechanisms underlying the translocation of DNA resulting from such motors, which are discussed next.

### 3.2.1. Model 1

The force of DNA movement is Brownian motion (**17,203,204**). The motor is a ratchet (**17**) used simply to ensure that DNA moves in one direction, but not the opposite.

### 3.2.2. Model 2

DNA is translocated through the axial hole of the portal vertex, much like a threaded rod processing through a nut, and thus DNA packaging is achieved by

utilizing the “threaded” helical nature of dsDNA (**142**). The motor, composed of the pRNA and connector, operates like a hex nut to drive a bolt (**143**). Evidence for this model would include establishing that DNA translocates regularly at a fixed ratio of distance moved to the number of motor turns.

### 3.2.3. Model 3

The fivefold/sixfold symmetry mismatch and sequential contraction and relaxation of motor components generates the force required for motor rotation (**142,143**). If this model is correct, discrete steps in  $12^\circ$  intervals in component rotation will be found.

### 3.2.4. Model 4

DNA located in the central channel interacts with one subunit of the portal (**137**). A  $12^\circ$  rotation of the narrow end of the connector leads to lengthwise expansion of the connector via a slight change in the angle of the long helices; the wide end of the connector follows the narrow end. Such a “following” allows the structure to relax and contract while translating 2 bp of DNA into the capsid (**137**). This model implies that one complete turn of the connector transfers 60 bp of DNA into the procapsid.

## 4. Applications of the $\phi$ 29 Nanomotor in Research and Nanotechnology

### 4.1. A Nanomotor With Potential to Be Incorporated Into Nanodevices

The ability to harness and utilize nanomotors has the potential to expand and revolutionize the field of nanotechnology (**205–207**). One viable option that has been pursued for the development of mechanical parts for nanotechnology is to incorporate the  $\phi$ 29 motor and other motors and their constituent parts into nanodevices. Techniques generally involve the characterization, manipulation, modification, control, creation, and/or assembly of organized materials on the nanoscale level (**208–210**). These materials can then be used as building blocks for the construction of larger devices and systems (**211–214**). Nanotechnological endeavors are expected to play critical roles in many scientific disciplines, including chemistry, physics, biology, medicine, materials science, engineering, and computer technology.

Several factors combine to make  $\phi$ 29 pRNA an ideal choice for applications in nanotechnology and other fields. It is readily reproducible, as evidenced by the recent development of a defined in vitro  $\phi$ 29 DNA-packaging system, whereby with purified procapsid, gp16, and pRNA, up to 90% of DNA-gp3 can be packaged (**78**). This process has been utilized to quantify the forces involved in DNA translocation with an optical trap (**199,215**). The  $\phi$ 29 DNA-packaging motor has, through this method, been confirmed as the strongest



known nanomotor, with a stalling force of 57 pN (199). Perhaps most importantly, however,  $\phi$ 29 pRNA is readily maneuverable and controllable, tending strongly toward interactions resulting in the formation of dimers, trimers, and hexamers. Complementary loop sequence production procedures allow for the formation of predefined pRNA multimers, modifiable at the earliest possible stage of the construction of larger structures and systems. pRNA's two domains are independent and tightly self-folded. As many as 120 nucleotides can be extended from the 3' end of pRNA without hindering its procapsid-binding or DNA-packaging activity (216,217).

#### **4.2. Polyvalent Gene Delivery System Using Motor pRNA**

Antigen assays and Southern blot analyses have demonstrated that  $\phi$ 29 pRNA can chaperone and escort the hammerhead ribozyme to function in the cell, enhancing cleavage efficiency and the inhibition effect of the ribozyme on hepatitis B virus. Such an increase in ribozymal activity likely results from pRNA's ability to prevent the ribozyme from misfolding and to protect it from degradation by exonucleases. It has been successfully demonstrated that exogenous RNA can be connected to the end of pRNA without affecting pRNA folding. At least 120 nonspecific bases can be extended from the 3' end of aptRNA without hindering folding or function of the pRNA, which indicates that the 117-base pRNA was folded independently of bases extended from its 3' end. These findings suggest that therapeutic RNA molecules could be placed between the 3' and 5' ends of the pRNA and would be able to fold without being influenced by the original pRNA sequence.

$\phi$ 29 pRNA tends strongly toward the formation of dimers (158,162, 174,218), and dimers are the primary building blocks of hexamers (164,175, 176,200). The formation of monomers and dimers can be controlled through manipulation and control of the sequences of the two interacting loops (158,162,174,176,218). The formation of pRNA dimers may also assist in stabilizing pRNA/ribozyme chimeric molecules. As long as the openings of the circularly permuted pRNAs are close enough to an area of dimer formation, the tertiary structure can help prevent exonucleases from accessing the ends of the RNA molecules.

The formation of dimers and hexamers also facilitates the delivery of multiple therapeutic agents. For example, one of the pRNA subunits of a hexamer could carry the hammerhead ribozyme, and the other pRNA subunit could carry a hairpin ribozyme or an antisense RNA. Applications of multiple therapeutic agents might enhance the efficiency of in vivo therapy. The multivalent subunits of pRNA show strong potential to facilitate specific targeting and delivery of ribozymes. One of the subunits could, for example, be utilized to carry an RNA molecule that interacts with a cell-surface receptor. Binding of dimer



or hexamer pRNA to the specific receptor would enable specific delivery of the RNA complex to the cell via endocytosis. Specific receptor-binding RNA molecules can be isolated through systematic evolution of ligands by exponential enrichment (SELEX) (219,220). Starting from a library containing random RNA sequences, in vitro evolution techniques allow for the selection of RNA molecules that are able to bind a specific ligand or receptor (221–224). The chimeric RNA carrying the hammerhead ribozyme and the chimeric RNA carrying the antireceptor can be mixed to form dimers via inter-RNA loop/loop interaction, as reported previously (164,175,176,200).

### **4.3. DNA-Packaging Motor as a DNA-Sequencing Apparatus or Molecular Sorter**

Another burgeoning area of interest in biology is the development of efficient and sensitive analytical tools that can be used to probe and manipulate single molecules. Given recent projects mapping bacterial, human, and other mammalian genomes, new types of arrays and methodologies will be required to analyze, interpret, and utilize genomic information efficiently and inexpensively. Scientists are working to develop a nanopore-based DNA-sequencing device (225). Such a device will recognize a single base pair, based on the electrical signals generated through the interaction of the bases of the DNA with a pore. A similar concept may be useful for single-molecule analysis of other biological molecules. The  $\phi$ 29 DNA-packaging motor has the potential to be developed into a DNA-sequencing apparatus, since the DNA-packaging process involves movement of the DNA through a 3.6-nm pore surrounded by six RNAs that can be modified to accept chemical or electrical signals.

### **4.4. Model for Study of RNA Dimers and Trimers in Other Living Systems**

Stable pRNA dimers and trimers in the absence of protein have already been isolated (164). Dimerization/trimerization assays provide simple and stable systems for studying structural solutions to pRNA complexes and for investigating the mechanisms of RNA/RNA interactions. RNA dimerization and oligomerization have been found to play an important role in many living systems. Dimerization of retroviral genomic RNA is critical to many stages in the retroviral life cycle, including translation, reverse transcription, RNA encapsidation, and virion assembly (226–228). For instance, RNA-RNA intermolecular interactions are required for the formation of a specific ribonucleoprotein particle, *bicoid* mRNA 3' UTR-STAUFIN, that determines the formation of the anterior pattern of the *Drosophila* embryo (229). RNA-RNA interaction is also an essential step in the cleavage reaction of RNase P on tRNA (230–232). Replication of plasmid ColE1 is regulated by plasmid-speci-

fied small RNAs (RNA I and RNA II) that form complexes through complementary RNA stem-loop interactions (233).

#### 4.5. A Model for Design of New Antiviral Strategies

Extensive investigation into DNA packaging of the dsDNA viruses documents certain common features in this step of the viral life cycle. Commonalities include the use of a pair of noncapsid enzymes to translocate viral DNA into a procapsid coupled with the hydrolysis of ATP (28–30,38,59,143,152,191,234–236). Similarities in DNA packaging between dsDNA bacteriophages and herpes viruses, adenovirus, parvovirus, and pox viruses (as mentioned in **Subheading 1.**) justify the use of  $\phi 29$  as a model system for the design of new antiviral strategies. Using  $\phi 29$  pRNA as a target, several methods have been modeled (170,171,173) for the inhibition of viral assembly.

##### 4.5.1. Inhibition of $\phi 29$ Assembly by Antisense DNA Targeting pRNA In Vitro

Antisense oligos include antisense RNA and antisense DNA. They are small, regulatory, single-stranded polynucleotides that bind to complementary regions on a specific target in order to control their biological function. Antisense DNA could bind to pRNA and cause a change in pRNA electrophoretic mobility (170). Antisense DNA oligos were shown to hybridize to  $\phi 29$  pRNA by gel shift assays (170).

$\phi 29$  pRNA contains two functional domains. One domain is located at the central region and is required for procapsid binding. The other domain, consisting of paired 5' and 3' ends, is needed for DNA translocation into procapsids but is not required for procapsid binding. Oligo P6 targeting the left-hand loop of the procapsid-binding domain could block the binding of pRNA to procapsids, resulting in the inhibition of  $\phi 29$  assembly in vitro. Oligos P11 and P15 targeting either the 5' or the 3' end of the pRNA, respectively, do not prevent pRNA from binding to procapsid, but strongly inhibit DNA packaging (166,170).

##### 4.5.2. Complete Inhibition of $\phi 29$ Assembly With Mutant pRNA In Vitro

$\phi 29$  is being used as a model to explore new avenues in antiviral research beyond in vitro inhibition with antisense oligos targeting pRNA. As already noted, pRNA contains two functional domains. Sequence alterations that disrupt base pairing at the 5'/3' ends of the DNA-translocating domain result in mutant pRNAs that are completely inactive in phage assembly in vitro but still retain WT procapsid-binding affinity (159,166,172,173). These mutant pRNAs are able to compete with WT pRNAs for procapsid binding and efficiently inhibit viral assembly both in vitro and in vivo (173).

For in vivo studies, a plasmid expressing a pRNA with a 4-base mutation at the 3' end was constructed and transformed into host cells. Cells harboring this plasmid were completely resistant to plaque formation by WT  $\phi$ 29. The interesting result here is that "complete" inhibition was gained, which indicates that factors involved in viral assembly can be utilized for efficient and target-specific antiviral treatment. This high level of efficiency has resulted from two pivotal features. First, since the two domains are quite distinct and separate, mutation of the packaging domain results in pRNA with no DNA-packaging activity, but procapsid-binding competence remains intact. Second, six pRNAs are involved in the packaging of one genome. This high-order dependence of pRNA results in a correspondingly higher order of inhibitive effects, since blocking only one of the six positions could result in complete cessation of the assembly of virions (172). The principle of using molecules containing two functional domains and requiring multiple-copy involvement as inhibitors could be applied to gene therapy, intracellular immunization, antiviral drug design, and the construction of transgenic plants resistant to viral infection, using certain viral structural proteins, enzymes, and other RNAs involved in the viral life cycle.

#### **4.6. Similar Mechanism Between Viral DNA Translocation and Other Nucleic Acid Sliding/Riding Processes**

There is a group of nucleic acid-binding proteins that plays a similar role in DNA or RNA riding or sliding related to DNA replication, translocation, recombination, RNA packaging, and RNA transcription (175,237–240). This group can be subdivided into two subsets: proteins that bind nucleic acid and proteins that act on nucleic acid. The chief feature common to both subsets is that they interact with RNA or DNA in a polymer conformation and with a ring-shaped morphology. Most of the proteins in this group are also hexameric.

The subset that acts on nucleic acid includes helicase (241,242); *E. coli* transcription termination protein Rho (243,244); the yeast DNA polymerase processivity factor (245); bovine papillomavirus E1 replication initiator (246); and the *E. coli* DNA polymerase III holoenzyme (247,248) and dsRNA-packaging motor (239,240), which exist as hexamers (241,249–252). Although the mechanisms of this kind of DNA–protein interaction remain to be elucidated, the finding that six copies of pRNA are attached to a sixfold symmetrical connector during DNA translocation indicates that it might have something in common with these hexamers. The processes of both viral DNA packaging and DNA (or RNA) replication (or RNA transcription) involve the relative motion of two components, one of which is nucleic acid. It would be intriguing to show how pRNA may play a role similar to that of the protein enzymes, such as DNAS-helicase or the termination factor Rho.

#### **4.7. Insight Into Mechanisms of Macromolecular Translocation Through Cellular Membrane Wall**

Migration or transportation of macromolecules, such as proteins or nucleic acids, through a barrier or cell membrane is a common process in life systems. After transcription in the nucleus, mRNA and tRNA must pass the nuclear membrane to reach the translation machinery in the cytoplasm. Similarly, nuclear proteins must pass from the cytoplasm, where they are synthesized, to the nucleus, where they function. After infection or transfection, most viral or plasmid DNA must pass through the nuclear membrane in order to serve as a template for gene expression (253). The Rev protein of human immunodeficiency virus assists in the translocation of viral mRNA from the nucleus to the cytoplasm through a nuclear pore (254,255). Varieties of proteins and other elements migrate into and out of the cell and nucleus to perform their respective functions. Molecular migration or translocation is also manifest in the tracking and rail riding of enhancers or transcription factors along DNA (251), the translocation of the transcription termination protein Rho along RNA (252), and the migration of helicases along single-stranded DNA during DNA replication (241,256–258).

One of the most complex and intricate translocation processes is viral DNA encapsidation. The study of DNA encapsidation could provide hints for macromolecular translocation through cell membranes.

### **5. Conclusion**

The  $\phi 29$  DNA-packaging motor serves as an effective model for the study of dsDNA viral packaging. The development of a defined in vitro packaging system utilizing purified  $\phi 29$  components will aid further research into both the specific attributes of  $\phi 29$  packaging and DNA packaging in general. This will provide for a number of technological advances, including the targeted delivery of therapeutic agents to cells, precise single-molecule sequencing techniques, and direct attachment of various motor parts to nanodevices. In addition,  $\phi 29$ 's strong tendency to form dimers, trimers, and hexamers can potentially be harnessed and utilized to construct self-assembling arrays that have far-ranging technological possibilities, including the development of ultrahigh-density memory storage systems and the isolation and separation of multiple pathogens in medical diagnoses. Ongoing research into specific motor parts and overall motor function is making such important goals increasingly realizable.

### **Acknowledgments**

I thank Jeremy Hall for his great contribution to the preparation of the manuscript. The work in the authors' laboratory was supported by National Insti-

tutes of Health grants GM59944 of EB3730 from the program of nanoscience and nanotechnology in Biology and Medicine, GM60529, and by National Science Foundation grant MCB-9723923.

## References

1. Kerr, C. and Sadowski, P. D. (1974) Packaging and maturation of DNA of bacteriophage T7 in vitro. *Proc. Natl. Acad. Sci. USA* **71**, 3545–3549.
2. Kaiser, A. D., Syvanen, M., and Masuda, T. (1975) DNA packaging steps in bacteriophage lambda head assembly. *J. Mol. Biol.* **91**, 175–186.
3. Pruss, G. J., Wang, J. C., and Calendar, R. (1975) *In vitro* packaging of covalently closed monomers of bacteriophage DNA. *J. Mol. Biol.* **98**, 465–478.
4. Hohn, B. (1975) DNA as substrate for packaging into bacteriophage lambda, in vitro. *J. Mol. Biol.* **98**, 93–106.
5. Bjornsti, M. A., Reilly, B. E., and Anderson, D. L. (1983) Morphogenesis of bacteriophage  $\phi$ 29 of *Bacillus subtilis*: oriented and quantized *in vitro* packaging of DNA protein gp3. *J. Virol.* **45**, 383–396.
6. Gope, R. and Serwer, P. (1983) Bacteriophage P22 in vitro DNA packaging monitored by agarose gel electrophoresis: rate of DNA entry into capsids. *J. Virol.* **47**, 96–105.
7. Hamada, K., Fujisawa, H., and Minagawa, T. (1986) A defined *in vitro* system for packaging of bacteriophage T3 DNA. *Virology* **151**, 119–123.
8. Guo, P., Grimes, S., and Anderson, D. (1986) A defined system for in vitro packaging of DNA-gp3 of the *Bacillus subtilis* bacteriophage  $\phi$ 29. *Proc. Natl. Acad. Sci. USA* **83**, 3505–3509.
9. Serwer, P. (1988) The source of energy for bacteriophage DNA packaging: an osmotic pump explains the data. *Biopolymers* **27**, 165–169.
10. Furth, P. A., Hennighausen, L., Baker, C., Beatty, B., and Woychick, R. (1991) The variability in activity of the universally expressed human cytomegalovirus immediate early gene 1 enhancer/promoter in transgenic mice. *Nucleic Acids Res.* **19**, 6205–6208.
11. Graeble, M. and Hearing, P. (1992) *Cis* and *trans* requirements for the selective packaging of adenovirus type 5 DNA. *J. Virol.* **66**, 723–731.
12. Higgins, R. R. and Becker, A. (1995) Interaction of terminase, the DNA packaging enzyme of phage  $\lambda$ , with its cos DNA substrate. *J. Mol. Biol.* **252**, 31–45.
13. Hang, J. Q., Catalano, C. E., and Feiss, M. (2001) The functional asymmetry of cosN, the nicking site for bacteriophage lambda DNA packaging, is dependent on the terminase binding site, cosB. *Biochemistry* **40**, 13,370–13,377.
14. Hohn, T. (1976) Packaging of genomes in bacteriophages: a comparison of ssRNA bacteriophages and dsDNA bacteriophages. *Philos. Trans. R. Soc. Lond. Ser. B* **276**, 143–150.
15. Serwer, P. (2003) Models of bacteriophage DNA packaging motors. *J. Struct. Biol.* **141**, 179–188.
16. Earnshaw, W. C. and Casjens, S. R. (1980) DNA packaging by the double-stranded DNA bacteriophages. *Cell* **21**, 319–331.

17. Huang, L. P. and Guo, P. (2003) Use of acetone to attain highly active and soluble DNA packaging protein gp16 of phi29 for ATPase assay. *Virology* **312**(2), 449–457.
18. Hwang, J. S. and Bogner, E. (2002) ATPase activity of the terminase subunit pUL56 of human cytomegalovirus. *J. Biol. Chem.* **277**, 6943–6948.
19. Hwang, Y., Hang, J. Q., Neagle, J., Duffy, C., and Feiss, M. (2000) Endonuclease and helicase activities of bacteriophage lambda terminase: changing nearby residue 515 restores activity to the gpA K497D mutant enzyme. *Virology* **277**, 204–214.
20. Catalano, C. E. (2000) The terminase enzyme from bacteriophage lambda: a DNA-packaging machine. *Cell Mol. Life Sci.* **57**, 128–148.
21. Dasgupta, A. and Wilson, D. W. (1999) ATP depletion blocks herpes simplex virus DNA packaging and capsid maturation. *J. Virol.* **73**(3), 2006–2015.
22. Rubinchik, S., Parris, W., and Gold, M. (1994) The in-vitro ATPases of bacteriophage-lambda terminase and its large subunit, gene-product-A—the relationship with their DNA helicase and packaging activities. *J. Biol. Chem.* **269**, 13,586–13,593.
23. Tomka, M. A. and Catalano, C. E. (1993) Kinetic characterization of the ATPase activity of the DNA packaging enzyme from bacteriophage lambda. *Biochemistry* **32**, 11,992–11,997.
24. Koonin, E. V., Senkhvich, T. G., and Chernos, V. I. (1993) Gene A32 product of vaccinia virus may be an ATPase involved in viral DNA packaging as indicated by sequence comparisons with other putative viral ATPases. *Virus Genes* **7**, 89–94.
25. Morita, M., Tasaka, M., and Fujisawa, H. (1993) DNA packaging ATPase of bacteriophage T3. *Virology* **193**, 748–752.
26. Hamada, K., Fujisawa, H., and Minagawa, T. (1987) Characterization of ATPase activity of a defined in vitro system for packaging of bacteriophage T3 DNA. *Virology* **159**, 244–249.
27. Guo, P., Peterson, C., and Anderson, D. (1987) Prohead and DNA-gp3-dependent ATPase activity of the DNA packaging protein gp16 of bacteriophage  $\phi$ 29. *J. Mol. Biol.* **197**, 229–236.
28. Javey, A., Guo, J., Wang, Q., Lundstrom, M., and Dai, H. (2003) Ballistic carbon nanotube field-effect transistors. *Nature* **424**, 654–657.
29. Zuker, M. (1989) On finding all suboptimal foldings of an RNA molecule. *Science* **244**, 48–52.
30. Casjens, S. (1985) Nucleic acid packaging by viruses in *Virus Structure and Assembly* (Casjens, S., ed.), Jones & Bartlett, Portola Valley, California, pp. 75–147.
31. Black, L. W. (1989) DNA Packaging in dsDNA bacteriophages. *Annu. Rev. Microbiol.* **43**, 267–292.
32. Bazinet, C. and King, J. (1985) The DNA translocation vertex of dsDNA bacteriophages. *Annu. Rev. Microbiol.* **39**, 109–129.
33. Anderson, D. L. and Reilly, B. (1993) Morphogenesis of bacteriophage  $\phi$ 29, in *Bacillus subtilis and Other Gram-Positive Bacteria: Biochemistry, Physiology, and Molecular Genetics* (Sonenshein, A. L., Hoch, J. A., and Losick, R., eds.), American Society for Microbiology, Washington, DC, pp. 859–867.



34. Rao, V. B. and Black, L. W. (1988) Cloning, overexpression and purification of the terminase proteins gp16 and gp17 of bacteriophage T4: construction of a defined *in vitro* DNA packaging system using purified terminase proteins. *J. Mol. Biol.* **200**, 475–488.
35. Becker, A. and Gold, M. (1988) Prediction of an ATP reactive center in the small subunit, gpNul of phage lambda terminase enzyme. *J. Mol. Biol.* **199**, 219–222.
36. Catalano, C. E., Cue, D., and Feiss, M. (1995) Virus DNA packaging: the strategy used by phage lambda. *Mol. Microbiol.* **16**, 1075–1086.
37. Yamada, M., Fujisawa, H., Kato, H., Hamada, K., and Minagawa, T. (1986) Cloning and sequencing of the genetic right end of bacteriophage T3 DNA. *Virology* **151**, 350–361.
38. Son, M., Hayes, S. J., and Serwer, P. (1988) Concatemerization and packaging of bacteriophage T7 DNA *in vitro*: determination of the concatemers' length and appearance kinetics by use of rotating gel electrophoresis. *Virology* **162**, 38–46.
39. Dunn, J. J. and Studier, F. W. (1983) Complete nucleotide sequence of bacteriophage T7 DNA and the locations of T7 genetic elements. *J. Mol. Biol.* **166**, 477–535.
40. Feiss, M., Frackman, S., and Sippy, J. (1985) Essential interaction between lambda-doid phage 21 terminase and the E. coli integrative host factor. *J. Mol. Biol.* **183**, 239–249.
41. Casjens, S., Huang, W. M., Hayden, M., and Parr, R. (1987) Initiation of bacteriophage P22 DNA packaging series: analysis of a mutant which alters the DNA target specificity of the packaging apparatus. *J. Mol. Biol.* **194**, 411–422.
42. Prasad, B. V. V., Prevelige, P. E., Marietta, E., Chen, R. O., Thomas, D., King, J., and Chiu, W. (1993) Three-dimensional transformation of capsids associated with genome packaging in a bacterial virus. *J. Mol. Biol.* **231**, 65–74.
43. Galisteo, M. and King, J. (1993) Conformational transformations in the protein lattice of phage P22 procapsids. *Biophys. J.* **65**, 227–235.
44. Skorupski, K., Pierce, J. C., Sauer, B., and Sternberg, N. (1992) Bacteriophage P1 genes involved in the recognition and cleavage of the phage packaging site (pac). *J. Mol. Biol.* **223**, 977–989.
45. Pfister, P., Wasserfallen, A., Stettler, R., and Leisinger, T. (1998) Molecular analysis of Methanobacterium phage psiM2. *Mol. Microbiol.* **30**, 233–244.
46. Desiere, F., Lucchini, S., and Brussow, H. (1998) Evolution of Streptococcus thermophilus bacteriophage genomes by modular exchanges followed by point mutations and small deletions and insertions. *Virology* **241**, 345–356.
47. Newcomb, W. W., Juhas, R. M., Thomsen, D. R., Homa, F. L., Burch, A. D., Weller, S. K., and Brown, J. C. (2001) The UL6 gene product forms the portal for entry of DNA into the herpes simplex virus capsid. *J. Virol.* **75**, 10,923–10,932.
48. Yu, D. and Weller, S. K. (1998) Generic analysis of the UL15 gene locus for the putative terminase of herpes simplex virus type 1. *Virology* **243**, 32–44.
49. Salmon, B. and Baines, J. D. (1998) Herpes simplex virus DNA cleavage and packaging: association of multiple forms of U(L)15-encoded proteins with



- B capsids requires at least the U(L)6, U(L)17, and U(L)28 genes. *J. Virol.* **72**, 3045–3050.
50. Scheffczik, H., Savva, C. G., Holzenburg, A., Kolesnikova, L., and Bogner, E. (2002) The terminase subunits pUL56 and pUL89 of human cytomegalovirus are DNA-metabolizing proteins with toroidal structure. *Nucleic Acids Res.* **30**, 1695–1703.
  51. Schmid, S. I. and Hearing, P. (1997) Bipartite structure and functional independence of adenovirus type 5 packaging elements. *J. Virol.* **71**, 3375–3384.
  52. Bett, A., Prevec, L., and Graham, F. (1993) Packaging capacity and stability of human adenovirus type 5 vectors. *J. Virol.* **67**, 5911–5921.
  53. Zhang, W., Low, J. A., Christensen, J. B., and Imperiale, M. J. (2001) Role for the adenovirus IVa2 protein in packaging of viral DNA. *J. Virol.* **75**, 10,446–10,454.
  54. Koonin, E. V., Senkevich, V. I., and Chernos, V. I. (1993) Gene A32 product of vaccinia virus may be an ATPase involved in viral DNA packaging as indicated by sequence comparisons with other putative viral ATPases. *Virus Genes* **7**, 89–94.
  55. Cassetti, M. C., Merchlinsky, M., Wolffe, E. J., Weiserg, A. S., and Moss, B. (1998) DNA package mutant: repression of the vaccinia virus A32 gene results in noninfectious, DNA-deficient, spherical, enveloped particles. *J. Virol.* **72**(7), 5769–5780.
  56. Feiss, M., Sippy, J., and Miller, G. (1985) Processive action of terminase during sequential packaging of bacteriophage lambda chromosomes. *J. Mol. Biol.* **186**, 759–771.
  57. Frackman, S., Siegele, D. A., and Feiss, M. (1984) A functional domain of bacteriophage  $\lambda$  terminase for prohead binding. *J. Mol. Biol.* **183**, 283–300.
  58. Frackman, S., Siegele, D. A., and Feiss, M. (1985) The terminase of bacteriophage  $\lambda$ : functional domains for *cosB* binding and multimer assembly. *J. Mol. Biol.* **180**, 283–300.
  59. Shibata, H., Fujisawa, H., and Minagawa, T. (1987) Early events in a defined *in vitro* system for packaging of bacteriophage T3 DNA. *Virology* **159**, 250–258.
  60. Shibata, H., Fujisawa, H., and Minagawa, T. (1987) Characterization of the bacteriophage T3 DNA packaging reaction *in vitro* in a defined system. *J. Mol. Biol.* **196**, 845–851.
  61. Shinder, G. and Gold, M. (1988) The Nu1 subunit of bacteriophage lambda terminase binds to specific sites in *cos* DNA. *J. Virol.* **62**, 387–392.
  62. Sternberg, N. and Coulby, J. (1987) Recognition and cleavage of the bacteriophage P1 packaging site (*pac*). I. Differential processing of the cleaved ends *in vivo*. *J. Mol. Biol.* **194**, 453–468.
  63. Sternberg, N. and Coulby, J. (1987) Recognition and cleavage of the bacteriophage P1 packaging site (*pac*). II. Functional limits of *pac* and location of *pac* cleavage termini. *J. Mol. Biol.* **194**, 469–479.
  64. Wu, W.-F., Christiansen, S., and Feiss, M. (1988) Domains for protein-protein interactions at the N and C termini of the large subunit of bacteriophage  $\lambda$  terminase. *Genetics* **119**, 477–484.

65. Pruss, G. and Calendar, R. (1978) Maturation of bacteriophage P2 DNA. *Virology* **86**, 454–467.
66. Bowden, D. W. and Calendar, R. (1979) Maturation of bacteriophage P2 DNA *in vitro*: a complex, site-specific system for DNA cleavage. *J. Mol. Biol.* **129**, 1–18.
67. Bowden, D. W. and Modrich, P. (1985) *In vitro* maturation of circular bacteriophage P2 DNA: purification of *ter* components and characterization of the reaction. *J. Biol. Chem.* **260**, 6999–7007.
68. Backhaus, H. (1985) DNA packaging initiation of *Salmonella* bacteriophage P22: determination of cut sites within the DNA sequence coding for gene 3. *J. Virol.* **55**, 458–465.
69. Poteete, A. R. and Botstein, D. (1979) Purification and properties of proteins essential to DNA encapsidation by phage 22. *Virology* **95**, 565–573.
70. Schmieger, H. and Koch, E. (1987) *In vitro* assay of packaging protein gp3 of *Salmonella* phage P22. *Intervirology* **28**, 157–162.
71. Strobel, E., Behnisch, W., and Schmieger, H. (1984) *In vitro* packaging of mature phage DNA by *Salmonella* phage P22. *Virology* **133**, 158–165.
72. Sun, M., Louie, D., and Serwer, P. (1999) Single-event analysis of the packaging of bacteriophage T7 DNA concatemers *in vitro*. *Biophys. J.* **77**(3), 1627–1637.
73. Endy, D., Kong, D., and Yin, J. (1997) Intracellular kinetics of a growing virus: a genetically structured simulation for bacteriophage T7. *Biotechnol. Bioeng.* **55**, 375–389.
74. Guo, P., Bailey, S., Bodley, J. W., and Anderson, D. (1987) Characterization of the small RNA of the bacteriophage  $\phi$ 29 DNA packaging machine. *Nucleic Acids Res.* **15**, 7081–7090.
75. Shu, D. and Guo, P. (2003) A viral RNA that binds ATP and contains an motif similar to an ATP-binding aptamer from SELEX. *J. Biol. Chem.* **278**(9), 7119–7125.
76. Bjornsti, M. A., Reilly, B. E., and Anderson, D. L. (1982) Morphogenesis of bacteriophage  $\phi$ 29 of *Bacillus subtilis*: DNA-gp3 intermediate in *in vivo* and *in vitro* assembly. *J. Virol.* **41**, 408–517.
77. Prieto, I., Lázaro, J. M., García, J. A., Hermoso, J. M., and Salas, M. (1984) Purification in a functional form of the terminal protein of *Bacillus subtilis* phage  $\phi$ 29. *Proc. Natl. Acad. Sci. USA* **81**, 1639–1643.
78. Deiss, L. and Frenkel, N. (1986) Herpes simplex virus amplicon: cleavage of concatemeric DNA is linked to packaging and involves amplification of the terminally reiterated a sequence. *J. Virol.* **57**, 933–941.
79. Newcomb, W. W., Brown, J. C., Booy, F. P., and Steven, A. C. (1989) Nucleocapsid mass and capsomer protein stoichiometry in equine herpesvirus 1: scanning transmission electron microscopic study. *J. Virol.* **63**, 3777–3783.
80. Lee, J. Y., Irmiere, A., and Gibson, W. (1988) Primate cytomegalovirus assembly: evidence that DNA packaging occurs subsequent to B capsid assembly. *Virology* **167**, 87–96.
81. Guo, P., Scholz, E., Turek, J., Nordgren, R., and Maloney, B. (1993) Assembly pathway of avian infectious laryngotracheitis virus. *Am. J. Vet. Res.* **54**, 2031–2039.

82. Gibson, W. and Roizman, B. (1972) Proteins specified by herpes simplex virus 8. Characterization and composition of multiple capsid forms of subtypes 1 and 2. *J. Virol.* **10**, 1044–1052.
83. Booy, F. P., Newcomb, W. W., Trus, B. L., Brown, J. C., Baker, T. S., and Steven, A. C. (1991) Liquid-crystalline, phage-like packaging of encapsidated DNA in herpes simplex virus. *Cell* **64**, 1007–1015.
84. Wieczorek, D. J. and Feiss, M. (2001) Defining cosQ, the site required for termination of bacteriophage lambda DNA packaging. *Genetics* **158**, 495–506.
85. McNabb, D. S. and Courtney, R. J. (1992) Analysis of the UL36 open reading frame encoding the large tegument protein (ICP1/2) of herpes simplex virus type 1. *J. Virol.* **66**, 7581–7584.
86. DeLange, A. M., Reddy, M., Scraba, D., Upton, C., and McFadden, G. (1986) Replication and resolution of cloned poxvirus telomeres *in vivo* generates linear minichromosomes with intact viral hairpin termini. *J. Virol.* **59**, 249–259.
87. Parsons, B. L. and Pickup, D. J. (1990) Transcription of orthopoxvirus telomeres at late times during infection. *Virology* **175**, 69–80.
88. Moss, B. (1990) Poxviridae and their replication, in *Virology* (Fields, B. N. and Knipe, D. M., eds.), Raven, New York, pp. 2079–2111.
89. Zhang, W. and Imperiale, M. J. (2000) Interaction of the adenovirus IVa2 protein with viral packaging sequences. *J. Virol.* **74**, 2687–2693.
90. Casjens, S. and Hendrix, R. (1988) Control mechanisms in dsDNA bacteriophage assembly, in *The Bacteriophages*, vol. 1. (Calendar, R., ed.), Plenum, New York, pp. 15–92.
91. Guo, P. (1994) Introduction: principles, perspectives, and potential applications in viral assembly. *Semin. Virol.* **5**(1), 1–3.
92. Hendrix, R. W. and Garcea, R. L. (1994) Capsid assembly of dsDNA viruses. *Semin. Virol.* **5**, 15–26.
93. Guo, P., Erickson, S., and Anderson, D. (1987) A small viral RNA is required for *in vitro* packaging of bacteriophage  $\phi$ 29 DNA. *Science* **236**, 690–694.
94. Guo, P., Peterson, C., and Anderson, D. (1987) Initiation events in *in vitro* packaging of bacteriophage  $\phi$ 29 DNA-gp3. *J. Mol. Biol.* **197**, 219–228.
95. Guo, P., Erickson, S., Xu, W., Olson, N., Baker, T. S., and Anderson, D. (1991) Regulation of the phage  $\phi$ 29 prohead shape and size by the portal vertex. *Virology* **183**, 366–373.
96. Guo, P., Rajogopal, B., Anderson, D., Erickson, S., and Lee, C.-S. (1991) sRNA of bacteriophage  $\phi$ 29 of *B. subtilis* mediates DNA packaging of  $\phi$ 29 proheads assembled in *E. coli*. *Virology* **185**, 395–400.
97. Lee, C. S. and Guo, P. (1995) *In vitro* assembly of infectious virions of ds-DNA phage  $\phi$ 29 from cloned gene products and synthetic nucleic acids. *J. Virol.* **69**, 5018–5023.
98. Lee, C. S. and Guo, P. (1994) A highly sensitive system for the *in vitro* assembly of bacteriophage  $\phi$ 29 of *Bacillus subtilis*. *Virology* **202**, 1039–1042.
99. Tonegawa, S. and Hayashi, M. (1970) Intermediates in the assembly of fX174. *J. Mol. Biol.* **48**, 219–242.

100. Laemmli, U. (1970) Cleavage of structural proteins during the assembly of the head of bacteriophage T4. *Nature* **227**, 680–685.
101. Laemmli, U., Molbert, E., Showe, M., and Kellenberger, E. (1970) Form determining function of the genes required for the assembly of the bacteriophage T4. *J. Mol. Biol.* **49**, 99–113.
102. Kaiser, D. and Masuda, T. (1973) *In vitro* assembly of bacteriophage lambda heads. *Proc. Natl. Acad. Sci. USA* **70**, 260–264.
103. King, J. and Casjens, S. (1974) Catalytic head assembly protein in virus morphogenesis. *Nature* **251**, 112–119.
104. Israel, J. V., Anderson, T. H., and Levine, M. (1967) *In vitro* morphogenesis of phage p22 from heads and base-plate parts. *Proc. Natl. Acad. Sci. USA* **57**, 284–291.
105. Becker, A., Marko, M., and Gold, M. (1977) Early events in the *in vitro* packaging of bacteriophage DNA. *Virology* **78**, 291–305.
106. Miyazaki, J., Fugisawa, H., and Minagawa, T. (1978) Biological activity of purified bacteriophage T3 prohead and prohead-like structures as precursors for *in vitro* head assembly. *Virology* **91**, 283–290.
107. Mettenleiter, T. and Rauh, I. (1990) A glycoprotein gX- $\beta$ -galactosidase fusion gene as insertional marker for rapid identification of pseudorabies virus mutants. *J. Virol. Methods* **30**, 55–66.
108. Poteete, A. R., Jarvik, V., and Botstein, D. (1979) Encapsulation of phage P22 DNA *in vitro*. *Virology* **95**, 550–564.
109. Bjornsti, M. A., Reilly, B. E., and Anderson, D. L. (1981) *In vitro* assembly of the *Bacillus subtilis* bacteriophage  $\phi$ 29. *Proc. Natl. Acad. Sci. USA* **78**, 5861–5865.
110. Fuller, M. and King, J. (1982) Assembly *in vitro* of bacteriophage P22 procapsids from purified coat and scaffolding subunits. *J. Mol. Biol.* **156**, 633–665.
111. Aoyama, A., Hamatake, R. K., and Hayashi, M. (1983) *In vitro* synthesis of bacteriophage  $\phi$ X174 by purified components. *Proc. Natl. Acad. Sci. USA* **80**, 4195–4199.
112. Hwang, Y. and Feiss, M. (1997) A defined system for *in vitro* lambda DNA packaging. *Virology* **211**, 367–376.
113. Kellenberger, E. and Wunderli-Allenspach, H. (1995) Electron microscopic studies on intracellular phage development—history and perspectives. *Micron* **26**, 213–245.
114. Tao, Y., Olson, N. H., Xu, W., Anderson, D. L., Rossmann, M. G., and Baker, T. S. (1998) Assembly of a tailed bacterial virus and its genome release studied in three dimensions. *Cell* **95**, 431–437.
115. Lee, C. S. and Guo, P. (1995) Sequential interactions of structural proteins in phage  $\phi$ 29 procapsid assembly. *J. Virol.* **69**, 5024–5032.
116. Murialdo, H. and Becker, A. (1977) Assembly of biologically active proheads of bacteriophage lambda *in vitro*. *Proc. Natl. Acad. Sci. USA* **74**, 906–910.
117. Shaw, J. E. and Murialdo, H. (1980) Morphogenetic genes C and Nu3 overlap in bacteriophage lambda. *Nature* **283**, 30–35.
118. Katsura, I. (1983) Structure and inherent properties of bacteriophage lambda head shell. IV. Small head mutants. *J. Mol. Biol.* **171**, 297–317.

119. Katsura, I. (1986) Structure and inherent properties of the bacteriophage lambda head shell. V. Amber mutants in gene E. *J. Mol. Biol.* **190**, 577–586.
120. Katsura, I. (1989) Structure and inherent properties of the bacteriophage lambda head shell. VI. DNA packaging defective mutants in the major capsid protein. *J. Mol. Biol.* **205**, 397–405.
121. Mindich, L., Qiao, X., Qiao, J., Onodera, S., Romantschuk, M., and Hoogstraten, D. (1999) Isolation of additional bacteriophages with genomes of segmented double-stranded RNA. *J. Bacteriol.* **181**, 4505–4508.
122. Traub, F. and Maeder, M. (1984) Formation of the prohead core of bacteriophage T4 *in vivo*. *J. Virol.* **49**, 892–901.
123. Traub, F., Keller, B., Kuhn, A., and Maeder, M. (1984) Isolation of the prohead core of bacteriophage T4 after cross-linking and determination of protein composition. *J. Virol.* **49**, 902–908.
124. Kuhn, A., Keller, B., Maeder, M., and Traub, F. (1987) Prohead core of bacteriophage T4 can act as an intermediate in the T4 head assembly pathway. *J. Virol.* **61**, 113–118.
125. Thomsen, D. R., Roof, L. L., and Homa, F. L. (1994) Assembly of herpes simplex virus (HSV) intermediate capsids in insect cells infected with recombinant baculoviruses expressing HSV capsid proteins. *J. Virol.* **68**, 2442–2457.
126. Tatman, J. D., Preston, V. G., Nicholson, R. M., Elliott, R. M., and Rixon, F. J. (1994) Assembly of herpes simplex virus type 1 capsids using a panel of recombinant baculoviruses. *J. Gen. Virol.* **75**, 1101–1113.
127. Newcomb, W., Homa, F. L., Thomsen, D. L., Ye, Z., and Brown, J. (1994) Cell-free assembly of the herpes simplex capsid. *J. Virol.* **68**, 6059–6063.
128. Guasch, A., Pous, J., Ibarra, B., Gomis-Ruth, F. X., Valpuesta, J. M., Sousa, N., Carrascosa, J. L., and Coll, M. (2002) Detailed architecture of a DNA translocating machine: the high-resolution structure of the bacteriophage phi29 connector particle. *J. Mol. Biol.* **315**, 663–676.
129. Simpson, A. A., Tao, Y., Leiman, P. G., et al. (2000) Structure of the bacteriophage phi29 DNA packaging motor. *Nature* **408**, 745–750.
130. Valpuesta, J. M., Fujisawa, H., Marco, S., Carazo, J. M., and Carrascosa, J. (1992) Three-dimensional structure of T3 connector purified from overexpressing bacteria. *J. Mol. Biol.* **224**, 103–112.
131. Rishovd, S., Holzenburg, A., Johansen, B. V., and Lindqvist, B. H. (1998) Bacteriophage P2 and P4 morphogenesis: structure and function of the connector. *Virology* **245**, 11–17.
132. Kochan, J., Carrascosa, J. L., and Murialdo, H. (1984) Bacteriophage lambda preconnectors: purification and structure. *J. Mol. Biol.* **174**, 433–447.
133. Donate, L. E., Herranz, L., Secilla, J. P., Carazo, J. M., Fujisawa, H., and Carrascosa, J. L. (1988) Bacteriophage T3 connector: three-dimensional structure and comparison with other viral head-tail connecting regions. *J. Mol. Biol.* **201**, 91–100.
134. Hendrix, R. W. (1978) Symmetry mismatch and DNA packaging in large bacteriophages. *Proc. Natl. Acad. Sci. USA* **75**, 4779–4783.

135. Chen, C. and Guo, P. (1997) Sequential action of six virus-encoded DNA-packaging RNAs during phage  $\phi$ 29 genomic DNA translocation. *J. Virol.* **71**, 3864–3871.
136. Salas, M. (1988) Phages with protein attached to the DNA ends, in *The Bacteriophages*, vol. 1 (Calendar, R., ed.), Plenum, New York, pp. 169–191.
137. Bravo, A., Hermoso, J. M., and Salas, M. (1994) In vivo functional relationships among terminal proteins of *Bacillus subtilis*  $\phi$ 29-related phages. *Gene* **148**, 107–112.
138. Blanco, L., Lazaro, J. M., de Vega, M., Bonnin, A., and Salas, M. (1994) Terminal protein-primed DNA amplification. *Proc. Natl. Acad. Sci. USA* **91**, 12,198–12,202.
139. Salas, M. (1991) Protein-priming of DNA replication. *Annu. Rev. Biochem.* **60**, 39–71.
140. Bravo, A., Hermoso, J. M., and Salas, M. (1994) In vivo functional relationships among terminal proteins of *Bacillus subtilis*  $\phi$ 29-related phage. *Gene* **148**, 107–112.
141. Donate, L. E., Valpuesta, J. M., Rocher, A., Mendez, E., Rojo, F., Salas, M., and Carrascosa, J. L. (1992) Role of the amino-terminal domain of bacteriophage  $\phi$ 29 connector in DNA binding and packaging. *J. Biol. Chem.* **267**, 10,919–10,924.
142. Franklin, J. (1992) A DNA packaging protein of phage T4, the product of gene 17, binds cooperatively to single-stranded DNA. PhD thesis, Vanderbilt University, Nashville, TN.
143. Higgins, R. R., Lucko, H. J., and Becker, A. (1988) Mechanism of *cos* DNA cleavage by bacteriophage lambda terminase-multiple roles of ATP. *Cell* **54**, 765–775.
144. Parris, W., Davidson, A., Keeler, C. L., Jr., and Gold, M. (1988) The Nu1 subunit of bacteriophage  $\lambda$  terminase. *J. Biol. Chem.* **263**, 8413–8419.
145. Kimura, M. and Fujisawa, H. (1991) Dissection of the functional domains of the packaging protein of bacteriophage T3 by site-directed mutagenesis. *Virology* **180**, 709–715.
146. Eppler, K., Wyckoff, E., Goates, J., Parr, R., and Casjens, S. (1991) Nucleotide sequence of the bacteriophage P22 genes required for DNA packaging. *Virology* **183**, 519–538.
147. Grimes, S. and Anderson, D. (1990) RNA dependence of the bacteriophage  $\phi$ 29 DNA packaging ATPase. *Mol. Biol.* **215**, 559–566.
148. Ibarra, B., Valpuesta, J. M., and Carrascosa, J. L. (2001) Purification and functional characterization of p16, the ATPase of the bacteriophage  $\phi$ 29 packaging machinery. *Nucleic Acids Res.* **29**(21), 4264–4273.
149. Hoeprich, S. and Guo, P. (2002) Computer modeling of three-dimensional structure of DNA-packaging RNA(pRNA) monomer, dimer, and hexamer of  $\phi$ 29 DNA packaging motor. *J. Biol. Chem.* **277**(23), 20,794–20,803.



150. Garver, K. and Guo, P. (1997) Boundary of pRNA functional domains and minimum pRNA sequence requirement for specific connector binding and DNA packaging of phage phi29. *RNA* **3**, 1068–1079.
151. Chen, C. and Guo, P. (1997) Magnesium-induced conformational change of packaging RNA for procapsid recognition and binding during phage phi29 DNA encapsidation. *J. Virol.* **71**, 495–500.
152. Bailey, S., Wichitwechkarn, J., Johnson, D., Reilly, B., Anderson, D., and Bodley, J. W. (1990) Phylogenetic analysis and secondary structure of the *Bacillus subtilis* bacteriophage RNA required for DNA packaging. *J. Biol. Chem.* **265**, 22,365–22,370.
153. Chen, C., Zhang, C., and Guo, P. (1999) Sequence requirement for hand-in-hand interaction in formation of pRNA dimers and hexamers to gear phi29 DNA translocation motor. *RNA* **5**, 805–818.
154. Reid, R. J. D., Bodley, J. W., and Anderson, D. (1994) Characterization of the prohead-pRNA interaction of bacteriophage phi29. *J. Biol. Chem.* **269**, 5157–5162.
155. Chen, C., Sheng, S., Shao, Z., and Guo, P. (2000) A dimer as a building block in assembling RNA: a hexamer that gears bacterial virus phi29 DNA-translocating machinery. *J. Biol. Chem.* **275**(23), 17,510–17,516.
156. Reid, R. J. D., Zhang, F., Benson, S., and Anderson, D. (1994) Probing the structure of bacteriophage phi29 prohead RNA with specific mutations. *J. Biol. Chem.* **269**, 18,656–18,661.
157. Zhang, C. L., Lee, C.-S., and Guo, P. (1994) The proximate 5' and 3' ends of the 120-base viral RNA (pRNA) are crucial for the packaging of bacteriophage phi29 DNA. *Virology* **201**, 77–85.
158. Zhang, C. L., Tellinghuisen, T., and Guo, P. (1995) Conformation of the helical structure of the 5'/3' termini of the essential DNA packaging pRNA of phage phi29. *RNA* **1**, 1041–1050.
159. Wichitwechkarn, J., Johnson, D., and Anderson, D. (1992) Mutant prohead RNAs in vitro packaging of bacteriophage phi29 DNA-gp3. *Mol. Biol.* **223**, 991–998.
160. Zhang, C. L., Tellinghuisen, T., and Guo, P. (1997) Use of circular permutation to assess six bulges and four loops of DNA-packaging pRNA of bacteriophage phi29. *RNA* **3**, 315–322.
161. Zhang, C. L., Garver, K., and Guo, P. (1995) Inhibition of phage phi29 assembly by antisense oligonucleotides targeting viral pRNA essential for DNA packaging. *Virology* **211**, 568–576.
162. Trottier, M., Garver, K., Zhang, C., and Guo, P. (1997) DNA-packaging pRNA as target for complete inhibition of viral assembly in vitro and in vivo. *Nucleic Acids Symp. Ser.* **36**, 187–189.
163. Trottier, M. and Guo, P. (1997) Approaches to determine stoichiometry of viral assembly components. *J. Virol.* **71**, 487–494.
164. Trottier, M., Zhang, C. L., and Guo, P. (1996) Complete inhibition of virion assembly *in vivo* with mutant pRNA essential for phage phi29 DNA packaging. *J. Virol.* **70**, 55–61.



165. Trottier, M., Mat-Arip, Y., Zhang, C., Chen, C., Sheng, S., Shao, Z., and Guo, P. (2000) Probing the structure of monomers and dimers of the bacterial virus phi29 hexamer RNA complex by chemical modification. *RNA* **6**, 1257–1266.
166. Guo, P., Zhang, C., Chen, C., Trottier, M., and Garver, K. (1998) Inter-RNA interaction of phage phi29 pRNA to form a hexameric complex for viral DNA transportation. *Mol. Cell.* **2**, 149–155.
167. Zhang, F., Lemieux, S., Wu, X., St.-Arnaud, S., McMurray, C. T., Major, F., and Anderson, D. (1998) Function of hexameric RNA in packaging of bacteriophage phi29 DNA in vitro. *Mol. Cell.* **2**, 141–147.
168. Wichitwechkarn, J., Bailey, S., Bodley, J. W., and Anderson, D. (1989) Prohead RNA of bacteriophage  $\phi$ 29: size, stoichiometry and biological activity. *Nucleic Acids Res.* **17(9)**, 3459–3468.
169. Chen, C., Trottier, M., and Guo, P. (1997) New approaches to stoichiometry determination and mechanism investigation on RNA involved in intermediate reactions. *Nucleic Acids Symp. Ser.* **36**, 190–193.
170. Shu, D., Huang, L., and Guo, P. (2003) A simple mathematical formula for stoichiometry quantitation of viral and nanobiological assemblage using slopes of log/log plot curves. *J. Virol Methods* **115(1)**, 19–30.
171. Guo, P. (2002) Structure and function of phi29 hexameric RNA that drive viral DNA packaging motor: review. *Prog. Nucl. Acid Res. Mol. Biol.* **72**, 415–472.
172. Peterson, C., Simon, M., Hodges, J., Mertens, P., Higgins, L., Egelman, E., and Anderson, D. (2001) Composition and mass of the bacteriophage phi29 prohead and virion. *J. Struct. Biol.* **135**, 18–25.
173. Anderson, D. L., Hickman, H. H., and Reilly, B. E. (1966) Structure of *Bacillus subtilis* bacteriophage  $\phi$ 29 and the length of  $\phi$ 29 deoxyribonucleic acid. *J. Bacteriol.* **91**, 2081–2089.
174. Carrascosa, J. L., Mendez, E., Corral, J., Rubio, V., Ramirez, G., Salas, M., and Vinuela, E. (1981) Structural organization of *Bacillus subtilis* phage  $\phi$ 29: a model. *Virology* **111**, 401–413.
175. Villanueva, N. and Salas, M. (1981) Adsorption of bacteriophage phi 29 to *Bacillus subtilis* through the neck appendage of the viral particle. *J. Virol.* **38(1)**, 15–19.
176. Villanueva, N., Lazaro, J. M., and Salas, M. (1981) Purification, properties and assembly of the neck-appendage protein of the *Bacillus subtilis* phage phi 29. *Eur. J. Biochem.* **117**, 499–505.
177. Hohn, T., Wurtz, M., and Hohn, B. (1976) Capsid transformation during packaging of bacteriophage  $\lambda$  DNA. *Philos. Trans. R. Soc. Lond. Ser. B* **276**, 51–61.
178. Davidson, A. and Gold, M. (1987) A novel *in vitro* DNA packaging system demonstrating a direct role for the bacteriophage  $\lambda$  FI gene product. *Virology* **161**, 305–314.
179. Gold, M. and Becker, A. (1983) The bacteriophage  $\lambda$  terminase: partial purification and preliminary characterization of properties. *J. Biol. Chem.* **258**, 14,619–14,625.

180. Becker, A., Murialdo, H., Lucko, H., and Morell, J. (1988) Bacteriophage lambda DNA packaging: the product of the F1 gene promotes the incorporation of the prohead to the DNA-terminase complex. *J. Mol. Biol.* **199**, 597–607.
181. White, J. H. and Richardson, C. C. (1987) Gene 18 protein of bacteriophage T7. Overproduction, purification, and characterization. *J. Biol. Chem.* **262**, 8845–8850.
182. Guo, P. (2002) Methods for structural and functional analysis of an RNA hexamer of bacterial virus phi29 DNA packaging motor. *Acta Biochim. Biophys. Sinica* **34**(5), 533–543.
183. Zhang, C. L., Trottier, M., and Guo, P. X. (1995) Circularly permuted viral pRNA active and specific in the packaging of bacteriophage  $\phi$ 29 DNA. *Virology* **207**, 442–451.
184. Wu, T., Ruan, K., and Liu, W. (1996) A fluorescence-labeling method for sequencing small RNA on polyacrylamide gel. *Nucleic Acids Res.* **24**, 3472, 3473.
185. Babcock, M. S., Pednault, E. P. D., and Olson, W. K. (1994) Nucleic acid structure analysis: mathematics for local cartesian and helical structure parameters that are truly comparable between structures. *J. Mol. Biol.* **237**, 125–156.
186. Gautheret, D. and Cedergren, R. (1993) Modeling the three-dimensional structure of RNA. *FASEB J.* **7**, 97–105.
187. Jimenez, J., Santisteban, A., Carazo, J. M., and Carrascosa, J. L. (1986) Computer graphic display method for visualizing three-dimensional biological structures. *Science* **232**, 1113–1115.
188. Carazo, J. M., Donate, L. E., Herranz, L., Secilla, J. P., and Carrascosa, J. L. (1986) Three-dimensional reconstruction of the connector of bacteriophage  $\phi$ 29 at 1.8 nm resolution. *J. Mol. Biol.* **192**, 853–867.
189. Smith, D. E., Tans, S. J., Smith, S. B., Grimes, S., Anderson, D. L., and Bustamante, C. (2001) The bacteriophage phi29 portal motor can package DNA against a large internal force. *Nature* **413**, 748–752.
190. Hendrix, R. W. (1998) Bacteriophage DNA packaging: RNA gears in a DNA transport machine [minireview]. *Cell* **94**, 147–150.
191. Dubé, P., Tavares, P., Lurz, R., and van Heel, M. (1993) The portal protein of bacteriophage SPP1: a DNA pump with 13-fold symmetry. *EMBO J.* **12**, 1303–1309.
192. Turnquist, S., Simon, M., Egelman, E., and Anderson, D. (1992) Supercoiled DNA wraps around the bacteriophage  $\phi$ 29 head-tail connector. *Proc. Natl. Acad. Sci. USA* **89**, 10,479–10,483.
193. Astumian, R. D. (1997) Thermodynamics and kinetics of a Brownian motor. *Science* **276**, 917–922.
194. Leibler, S. (1994) Brownian motion: moving forward noisily. *Nature* **370**, 412, 413.
195. Soong, R. K., Bachand, G. D., Neves, H. P., Olkhovets, A. G., Craighead, H. G., and Montemagno, C. D. (2000) Powering an inorganic nanodevice with a biomolecular motor. *Science* **290**, 1555–1558.
196. Baneyx, G. and Vogel, V. (1999) Self-assembly of fibronectin into fibrillar networks underneath dipalmitoyl phosphatidylcholine monolayers: role of lipid matrix and tensile forces. *Proc. Natl. Acad. Sci. USA* **96**, 12,518–12,523.

197. Hess, H. and Vogel, V. (2001) Molecular shuttles based on motor proteins: active transport in synthetic environments. *Rev. Mol. Biotechnol.* **82**, 67–85.
198. Niemeyer, C. M. (2002) The developments of semisynthetic DNA-protein conjugates. *Trends Biotechnol.* **20**, 395–401.
199. Schmidt, O. G. and Eberl, K. (2001) Nanotechnology: thin solid films roll up into nanotubes. *Nature* **410**, 168.
200. Modi, A., Koratkar, N., Lass, E., Wei, B., and Ajayan, P. M. (2003) Miniaturized gas ionization sensors using carbon nanotubes. *Nature* **424**, 171–174.
201. Credo, G. M., Boal, A. K., Das, K., Galow, T. H., Rotello, V. M., Feldheim, D. L., and Gorman, C. B. (2002) Supramolecular assembly on surfaces: manipulating conductance in noncovalently modified mesoscale structures. *J. Am. Chem. Soc.* **124**, 9036–9037.
202. Baneyx, G., Baugh, L., and Vogel, V. (2002) Supramolecular chemistry and self-assembly special feature: fibronectin extension and unfolding within cell matrix fibrils controlled by cytoskeletal tension. *Proc. Natl. Acad. Sci. USA* **99**, 5139–5143.
203. Hyman, P., Valluzzi, R., and Goldberg, E. (2002) Design of protein struts for self-assembling nanoconstructs. *Proc. Natl. Acad. Sci. USA* **99**, 8488–8493.
204. Goldberger, J., He, R., Zhang, Y., Lee, S., Yan, H., Choi, H. J., and Yang, P. (2003) Single-crystal gallium nitride nanotubes. *Nature* **422**, 599–602.
205. Davenport, R. J. (2001) Crossover research yield scents and sensitivity—watching a virus get stuffed. *Science* **291**, 2071–2072.
206. Hoeprich, S., Zhou, Q., Guo, S., Shu, D., Qi, G., Wang, Y., and Guo, P. (2003) Bacterial virus phi29 pRNA as a hammerhead ribozyme escort to destroy hepatitis B virus. *Gene Ther.* **10(15)**, 1258–1267.
207. Shu, D., Huang, L., Hoeprich, S., and Guo, P. (2003) Construction of phi29 DNA-packaging RNA (pRNA) Monomers, dimers and trimers with variable sizes and shapes as potential parts for nano-devices. *J. Nanosci. Nanotechnol.* **4**, 295–302.
208. Mat-Arip, Y., Garver, K., Chen, C., Sheng, S., Shao, Z., and Guo, P. (2001) Three-dimensional interaction of phi29 pRNA dimer probed by chemical modification interference, cryo-AFM, and cross-linking. *J. Biol. Chem.* **276**, 32,575–32,584.
209. Tuerk, G. and Gold, L. (1990) Systematic evolution of ligands by exponential enrichment: RNA ligands to bacteriophage T4 DNA polymerase. *Science* **249**, 505–510.
210. Ellington, A. D. and Szostak, J. W. (1990) *In vitro* selection of RNA molecules that bind specific ligands. *Nature* **346**, 818–822.
211. Ciesiolka, J., Gorski, J., and Yarus, M. (1995) Selection of an RNA domain that binds Zn<sup>++</sup>. *RNA* **1**, 538–550.
212. Klug, S. J. and Famulok, M. (1994) All you wanted to know about SELEX. *Mol. Biol. Rep.* **20**, 97–107.
213. Wang, C., Jin, Y. X., and Wang, D. B. (1998) Selection with SELEX method of small RNA molecules specifically binding to starch. *Sheng Wu Hua Xue. Yu Sheng Wu Wu Li Xue. Bao. (Shanghai)* **30**, 402–404.

214. Shtatland, T., Gill, S. C., Javornik, B. E., Johansson, H. E., Singer, B. S., Uhlenbeck, O. C., Zichi, D. A., and Gold, L. (2000) Interactions of *Escherichia coli* RNA with bacteriophage MS2 coat protein: genomic SELEX. *Nucleic Acids Res.* **28**, E93.
215. Deamer, D. W. and Akeson, M. (2000) Nanopores and nucleic acids: prospects for ultrarapid sequencing. *Trends Biotechnol.* **18**, 147–151.
216. Sundquist, W. I. and Heaphy, S. (1993) Evidence for interstand quadruplex formation in the dimerization of human immunodeficiency virus 1 genomic RNA. *Proc. Natl. Acad. Sci. USA* **90**, 3393–3397.
217. Skripkin, E., Paillart, J. C., Marquet, R., Ehresmann, B., and Ehresmann, C. (1994) Identification of the primary site of the human immunodeficiency virus type 1 RNA dimerization in vitro. *Proc. Natl. Acad. Sci. USA* **91**, 4945–4949.
218. Paillart, J. C., Skripkin, E., Ehresmann, B., Ehresmann, C., and Marquet, R. (1996) A loop-loop “kissing” complex is the essential part of the dimer linkage of genomic HIV-1 RNA. *Proc. Natl. Acad. Sci. USA* **93**, 5572–5577.
219. Ferrandon, D., Koch, I., Westhof, E., and Nusslein-Volhard, C. (1997) RNA-RNA interaction is required for the formation of specific bicoid mRNA 3' UTR-STAUEN ribonucleoprotein particles. *EMBO J.* **16**, 1751–1758.
220. Guerrier-Takada, C., Gardiner, K., Marsh, T., Pace, N., and Altman, S. (1983) The RNA moiety of ribonuclease P is the catalytic subunit of the enzyme. *Cell* **35**, 849–857.
221. Oh, B. K. and Pace, N. R. (1994) Interaction of the 3'-end of tRNA with ribonuclease P RNA. *Nucleic Acids Res.* **22**(20), 4087–4094.
222. Baer, M. F., Reilly, R. M., McCorkle, G. M., Hai, T. Y., Altman, S., and Raj Bhandary, U. L. (1988) The recognition by RNase P of precursor tRNAs. *J. Biol. Chem.* **263**, 2344–2351.
223. Eguchi, Y. and Tomizawa, J. (1990) Complex formed by complementary RNA stem-loops and its stabilization by a protein: function of ColE1 Rom protein. *Cell* **60**, 199–209.
224. Panuska, J. R. and Goldthwait, D. A. (1980) A DNA dependent ATPase from T4-infected *E. coli*: purification and properties of a 63,000-dalton enzyme and its conversion to a 22,000-dalton form. *J. Biol. Chem.* **255**, 5208–5214.
225. Guo, P. and Trottier, M. (1994) Biological and biochemical properties of the small viral RNA (pRNA) essential for the packaging of the double-stranded DNA of phage  $\phi$ 29. *Semin. Virol.* **5**, 27–37.
226. Serwer, P. (1988) The source of energy for bacteriophage DNA packaging: an osmotic pump explains the data. *Biopolymers* **27**, 165–169.
227. Ellison, V. and Stillman, B. (2001) Opening of the clamp: an intimate view of an ATP-driven biological machine. *Cell* **106**, 655–660.
228. Hingorani, M. M. and O'Donnell, M. (2000) Sliding clamps: a (tail)ored fit. *Curr. Biol.* **10**, 25–29.
229. Kainov, D. E., Pirttimaa, M., Tuma, R., Butcher, S. J., Thomas, G. J., Jr., Bamford, D. H., and Makeyev, E. V. (2003) RNA packaging device of double-

- stranded RNA bacteriophages, possibly as simple as hexamer of P4 protein. *J. Biol. Chem.* **278**, 48,084–48,091.
230. Lisal, J., Kainov, D. E., Bamford, D. H., George, J. T., and Tuma, R. (2003) Enzymatic mechanism of RNA translocation in dsRNA bacteriophages. *J. Biol. Chem.* **279**, 1343–1350.
231. West, S. C. (1996) DNA helicases: new breeds of translocating motors and molecular pumps. *Cell* **86**, 177–180.
232. Niedenzu, T., Roleke, D., Bains, G., Scherzinger, E., and Saenger, W. (2001) Crystal structure of the hexameric replicative helicase RepA of plasmid RSF1010. *J. Mol. Biol.* **306**, 479–487.
233. Gogol, E. P., Seifried, S. E., and von Hippel, P. H. (1991) Structure and assembly of the Escherichia coli transcription termination factor rho and its interaction with RNA. I. Cryoelectron microscopic studies. *J. Mol. Biol.* **221**, 1127–1138.
234. Burgess, B. R. and Richardson, J. P. (2001) RNA passes through the hole of the protein hexamer in the complex with the Escherichia coli Rho factor. *J. Biol. Chem.* **276**, 4182–4189.
235. Bowers, J., Tran, P. T., Joshi, A., Liskay, R. M., and Alani, E. (2001) MSH-MLH complexes formed at a DNA mismatch are disrupted by the PCNA sliding clamp. *J. Mol. Biol.* **306**, 957–968.
236. Sedman, J. and Stenlund, A. (1998) The papillomavirus E1 protein forms a DNA-dependent hexameric complex with ATPase and DNA helicase activities. *J. Virol.* **72**, 6893–6897.
237. Leu, F. P. and O'Donnell, M. (2001) Interplay of a clamp loader subunits in opening the  $\beta$  sliding clamp of E. coli DNA polymerase III holoenzyme. *J. Biol. Chem.* **276**, 47,185–47,194.
238. Song, M. S., Dallmann, H. G., and McHenry, C. S. (2001) Carboxyl-terminal domain III of the delta subunit of the DNA polymerase III holoenzyme binds delta. *J. Biol. Chem.* **276**, 40,668–40,679.
239. Geiduschek, E. P. (1997) Riding the (mono)rails: the structure of catenated DNA-tracking proteins. *Chem. Biol.* **2**, 123–125.
240. Young, M. C., Schultz, D. E., Ring, D., and von Hippel, P. H. (1994) Kinetic parameters of the translocation of bacteriophage T4 gene 41 protein helicase on single-stranded DNA. *J. Mol. Biol.* **235**, 1447–1458.
241. Herendeen, D. R., Kassavetis, G. A., and Geiduschek, E. P. (1992) A transcriptional enhancer whose function imposes a requirement that proteins track along DNA. *Science* **256**, 1298–1303.
242. Geiselman, J., Wang, Y., Seifried, S. E., and von Hippel, P. H. (1993) A physical model for the translocation and helicase activities of Escherichia coli transcription termination protein rho. *Proc. Natl. Acad. Sci. USA* **90**, 7754–7758.
243. Davis, L. I. (1995) The nuclear pore complex. *Annu. Rev. Biochem.* **64**, 865–896.
244. Krug, R. M. (1993) The regulation of export of mRNA from nucleus to cytoplasm. *Curr. Opin. Cell Biol.* **5**, 944–949.
245. Pfeifer, K., Weiler, B. E., Ugarkovic, D., Bachmann, M., Schroder, H. C., and Muller, W. E. (1991) Evidence for a direct interaction of Rev protein with nuclear envelope mRNA-translocation system. *Eur. J. Biochem.* **199**, 53–64.

246. Young, M., Kuhl, S., and von Hippel, P. (1994) Kinetic theory of ATP-driven translocases on one-dimensional polymer lattices. *J. Mol. Biol.* **235**, 1436–1446.
247. Egelman, E. H. (1996) Homomorphous hexameric helicases: tales from the ring cycle. *Structure* **4**, 759–762.
248. San Martin, M. C., Gruss, C., and Carazo, J. M. (1997) Six molecules of SV40 large T antigen assemble in a propeller-shaped particle around a channel. *J. Mol. Biol.* **268**, 15–20.
249. Huang, L. P. and Guo, P. (2003) Use of PEG to acquire highly soluble DNA-packaging enzyme gp16 of bacterial virus phi29 for stoichiometry quantification. *J. Virol. Methods* **109**, 235–244.
250. Peterson, C., Simon, M., Hodges, J., Mertens, P., Higgins, L., Egelman, E., and Anderson, D. (2001) Composition and Mass of the Bacteriophage phi29 Prohead and Virion. *J. Struct. Biol.* **135**, 18–25.

## Construction of Ordered Protein Arrays

Jarrold Clark, Taras Shevchuk, Piotr M. Swiderski, Rajesh Dabur,  
Laura E. Crocitto, Yaroslav I. Buryanov, and Steven S. Smith

### Summary

Artificially ordered protein arrays provide a facile approach to a variety of problems in biology and nanoscience. Current demonstration systems use either nucleic acid tethers or methyltransferase fusions in order to target proteins or peptides of interest to nucleic acid scaffolds. These demonstrations point to the large number of useful devices and assemblies that can be envisioned using this approach, including smart biological probes and drug delivery systems. In principle, these systems are now capable of imitating the earliest forms of prebiotic organisms and can be expected to reach the complexity of a small virus in the near future. Third-generation methyltransferase inhibitors provide an example of a smart chemotherapeutics that can be constructed with this approach. We describe the use of mechanistic enzymology, computer-aided design, and microfluidic chip-based capillary electrophoresis in assessing the final assembly and testing of designs of this type.

**Key Words:** Bionanotechnology; DNA methyltransferase; protein ordering; protein targeting; DNA scaffold; inhibitor design; inhibitor delivery; smart chemotherapeutics; macromolecular carcerand; microfluidics.

### 1. Introduction

Bionanotechnology is an emerging field placed squarely at the interface between biotechnology and nanotechnology. Like other nanotechnologies, its goal is the production of useful materials and devices. Much of the technology in this area is biomimetic, meaning that it seeks to mimic biological processes. Most of the approaches taken to date are a form of macromolecular natural product chemistry aimed at producing macromolecular machines from nucleic acids and proteins. Biosensors (**1**), two-dimensional crystals (**2**), electronic circuitry (**3**), and a fueled oscillator (**4**) have all been described.

From: *Methods in Molecular Biology*, vol. 300:  
*Protein Nanotechnology, Protocols, Instrumentation, and Applications*  
Edited by: T. Vo-Dinh © Humana Press Inc., Totowa, NJ



The technology is now capable of imitating prebiotic molecular evolution. According to current thinking, the earliest form of organization in prebiology may have generated supramolecular aggregates called metabolosomes (5), which ultimately gave rise to translation (6). Prior to the appearance of translation, we think the RNA world was an evolving system in which RNA played the only structural and catalytic roles. Metabolosomes are viewed as assemblies in which nucleic acid base-pairing rules order different functions along a nucleic acid scaffold. Base pairing between a short region of the nucleic acid scaffold and a short region of the functionalized adapter RNAs is thought to have generated the appropriate alignment of the functionalities (5). Niemeyer et al. (7,8) have successfully utilized this approach in developing a bionanotechnology of ordered supramolecular assemblies.

In their initial experiments, they ordered the thermostable protein streptavidin along the screw axis of a DNA helix (8) by using biotinylated DNA as the adapter. The streptavidin protein binds to the end of the DNA owing to the innate capacity of streptavidin to bind extremely tightly to biotin. A DNA or an RNA molecule was then used as a scaffold to sequester and align the tethered streptavidin molecules (8) much as originally envisioned (5) for the metabolosome. When DNA is used as the organizing molecule, the streptavidin moieties are expected to be arrayed around the screw axis of the DNA molecule (36°/bp); however, when RNA is used, this orientation is expected to be in accordance with the screw axis of the RNA-DNA hybrid (30°/bp).

Streptavidin aggregates also provide the opportunity for secondary assembly. For example, by adding biotin to both of the 5' ends of complementary oligodeoxynucleotides, it has been possible to form ring structures or networks of DNA linked by two, three, or four biotin contacts per streptavidin residue (7). Moreover, the streptavidin molecule binds biotin with a stoichiometry of four biotin residues per protein moiety. This leaves three unused sites on the DNA-streptavidin conjugate. These unused sites have been used to attach biotinylated antibodies to DNA-tethered streptavidin (8). This permits the derivatization of microstructured surface arrays of DNA using the base-pairing complementarity of the array so as to convert it into a protein array of different antigen specificities (8).

Biotinylated proteins can be linked to avidin and then targeted to DNA- or RNA-organizing molecules provided that they can withstand the extended exposure to temperatures above 50°C required for the annealing process. Alternatively, biotinylated proteins can be sequestered without regard to order along an organizing DNA or RNA molecule by incubating them at low temperature with streptavidin molecules tethered to DNA or RNA. Using these methods, the effects of protein proximity have also been studied with this system. In an example of this approach, the NADPH oxidoreductase was placed

adjacent to luciferase in order to improve the properties of light emission by the system that is normally coupled by these enzymes. A measurable improvement was observed (9). In summary, the tethered adapter technology studied by Niemeyer et al. has generated several interesting and potentially useful nanoscale assemblies containing ordered protein arrays.

We have developed an alternative approach to the construction of ordered protein arrays. This approach is analogous to a later stage in prebiotic evolution after nucleic acid complementarity had allowed metabolosomes to evolve translation. The advent of translation permitted prebiotic systems to produce peptides and proteins that provided additional flexibility to supramolecular aggregates. The flexibility provided by sequence-specific interaction between nucleic acids and proteins is thought to have allowed these supramolecular aggregates to move past the RNA world into the modern molecular biology that forms the current basis of the living state. The bionanotechnology that we have developed for the construction of ordered protein arrays is based on protein–nucleic acid interaction (10,11). The technology's current state suggests that it will permit the construction of programmable devices with a degree of sophistication equal to that of the most advanced prebiotic metabolosomes and perhaps that of small viruses.

## 2. Ordered Assembly of a Three-Address Array

The fundamental principle of ordered assembly of a three-address array is the capacity of DNA methyltransferases to form covalent linkages with DNA in the reaction depicted in **Fig. 1**. This property, coupled with their selectivity for defined nucleic acid sequences, allows DNA methyltransferases to serve as targeting agents for fusion proteins directed to specific sites on a DNA scaffold (11). In what follows, the decoration of a Y-Junction recombination intermediate serves as an example of the methodology employed in ordering proteins using this technology.

### 2.1. Molecular Models

Although not always possible or absolutely necessary, we have found it useful in most cases to prepare at least preliminary molecular models of the assemblies under consideration. In this case (**Fig. 2**), molecular models of the Y-Junction recombination intermediate were constructed in Insight II (Accelrys, San Diego, CA). The DNA builder was used to extend the DNA present in the three-dimensional structure of the M·HhaI protein–DNA complex (12) obtained from the Protein Data Bank (13) with PDB ID:1MTH. The arms were linked at the center to form a model of the Y-Junction having an accurate sequence. Assisted model building with energy refinement molecular force field (14) was used to minimize the structure while constraining the DNA and protein struc-

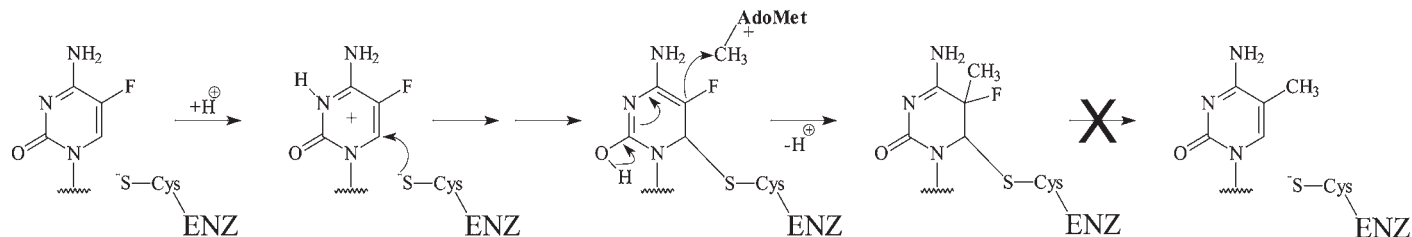


Fig. 1. DNA methyltransferase mechanism of action. Methyltransferases make a nucleophilic attack on C6 of cytosine or 5-fluorocytosine. This breaks the 5-6 double bond in the ring and activates C5 for methyltransfer. After the methyl group is transferred from *S*-adenosyl-[L]-methionine (AdoMet) to C5 of cytosine, the hydrogen at C5 and the enzyme nucleophile at C6 are removed by  $\beta$ -elimination. When fluorine is present at C5, this cannot occur because of the strength of the fluorine-carbon bond. Thus, the progress of the reaction is blocked, leaving a covalent linkage between the enzyme and the cytosine ring targeted by the enzyme. In the case of *M•EcoRII*, it is the second cytosine in the CCWGG recognition sequence that is attacked, in which W stands for A or T. *M•HhaI* attacks the first cytosine in the GCGC sequence, and human Dnmt1 (hDnmt1) attacks the cytosine in the CG dinucleotide.

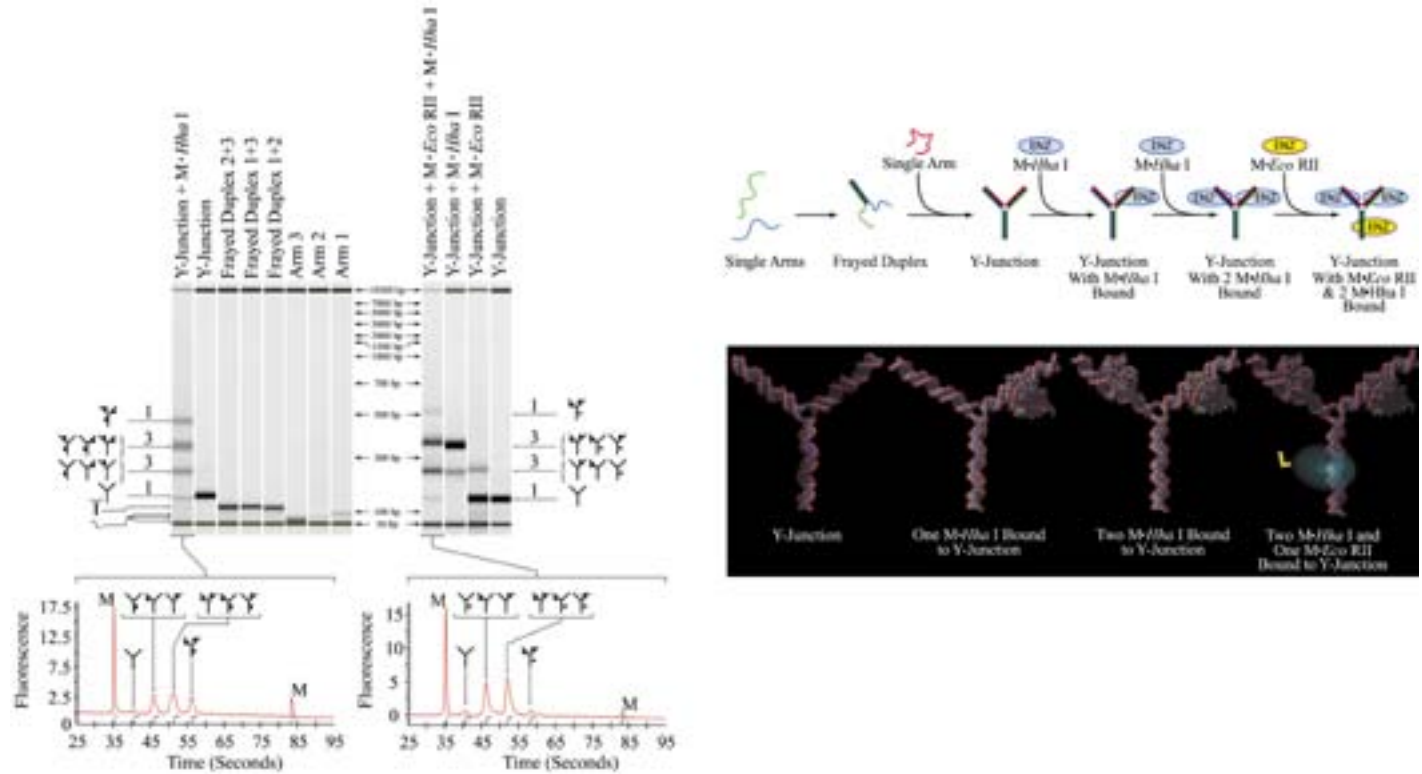


Fig. 2. Assembly of a three-address nucleoprotein array. A schematic of the final assembly process for the machine is depicted in the upper right. The black panel in the lower right depicts molecular models of the predicted intermediates in the assembly of the three-address array once the duplex Y-Junction itself is formed. In the last frame of the molecular model panel, NLS-M•EcoRII is depicted as an ovoid with a crooked appendage depicting the NLS peptide. (Figure 2 caption continued on next page.)

tures in the arms beyond the 10 bp at the center of the junction. The energies of the resulting structures were minimized with respect to molecular mechanics until the RMS force was  $<0.1$  (kcal/mol)/Å. Following molecular mechanics, each structure was further minimized with 1000 steps of simple dynamics. We did not attempt to prepare a molecular model of the nuclear localization signal (NLS)-M•EcoRII fusion protein because a crystal structure for M•EcoRII was not available. Current information on this protein (15) suggested that a 30-bp arm on the Y-Junction could accommodate the fusion protein in the environment created by the linking of M•HhaI proteins to the adjacent arms of the Y-Junction.

## 2.2. Preparation of Oligodeoxynucleotide

5-Fluorodeoxycytidine was introduced as the TMP-F-dU-CE convertible phosphoramidite (Glen Research, Sterling, VA). All other bases were introduced with standard phosphoramidite chemistry. Concentrations were measured by absorbance spectroscopy at 260 nm. Duplexes and Y-Junctions were formed by mixing equimolar amounts of oligodeoxynucleotides in 10 mM Tris-HCl (pH 7.2), 1 mM EDTA, and 100 mM NaCl, so as to give a final concentration of 6  $\mu$ M. Annealing was carried out at 95°C for 5 min, 50°C for 60 min, room temperature for 10 min, and then put on ice for 10 min. The Y-Junction oligodeoxynucleotide sequences employed in this study were as follows:

---

Fig. 2. (continued from previous page) Mobility shift detection of nucleoprotein complexes was carried out using a newly developed microfluidics chip method (20). This method employs the Bioanalyzer system (Agilent, Palo Alto, CA) and LabChip® microfluidics chips (Caliper Technologies, Mountain View, CA) normally employed in nucleic acid detection and characterization (56,57). DNA 7500, chips designed for the separation of DNA duplexes over the range of 15 to 7500 bp, were used in the analysis. Each of the three single strands migrate at their expected lengths. Frayed duplexes formed by each of the combinations of two strands migrate with an apparent mobility corresponding to about 110-bp duplex markers. The Y-Junction forms readily when all three strands are annealed (rightmost lane in the DNA 500 chip virtual gel panel). It has a mobility corresponding to that of a 150-bp duplex in the 7500 chip. The Y-Junction bound to the fusion protein exhibits a mobility corresponding to that of a 270-bp duplex. When M•HhaI was introduced into the reaction, the expected set of intermediates was observed when three addresses for M•HhaI were present (leftmost lane in the DNA chip virtual gel panel) and inset mobility scan depiction, lower left). Alternatively, when one address for NLS-M•EcoRII and two addresses for M•HhaI were present on the junction, a different set of intermediate forms was observed (right lane of the DNA chip virtual gel panel and the inset mobility scan depiction, lower right).

- |                                                                       |   |
|-----------------------------------------------------------------------|---|
| M                                                                     | F |
| 1. 5'-GCTGGCTATGCCACCAGGTGAGGCTAACTGAGGTAGCACGACCGCGCTACAATCTGGTGA-3' |   |
| M                                                                     | F |
| 2. 5'-TCACCAGATTGTAGCGCGGTCTGCTACCTGGTTCCACCAGATGCGCGTGACCTGTAGTT-3'  |   |
| M                                                                     | F |
| 3. 5'-AACTACAGGTCACGCGCATCTGGTGGAACCCAGTTAGCCTCACCTGGTGGCATAGCCAGC-3' |   |

in which M indicates 5-methyl and F indicates a 5-fluoro moiety on cytosine.

### 2.3. Monitoring Y-Junction Assembly With Microfluidics Chips

In the past, we have used polyacrylamide gel electrophoresis (PAGE) to monitor assembly of DNA scaffolds (*11,16*); however, this methodology is time-consuming and, in general, requires the use of  $^{32}\text{P}$  end labeling. More recently, we have used microfluidics chip systems for this analysis because it is very rapid, requires negligible amounts of sample, and does not require the use of radiolabeled DNA.

The DNA 500 LabChip or the DNA 7500 LabChip can be used for the detection of retardation products. Nine microliters of gel dye mix was added to the appropriate well, and the chip was primed with 0.8 mL of air for 30 s. When the DNA 500 LabChip was employed, 5  $\mu\text{L}$  of the gel dye mix was added to each well, and 1  $\mu\text{L}$  of the 500 chip ladder was added to the ladder well. When the DNA 7500 LabChip was employed, 5  $\mu\text{L}$  of the internal marker mix and 1  $\mu\text{L}$  of the 7500 chip ladder were added to the ladder well. Nine microliters of gel dye mix was then added to each of the two gel reservoir wells. One microliter from each reaction was added to 1 of the 12 sample wells. The chip was then vortexed at 2400 rpm for 1 min. Finally, the chip was placed in an Agilent 2100 Bioanalyzer and processed within 5 min.

A schematic of the steps in the assembly of the Y-Junction is given in **Fig. 2** (first three steps in the upper right panel). Representative results of an analysis of this type are also depicted in **Fig. 2** (leftmost virtual gel, lanes 1–7 right to left).

### 2.4. Cloning and Expression of the NLS-M•EcoRII Fusion

The construction and expression of fusion proteins using recombinant DNA techniques is an essential component of this technology. Each fusion is different and requires an approach tailored to the nature of the targeting methyltransferase and the targeted fusion protein. Expression of the fusion must be followed by at least partial purification. The cloning, expression, and purification of the NLS-M•EcoRII fusion is given as a simple example.

Plasmid pRT103 containing the M•EcoRII-NLS fusion protein was constructed by inserting an NLS cassette at the *Nco*I site in the multipurpose clon-

ing site of pRT103. The full-length M•EcoRII sequence was isolated from a pBR322 clone and ligated into the *Bam*HI site of the multipurpose cloning site in the pRT103 (17). This resulted in an in-frame NLS sequence at the N-terminus of the M•EcoRII, under the control of the plant 35-S CaMV promoter, which is effective in promoting transcription in *Escherichia coli*. The mammalian nuclear localization signal is located at the 5' end of the transcript. The bacterial translation stop signal from CaMV is located 3' to the *Bam*HI site. The plasmid was transfected into *E. coli* GM2163 (New England Biolabs) for continuous expression under the control of the 35-S promoter. Bacteria were grown aerobically in Luria broth until they reached stationary state.

Although this particular fusion was formed using restriction cleavage and ligation, we have also found it both convenient and effective to use polymerase chain reaction (PCR) to amplify fusion proteins and the targeting methyltransferases. High-fidelity polymerases are effective in this application, and the use of PCR permits the introduction of any desired restriction site in the bounding primers, thereby facilitating assembly of plasmid systems for fusion production.

#### 2.4.1. Purification

Purification of the fusion protein was essentially as described previously (18,19). The cells were lysed in a buffer containing 50 mM Tris-HCl (pH 7.8), 10% (v/v) glycerol, 1 mM EDTA, and 750 µg/mL of lysozyme (Sigma, St. Louis, MO). After 30 min at 0°C, the mixture was incubated for 5 min at 20°C. The viscous mixture was sonicated in 15-s bursts, with 1 min of cooling at 0°C between bursts at the microtip maximum setting with a Branson Sonicator (Branson, Danbury, CT). The temperature during sonication was maintained below 15°C. Cellular debris was removed by centrifuging at 5000g for 10 min. The supernatant fluid was then mixed with an equal volume of DEAE Sepharose (Pharmacia, Uppsala, Sweden) that had been equilibrated with a buffer containing 50 mM Tris-HCl (pH 7.8), 10% (v/v) glycerol, 1 mM EDTA, and 150 mM NaCl. After stirring for 30 min, the unbound material was collected by filtration.

The filtrate was then mixed with 0.5 vol of precycled phosphocellulose (P-11; Whatman, Maidstone, UK). After stirring for 30 min, the mixture was filtered and the P-11 cake was resuspended in 2 vol of the same buffer containing 150 mM NaCl. The cake was again collected by filtration and resuspended in 2 vol of the same buffer containing 400 mM NaCl. Elution was carried out by filtration. The filtered fluid (approx 170 mg of protein) was collected and dialyzed to 150 mM NaCl in the elution buffer. The dialyzed material was applied to two tandemly linked 5-mL Cibacron-blue Econo-Pak fast protein liquid chromatography (FPLC) columns (Bio-Rad, Hercules, CA). The column was



washed with 50 mL of the same buffer containing 180 mM salt. Elution was carried out with a step increase in salt concentration to 1.5 M NaCl in the same buffer. Gradients were prepared and protein detection was carried out with a Waters Millennium 32 System (Waters, Milford MA). Active fractions were then concentrated using Centricon-10 concentrators (Amicon, Beverly, MA). Unlike the M•*HhaI* preparation that was essentially homogeneous by PAGE, the M•*EcoRII*-NLS fusion preparation contained approx 15 visible bands on polyacrylamide gels stained with Coomassie blue R250 (Sigma), suggesting that it made up about 20% of the visible protein. M•*HhaI* was purified as previously described (11).

#### 2.4.2. Protein Coupling Conditions

Annealed Y-Junction at concentrations ranging from 0.37 to 1.5  $\mu$ M was exposed to concentrations of M•*HhaI* ranging from 0.81 to 2.43  $\mu$ M in a binding buffer containing 50 mM Tris-HCl (pH 7.8), 10 mM EDTA, 5 mM  $\beta$ -mercaptoethanol, and 80  $\mu$ M AdoMet. The final volume of the reaction was 10  $\mu$ L. The reaction was then incubated for 2.5 h at 37°C.

### 2.5. Monitoring Final Assembly With Microfluidics Chip-Based Protein Mobility Shift

Electrophoretic mobility shift analysis (EMSA) is a well-characterized and widely employed technique for the analysis of protein–DNA interaction and of transcription factor combinatorics. As currently implemented, EMSA generally involves the use of radiolabeled DNA and PAGE. We have noted (20) that this technique could be effectively implemented with microfluidics chips designed for the separation of DNA fragments. To accomplish this, samples were run on a 2100 Bioanalyzer (Agilent) using a DNA 500 LabChip or a DNA 7500 LabChip (Caliper Technologies) according to the manufacturer's instructions. **Figure 2** (right virtual gel panel) depicts the results of monitoring the final assembly obtained by mixing the duplex Y-Junction with a mixture of the NLS-M•*EcoRII* fusion protein and M•*HhaI*. When M•*HhaI* addresses were present on each arm of the Y-Junction, the expected intermediates were observed (Y-Junction + M•*HhaI* I; see left virtual gel and inset scanned panel in **Fig. 2**).

## 3. Applications of Ordered Arrays in Smart Drug Design

The design progression for DNA methyltransferase inhibitors is depicted in **Fig. 3**. Here we see small molecules that must be incorporated into DNA as the first generation of such inhibitors. Single-strand conformers (SSCs) that display the methyltransferase recognition motif and target the enzyme to an inhibitory target are the second-generation inhibitors. Third- and fourth-generation inhibitors can be approached with the bionanotechnology of ordered protein arrays as described in **Subheadings 3.4.** and **3.5.**

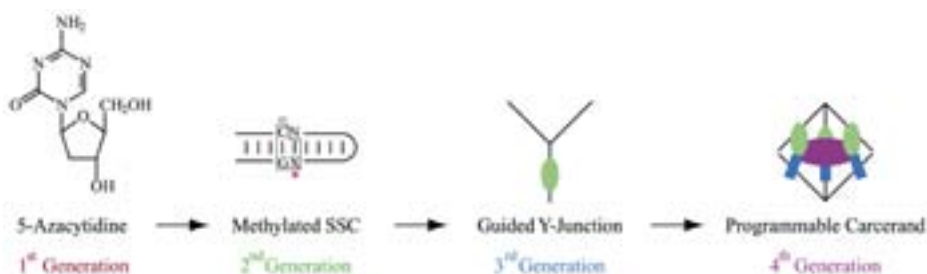


Fig. 3. Schematic of design progression. First-generation inhibitors are small molecules with the capacity to become incorporated in DNA and trap methyltransferases. Second-generation inhibitors are single-strand conformers (SSCs) that carry a methyltransferase trap. In this figure, the three-nucleotide recognition motif characteristic of hDnmt1 is marked with an L-shaped box. The third-generation inhibitors are recombination intermediates with binding sites for methylation activators linked to methyltransferase traps. They are guided to the nucleus of the cell by linked proteins with nuclear localization signals. Fourth-generation inhibitors are self-assembling and programmable hemi carcerands that are capable of sensing their environment and disgoring or exposing an encapsulated or protected entity at a desired cellular or intracellular location.

### 3.1. Tumor Biology of DNA Methyltransferase Inhibition

Although we are only beginning to understand fully the complexities of *selective* gene activation and repression in normal cells, these processes appear to be mediated by targeted recruitment of chromatin remodeling factors coupled with developmentally regulated protein–protein and protein–DNA interaction combinatorics resulting in promoter activation or repression. Once established, tissue-specific patterns of gene silencing appear to be stably maintained by a self-reinforcing network of protein and DNA modifications involving histone methylation, histone hypoacetylation, and cytosine methylation (21). These modifications do not appear to *control* gene silencing in the sense that they do not initiate gene silencing during normal differentiation. However, they are clearly important hallmarks of silenced genes in mammals that are established by cofactors and changes in nucleic acid structure that alter the activity and specificity of methyltransferases and deacetylases (22–26).

What is interesting is the general randomization of gene expression patterns during tumorigenesis resulting from the complex interplay of irreversible genetic damage and natural selection during tumor progression. In addition to the attendant alterations in genome structure associated with this process, alterations in patterns of gene expression are clonally established that result in ectopic gene expression and ectopic gene silencing.

Given that clones of tumor cells that are capable of continued expansion have achieved a degree of adaptation to the local environment during tumorigenesis, it is reasonable to suggest that wholesale disruption of the clonally established patterns of gene expression that they have achieved would at least slow their proliferation. This concept has led to a search for methods by which stable patterns of heterochromatinization can be disrupted. As expected, histone deacetylase inhibitors and DNA (cytosine-5) methyltransferase inhibitors act synergistically (27,28) to destabilize the self-reinforcing modification network in heterochromatin permitting the nonspecific reactivation of silent genes. However, the inhibition of either histone deacetylase or DNA (cytosine-5) methyltransferase is generally sufficient for reactivation. Of these, the DNA methyltransferase inhibitors have received the most attention as potential chemotherapeutic agents (*see refs. 29–31* for reviews).

### 3.2. First-Generation Inhibitors

The current armamentarium of inhibitors for which at least preliminary human trials have been conducted consists of a series of soluble small molecules that act by becoming incorporated into DNA (29–32).

As with most general attacks on the machinery of the cell, key parameters in the efficacy of the approach have been the intrinsic sensitivity of the target tumor, the biodistribution of the inhibitory drugs, and the avoidance of potential side effects (29–32). Among the potential side effects unique to this approach is the real potential for the release of undesirable activities such as multidrug resistance from gene silencing (33).

Although the patient samples are currently very small, significant responses to the DNA methyltransferase inhibitor decitabine (2'deoxy-5-azacytidine) have been seen with acute leukemias. Complete responses in as many as 33% of patients have been reported for relapsed chronic myelogenous leukemia, with 20 to 30% for relapsed acute myelogenous leukemia (34). Responses with solid tumors have been less frequent, with melanoma the highest at 5% for the DNA methyltransferase inhibitor 5,6-dihydro-5-azacytidine (35).

With prostate cancer, although methylation abnormalities have been widely reported in cell lines and clinical specimens, clinical studies with methyltransferase inhibitors are very limited. Nevertheless, decitabine induces cellular differentiation in PC3 and DU145 cell lines (36). Moreover, in a limited patient study, it has been reported that decitabine is well tolerated and gave stable responses in 2 of 12 cases of metastatic D2 prostate cancer (36).

### 3.3. Second-Generation Inhibitors

It is clearly too early to tell whether or not the aforementioned first-generation methyltransferase inhibitors will have chemotherapeutic value alone or in

combination chemotherapy (29,31). Even so, two new directions in the inhibition of methyltransferases are being explored. Both first-generation inhibitors of DNA methyltransferase (32) and second-generation inhibitors of methyltransferase action are under study (37–41). The use of second-generation inhibitors should avoid the side effects produced by the necessity of random incorporation into DNA required for decitabine action because second-generation inhibitors are DNA analogs that act as direct inhibitors of the methyltransferase (38,40,42,43).

Although the second-generation inhibitors do not use ordered protein arrays or bionanotechnology *per se*, they are potential components of the third-generation inhibitors, as described in **Subheading 3.4**. Thus, it is valuable to review their design properties.

### 3.3.1. Electronic Structure Activity Relations-Identified Targets and DNA Methyltransferase Inhibitor Design

Electronic structure activity relations (ESAR) have successfully predicted the effects of the mechanism-based inhibitors FdC (11), dU (44), and 2-pyrimidinone (45) on bacterial enzyme. Thus, it appears to be of general utility in determining the effects that a candidate inhibitor will have on methyltransferase action. An algorithm for analyzing candidate targets is depicted in **Fig. 4**. The results of calculations using the algorithm for a series of known and likely inhibitors of methyltransferases are depicted graphically in **Fig. 5**. In light of the known parameters of the human DNA (cytosine-5)methyltransferase, generally termed Dnmt1, the data indicate that the candidate second-generation inhibitors of the enzyme should have the following characteristics:

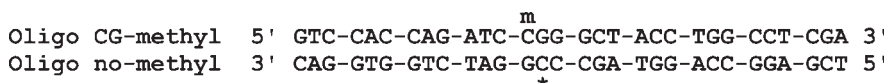
1. They should generally present a duplex region (that may contain mispairs) comprising about 28 bp of duplex in a hairpin formed of a single strand (46,47) or duplex formed from two fully or partially complementary oligodeoxynucleotides (48).
2. The partial duplex should contain nonproductive (44) or weakly productive three-nucleotide motifs (38,48). As defined in the cited references, a three-nucleotide recognition motif consists of a cytosine or preferably a 5-methylcytosine on one strand that is paired with a guanine or an inosine residue that is 3' to the targeted base. In short, this motif defines the targeted base. It is depicted in **Fig. 3** (second-generation panel).
3. These nonproductive motifs should target the enzyme to a nonproductive or base-modified nucleotide in which the reference absolute value of the frontier orbital energy difference (see **Fig. 4**) for nucleophilic attack is  $>0.73797$  eV, or  $>7.39287$  eV for methyltransfer based on the data given in (43).

The hairpin molecules described in **refs. 38, 41, 46, and 49** satisfy these criteria with frontier orbital energy differences for methyl transfer exceeding the requirement in point no. 3 for a normally paired nucleotide analog.

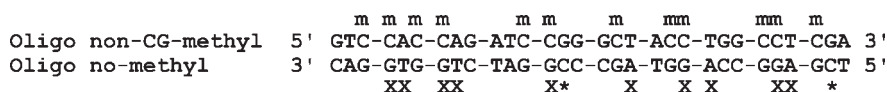
### 3.3.2. Multiply Mistargeted Bases

Saturation curves for a productive substrate ( $^dCS_1$ ) and a multiply mistargeted nonproductive substrate ( $^{Nd}CS_2$ ) are depicted in **Fig. 5**. The sequences are as follows:

1.  $^dCS_1$ : CG-methylated oligo targeting normally paired dC



2.  $^{Nd}CS_2$ : non-CG-methylated oligo targeting normally paired dC, dT, dA, and dG



in which x indicates a mistargeted base, \* indicates an appropriately targeted base, and m indicates a targeting methyl group.

Since previous work with substrate  $^dCS_1$  (**50,51**) has shown that tritium incorporation is confined almost exclusively to the methyl-targeted cytosine (\*), tritium incorporation into substrate  $^{Nd}CS_2$  is likely to be directed to the two productive sites in the substrate or other cytosine residues in the oligodeoxynucleotide. Based on the ESAR, 10 of the 12 targeted sites will produce nonproductive binding of the enzyme to sites targeting dT, dG, or dA where LUMO energies exceed that required for nucleophilic attack. The human enzyme has a footprint in the range of 28 bp (**48**), suggesting that it would generally bind only once to an oligodeoxynucleotide of this type with a probability of 10/12 (0.833) of binding to a nonproductive site. Thus, the low  $V_m$  and low  $K_m$  observed for this substrate strongly suggest that the bulk of the interaction with the substrate is at nonproductively targeted dA, dG, and dT sites. Uniform methylation also raises the  $T_m$  of the oligodeoxynucleotide from 74 to 80°C (data not shown), suggesting that the enzyme may also be able to bind at methylated targeting sites but be slowed by the additional energy required to disrupt the base-stacking interactions as the bases are flipped out of the helix.

Given that the kinetics monitor tritium incorporation into either substrate, the kinetics are described by the reaction scheme given in **Fig. 5A**, left. The general equations describing this reaction (**52**) are as follows:

$$v = (V_{m1}[S_1]/K_{m1} + V_{m2}[S_2]/K_{m2}) / (1 + [S_1]/K_{m1} + [S_2]/K_{m2}) \quad (1)$$

$$K_{m2} = K_{m1}[S_2](v - V_{m2}) / (V_{m1}[S_1] - v([S_1] + K_{m1})) \quad (2)$$

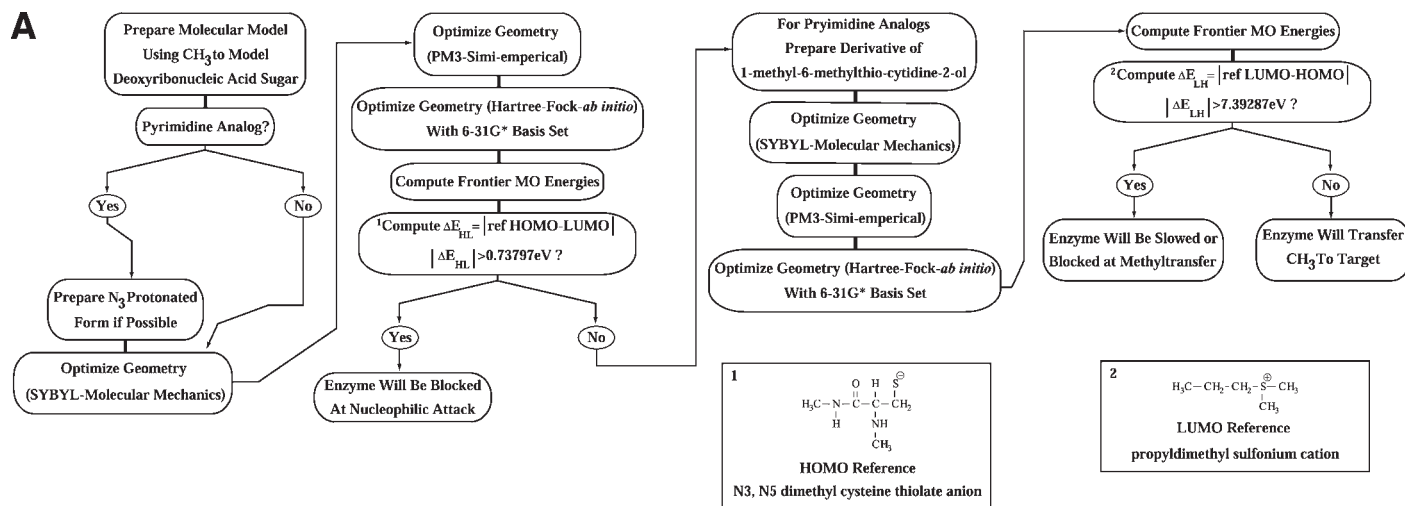


Fig. 4. ESAR for second-generation methyltransferase inhibitors. **(A)** ESAR algorithm for deciding whether nucleophilic attack or methyltransfer will be affected in inhibition. **(B)** Frontier orbital picture comparing models of targets that permit nucleophilic attack at a cytosine model compound (acceptor attacked) with models of targets that do not permit nucleophilic attack (acceptor not attacked): (I) 1-methyl-5-pyrimidinone cation (N3 protonated); (II) 1-methyl-5-fluorocytosine cation (N3 protonated); (III) 1-methyl-5-azacytosine cation (N3 protonated); (IV) 1-methylcytosine cation (N3 protonated); (V) 1-methyl-4-thiouracil; (VI) 1-methyl-3-bromouracil; (VII) 1-methyl-2-pyrimidinone; (VIII) 1-methyl-5-fluorouracil; (IX) 1-methyluracil; (X) 1-methylpseudouracil ( $\psi$ ); (XI) 1-methylthymine; (XII) 1-methyl-5-azacytosine; (XIII) 1-methylcytosine; (XIV) 9-methyl-8-oxoguanine; (XV) 9-methyladenine; (XVI) 9-methylguanine; (XVII) 9-methyl-7-deazaguanine; (XXII) N3, N5 dimethyl cysteine thiolate anion.

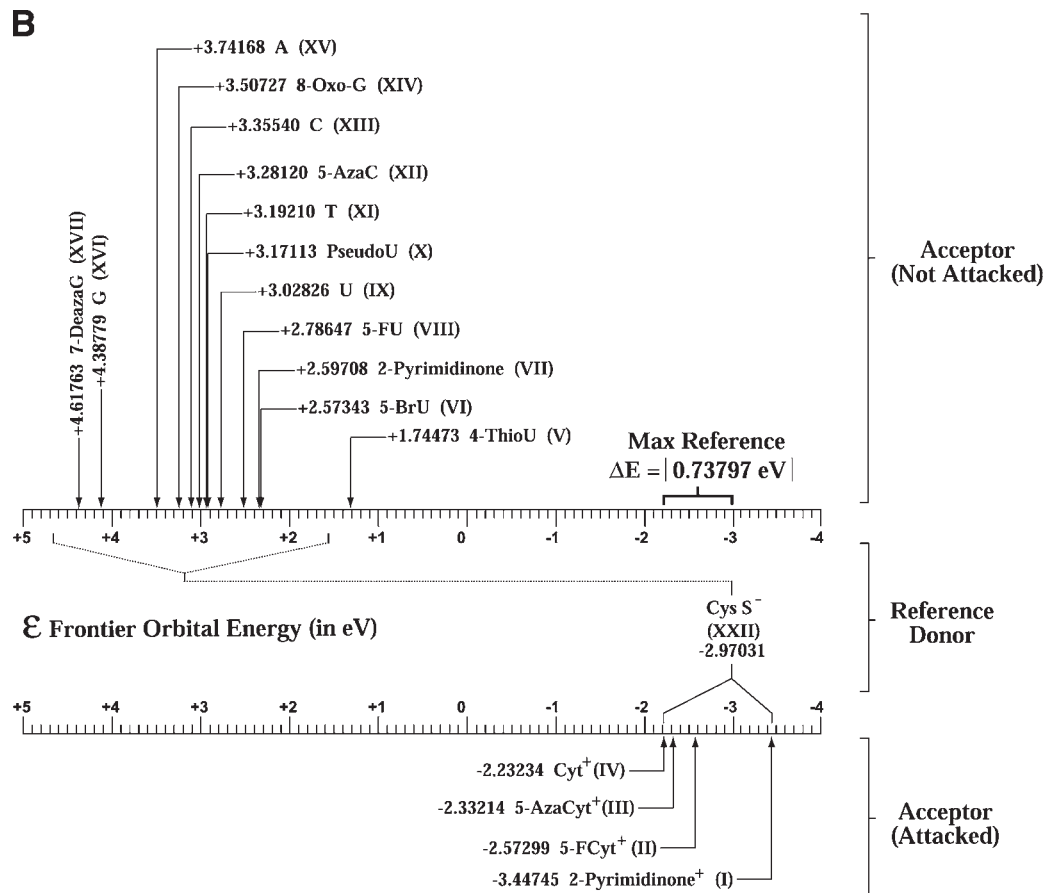


Fig. 4. (continued)



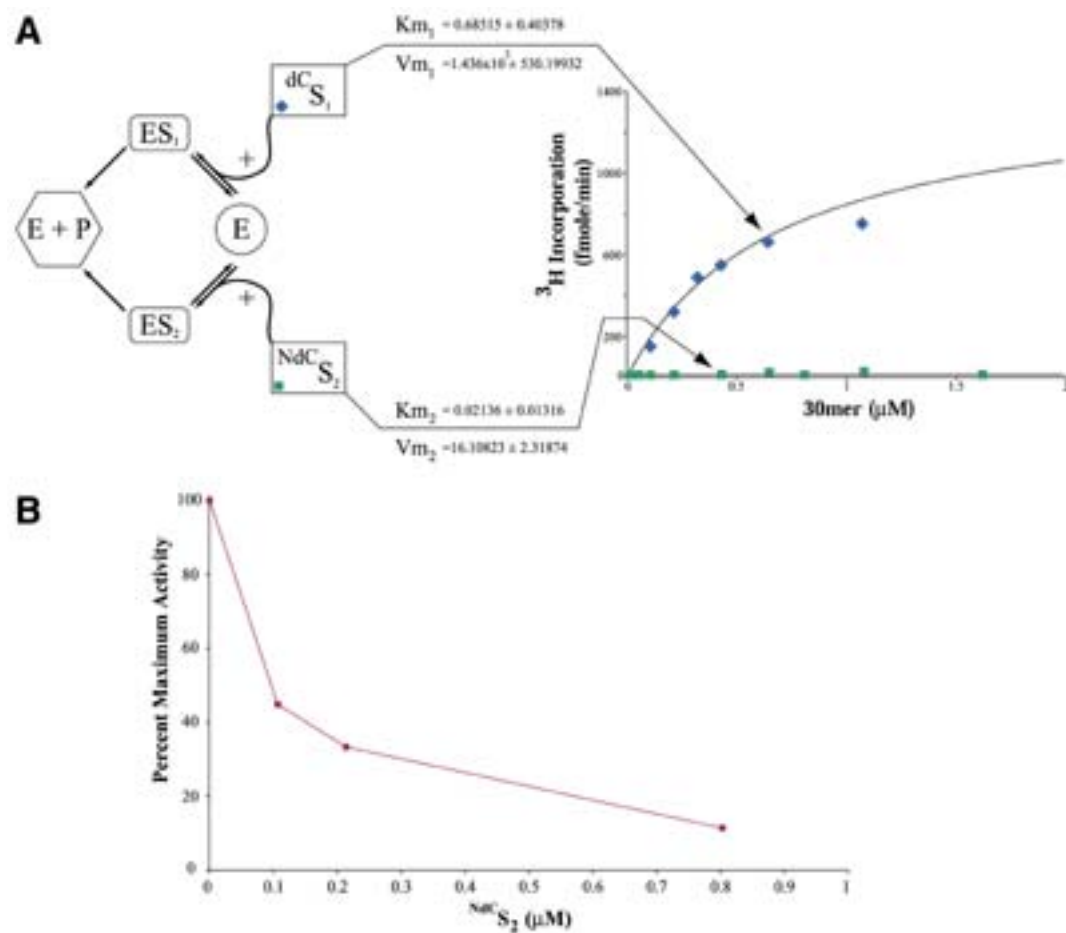


Fig. 5.

### 3.3.3. Singly Mistargeted Mismatched Bases

Although the methyltransferase reaction involves both AdoMet and DNA as substrates, at constant AdoMet concentrations, the DNA saturation kinetics are hyperbolic for either the highly productive or weakly productive substrate. When a constant concentration of the productive substrate is present and varying amounts of the weakly productive substrate are added, inhibition by the weakly productive substrate follows the kinetics predicted for a two-DNA substrate system. In many cases, incorporation into weakly productive competing substrates is very low. This makes it difficult to estimate  $Km_2$  from direct saturation experiments. In these cases, we have found it useful to arrive at an upper limit for  $Vm_2$  and determine an average value for  $Km_2$  from **Eq. 2**.

In general, we have noted that multiply mistargeted second-generation inhibitors are more potent than singly mistargeted inhibitors based on side-by-side comparisons. An inhibition curve for the multiply mistargeted inhibitor  $^{Nd}CS_2$  is provided in **Fig. 5B**.

### 3.4. Third-Generation Inhibitors

One form of third-generation inhibitors under study comprises recombination intermediates with binding sites for methylation activators that are linked to methyltransferase traps like those found in second-generation inhibitors. These inhibitors are to be guided to the nucleus of the cell by linked proteins with nuclear localization signals, as shown schematically in **Fig. 6**. The design parameters of such an inhibitor are given in **Fig. 7**. To construct this machine, the NLS-M•EcoRII fusion was cloned and the fusion protein was purified as described in **Subheading 2.4**. Final assembly was monitored by mobility shift analysis using a Bioanalyzer 2100 and DNA analysis microfluidics chips. As can be seen in **Fig. 2**, each step in the final assembly process could be monitored by the appearance of the expected intermediate in the microfluidics analysis. The data clearly show that methyltransferase-directed nucleoprotein

---

**Fig. 5.** (*previous page*) Nucleic acid-based inhibitor action. **(A)** Saturation plots for hemimethylated DNA and non-CG methylated DNA. Although each substrate carries methyl groups at cytosines on only one strand, the hemimethylated substrate ( $^{d}CS_1$ ) targets hDnmt1 to a single cytosine residue. The second substrate ( $^{Nd}CS_2$ ) mistargets the enzyme to dG, dA, and dT residues as well. Based on the two-substrate reaction scheme on the right, increasing the concentration of ( $^{Nd}CS_2$ ) at a constant concentration of ( $^{d}CS_1$ ) is expected to inhibit the enzyme. **(B)** Inhibition of human DNA methyltransferase by singly and multiply mistargeted substrate analogs. The active substrate ( $^{d}CS_1$ ) gives rapid incorporation of  $^3H$ -methyl groups from AdoMet into DNA (normalized to 100% activity). This ongoing reaction was inhibited by increasing the amounts of a second substrate,  $^{Nd}CS_2$ .

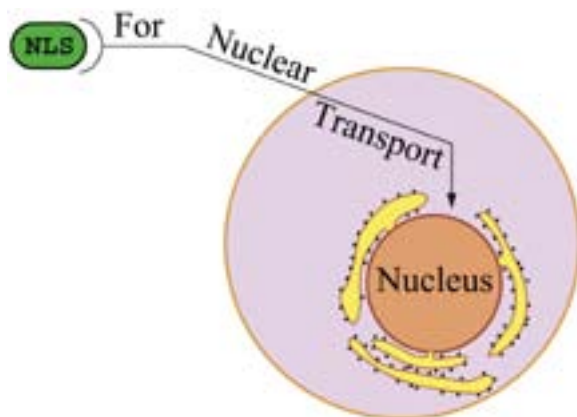


Fig. 6. Schematic of effect of NLS in directing protein transport to the nucleus.

assembly can be used to produce a machine for inhibition of human DNA methyltransferase based on a bionanotechnological design (*see* **Fig. 2**, Y-Junction + M•*Eco*RII lane). The design is now being tested for its efficacy in the inhibition of hDnmt1 *in vitro* and *in vivo*.

More sophisticated designs based on arrayed protein signals or binding sites are possible. Designs of this type, however, would require four-arm or X-Junctions in order to accommodate the arrayed functions. A detailed discussion of these designs is beyond the scope of this chapter.

### 3.5. Fourth-Generation Inhibitors

Fourth-generation inhibitors are analogous to the small-molecule carcerands first studied by Warmuth and Yoon (**53**). These self-assembling and programmable macromolecular hemi carcerands (**54**) would be capable of sensing their environment and disgorging or uncoating an encapsulated or hidden entity at a desired cellular or intracellular location. A representative design is given in **Fig. 8**. The value of using an ordered protein array in a design of this type is the availability of DNA-binding proteins that bind to DNA or release only in the presence of a small-molecule ligand. Many proteins of this type are known, and it will be possible to engineer responses to desired ligands that will cause the hemi carcerand to disassemble in the presence of high local concentrations of the ligand. Disassembly could be used to release a macromolecule or expose the internal surface of the structure so as to attack or modify certain cellular systems localized in the region of high ligand concentration.

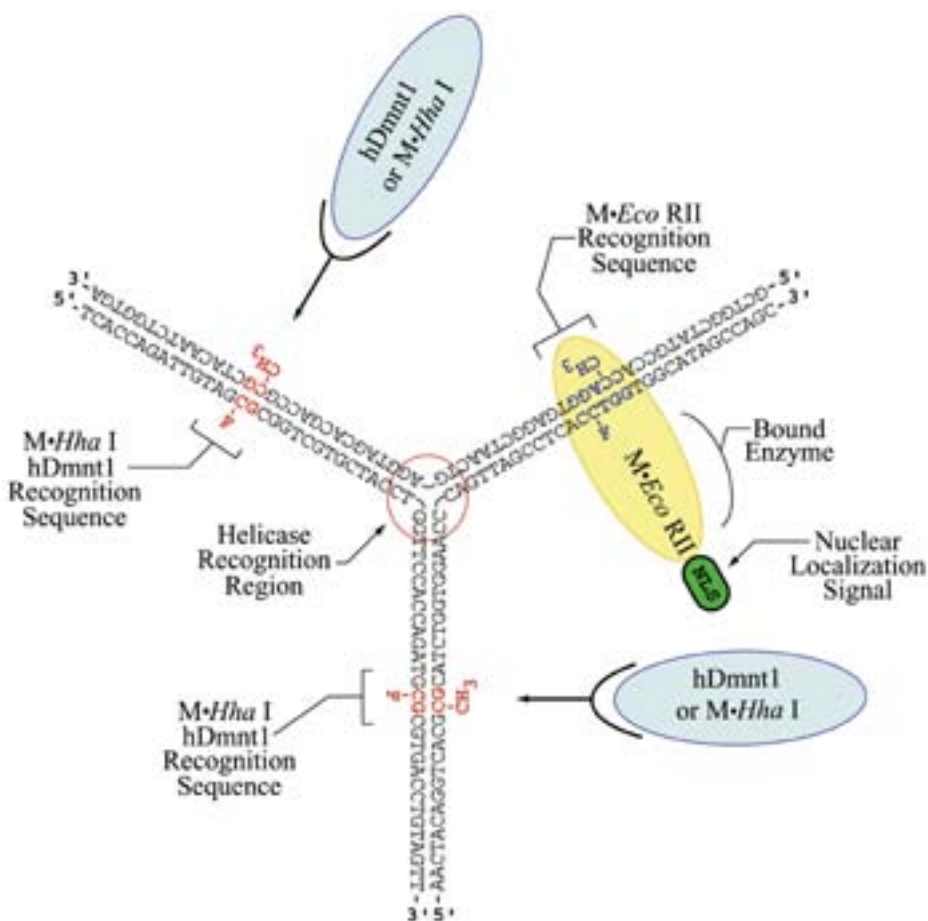


Fig. 7. Bionanotechnological machine for inhibition of human DNA methyltransferase: a guided Y-Junction. This machine comprises a Y-Junction protein array scaffold that can act as a recombination intermediate so as to activate further the already activated methyltransferase targeting sites (hDnmt1 recognition sequence). The device also has the potential to attract helicases (helicase recognition region). The arms of the Y-Junction carrying the human recognition sequences are each 30 bp long. Thus, they each present an adequate kinetic footprint for the hDnmt1 at each of the dual trapping regions of the inhibitor. The entire system is stabilized by the presence of a trapped bacterial methyltransferase (M•EcoRII) carrying an NLS that is designed to link the machine to the cellular nuclear transport system so as to place it effectively in the cell nucleus where the bulk of hDnmt1 acts.



Fig. 8. Self-assembling trigonal dipyramid as a macromolecular carcerand. A methyltransferase-targeted DNA-binding protein is used to decorate a Y-Junction so as to place the fusion proteins on the same face of the helix in each arm of the Y-Junction. The targeted Y-Junction contains binding sites for the DNA-binding protein on each of its arms. Mixing the two components should result in a closed structure with the edge topology of a trigonal dipyramid (Johnson Solid). The resulting lumen could be used to house a macromolecule, or to hide an inhibitory nucleic acid surface. Disassembly of the structure (not shown) would occur if a ligand-sensitive DNA-binding protein were used as the fusion protein of choice to produce a hemi carcerand. Depending on the choice of fusion, the hemi carcerand would disassemble in a region of low or high ligand concentration because DNA binding or release by the fusion would be induced by changes in ligand concentration.

#### 4. Conclusion

Ordered protein arrays provide a facile approach to a variety of problems in biology and nanoscience. Current demonstration systems use either nucleic acid tethers (55) or methyltransferase fusions (54) in protein targeting to nucleic acid scaffolds. These systems are now capable of imitating the earliest forms of prebiotic organisms and can be expected to reach the complexity of a small virus in the near future. The use of microfluidics chips in assessing final assembly of these designs (20) should facilitate their construction and testing. The number of assemblies that can be contemplated is quite large, ranging from tethered enzyme couples (9) to the smart chemotherapeutic agents described here. Thus, one can anticipate that a large number of interesting and complex array-based assemblies and devices will appear in the near future.

## References

1. Yun, C. S., Khitrov, G. A., Vergona, D. E., Reich, N. O., and Strouse, G. F. (2002) Enzymatic manipulation of DNA-nanomaterial constructs. *J. Am. Chem. Soc.* **124**, 7644, 7645.
2. Seeman, N. C. (1991) Construction of three-dimensional stick figures from branched DNA. *DNA Cell. Biol.* **10**, 475–486.
3. Gil, A., de Pablo, P. J., Colchero, J., Gómez-Herrero, J., and Baró, A. M. (2002) Electrostatic scanning force microscopy images of long molecules: single-walled carbon nanotubes and DNA. *Nanotechnology* **13**, 309–313.
4. Yurke, B., Turberfield, A. J., Mills, A. P. Jr., Simmel, F. C., and Neumann, J. L. (2000) A DNA-fuelled molecular machine made of DNA. *Nature* **406**, 605–608.
5. Gibson, T. J. and Lamond, A. I. (1990) Metabolic complexity in the RNA world and implications for the origin of protein synthesis. *J. Mol. Evol.* **30**, 7–15.
6. Woese, C. R. (2002) On the evolution of cells. *Proc. Natl. Acad. Sci. USA* **99**, 8742–8747.
7. Niemeyer, C. M., Adler, M., Gao, S., and Chi, L. (2000) Supramolecular nanocircles consisting of streptavidin and DNA. *Angew. Chem. Int. Ed. Engl.* **39**, 3055–3059.
8. Niemeyer, C. M., Sano, T., Smith, C. L., and Cantor, C. R. (1994) Oligonucleotide-directed self-assembly of proteins: semisynthetic DNA—streptavidin hybrid molecules as connectors for the generation of macroscopic arrays and the construction of supramolecular bioconjugates. *Nucleic Acids Res.* **22**, 5530–5539.
9. Niemeyer, C. M., Koehler, J., and Wuerdemann, C. (2002) DNA-directed assembly of bienzymic complexes from in vivo biotinylated NAD(P)H:FMN oxidoreductase and luciferase. *Chembiochem.* **3**, 242–245.
10. Smith, S. S. (1995) Nucleoprotein-based nanoscale fabrication. *Biol. Biomed. Sci. Technol. Div.* Office of Naval Research (ONR) 34196-3, 161, 162.
11. Smith, S. S., Niu, L., Baker, D. J., Wendel, J. A., Kane, S. E., and Joy, D. S. (1997) Nucleoprotein-based nanoscale assembly. *Proc. Natl. Acad. Sci. USA* **94**, 2162–2167.
12. Klimasauskas, S., Kumar, S., Roberts, R. J., and Cheng, X. (1994) HhaI methyltransferase flips its target base out of the DNA helix. *Cell* **76**, 357–369.
13. Berman, H. M., Westbrook, J., Feng, Z., Gilliland, G., Bhat, T. N., Weissig, H., Shindyalov, I. N., and Bourne, P. E. (2000) The protein data bank. *Nucleic Acids Res.* **28**, 235–242.
14. Ponder, J. W. and Case, D. A. (2003) Force fields for protein simulations. *Adv. Protein Chem.* **66**, 27–85.
15. Schroeder, S. G. and Samudzi, C. T. (1997) Structural studies of EcoRII methylase: exploring similarities among methylases. *Protein Eng.* **10**, 1385–1393.
16. Smith, S. S. (2001) A self-assembling nanoscale camshaft: implications for nanoscale materials and devices constructed from proteins and nucleic acids. *Nano Lett.* **1**, 51–56.
17. Topfer, R., Matzeit, V., Gronenborn, B., Schell, J., and Steinbiss, H. H. (1987) A set of plant expression vectors for transcriptional and translational fusions. *Nucleic Acids Res.* **15**, 5890.

18. Kosykh, V. G., Solonin, A. S., Buryanov Y. I., and Bayev, A. A. (1981) Overproduction of the EcoRII endonuclease and methylase by *Escherichia coli* strains carrying recombinant plasmids constructed in vitro. *Biochim. Biophys. Acta* **655**, 102–106.
19. Buryanov, Y. I., Bogdarina, I. G., and Bayev, A. A. (1978) Site specificity and chromatographic properties of *E. coli* K12 and EcoRII DNA-cytosine methylases. *FEBS Lett.* **88**, 251–254.
20. Clark, J., Shevchuk, T., Swiderski, P. M., Dabur, R., Crocitto, L. E., Buryanov, Y. I., and Smith, S. S. (2003) Mobility-shift analysis with microfluidics chips. *Biotechniques* **35**, 548–554.
21. Richards, E. J. and Elgin, S. C. (2002). Epigenetic codes for heterochromatin formation and silencing: rounding up the usual suspects. *Cell* **108**, 489–500.
22. Smith, S. S. and Crocitto, L. (1999) DNA methylation in eukaryotic chromosome stability revisited: DNA methyltransferase in the management of DNA conformation space. *Mol. Carcinog.* **26**, 1–9.
23. Smith, S. S. (2000) Gilbert's conjecture: the search for DNA (cytosine-5) demethylases and the emergence of new functions for eukaryotic DNA (cytosine-5) methyltransferases. *J. Mol. Biol.* **302**, 1–7.
24. Baylin, S. and Bestor, T. H. (2002) Altered methylation patterns in cancer cell genomes: cause or consequence? *Cancer Cell* **1**, 299–305.
25. Smith, S. S. (1994) Biological implications of the mechanism of action of human DNA (cytosine-5)methyltransferase. *Prog. Nucleic Acid Res. Mol. Biol.* **49**, 65–111.
26. Smith, S. S., Laayoun, A., Lingeman, R. G., Baker, D. J., and Riley, J. (1994) Hypermethylation of telomere-like foldbacks at codon 12 of the human c-Ha-ras gene and the trinucleotide repeat of the FMR-1 gene of fragile X. *J. Mol. Biol.* **243**, 143–151.
27. Chiurazzi, P., Pomponi, M. G., Pietrobono, R., Bakker, C. E., Neri, G., and Oostra, B. A. (1999) Synergistic effect of histone hyperacetylation and DNA demethylation in the reactivation of the FMR1 gene. *Hum. Mol. Genet.* **8**, 2317–2323.
28. Cameron, E. E., Bachman, K. E., Myohanen, S., Herman, J. G., and Baylin, S. B. (1999) Synergy of demethylation and histone deacetylase inhibition in the re-expression of genes silenced in cancer. *Nat. Genet.* **21**, 103–107.
29. Goffin, J. and Eisenhauer, E. (2002) DNA methyltransferase inhibitors: state of the art. *Ann. Oncol.* **13**, 1699–1716.
30. Brown, R. and Strathdee, G. (2002) Epigenetic cancer therapies: DNA methyltransferase inhibitors. *Expert Opin. Investig. Drugs* **11**, 747–754.
31. Christman, J. K. (2002) 5-Azacytidine and 5-aza-2'-deoxycytidine as inhibitors of DNA methylation: mechanistic studies and their implications for cancer therapy. *Oncogene* **21**, 5483–5495.
32. Stewart, D. J., Donehower, R. C., Eisenhauer, E. A., Wainman, N., Shah, A. K., Bonfils, C., MacLeod, A. R., Besterman, J. M., and Reid, G. K. (2003) A phase I pharmacokinetic and pharmacodynamic study of the DNA methyltransferase 1 inhibitor MG98 administered twice weekly. *Ann. Oncol.* **14**, 766–774.



33. El-Osta, A. (2003) On the use of DNA methylation inhibitors and the reversal of transcriptional silencing. *Blood* **101**, 1656; author reply 1657, 1658.
34. Momparler, R. L., Rivard, G. E., and Gyger, M. (1985) Clinical trial on 5-aza-2'-deoxycytidine in patients with acute leukemia. *Pharmacol. Ther.* **30**, 277–286.
35. Creagan, E. T., Schaid, D. J., Hartmann, L. C., and Loprinzi, C. L. (1993) A phase II study of 5,6-dihydro-5-azacytidine hydrochloride in disseminated malignant melanoma. *Am. J. Clin. Oncol.* **16**, 243, 244.
36. Thibault, A., Figg, W. D., Bergan, R. C., Lush, R. M., Myers, C. E., Tompkins, A., Reed, E., and Samid, D. (1998) A phase II study of 5-aza-2'-deoxycytidine (decitabine) in hormone independent metastatic (D2) prostate cancer. *Tumori* **84**, 87–89.
37. Smith, S. S., Lingeman, R. G., and Kaplan, B. E. (1992) Recognition of foldback DNA by the human DNA (cytosine-5)-methyltransferase. *Biochemistry* **31**, 850–854.
38. Smith, S. S., Kaplan, B. E., Sowers, L. C., and Newman, E. M. (1992) Mechanism of human methyl-directed DNA methyltransferase and the fidelity of cytosine methylation. *Proc. Natl. Acad. Sci. USA* **89**, 4744–4748.
39. Knox, J. D., Araujo, F. D., Bigey, P., Slack, A. D., Price, G. B., Zannis-Hadjopoulos, M., and Szyf, M. (2000) Inhibition of DNA methyltransferase inhibits DNA replication. *J. Biol. Chem.* **275**, 17,986–17,990.
40. Bigey, P., Knox, J. D., Croteau, S., Bhattacharya, S. K., Theberge, J., and Szyf, M. (1999) Modified oligonucleotides as bona fide antagonists of proteins interacting with DNA: hairpin antagonists of the human DNA methyltransferase. *J. Biol. Chem.* **274**, 4594–4606.
41. Smith, S. S. and Kaplan, B. E. (1996) Mechanism-based inhibitors of DNA methyltransferase. US patent 5,503,975.
42. Kho, M. R., Baker, D. J., Laayoun, A., and Smith, S. S. (1998) Stalling of human DNA (cytosine-5) methyltransferase at single-strand conformers from a site of dynamic mutation. *J. Mol. Biol.* **275**, 67–79.
43. Clark, J., Shevchuk, T., Kho, M. R., and Smith, S. S. (2003) Methods for the design and analysis of oligodeoxynucleotide-based DNA (cytosine-5)methyltransferase inhibitors. *Anal. Biochem.* **321**, 50–64.
44. Wendel, J. A. and Smith, S. S. (1998) Uracil as an alternative to 5-fluorocytosine in addressable protein targeting. *Nanotechnology* **9**, 297–304.
45. Zhou, L., Cheng, X., Connolly, B. A., Dickman, M. J., Hurd, P. J., and Hornby, D. P. (2002) Zebularine: a novel DNA methylation inhibitor that forms a covalent complex with DNA methyltransferases. *J. Mol. Biol.* **321**, 591–599.
46. Smith, S. S., Lingeman, R. G., and Kaplan, B. E. (1992) Recognition of foldback DNA by the human DNA (cytosine-5)-methyltransferase. *Biochemistry* **31**, 850–854.
47. Christman, J. K., Sheikhejad, G., Marasco, C. J., and Sufrin, J. R. (1995) 5-Methyl-2'-deoxycytidine in single-stranded DNA can act in cis to signal de novo DNA methylation. *Proc. Natl. Acad. Sci. USA* **92**, 7347–7351.
48. Laayoun, A. and Smith, S. S. (1995) Methylation of slipped duplexes, snapbacks and cruciforms by human DNA(cytosine-5)methyltransferase. *Nucleic Acids Res.* **23**, 1584–1589.

49. Szyf, M. (1998) Targeting DNA methyltransferase in cancer. *Cancer Metastasis Rev.* **17**, 219–231.
50. Smith, S. S., Hardy, T. A., and Baker, D. J. (1987) Human DNA (cytosine-5)methyltransferase selectively methylates duplex DNA containing mispairs. *Nucleic Acids Res.* **15**, 6899–6916.
51. Smith, S. S., Kan, J. L., Baker, D. J., Kaplan, B. E., and Dembek, P. (1991) Recognition of unusual DNA structures by human DNA (cytosine-5)methyltransferase. *J. Mol. Biol.* **217**, 39–51.
52. Chaplin, M. F. and Bucke, C. (1990) *Enzyme Technology*, University Press, Cambridge.
53. Warmuth, R. and Yoon, J. (2001) Recent highlights in hemicarcerand chemistry. *Acc. Chem. Res.* **34**, 95–105.
54. Smith, S. S. (2002) Designs for the self-assembly of open and closed macromolecular structures and a molecular switch using DNA methyltransferase to order proteins on nucleic acid scaffolds. *Nanotechnology* **13**, 413–419.
55. Niemeyer, C. M. (2000) Self-assembled nanostructures based on DNA: towards the development of nanobiotechnology. *Curr. Opin. Cell Biol.* **4**, 609–618.
56. Fuller, R. A., Clark, J., Kretzner, L., Korn, D., Blair, S. L., Crocitto, L. E., and Smith, S. S. (2003) Use of microfluidics chips for the detection of human telomerase RNA. *Anal. Biochem.* **313**, 331–334.
57. Nachamkin, I., Panaro, N. J., Li, M., Ung, H., Yuen, P. K., Kricka, L. J., and Wilding, P. (2001) Agilent 2100 bioanalyzer for restriction fragment length polymorphism analysis of the *Campylobacter jejuni* flagellin gene. *J. Clin. Microbiol.* **39**, 754–757.

## Bioengineering and Characterization of DNA–Protein Assemblies Floating on Supported Membranes

Wilfrid Boireau, Anthony C. Duncan, and Denis Pompon

### Summary

This chapter describes the design, practical construction, and characterization of P-DNA and their applications in building a new generation of DNA chips. P-DNAs are artificial covalent assemblies involving a histidine tag head able to bind to modified phospholipids, a core protein domain derived from cytochrome b5 by genetic engineering that features specific spectroscopic and electrochemical properties useful for detection, a synthetic linker acting as a spacer, and an oligonucleotide acting as a probe. P-DNA has the property of being able to efficiently self-associate to a supported bilayer including nickel-iminodiacetate-modified phospholipids. The construction of P-DNA and its interaction with a complementary oligonucleotide sequence can be monitored in real time by surface plasmon resonance using a Biacore system or equivalent. P-DNA chips feature unique properties including tunable surface density of probes; very low nonspecific interaction with external DNA; lateral mobility, minimizing steric interaction; optimization of hybridization efficiency; and, potentially, recognition by multiple probes of a single target and perfectly defined and homogeneous structure, permitting high density up to a compact monolayer. Potential applications of this new device are multiple, including high-sensitivity and high-selectivity chips for DNA–DNA, DNA–RNA, or DNA–protein interactions.

**Key Words:** DNA chip; supramolecular assemblies; surface plasmon resonance; artificial protein-DNA structure; supported membrane; lateral mobility; cytochrome; dynamic.

### 1. Introduction

Designing artificial supramolecular assemblies containing both protein and nucleic acid is still a challenge. Few models in the literature deal with this kind of molecular construction in order to develop DNA or bioelectronic devices. Most DNA chip sensors are designed using poorly controlled adsorption or

From: *Methods in Molecular Biology*, vol. 300:  
*Protein Nanotechnology, Protocols, Instrumentation, and Applications*  
Edited by: T. Vo-Dinh © Humana Press Inc., Totowa, NJ

covalent attachment of the probes, which leads to uncontrolled pattern and geometry, severely limiting applications. A critical aspect for bioinorganic devices is the contact of the inorganic template (or substrate) with the biological components. Strong interaction of biomolecules with the support yields a random immobilization that impairs self-organization. Biomolecular structures by themselves are frequently denatured on interaction with the support, leading to loss of function.

To isolate inorganic support from biomolecules, several types of support functionalization have been evaluated, including supported lipid bilayers that mimic natural membranes. Most of the common substrates can be covered with a supported membrane resulting from vesicular spreading or Langmuir-Blodgett layer deposition. Such a bilayer has several advantages: (1) it acts as a cushion isolating and protecting the metallic or inorganic support, (2) it constitutes a biomimetic environment limiting nonspecific adsorption and denaturation of biomolecules, and (3) it can be easily functionalized to allow specific attachment of biomolecules through a floating artificial anchor attached on one side to the bilayer by hydrophobic interactions and on the opposite side to the biomolecule by a specifically engineered link. This interfacing confers unique properties such as lateral mobility of biomolecules that are maintained close to the surface by the anchor while not interacting directly with the support.

This chapter describes an original molecular device associating protein and nucleic acid components with a supported membrane interface to set up highly ordered nanostructures of interest for biosensors. This molecular Lego is composed of two parts: a supramolecular assembly composed of a modified oligonucleotide covalently linked to a genetically modified protein via a homobifunctional linker, and a supported bilayer including functionalized phospholipids that can specifically capture the previous assembly. Unique properties of this device result both from the lateral mobility permitted by the floating structure that allows in turn some easy bidimensional structural reorganization and from the specific properties of the embedded recombinant protein that was designed to give the device additional optical and electronic properties of critical interest for biosensors. This chapter also describes how such assembly can be implemented to set up conformation-sensitive devices with potential application in the detection of the interaction of a single molecule or in the detection of geometric transition in nucleic acids in response to interacting proteins or ligands.

## 2. Materials

Dimyristoyl phosphatidyl choline (DMPC), dioleoyl phosphatidyl choline (DOPC), and octyl glucoside were purchased from Sigma (St. Louis, MO).

1,2-Dioleoyl-*sn*-glycero-3[(*N*(5-amino-1-carboxypentyl)] iminodiacetic acid succinyl (DOGS) was purchased from Aventi Polar Lipids. Cis-[PtCl<sub>2</sub>(NH<sub>3</sub>)<sub>2</sub>] was kindly provided by Johnson Matthey (London, UK). 1,4-Di-[3'-(2'-pyridyldithio)propionamido]-butane (DPDPB) was provided by Pierce (Rockford, IL). DPDPB is insoluble in aqueous buffers and was first dissolved in dimethyl sulfoxide (DMSO) (20 mM) before dilution. Oligonucleotides were provided by Eurogentec.

Surface plasmon resonance (SPR) experiments were run on BIAcore X and 3000 (BIAcore, Uppsala, Sweden) at 25°C, with a flow rate of 2–50 µL/min, in 50 mM sodium phosphate solution (pH 7.5) (buffer P1). Sensor chip HPA precoated with octadecylmercaptan (OM) was purchased from BIAcore or prepared from a standard J1 chip or SIA kit as follows: a 1 mM solution of OM in an ethanol/water solution (4:1 [v/v]) was sonicated for 20 min using a Transsonic 310 at maximum power. J1 sensor chips were treated overnight and rinsed with ultrapure ethanol and water prior to drying under nitrogen.

Single-stranded DNA (ssDNA) (5'-CTATCATTTGCTTACTATTC-3') and the complementary oligonucleotide were provided by Eurogentec. DPDPB is insoluble in aqueous buffers and was first dissolved in a stock solution of DMSO (20 mM). The concentration of DPDPB can be calculated by spectroscopy using  $A_{237\text{ nm}} = 1.2 \times 10^4 \text{ M}^{-1} \text{ cm}^{-1}$  and  $A_{287\text{ nm}} = 8.8 \times 10^3 \text{ M}^{-1} \text{ cm}^{-1}$ . Its functionality was monitored directly or by the absorbance ( $A_{344\text{ nm}} = 8.08 \times 10^3 \text{ M}^{-1} \text{ cm}^{-1}$ ) of pyridine-2-thione released on reduction. A mixture of modified ssDNA and cytochrome b5 with DPDPB must contain <10% (v/v) DMSO in buffer solution.

### 3. Methods

#### 3.1. Protocols and Instrumentation

##### 3.1.1. Molecular Engineering of Cytochrome b5

Cytochrome b5 is an electron carrier protein encompassing an iron protoporphyrin IX as a redox cofactor. This protein is naturally anchored onto the endoplasmic reticulum membrane of cells through a C-terminal hydrophobic amino acid sequence (**Fig. 1**). The globular redox domain is hydrophilic and does not interact with membranes. This domain features a high absorbancy at 413 nm for the oxidized form that shifts to 423 nm on reduction. An engineered protein (Hb5-[His]<sub>4</sub>) was derived from human microsomal cytochrome b5 by genetic engineering resulting in the substitution of the 26 C-terminal amino acid residues by the –NGHHHH–COOH sequence. This engineered protein was soluble and presented a C-terminal histidine tag that can coordinate a nickel-iminodiacetate-ended synthetic linker.

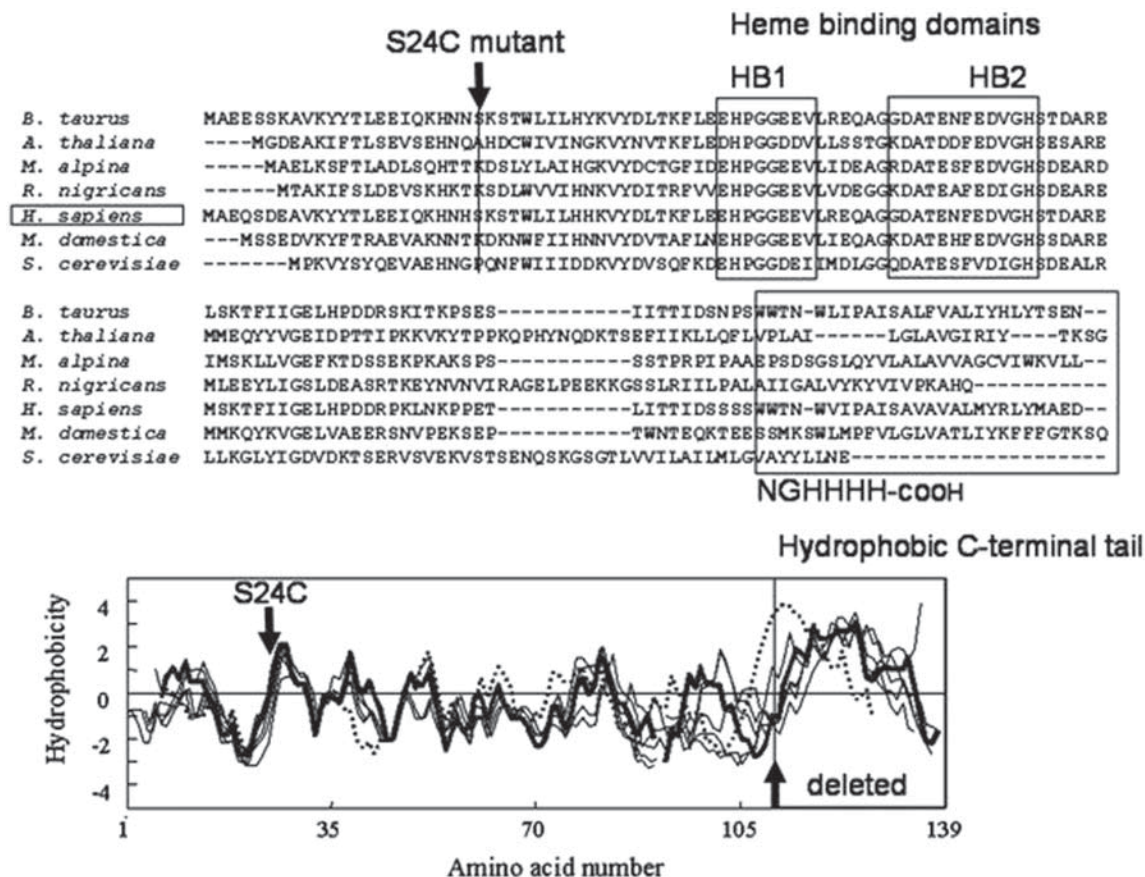


Fig. 1.

Engineering was performed on human b5 cDNA by polymerase chain reaction amplification using the 5'-GGCTGGATCCTTAATGGTGGTGATGTC CGTTACTGGAAGTGAATCAATAGTAGTG-3' oligonucleotide as a reverse primer and an oligonucleotide covering the 24 first bases of the 5' end of the cDNA open reading frame as a direct primer. The amplified cDNA was subcloned into pCR<sup>®</sup>2.1-TOPO<sup>®</sup> using the TOPO TA cloning kit (Invitrogen, Carlsbad, CA) and was checked by sequencing. The Hb5-(His)<sub>4</sub> coding sequence was extracted from pCR2.1 by *Sph*I-*Bam*HI double digestion and was ligated into the *Sph*I-*Bam*HI-digested pUHE25-2 expression vector (*I*) giving pUHE-[Hb5-(His)<sub>4</sub>]. Owing to the construction, this vector expresses a cytochrome b5 protein containing an additional leucine residue immediately following the initiation codon in addition to the C-terminal substitution.

Serine 24 in Hb5-(His)<sub>4</sub> (serine 23 of original human b5) was changed to cysteine by site-directed mutagenesis on pUHE-[Hb5-(His)<sub>4</sub>] using a Quick-Change site-directed mutagenesis kit (Stratagene) following the manufacturer's recommendations. Mutation was checked by sequencing.

### 3.1.2. Expression of Engineered Cytochrome b5

The same procedure was used for expression of [Hb5-(His)<sub>4</sub>] and its S24C derivative. XL1-Blue<sup>™</sup> cells transformed by pUHE-[Hb5-(His)<sub>4</sub>] were grown in 1 L of Terrific Broth supplemented with ampicillin (100 mg/L) at room temperature for 48 h. Isopropyl thiogalactoside and  $\delta$ -amino levulinic acid hydrochloride (Sigma) were added at a final concentration of 0.5 mM when the OD<sub>600</sub> reached 10. Induction took place for 30 h at 24°C. Cells were harvested and resuspended in 50 mL of 20 mM Tris-HCl buffer, pH 8.0. Cell walls were broken by the conjugated effects of lysozyme (1.25 mg/mL) and by sonication (4  $\times$  180s with 50% active cycles, using a Vibracell from Bioblock-Scientific) at 4°C in the presence of Cocktail Protease Inhibitors (Sigma), DNase (Sigma), and RNase (Boehringer). The 10,000g supernatant was applied to a 1.5  $\times$  7 cm column of Ni<sup>2+</sup>/iminodiacetate immobilized on agarose (Sigma) equilibrated with 25 mL of buffer P1. After thoroughly washing the column with buffer P1,

---

Fig. 1. (*previous page*) Sequence alignments of microsomal cytochromes b5. Aligned sequences are from mammalian, insect, plant, and fungal origins. (**Top**) Boxes HB1 and HB2 indicate conserved sequences surrounding the histidyl residues that are ligands of the heme iron. S24C labels the position mutated in this work in the human sequence to introduce a unique cysteinyl residue. The large box indicates the hydrophobic C-terminal sequence tail anchoring the natural enzyme to the membrane and the engineered C-terminal sequence (bold large letters). (**Bottom**) Corresponding hydrophobic index profiles. The arrow under S24C indicates the mutated position. The box labeled "deleted" indicates the deleted hydrophobic C-terminal sequence.



[Hb5-(His)<sub>4</sub>] was eluted with a 1 mg/mL solution of L-histidine. After purification, the protein was characterized by mass spectroscopy analysis (observed = 13,109; expected = 13,129).

### 3.1.3. Coupling of ssDNA to Engineered Cytochrome b5 Via a cis-Platin Bridge

To constitute a well-defined covalent link between the ssDNA of interest and cytochrome b5, *cis*-[Pt(NH<sub>3</sub>)<sub>2</sub>(H<sub>2</sub>O)<sub>2</sub>]<sup>2+</sup> was used as a crosslinking reagent. This approach has the advantage of forming a short linkage between the protein and the nucleic acid while preserving most of the hybridization properties of the ssDNA moiety. A drawback is the requirement for specific nucleic acid sequences that include a unique guanine that acts as a target at its N7 position for the cisplatin link (2). *Cis*-[Pt(NH<sub>3</sub>)<sub>2</sub>(H<sub>2</sub>O)<sub>2</sub>]<sup>2+</sup> (cisplatin) was prepared by dissolving a suspension of *cis*-[Pt(NO<sub>3</sub>)<sub>2</sub>(NH<sub>3</sub>)<sub>2</sub>] in water, formed by reaction of *cis*-[PtCl<sub>2</sub>(NH<sub>3</sub>)<sub>2</sub>] with silver nitrate. The ssDNA oligonucleotide (5'-CTA TCATTTGCTTACTATTC-3') was chosen as a model DNA fitting the previous requirements. Methylation analysis and Maxam-Gilbert sequencing (3,4) indicated that a single platination occurred at the N7 position of the unique guanine present on this oligonucleotide.

For formation of the cisplatin link, [Hb5-(His)<sub>4</sub>] and ssDNA (100–200 μM) were incubated in the presence of 5 molar eq of platinum complex in buffer P1 for 5 h at 25°C. The resulting complex (90 μM) was incubated with 1.5 eq of ssDNA for 50 h at 25°C. The [Hb5-(His)<sub>4</sub>]-Pt-ssDNA (P-DNA) was purified from the excess reagent using Ni<sup>2+</sup> iminodiacetic acid immobilized on agarose (Sigma). The protein was eluted with 1 M imidazole acetate in P1 buffer. The purification steps were monitored using the radiodetection of the 5'-end <sup>32</sup>P-labeled DNA and optical absorption monitoring at 413 nm for the cytochrome b5 and at 260 nm for the DNA. Results were consistent with formation of an equimolecular complex between [Hb5-(His)<sub>4</sub>] and the ssDNA based on ε<sub>413 nm</sub> = 117 mM<sup>-1</sup>·cm<sup>-1</sup> for [Hb5-(His)<sub>4</sub>] and ε<sub>260 nm</sub> = 180 mM<sup>-1</sup>·cm<sup>-1</sup> for the ssDNA. Control of P-DNA structure was routinely assessed by sodium dodecyl sulfate polyacrylamide gel electrophoresis analysis (5).

### 3.1.4. Coupling of ssDNA to Engineered Cytochrome b5 Through Homobifunctional Crosslinker

An alternate strategy was conceived to make it possible to combine any type of nucleic acid with cytochrome b5. This strategy consisted of creating, by site-directed mutagenesis, a unique attachment site on cytochrome b5 for a bifunctional crosslinker also able to couple with a modified nucleic acid. The homobifunctional linker DPDPB is a 16 Å linker that can form disulfide bonds with both thiolate-containing ssDNA and protein (Fig. 2). ssDNA modified by

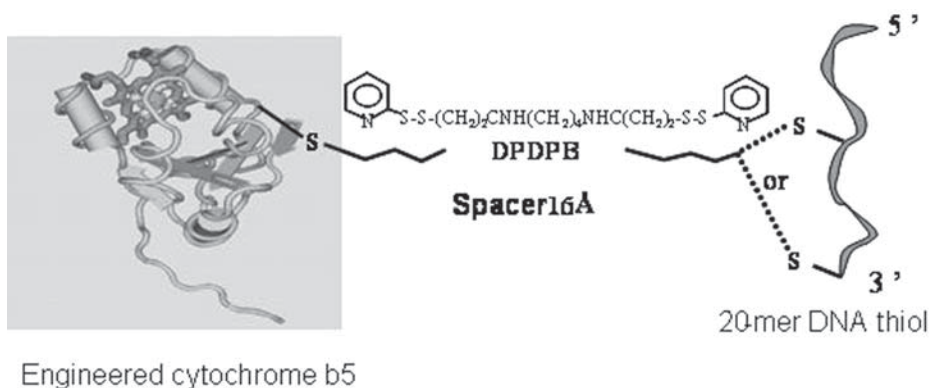


Fig. 2. Schematic structure of DPDPB-coupled P-DNA. Cytochrome b5 was coupled to ssDNA through a DPDPB bifunctional linker. DPDPB reaction led to insertion of a 16Å linker between the cytochrome b5 thiolate and the thiol-modified oligonucleotide.

a thiol group linked to the 3' or 5' end via a  $(-\text{CH}_2-)_3$  or  $(-\text{CH}_2-)_6$  spacer was provided by Eurogentec. The unmodified cytochrome b5 contains no endogenous cysteinyl residue. The S24C mutation was introduced to add a solvent-accessible cysteine at the periphery of the protein without disturbing the cytochrome folding (preservation of its spectroscopic and electrochemical properties). Based on the three-dimensional structure, this substitution localizes far away from the C-terminal histidine tag, thus allowing two independent and noninteracting links of cytochrome b5 with external elements.

#### 3.1.4.1. OLIGONUCLEOTIDE COUPLING WITH DPDPB

A specific protocol has been designed to optimize the yield of adduct synthesis. A solution of the thiolated ssDNA was incubated at 30°C for 10 min with dithiothreitol (DTT) at a 1:100 molecular ratio to cleave potential preexisting disulfide bridges. Excess unreacted DTT had to be eliminated before carrying out ssDNA coupling with the DPDPB reagent. For this purpose, a gel-exclusion chromatography on Sephadex G25 (Pharmacia) was performed. The coupling step was for 4 h at 30°C at a molar ratio of 1:20 between the desalted ssDNA and DPDPB. Following this step, coupled ssDNA was purified from excess reagent by separation onto a weak anion-exchange column (DEAE cellulose; Pharmacia). After a low-salt (0.1 M NaCl) wash, the ssDNA-PB adduct was eluted with 1.5 M NaCl. This led to highly concentrated fractions of the ssDNA-PB adduct from which a small amount (1 nmol) was withdrawn to evaluate the coupling efficiency. This was determined by monitoring the change in absorption at 344 nm following the addition of excess DTT. This chemical

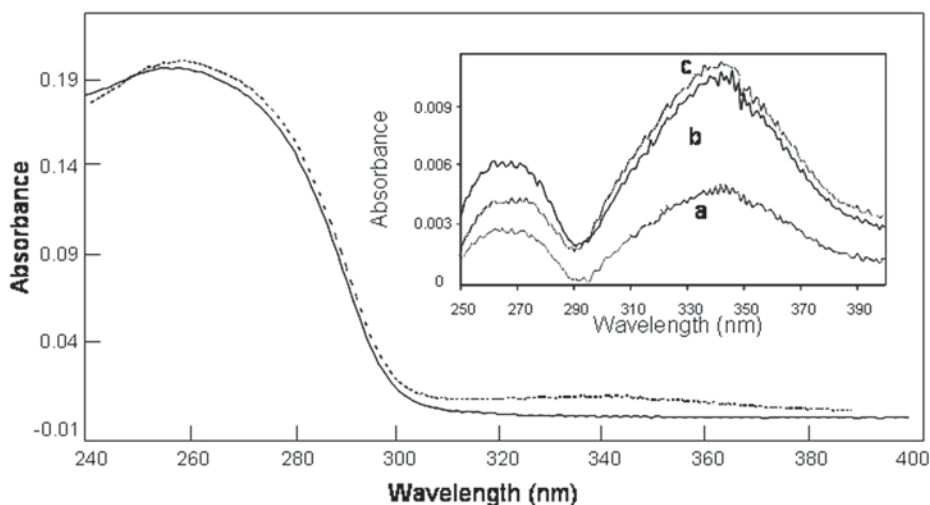


Fig. 3. Spectral characterization of adducts between DPD PB and ssDNA. Coupling and purification were performed as described in the text. Spectra were recorded for ssDNA prior to mixing with DPD PB (solid line) and after coupling and purification (dashed line). Titration of the remaining thiopyridine functionalization on the adduct can be performed by cleavage with DTT, which allows the release of the strongly absorbing pyridine 2-thione chromophore ( $\epsilon_{343 \text{ nm}} = 8080 \text{ M}^{-1} \cdot \text{cm}^{-1}$ ). Increasing the molar ratio of the DTT/adduct gave rise to corresponding increases in the  $A_{343 \text{ nm}}$  signal until saturation: (a) 10/1, (b) 50/1, (c) 100/1.

cleaves the uncoupled end of the linker releasing the pyridine-2-thione that was monitored at 344 nm ( $8.1 \times 10^3 \text{ M}^{-1} \text{ cm}^{-1}$ ), as presented in **Fig. 3**. Up to 80% of the initial ssDNA was found to be coupled to DPD PB, and the ssDNA-PB adduct was kept at 4°C for a few days without any detectable loss of reactivity (*see Note 1*).

#### 3.1.4.2. COUPLING OF S24C MUTANT OF Hb5(His)<sub>4</sub> PROTEIN TO ssDNA-PB ADDUCT

The second step of the assembly formation involves reaction of the protein with the ssDNA-PB adduct. During the purification process of the cysteine-containing protein, we noticed a high level of spontaneous dimer formation through a disulfide bond. This dimer was reduced by incubation of the purified protein with DDT as already described for the modified oligonucleotide (same time, temperature, and molar ratios). Similarly, the excess DTT was removed immediately before the coupling step by a rapid gel chromatography on Sephadex G50. The protein eluted into the dead volume of the column and was directly collected into the solution of purified ssDNA-PB adduct to reach a final molar ratio of 1 protein for 10 modified oligonucleotides. After at least

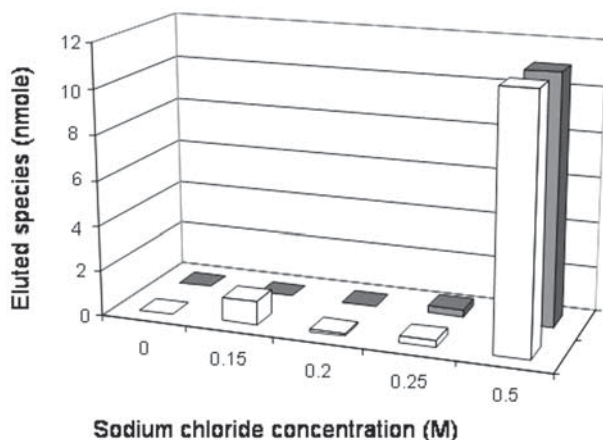


Fig. 4. Elution profile of DPDPB-coupled P-DNA purification on DEAE-cellulose column. As described in the text, a combination of chromatographic steps was required to obtain pure P-DNA. The last step involved an anion-exchange column (DEAE-cellulose) and was used in order to separate the different negatively charged species. A salt gradient allowed resolution of free cytochrome b5 from P-DNA. Solid boxes represent the ssDNA elution profile as deduced from ultraviolet absorbance; open boxes represent the cytochrome b5 elution profile as deduced from visible light absorbance.

2 h of coupling at room temperature in buffer P1, the final adduct was purified by combined chromatographies. Metal chelate chromatography was used to eliminate all the histidine tag-free species (i.e., nonprotein species). Following a wash step with a saline solution, the nickel-iminodiacetate column was eluted by a solution of histidine (1 mg/mL) or of EDTA (1 mM). Three species may still coexist in the eluate: monomeric and dimeric uncoupled proteins and the complex. Final purification was achieved by loading the previous eluate onto a DEAE Sepharose gel column that binds the three species but with differential affinities. Owing to the negative charges on DNA phosphate groups, the P-DNA complex is much more tightly bound than uncoupled proteins. A salt gradient allowed gradual elution of the species, as illustrated in **Fig. 4**. P-DNA eluted at the higher salt concentration. Routinely, this procedure resulted in a high yield of P-DNA synthesis (up to 75%). Spectrophotometric analysis of P-DNA was performed, and spectroscopic properties were compared with those of the uncoupled cytochrome b5 and ssDNA macromolecules (**Fig. 5**). P-DNA exhibits two major absorbance peaks corresponding to the nucleic acid and protein moieties, at 260 and 412 nm, respectively. For calculations, the absorbance at 260 nm has to be corrected to take into account the contribution of the Hb5-(His)<sub>4</sub> protein at this wavelength (about 20% of the 413-nm absorbance value).

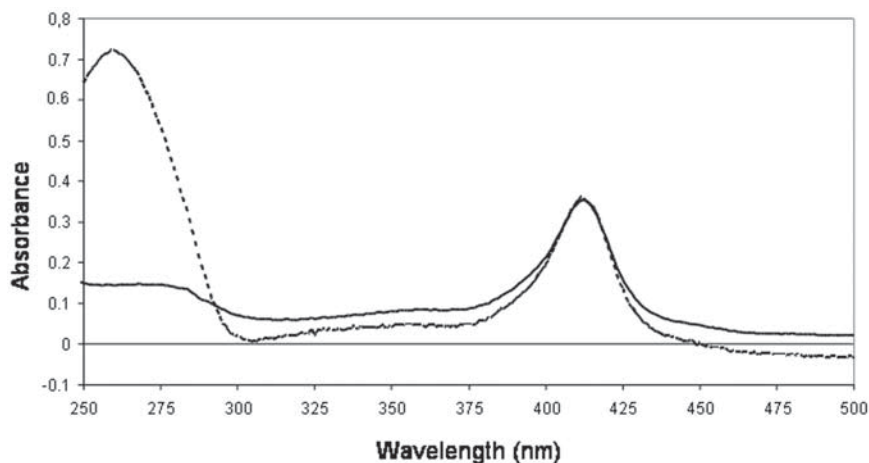


Fig. 5. Spectral characterization of [Hb5]His<sub>4</sub> and P-DNA. Absorption spectra of Hb5(His<sub>4</sub>) (solid line) and of purified P-DNA resulting from DPDPB-mediated coupling of Hb5(His<sub>4</sub>) with ssDNA (dashed line).

### 3.1.5. Conclusions

The formation of highly ordered and homogeneous supramolecular assemblies requires fully defined molecular components able to associate together in a fully defined and unique manner. We thus engineered a small globular protein, cytochrome b5, that exhibits a stable folding as well as useful specific spectroscopic and redox properties facilitating detection and characterization. Molecular engineering was used to introduce two types of functionalization: one allowing the controlled association of the final complex with a supported bilayer, and the other allowing a unique linkage to a nucleic acid moiety. This link was designed to avoid any disturbances of the protein structure, which, in the final complex, conserves unchanged redox and spectral properties. Moreover, this link allows a sufficient intramolecular flexibility to limit and even avoid any interference from the protein moiety that could affect the hybridization properties of the nucleic acid domain. The use of a distal homobifunctional synthetic crosslinker enabled further reduction of steric hindrance and, thus, higher yield and increased specific DNA base-pairing recognition.

A specific optimized protocol was designed to implement the reaction of the single-strand oligonucleotide with the DPDPB coupling agent under mild reaction conditions. Prior to reacting the oligonucleotide-spacer adduct with the protein, a spectroscopic assay requiring only a very limited amount of adduct (<1 nmol) was designed in order to quantify coupling efficiency. The yield of the coupling between the oligonucleotide-spacer adduct and the pro-

tein could also be assessed by spectroscopic methods taking advantage of the well-defined absorption of DNA and cytochrome b5 at 260 and 412 nm, respectively.

### 3.2. P-DNA Applications

A biosensor must combine biological recognition processes with signal transduction, allowing detection. Sensitivity of this detection increases when the size of the detection system decreases. SPR technology is a suitable detection system that requires no preliminary labeling of samples to monitor, and that provides real-time kinetics of biomolecule assembly (6). The generation of an evanescent wave requires a metal-coated template that also acts as an assembly support. These devices detect time-dependent changes in the refractive index at the surface of the sensor and give a signal (the sensorgram) proportional to the mass of the molecules bound to the surface. The sensitivity of SPR exponentially decreases with the distance between the interface and the recognition assemblies and becomes negligible for distances exceeding 300 nm. The classic BIAcore technology, which is essentially based on chips exhibiting a 100-nm polymer cushion (a dextran matrix on a gold surface), is not optimal for sensitivity. Supported lipidic membranes allow a closer distance, and thus a potentially optimized limit of detection, and also feature biomimetic properties limiting nonspecific interactions.

#### 3.2.1. Setup of Hybrid Bilayer Onto Gold Surface

A hybrid bilayer composed of a dense octadecyl mercaptan monolayer self-assembled onto a gold substrate overlaid by a free-floating phospholipid upper layer could be obtained by interaction of a liposome suspension with the OM-functionalized gold substrate (7). Kinetics of the hybrid bilayer formation was monitored by using SPR technology. Based on experimental and theoretical calibrations, a signal of 1 RU was found to correspond to a mass of 1 pg/mm<sup>2</sup> (8) and 700 resonance unit (RU) to a monolayer 1-nm thick (9). Fusion of small unilamellar vesicles of phospholipids (1 mM in buffer P1 at 25°C) with the self-assembled OM monolayer was performed. To reach a highly packed monolayer, a 20-min incubation was required. To remove excess material resulting from vesicular interdigitations, a 20 mM sodium hydroxide solution is injected until a stable signal is reached (*see Note 2*). Routinely, we measured values of 1700 and 1900 ± 300 RU for fusion of, respectively, DMPC and DOPC vesicles. This is in good agreement with previously published values (10). Nevertheless, it appeared important to control the integrity of the planar lipidic upper layer by injecting some polar proteins. Injection of a 1 μM solution of Hb5[His]<sub>4</sub> did not produce any signal, indicating the absence of nonspecific interactions with uncovered gold or hydrophobic layers (5). To confer

metal chelate affinity properties to the supported membrane, 10% (by mole) of a synthetic modified phospholipid (DOGS) bearing a nickel-iminodiacetate head was incorporated into the DMPC- or DOPC-containing vesicles used for the fusion step. Functionalized and nonfunctionalized vesicles behaved similarly toward the OM monolayer (*see Note 3*) (formation of uniform hybrid bilayer).

### 3.2.2. Interaction of Various Types of Cytochrome b5 With Supported Membranes

#### 3.2.2.1. NATIVE HUMAN CYTOCHROME B5

Native human cytochrome b5 is an extrinsic membrane protein with a natural transmembrane anchor domain composed of 26 amino acids at its carboxy terminus. We studied the incorporation of this protein into a hybrid bilayer by SPR in a 0.1 to 3  $\mu\text{M}$  range of concentration. Cytochrome b5 exhibited a high affinity for the supported bilayer but, surprisingly, at the highest concentrations tested acted as a macromolecular detergent by destroying the lipidic layer. Based on the Langmuir model proposed in the BIAevaluation software (BIAcore), a dissociation constant of 20 nM was evaluated, which is the same order of magnitude as the value calculated for rabbit cytochrome b5 (*11*). With an appropriate concentration (i.e.,  $<1 \mu\text{M}$ ), a monolayer of cytochrome b5 can be reconstituted highly packed onto the biosensor surface, giving an SPR signal of 1000 RU, which represents a coverage of 8 pmol/cm<sup>2</sup> (*12*). Although this membranous protein has a strong affinity for the hybrid bilayer, several factors make its use difficult, such as aggregation in solution, solubilization with detergent, and destruction of the bilayer.

#### 3.2.2.2. Hb5(His)<sub>4</sub> PROTEIN

It was previously reported that a membrane anchor-free cytochrome b5 containing a hexa-histidine tag could be incorporated with a relatively high affinity ( $>1 \mu\text{M}$ ) into a metal chelate monolayer (*13*). In our case, the -NGHHHH C-terminal extension was added to a modified human microsomal cytochrome b5 deleted of its natural C-terminal polypeptidic membrane anchor. Binding of the Hb5(His)<sub>4</sub> protein to the DOGS-doped supported bilayer was analyzed by SPR (**Fig. 6**, curve B). Typically, a unique injection of Hb5(His)<sub>4</sub> was performed at 1  $\mu\text{M}$  concentration (**Fig. 6**, curve B, **step 1**). A small decrease in the signal was observed on washing with buffer (**Fig. 6**, curve B, **step 2**), which probably reflected conditions of thermodynamic equilibration. Classically, the signal reaches values of 200 RU in the condition of excess lipid anchor inside the lipidic monolayer (10% DOGS). Injections of free L-histidine strongly decreased the signal (not shown), as expected for a nickel-chelating agent having the ability to disrupt the metal-mediated linkage. A dissociation constant of



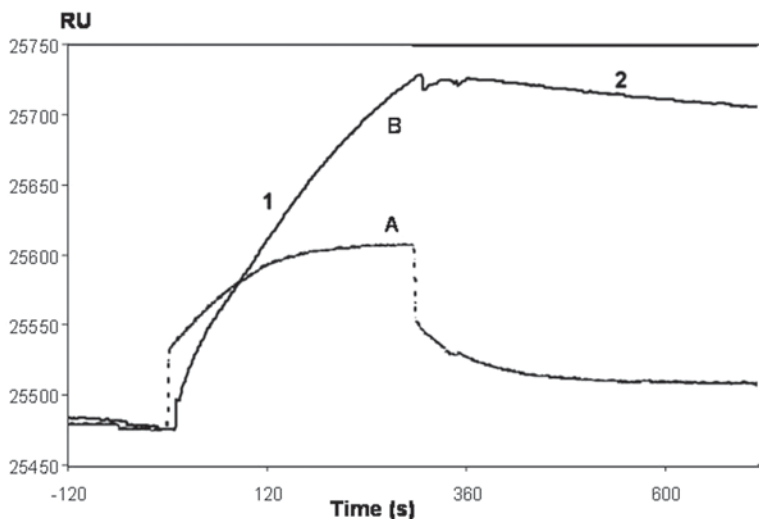


Fig. 6. Sensorgram of DNA-free [Hb5]His<sub>4</sub> and P-DNA interaction with membrane. The left baseline corresponds to the hybrid bilayer (DPMC/DOGS [10/1 by mole]) structure. Two injections were performed in order to analyze the kinetics of Hb5(His<sub>4</sub>) (curve B) and P-DNA (curve A) association/dissociation: 1. 1  $\mu$ M Hb5(His<sub>4</sub>) and P-DNA were injected at 25°C with a flow rate of 10  $\mu$ L/min; 2. washing step.

50 nM was deduced for Hb5[His]<sub>4</sub>. This value is very close to the value for the native protein and is much lower than the one (>1 mM) reported for the acylated soluble proteins (14). This is an important result that validates the strategy of cytochrome b5 molecular engineering because (1) the modification of the type of membrane attachment (chelate vs hydrophobic binding) did not alter the affinity for the lipid matrix; (2) in contrast to the natural b5, the engineered protein used did not tend to destroy the hybrid bilayer (even for large concentrations above 25  $\mu$ M) and did not interact with a DOGS-free hybrid bilayer; and (3) the protein layer can be removed in gentle aqueous conditions by chelate competitors, which makes biosensor regeneration easy to carry out.

### 3.2.3. Building of P-DNA Chips

#### 3.2.3.1. INTERACTION OF VARIOUS P-DNAs WITH HYBRID BILAYER

SPR experiments have been performed to test the ability of *cis*platin- and DPDPB-coupled P-DNA to form supramolecular assemblies with the nickel-iminodiacetate-functionalized bilayer. As illustrated in Fig. 6, curve A, when a 1  $\mu$ M solution of DPDPB-coupled P-DNA was injected in the same conditions as for Hb5[His]<sub>4</sub>, a 30-RU response signal was observed. To reach a level of coverage similar to the one observed with Hb5-(His)<sub>4</sub>, a longer injection was

necessary. Under experimental conditions that give rise to a saturation with uncoupled Hb5-(His<sub>4</sub>), the response for P-DNA was far from saturation with a coverage density about twofold lower. A value of 300 RU corresponding to coverage of 1.25 pmol/cm<sup>2</sup> of P-DNA was observed after a binding time of 20 min (5).

Kinetic constants were evaluated in a range of concentration between 0.1 and 2.5  $\mu$ M at 25°C and illustrated a lower affinity ( $K_D = 0.5\text{--}1\ \mu$ M) of P-DNA for the supported bilayers compared with what was observed with the DNA-free protein. The decrease in the affinity could be explained by the larger size and the strong negative charge of the P-DNA compared with the uncoupled protein. Therefore, the ssDNA moiety of the complex probably introduces some steric hindrance as well as some electrostatic repulsive interactions with the negatively charged membrane surface that together reduce the affinity of the complex for the bilayer. However, this reduced affinity is not a major drawback because the supramolecular complex once formed was found to be stable enough to allow most interactions to take place. This indicates that the large size of the complex does not cause a rapid extraction of the lipid anchors from the phospholipid matrix, or a rapid break of the chelate-mediated link. Preliminary experiments indicated that the complex can be further stabilized by lowering the temperature, probably because the induced phase transition of the lipid layer likely slows down the residual extraction of the anchor lipid from the bilayers.

### 3.2.3.2. SPECTROSCOPIC AND SPR ANALYSIS OF HYBRIDIZATION

To evaluate the influence of protein coupling on the hybridization properties of the ssDNA, the melting temperature of the double-stranded DNA formed by hybridization of a free ssDNA sequence complementary to the nucleic acid part of the P-DNA was determined. Melting temperatures of DNA duplexes were determined on a Uvikon 941 spectrophotometer using Bio-Tek software (Bio-Tek Kontron, St Quentin en Yvelines, France). Free ssDNA or P-DNA (cisplatinium coupled) was incubated with the complementary ssDNA at a final concentration of 0.5  $\mu$ M in 0.1 M NaClO<sub>4</sub>, pH 4.0. The duplex sample was heated at 80°C (for the free ssDNA) or 65°C (for P-DNA), and the temperature was allowed to decrease to 2.5°C at a rate of 1°C/min. Absorbance changes were monitored at 260 nm. Samples were then heated at a rate of 1°C/min from 2.5 to 60°C in order to check that hybridization and fusion curves were consistent. The melting temperatures in 0.1 M NaClO<sub>4</sub>, pH 4.0, were found to be 45 and 23°C for the free duplex and the [Hb5-(His)<sub>4</sub>] complex, respectively (Fig. 7). This result suggested that the stability of the duplex DNA was significantly reduced on coupling to [Hb5-(His)<sub>4</sub>]. Steric interaction with the protein

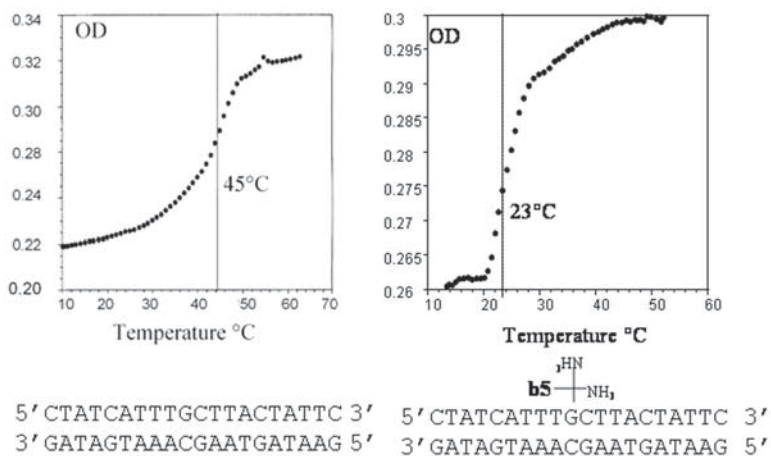


Fig. 7. Melting analysis of double-stranded free DNA and cisplatinum-coupled P-DNA. The melting of each 20-base-long double-stranded oligonucleotide was analyzed by duplex optical adsorption at 260 nm in 0.1 NaClO<sub>4</sub>, pH 4.0, with the temperature scanning rate set at 1°C/min.

moiety and/or geometric distortion of duplex DNA owing to guanine platination likely contributed to the phenomenon (15). Nevertheless, the fusion curve for P-DNA showed a clear single-step transition, suggesting that a real hybridization and not some nonspecific interactions had occurred. In addition, control experiments with unrelated DNA sequences of similar length did not exhibit any signal (5).

Hybridization of the bilayer-coated P-DNA (1 pmol/cm<sup>2</sup> of membrane) with the complementary nucleotide sequence was realized at different temperatures below 30°C. In such conditions, the duplex DNA within the complex in solution was found to be stable based on the previous fusion curve analysis. Complementary ssDNA (50 µg/mL in buffer P1 or phosphate-buffered saline) was injected onto the membrane-bound device. Based on RU signal, hybridization was only observed for sodium chloride concentrations >150 mM (Fig. 8). This result is consistent with the expected stabilization of DNA duplex by reduction of the DNA negative-charge electrostatic repulsion following increases in ionic strength. Under such conditions, the observed response of 55 RU was half that expected for a full hybridization. Furthermore, when a noncomplementary ssDNA was injected, no signal was observed, highly suggesting that observed signals resulted from a specific interaction.

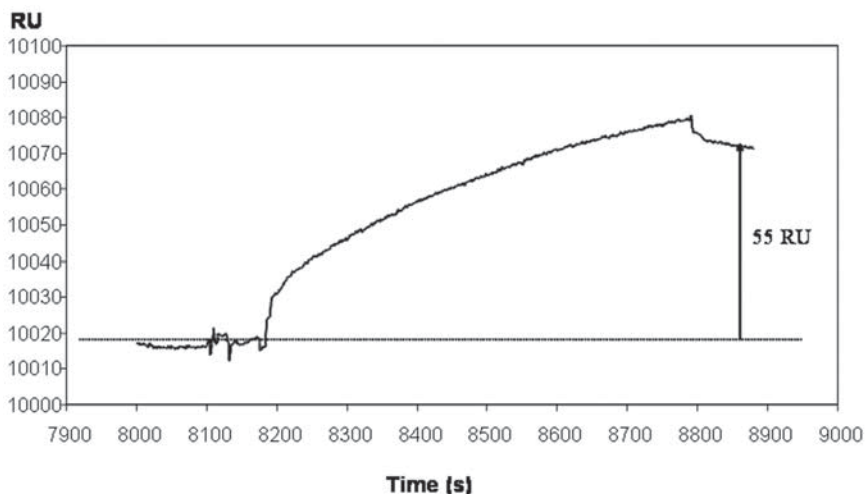


Fig. 8. SPR hybridization of DPDPB-coupled P-DNA with complementary oligonucleotide. The initial baseline corresponds to the deposition of  $1.25 \text{ pmol/cm}^2$  of P-DNA onto the lipidic upper layer. A single injection of complementary ssDNA yielded a specific stable association response (55 RU) after washing. The complementary ssDNA concentration was  $25 \text{ }\mu\text{g}/\mu\text{L}$ , and the flow rate during the injection was  $10 \text{ }\mu\text{L}/\text{min}$  at  $25^\circ\text{C}$ .

#### 3.2.4. Unique Properties of P-DNA Chips

The designed device is a much more well-defined molecular organization than the stochastic one observed in classic DNA chips resulting from the random deposit of oligoprobes on a poorly defined support layer generally constituted of a positively charged polymer that acts as a nonspecific binder for the nucleic acids. Because of the limited affinity of such interaction, additional crosslinking of nucleic acids is generally required to stabilize the device. Such crosslinking could partially depreciate the nucleic acids' properties. Data indicate that in such a classic chip only a few percent of probes are really accessible for hybridization, thus dramatically limiting sensibility. The P-DNA concept minimizes nonspecific interactions since the negatively charged supported membrane does not interact with DNA and, on the contrary, it maximizes the base-pairing specific recognition by presenting the probe oligonucleotide in solution away from the interface. Additionally, the unique lateral mobility properties of the device favor probe accessibility even in conditions leading to a high level of probe saturation.

P-DNA chip design includes the possibility of accurately controlling the density of immobilized probe onto the biomimetic layer, allowing optimization of the ratio between sensitivity and specificity for particular applications.

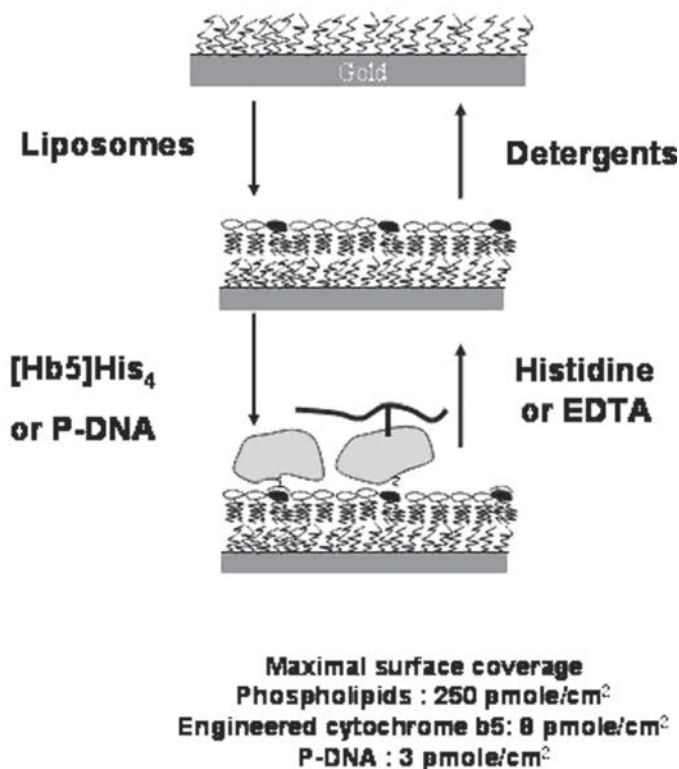


Fig. 9. Schematic for reversible self-assembly of P-DNA.

The coverage density can be accessed by SPR. Calculated saturating densities for phospholipids, cytochrome b5, and P-DNA on the sensor are summarized in **Fig. 9**. A remarkable advantage of SPR is that it allows real-time monitoring of the variation in density when varying the DOGS dosage in the lipid layer. Another advantage is the controlled reversibility of the self-assembling reactions that make chip regeneration possible (**Fig. 10**).

#### 4. Notes

1. The presented strategy for the coupling of engineered cytochrome b5 with the oligoprobes involved a homobifunctional linker and thiolated oligonucleotides. This approach works well but is rather tricky to implement because of the difficulty in reproducibly synthesizing thiolated oligonucleotides of good quality, the rather high cost of such synthesis, the need to deal with oxygen-dependent oxidation of thiolated DNA, the need to tightly control the coupling step with the homofunctionalized linker to avoid formation of cytochrome b5 or oligoprobe homodimers, and the resulting need for a good purification that leads to some

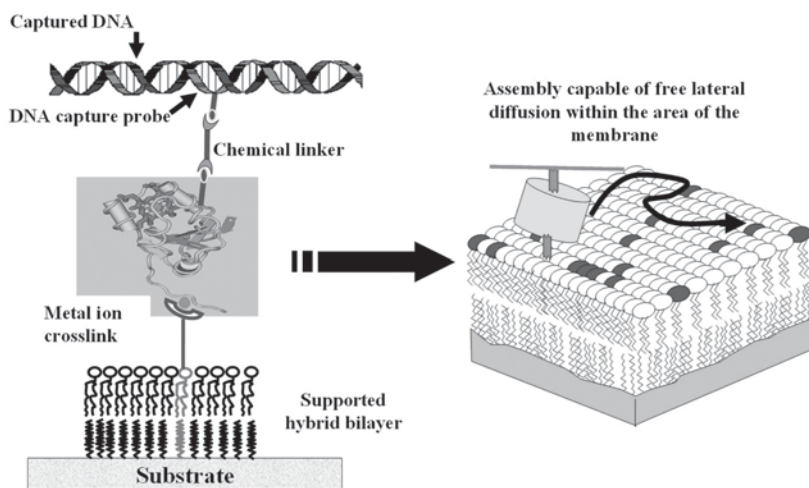


Fig. 10. P-DNA as floating DNA sensor capable of lateral diffusion.

decrease in final complex yields. To solve these drawbacks, we recently modified the procedure by using amino-modified instead of thiolated oligonucleotides. Such amino-modified oligoprobes (commercially available as 3'-, 5'-, or internal base modifications) are widely used in classic chip technology; they also are simpler to synthesize at much lower costs. The homobifunctional linker has to be changed for a heterobifunctional linker including both a thiol-reactive and an amine-reactive extremity. A large number of such linkers are available from commercial sources. The coupling of the linker with the oligoprobe was first performed. This led to a single possible product with no possibility of dimer formation. The purified adduct was then coupled to the modified cytochrome b5 as previously described for the homobifunctional linker. Globally, the yield is improved and the costs and number of building steps are reduced.

2. Self-assembly of supported lipid bilayers by liposome (or small unilamellar vesicle) fusion is classic and well described in the literature. However, this process can lead to a coverage being incomplete owing to the presence of impurities in the substrate or in the vesicle solution. An alternate cause can also be a too large dispersion of the vesicle sizes. The process can also lead to multilayer formation when incubation time for the fusion step is too long or when an unadapted phospholipid composition is used. These multilayers introduce heterogeneities and instabilities in chips. To limit and control such phenomena during SPR monitoring of vesicle fusion, each injection of phospholipid (typically 1 mM at 25°C for 20 min) was followed by repeated injections of 20 mM sodium hydroxide in order to remove phospholipid digitations resulting from incomplete vesicle fusion. This can account for up to 20% of the SPR signal and causes major signal instabilities. The preparation of vesicle solutions implies repeated sonications, which can cause a progressive chemical degradation of phospholipids, particu-

larly metal dissociation from those modified with nickel iminodiacetate. It is thus useful following the construction of bilayer to reload the modified lipid (DOGS) with nickel by injecting a 50 mM nickel chloride solution in sodium acetate buffer, pH 6.0. This step is also required following biochip regeneration by histidine or EDTA injections.

3. Each step of the whole chip setup has to be carefully controlled by systematic SPR measurements. For example, the binding of Hb5(His)<sub>4</sub> is evaluated on a supported phospholipid bilayer including 10% mol/mol DOGS. It is highly recommended that one test that no interaction can be detected when only DOPC or DMPC but no modified lipid is included, and also that one check the integrity of the supported layer by verifying the absence of interaction of a protein such as cytochrome-*c*, which normally does not interact with bilayers of good quality.

## Acknowledgments

We thank Marie Agnès Sari and Sophie Bombard from the Laboratory of Biochemistry and Technology, University of Paris V, France, for engineering the *cis*platinum-coupled P-DNA complex and conducting hybridization characterizations by spectrophotometry; Jean Christophe Zeeh and Pierre Emmanuel Puig from FEMTO-ST Institute, LPMO Department, LPMO, Besançon, for help with the experiments; Didier Dupont from INRA, Poligny, France, for help with the SPR instrumentation; and Philippe Urban for editing the manuscript for correct use of language.

## References

1. Bujard, H., Gentz, R., Lanzer, M., Stüber, D., Müller, M., Ibrahimi, I., Häuptle, M. T., and Dobberstein, B. (1987) A T5 promoter-based transcription-translation system for the analysis of proteins in vitro and in vivo, in *Methods in Enzymology*, vol. 155 (Wu, R. and Grossmann, L., eds.), Academic Press Inc., San Diego, CA, pp. 416–433.
2. Lepre, C. A. and Lippard, S. J. (1990) Interaction of platinum antitumor compounds with DNA. *Nucleic Acids Mol. Biol.* **4**, 9–38.
3. Maxam, A. H. and Gilbert, W. (1980) *Methods Enzymol.* **65**, 499–560.
4. Comess, K. M., Costello, C. E., and Lippard, S. J. (1990) Identification and characterization of a novel linkage isomerization in the reaction of trans-diamminedichloroplatinum(II) with 5'-d(TCTACGCGTTCT). *Biochemistry* **29**, 2102–2110.
5. Boireau, W., Bombard, S., Sari, M. A., and Pompon, D. (2002) Bioengineering and characterization of DNA-protein assemblies floating on supported membranes. *Biotechnol. Bioeng.* **77**, 225–231.
6. Jönsson, U., Fägerstam, L., Ivarsson, B., et al. (1991) Real-time biospecific interaction analysis using surface plasmon resonance and a sensor chip technology. *Biotechniques* **11**, 620–627.



7. Kalb, E., Frey, S., and Tamm, L. K. (1992) Formation of supported planar bilayer by fusion of vesicles to supported phospholipid monolayers. *Biochim. Biophys. Acta* **1103**, 307–316.
8. Stenberg, E., Persson, B., Roos, H., and Urbaniczky, C. (1991) Quantitative determination of surface concentration of protein with surface plasmon resonance using radiolabeled proteins. *J. Colloid Inter. Sci.* **143**, 513–526.
9. Sigal, G. B., Mrksich, M., and Whitesides, G. M. (1997) Using surface plasmon resonance spectroscopy to measure the association of detergent with self-assembled monolayers of hexadecanethiolate on gold. *Langmuir* **13**, 2749–2755.
10. Pierrat, O., Lechat, N., Bourdillon, C., and Laval, J. M. (1997) Electrochemical and surface plasmon resonance characterization of the step-by-step self assembly of a biomimetic structure onto an electrode surface. *Langmuir* **13**, 4112–4118.
11. Tetryachenko-Ladokhina, V. G., Ladokhin, A. S., Liming, W., Steggles, A. W., and Holloway, P. W. (1993) Amino acid substitutions in the membrane-binding domain of cytochrome b5 alter its membrane-binding properties. *Biochim. Biophys. Acta Biomembr.* **1153**, 163–169.
12. Boireau, W. (1999) PhD thesis, Electrochemistry of cytochrome b5 in solution and reconstituted inside lipidic bilayers. University of Technology, Compiègne, France.
13. Ng, K., Pack, D. W., Sasaki, D. Y., and Arnold, F. H. (1995) Engineering protein-lipid interactions: targeting of histidine-tagged proteins to metal-chelating lipid monolayers. *Langmuir* **11**, 4048–4055.
14. Lange, C. and Koch, K. W. (1997) Calcium-dependent binding of recoverin to membranes monitored by surface plasmon resonance spectroscopy in real time. *Biochemistry* **36**, 12,019–12,026.
15. Fouchet, M. H., Gauthier, C., Guittet, E., Girault, J. P., Igolen, J., and Chottard, J. C. (1992) Synthesis and characterization of a d(ApG) platined nanonucleotide duplex. *Biochem. Biophys. Res. Commun.* **182**, 555–560.

## Nanosystems for Biosensing

### *Multianalyte Immunoassay on a Protein Chip*

Eiichi Tamiya, Zheng-liang Zhi, Yasutaka Morita, and Quamrul Hasan

#### Summary

This chapter describes the construction of addressable two-dimensional (2D) microarrays via the random fluidic self-assembly of metallic particles and the use of these arrays as platforms for constructing protein chips for bioassays. These arrays will be useful as platforms for constructing protein chips for bioassays in a broad range of applications. The basic units in the assembly are microfabricated particles, which carry a straightforward visible code, and the corresponding array template patterned on a glass substrate. On one face, the particles consist of a hydrophobic and magnetic Ni-polytetrafluoroethylene (Ni-PTFE) composite layer; the other face has a gold layer that was modified for biomolecular attachment. We use photoresist patterning to create an array template with spatially discrete microwells into which an Ni-PTFE hydrophobic composite layer and a hydrophobic photoadhesive coating are electrodeposited. After biomaterial attachment and binding processes in bulk, the particles are randomly self-assembled onto the lubricated bonding sites on the chip substrate. This self-assembly process is driven by a combination of magnetic, hydrophobic, and capillary interactions. The encoding symbol carried by each particle is used to identify the target attached to the particle surface. This model system demonstrates the utility of the protein chip array for conducting simultaneous multianalyte immunoassays of human immunoglobulins (IgA, IgG, and IgM).

**Key Words:** Protein chip; biochip; nanosystem; biosensing; microparticle array; self-assembly; encoding; multianalyte immunoassay.

#### 1. Introduction

The fabrication of high-throughput and cost-effective bioassay systems for solution-phase multianalyte parallel detection is critically dependent on arrays of biofunctional biomolecular features arranged on a highly integrated chip (**1**). Generally, conventional techniques for biomaterial patterning on a biochip

From: *Methods in Molecular Biology*, vol. 300:  
*Protein Nanotechnology, Protocols, Instrumentation, and Applications*  
Edited by: T. Vo-Dinh © Humana Press Inc., Totowa, NJ

involve direct application of the biocomponents onto the substrate surface using any one of several techniques: microcontact printing (2–4), robotic spotting (5–7), and site-selective photodeposition synthesis (8–10). However, these procedures require sophisticated high-precision devices and are both costly and time-consuming. Typical planar arrays also have several technical drawbacks, such as slow diffusion of targets to the binding surface and nonuniform size of the arrayed features. In an effort to overcome these problems, Goodey et al. (11), Christodoulides et al. (12), and Curey et al. (13) developed a versatile platform that uses an on-chip, microcavity-accommodated microbead array for the parallel detection of multiple components in a complex fluid. In this implementation, however, the array was fabricated by sequentially placing individual beads into the on-chip microcavities, one at a time. Practically, this methodology is extremely cumbersome, particularly when the application calls for the assembly of high-density arrays of small beads. Michael et al. (14) and Walt (15) proposed another method, in which a random and high-density optical biosensor array is created by randomly dispersing encoded microspheres at the distal end of the fiber bundles. This approach, although overcoming the typical shortcomings associated with the planar-surface technique, requires an optical-encoding chemistry for individual microspheres in order to identify each sensor settled in the array.

Several articles have reported on the development of large-scale integrated picoliter microchamber arrays for polymerase chain reaction (16), the introduction of a novel nanoliter dispensing system suitable for DNA amplification on a microchamber array chip (17), the development of a new approach for manufacturing encoded microstructures used as versatile building blocks for miniaturized multiplex bioassays (18), and the construction of a protein chip array (19).

This chapter describes a two-step methodology for constructing a protein chip array. First, biocomponents are immobilized individually on micro-machined, encoded microcarriers (rectangular metallic particles bearing an engraved signature), and specific binding to multiple targets is carried out in a bulk solution. Second, the particles are arranged onto the complementary binding sites on an array template and subsequently detected. The encoding symbol carried by the microparticles is a straightforward visible feature, introduced while the particles were being manufactured. Thus, this approach does not require additional sophisticated chemistry to incorporate an encoding element. The encoding symbol is used as the signature of the individual arrayed particle and identifies the target/compound attached to each particle surface.

Self-assembly is used to arrange the organized structures on a chip substrate, and to construct the particle array. Generating high-dimensional arrays

of structures using self-assembly of small objects is a common technique in biology, chemistry, and physics (20). The components to be assembled can be either spheres (21) or nonspheres (22–29), with a wide range of sizes, from a few nanometers (21) to several millimeters (24–29). So far, self-assembly techniques have been developed for a range of practical applications, including fabrication of microelectronic device elements (24,30,31), photonic band-gap structures (32), and other three-dimensional structures from colloid particles (33,34). Various kinds of weak interactions, such as electrostatic, magnetic, hydrophobic, and capillary, can drive the assembly (22,23). To promote the self-assembly process for larger objects, researchers have typically exploited capillary interactions in combination with a lubrication process (22–30).

For the process described here, we introduce hydrophobic and magnetic Ni-polytetrafluoroethylene (Ni-PTFE) composite layers in the interaction areas of both the assembling pieces and the spatially discrete microwells on the array template. The individual particles carrying immobilized biocomponents are then allowed to assemble randomly onto the array template, promoted by a combination of selective short-range forces including magnetic, hydrophobic, and capillary interactions. This approach combines the advantages of a typical microsphere-based array, providing high flexibility in array implementation and use (15), with the simplicity of the interrogation technologies available for a planar chip array. The utility of the constructed particle array platform is shown here as a model system for simultaneous multianalyte immunoassays of human immunoglobulins (IgA, IgG, and IgM) (19).

## 2. Materials

For the study described here, negative photoresist XP SU-8 50, developer, Nano Remover PG photoresist remover, and XP SU-8 release layer were purchased from Microchem (Newton, MA). Supersignal enzyme-linked immunosorbent assay femto maximum sensitivity substrate was obtained from Pierce (Rockford, IL). All the antibodies (developed in goat), antigens (human IgA, IgG, and IgM), and peroxidase-conjugated antibodies were obtained from Sigma (St. Louis, MO) and used as received. Metaflon FS Ni-PTFE dispersion electroplating solution, containing nickel sulfamate ( $\text{Ni}^{2+}$  100 g/L) plus fine PTFE particles (diameter: approx 0.2  $\mu\text{m}$ ; concentration: 50 g/L), was purchased from C. Uyemura & Co (Osaka, Japan). 16-Mercaptohexadecanoic acid (90%) was obtained from Aldrich (Milwaukee, WI). 1-Hexadecanethiol was obtained from Wako (Osaka, Japan). Other chemicals used in this study were of reagent grade and purchased from local commercial sources. The photomasks were designed with Illustrator 9.01 (Adobe) and printed on a transparency film using a high-resolution laser printer system.

### 3. Methods

#### 3.1. Photolithographic Patterning

Cleaned glass slides ( $38 \times 26$  mm) served as the substrate for the deposition by evaporation of 20 nmol of Cr and then 200 nmol of Cu that was used as a conducting seed layer and later also as the sacrificial release layer. A Karl Suss MJB 3 mask aligner (Zeiss, Oberkochen, Germany) in contact mode, powered by a 350-W mercury ultraviolet (UV) light source, was used for contact photolithography. The metal-coated substrates were first spin coated with a 2- $\mu$ m XP SU-8 release layer, according to the protocol provided by the manufacturer (<http://www.microchem.com>). Next, they were spin coated with an approx 50- $\mu$ m layer of SU-8 50 photoresist thick film and structured using standard photolithographic procedures. Two kinds of resist patterning templates were fabricated, one for particle preparation and another for the array template (chip substrate); the template fabrication process is described in **Subheading 3.7**.

For the particle fabrication template, a  $48 \times 24$  microwell array with a  $400 \times 200$   $\mu$ m electrochemically active area in each well and a 50- $\mu$ m separation space between the wells was designed on a  $30 \times 20$  mm substrate area. The coding symbol was located at an upright area of each microwell. The array template had a  $20 \times 20$  mm effect area consisting of  $21 \times 21$  microwells in shapes and sizes that complemented the fabricated pieces.

#### 3.2. Electrodeposition

The photoresist-patterned substrates were cleaned for 2 min using reactive-ion etching with an  $O_2$  plasma. This treatment oxidized the hydrophobic SU-8 photoresist surface, thus making it hydrophilic (contact angle:  $<20^\circ$ ), as was required for the selective binding of the particles to the microwells on the array template. Electrodeposition of an Ni-PTFE composite layer in the microwell areas was carried out using an electroplating bath at  $50^\circ\text{C}$  for 30 min for particle preparation and 1 h for array template preparation, with a current density of approx  $0.1 \text{ mA/mm}^2$  based on the active area of the substrate. The microwell areas prepared using this procedure had a smooth, hydrophobic, and magnetic surface, in contrast to the other areas, which remained hydrophilic.

#### 3.3. Particle Fabrication

Following electrodeposition of the Ni-PTFE composite layer (approx 6  $\mu$ m thick), the patterned particle fabrication and array templates were deposited sequentially on top of the photoresist by evaporation with a 0.02- $\mu$ m layer of Cr and a 0.3- $\mu$ m layer of Au. The metallized resist pattern on the chip was then lifted after immersion in an SU-8 Remover PG solution at  $80^\circ\text{C}$  for 10 to 20 min. The particles were finally liberated from the underlying substrate by dissolving the sacrificial Cu layer with an etchant containing sodium hypochlorite (0.2 M),

ammonia (0.7 M), and ammonium carbonate (2.6 M). The particles were transferred and stored in an Eppendorf-type tube filled with ethanol. They exhibited an instantaneous attraction when a magnet was moved close to the tube containing the particle suspension, thus confirming their magnetic properties.

### **3.4. On-Particle Immunoassays for IgA, IgG, and IgM**

The fabricated particles were coated with a self-assembled monolayer (SAM) by soaking them for 24 h in a 1 mM solution of 16-mercaptohexadecanoic acid in ethanol. The particles carrying the carboxylic acid-terminated thiol monolayer were washed using ethanol and transferred into a 0.5-mL Eppendorf-type tube. Four sets of particles were then treated with 100  $\mu$ L of a solution containing 2  $\mu$ g/mL of antibodies against either IgA, IgG, IgM, or 2% casein (as a negative control) in 50 mM phosphate-buffered saline (PBS) with 138 mM NaCl (pH 7.4) for 3 h at room temperature with rotating agitation. They were subsequently passivated with 2% casein (sodium salt) for 1 h to prevent non-specific adsorption of proteins during subsequent steps. Finally, the particles were rinsed three times with 10 mM PBS (pH 7.4) containing 0.01% Tween-20.

The sets, each containing 10–20 particles with immobilized individual antibodies, were combined in a 0.5-mL Eppendorf-type tube. A 100- $\mu$ L sample containing a mixture of IgA, IgG, and IgM was added and incubated for 1 h. The particles were subsequently rinsed, and a 100- $\mu$ L mixture of three peroxidase-conjugated reporter antibodies, each with a concentration of 4  $\mu$ g/mL, was added for 1 h to form sandwich immunobinding complexes on the particles and rinsed. The immunotreated particles were then applied onto the array template and finally detected, as described in **Subheadings 3.5.** and **3.6.**

For calibration purposes, six standards with antigen concentrations between 0.001 and 10  $\mu$ g/mL were tested individually, each with one set of particles. A calibration with several standards on a single experiment was also tested. In this case, three sets of particles were first immobilized with the same antibody and blocked in separate tubes; standards containing three different concentrations of the analyte were then added to the particles individually and incubated. The particles were washed and combined, and peroxidase-conjugated reporter antibody was added to form the sandwich immunobinding complexes.

### **3.5. Assembly of Particle Array**

An SU-8 photoresist-patterned array template with an electrodeposited Ni-PTFE layer on the surface of its microwells was magnetized, using a permanent magnet, for 2 h. The template was then coated with an SAM of 16-hexadecanethiol for 12 to 24 h and lubricated with a thin hydrophobic photocurable adhesive film following the procedure described by Srinivasan et al. (30).

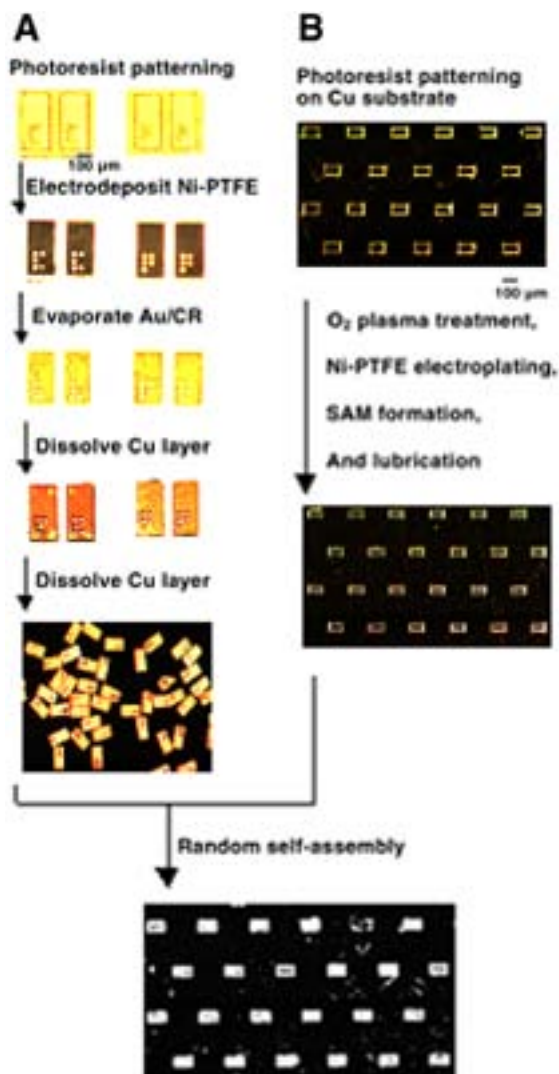


Fig. 1. Protocol used for fabrication and self-assembly of particle array on a protein chip substrate. **(A)** Fabrication of encoded multilayer particles. SU-8 50 photoresist was patterned as a template on a Cu-coated glass substrate, and an Ni-PTFE layer (approx 6  $\mu\text{m}$  thick) was electrodeposited on the open area of the microwells. After evaporation of Cr (20 nm) and Au (300 nm) on the entire chip surface, the metallized SU-8 photoresist was lifted off using SU-8 Remover PG solution. Finally, the particles were released from the underlying substrate by dissolving the Cu sacrificial layer. Only two types of encoded particles are shown here as examples. **(B)** Fabrication of a microwell array template on a chip substrate. An SU-8 photoresist (approx 50  $\mu\text{m}$  thick)-patterned microwell array on a Cu-covered glass slide was treated with O<sub>2</sub> plasma,



The photocurable adhesive consisted of 96:2:2 (w/w/w) dodecylmethacrylate/benzoin isobutyl ether/1,6-hexanediol diacrylate (22,23). After rinsing in distilled water, the chip was transferred to a 100-mL vessel; a continuously flowing water stream (containing 0.1 M NaCl) was maintained over the chip surface with the aid of a pump. Particles were then added slowly, using a Pasteur pipet, and settled onto the surface of the chip substrate. The pieces moved across the surface and finally settled onto the microwell sites covered with the photo-adhesive layer, forming a particle array. After exposure to UV radiation (100 W) for 20 min, the pieces were fixed in place. Excess particles that were not bound to the microwells were removed by washing.

### 3.6. Detection of Chemiluminescence Signal

The chemiluminescence from multiple particle spots located on the substrate was magnified by an MZFLIII microscope (Leica, Heerbrugg, Switzerland) and imaged using a charge-coupled device camera detector (ZVS-3C75DE; Carl Zeiss, Oberkochen, Germany). The images were then analyzed using IPLab Spectrum P software. The chemiluminescence signals from the microscopic particle zones were captured with a 30-s acquisition time.

To initiate the luminescence reaction, 0.1 mL of a mixture of the chemiluminescence substrates comprising luminol and  $\text{H}_2\text{O}_2$  was pipeted onto the particle-settled substrate. The peroxidase-conjugated antibodies, fixed on the particle surface through immunobinding, emitted localized chemiluminescent signals. By reading the encoding signature of the particle at a given location on the substrate, we were able to identify the targets bound onto the individual particles.

### 3.7. Fabrication and Assembly of Particle Array on a Protein Chip Substrate

Micromachining techniques were employed to manufacture the encoded multilayer particles and the corresponding array templates. Primarily, these techniques involved a combination of photolithography and lift-off, electroplating-through-mask (35), metal thermal evaporation, and wet etching. The typical process for the fabrication of the particles and the array template on a chip substrate is outlined in **Fig. 1**.

---

(*Fig. 1. caption continued*) and an Ni-PTFE layer (~6  $\mu\text{m}$  thick) was electrodeposited on the open area of the microwells. The hydrophobic Ni-PTFE structures were then magnetized with a permanent magnet and further coated with a thin photoadhesive film through hydrophobic interactions. The chip substrate was next immersed in a fluid water system, and the particle suspension was added slowly to allow the self-assembly process. Finally, curing the adhesive by exposure to UV radiation provided mechanically stable particle arrays that could be used for detection.

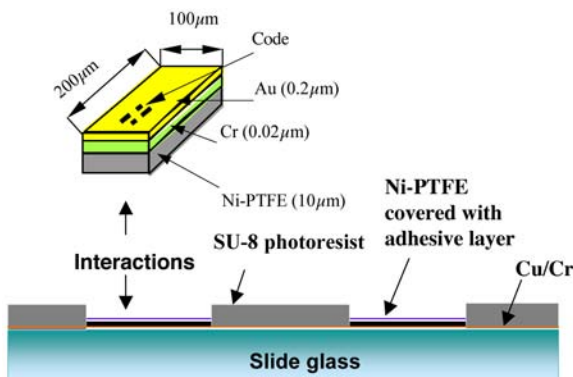


Fig. 2. Schematic representation of interaction of encoded particles with microwell surface of array template on a protein chip substrate.

To fabricate the array template, the surface of the substrate was patterned into defined hydrophobic (in microwells) and hydrophilic surface regions (the remaining area). An  $O_2$  plasma etching for the photolithographically patterned resist layer was found to render the surface hydrophilic. Then, an electrodeposited Ni-PTFE layer (approx  $6\ \mu\text{m}$  thick) on the microwell areas on the array template made these areas hydrophobic. These areas were further coated with an SAM of 16-hexadecanethiol, which rendered the microwell surface ultrahydrophobic. With such a process, the microwell areas on the substrate became hydrophobic (also magnetic) while the other regions remained hydrophilic, thus facilitating the further coating of a hydrophobic, photo-adhesive thin layer onto the microwell areas.

**Figure 2** illustrates the principles underlying the self-assembly process, based on a combination of magnetic, hydrophobic, and capillary interactions.

### 3.8. Summary of Multianalyte Immunoassay Process

The multianalyte capacity of the present approach was tested and demonstrated for parallel determination of three independent analyses of human immunoglobulins (IgA, IgG, and IgM). The sandwich immunoassay format uses particles with immobilized antibodies, peroxidase-labeled reporter antibodies, and the luminol-based chemiluminescence detection system. The particle surface of gold when passivated with an SAM of 16-mercaptohexadecanoic acid is easily compatible with available biomolecular coupling chemistries (by adsorption) and luminescence-based detection techniques (35). The typical assay protocol for the particle-based multianalyte immunoassay is outlined in **Fig. 3**.

Calibration curves for the three antigens were obtained individually by using mean values of triplicates of integrated particle light intensities plotted against the antigen concentration values, as shown in **Fig. 4**.

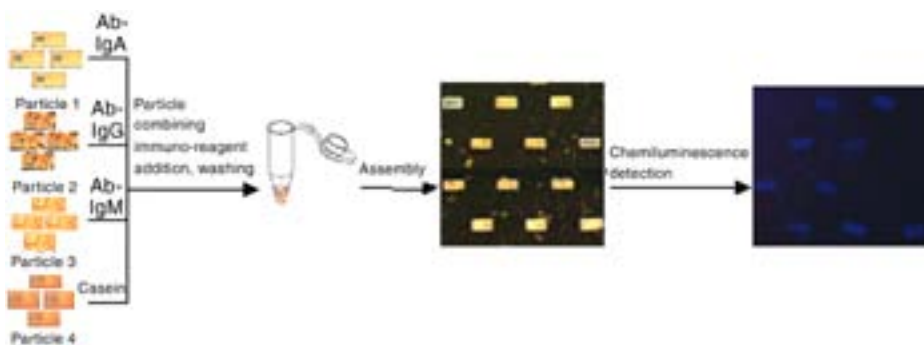


Fig. 3. Process leading to multianalyte immunoassays in parallel with arrayed particles on a protein chip substrate. Separate subsets of particles bearing an identifiable code were each tagged with a specific antibody. After combining the sets into a plastic tube, immunoreagents for a sandwich assay were added sequentially, and the particles were then assembled onto an array template in a random fashion. The encoding signature identified the individual particle registration and, subsequently, the assay target at each given location on the substrate.

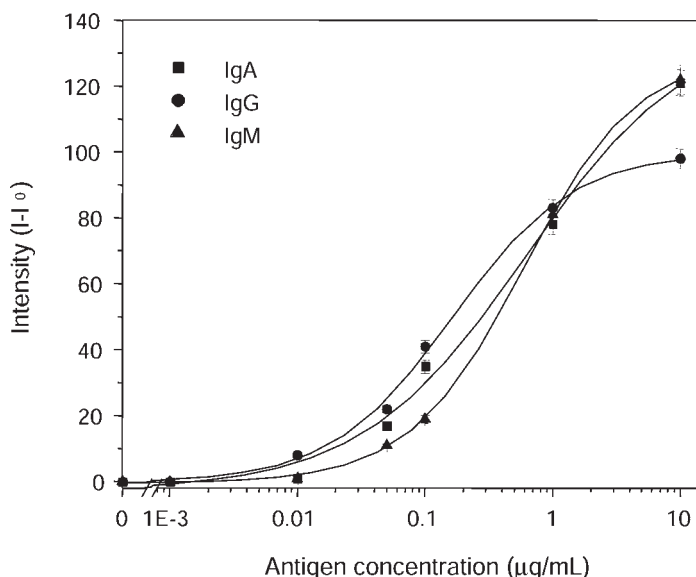


Fig. 4. Calibration curves for IgA, IgG, and IgM multianalyte immunoassays on microfabricated particles with chemiluminescent detection. The intensity data derived from the individual particles were subtracted from a background value.

All the curves show a sigmoidal binding behavior. The determination ranges for IgA, IgG, and IgM were typically from 10 ng/mL to 1  $\mu$ g/mL, and the detection limits were approx 10 ng/mL. The detection limits achieved in this work mainly depended on the affinity of antibodies and antigens, as happens in conventional immunoassays.

For quantitative analysis, it is necessary to carry out calibration with several standards on a single chip. To accomplish this goal, the experimental protocol was altered slightly: different sets of the particles were first immobilized with the same antibody and blocked in separate tubes; standards containing a certain concentration of the analyte were then added to the particles individually and incubated. Peroxidase-conjugated reporter antibody was subsequently added to form the sandwich immuno-binding complexes. The procedure used for the particle fabrication by micromachining techniques is amenable to mass production at low cost and is thus suitable for applications that extend beyond the laboratory.

#### 4. Conclusion

This chapter has outlined the template-directed self-assembly of a randomly ordered, addressable particle array that could be used for miniaturized multianalyte immunoassays. The approach described here provides a versatile building block for parallel bioassays in a combinatorial fashion. The benefits of this method include improved flexibility in assay implementation, and the ability to avoid overlap or particle aggregation between adjacent particles during detection. Moreover, including multiple copies of each kind of particle and control particles in a single operation improves precision through signal averaging and simultaneously minimizes the probability of false results (either positive or negative) that might occur if a single sensor was used in the assay. Because of the unique fabrication procedure and potentially high level of encoding capability, the particles fabricated by this method—once optimized regarding array-assembling efficiency—could also be widely applied in genomics, proteomics, combinatorial chemistry, and other high-throughput bioscreening and bioassay applications.

#### Acknowledgments

We thank Prof. R. B. DiGiovanni and J. A. Steeh for editing assistance. This work was partially funded by a grant-in-aid for Scientific Research Priority Area (A) of MEXT, Research for Future Program from the JSPS, and the 21st Century Center of Excellence Program on Technology Creation Based on Knowledge Science at JAIST.

## References

1. Sanders, G. H. W. and Manz, A. (2000) Chip-based microsystems for genomic and proteomic analysis. *Trends Anal. Chem.* **19**, 364–378.
2. Jackman, R. J., Wilbur, J. L., and Whitesides, G. M. (1995) Fabrication of submicrometer features on curved substrates by microcontact printing. *Science* **269**, 664–666.
3. Bernard, A., Fitzli, D., Sonderegger, P., Delamarche, E., Michel, B., Bosshard, H. R., and Biebuyck, H. (2001) Affinity capture of proteins from solution and their dissociation by contact printing. *Nat. Biotechnol.* **19**, 866–869.
4. Okamoto, T., Suzuki, T., and Yamamoto, N. (2000) Microarray fabrication with covalent attachment of DNA using bubble jet technology. *Nat. Biotechnol.* **18**, 438–441.
5. MacBeath, G. M. and Schreiber, S. L. (2000) Printing proteins as microarrays for high-throughput function determination. *Science* **289**, 1760–1763.
6. Wiese, R., Belosludtsev, Y., Powdrill, T., Thompson, P., and Hogan, M. (2001) Simultaneous multianalyte ELISA performed on a microarray platform. *Clin. Chem.* **47**, 1451–1457.
7. Lee, K. B., Park, S. J., Mirkin, C. A., Smith, J. C., and Mrksich, M. (2002) Protein nanoarrays generated by dip-pen nanolithography. *Science* **295**, 1702–1705.
8. Schena, M., Shalon, D., Davis, R. W., and Brown, P. O. (1995) Quantitative monitoring of gene expression patterns with a complementary DNA microarray. *Science* **270**, 467–470.
9. Fodor, S. P. A., Read, J. L., Pirrung, M. C., Stryer, L., Lu, A. T., and Solas, D. (1991) Light-directed, spatially addressable parallel chemical synthesis. *Science* **251**, 767–773.
10. Fodor, S. P. A., Rava, R. P., Huang, X. C., Pease, A. C., Holmes, C. P., and Adams, C. L. (1993) Multiplexed biochemical assays with biological chips. *Nature* **364**, 555, 556.
11. Goodey, A., Lavigne, J. J., Savoy, S. M., et al. (2001) Development of multi-analyte sensor arrays composed of chemically derivatized polymeric microspheres localized in micromachined cavities. *J. Am. Chem. Soc.* **123**, 2559–2570.
12. Christodoulides, N., Tran, M., Floriano, P. N., Rodriguez, M., Goodey, A., Ali, M., Neikirk, D., and McDevitt, J. T. (2002) A microchip-based multianalyte assay system for the assessment of cardiac risk. *Anal. Chem.* **74**, 3030–3036.
13. Curey, T. E., Salazar, M. A., Oliveira, P., Javier, J., Dennis, P. J., Rao, P., and Shear, J. B. (2002) Enzyme-based sensor arrays for rapid characterization of complex disaccharide solutions. *Anal. Biochem.* **303**, 42–48.
14. Michael, K. L., Taylor, L. C., Schultz, S. L., and Walt, D. R. (1998) Randomly ordered addressable high-density optical sensor arrays. *Anal. Chem.* **70**, 1242–1248.
15. Walt, D. R. (2000) Bead-based fiber-optic arrays. *Science* **287**, 451, 452.
16. Nagai, H., Murakami, Y., Morita, Y., Yokoyama, K., and Tamiya, E. (2001) Development of a microchamber array for picoliter PCR. *Anal. Chem.* **73**, 1043–1047.

17. Matsubara, Y., Kobayashi, M., Morita, Y., and Tamiya, E. (2002) Application of a microchamber array for DNA amplification using a novel dispensing method. *Arch. Histol. Cytol.* **65**(5), 481–488.
18. Zhi, Z. L., Morita, Y., Hasan, Q., and Tamiya, E. (2003) Micromachining microcarrier-based biomolecular encoding for miniaturized and multiplexed immunoassay. *Anal. Chem.* **75**, 4125–4131.
19. Zhi, Z. L., Murakami, Y., Morita, Y., Hasan, Q., and Tamiya, E. (2003) Multianalyte immunoassay with self-assembled addressable microparticle array on a chip. *Anal. Biochem.* **318**, 236–243.
20. Whitesides, G. M. and Grzybowski, B. (2002) Self-assembly at all scales. *Science* **295**, 2418–2421.
21. Boal, A. K., Ilhan, F., DeRouchey, J. E., Thurn-Albrecht, T., Russell, T. P., and Rotello, V. M. (2000) Self-assembly of nanoparticles into structured spherical and network aggregates. *Nature* **404**, 746–748.
22. Clark, T. D., Tien, J., Duffy, D. C., Paul, K. E., and Whitesides, G. M. (2001) Self-assembly of 10- $\mu$ m-sized objects into ordered three-dimensional arrays. *J. Am. Chem. Soc.* **123**, 7677–7682.
23. Clark, T. D., Ferrigno, R., Tien, J., Paul, K. E., and Whitesides, G. M. (2002) Template-directed self-assembly of 10- $\mu$ m-sized hexagonal plates. *J. Am. Chem. Soc.* **124**, 5419–5426.
24. Gracias, D. H., Tien, J., Breen, T. L., Hsu, C., and Whitesides, G. M. (2000) Forming electrical networks in three dimensions by self-assembly. *Science* **289**, 1170–1172.
25. Terfort, A., Bowden, N., and Whitesides, G. M. (1997) Three-dimensional self-assembly of millimetre-scale components. *Nature* **386**, 162–164.
26. Grzybowski, B. A., Stone, H. A., and Whitesides, G. M. (2000) Dynamic self-assembly of magnetized, millimeter-sized objects rotating at a liquid-air interface. *Nature* **405**, 1033–1036.
27. Tien, J., Breen, T. L., and Whitesides, G. M. (1998) Crystallization of millimeter-scale objects with use of capillary forces. *J. Am. Chem. Soc.* **120**, 12,670–12,671.
28. Breen, T. J., Tien, J., Oliver, S. R. J., Hadzic, T., and Whitesides, G. M. (1999) Design and self-assembly of open, regular, 3D mesostructures. *Science* **284**, 948–951.
29. Oliver, S. R. J., Clark, T. D., Bowden, N., and Whitesides, G. M. (2001) Three-dimensional self-assembly of complex, millimeter-scale structures through capillary bonding. *J. Am. Chem. Soc.* **123**, 8119, 8120.
30. Srinivasan, U., Liepmann, D., and Howe, R. T. (2001) Microstructure to substrate self-assembly using capillary forces. *J. Microelectromech. Syst.* **10**, 17–24.
31. Gittins, D. I., Bethell, D., Schirin, D. J., and Nichols, R. J. (2000) A nanometerscale electronic switch consisting of a metal cluster and redox-addressable groups. *Nature* **408**, 67–69.
32. Joannopoulos, J. D. (2001) Self-assembly lights up. *Nature* **414**, 257, 258.

33. Li, M., Schnablegger, H., and Mann, S. (1999) Coupled synthesis and self-assembly of nanoparticles to give structures with controlled organization. *Nature* **402**, 393–395.
34. Cheng, Z., Russel, W. B., and Chaikin, P. M. (1999) Controlled growth of hardsphere colloidal crystals. *Nature* **401**, 893–895.
35. Nicewarner-Pena, S. R., Freeman, R. G., Reiss, B. D., He, L., Pena, D. J., Walton, I. D., Cromer, R., Keating, C. D., and Natan, M. J. (2001) Submicrometer metallic barcodes. *Science* **294**, 137–141.





## Optical Nanosensors for Detecting Proteins and Biomarkers in Individual Living Cells

Tuan Vo-Dinh

### Summary

Recently, nanotechnology has been revolutionizing important areas in molecular biology and medicine, especially diagnostics and therapy at the molecular and cellular levels. The combination of nanotechnology, biology, advanced materials, and photonics opens up the possibility of detecting and manipulating atoms and molecules using nanodevices. This capability has the potential for a wide variety of medical uses at the cellular level. One of the most recent technological advances has been in the area of nanosensors. This chapter describes the principle of optical nanosensors, their development, and their applications for in vivo analysis of proteins and biomarkers in individual living cells. Nanosensors were fabricated with optical fibers pulled down to tips with distal ends in nanoscale dimensions. Nanosensors with immobilized bioreceptor probes (e.g., antibodies, enzyme substrate) that are selective to target analyte molecules are also referred to as nanobiosensors. Laser light is launched into the fiber, and the resulting evanescent field at the tip of the fiber is used to excite target molecules bound to the antibody molecules. A photometric detection system is used to detect the optical signal (e.g., fluorescence) originating from the analyte molecules or from the analyte-bioreceptor reaction.

**Key Words:** Nanosensor; nanoprobe; nanotechnology; biosensor; antibody; single cell; benzopyrene tetrol; cancer.

### 1. Introduction

Minimally invasive analysis of proteins and related cellular signaling pathways inside single intact cells is becoming increasingly important because cells in a population respond asynchronously to external stimuli. There is a need to further our understanding of basic cellular signaling processes in order to obtain new information that is not available from population-averaged cellular measurements. A further advantage of living-cell analysis is that it allows us to

From: *Methods in Molecular Biology*, vol. 300:  
*Protein Nanotechnology, Protocols, Instrumentation, and Applications*  
Edited by: T. Vo-Dinh © Humana Press Inc., Totowa, NJ

understand the exact pathways by which signaling pathways move through the architecture of the cell. Not only is there a need to resolve such measurements temporally; there is also a need to resolve them spatially. For these reasons, continued progress in cellular physiology requires new protein measurement strategies that can be applied to individual cells with great temporal and spatial resolution.

Advances in nanotechnology and photonics have recently led to a new generation of devices for probing the cellular machinery, elucidating intimate life processes occurring at the molecular level that were heretofore invisible to human inquiry (*1*). Recent advances in nanotechnology have led to the development of biosensor devices having nanoscale dimensions; such sizes make them suitable for probing biomolecules such as proteins inside individual living single cells. These nanotools could provide new information that could greatly improve our understanding of cellular function, thereby revolutionizing cell biology.

Fiberoptic sensors provide useful tools for remote *in situ* monitoring. Nanoscale fiberoptic sensors would be suitable for sensing intracellular/intercellular physiological and biological parameters in microenvironments. A wide variety of fiberoptic chemical sensors and biosensors have been developed in our laboratory for environmental and biochemical monitoring (*2–9*). Submicron fibers have been developed for use in near-field optics (*10,11*). Tapered fibers with submicron tip diameters between 20 and 500 nm have also been developed for near-field scanning optical microscopy (NSOM). NSOM was used to achieve subwavelength 100-nm spatial resolution in Raman detection (*12,13*). Tan et al. (*14,15*) have developed and used chemical nanosensors to perform measurements of calcium and nitric oxide, among other physicochemicals in single cells. Vo-Dinh et al. have developed nanosensors with antibody probes (*16–23*) and enzyme substrate-based probes (*24*) to detect biochemical targets and proteins inside living single cells. This chapter describes the operating principle, instrumentation, protocols, and applications of optical nanosensors.

## **2. Principle of Biosensors and Nanosensors**

### **2.1. Near-Field Optics and Nanosensors**

Nanofibers were originally developed for use in NSOM, which is a technique involving light sources or detectors that are smaller than the wavelength of light (*10*). The first method developed for performing these experiments was to place a pinhole in front of the detector, thus effectively reducing the detector's size. In a later variation of these pinholes, an excitation probe with dimensions smaller than the wavelength of the light was used for sample inter-

rogation. Betzig and Chichester (*11*) developed one such probe capable of obtaining measurements with a spatial resolution of approx 12 nm. The probe was constructed by using a micropipet puller to pull a single-mode optical fiber to a tip diameter of 20 nm and then coating the walls of the fiber with 100 nm of aluminum to confine the excitation radiation to the tip. With this nanoprobe, images of a pattern were reconstructed from a raster scan performed in the illumination mode, with the probe acting as a localized light source.

Near-field microscopy has received great interest resulting from its extremely high spatial resolution (subwavelength) (*10*). For example, a relatively new method known as near-field surface-enhanced Raman spectroscopy (NF-SERS) has been used for the measurement of single-dye and dye-labeled DNA molecules with a resolution of 100 nm (*12,13*). In this work, DNA strands labeled with the dye brilliant cresyl blue were spotted onto a SERS-active substrate that was prepared by evaporation of silver on a nanoparticle-coated substrate. The silver-coated nanostructured substrates are capable of inducing the SERS effect, which can enhance the Raman signal of the adsorbate molecules up to  $10^8$  times (*25*). NF-SERS spectra were collected by illuminating the sample using the nanoprobe and detecting the SERS signals using a spectrometer equipped with a charge-coupled device (CCD). Raster scanning the fiber probe over the sample and normalizing for surface topography using Rayleigh scattered light produced a two-dimensional (2D) SERS image of the DNA on the surface of the substrate with subwavelength spatial resolution. Near-field optical microscopy promises to be an area of growing research that could provide an imaging tool for monitoring individual cells and even biological molecules. Single-molecule detection and imaging schemes using nanofibers could open new possibilities in the investigation of the complex biochemical reactions and pathways in biological and cellular systems.

## **2.2. Biosensor Components**

Over the years, new techniques in biosensing have set the stage for great advances in the field of biological research. The two fundamental operating principles of a biosensor are biological recognition and sensing. Therefore, a biosensor can be generally defined as a device that consists of two basic components connected in series: (1) a biological recognition element, often called a bioreceptor; and (2) a transducer (*4,18*). The biosensor detects molecules and transforms this recognition into another type of signal using a transducer. The interaction of the analyte with the bioreceptor is designed to produce an effect measured by the transducer, which converts the information into a measurable effect, such as an electrical signal. A bioreceptor is a biological molecular species (e.g., an antibody, an enzyme, a protein, or a nucleic acid) or a living biological system (e.g., cells, tissue, or whole organisms) that uses

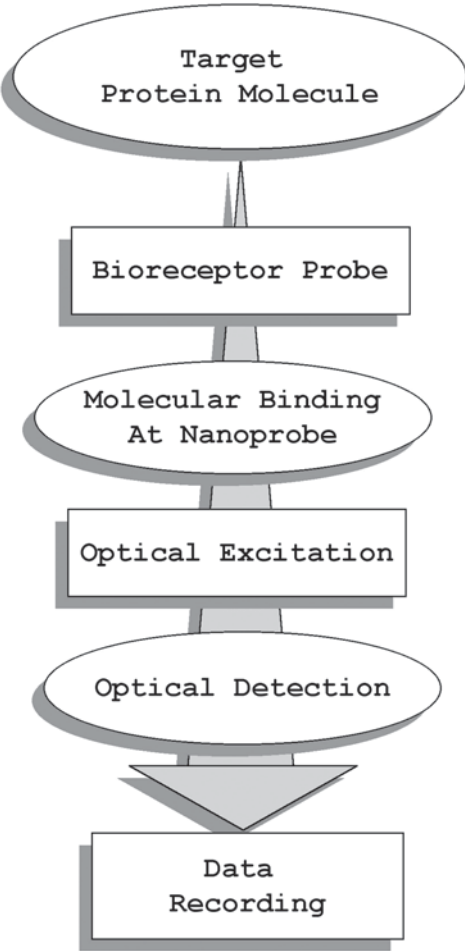


Fig. 1. Principle of biosensing system.

biochemical mechanisms for recognition. The main purpose of the recognition system is to provide the sensor with a high degree of selectivity for the analyte to be measured.

Several transduction methods are used in biosensors. The three main methods are based on optical detection, electrochemical detection, and mass-based detection. Other detection methods include voltaic and magnetic. New types of biosensor transducers are continually being developed. Each of the three main classes contains many different subclasses, creating a large number of possible transduction methods or combinations of methods. This chapter focuses on optical transduction methods. **Figure 1** illustrates the conceptual principle of

the biosensing process using a bioreceptor probe and an optical detection method.

Recent advances in nanotechnology leading to the development of submicron optical fibers have opened new horizons for intracellular measurements. Typically, the tip diameter of the optical fiber used in these sensors ranges between 20 and 100 nm. These sensors are based on the same basic principles as more conventional optical biosensors, except for the excitation process. Because the diameter of the optical fiber's tip is significantly less than the wavelength of light used for excitation of the analyte, photons cannot escape from the tip of the fiber to be absorbed by the species of interest, as is the case in larger fiberoptic sensors. Instead, in a fiberoptic nanosensor, after the photons have traveled as far down the fiber as possible, excitons or evanescent fields continue to travel through the remainder of the tip, providing excitation for the fluorescent species of interest present in the biosensing layer. An additional feature of evanescent excitation is that only species that are in extremely close proximity to the fiber's nanoprobe can be excited, thereby precluding the excitation of interfering fluorescent species elsewhere on the sample. Thus, any signal collected is from molecular species extremely close to the fiber (within the 100-nm near-field environment). This feature allows for an unprecedented level of localization.

### **2.3. Bioreceptors**

The key to specificity with biosensor technologies lies in the bioreceptor molecules used. Bioreceptors are responsible for binding the analyte of interest to the sensor for measurement. Bioreceptors can take many forms and are as numerous as the different analytes that have been monitored using biosensors. However, bioreceptors can generally be classified into five major categories: antibodies/antigens, enzymes, nucleic acids/DNA, cellular structures/cells, and biomimetics. This chapter deals with biosensor systems using antibody probes, often called immunosensors, with optical detection. Another type of probe that involves an enzyme substrate is discussed in **Subheading 4**.

Immunological reactions involving the antigen-antibody binding reaction provide the basis for the specificity of immunoassays. Antibodies are complex biomolecules, made up of hundreds of individual amino acids arranged in a highly ordered sequence. Antibodies are produced by immune system cells when such cells are exposed to substances or molecules called antigens. The antibodies called forth following antigen exposure have recognition or binding sites for specific molecular structures (or substructures) of the antigen. The way in which an antigen and an antigen-specific antibody interact is analogous to a lock-and-key fit, in which specific configurations of a unique key enable it to open a lock. In the same way, an antigen-specific antibody fits its unique

antigen in a highly specific manner, so that the three-dimensional (3D) structures of antigen and antibody molecules are complementary. Owing to this 3D shape fitting, and the diversity inherent in individual antibody makeup, it is possible to find an antibody that can recognize and bind to any one of a large variety of molecular shapes.

This unique property of antibodies is the key to their usefulness in immunosensors; their ability to recognize molecular structures allows one to develop antibodies that bind specifically to chemicals, biomolecules, micro-organism components, and so on. One can then use such antibodies as specific probes to recognize and bind to an analyte of interest that is present, even in extremely small amounts, within a large number of other chemical substances. Since the first development of a remote fiberoptics immunosensor for *in situ* detection of the chemical carcinogen benzo[*a*]pyrene (BaP) (2), antibodies have become commonly used as bioreceptors in biosensors.

### 3. Materials and Methods

#### 3.1. Fabrication of Fiberoptics Nanoprobes

This section describes the protocols and instruments used in the fabrication of fiberoptics nanoprobes. Since fiberoptic nanoprobes are not commercially available, investigators must fabricate them in their own laboratories. Two methods are generally used for preparing the nanofiber tips. The so-called heat-and-pull method is the most commonly used. This method consists of local heating of a glass fiber using a laser or a filament and subsequently pulling the fiber apart. The shape of the nanofiber tips obtained depends on controllable experimental parameters such as the temperature and the timing of the procedure. The second method, often referred to as Turner's method, involves chemical etching of glass fibers. In a variation of the standard etching scheme, the taper is formed inside the polymer cladding of the glass fibers.

The experimental procedures for the fabrication of nanofibers using the heat-and-pull procedure, used by our laboratory, is schematically shown in **Fig. 2 (21)**. The heat-and-pull procedure consists of pulling a larger silica optical fiber to produce the tapered nanotip fiber using a special fiber-pulling device (Sutter Instruments P-2000). This method yields fibers with submicron diameters. One end of a 600- $\mu\text{m}$  silica/silica fiber is polished to a 0.3- $\mu\text{m}$  finish with an Ultratec fiber polisher. The other end of the optical fiber is then pulled to a submicron length using a fiber puller. A scanning electron microscopy photograph of one of the fiber probes fabricated for studies is shown in **Fig. 3**. The distal end of the nanofiber is approx 30 nm.

To prevent leakage of the excitation light on the tapered side of the fiber, the sidewall of the tapered end is then coated with a thin layer (100 nm thick) of



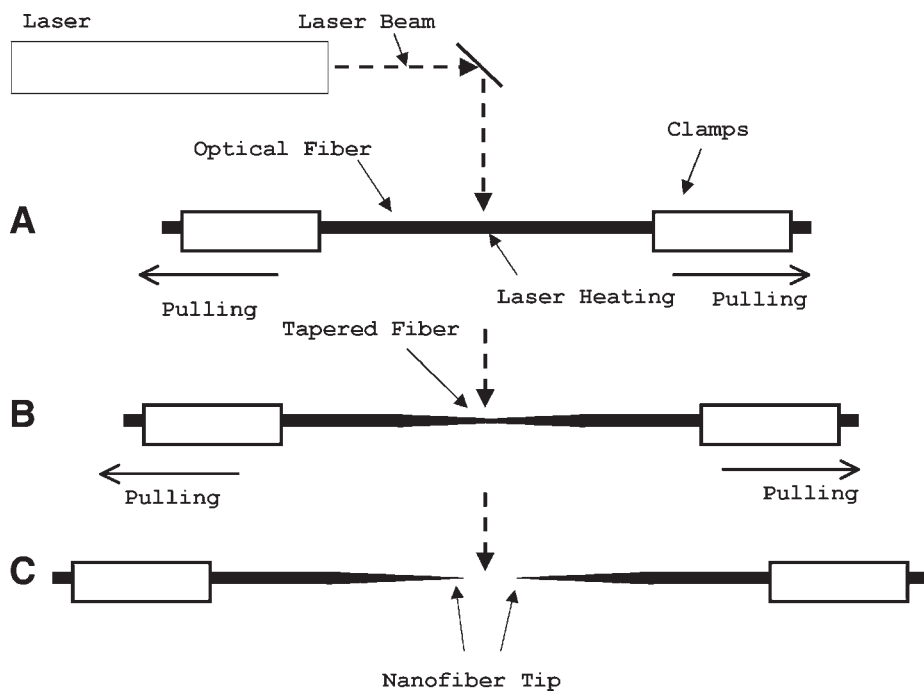


Fig. 2. Fabrication of nanofibers using heat-and-pull technique.

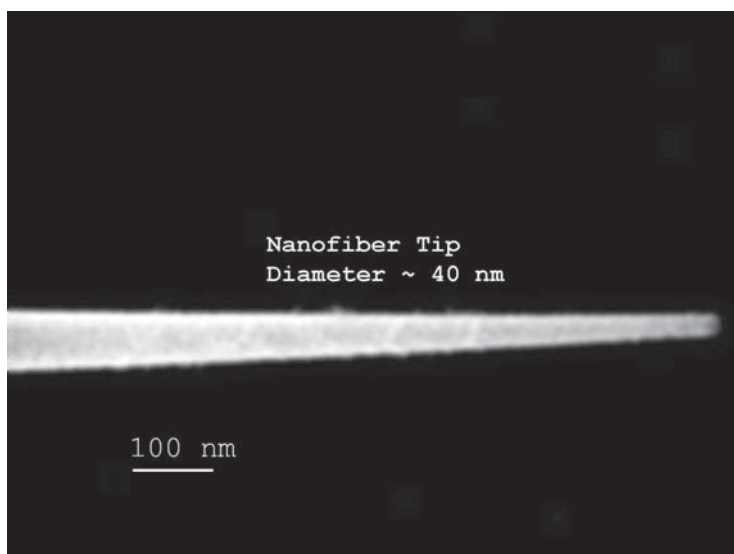


Fig. 3. Scanning electron micrograph of uncoated nanoprobe. The size of the fiber tip diameter is approx 40 nm.

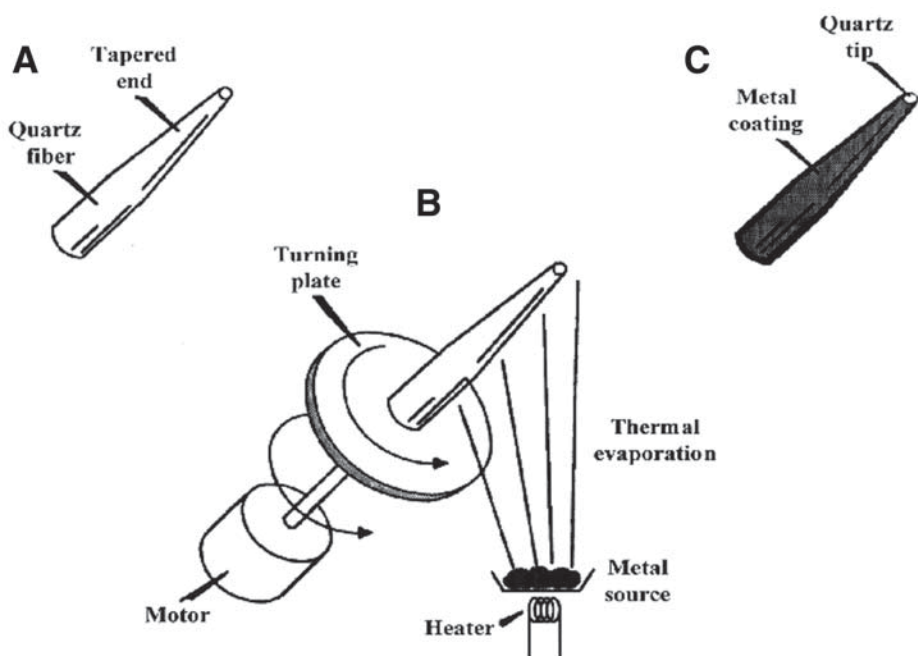


Fig. 4. Protocol used for coating nanofiber tip with silver: (A) uncoated fiber tip; (B) fiber coating using metal evaporation over rotating tip; (C) coated fiber. (From **ref. 21**.)

metal, such as silver, aluminum, or gold, using a thermal evaporation metal-coating device. The coating procedure is schematically illustrated in **Fig. 4 (21)**. The metal coating is only for the sidewall and leaves the distal end of the fiber free for subsequent binding with bioreceptors. The fiber probe is attached to a rotating plate inside a thermal evaporation chamber (**4,19,21**). The fiber axis and the evaporation direction form an angle of approx  $45^\circ$ . While the probe is rotated, the metal is allowed to evaporate onto the tapered side of the fiber tip to form a thin coating. The tapered end is coated with 300 to 400 nm of silver in a Cooke Vacuum Evaporator system using a thermal source at  $10^{-6}$  torr. Since the fiber tip is pointed away from the metal source, it remains free from any metal coating. With the metal coating, the size of the probe tip is approx 250 to 300 nm (**Fig. 5**).

Another method for fabricating optical nanofibers involves chemical etching using HF. There are two variations of the HF etching method: one method involves the use of a mixture of HF acid and organic solvent, known as Turner etching (**26**); and the other uses only HF, known as tube etching (**27–29**). In the Turner method, a fiber is placed in the meniscus between the HF and the

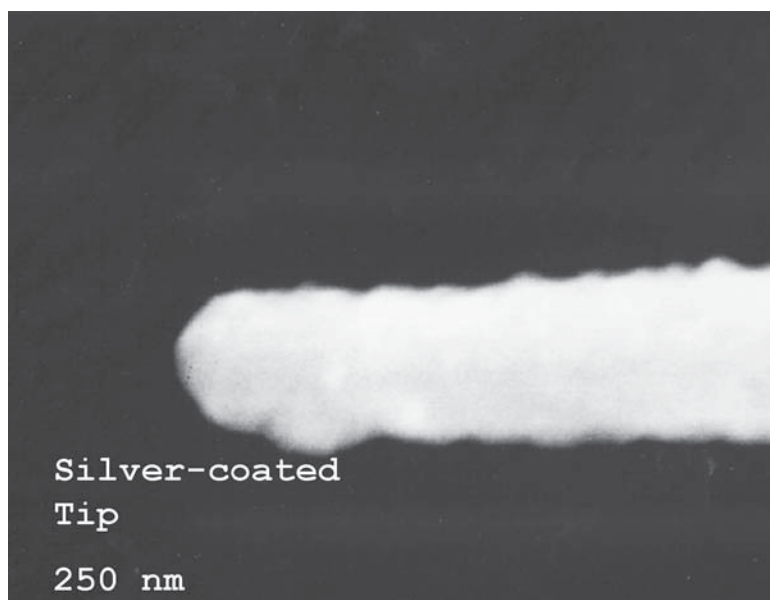


Fig. 5. Scanning electron micrograph of fiberoptics nanosensor with silver-coated sidewall.

organic overlayer; over time, a small tip with a smooth, large, angled taper is formed. This large taper angle provides much more light at the tip of the fiber, and the additional light, in turn, greatly increases the sensitivity of the nanosensors.

The reproducibility of the Turner method is strongly affected by environmental parameters such as temperature and vibration because of the dual chemical nature of the etching process. To avoid this problem, researchers developed a variation of the etching method involving tube etching. In this procedure, an optical fiber with a silica core and an organic cladding material is placed in an HF solution. The HF slowly dissolves the silica core, producing a fiber with a large taper angle and a nanometer-size tip. The HF begins first to dissolve the fiber's silica core, while not affecting the organic cladding material. This unaffected cladding creates localized convective currents in the HF solution, which cause a tip to be formed. After a period of time, more of the silica core is dissolved until the dissolved silica emerges above the surface of the HF solution. At this juncture, the HF is drawn up the cladding walls via capillary action and runs down the silica core to produce a nanometer-size tip. By varying the time of HF exposure and the depth to which the fiber is submerged in the HF solution, one can control the size of the fiber tip and the angle of the taper.

Once the tip has been formed, the protruding cladding can be removed either with a suitable organic solvent or by simply burning it off. Nanotips fabricated using etching procedures, which can be designed to have sharp tips, have been used in NSOM studies to detect SERS-labeled DNA molecules on solid substrates at subwavelength spatial resolution (12,13).

### **3.2. Immobilization of Bioreceptors Onto a Nanoprobe**

The preparation of nanosensor probes involves covalent immobilization of receptors onto the nanofiber tip. For antibody binding, several strategies can be used to retain the antibody at the sensing probe. Whatever procedure is involved, one requirement is that the antibody retain its antigen-binding activity as much as possible. Perhaps the easiest procedure involves enclosure of the antibody in solution within a semipermeable membrane cap that fits over the end of the sensor (2). However, this design is more complicated and would increase the size of the tip of the nanosensor.

Antibodies can be immobilized onto nanofiber probes by using a chemical immobilization method. The fiber is derivatized in 10% GOPS in H<sub>2</sub>O (v/v) at 90°C for 3 h. The pH of the mixture is maintained below 3.0 with concentrated HCl (1 M). After derivatization, the fiber is washed in ethanol and dried overnight in a vacuum oven at 105°C. The fiber is then coated with silver as described previously. The derivatized fiber is activated in a solution of 100 mg/mL of 1,1' carbonyldiimidazole in acetonitrile for 20 min, followed by rinsing with acetonitrile and then phosphate-buffered saline (PBS). The fiber tip is then incubated in a 1.2 mg/mL antibody solution (PBS solvent) for 4 d at 4°C and stored overnight in PBS to hydrolyze any unreacted sites. The fibers are stored at 4°C with the antibody-immobilized tips stored in PBS. This procedure has been shown to maintain >95% antibody activity (21).

### **3.3. Experimental Protocol**

This section provides a description of the protocols used for growing cell cultures for analysis using the nanosensors. Cell cultures were grown in a water-jacketed cell culture incubator at 37°C in an atmosphere of 5% CO<sub>2</sub> in air. Clone 9 cells, a rat liver epithelial cell line, were grown in Ham's F-12 medium (Gibco) supplemented with 10% fetal bovine serum and an additional 1 mM glutamine (Gibco). In preparation for an experiment,  $1 \times 10^5$  cells in 5 mL of medium were seeded into standard dishes (Corning Costar). Growth of the cells was monitored daily by microscopic observation. When the cells reached a state of confluence of 50 to 60%, the analyte solution was added and left in contact with the cells for 18 h (i.e., overnight). This procedure is designed to incubate the cells with the analyte molecules for subsequent monitoring using the nanosensors.

The growth conditions were chosen so that the cells would be in log phase growth during the chemical treatment but would not be so close to confluence that a confluent monolayer would form by the termination of the chemical exposure. The analyte solution was prepared as a 1 mM stock solution in reagent-grade methanol and further diluted in reagent-grade ethanol (95%) prior to addition to the cells. Following chemical treatment, the medium containing the analyte was aspirated and replaced with standard growth medium prior to the nanoprobe procedure.

Monitoring target analyte molecules in single cells was then performed using antibody nanoprobe as follows: a culture dish of cells was placed on a prewarmed microscope stage, and the nanoprobe, mounted on a micropipet holder, was moved into position (i.e., in the same plane as the cells), using bright-field microscopic illumination, so that the tip was outside the cell to be probed. The total magnification was usually  $\times 400$ . Under no room light and no microscopic illumination, the laser shutter was opened to illuminate the optical fiber for excitation of the analyte molecules bound on the antibodies at the fiber tip. Usually, if the silver coating on the nanoprobe was appropriate, no light leaked out of the sidewall of the tapered fiber. Only a faint glow of laser excitation at the tip could be observed on the nanoprobe. A reading was first taken with the nanoprobe outside the cell and the laser shutter closed. The nanoprobe was then moved into the cell, inside the cell membrane and extending into the cellular compartments of interest. The laser was again opened, and readings were taken and recorded as a function of the time during which the nanoprobe was inside the cell.

### **3.4. Optical Detection Instrument**

The optical detection system used for monitoring single cells with the nanosensor is schematically illustrated in **Fig. 6 (18–21)**. Laser excitation light (either the 325-nm line of an HeCd laser [Omnichrome; 8-mW laser power] or the 488-nm line of an argon ion laser [Coherent; 10 mW]) was focused onto a 600- $\mu\text{m}$  delivery fiber, which was connected to the nanofiber through an SMA connector. The nanofiber was secured to a micromanipulator on a microscope. The experimental setup used to probe single cells was adapted to this purpose from a standard micromanipulation/microinjection apparatus. A Nikon Diaphot 300 inverted microscope with a Diaphot 300/Diaphot 200 Incubator to maintain the cell cultures at approx 37°C on the microscope stage was used for these experiments. The micromanipulation equipment used consisted of MN-2 Narishige 3D manipulators for coarse adjustment, and Narishige MMW-23 3D hydraulic micromanipulators for final movements. The optical fiber nanoprobe was mounted on a micropipet holder (World Precision Instruments). The fluorescence emitted from the cells was collected by the microscope objective and

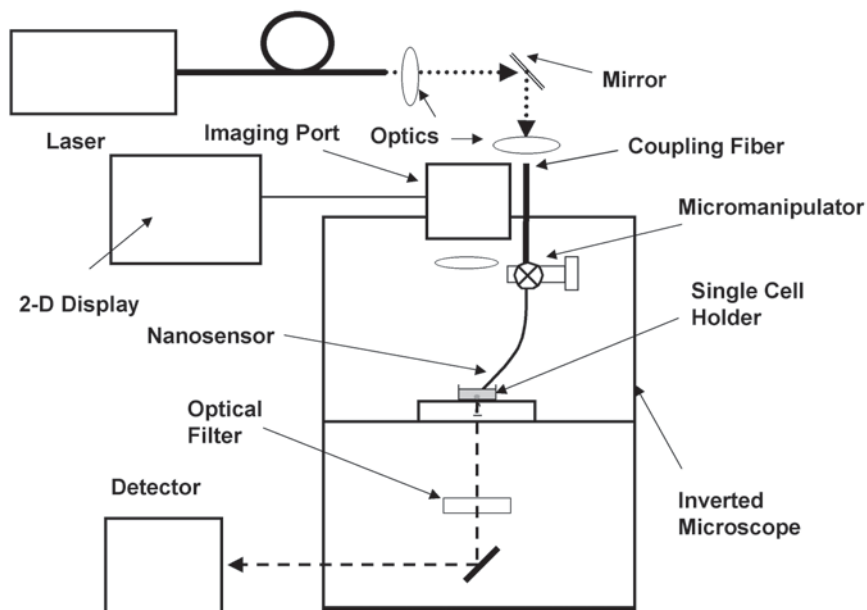


Fig. 6. Instrument using nanosensors for fluorescence measurements of single cells.

passed through an appropriate long-pass dichroic mirror to eliminate the laser excitation scatter light. The fluorescence beam was then focused onto a photomultiplier tube (PMT) for detection. The output from the PMT was passed through a picoammeter and recorded on a strip chart recorder or a personal computer for further data treatment. To record the fluorescence of analyte molecules binding to antibodies at the fiber tip, a Hamamatsu PMT detector assembly (HC125-2) was mounted in the front port of the Diaphot 300 microscope, and fluorescence was collected via this optical path (80% of available light at the focal plane can be collected through the front port). A CCD mounted onto another port of the microscope could be used to record images of the nanosensor monitoring single cells.

## 4. Applications

### 4.1. Monitoring Biomarkers in Single Living Cells

The nanoscale size of this new class of sensors allows for measurements in the smallest of environments. One such environment that has evoked a great deal of interest is that of individual cells. Using these nanosensors, it has become possible to probe individual chemical species in specific locations throughout a cell. Previously, such measurements could be performed only by

fluorescence microscopy, in which a fluorescent dye was inserted into a cell and allowed to diffuse throughout the cell. Depending on the fluorescent dye that was chosen, changes in the fluorescence properties of the dye could then be monitored, in an imaging modality, as the dye came in contact with the analyte of interest. Since this technique relies on imaging the fluorescent dye, it requires the homogeneous dispersion of the dye through the various locations in the cell, which is limited by intracellular conditions (e.g., pH) or often does not even occur owing to compartmentalization by the cell. Fiberoptic nanosensors, therefore, could offer significant improvements over such methods and eliminate the problems associated with cellular diffusion.

Nanosensors with antibody-based probes to measure specific fluorescent targets inside a single cell have been demonstrated (18–23). Because cells are very small (1–10  $\mu\text{m}$ ), the success of intracellular investigations depends on several factors, including the sensitivity of the measurement system, the selectivity of the probe, and the small size of the nanofiber probes. Vo-Dinh et al. (21) reported the smallest cells to be nondestructively probed with a fiberoptic nanobiosensor. In their work, the antibody probe was targeted for benzo[*a*]-pyrene tetrol (BPT), an important biological compound, which was used as a biomarker of human exposure to the carcinogen BaP, a polycyclic aromatic hydrocarbon of great environmental and toxicological interest because of its mutagenic/carcinogenic properties and its ubiquitous presence in the environment. BaP has been identified as a chemical carcinogen in laboratory animal studies. The small size of the probe allowed manipulation of the nanosensor at specific locations within the cells. Before measurements, the cells were incubated with BPT using the experimental procedures described previously. Interrogation of single cells for the presence of BPT was then carried out using antibody nanoprobe for excitation and a photometric system for fluorescence signal detection.

Nanosensors for BPT were used to measure the intracellular concentrations of BPT in the cytoplasm of two different cell lines: human mammary carcinoma cells and rat liver epithelial cells (Clone 9). The rat liver epithelial cells were used as the model cell system after treatment of the culturing media with an excess of BPT. **Figure 7** shows a digital image of the nanosensor actually being inserted into a single human mammary carcinoma cell. The results demonstrated the possibility of *in situ* measurements of BPT inside a single cell.

Note that these nanosensors were equipped with single-use bioprobes because the probes were used to obtain only one measurement at a specific time and could not be reused owing to the strong association constant of the antibody-antigen binding process. Antibody probes can be regenerated, however, using ultrasound methods. Our laboratory has successfully developed a method using ultrasound (US) to noninvasively release antigen molecules from





Fig. 7. Monitoring of single human mammary carcinoma cell using fiberoptic nanosensor.

the antibodies and therefore regenerate antibody-based biosensors (30). The results of measurements with an antibody probe for the breast cancer antigen illustrate the effectiveness and the potential of the regenerable immunosensor. In this instance, US regeneration attained a 65% removal of the antigens bound to the monoclonal antibodies immobilized on the fiber surface. The US regeneration scheme is a nondestructive approach that has a great potential for application to nanosensors. The results demonstrate the effectiveness of this US-based approach in releasing the antigen from the antibody probe.

We have performed multiple calibration measurements of solutions containing different BPT concentrations to obtain quantitative estimates of the number of BPT molecules detected. Up to five recordings of the fluorescence signals could be taken with each measurement using a specific nanoprobe. For these calibration measurements, the fibers were placed in Petri dishes containing solutions of BPT with concentrations ranging from  $1.56 \times 10^{-10}$  to  $1.56 \times 10^{-8}$  M. By plotting the increase in fluorescence from one concentration to the next vs the concentration of BPT, and fitting these data with an exponential function in order to simulate a saturated condition, we determined a concentration of  $(9.6 \pm 0.2) \times 10^{-11}$  M for BPT in the individual cell investigated (17–21).

Nanosensors were also developed for *in situ* measurements of the carcinogen BaP (30). Detection of BaP transport inside single cells is of great biomedical interest, because it can serve as a means for monitoring BaP exposure,

which can lead to DNA damage (28). To perform these measurements, it was necessary to use antibodies targeted to BaP. The fluorescent BaP molecules were bound by interaction with the immobilized antibody receptor, forming a receptor-ligand complex. Following laser excitation of this complex, a fluorescence response from BaP provided a basis for the quantification of BaP concentration in the cell being monitored. The fluorescence signal generated allows for a high sensitivity of detection. The intracellular measurements of BaP depend on the reaction times involved. The reaction time established in this study for antibody-BaP complexing was 5 min. This was used as a standard time to enable calibration from fiber to fiber. In addition, the nanosensors were calibrated through standard analytical procedures using measurements of known concentration of reference solutions.

#### ***4.2. Detection of Caspase Proteins Signaling Apoptosis in Single Living Cells***

Over the last few years, there has been increasing interest in developing instruments and techniques for monitoring the onset of apoptosis in living cells. It has become increasingly apparent that the mitochondria play a major role in the apoptosis process. The key mitochondrial components regulating apoptosis exert their effects at two control points—the permeability transition pore complex (PTPC) situated at points where the inner and outer mitochondrial membranes come into close proximity, and the apoptosome located just outside the mitochondria. As shown in **Fig. 8**, anticancer drugs often induce apoptosis in cells, acting on the PTPC to induce the release of proapoptotic factors from the mitochondria. These factors stimulate the assembly of the apoptosome and the subsequent activation of the initiator caspase-9 and effector caspase-3, leading to apoptosis. The apoptosome is a major control point where caspase-9 and caspase-3 interact and activate one another. Caspase-9 processes caspase-3 at the apoptosome, thereby activating it. A feedback loop, in which processed caspase-3 cleaves and activates caspase-9, amplifies the production of activated caspases. A second positive feedback loop links the apoptosome and PTPC. Caspase-3 cleaves a number of components of the mitochondrial electron transport chain. These operations trigger the stepped-up production of reactive oxygen species (ROS) and efflux of cytochrome-c, which then acts at the apoptosome to amplify the amount of activated caspase-9 and caspase-3.

We have performed measurements to investigate the application and utility of nanosensors for monitoring the onset of the mitochondrial pathway of apoptosis in a single living cell by detecting enzymatic activities of caspase-9 (24). Minimally invasive analysis of single live MCF-7 cells for caspase-9 activity was demonstrated using the optical nanosensor, which employed a modification of an immunochemical assay format for the immobilization of

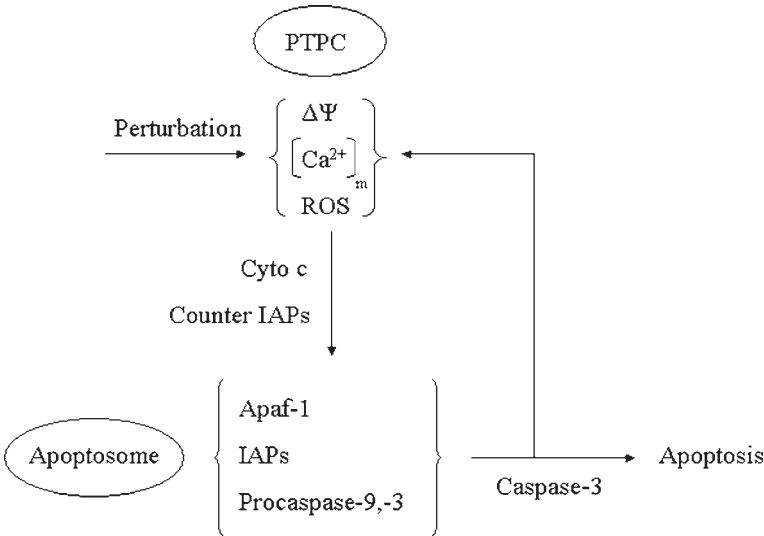


Fig. 8. Schematic diagram of mitochondrial apoptosis control unit.

the nonfluorescent enzyme substrate leucine-glutamic acid-histidine-aspartic acid-7-amino-4-methyl coumarin (LEHD-AMC). LEHD-AMC covalently attached to the tip of an optical nanosensor was cleaved during apoptosis by caspase-9, generating free AMC. An evanescent field was used to excite cleaved AMC, and the resulting fluorescence signal was detected. By quantitatively monitoring the changes in fluorescence signals, we detected caspase-9 activity within a single living MCF-7 cell. Photodynamic therapy protocols employing  $\delta$ -aminolevulinic acid (ALA) were used to induce apoptosis (32) in MCF-7 cells. The substrate LEHD-AMC was cleaved by caspase-9, and the released AMC molecules were excited and emitted a fluorescence signal. By comparing the fluorescence from an apoptotic cell and an uninduced control, we detected and identified caspase-9 activity.

The results show that for the treated control group of cells, the fluorescence signal relative to the experimental group was insignificant. The fluorescence signals obtained from the cells that were both incubated with ALA and photoactivated were much higher than the signal obtained from both control groups. The presence and detection of cleaved AMC in single live MCF-7 cells as a result of these experiments is representative of caspase-9 activity and a hallmark of apoptosis. These results indicate that AMC, and hence apoptosis, can be monitored and measured using optical nanosensors within single living cells. These studies show the possibility of studying cells without having to disrupt the physiological makeup and, in the process, interfere with cellular biochemistry.

## 5. Conclusion

The nanosensor technologies described in this chapter belong to a new generation of nanotools that could dramatically change our fundamental understanding of the life process itself. Dynamic information on signaling processes inside living cells is important to a fundamental understanding of cellular processes. Many traditional microscopy techniques involve incubating cells with fluorescent dyes or nanoparticles and examining the interaction of these dyes with compounds of interest. However, when a dye or nanoparticle is incubated into a cell, it is transported to intracellular sites that may or may not be where it is most likely to stay and not to areas that the investigator would like to monitor. The fluorescence signals, which are supposed to reflect the interaction of the dyes with chemicals of interest, are generally directly related to dye concentration as opposed to analyte concentration. Only with optical nanosensors can excitation light be delivered to specific locations inside cells. To date, the nanosensor is the only technology that can be used to measure biotargets in a living cell without affecting cell viability. Combined with the exquisite molecular recognition of antibody probes, nanosensors have great potential to serve as powerful tools for exploring biomolecular processes in the subcompartments of living cells.

Nanosensors could ultimately lead to the development of new modalities for early diagnostics and medical treatment and prevention beyond the cellular level to that of individual organelles and even DNA, the building block of life. Today, research in biomedical science and engineering at the molecular level is growing exponentially because of the availability of these new investigative nanotools. These new analytical tools are capable of probing the nanometer world and will make it possible to characterize the chemical and mechanical properties of cells, probe the working of molecular protein machines, and discover novel phenomena and processes and also will provide science with a wide range of tools, materials, devices, and systems with unique capabilities. The marriage of genomics, electronics, biomaterials, and photonics is expected to revolutionize many areas of medicine in the twenty-first century. This ultimate technology convergence will open new horizons for the discovery of new tools and biomarkers for detection, diagnosis, and prevention studies, and new targets for therapeutic development.

## Acknowledgments

I acknowledge the contributions of G. D. Griffin, J. P. Alarie, B. M. Cullum, and P. Kasili. This research was sponsored by the LDRD Project (Advanced Nanosensors), and by the US Department of Energy. Oak Ridge National Laboratory is managed for the Department of Energy by UT-Battelle, LLC, under contract DE-AC05-00OR22725.

## References

1. Zandonella, C. (2003) The tiny tool kit. *Nature* **423**, 10–12.
2. Vo-Dinh, T., Tromberg, B. J., Griffin, G. D., Ambrose, K. R., Sepaniak, M. J., and Gardenhire, E. M. (1987) Antibody-based fiberoptics biosensor for the carcinogen benzo(a)pyrene. *Appl. Spectrosc.* **41(5)**, 735–738.
3. Vo-Dinh, T. G. G. D. and Sepaniak, M. J. (1991) Optical antibody biosensor, in *Fiber Optic Chemical Sensors and Biosensors* (Wolfbeis, O. S., eds.), CRC Press, Boca Raton, FL, pp. 217–257.
4. Vo-Dinh, T., Sepaniak, M. J., Griffin, G. D., and Alarie, J. P. (1993) Immunosensors: principles and applications. *Immunomethods* **3**, 85–90.
5. Alarie, J. P. and Vo-Dinh, T. (1996) Antibody-based submicron biosensor for benzo a pyrene DNA adduct. *Polycyclic Aromatic Compounds* **8(1)**, 45–52.
6. Alarie J. P. and Vo-Dinh, T. (1991) A fiber optic cyclodextrin-based sensor. *Talanta* **38**, 529–534.
7. Tromberg, B. J., Sepaniak, M. J., Alarie, J. P., Vo-Dinh, T., and Santella, S. M. (1998) Development of antibody-based fiberoptics sensor for the detection of benzo(a)pyrene metabolite. *Anal. Chem.* **60**, 1901–1905.
8. Alarie, J. P., Bowyer, J. R., Sepaniak, M. J., Hoyt, A. M., and Vo-Dinh, T. (1990) Fluorescence monitoring of benzo(a)pyrene metabolite using a regenerable immunochemical-based fiber optic sensor. *Anal. Chim. Acta* **236**, 237–243.
9. Bowyer, J. R. Alarie, J. P., Sepaniak, M. J., Vo-Dinh, T., and Thompson, R. Q. (1991) Construction and evaluation of regenerable, fluoroimmunochemical-based fiber optic biosensor. *Analyst* **116**, 117.
10. Pohl, D. W. (1984) Scanning near-field optical microscopy, in *Advances in Optical and Electron Microscopy* (Sheppard, C. J. R. a. M., T., ed.), Academic, London.
11. Betzig, E. and Chichester, R. J. (1993) Single molecules observed by near-field scanning optical microscopy. *Science* **262(5138)**, 1422–1425.
12. Zeisel, D., Deckert, V., Zenobi, R., and Vo-Dinh, T. (1998) Near-field surface-enhanced Raman spectroscopy of dye molecules adsorbed on silver island films. *Chem. Phys. Lett.* **283(5–6)**, 381–385.
13. Deckert, V., Zeisel, D., Zenobi, R., and Vo-Dinh, T. (1998) Near-field surface enhanced Raman imaging of dye-labeled DNA with 100-nm resolution. *Anal. Chem.* **70(13)**, 2646–2650.
14. Tan, W. H., Shi, Z. Y., and Kopelman, R. (1992) Development of submicron chemical fiber optic sensors. *Anal. Chem.* **64(23)**, 2985–2990.
15. Tan, W. H., Shi, Z. Y., Smith, S., Birnbaum, D., and Kopelman, R. (1992) Submicrometer intracellular chemical optical fiber sensors. *Science* **258(5083)**, 778–781.
16. Cullum, B. M., Griffin, G. D., Miller, G. H., and Vo-Dinh, T. (2000) Intracellular measurements in mammary carcinoma cells using fiber-optic nanosensors. *Anal. Biochem.* **277(1)**, 25–32.
17. Vo-Dinh, T. G. G. D., Alarie, J. P., Cullum, B. M., Sumpter, B., and Noid, D. (2000) Development of nanosensors and bioprobes. *J. Nanoparticle Res.* **2**, 17.

18. Vo-Dinh, T. and Cullum, B. (2000) Biosensors and biochips: advances in biological and medical diagnostics. *Fresenius J. Anal. Chem.* **366**(6–7), 540–551.
19. Cullum, B. M. and Vo-Dinh, T. (2000) The development of optical nanosensors for biological measurements. *Trends Biotechnol.* **18**(9), 388–393.
20. Vo-Dinh, T., Cullum, B. M., and Stokes, D. L. (2001) Nanosensors and biochips: frontiers in biomolecular diagnostics. *Sens. Actuators B* **74**, 2.
21. Vo-Dinh, T., Alarie, J. P., Cullum, B. M., and Griffin, G. D. (2000) Antibody-based nanoprobe for measurement of a fluorescent analyte in a single cell. *Nat. Biotechnol.* **18**(7), 764–767.
22. Vo-Dinh, T. (2003) Nanobiosensors: probing the sanctuary of individual cells. *J. Cell. Biochem. Suppl.* **39**, 154–161.
23. Kasili, P. M., Cullum, B. M., Griffin, G. D., and Vo-Dinh, T. (2002) Nanosensor for in-vivo measurement of the carcinogen benzo [a] pyrene in a single cell. *J. Nanosci. Nanotechnol.* **6**, 653.
24. Kasili, P. M., Song, J. M., and Vo-Dinh, T. (2004) Optical sensor for the detection activity of caspase 9 in a single cell. *J. Am. Chem. Soc.*, in press.
25. Vo-Dinh, T. (1998) Surface-enhanced Raman spectroscopy using metallic nanostructures. *Trends Anal. Chem.* **17**, 557.
26. Turner, D. R. (1984) US patent no. 4,469,554.
27. Hoffmann, P., Dutoit, B., and Salathe, R. P. (1995) Comparison of mechanically drawn and protection layer chemically etched optical fiber tips. *Ultramicroscopy* **61**(1–4), 165–170.
28. Lambelet, P., Sayah, A., Pfeffer, M., Philipona, C., and Marquis-Weible F. (1998) Chemically etched fiber tips for near-field optical microscopy: a process for smoother tips. *Appl. Opt.* **37**, 7289–7292.
29. Stockle, R., Fokas, C., Deckert, V., Zenobi, R., Sick, B., Hecht, B., and Wild, U. P. (1999) High-quality near-field optical probes by tube etching. *Appl. Phys. Lett.* **75**(2), 160–162.
30. Morena-Bondi, M., Mobley, J., Alarie, J. P., and Vo-Dinh, T. (2000) Antibody-based biosensor for breast cancer with ultrasonic regeneration. *J. Biomed. Opt.* **5**(3), 350.
31. Ricci, J. E., Gottlieb, R. A., and Green, D. R. (2003) Caspase-mediated loss of mitochondrial function and generation of reactive oxygen species during apoptosis. *J. Cell Biol.* **160**, 65–75.
32. Hengartner, M. O. (2002) Apoptosis—DNA destroyers. *Nature* **412**, 27–29.





## Nanoelectrodes Integrated in Atomic Force Microscopy Cantilevers for Imaging of *In Situ* Enzyme Activity

Angelika Kueng, Christine Kranz, Alois Lugstein, Emmerich Bertagnolli, and Boris Mizaikoff

### Summary

For investigation of laterally resolved information on biological activity, techniques for simultaneously obtaining complementary information correlated in time and space are required. In this context, recent developments in scanning probe microscopy are aimed at information on the sample topography and simultaneously on the physical and chemical properties at the nanometer scale. With the integration of submicro- and nanoelectrodes into atomic force microscopy (AFM) probes using microfabrication techniques, an elegant approach combining scanning electrochemical microscopy with AFM is demonstrated. This instrumentation enables simultaneous imaging of topography and obtainment of laterally resolved electrochemical information in AFM tapping mode. Hence, topographical and electrochemical information on soft surfaces (e.g., biological species) and polymers can be obtained. The functionality of tip-integrated electrodes is demonstrated by simultaneous electrochemical and topographical studies of an enzyme-modified micropattern.

**Key Words:** Scanning electrochemical microscopy; atomic force microscopy; enzyme activity; tapping mode; bifunctional scanning probe tips.

### 1. Introduction

Recent developments in the combination of scanning probe techniques are aimed at complementary, simultaneously obtained information about physical and chemical surface properties with high spatial resolution. Because many biochemically relevant processes are based on redox chemistry and electrochemical conversion of molecules, techniques gathering laterally resolved information on coupled oxidation-reduction processes are of particular interest. The combination of atomic force microscopy (AFM) (*1*) with scanning

From: *Methods in Molecular Biology*, vol. 300:  
*Protein Nanotechnology, Protocols, Instrumentation, and Applications*  
Edited by: T. Vo-Dinh © Humana Press Inc., Totowa, NJ

electrochemical microscopy (SECM) (2–4) is a particularly attractive strategy for achieving complementary electrochemical and topographical information with high lateral resolution in a single time- and space-correlated measurement (5). Microfabrication including focused ion beam (FIB) technology of submicro- and nanoelectrodes integrated into conventional AFM tips is an elegant and versatile approach combining SECM and AFM (6,7). The terms AFM and SECM are used for the instrument as well as the technique. An electroactive area is integrated at an exactly defined distance above the apex of the AFM tip (8), enabling contact mode and tapping mode operation (9). Application of AFM tapping mode (10) is a prerequisite for successfully imaging soft biological samples or polymers (11–13).

To illustrate the functionality and capability of this method, bifunctional probes with integrated electrodes are applied to simultaneously image topographical and electrochemical properties of a biologically active sample in AFM tapping mode. As an example, the activity of the oxidoreductase glucose oxidase immobilized at a periodic micropattern of a soft polymer matrix is electrochemically imaged during mapping of the topography (14). This concept is currently extended to AFM tip-integrated electrochemical biosensors for biomedical applications (15–17).

## 2. Materials

1. Atomic force microscope equipped with a tapping mode liquid cell (e.g., Nanoscope III; Digital Instruments, Santa Barbara, CA).
2. Bipotentiostat (Model 832A, CH-Instrument, Austin, TX).
3. FIB system.
4. DC-sputterer equipped with a Ti target.
5. RF-sputterer equipped with an Au or Pt target.
6. Vapor deposition polymerization (VDP) system or plasma-enhanced chemical vapor deposition (PECVD).
7. Silicon nitride AFM cantilevers with a length of 200  $\mu\text{m}$ , an integrated pyramidal tip (base:  $4 \times 4 \mu\text{m}$ ; height: 2.86  $\mu\text{m}$ ), and a spring constant of approx 0.06  $\text{Nm}^{-1}$ .
8. Micropatterned gold/silicon nitride sample (Quantifoil, Jena, Germany).
9. Chloro-*p*-xylylene (parylene C).
10. Pt wire (diameter: 1 mm) as counterelectrode.
11. Ag/AgCl reference electrode or oxidized Ag wire (diameter: 1 mm) serving as a quasireference electrode (AgQRef).
12. Insulating varnish (RS Components, Northants UK).
13. Glucose oxidase (150,000 U/g, solid, from *Aspergillus niger*); store at  $-20^\circ\text{C}$ .
14. Potassium ferrocyanide.
15. Potassium chloride.
16. 0.1 M Phosphate buffer (pH 7.0); store at  $4^\circ\text{C}$ .
17. Glucose.
18. EDP, Elektrodepositionslack Glassphor ZQ 8-43225, Canguard (BASF Farben und Lacke, Münster, Germany).

### 3. Methods

#### 3.1. Preparation of AFM-SECM Tip

The steps described in **Subheadings 3.1.1.–3.1.3.** outline the procedure for preparation of the AFM-SECM tip including the metallization and insulation of the cantilever, the FIB cutting process to expose the electroactive area, and the characterization of the tip-integrated electrodes.

##### 3.1.1. Metallization and Insulation of AFM Cantilevers

The silicon nitride AFM cantilevers were DC sputtered (CVC Products) with a 3-nm Ti adhesion layer (working pressure: 6 mtorr; power: 350 W; under argon). Subsequently, a 100-nm uniform gold layer was deposited using an RF-sputterer (working pressure: 6 mtorr; power: 150 W; under argon) to minimize mechanical stress on the cantilevers (*see Note 1*). To insulate the gold-coated cantilever, 700 nm of parylene C was deposited by VDP (*see Note 2*) (**18**). The polymerization process includes the following steps:

1. Initial vaporization at 150°C, 1.0 torr.
2. Cleaving into monomeric radicals by pyrolysis at 680°C, 0.5 torr.
3. Adsorption of the monomeric radical onto the sample (cantilever) surface and simultaneous polymerization.

##### 3.1.2. FIB Milling of AFM-SECM Cantilevers

**Figure 1** schematically illustrates the fabrication steps of an integrated frame microelectrode along with the FIB images of the milling processes. All modifications were carried out in a two-lens FIB system (Micrion 2500) utilizing a beam of Ga<sup>+</sup> ions at 50 keV.

**Figure 1A** shows the cantilever after coating with the metal layer and the insulation layer. The first FIB-milling step, diametrically opposed cuttings, as illustrated in **Fig. 1B**, determines the size of the integrated microelectrode. The same cutting procedure was repeated in a second step at the frontal areas of the pyramidal tip after a 90° turn of the cantilever (**Fig. 1C**). The following milling step (**Fig. 1D**) comprises reshaping the AFM tip and adjusting its length in correlation with the integrated electrode area. For optimum current responses according to SECM theory (**19**), the reshaped AFM tip (tip-substrate separation) should be  $<0.7 \times$  electrode edge length (**Fig. 1F**). This milling step must be repeated again at the side and the frontal areas of the pillar to reshape the nonconducting original AFM tip. **Figure 1E** shows the integrated microelectrode after a final single-pass milling step to remove accumulated material resulting from previous cutting steps from the electroactive surface. Because of the reshaped AFM tip, this procedure ensures high resolution in topography and a precisely defined and constant distance between the integrated electrode

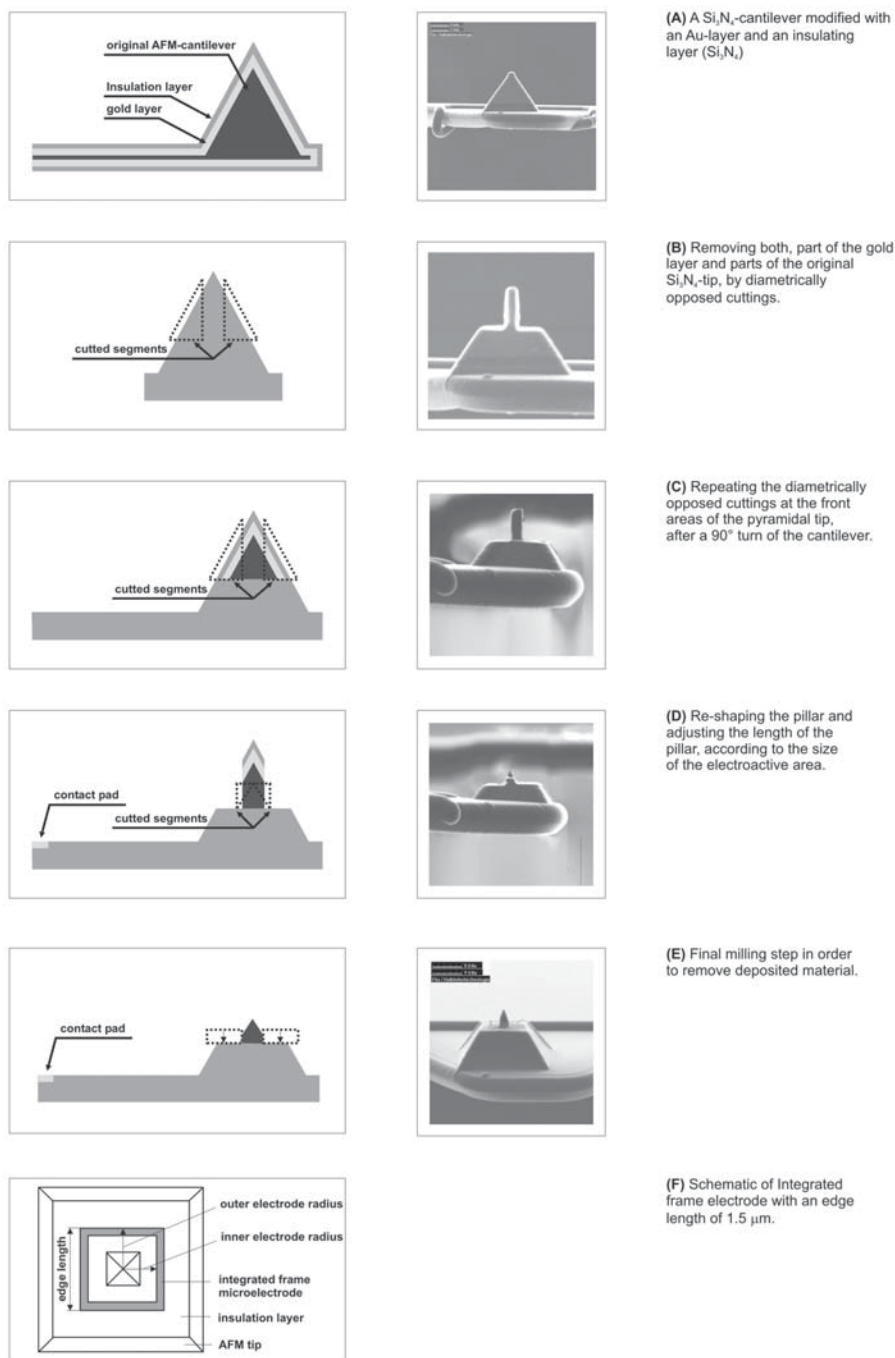


Fig. 1. (A–F) Modification steps of coated AFM tip using FIB technique showing (left) schematic view of processing step and (right) corresponding FIB images. (From ref. 6 with permission.)

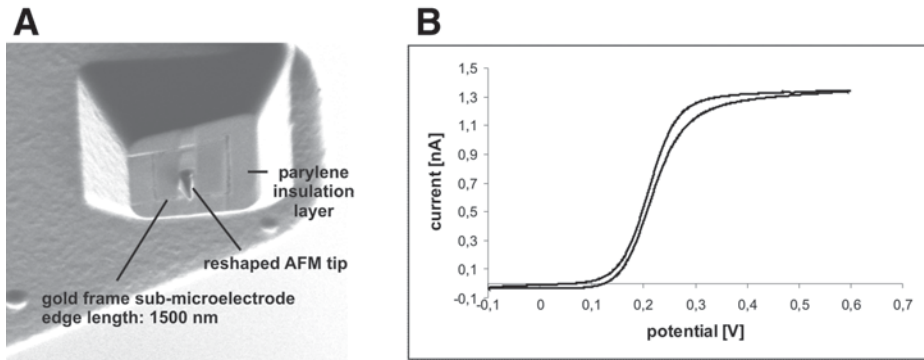


Fig. 2. (A) FIB images of integrated frame submicroelectrode with edge length of 1500 nm and tip height of 800 nm; (B) cyclic voltammogram recorded at this frame submicroelectrode for oxidation of 0.01 mol/L of  $K_4[Fe(CN)_6]$  in 0.5 mol/L of KCl (scan rate: 100 mV/s).

and the sample surface within the working distance for electrochemical imaging of the surface properties.

### 3.1.3. Electrochemical Characterization of Tip-Integrated Frame Microelectrodes

Electrochemical characterization of the integrated microelectrodes was done by cyclic voltammetry using 0.01 mol/L of  $K_4[Fe(CN)_6]$  in 0.5 mol/L of KCl as a supporting electrolyte (**Fig. 2B**). Currently, no theoretical description for square-frame electrode geometries is available in the literature. Development of a suitable theory is in progress. Hence, the theoretical description of ring microelectrodes was used for characterization of the electrochemical behavior. The steady-state current response of a ring microelectrode can be described using **Eqs. 1–3 (20,21)**:

$$I_d = nFDc^* l_0 \quad (1)$$

in which

$$l_0 = \frac{\pi^2(a+b)}{\ln[16(a+b)/(b-a)]} \quad (2)$$

for  $a/b > 0.91$ , and

$$l_0 = \frac{\pi^2(a+b)}{\ln[32a/(b-a) + \exp(\pi^2/4)]} \quad (3)$$

for all other ratios  $a/b$ . In **Eqs. 1–3**,  $D$  and  $c^*$  are the diffusion coefficient and the bulk concentration of the redox mediator, respectively;  $F$  is the Faraday constant;  $n$  is the number of transferred electrons;  $a$  is the inner electrode radius; and  $b$  is the outer electrode radius (see **Fig. 1F**). Based on **Eqs. 1** and **2**, the theoretical steady-state current for the oxidation of 0.01 mol/L of  $[\text{Fe}(\text{CN})_6]^{4-}$  with  $n = 1$  for the cyclic voltammogram of the frame microelectrode shown in **Fig. 2A** (inner radius  $a = 650$  nm; outer radius  $b = 750$  nm; ratio  $a/b = 0.867$ ) is calculated to be 1.65 nA (diffusion coefficient:  $6.7 \times 10^{-6}$  cm<sup>2</sup>/s [4]). The experimentally observed steady-state current is 1.4 nA. However, it has to be considered that the diffusion behavior towards a frame electrode differs from the ring geometry owing to additional effects occurring at the edges of the frame geometry.

### 3.2. Preparation of Sample

The simultaneous imaging of the topographical and electrochemical properties of a soft biological sample with bifunctional AFM-SECM probes is described. As a test sample, the pores of a periodic microstructure were filled with a soft polymer matrix entrapping the enzyme glucose oxidase (**14**) (see **Note 3**).

**Figure 3** illustrates the fabrication steps of the sample surface along with AFM images. A periodically micropatterned silicon nitride layer (450-nm layer thickness) was deposited onto a gold-coated silicon wafer (see **Note 4**). The conductive gold layer was used as a working electrode to electrochemically deposit the glucose oxidase-containing polymer films based on pH shift-induced precipitation (**Fig. 3A,B**) (**22**). A solution containing glucose oxidase (5 mg/mL of water) and Canguard polymer suspension (70  $\mu\text{L}$ /mL of water) was stored for at least 30 min at 4°C before it was used. A three-electrode setup was used with an oxidized silver wire operating as the AgQRef, a platinum wire as the auxiliary electrode, and the conductive gold layer of the micropattern as the working electrode. For polymer film formation with the enzyme present in solution, a potential-pulse profile (2200 mV for 0.2 s, 800 mV for 1 s, and 0 mV for 5 s vs AgQRef) was applied 12 times, leading to the precipitation of the polymer in the pores entrapping the enzyme. The sample was rinsed with water and phosphate buffer and stored for at least 12 h at 4°C before analysis with AFM-SECM.

### 3.3. Simultaneous Topographical and Electrochemical Imaging of Enzyme Activity

The experimental setup and the parameters for AFM-SECM imaging of enzyme activity are described in **Subheadings 3.3.1–3.3.4**. This includes a description of the instrumentation, the parameters chosen for AFM tapping mode, and the parameters for simultaneous electrochemical imaging.

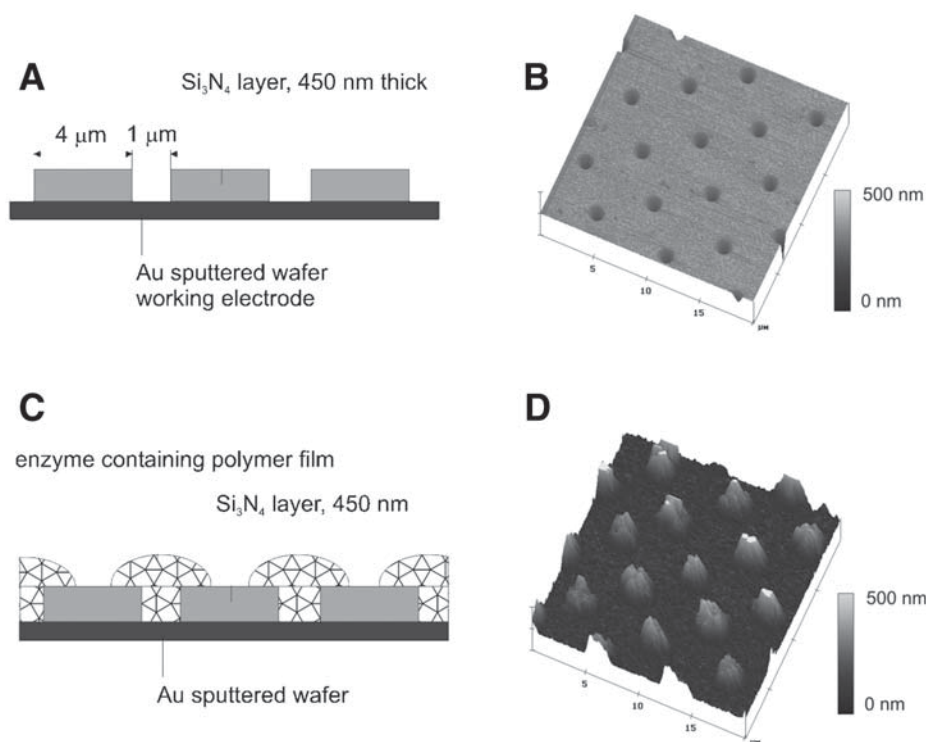


Fig. 3. Schematic view of sample and corresponding AFM contact mode images (A,B) before and (C,D) after precipitation of enzyme containing polymer film.

### 3.3.1. Instrumentation: Experimental Setup

The modified tip was mounted into a Nanoscope III, equipped with a tapping mode fluid cell using the liquid inlet and outlet for positioning a Pt wire as the counterelectrode and an oxidized Ag wire as the AgQRef. The electrical contact for the integrated electrode is provided by the gold spring holding the cantilever in the fluid cell. The spring is pressed onto a small exposed area of the gold layer at the end of the cantilever mount. The contact window was opened by mechanically scratching the insulation layer with a needle or tweezers with sharp, pointy ends. After contacting, the cantilever mount was protected by an insulation varnish applied with a fine microbrush.

An overview of the experimental setup is shown in **Fig. 4**. The electrochemical experiment is controlled with a bipotentiostat, and the electrochemical signal is read into an additional AD channel of the AFM instrument, which is provided by all conventional atomic force microscopes (*see Note 5*). Thus, the current measured with the integrated electrode can be directly correlated to the topographical information obtained by the reshaped AFM tip.





### 3.3.2. Tapping Mode Imaging

For simultaneous topographical and electrochemical imaging of the enzyme activity, the integrated electrode is scanned over the sample surface in AFM tapping mode using the DI tapping mode liquid cell filled with air-saturated phosphate buffer. The parameters for AFM tapping mode imaging are as follows:

1. Drive frequency: 32.4 V (*see Note 6*).
2. Drive amplitude: 5 V (*see Note 7*).
3. Scan rate: 2 Hz (*see Note 8*).
4. Set point: 0.6 V (*see Note 9*).
5. Sampling rate:  $256 \times 256$ .

The integral gain and proportional gain should be optimized for every measurement so that the height image shows the sharpest contrast and there are minimal variations in the amplitude image (the error signal).

### 3.3.3. Electrochemical Imaging

For localized detection of glucose oxidase activity, the generation-collection mode of SECM (**23**) has been applied. In the presence of the substrate glucose,  $\text{H}_2\text{O}_2$  is locally generated as a byproduct of the enzymatic reaction. Glucose oxidase catalyzes the oxidation of glucose to gluconolactone, and the electron acceptor oxygen of the enzymatic reaction is reduced to  $\text{H}_2\text{O}_2$  (**Fig. 4B**).  $\text{H}_2\text{O}_2$  is directly detected at the integrated electrode using amperometry at a constant applied potential of 750 mV vs AgQRef. A schematic of the involved reactions and the measurement principle is given in **Fig. 4B**.

The parameters for electrochemical imaging are as follows:

1. Technique: amperometry.
2. Counterelectrode: Pt wire.
3. Quasi-reference electrode: oxidized Ag wire.
4. Tip potential: 750 mV vs AgQRef.
5. Sample interval: 0.0025 s.
6. Liquid: for negative control, phosphate buffer (0.1 M, pH 7.0), air saturated; for positive control, add 50 mM glucose.

### 3.3.4. Simultaneous AFM-SECM Imaging

The tip was engaged to the surface and the image quality optimized (*see Subheading 3.3.1.*) showing the topographic features of the polymer spots. Subsequently, the potential was applied to the integrated electrode and the current was recorded as a negative control image (**Fig. 5A–C**). In the absence of glucose in solution, the current recorded at the electrode during AFM tapping mode imaging of the enzyme containing polymer spots was negligible and

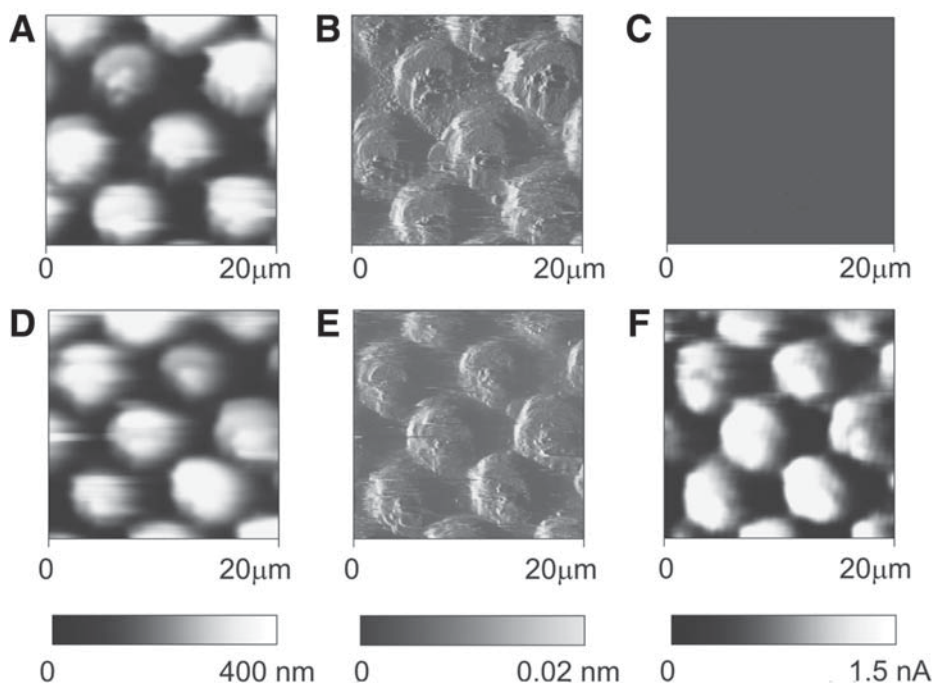


Fig. 5. Simultaneously recorded height and current images of glucose oxidase activity in AFM tapping mode with free-drive amplitude of 5 V and drive frequency of 32.4 kHz. Top view of the height (**A,D**), corresponding amplitude (**B,E**), and simultaneously recorded current (**C,F**) images recorded in air-saturated phosphate buffer (0.1 mol/L, pH 7.4) in the absence (**A–C**) and presence (**D–F**) (50 mM) of the substrate glucose in solution is shown. The tip was held at a potential of 750 mV vs AgQRef. Electrode edge length: 770 nm; tip height: 700 nm. (From **ref. 14** with permission.)

revealed no electrochemical features (**Fig. 5C**). For mapping the enzyme activity, the tip was retracted and the fluid cell was filled with phosphate buffer containing 50 mM glucose. After reengagement of the tip, the scanning procedure was repeated. In the presence of glucose, an increase in the current recorded at the nanoelectrode was obtained owing to the localized production of  $\text{H}_2\text{O}_2$  when the tip was scanned across the glucose oxidase containing polymer spots (**Fig. 5F**). The periodicity of the pattern in the electrochemical image corresponds well with the topography provided by the integrated AFM tip. Furthermore, the topography features in the negative and positive control are unaltered but do not give any information about the immobilized enzyme activity.

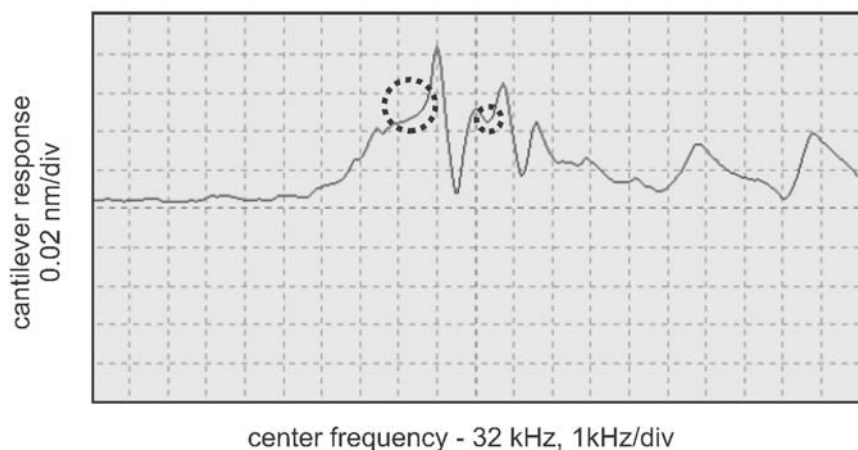


Fig. 6. Frequency spectrum of modified cantilever coated with 100 nm of Au and insulated with 700 nm of parylene C.

#### 4. Notes

1. Alternatively, a 50-nm Pt layer can be deposited as an electrode material (working pressure: 6 mtorr; power: 30 W; under argon). Higher power results in bending of the cantilever.
2. The metallized cantilevers can also be insulated by applying an 800-nm-thick layer of silicon nitride deposited by PECVD. Dense and well-defined insulation layers are particularly achievable when the process is repeated several times ( $6 \times 5$  min PECVD deposition, resulting in approx 800 nm of  $\text{Si}_3\text{N}_4$ ) (6).
3. The described immobilization protocol can be applied to a number of other proteins. For example, entrapment of catalase, lactate oxidase, pyrovate oxidase,  $\text{NAD}^+$ -dependent glucose dehydrogenase, pyrroloquinoline quinone (PQQ)-dependent glucose dehydrogenase, quinohemoprotein alcohol dehydrogenase, and alcohol dehydrogenase has been reported in the literature (22).
4. The periodically micropatterned wafer was purchased from Quantifoil. Any micro-electrode array can be used for this purpose.
5. Digital Instruments offers a phase box for reading in up to four additional signals.
6. Despite deposition of 100 nm of gold and 700 nm of parylene C, the properties of the initial silicon nitride cantilever remain virtually unaltered compared with unmodified  $\text{Si}_3\text{N}_4$  cantilevers (9). Anyway, the optimal drive frequency varies for different samples, fluids, fluid volumes, and cantilevers, and, hence, the drive frequency has to be chosen manually following the DI operation instructions. The best frequencies appear to be on the side of a peak or in a shallow valley between peaks. A typical frequency spectrum of a modified cantilever is depicted in **Fig. 6**. The regions circled show typical operation frequencies that produce good fluid tapping images.

7. The drive amplitude is adjusted until the desired cantilever response amplitude is obtained. For samples with small variations in height, usually drive amplitudes of 2 to 5 V are required. Good results are usually not obtained on soft samples if it is necessary to use drive amplitudes above 10 V.
8. In general, low scan rates of 1 Hz or lower are advantageous in order to avoid convective effects.
9. The set point can be adjusted by monitoring the image quality. Increase the set point in small increments until the cantilever pulls off the surface. Then reduce the set point in small increments until an image appears and the image is optimized. Usually the best images are obtained at set points just below where an image appears.

## Acknowledgments

This work was supported by the National Science Foundation (grant 0216368 within the program Biocomplexity in the Environment), the National Institute of Health (grant EB00058), and the Fonds zur Förderung der wissenschaftlichen Forschung Austria (grants P14122-CHE and J2230).

## References

1. Binnig, G., Quate, C. F., and Gerber, C. (1986) Atomic force microscopy. *Phys. Rev. Lett.* **56**, 930–933.
2. Liu, H. Y., Fan, F.-R. F., Lin, C. W., and Bard, A. J. (1986) Scanning electrochemical and tunneling ultramicroelectrode microscope for high-resolution examination of electrode surfaces in solution. *J. Am. Chem. Soc.* **108**, 3838, 3839.
3. Engstrom, R. C., Weber, M., Wunder, D. J., Burgess, R., and Winkquist, S. (1986) Measurements within the diffusion layer using a microelectrode probe. *Anal. Chem.* **58**, 844–848.
4. Kwak, J. and Bard, A. J. (1989) Scanning electrochemical microscopy: theory of the feedback mode. *Anal. Chem.* **61**, 1221–1227.
5. Gardner, C. E. and Macpherson, J. V. (2002) Atomic force microscopy probes go electrochemical. *Anal. Chem.* **74**, 576A–584A.
6. Kranz, C., Friedbacher, G., Mizaikoff, B., Lugstein, A., Smoliner, J., and Bertagnolli, E. (2001) Integrating an ultramicroelectrode in an AFM cantilever: combined technology for enhanced information. *Anal. Chem.* **73**, 2491–2500.
7. Krantz, C., Mizaikoff, B., Lugstein, A., and Bertagnolli, E. (2002) Integrating an ultramicroelectrode in an AFM cantilever: toward the development of combined microsensing imaging tools: in *Environmental Electrochemistry Analysis of Trace Element Biogeochemistry* (Taillefert, M. and Rozan, T. F., eds.), American Chemical Society, Washington, DC, pp. 320–333.
8. Lugstein, A., Bertagnolli, E., Kranz, C., Kueng, A., and Mizaikoff, B. (2002) Integrating micro- and nanoelectrodes into atomic force microscopy cantilevers using focused ion beam techniques. *Appl. Phys. Lett.* **81**, 349–351.

9. Kueng, A., Kranz, C., Mizaikoff, B., Lugstein, A., and Bertagnolli, E. (2003) Combined scanning electrochemical atomic force microscopy for tapping mode imaging. *Appl. Phys. Lett.* **82**, 1592–1594.
10. Hansma, P. K., Cleveland, J. P., Radmacher, M., et al. (1994) Tapping mode atomic force microscopy in liquids. *Appl. Phys. Lett.* **64**, 1738–1740.
11. Putman, C. A. J., van der Werf, K. O., De Grooth, B. G., Van Hulst, N. F., and Greve, J. (1994) Tapping mode atomic force microscopy in liquid. *Appl. Phys. Lett.* **64**, 2454–2456.
12. Le Grimellec, C., Giocondi, M. C., Pujol, R., and Lesniewska, E. (2000) Tapping mode atomic force microscopy allows the in situ imaging of fragile membrane structures and of intact cell surfaces at high resolution. *Single Molecules* **1**, 105–107.
13. Knoll, A., Magerle, R., and Krausch, G. (2001) Tapping mode atomic force microscopy on polymers: where is the true sample surface? *Macromolecules* **34**, 4159–4165.
14. Kueng, A., Kranz, C., Lugstein, A., Bertagnolli, E., and Mizaikoff, B. (2003) Integrated AFM-SECM in tapping mode: simultaneous topographical and electrochemical imaging of enzyme activity. *Angew. Chem. Int. Ed.* **42**, 3237–3240.
15. Kueng, A., Kranz, C., and Mizaikoff, B. (2003) Scanning probe microscopy with integrated biosensors. *Sens. Lett.* **1**, 2–15.
16. Kueng, A., Kranz, C., and Mizaikoff, B. (2004) Amperometric ATP-biosensor based on polymer entrapped enzymes. *Biosens. Bioelectron.* **19**, 1301–1307.
17. Kranz, C., Kueng, A., Lugstein, A., Bertagnolli, E., and Mizaikoff, B. (2004) Mapping of enzyme activity by detection of enzymatic products during AFM imaging with integrated SECM-AFM probes. *Ultramicroscopy* **100**, 127–134.
18. Heintz, E. L. H., Kranz, C., Mizaikoff, B., Noh, H.-S., Hesketh, P., Lugstein, A., and Bertagnolli, E. (2001) Characterization of parylene coated combined scanning probe tips for in-situ electrochemical and topographical imaging, in *Proceedings of the IEEE Nanotechnology Conference*.
19. Lee, Y., Amemys, S., and Bard, A. J. (2001) Scanning electrochemical microscopy. 41. Theory and characterization of ring electrodes. *Anal. Chem.* **73**, 2261–2267.
20. Smythe, W. R. (1951) The capacitance of a circular annulus. *J. Appl. Phys.* **22**, 1499–1501.
21. Szabo, A. J. (1987) Theory of current at microelectrodes: application to ring electrodes. *J. Phys. Chem.* **91**, 3108–3111.
22. Kurzawa, C., Hengstenberg, A., and Schuhmann, W. (2002) Immobilization method for the preparation of biosensors based on pH shift-induced deposition of biomolecule-containing polymer films. *Anal. Chem.* **74**, 355–361.
23. Wittstock, G. (2001) Modification and characterization of artificially patterned enzymatically active surfaces by scanning electrochemical microscopy. *Fresenius J. Anal. Chem.* **370**, 303–315.





## Protein Amyloidose Misfolding

### *Mechanisms, Detection, and Pathological Implications*

Nigil Satish Jeyashekar, Ajit Sadana, and Tuan Vo-Dinh

#### Summary

A variety of diseases result because of misfolded protein that deposits in extracellular space in the body. These deposits can be amorphous (disordered) or fibrillar (ordered). Inclusion bodies are an example of amorphous aggregates, and amyloid fibril is an example of fibrillar or ordered aggregates. In this chapter, we discuss a class of diseases caused by fibrillar aggregate deposits or amyloid fibrils called amyloidosis. We also review mechanisms by which different proteins misfold to form amyloid fibrils. Each amyloid fibril formed from a different protein causes a different disease by affecting a different organ in the body. However, the characteristics of different amyloid fibrils, namely structure and morphology, observed by electron microscopy and X-ray fiber diffraction appear to be quite similar in nature. We present therapeutic strategies developed to eliminate amyloid fibril formation. These strategies could possibly avert a whole class of fatal diseases caused by amyloid fibril deposition owing to similar characteristics of the amyloid fibrils.

**Key Words:** Amyloid fibril formation; protein folding; transthyretin; lysozyme; immunoglobulin; Alzheimer disease; prions.

#### 1. Introduction

Protein folding whereby the protein acquires its native and active structure starting from a linear inactive state (in which the information for its coding is contained in its amino acid sequence) is a central problem in biology. During folding, certain proteins fail to acquire the native and active state and precipitate as an insoluble “mass.” In vivo, the insoluble mass deposits in extracellular spaces in various organs in the human body, leading to lethal diseases that initially result in organ failure and eventually lead to organ death. The deposits could be either amorphous aggregates, such as inclusion bodies or disordered

aggregates or fibrillar aggregates, such as amyloid fibrils. The diseases caused owing to deposition of amyloid fibrils are called amyloidosis. The precursor proteins that misfold to form amyloid fibrils are amyloidogenic proteins.

Sixteen different amyloidogenic proteins have been identified to form cross- $\beta$  fibril components owing to misfolding. They result in different clinical syndromes (*1,2*). The most familiar include Alzheimer disease and transmissible spongiform encephalopathies (TSEs), prion diseases such as bovine spongiform encephalopathy or mad cow disease (consumption of tainted meat causes Creutzfeldt-Jacob disease in humans; in cows it is called mad cow disease). Molecular chaperones such as chaperonins that include heat-shock proteins, groEL, hsp60 family, and the hsp90 family are proteins that help in the proper assembly of proteins while folding to attain the native state. The excess unfolded proteins and misfolded proteins are removed by proteolytic degradation. This is the *quality control* mechanism. The amyloid fibrils that are formed overcome all the chaperone-mediated folding and degradation mechanisms to deposit in extracellular spaces in the human body, causing fatal diseases.

This chapter reviews different mechanisms by which amyloid fibrils are formed from precursor proteins. Amyloid fibrils formed from different amyloidogenic proteins have been characterized to have similar structural and morphological characteristics, as observed from Congo red staining, electron microscopy, and X-ray fiber diffraction data. Therapeutic strategies to inhibit or eliminate fibril formation for different precursor proteins have been reviewed. These strategies include surgical gene therapy, genetic engineering, artificial chaperones, and stabilizing ligands. The therapeutic strategies developed eliminate the formation of fibrils. This could possibly lead to a decline in the lethal class of diseases such as amyloidosis owing to the similar characteristics of these types of diseases.

## 2. Mechanisms of Amyloid Fibril Formation

The fundamental model for protein aggregation is shown in **Fig. 1**. The native forms, ordered aggregates (amyloid fibrils), and amorphous aggregates (inclusion bodies) are formed from the unfolded protein through intermediates. The intermediate can be considered a building block, and the native state is formed by intermolecular interaction of hydrophobic faces of such building blocks (*3*). Aggregates are formed when hydrophobic surfaces interact in an intermolecular manner, and three-dimensional (3D) propagation of such intermediates forms larger aggregates. The aggregates precipitate once the solubility limit is exceeded. The intermediates are prone to aggregation because they have large patches of contiguous surface hydrophobicity. The hydrophobic surfaces are relatively sealed within the structure in the final folded state.

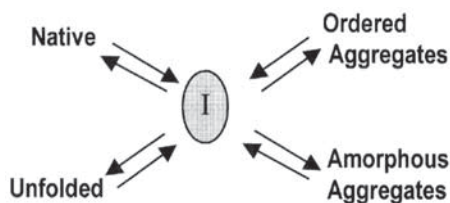


Fig. 1. Basic protein-folding mechanism (3).

### 2.1. Concept of Crowding

The various stages of protein folding may take place either in a single fluid medium or in a series of compartmental fluid media. In both cases, macromolecules occupy a large fraction of the total volume of the fluid. Such fluid media are generally referred to as “crowded” rather than concentrated because no macromolecule may be present at a high concentration (4,5). Crowding would enhance the rate and equilibrium constants for formation of amyloid-like aggregates. Competitive steps exist in protein folding to prevent it from forming amyloid fibrils. Nevertheless, a sustained condition of overcrowding would enhance any preexisting propensity of partially unfolded protein to form amyloid and/or inclusion bodies (4).

### 2.2. Conformational Change Hypothesis

The conformational change hypothesis indicates that tertiary structural changes under partially denaturing conditions convert 1 of the 16 normally soluble and functional human proteins into an alternative conformation. This alternative conformation subsequently undergoes self-assembly into amyloid fibril. This is the putative causative agent in amyloid diseases (6).

### 2.3. Fibril Characteristics

Amyloid fibril formation refers to an *in vivo* process in which 1 of the 16 human amyloidogenic proteins abnormally self-assembles into a fibril 60 to 100 Å in width and of variable length. Amyloid plaque is characterized by three features (3): A characteristic birefringent staining using Congo red, fibrous morphology observed by electron microscopy, and a distinctive X-ray fiber diffraction pattern consistent with a high  $\beta$ -sheet content.

Amyloid fibrils are generally 7 to 12 nm in diameter and can be dissociated by a high concentration of denaturant. Fiber diffraction studies have suggested that the core structure of amyloid fibrils is a cross- $\beta$  structure, involving  $\beta$  strands running perpendicular to the axis of the fibril. The strands interact to form  $\beta$  sheets with their planes parallel to the axis of the fibril (3). Each amyloid fibril is considered to be made up of a bundle of fibrous “protofilament.”

Each protofilament is a cytoplasmic microtubule, with a 25-nm od and 5-nm-thick walls, packed in a helix and associated with various proteins. Depending on the protein or peptide, four to five protofilaments intertwine to form a fibril, with a characteristic diameter of approx 10 nm (3).

The ability to form an amyloid is a generic property of polypeptide chains. An increase in the concentration of precursor and subsequent amyloid formation may be brought about by mutation, and improper posttranslational modification (4). The increased incidence of amyloid disease in the aged may be a direct consequence of increased total intracellular protein concentration crowding (or, equivalently, a decrease in cell water content) in the cells of aging tissues. This is supported by evidence for a significant decrease in water content in brain and liver cells with advancing age (4). Amyloid fibrils are an apparently inert, insoluble, mainly extracellular protein polymer that kills the cell without tissue necrosis but by the activation of the apoptotic mechanism (6).

Although there are 16 different amyloidogenic precursor proteins involved in amyloid fibrils formation, the following section restricts discussion regarding protein function, the mechanism of folding, and the characteristics of amyloid aggregate formation to the clinically important proteins transthyretin (TTR), immunoglobulin, A $\beta$  peptide involved in Alzheimer disease, lysozyme, and prions. A few characteristics of  $\beta$ -2 microglobulin and apolipoprotein are also discussed.

### 3. Clinically Important Proteins Involved in Amyloidic Diseases

#### 3.1. *Transthyretin*

TTR is involved in two amyloid diseases: familial amyloidotic polyneuropathy (FAP) and senile systemic amyloidosis. A partially folded monomeric intermediate, populated at a low pH, has been implicated in in vitro amyloid formation from TTR (3).

TTR transports thyroxine by direct binding and transports retinol indirectly by binding to the retinol-binding protein. In certain individuals, wild-type (WT) TTR is converted to amyloid, which appears to cause senile systemic amyloidosis around the age of 80. This type of amyloid is characterized by heavy amyloid deposits in the heart, leading to congestive heart failure. Alternatively, 1 of 54 TTR mutants deposited systemically as amyloid can cause peripheral neuropathy or organ dysfunction. This typically has a much earlier onset. These diseases are broadly referred to as FAPs (7). The FAP mutations appear to function by destabilizing the native protein-folded structure, and by making the amyloidogenic intermediate more accessible relative to the folded state under mildly denaturing conditions. These mutations do not alter the native folded structure. Destabilization increases the steady-state concentration of the monomeric amyloidogenic intermediate. This, in turn, increases the mass of

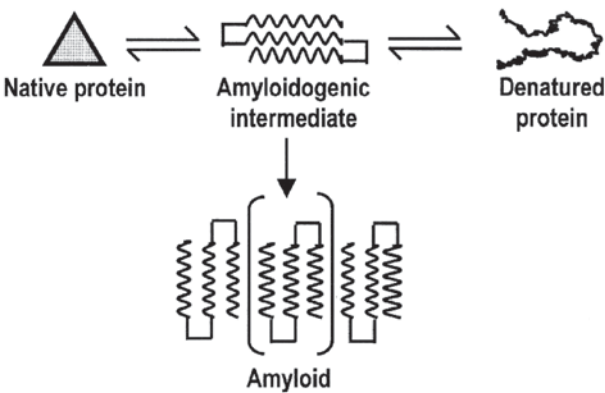


Fig. 2. Mechanism of TTR misfolding to form amyloid (I).

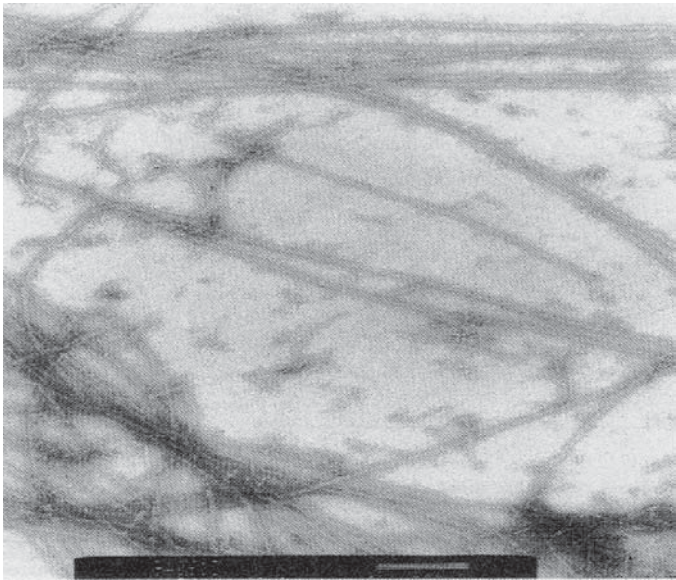


Fig. 3. Electron micrograph of TTR amyloid fibrils (II).

the amyloid formed, thereby lowering the age of disease onset (I). The amyloidogenic intermediate undergoes self-assembly into several quaternary structures that lead to TTR amyloid fibril formation at physiological TTR concentrations (8). The mechanism is shown in Fig. 1.

FAP variants denature to the amyloidogenic intermediate much more quickly than the WT TTR. This facilitates an increased concentration of the amyloidogenic intermediate, thus predisposing individuals with these muta-

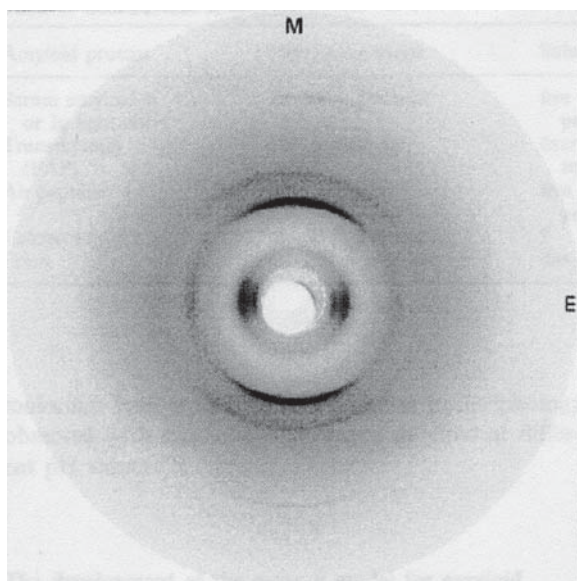


Fig. 4. X-ray fiber diffraction of TTR amyloid fibril (9). M represents meridional reflection; E represents equatorial reflection.

tions to fibril formation and disease. The increased rate of formation of the amyloidogenic intermediate for the FAP variants could be especially important, since the duration of TTR's residence in the lysosome (the likely intracellular site for the amyloid conversion process) could be relatively short. The self-assembly process may not be a nucleated condensation polymerization but, instead, appears to involve the self-assembly of quaternary structures of increasing complexity (7).

The high-resolution pattern of the structure of amyloid fibrils derived from TTR variants was in agreement with the cross- $\beta$  structure and revealed a new repeat of 115 Å. **Figures 2 and 3** represent high resolution electron micrograph and X-ray fiber diffraction patterns of TTR amyloid fibril. This can be interpreted as a repeating unit of 24  $\beta$  strands that forms a complete helical turn of the  $\beta$  sheet about an axis parallel to the fiber axis (3). At present, the thyroxine-binding site appears to present the most promising target for pharmacological inhibition of the conformational changes responsible for fibril formation. In addition, flufenamic acid and diclofenac (9) act as a powerful inhibitor for fibril formation (8).

### 3.2. Lysozyme

Lysozyme is known to have a protective effect against bacterial infection through its capacity to hydrolyze the bacterial cell wall. Lysozyme catalyzes



the hydrolysis of natural and synthetic polymers of  $\beta(1-4)$ -linked units of *N*-acetylglucosamine and *N*-acetylmuramic acid by binding to the substrate (8). Lysozyme synthesis occurs in all human tissues. This protein is present in all biological fluids, from tears to plasma, where it is mainly sustained by neutrophils, leukocytes, and monocytes. Lysozyme is rapidly removed from plasma by kidney filtration, and it has been calculated that in 1 h approx 76% of plasma lysozyme is excreted in the urine. Lysozyme distribution data have been analyzed, and it is suggested that there is a certain discrepancy between the synthesis and tissue localization of radiolabeled lysozyme in the liver and spleen. However, the two organs are able to take up more than 25% of the circulating enzyme. This suggests that the circulating lysozyme is physiologically taken up by the liver and spleen structures. Note that the two organs are heavily involved in this type of amyloidosis.

Two naturally occurring variants of human lysozyme, Ile56Thr and Asp67His, have been found to be amyloidogenic, apparently causing hereditary nonneuropathic systemic amyloidosis. Both mutants are significantly less stable than the WT protein and have populated partially folded intermediates at 37°C that are assumed to be the precursors of amyloid (1,3). Both of these species have single amino acid mutations, either threonine for isoleucine at position 56 or histidine for aspartate at position 67 (8). Unlike TTR amyloidosis, WT lysozyme appears incapable of amyloid fibril formation (7). In the case of the two known disease-related human lysozyme variants, fibrils form most readily at low pH or at slightly elevated temperatures (10). The decreased protein stability, rather than the altered folding kinetics, is a common feature of the two variants. The lower stability of the native state results in the population of a partially folded state that is very similar to the major intermediate populated on the folding pathway of the WT protein (10).

The unfolded region of the intermediate is primarily in the  $\beta$  domain of the protein. This indicates that the aggregation process might be initiated by the intermolecular association of the  $\beta$  strands that are involved in the intramolecular interactions in the native structure (10). The key to both amyloidogenic mutations in human lysozyme apparently lies in the effect that they produce at the interface between the  $\alpha$  and  $\beta$  domains. Residue 56 acts as an anchor of the  $\beta$  domain onto the  $\alpha$  domain (11). The formation of the native state for the major fraction of the lysozyme is retarded compared with the direct folding process. Partially structured intermediates that transiently populate seem to be kinetically trapped in a conformation that can only slowly reach the native state (12). Stabilization of the intermediate, rather than the equilibrium instability, is a crucial factor in amyloidogenicity of human lysozyme (13,14). The mechanism for amyloid formation in lysozyme is shown in Fig. 5 (13).



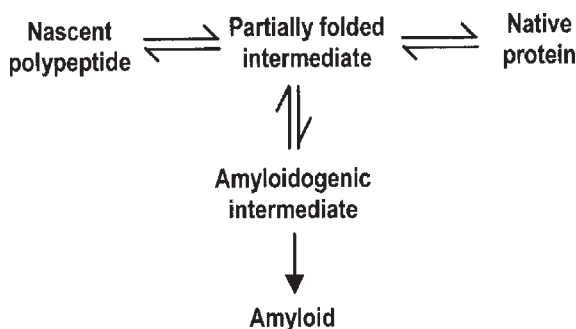


Fig. 5. Lysozyme folding mechanism and amyloid fibril formation (9).

### 3.3. Immunoglobulin

Light-chain amyloidosis is observed in approx 10% of those individuals experiencing monoclonal light-chain overproduction. This leads to malfunction of the peripheral nervous system, organ dysfunction, and death, usually within 5 yr. The conversion of immunoglobulin (Ig) light chain into an amyloid under acidic and partially denaturing conditions proceeds through at least one conformational intermediate that is readily accessible to some light chains but not to all. Domain stability is inversely proportional to the extent of amyloid fibril formation. It is the conformational intermediates rather than the native state that render the protein capable of amyloid fibril formation (1).

Some mutations leading to amyloid fibril formation in TTR, lysozyme, and Ig variable light ( $V_L$ )-chain domains are also observed to result in a decreased stability of the native state. In such cases, there is differential destabilization of the native conformation compared with aggregating intermediate conformation that results in the population of the aggregating conformation (3).

### 3.4. A $\beta$ Peptide and Alzheimer's Disease

Alzheimer's disease, which leads to dementia and eventual death, is characterized by the presence of amyloid fibrils surrounded by dead and dying neurons in the brain tissue (15). The principal component of the fibrils is the  $\beta$ -amyloid peptide, a 39- to 43-residue peptide of known sequence but unknown function, which is found in normal human tissue and is derived from a larger protein precursor (1,8). The A $\beta$  amyloid polypeptide is generated by two distinct proteolytic events referable to  $\beta$  and  $\gamma$  secretase. The A $\beta$  aggregates can induce neurotoxicity, loss of presynaptic terminals, and development of dystrophic neuritis. The degree of toxicity is dependent on the level of aggregation (8). A $\beta$  adopts a metastable structure in its soluble state that most likely becomes more structured on formation of the amyloidogenic intermediate. In fact,

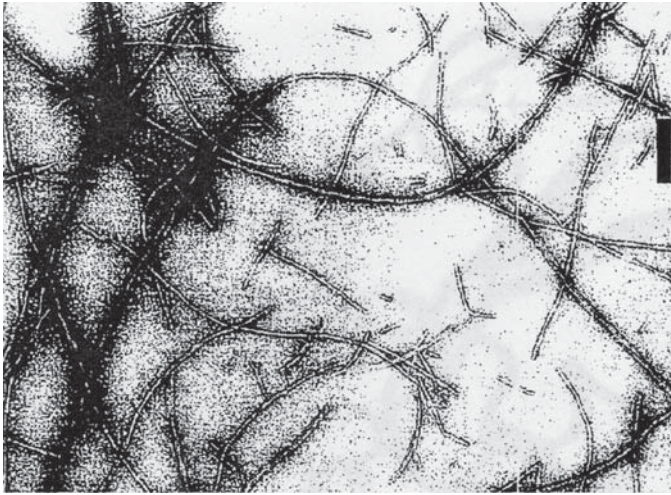


Fig. 6. Electron micrograph showing amyloid fibrils formed from lysozyme (10).

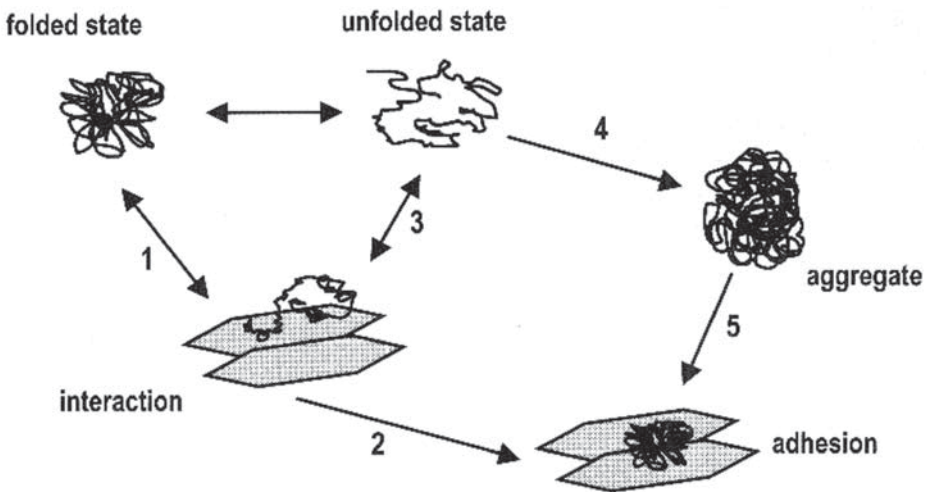


Fig. 7. Fibril formation mechanism owing to  $\beta$  (25-35) amyloid interaction with folded state (16).

the assembly of the  $A\beta$  helical structures may drive the increase in secondary and quaternary  $\beta$ -sheet structure (7).  $A\beta$  micelles form above a certain critical  $A\beta$  concentration. Fibrils nucleate within these micelles, and these fibrils grow through the irreversible binding of monomers to the fibril ends (7).

The native, soluble, and folded states interact with the  $\beta$  (25-35) amyloid (step 1 in Fig. 7). The amyloid-protein complex forms aggregates and deposits

(**step 2**). In some cases, the amyloid exerts a force to unfold the protein on the surface of the amyloid fibril (**step 3**). The unfolded or partially unfolded state has a stronger propensity to aggregate. This results in amorphous aggregates, which adhere strongly to the surface of the amyloid fibril and undergo irreversible deposition. The  $\beta$  (25-35) amyloid interacts with the native protein and destroys its native conformation. This leads to the formation of pathological aggregates. The action of  $\beta$  (25-35) amyloid is exactly opposite that of a chaperone, which helps proteins fold correctly. Hence,  $\beta$  (25-35) is termed an *antichaperone* (**16**). Fibrillar A $\beta$  that deposits in cerebral vessels can effectively localize and enhance the anticoagulant functions A $\beta$ PP. This contributes to a microenvironment conducive to hemorrhaging (**17**). The demonstration that certain compounds such as Congo red, anthracyclines, and rifampicin can avidly bind to the fibrils and, without modifying their overall structure, annihilate their cytotoxic power suggests a useful therapeutic strategy (**6**).

### 3.5. Prions

Prions might represent a distinct class of infectious agents that are proteinaceous and devoid of nucleic acid. The prion is an abnormal form of a host-encoded protein that can interact with its normal counterpart and cause it to become abnormal. This adaptation of the word *prion* involves a broadening of the definition from a focus on the proteinaceous infectious agent of TSE diseases to include infectious proteins or protein-based genetic elements (**18**). The prion hypothesis asserts that an abnormal form of PrP, probably the aggregated, amyloidogenic protease-resistant form (PrP-res or PrP<sup>Sc</sup>), is the infectious agent that propagates by inducing a change in the normal, protease-sensitive PrP (PrP-sen or PrP<sup>C</sup>). PrP-res is usually correlated with TSE infectivity and can induce PrP-sen to convert to the protease-resistant, aggregated state in cell-free reaction (**18**). The aggregate formed in this case induces further aggregation of the normal form of the protein. Hence, prions are termed *infectious*, unlike other forms of amyloidogenic proteins. However, prionogenic aggregates possess fibrillar structure, as observed from electron micrographs and X-ray fiber diffraction (**11,18**). These aggregates stain with Congo red dye (**18**), suggesting that the prions are amyloid in nature.

The “seeding” mechanism, also known as nucleated polymerization has been proposed as a model for prion aggregation. Studies involving these mechanisms are of utmost importance because the disease is transmitted across species barrier, from cattle (cow, lamb) to humans, hence the name TSE. PrP<sup>Sc</sup> can adopt a fibrillar structure similar to an amyloid. A possible therapeutic approach is to design peptidomimetics that prevent the assembly of prionogenic intermediate into a prion particle (**19**). Two models of amyloid prion formation are presented in **Figs. 8,9**.

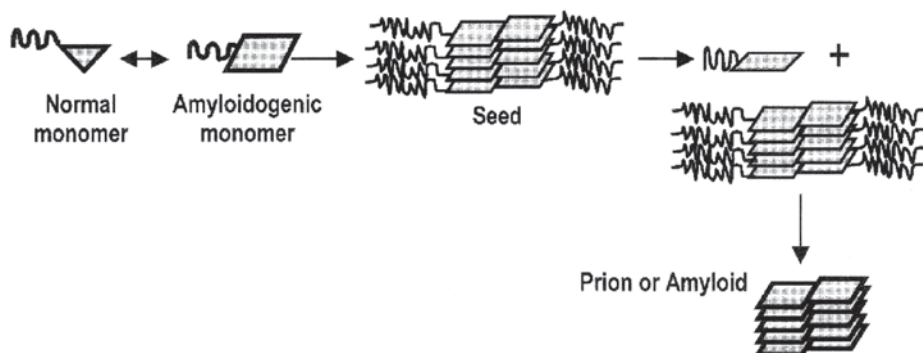


Fig. 8. Nucleation model for amyloid prion formation (18).

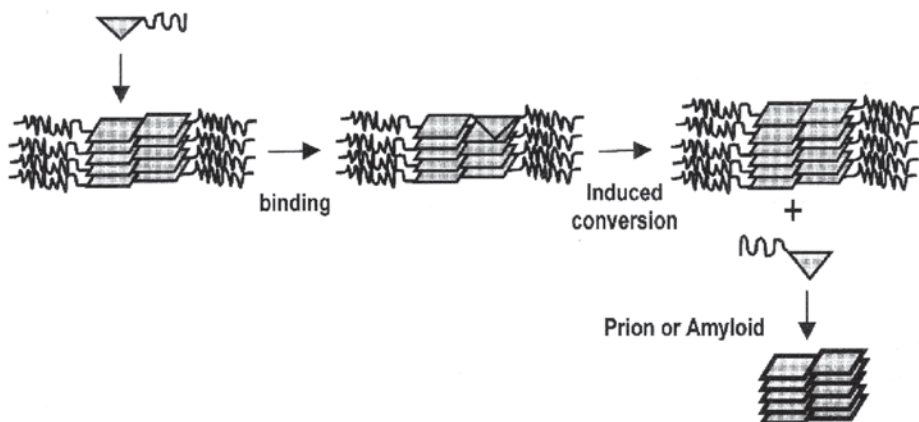


Fig. 9. Autocatalytic model for amyloid prion formation (18).

#### 4. Common Fibril Characteristics

Fibril diffraction data from amyloid fibrils composed of different precursor proteins are virtually identical. This suggests that the structure of amyloid is common, despite the lack of primary or tertiary structural homology among the 17 precursor proteins (7). A range of experiments, particularly X-ray fiber diffraction, indicates that the fibrils have extensive  $\beta$ -sheet character. These sheets run perpendicular to the fibril axis to generate what is described as a cross- $\beta$  structure. This observation is remarkable in view of the fact that the soluble native forms of the proteins associated with these diseases vary quite considerably in their nature. This similarity of the fibrillar forms of the proteins prompted the proposal that there are strong similarities in the inherent structure of amyloid fibrils and in the mechanism by which they are formed (10).

Furthermore, there is a body of evidence indicating that the different amyloid fibrils that are composed of different proteins have the same molecular form. All amyloid fibrils seem to exhibit the following molecular properties, which are now considered to be diagnostic for amyloid (**II**):

1. *Appearance in the electron microscope.* Amyloid fibrils examined under the electron microscope show almost uniform fibrils about 100 Å in diameter. The fibrils are straight and unbranched and show a smooth surface lacking any very obvious surface features.
2. *Tinctorial properties.* All amyloid fibrils can be stained with the diazo dye Congo red and exhibit an apple-green birefringence, which is the most widely used diagnostic for amyloid. It is likely that the Congo red molecule is bound and ordered in a specific way by the amyloid fibrils. However, the interaction remains to be characterized.
3. *X-ray diffraction pattern.* Amyloid fibrils give rise to characteristic X-ray fiber diffraction patterns dominated by relatively sharp and intense 4.7-Å meridional and weaker and more diffuse 10-Å equatorial reflections.

The X-ray pattern is indicative of a particular type of  $\beta$ -sheet structure, known as cross- $\beta$  structure. The  $\beta$  sheets are arranged parallel to the axis of the fibers with their constituent  $\beta$  strands perpendicular to the fiber axis. These same characteristics seem to occur in amyloid fibril from different amyloid diseases and from different precursor proteins. Each amyloid aggregate is a fibril, which is composed of several protofilaments whose subunit is termed a *subprotofilament*. Ex vivo fibrils formed from an Ig light chain are found to be 75 to 80 Å in diameter and are composed of five or six protofilaments each about 25 to 30 Å wide arranged parallel to one another. The protofilaments appear to be composed of two or three subunit strands 10 to 15 Å wide and are called subprotofilaments. They are helically arranged with a 30- to 50-Å repeat (**II**). The substructure of different amyloid fibrils with their dimensions are given in **Table 1**.

Amyloid fibrils derived from different polypeptide precursors may be composed of different numbers and arrangements of protofilaments. Variations can combine to produce variability in the transverse dimensions of amyloid fibrils. However, the degree of variability can be accommodated within a common molecular structure of amyloid fibril.

All amyloid fibrils contain  $\beta$ -sheet structure in which the peptide strands are aligned orthogonal to the direction of fibril growth (**15**). The core structure of the TTR amyloid fibril, which is a continuous  $\beta$ -sheet helix, can be extended to other amyloids formed by proteins as diverse as lysozyme and Ig light chain (**18**). Fibrils are an epiphenomenon linked to disease (**15**). The ability to form amyloid fibrils is not a characteristic associated wholly or primarily with those proteins found to be associated with amyloidoses. This is a property that could be common to many or indeed all proteins under appropriate conditions (**10**).

**Table 1**  
**Substructure of Amyloid Fibrils With Dimensions (9)**

Amyloid protein	Fibril dimension	Substructure
Serum amyloid A or Ig light chain	75- to 80-Å diameter	Five 25- to 35-Å protofilaments in pentagonal array
TTR (FAP)	130-Å diameter	Four 50- to 60-Å protofilaments in square section array
A $\beta$ peptide	90-Å diameter	Five to six 20- to 30-Å protofilaments in pentagonal or hexagonal array
Calcitonin	50- to 60-Å diameter	—
Prion	60- to 200-Å ribbons	Flat assembly of protofilaments

Thus, the fibrils from different peptides and proteins are, in reality, variations on a common theme.

The dimensions of the protofilaments, and the lengths of the  $\beta$  strands within them, may be determined simply by the physiochemical properties of an unfolded polypeptide chain (10). In other words, the potential to form an amyloid can be predicted based on the physiochemical properties of the proteins (20,21). The nature of the polypeptide of the fibrils is used to define the type of amyloidoses, and it affects the pathology of the disease state. Nevertheless, all amyloid fibrils, regardless of the character of the precursor or the site of deposition in the body, appear to have a related ultrastructure and a closely similar molecular core structure (11).

## 5. X-Ray Diffraction Studies of Amyloid Fibrils

Fibrous protein samples, like amyloid are usually exposed to the X-ray beam with the long axis of the fibrils more or less perpendicular to the direction of the beam. The X-ray reflections are then distinguished by their direction with reference to the fiber axis and their distance from the center of the pattern: meridional reflections are defined as those lying parallel to the fiber axis, and equatorial reflections are those positioned at right angles to the fiber axis.

The earliest reported fiber diffraction investigations of serum amyloid A and light-chain amyloid indicated an intense meridional reflection at 4.68 Å and an equatorial reflection at 9.8 Å. This is characteristic of the cross- $\beta$  structure and occurs only if the amyloid fibrils are protofilaments composed of two or more  $\beta$  sheets. Purified amyloid fibril cores isolated from senile systemic plaques associated with Alzheimer disease show reflections at 4.76 Å and approx 10.6 Å. Prion rods exhibit a prominent interstrand spacing at 4.72 Å, and an equatorial spacing at 8.26 Å.



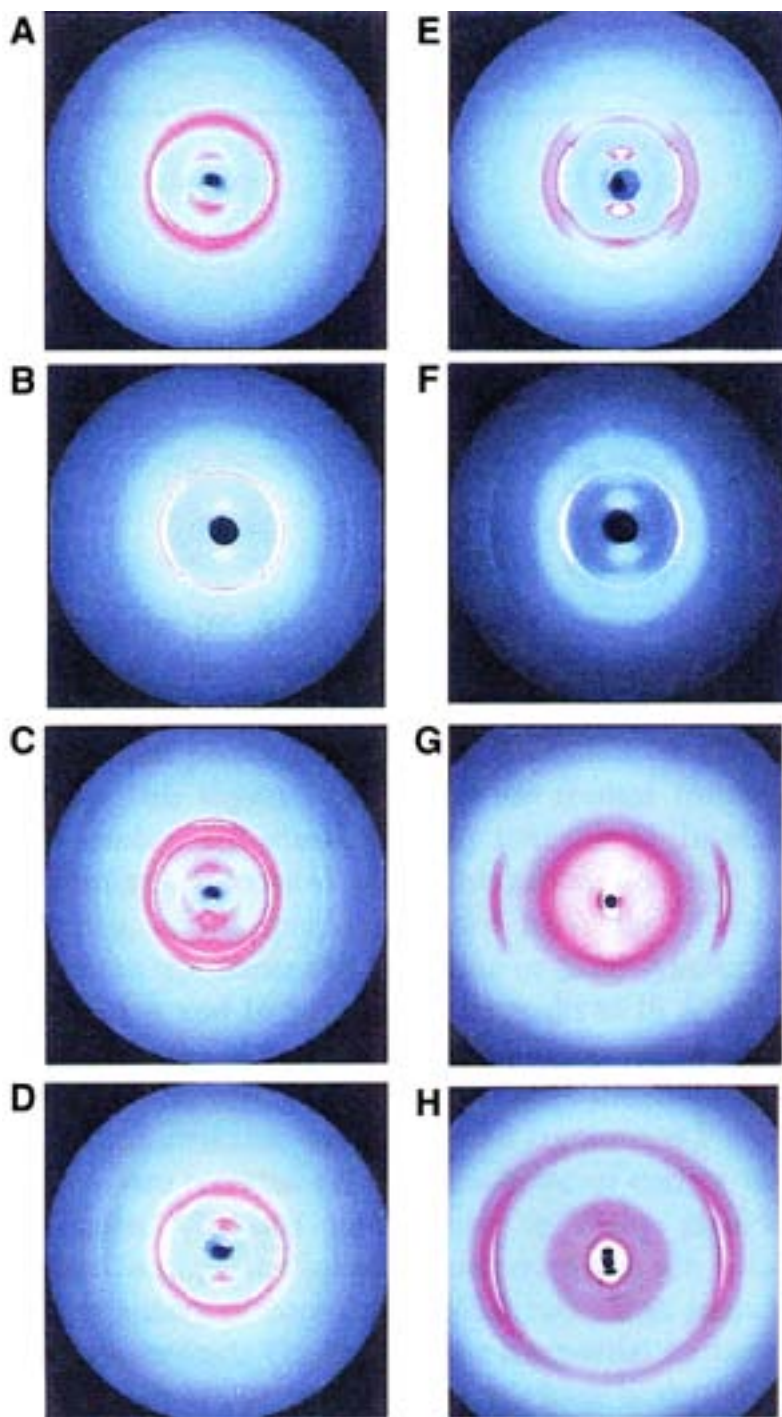


Fig. 10. X-ray fiber diffraction showing eight different amyloid fibrils from different proteins having the same core structure: (A,B,E) TTR; (C) apolipoprotein; (D) Ig; (F) islet-associated peptide; (G) serum amyloid A; (H) lysozyme (II).



The most thoroughly studied amyloid fibrils to date have been those extracted from Swedish patients with FAP. X-ray diffraction was used to study the molecular structure of various amyloid fibrils, including *ex vivo* fibrils from patients with Ig light chain, serum amyloid A, apolipoprotein A-1, TTR (two different variants), lysozyme amyloidoses, and synthetic amyloid fibrils formed from amyloidogenic fragments of TTR. The islet-associated polypeptide and the high-resolution images are shown in **Fig. 10**. It can be seen in **Fig. 10** that in spite of the large differences in the size and structures of the polypeptide precursors of the fibrils, the similarities in the diffraction patterns are quite marked. This indicates that different amyloid fibrils actually share a common molecular skeleton on the fibril axis, with the same atomic spacings (*11*).

The similarity in the diffraction over the medium- and high-angle regions of the meridional X-ray pattern can only occur if the fibrils have well-defined and closely similar molecular structures, at least insofar as their ordered core components are concerned. Thus, apparently most, if not all, amyloid fibrils have as their core structure the continuous  $\beta$ -sheet helix that has been described in detail for the TTR amyloid fibril. A model of the amyloid protofilament, containing helically twisted  $\beta$  sheets, gives reasonable agreement with the major features of the fiber diffraction patterns exhibited by all amyloid fibrils examined so far. Within this framework, there are many possibilities for fibrils to be composed of different numbers or arrangements of protofilaments. In addition, protofilaments may vary in diameter as a result of the need to incorporate different-sized loops linking the  $\beta$  strands.

It is also possible that some amyloids may be composed of only one pair of  $\beta$  sheets, rather than the two pairs of sheets thought to compose the TTR amyloid protofilament. In spite of the possibility of these considerable variations, the common core structure indicated by the diffraction patterns is evidence that the amyloid fibrils do have a well-defined generic molecular structure that accounts for their characteristic disease-forming properties (*11*). The closely similar cross- $\beta$  fiber diffraction patterns exhibited by amyloid fibrils indicate that this underlying ordered structure is primarily a  $\beta$  sheet. Also, the constituent  $\beta$  strands lying at right angles to the fiber axis (*11*).

## 6. Unified Mechanism of Amyloid Formation

The conformational properties of all proteins should be considered in terms of the multiple steady states that are accessible to such structures (*10*). The unified mechanism in **Fig. 11** suggests the various structures awaiting a polypeptide chain after biosynthesis, which includes the mechanism of amyloid fibril formation (*10,22*). In addition, if the protein is able to fold rapidly, any partially folded species will have a short lifetime, reducing the probability that intermolecular interactions will occur. Moreover, once folded, the native state

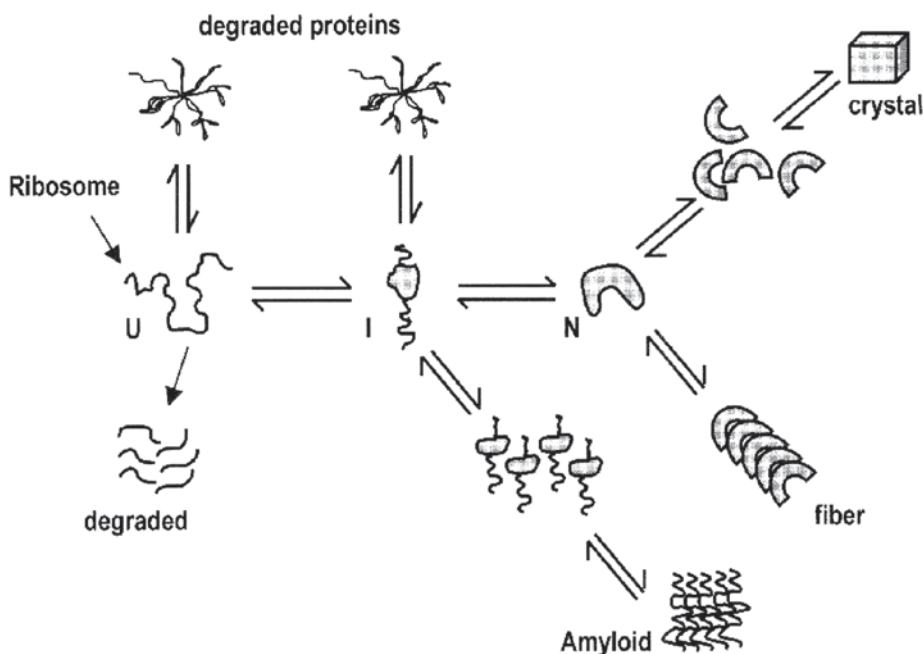


Fig. 11. Unified mechanism of amyloid fibril formation (10,22).

is generally a high-compact structure that conceals the polypeptide main chain within its interior. Such a state is protected from aggregation except through the interactions of surface side chains (as is the case of protein crystals). This state is unable to form the strong intermolecular hydrogen bonds associated with the polypeptide backbone. If the native state is maintained under appropriate folding conditions, then aggregation to amyloid fibrils will be resisted by the kinetic barrier associated with unfolding, even if the aggregated state is thermodynamically more stable (10).

Parkinson disease, caused by mutations in the gene encoding  $\alpha$ -synuclein, is characterized by cytoplasmic neuronal deposits. These deposits are lewy bodies in the affected regions of the brain and resemble amyloid fibrils. This has been determined by morphological studies such as atomic force and electron microscopies, distinctive dye-binding properties (Congo red & thioflavin T), and antiparallel  $\beta$ -sheet structure (Fourier transform infrared spectroscopy and circular dichroism spectroscopy) (23).

## 7. Therapeutic Strategies

The generic picture of amyloid structure and the mechanism of its formation provide a conceptual framework for linking various pathological conditions

associated with the deposition of this material. This suggests possible general approaches to the prevention or treatment of the whole family of amyloid diseases (10). A system of artificial chaperones (detergents and cyclodextrin) has been successfully used to minimize aggregation in the renaturation of denatured-reduced lysozyme. Osmolytes and other stabilizing ligands may decrease the amount of aggregation. This probably reflects differential stabilization of the native state. Osmolytes have been shown to inhibit prion formation in the scrapie system, consistent with the involvement of protein conformational changes in the formation of prions (3).

Seeding as in the case of prion protein increases the rate of amyloid formation. Hence, reducing seeding, by introducing a ligand that probably binds and stabilizes the native state, would decrease aggregate formation. The surgical gene therapy method of treating FAP, in which the FAP mutation is replaced with the WT TTR, causes (1) cessation of fibril formation, (2) clearance of the amyloid already deposited, and (3) clinical improvement where complications from transplantation do not occur (7). This works by modification of the protein sequence (10). Aggregation is minimized, leading to elimination or a decrease in the clinical symptoms.

For example, small proteins, such as acylphosphatase, have shown that this is likely to be a general method of reducing the tendency to form amyloid fibrils under conditions in which the native state of the protein has low stability (10). In addition to these therapeutic strategies, other techniques are designed to inhibit amyloid formation either by blocking fibril growth or by stabilizing the  $\alpha$ -helical or random coil structures. This prevents the  $\beta$  peptide from precipitating to an amyloid structure and becoming toxic to nerve cells (24). Novel therapeutic strategies like genetic engineering (25) to eliminate amyloid fibril formation could be promising for eliminating a whole class of fatal diseases caused by protein misfolding. This may be facilitated by the fact that fibrils have the same core structure and can be characterized by common properties.

## References

1. Kelly, J. W. (1996) Alternative conformations of amyloidogenic proteins govern their behavior. *Curr. Biol.* **6**, 11–17.
2. Yutani, K., Takayama, G., Goda, S., et al. (2000) The process of amyloid-like fibril formation by methionine aminopeptidase from a hyperthermophile, *Pyrococcus furiosus*. *Biochemistry* **39**, 2769–2777.
3. Fink, A. L. (1998) Protein aggregation: folding aggregates, inclusion bodies and amyloid. *Folding Design* **3**, R9–R23.
4. Minton, A. P. (2000) Implications of macromolecular crowding for protein assembly. *Curr. Opin. Struct. Biol.* **10**, 34–39.
5. Minton, A. P. (2000) Protein folding: thickening the broth. *Curr. Biol.* **10**, R97–R99.

6. Bellotti, V., Mangione, P., and Stoppini, M. (1999) Biological activity and pathological implications of misfolded proteins. *Cell. Mol. Life Sci.* **55**, 977–991.
7. Kelly, J. W. (1998) The alternative conformations of amyloidogenic proteins and their multi-step assembly pathways. *Curr. Opin. Struct. Biol.* **8**, 101–106.
8. Demchenko, A. P. (1999) Protein folding with molecular chaperones: stochastic process under control. *Biophysics* **45**, 404–410.
9. Oza, V. B., Smith, C., Raman, P., et al. (2002) *J. Med. Chem.* **45**, 321–332.
10. Dobson, C. M. (2001) The structural basis of protein folding and its links with human disease. *Philos. Trans. R. Soc. London Ser. B Biol. Sci.* **356**, 133–145.
11. Serpell, L. C., Sunde, M., and Blake, C. C. F. (1997) The molecular basis of amyloidosis. *Cell. Mol. Life Sci.* **53**, 871–887.
12. Kiefhaber, T. (1995) Kinetic traps in lysozyme folding. *Proc. Natl. Acad. Sci. USA* **92**, 9029–9033.
13. Takano, K., Funahashi, J., and Yutani, K. (2001) The stability and folding process of amyloidogenic mutant human lysozymes. *Eur. J. Biochem.* **268**, 155–159.
14. Canet, D., Sunde, M., Last, A. M., Miranker, A., Spencer, A., Robinson, C. V., and Dobson, C. M. (1999) Mechanistic studies of the folding of human lysozyme and the origin of amyloidogenic behavior in its disease-related variants. *Biochemistry* **38**, 6419–6427.
15. Lansbury, P. T., Jr. (1999) Evolution of amyloid: what normal protein folding may tell us about fibrillogenesis and disease. *Proc. Natl. Acad. Sci. USA* **96**, 3342–3344.
16. Konno, T. (2001) Amyloid-induced aggregation and precipitation of soluble proteins: an electrostatic contribution of the Alzheimer's  $\beta$ (25–35) amyloid fibril. *Biochemistry* **40**, 2148–2154.
17. Wagner, M. R., Keane, D. M., Melchor, J. P., Auspaker, K. R., and Van Nostrand, W. E. (2000) Fibrillar amyloid  $\beta$ -protein binds protease nexin-2/amyloid  $\beta$ -protein precursor: stimulation of its inhibition of coagulation factor XIa. *Biochemistry* **39**, 7420–7427.
18. Caughey, B. (2000) Transmissible spongiform encephalopathies, amyloidoses and yeast prions: common threads? *Nat. Med.* **6**, 751–754.
19. Kelly, J. W. (1998) The environmental dependency of protein folding best explains prion and Amyloid diseases. *Proc. Natl. Acad. Sci. USA* **95**, 930–932.
20. Gujjaro, J. I., Sunde, M., Jones, J. A., Campbell, I. D., and Dobson, C. M. (1998) Amyloid fibril formation by an SH3 domain. *Proc. Natl. Acad. Sci. USA* **95**, 4224–4228.
21. Kallijärvi, J., Haltia, M., and Baumann, M. (2001) Amphoterin includes a sequence motif which is homologous to the Alzheimer's  $\beta$ -amyloid peptide (A $\beta$ ), forms Amyloid fibrils in vitro, and binds avidly to A $\beta$ . *Biochemistry* **40**, 10,032–10,037.
22. Dobson, C. M. and Karplus, M. (1999) The fundamentals of protein folding: bringing together theory and experiment. *Curr. Opin. Struct. Biol.* **9**, 92–101.

23. Conway, K. A., Harper, J. D., and Lansbury, P. T., Jr. (2000) Fibrils formed in vitro from  $\alpha$ -synuclein and two mutant forms linked to Parkinson's disease are typical Amyloid. *Biochemistry* **39**, 2552–2563.
24. Ma, K., Clancy, E. L., Zhang, Y., Ray, D. G., Wollenberg, K., and Zagorski, M. G. (1999) Residue-specific  $pK_a$  measurements of the  $\beta$ -peptide and mechanism of pH-induced Amyloid formation. *J. Am. Chem. Soc.* **121**, 8698–8706.
25. Lee, S. C., Lee, M. J., Choi, I., and Yu, M. H. (1997) Genetically engineered human interleukin-6 variant with enhanced stability. *Biotechnol. Lett.* **19**, 885–888.



## Near-Field Scanning Optical Microscopy for Bioanalysis at Nanometer Resolution

Musundi B. Wabuyele, Mustafa Culha,  
Guy D. Griffin, Pierre M. Viallet, and Tuan Vo-Dinh

### Summary

The nondestructive imaging of biomolecules in nanometer domains in their original location and position as adsorbed or deposited on a surface is of garners considerable experimental interest. Near-field scanning optical microscopy (NSOM) is an emerging technique with its astonishing resolving power of  $<100$ -nm domains, and nondestructive nature compared with other scanning probe microscopic techniques is an emerging technique to achieve this goal. At the single-molecule level of resolution, it is possible to use the NSOM as a critical tool for visualization of proteins on surfaces to obtain more fundamental information about their orientation and locality without disturbing their original orientation and position, and level of interaction with the surface. Several areas of science and medicine can benefit from this type of study especially for biomedical and biochip applications. To illustrate possible applications, imaging of green fluorescent proteins and biomolecules associated with multidrug resistance proteins in tumor cells will be demonstrated using NSOM.

**Key Words:** Near-field scanning optical microscopy; protein; biomolecules; multidrug resistance transport protein; P-glycoprotein.

### 1. Introduction

Optical microscopy is an important technology that finds applications in scientific and technological arenas ranging from imaging of living specimens and characterization of advanced materials to the spectroscopic analysis of semiconductors. There is an increasing demand for higher spatial resolution to obtain more information about the given area of a sample or a molecule on a surface or in a cell. Disappointingly, conventional optics limits the resolution as determined by Abbé (1), to  $\lambda/2$  or 200 nm for visible light. In 1928, Synge (2) overcame this barrier by suggesting that light exciting an aperture is

From: *Methods in Molecular Biology*, vol. 300:  
*Protein Nanotechnology, Protocols, Instrumentation, and Applications*  
Edited by: T. Vo-Dinh © Humana Press Inc., Totowa, NJ



confined to roughly the dimensions of an aperture having subwavelength dimensions. Even though this principle was the first demonstrated in the microwave region of the spectrum in 1972 (3), it could be applied at optical wavelengths with the design and introduction of subwavelength aperture optical probes. Near-field scanning optical microscopy (NSOM) not only overcomes the diffraction limitation of conventional optics but also combines the enhanced lateral and vertical resolution allowing the use of characteristic scanning probe microscopies with simultaneous measurements of topographical and optical signals.

Scanning probe microscopy (SPM) was revolutionized by the development of high-resolution techniques such as scanning force microscopy (AFM) and scanning tunneling microscopy (STM). A high resolution of images of biological samples such as cells or DNA has been successfully demonstrated using AFM at a molecular level. However, only topographical information can be obtained because AFM acquires images based on the force interaction between the tip and the surface of the sample. Alternatively, samples for STM must be conductive. In contrast, NSOM probes do not come in contact with the sample; hence, it is noninvasive in nature and does not perturb the sample (*see Fig. 1*) (4). NSOM combines enhanced lateral and vertical resolution and has the ability to attain spatial resolution approaching nanometer scale. This is an apparent advantage over other scanning and optical techniques and can help researchers to understand phenomena is challenged by several areas of science including nanotechnology, biomaterial science, and biosciences.

NSOM is based on scanning a very small light source with dimensions smaller than its wavelength very close (in the near field) to the sample. The light source is a tapered optical fiber from one end and coated with aluminum on its outside walls. The light that is coupled to the fiber is radiated from the tapered and aluminum-coated end. This emanated light passes through an aperture (approx 50 to 100 nm) with an exponential attenuation away from the tip. As shown in **Fig. 2**, near-field illumination of the sample at a distance  $h_1$  less than the wavelength ( $\lambda$ ) of incident light gives high-resolution images compared with those obtained from far-field illumination in which the distance  $h_2 \gg \lambda$  and greater than the aperture. Thus, subwavelength details of the image are lost.

Over the past decade, NSOM has evolved into a new frontier in science (5) with a high impact and potential in various areas of research ranging from biomedical to analytical to biological sciences. Betzig and Chichesterd were among the first pioneers to investigate biological tissues using NSOM (6). Thin-tissue sections of the hippocampus region of monkey brain were imaged using NSOM. Other experiments have been performed in an attempt to distinguish single actin filaments in the cytoskeleton. The actin filaments were stained selectively with rhodamine-labeled phalloidin and imaged with NSOM

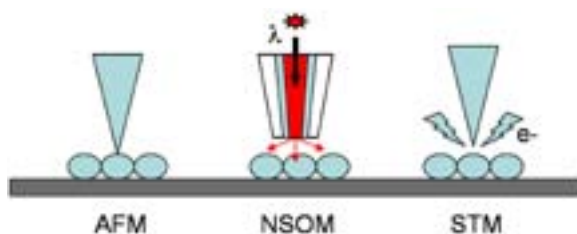


Fig. 1. Comparison of SPMs. AFM involves a cantilever being scanned over the surface of a sample. The measured cantilever deflections are used to generate topographical images. NSOM involves a tapered optical fiber probe coupled to a laser light and is used to excite fluorophores as the probe is scanned over the surface of a sample. STM uses a sharpened conducting tip with a bias voltage applied between the tip and the sample. When the tip is brought within about 10 Å of the sample, electrons ( $e^-$ ) from the sample begin to “tunnel” through the gap into the tip. The resulting tunneling current varies with tip-to-sample spacing, and it is the signal used to create an STM image.

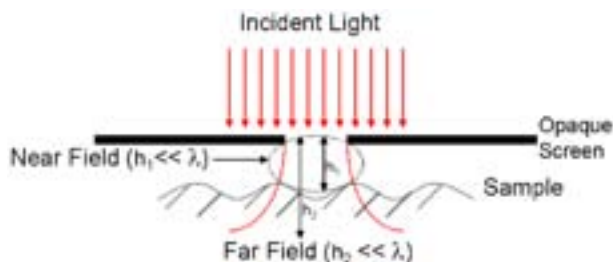


Fig. 2. Principles of NSOM. A subwavelength-size aperture confines the laser light and illuminates the sample in close proximity (typically <10 nm) with a depth of  $h_1$  (near field) and  $h_2$  (far field).

(7,8). Moers et al. (9) studied fluorescently labeled chromosomes by combining cytochemical and scanning probe techniques, which enabled the localization and identification of several fluorescently labeled genomic DNA fragments on a single chromosome with extraordinary resolution. In 1998, Garcia-Parajo et al. (10) studied the photodynamics of individual fluorescence molecules, which were localized with an accuracy of 1 nm. Later, Garcia-Parajo et al. (11) reported on studies of green fluorescent protein (GFP) as an individual marker for applications in molecular biology for detailed understanding of its photophysical and photodynamic properties. They investigated both individual S65T mutants of GFP on a glass surface and embedded in a water-pore gel. Kirsch et al. (12) studied the imaging of pUC18 relaxed circular plasmid DNA

spread on mica precoated with cetylpyridinium chloride. This study demonstrated the applicability of the shear force signal (topography) in conjunction with the optical signals from fluorescence to image biological macromolecules.

Several groups have demonstrated applications of NSOM in cell biological studies. These applications include the imaging of cytoskeleton components in 3T3 fibroblasts by Betzig et al. (13), as well as membrane mapping and colocalization of malarial and host skeletal proteins in red blood cells infected with the human malaria parasite *plasmodium falciparum* (14). Other studies used NSOM to detect activation-dependent clustering of the erB2 receptor, a member of the epidermal growth factor (EGF) family that is overexpressed in breast cancer patients (15). In another study, Deckert et al. (16) combined NSOM and surface-enhanced Raman scattering (SERS) to image brilliant cresyl blue-labeled DNA on Teflon nonospheres covered with evaporated silver layers. The imaging of fluorescently labeled DNA with high spatial resolution and single-molecule fluorescence sensitivity was demonstrated, and no sample deformation was observed under the reported experimental conditions (17). In another study, researchers used a planar silver island-based SERS substrate to generate SERS signals and a chemically etched, 200-nm optical fiber tip to deliver excitation radiation from an argon ion laser (488 nm). The tapered sides of the fiber tip were coated with a thick, opaque layer of metal to confine the excitation radiation to the 200-nm tip, hence permitting extremely localized sample excitation. This factor, combined with a substrate-to-fiber tip spacing of approx 0.1 nm, enabled the acquisition of spectral and spatial information, with subwavelength lateral resolution, for CFV and rhodamine 6G molecules (18,19) distributed on the silver island substrate. Furthermore, the SERS-NSOM technique demonstrated exceptional sensitivity. Spectra from as few as 300 molecules have been recorded. Schmalenberg et al. (20) studied imaging of laminin and bovine serum albumin proteins with AFM and NSOM on a patterned glass surface in both dry and hydrated environment.

The capability to generate patterned surfaces with biomolecules such as proteins for biosensor technology (21), for tissue engineering (22), and for fundamental studies of protein adsorption on surfaces for development of biocompatible materials is extremely important. As a result of extensive studies in genomics and proteomics, the biochip concept has been developed. A biochip is an array of dots, with each dot containing a small volume of proteins and fragments of DNA. In a protein biochip, the spots contain a range of proteins, and/or visualization of these proteins in their original location and position with NSOM in nanometer resolution may play a critical role in understanding their interaction with other molecules.

In the present study, we investigated the localization of multidrug resistance (MDR) transport proteins and their effect on chemotherapeutic drugs. The development of multi-drug resistance owing to expression of MDR proteins in cells has been a major hindrance to successful delivery of chemotherapeutic drugs. By this mechanism, cancer cells become resistant to many drugs of diverse structure and mechanism when exposed to this drug. Two kinds of proteins, multidrug resistance protein (MRP) and P-glycoprotein (P-gp), play a key role in the MDR phenomenon; however, their locality and mechanism of action still remain a subject of interest. In addition to the confocal microscopy and other biological techniques previously reported, we would like to apply the advantages of NSOM to determine the localization and effects of these proteins in the chemotherapeutic treatment of human cancers.

## **2. Materials**

### **2.1. Cell Lines**

Chinese hamster ovary (CHO) lines were obtained from the American Type Culture Collection (Manassas, VA). MTLN3 cells were kindly provided by Dr. Jeffrey E. Segall (Albert Einstein College of Medicine, Department of Anatomy and Structural Biology).

#### *2.1.1. Cell Culture and Fixation*

The cells were cultured (95% humidity, 5% CO<sub>2</sub>, 37°C) on glass chamber slides from Nalge Nunc (Naperville, IL) in F-12 (Invitrogen, Carlsbad, CA) with 10% fetal bovine serum (FBS) (Gibco, Grand Island, NY) for CHO, and 5% FBS in Dulbecco's modified Eagle's medium (Invitrogen) with 0.5% Pen/Strep for MTLN3 cells. When the cells reached 70 to 80% confluence (3 d), they were subcultured at a 1:20 split ratio for CHO and MTLN3. The cells were fixed with 4% paraformaldehyde for 5 min followed by multiple rinses with methanol followed by 100% cold ethanol.

#### *2.1.2. Cell Labeling With Drugs and Dyes*

Yellow-green fluorescent FluoSpheres beads and BODIPY® FL verapamil hydrochlorides were purchased from Molecular Probes. Doxorubicin (DOX) was obtained from Sigma (St. Louis, MO). Cells were incubated with the indicated dyes and drugs for 2 h in their respective medium in a 5% CO<sub>2</sub>, 37°C incubator. Prior to fixing, the cells were washed with phosphate-buffered saline buffer.

### **2.2. NSOM Instrumentation**

1. Instrument stage (base plate with mounted hardware).
2. Aurora-2 sensor head.

3. Electronic Control Unit-*Plus* (ECU-*Plus*) with I/O 10 and I/O MOD+ boards.
4. Aurora Control Unit.
5. Computer.
6. Video monitor.
7. NSOM fiberoptic tips.
8. Probe installation tool.
9. Fiber cleaver.
10. Fiber stripper tool.
11. Tool kit.
12. NSOM standard sample.
13. User's manual.
14. SPMLab software.
15. SPMLab Software Reference Manual.
16. Laser.
17. Laser coupler.
18. Vibration isolation table.

### 2.2.1. Setup of System

A TopoMetrix Aurora-2 Near-field Scanning Optical Microscope was used for our experiments. The Aurora-2 instrument is a platform for obtaining topographic and optical images. A sample is mounted on an X-Y scanning stage, which is controlled by a three-piezo scanner arrangement. The fiberoptic probe is mounted on the removable Aurora-2 microscope head and positioned above the sample. Topographic and optical images can be taken simultaneously. As shown in **Fig. 3**, the sample is laterally scanned beneath the fiber tip with a distance of 5 to 10 nm being maintained by monitoring the shear-force interaction between the lateral vibrating tip and the sample surface. The scanning process is controlled by the electronics of the SPM system. The optical components of the Aurora-2 system are used for taking NSOM data as well as for focusing the optics and monitoring the probe-sample approach. The rotating mirror (*see Fig. 4*) selects either the reflection or transmission objective. The two “flipper” mirrors can be manually flipped down to allow use of the photomultiplier tube (PMT) or optional hardware, such as a photon counter or spectrometer.

For NSOM imaging, multiple excitation sources can be used depending on what kind of chromophore is being investigated. A 488-nm argon-ion laser equipped with laser-line filter was used as an excitation source for our experiments. The emission light was collected via the transmission mode through a  $\times 40$ , 0.65N.A objective and through a set of filters, dichroic mirror (510DF10) and bandpass filter (520LP10), obtained from Omega Optical. The fluorescence signal was then detected by a PMT and analyzed with commercial software (SPMLab).

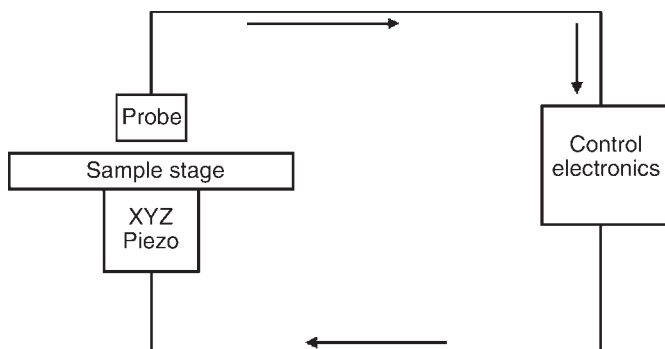


Fig. 3. Schematic layout of Aurora-2 system showing topography feedback loop. The sample is mounted on a scanning stage, which is controlled by a three-piezo scanner arrangement. The fiberoptic probe is mounted on the removable Aurora-2 microscope head and positioned above the sample.

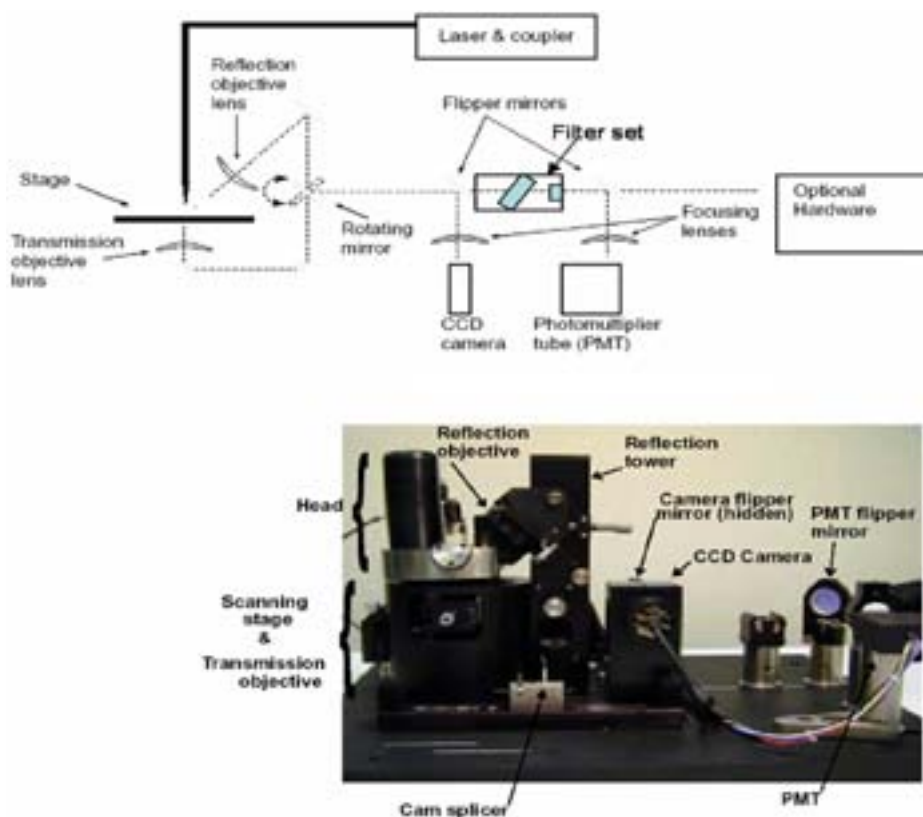


Fig. 4. Block diagram showing (A) light path and (B) components of Aurora-2 system. CCD, charge-coupled device.

### 3. Methods

The methods discussed next describe the sample and tip mounting, and laser coupling, as well as providing an example of the preparation of sample and experimental setup for simultaneous topographical and NSOM imaging of biomolecules in cells.

#### 3.1. Preparation of Sample

Samples are prepared on a thin optically transparent glass substrate. Cells were cultured and fixed on glass chambers that were 200  $\mu\text{m}$  thick. For good imaging, the sample has to be relatively flat. Typically, sample height features of  $<500$  nm in size and a scan range of  $30 \times 30 \mu\text{m}$  is acceptable. Rough surfaces make feedback difficult because the tip is easily damaged (*see Note 1*).

#### 3.2. Sample and Probe Mounting, and Laser Coupling

To mount the sample, the head must be removed and the sample slide can be simply taped to the stage (*see Notes 2–4*). The probe is installed to the probe cartridge with the help of a probe installation tool (*see Note 5*). After stripping away about 2.5 cm of the polymer buffer from the distal end of the fiber with the help of a fiber stripper tool, the end of the tip fiber is cleaved with the optical fiber cleaver (*see Note 6*). Finally, the fiber tip is inserted into the cam splicer (*see Fig. 3*). The transmission and reflection objectives also must be focused (*see Note 7*). The transmission objective is manually adjusted in X, Y, and Z (focus) with the translation knobs. The reflection objective is focused by manual rotation of the lens.

#### 3.3. Sample Imaging

An NSOM image is composed of both topographic and optical information. A topographic image is first taken, which helps to set up the scan parameters and to identify the surface features (*see Note 8*). Finally, the combined image topographic and optical scan is taken (*see Notes 9,10*). The topographic image is almost identical to noncontact mode of the AFM technique. For topographic scanning, the probe is brought into feedback. Once the tip is in the feedback position and the probe can track the topography of the sample at a near-field range, NSOM imaging can be performed. A block diagram of the experimental setup is shown in **Fig. 4**.

#### 3.4. Parameters for Topographical and NSOM Images

First the drive frequency for each probe is set to the resonant frequency of the tuning fork so that the magnitude of the tuning fork vibration can be maximized by adjusting the drive frequency. Typically, a frequency range between 90 and 100 kHz is selected for the tuning fork. After zooming in on the peak,



it is necessary for the amplitude to be about 5 V, which corresponds to approx 30 nA on the internal sensor signal. Fine-tuning the noncontact controls is then performed with the aim of having the drive amplitude as low as possible while maintaining the internal sensor signal constant and the root mean square noise (RMS)  $<0.1$ .

The tip is brought into the feedback via two approaches: “automatic” and “manual” feedback. The automatic feedback approach uses the automatic features programmed into the SPMlab software to lower the tip toward the sample surface. The manual feedback approach is more difficult and requires more care while lowering the tip to a distance within a few microns above the surface. The initial P-I-D setting for the topographical imaging was as follows:  $P = 1$ ,  $I = 0.05$ ,  $D = 0$ . The set point value was  $-64$  nA (*see Note 11*). Once the tip is in feedback with the surface, the P-I-D parameters were adjusted to optimize the scan (*see Note 12*).

Because the laser light heats and expands the tip, some adjustments have to be made to the P-I-D settings before taking the NSOM images. In addition, the tuning fork frequency has to be rechecked. Once the P-I-D settings are optimized, NSOM images can be obtained (*see Note 13*).

### 3.5. Results and Discussion

As previously shown in reviews by Dunn (21) and Deckert (23), NSOM has emerged as a powerful tool for biological applications. The high resolution has enabled the study of functional molecular complexes ranging from chromosomes to membrane domains. To establish the usefulness of NSOM for imaging biological molecules, we wanted to investigate colocalization of proteins and their effects on chemotherapeutic drugs within the substructure of cells and cellular organelles. A phenomenon called MDR, which results from the overexpression of drug transporter proteins that belong to an ATP-binding cassette family of proteins, is the focus of our study.

P-gp and multidrug resistance protein-1 (MRP-1) are the two main proteins that are thought to be responsible for the extrusion of cytotoxic natural product amphipathic drugs from cancer cells. Clearly, the resistance of tumor cells to chemotherapeutic drugs has been a major clinical problem, and the pharmacological reversal of the function of the MDR transporter proteins is a significant area of interest. These proteins are assumed to be located in the plasma membrane (24,25); however, studies have demonstrated their location in other cellular organelles such as the endoplasmic reticulum (26,27). Although numerous factors have been associated with the development of MDR, studies largely support the role of an energy-dependent pump system in either extruding or excluding chemotherapeutic drugs from cells (28–30). Initial NSOM experiments to validate our system were performed on tumor cells (MTLN3) transfected with GFPs. The proteins are expressed *in vivo* and therefore can serve as

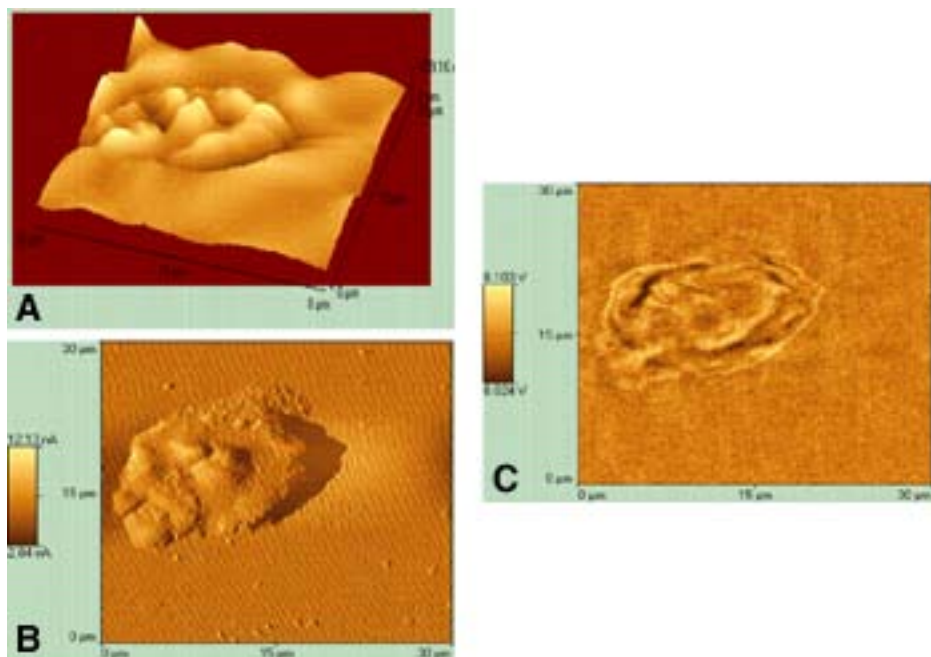


Fig. 5. MTLN3 tumor cells expressing GFP fusion proteins: (A) topography; (B) feedback internal signal; (C) fluorescence.

an indicator of internal structures and function within the cells. Previous studies have allowed visualization of the distribution of cell-surface EGF receptor (EGFR) in CHO cells that were stably transfected with a fusion construct of the EGFR and GFP. **Figure 5** shows topography, feedback internal signal, and fluorescence images of the MTLN3 tumor cells expressing the GFP fusion proteins. From these NSOM images, one can observe a homogeneous distribution of the protein in the cytoplasmic compartment of the cells.

Because of the superior resolution of NSOM, single-molecule studies have been carried out in which several hundred molecules per square micrometer can be observed. The level of sensitivity and accuracy has been proven to be far superior than for the far-field methods. Therefore, NSOM is an ideal technique for allowing independent observations of molecules at physiologically relevant packing densities. Additionally, the level of detail and sensitivity of NSOM allows colocalization studies in cases in which unprecedented information with high accuracy is required. We therefore chose to apply NSOM to study subcellular localization and the activity of MDR transport proteins. In this chapter, we do not show the specific locality of the proteins; nonethe-

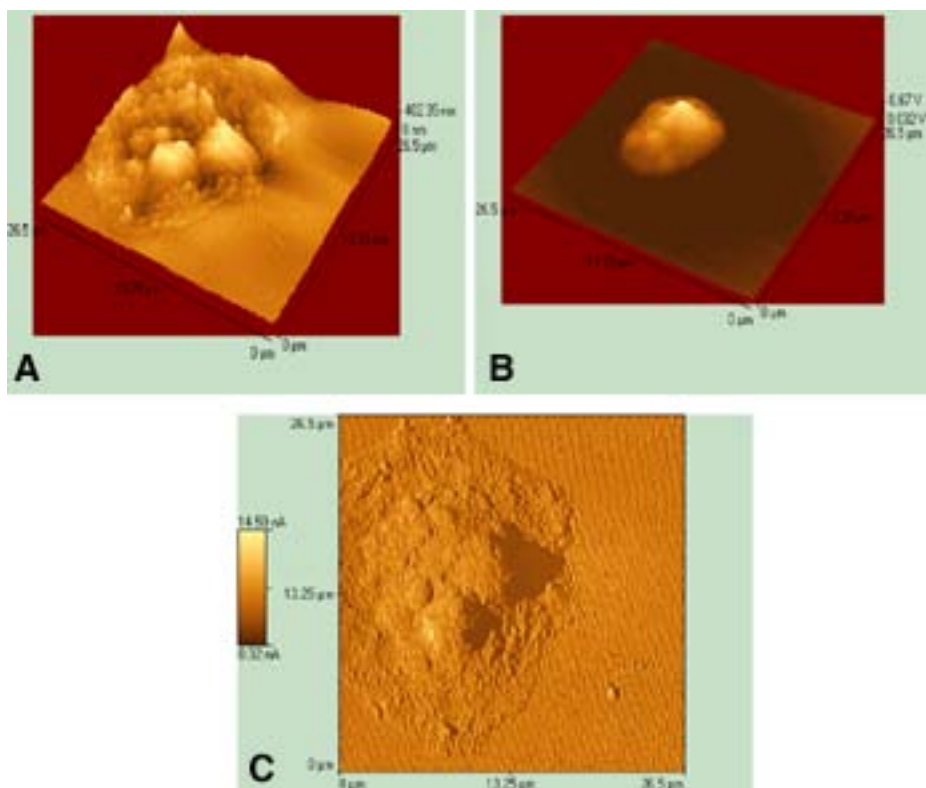


Fig. 6. NSOM image of CHO cells incubated with 5  $\mu\text{M}$  DOX: (A) topography; (B) fluorescence; (C) feedback internal signal.

less, we do demonstrate their effect on the localization of agents (drug and inhibitor) that interact with the proteins. Generally, MRP-1 and P-gp proteins are considered to be cell-surface localized and mediate drug resistance by lowering the total intracellular drug concentration (31,32). Several groups have tried to explain this MDR phenomenon and the mechanism of action using different models such as the energy-dependent pump system (30,33), but the localization of both proteins and the mechanism of action remain to be resolved.

To study the effect of MRP-1 transporters on the localization and accumulation of the anthracycline DOX and on yellow-green fluorescent FluoSpheres (data not shown), we used CHO and J774 cells (data not shown) that slightly expressed these proteins. The cells were incubated with 5  $\mu\text{M}$  DOX for 2 h at 37°C. They were then rinsed and fixed before imaging. **Figure 6** shows the topography and fluorescence images of CHO cells incubated with DOX. The fluorescence image clearly demonstrates nuclear localization of DOX.

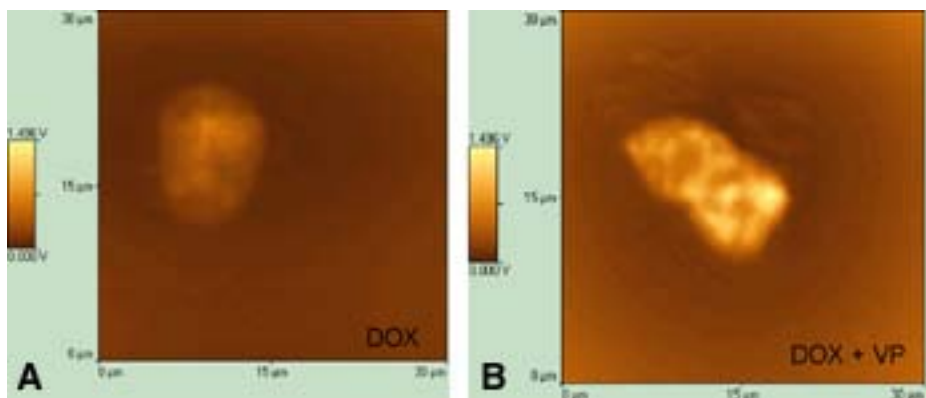


Fig. 7. NSOM images of CHO cells incubated with (A) 5  $\mu$ M DOX and (B) 5  $\mu$ M DOX + 5  $\mu$ M verapamil.

From the results in **Fig. 7**, we expected to see a high intracellular accumulation of drugs in cells that do not overly express the MDR transport proteins. However, suffice it to say that even cells that have not been exposed or transfected with these proteins do show some type of resistance. We demonstrated this phenomenon by inhibiting the function of the P-gp and MRP-1 proteins using an MDR reverser, verapamil. Interestingly, we observed that the addition of verapamil to CHO cells increased the cytotoxicity of DOX by fourfold. This kind of information clearly indicates that other factors (protein substrates) may also be associated with the drug resistance.

NSOM images of CHO cells that were incubated with only 5  $\mu$ M DOX and with both 5  $\mu$ M each of verapamil and DOX for 2 h at 37°C are shown in **Fig. 7**. Similar studies with cells transfected with MDR transporter proteins have been obtained (27,33). Conversely, the cells used in our study were normal CHO cells; thus, one would expect to observe little or no effect on the drug accumulation process. However, the results obtained with the CHO cells indicated that even normal cells may express these proteins at a level significant enough to efflux drugs from the cellular compartments. Therefore, the concentration and localization of multi-drug resistance proteins plays a vital role in the drug accumulation process. Using a highly sensitive technique with a high resolution such as NSOM provides unprecedented details on the effects of these MDR proteins. NSOM has therefore demonstrated that even in cases in which there is a low concentration of proteins, significant information can be obtained. Further studies are being conducted to localize the specific proteins and their activity in normal and tumor cells.

#### **4. Notes**

1. The fixed cells should be as flat as possible (<500 nm in height) so that the tip does not get out of feedback or become damaged.
2. To avoid damage to the piezo scanners, do not apply excessive force to the scanning stage.
3. To avoid damaging the piezo scanners, be careful not to touch the stage with the head.
4. To avoid damage to the probe and sample, handle the head with care, paying particular attention to the probe and probe mount on the bottom. Whenever the head is removed from the microscope stage, use the tip “up” button on the data acquisition tool bar to raise the tip a safe distance away from the sample. When placing the head on the stage, or when carefully setting it down on a table or other flat surface, turn the Z-height thumbscrews one full turn clockwise. Whenever the head is lowered using the Z motor or thumbscrews, watch the image on the video monitor to make sure that the probe does not crash into the sample or stage.
5. Because the probe is extremely fragile, handle it with care.
6. The NSOM probe is a fiber with one end tapered. Extra care is necessary while stripping off the cladding and cleaving the fiber.
7. First, the reflection objective should be used to locate the tip with the help of a camera. Second, the probe needs to be brought to the surface as close as possible, and the laser light coming out of the probe must be located using the transmission objective after turning off all the lights.
8. Once the probe is brought to feedback, the environment must be vibration free. Do not walk, open, or close the door; closing the door or walking by or touching the experimental setup table easily breaks the probe.
9. Exposure to light can damage the PMT. Thus, the light on the Aurora-2 must be off to prevent damage before the scan begins.
10. A sudden, dramatic increase in NSOM signal indicates a break in the tip, and the PMT voltage must immediately be lowered to prevent damage to the PMT.
11. Coupling the laser light into the probe is critical to obtain the optimum laser light. Do not couple the laser while the tip is in feedback.
12. The P-I-D setting should be low (especially the integral) so that the tip does not jump as it approaches the sample.
13. For the best topographic imaging, the P-I-D setting for each new tip has to be optimized.

#### **Acknowledgments**

This work was sponsored by the Office of Biological and Environmental Research, US Department of Energy, under contract DE-AC05-00OR22725 with UT-Battelle, LLC; and by the Laboratory Directed Research and Development Program (Advanced Plasmonics Sensor project) at Oak Ridge National Laboratory. M. Wabuyele and M. Culha are also supported by an appointment to the Oak Ridge National Laboratory Postdoctoral Research Associates Program, administered jointly by the Oak Ridge National Laboratory and Oak Ridge Institute for Science and Education.

## References

1. Abbe, E. (1873) Beitrage zur Theorie des Mikroskops und der mikroskopischen Wahrnehmung. *Arch. Mikros. Anat. Entwicklungsmech.* **9**, 413–468.
2. Syngé, E. H. (1928) A suggested method for extending microscopic resolution into the ultra-microscopic region. *Philos. Mag.* **6**, 356–362.
3. Ash, E. A. and Nicholls, G. (1972) Super-resolution aperture scanning microscope. *Nature (Lond.)* **237**, 510–512.
4. Mrksich, M. and Whitesides, G. M. (1995) Patterning self-assembled monolayers using microcontact printing: a new technology for biosensors. *Trends Biotechnol.* **13**, 228–235.
5. Lange, F., Cambi, A., Huijbens, R., de Bakker, B., Rensen, W., Garcia-Parajo, M., van Hulst, N., and Figdor, G. C. (2001) Cell biology beyond the diffraction limit: near-field scanning optical microscopy. *J. Cell Sci.* **114**, 4153–4160.
6. Betzig, E. and Chichester, R. (1993) Single molecules observed by near-field scanning optical microscopy. *Science* **262**, 1422–1424.
7. Zenobi, R. and Deckert, V. (2000) Scanning near-field optical microscopy and spectroscopy as a tool for chemical analysis. *Angew. Chem. Int. Ed.* **39**, 1747–1757.
8. Doyle, R. T., Szulzewski, M. J., and Haydon, P. G. (2001) Extraction of near-field fluorescence from composite signals to provide high resolution images of glial cells. *Biophys. J.* **80**, 2477–2482.
9. Moers, M. H., Kalle, W. H., Ruiter, A. G., Wiegant, J. C., Raap, A. K., Greve, J., de Grooth, B. G., and Van Hulst, N. F. (1996) Fluorescence in situ hybridization on human metaphase chromosomes detected by near-field scanning optical microscopy. *J. Microsc.* **182**, 40–45.
10. Garcia-Parajo, M. F., Veerman, J. A., Segers-Nolten, A. G., and Van Hulst, N. F. (1998) Near-field optical and shear-force microscopy of single fluorophores and DNA molecules. *Ultramicroscopy* **71**, 311–319.
11. Garcia-Parajo, M. F., Veerman, J. A., Segers-Nolten, G. M. J., de Grooth, B. G., Greve, J., and van Hulst, N. F. (1999) Visualising individual green fluorescent proteins with a near field optical microscope. *Cytometry* **36**, 239–246.
12. Kirsch, A. K., Meyer, C. K., and Jovin, T. M. (1997) Shear force imaging of DNA in a near-field scanning optical microscope. *J. Microsc.* **185**, 396–401.
13. Betzig, E., Chichester, R. J., Lanni, F., and Taylor, D. L. (1993) Near-field fluorescence imaging of skeletal actin. *Bioimaging* **1**, 129–135.
14. Enderle, T., Ha, T., Ogletree, D. F., Chemla, D. S., Magowan, C., and Weiss, S. (1997) Membrane specific mapping and colocalization of malarial and host skeletal proteins in the *Plasmodium falciparum* infected erythrocyte by dual-color near-field scanning optical microscopy. *Proc. Natl. Acad. Sci. USA* **94**, 520–525.
15. Nagy, P., Jenei, A., Kirsch, A. K., Szollosi, J., Damjanovich, S., and Jovin, T. M. (1999) Activation-dependent clustering of the erbB2 receptor tyrosine kinase



- detected by scanning near-field optical microscopy. *J. Cell. Sci.* **112**, 1733–1741.
16. Deckert, V., Zeisel, D., Zenobi, R., and Vo-Dinh, T. (1998) Near-field surface enhanced Raman imaging of dye-labeled DNA with 100-nm resolution. *Anal. Chem.* **70**, 2646–2650.
  17. Garcia-Parajo, M. F., Veerman, J. A., van Noort, S. J. T., de Grooth, B. G., Greve, J., and van Hulst, N. F. (1998) Near-field optical microscopy for DNA studies at the single molecular level. *Bioimaging* **6**, 43–53.
  18. Emory, S. R. and Nie, S. (1997) Near-field surface-enhanced Raman spectroscopy on single silver nanoparticles. *Anal. Chem.* **69**, 2631–2635.
  19. Zeisel, D., Deckert, V., Zenobi, R., and Vo-Dinh, T. (1998) Near-field surface-enhanced Raman spectroscopy of dye molecules adsorbed on silver island films. *Chem. Phys. Lett.* **283**, 381–385.
  20. Schmalenberg, K. E., Thompson, D. M., Buettner, H. M., Uhrich, K. E., and Garfias, L. F. (2002) In situ stepwise surface analysis of micropatterned glass substrates in liquids using functional near-field scanning optical microscopy. *Langmuir* **18**, 8593–8600.
  21. Dunn, R. C. (1999) Near-field scanning optical microscopy. *Chem. Rev.* **99**, 2891–2927.
  22. Merrit, M. V., Mrksich, M., and Whitesides, G. M. (1997) Using self-assembled monolayers to study the interactions of man-made materials with proteins, in *Principles of Tissue Engineering* (Lanza, R. P., Langer, R., and Chick, W., eds.), R. G. Landes Company, Austin, TX, pp. 211–223.
  23. Deckert, V. (2003) Near-field imaging in biological and biomedical applications, in *Biomedical Photonics Handbook* (Vo-Dinh, T., ed.), CRC Press, Boca Raton, FL, pp. 12–19.
  24. Zaman, G. J. R., Flens, M. J., van Leusden, M. R., et al. (1994) The human multidrug resistance-associated protein MRP is a plasma membrane drug-efflux pump. *Proc. Natl. Acad. Sci. USA* **91**, 8822–8826.
  25. Shapiro, A. B., Fox, K., Lam, P., and Ling, V. (1999) Stimulation of P-glycoprotein-mediated drug transport by prazosin and progesterone: evidence for a third drug-binding site. *Eur. J. Biochem.* **3**, 841–850.
  26. Krisnamachary, N. and Center, M. S. (1993) The MRP gene associated with a non-P-glycoprotein multidrug resistance encodes a 190-kDa membrane bound glycoprotein. *Cancer Res.* **53**, 3658–3661.
  27. Barrand, M. A., Heppell-Parton, A. C., Wright, K. A., Rabbits, P. H., and Twentyman, P. R. (1994) A 190-kilodalton protein overexpressed in non-P-glycoprotein-containing multidrug-resistant cells and its relationship to the MRP gene. *J. Natl. Cancer Inst.* **86**, 110–117.
  28. Borst, P. (1999) Multidrug resistance: a solvable problem? *Ann. Oncol.* **10**, 162–164.
  29. Sharom, F. J. (1997) The P-glycoprotein efflux pump: how does it transport drugs? *J. Membr. Biol.* **160**, 161–175.
  30. Sauna, E. Z., Smith, M. M., Muller, M., Kerr, M. K., and Ambudkar, V. S. (2001) The mechanism of action of multidrug-resistance-linked p-glycoprotein. *J. Bioenerg. Biomembr.* **33**, 481–491.



31. Stride, D. B., Cole, C. P. S., and Deeley, G. R. (1999) Localization of substrate specificity domain in the multidrug resistance proteins. *J. Biol. Chem.* **274**, 22,877–22,883.
32. Hamilton, K. O., Topp, E., Makagiansar, I., Siahaan, T., Yazdanian, M., and Audus, L. K. (2001) Multidrug resistance-associated protein-1 functional activity in Calu-3 cells. *J. Pharmacol. Exp. Ther.* **3**, 1199–1205.
33. Chen, Y., Pant, A. C., and Simon, M. S. (2001) P-Glycoprotein does not reduce substrate concentration from the extracellular leaflet of the plasma membrane in living cells. *Cancer Res.* **61**, 7763–7769.